



Atomic scale modeling of plasticity in chromium and other body-centered cubic transition metals

Baptiste Bienvenu

► To cite this version:

Baptiste Bienvenu. Atomic scale modeling of plasticity in chromium and other body-centered cubic transition metals. Materials Science [cond-mat.mtrl-sci]. Université Paris-Saclay, 2022. English. NNT : 2022UPASP072 . tel-03917543

HAL Id: tel-03917543

<https://theses.hal.science/tel-03917543>

Submitted on 2 Jan 2023

HAL is a multi-disciplinary open access archive for the deposit and dissemination of scientific research documents, whether they are published or not. The documents may come from teaching and research institutions in France or abroad, or from public or private research centers.

L'archive ouverte pluridisciplinaire **HAL**, est destinée au dépôt et à la diffusion de documents scientifiques de niveau recherche, publiés ou non, émanant des établissements d'enseignement et de recherche français ou étrangers, des laboratoires publics ou privés.

Atomic scale modeling of plasticity in chromium and other body-centered cubic transition metals

*Modélisation atomique de la plasticité du chrome et des autres
métaux de transition cubiques centrés*

Thèse de doctorat de l'université Paris-Saclay

École doctorale n° 564, Physique en Île-de-France (PIF)

Spécialité de doctorat : Physique

Graduate School : Physique. Réfèrent : Faculté des Sciences d'Orsay

Thèse préparée au **Service de Recherches de Métallurgie Physique (Université Paris-Saclay, CEA)** sous la direction d'**Emmanuel CLOUET**, Directeur de recherche CEA Saclay, et le co-encadrement de **Chu-Chun FU**, Ingénieure de recherche CEA Saclay

Thèse soutenue à Paris-Saclay, le 13 Juillet 2022, par

Baptiste BIENVENU

Composition du Jury

David RODNEY

Professeur, Institut Lumière Matière,
Université Claude Bernard Lyon 1

Charlotte BECQUART

Professeure, Unité Matériaux et Transformations,
Université de Lille

Laurent PIZZAGALLI

Directeur de recherche, Institut P', Université de Poitiers

Benoît DEVINCIRE

Directeur de recherche,
Laboratoire d'Etude des Microstructures, CNRS-ONERA

Maryam GHAZISAEIDI

Associate Professor, Ohio State University

Matous MROVEC

Research group leader, ICAMS

Emmanuel CLOUET

Directeur de recherche,
Service de Recherches de Métallurgie Physique, CEA Saclay

Président

Rapporteuse & Examinatrice

Rapporteur & Examineur

Examineur

Examinatrice

Examineur

Directeur de thèse



Acknowledgments, *remerciements*

I wish to warmly thank all members of the jury I had the pleasure to meet for the defense of this work, Charlotte Becquart and Laurent Pizzagalli for reviewing the following few dense pages, David Rodney for chairing the jury, and Maryam Ghazisaeidi, Benoît Devincere, and Matous Mrovec for their careful examination of this work. Each one of you helped make this a very pleasant afternoon of fruitful discussion. I will be expressing the following *remerciements* in french, which feels more natural.

Je remercie, pour plus de choses encore que je ne saurais en nommer, mon encadrant et directeur de thèse Emmanuel Clouet. Ce fut un immense plaisir et une chance de travailler ensemble et d'explorer ce riche sujet, avec toute ta confiance et ton savoir-faire. Rares ont été les journées où nous n'échangions pas autour de ces fameuses dislocations, il y avait toujours quelque chose à faire, et quel plaisir ! J'ai beaucoup appris durant ces trois ans. A ce titre, pour ton encadrement et ton expertise, je te remercie également chaleureusement, Chu Chun Fu.

J'ai aussi eu la chance de passer ces trois ans dans un environnement de travail, d'entente, et de discussion scientifique idéal, au SRMP, dirigé d'une sympathique main de maître par Jean-Luc Béchade. Ainsi, je remercie tous ceux avec qui j'ai eu l'occasion et le grand plaisir d'avoir travaillé, que ce soit au SRMP ou ailleurs, et notamment David Rodney, Lucile Dezerald et Daniel Caillard, mais aussi depuis mon stage au LEM avec Hakim Amara, Lorenzo Sponza et François Ducastelle.

Mes remerciements vont aussi à la direction du projet ICOMB, particulièrement Jean-Christophe Brachet et Hervé Palancher, qui nous ont permis d'explorer ce sujet avec un regard fondamental en nous fournissant les moyens nécessaires et en nous accordant leur confiance pour mener à bien ce travail de thèse.

Enfin, je souhaite remercier mes amis et ma famille, pour leur écoute sur des sujets qui n'étaient ni les leurs ni les miens il y a trois ans de cela, et pour qui ils n'ont plus aucun secret !

Table of contents

Acknowledgments, <i>remerciements</i>	2
I Introduction	8
II Literature review	10
1 Plasticity of body-centered cubic transition metals	11
1.1 Energetic description of dislocations	11
1.2 Dislocation glide in body-centered cubic metals	13
1.3 Non-Schmid effects and anomalous slip	16
2 Atomistic study of dislocations in body-centered cubic metals	18
2.1 <i>Ab initio</i> modeling of dislocations	18
2.1.1 Core structure of the $\frac{1}{2}\langle 111 \rangle$ screw dislocation	18
2.1.2 Peierls potential of the $\frac{1}{2}\langle 111 \rangle$ screw dislocation	20
2.1.3 Non-Schmid effects: screw dislocation trajectory and relaxation volume	21
2.2 Dislocation-based plasticity using interatomic potentials	24
3 The case of chromium	25
3.1 Magnetic phases of chromium	25
3.1.1 Experimental observations	25
3.1.2 Theoretical investigations	28
3.2 Elastic properties of chromium	29
3.3 Plasticity of chromium	30
III Methods	36
1 Energetic models	36
1.1 <i>Ab initio</i> density functional theory calculations	36
1.1.1 Solving Shrödinger's equation	36
1.1.2 Density functional theory	36
1.1.3 Exchange and correlation functional	37
1.1.4 Pseudo potential approximation	38
1.1.5 Plane wave basis	39
1.1.6 Sampling of the Brillouin zone	39
1.1.7 Spin-polarized density functional theory	39
1.2 Tight-binding formalism	40
1.3 Generalized Heisenberg and effective interaction models	42
1.4 Empirical interatomic potentials	43
2 Finite temperature simulations	45
2.1 Magnetic excitations	45
2.1.1 Metropolis Monte Carlo sampling	45
2.1.2 Thermodynamics using Metropolis Monte Carlo sampling	45
2.1.3 Including quantum statistics	47
2.2 Molecular dynamics simulations	49

3	Atomistic modeling of dislocations and plasticity of body-centered cubic metals	49
3.1	<i>Ab initio</i> modeling of dislocations	49
3.1.1	Simulation setup for dislocation modeling	50
3.1.2	Peierls potential and mobility of dislocations	52
3.1.3	Dislocation core dilatation field and eigenstrain model	53
3.2	Interatomic potentials and molecular dynamics simulation of dislocations	56
IV	Chapter 1: Bulk properties of bcc chromium	58
1	Magnetic phases	58
1.1	Stability of the different magnetic phases	58
1.2	Elastic properties of the magnetic phases	61
2	Generalized stacking faults	61
2.1	Simulation setup	62
2.2	Complete γ -surfaces in the NM phase	63
2.3	$\langle 111 \rangle$ slip mode in the NM and AF phases	64
2.4	$\langle 100 \rangle$ slip mode in the NM and AF phases	67
V	Chapter 2: Dislocations and plasticity in bcc chromium	70
1	Core properties of the $1/2\langle 111 \rangle$ screw dislocation	70
1.1	Impact of magnetism on the core structure of the $1/2\langle 111 \rangle$ screw dislocation	70
1.2	Core energy of the $1/2\langle 111 \rangle$ screw dislocation	72
1.3	Consequence of the magnetic fault in the AF phase	74
1.4	Peierls potential and lattice friction	75
1.5	Dislocation trajectory and relaxation volume	78
2	Non-Schmid effects and $\langle 111 \rangle\{110\}$ slip activity	80
2.1	Derivation of a yield criterion for uniaxial loading	80
2.2	Deviations from the Schmid law	83
3	Thermal activation and mobility law	87
3.1	Line tension model for kink-pair mechanism	87
3.2	Flow stress at finite temperature and mobility law	90
VI	Chapter 3: Magnetic excitations and plasticity of chromium	96
1	Finite temperature and magnetic excitations	96
1.1	Parametrization of a generalized Heisenberg model for chromium	96
1.2	Spin spirals and transverse magnetic excitations	100
1.3	Validation of the HL models	102
1.4	Thermodynamical magnetic properties of bulk bcc chromium	103
2	Magnetism and plasticity of chromium at finite temperature	105
2.1	Infinite magnetic faults	106
2.2	Magnetic fault bounded by two $1/2\langle 111 \rangle$ screw dislocations	110
2.3	Magnetic energy of the $1/2\langle 111 \rangle$ screw dislocation core	114

VII Chapter 4 - Non-Schmid effects across bcc transition metals	120
1 Core properties and mobility of $\frac{1}{2}\langle 111 \rangle$ screw dislocations	120
1.1 Peierls potential	120
1.2 Dislocation trajectory and relaxation volume	121
1.3 Peierls enthalpy barrier under applied stress	123
2 Uniaxial mechanical loading	124
2.1 Generalized yield criterion	124
2.2 Variations among bcc transition metals	125
3 Comparison to experiments at low temperature	126
3.1 Yield stress and slip activity	126
3.2 Tension/compression asymmetry	131
3.3 Tension/compression asymmetry at finite temperature	133
VIII Chapter 5 - Anomalous slip in bcc transition metals	136
1 Experimental literature review	136
2 <i>In situ</i> straining experiments	137
2.1 Experimental methods	138
2.2 Glide of isolated $\frac{1}{2}\langle 111 \rangle$ screw dislocations and networks in niobium	138
2.3 Rapid motion of multi-junctions in niobium	139
3 Atomistic simulations and elastic model	141
3.1 Relaxation of a four-dislocation node	142
3.2 Formation of a four-dislocation node	146
3.3 Formation of $\langle 100 \rangle$ junctions	147
3.3.1 Formation of $\langle 100 \rangle$ screw junctions under dynamic conditions	151
3.4 Discussion	153
IX Chapter 6 - $\langle 100 \rangle$ dislocations in bcc transition metals	156
1 Elasticity and $\langle 100 \rangle$ dislocations	156
1.1 Elasticity and relative stability of dislocations having different Burgers vectors	156
1.2 Formation of $\langle 100 \rangle$ junctions in bcc metals	157
1.3 Experimental observations of $\langle 100 \rangle$ dislocations	159
2 Core properties and mobility of $\langle 100 \rangle$ screw dislocations	160
2.1 $\langle 100 \rangle$ screw dislocations in chromium	160
2.2 Competition between $\frac{1}{2}\langle 111 \rangle\{110\}$ and $\langle 100 \rangle\{110\}$ slip in chromium	163
2.3 Thermal activation of $\langle 100 \rangle$ screw dislocations in chromium	166
2.4 $\langle 100 \rangle$ screw dislocations in all bcc transition metals	168
3 Larger scale simulations using molecular dynamics and interatomic potentials	171
3.1 Dislocation loops with $\frac{1}{2}\langle 111 \rangle$ and $\langle 100 \rangle$ Burgers vectors under strain	171
3.2 $\langle 100 \rangle$ dislocation sources	174
3.3 <i>Ab initio</i> calculation of the Peierls barrier of mixed $\langle 100 \rangle$ dislocations	176
3.4 Discussion	178

X	Conclusions and outlook	180
XI	Synthèse en français	184
XII	Bibliography	190
XIII	Appendices	200
Appendix A	Experimental yield stresses and athermal temperatures	200
Appendix B	Orientation and surface dependence of the energy of the magnetic fault bounded by two $\frac{1}{2}\langle 111 \rangle$ screw dislocations with the tight binding model	201
Appendix C	Free energy of model magnetic fault variations with temperature	203
Appendix C.1	Constant magnetic fault energy	203
Appendix C.2	Linearly decreasing magnetic fault energy	203
Appendix D	Adjustment of the elastic constants to ensure the symmetry of the $\frac{1}{2}\langle 111 \rangle$ and $\langle 100 \rangle$ screw dislocations trajectory in $\{110\}$ planes	204
Appendix D.1	$\frac{1}{2}\langle 111 \rangle$ screw dislocation	204
Appendix D.2	$\langle 100 \rangle$ screw dislocation	205
Appendix E	Influence of the entropic contribution on the predicted flow stress	206
Appendix E.1	Comparison with experiments	206
Appendix E.2	Influence of the approximation for the entropic contribution	207
Appendix F	Formation of $\langle 100 \rangle$ junctions of different characters from interaction between mixed $\frac{1}{2}\langle 111 \rangle$ dislocations	209

Introduction

Extreme working conditions are found inside the core of a nuclear reactor, among which the high irradiation dose and the highly corrosive environment, thus subjecting the components inside to constant evolution. The fuel cladding, made of zirconium-alloy, needs to endure these highly degrading conditions, in particular in accidental conditions, for instance in the event of a loss of coolant accident (LOCA), where the temperature inside the core of the reactor can rapidly increase, thus accelerating oxidation and degradation processes, which can lead to the failure of the cladding. Application of a thin coating layer of chromium (Cr), known for its high resistance to corrosion, on the fuel cladding is currently explored as a possible solution to prevent oxidation of the cladding [1–4]. Under these conditions (temperature, pressure, irradiation), the Cr coating needs to be able to deform plastically, to accommodate the deformation imposed by the cladding and the fuel. However, Cr shows a high transition temperature from brittle to ductile behavior, and which strongly depends on the purity of the sample [5]. Additionally, irradiation damages are known to induce a considerable hardening, further pushing the transition to ductile behavior towards high temperatures, with enhanced brittleness at low temperatures. Thus, depending on the material and the working temperature, the Cr coating may be subjected to deformation while in a brittle state, which would then result in initiation of cracks in the coating, and ultimately the loss of its protective properties. In this respect, it is necessary to have a good understanding of its plasticity to accurately predict its properties under working conditions.

Cr is one of the seven pure body-centered cubic (bcc) transition metals, a class of metal used for various structural components for applications under severe working conditions due to their interesting mechanical properties and high melting point. Plasticity of bcc transition metals operates through the motion of dislocations with a $\frac{1}{2}\langle 111 \rangle$ Burgers vector, the smallest periodicity vector of the bcc lattice. At low temperature, most particularly below the brittle to ductile transition, their motion is governed by the high lattice friction their screw orientation experiences, responsible for their alignment along this particular orientation, and impeding their motion. Among the seven pure bcc transition metals, Cr is the only one with an ordered magnetic structure close to antiferromagnetism at temperatures below ambient [6], before a transition to a disordered high-temperature paramagnetic phase where magnetism however still remains. In the temperature range where magnetic order prevails, atoms located on the two sub-lattices of the bcc structure (*i.e.* corner and center atoms) have a spin of opposite sign. Given that the $\frac{1}{2}\langle 111 \rangle$ Burgers vector of dislocations links two atoms with different magnetic moments, magnetic faults are expected to be generated as a consequence of the disruption of the magnetic order. Impact of magnetism on the properties of dislocations therefore needs to be addressed, in particular since the brittle to ductile transition temperature of pure Cr is close to the disappearance of magnetic order, both close to room temperature [5, 6]. The impact of magnetism also has to be addressed in the disordered paramagnetic phase, since magnetism persists. Plasticity of Cr therefore raises multiple questions (impact of magnetism, types of dislocations carrying plasticity), and has been the focus of few studies aiming at characterizing its mechanical properties. In particular, it is not clear whether Cr has a conventional plasticity with respect to all other bcc transition metals, which were thoroughly studied both experimentally and theoretically, which is not the case of Cr, partly because of the added complexity of accounting for its magnetic structure.

Modeling of plasticity at the atomic scale allows for incorporation of the fine properties of the dislocation core, needed to properly describe how they interact with the lattice as they move when subjected to applied stress. Such a modeling approach, based on atomistic simulations, has proven its ability to accurately account for the core of dislocations, linking their properties to the macroscopic mechanical behavior of bcc metals. Based on previous works, which laid the basis for the incorporation of all physical ingredients to account for the core properties of dislocations using *ab initio* calculations, one is now able to construct generalized yield criteria allowing for the prediction of the yield stress and slip activity as a function of the mechanical loading, directly from *ab initio* calculations. The results of such model can then be compared to experiments to test its ability to reproduce features of the yield behavior of bcc transition metals. Development of yield criteria across all bcc transition metals also allows to qualify differences between one another, in particular to conclude on the resemblance between Cr and other bcc metals.

Apart from these advances allowed by atomistic simulations, some mechanisms accounting for the plastic deformation of bcc transition metals are nevertheless still not fully understood or identified, and therefore need further investigation to explore new possibilities. In particular, anomalous slip, characterized by activity of dislocations in low-stressed planes in pure samples at low temperature, was first observed more than 50 years ago and still lacks proper explanation accounting for all of its features. It is also not clear if dislocations having a different Burgers vector than the conventional $\frac{1}{2}\langle 111 \rangle$ can actively participate to the plastic deformation of these metals. In particular, $\langle 100 \rangle$ dislocations, which are slightly longer in norm, are reported in all bcc transition metals, mostly as the junction product of two intersecting $\frac{1}{2}\langle 111 \rangle$ dislocations. Activity of these dislocations is often neglected when rationalizing plasticity of bcc transition metals, although their motion is reported experimentally in a few metals at room temperature. Therefore, a proper modeling of these dislocations is needed to understand in which conditions they can participate to the plastic deformation of these metals.

We begin this document with a review of the experimental literature regarding features of the plasticity of bcc transition metals, along with simulation works at the atomic scale aiming at their description (**Literature review**). We then present the different tools used in this work for all presented atomistic simulations, whether for dislocation modeling or for description of the magnetic properties of Cr (**Methods**). The results are structured in six different chapters, starting from the bulk properties of bcc Cr modeled using *ab initio* calculations, with a focus on its magnetic phases, their elastic properties, and the stacking fault energies in different planes (**Chapter 1**). We then present the properties of $\frac{1}{2}\langle 111 \rangle$ screw dislocations in bcc Cr modeled using *ab initio* calculations at 0 K. We focus on qualifying the impact of magnetism on their core properties and mobility, with parametrization of a yield criterion for prediction of slip activity and yield stress of single crystals subjected to uniaxial mechanical loading (**Chapter 2**). Using an effective interaction model for magnetic properties parametrized on *ab initio* data, coupled to Monte Carlo simulations, we then study finite temperature magnetism of bcc Cr, with a focus on the properties linked to its plasticity, and the properties of $\frac{1}{2}\langle 111 \rangle$ dislocations (**Chapter 3**). The yield criterion developed for Cr is then extended to all bcc transition metals, allowing for comparison between them to conclude on whether Cr shows a similar plastic behavior, and also to test the ability of the model to reproduce the experimental features of their plasticity (**Chapter 4**). We then present a new mechanism explaining anomalous slip in bcc transition metals, which is the result of a collaboration with Daniel Caillard (CEMES, CNRS, Toulouse), with coupled *in situ* straining experiments in a transmission electron microscope performed by Daniel Caillard and our atomistic simulations (**Chapter 5**). Finally, we explore possibilities for dislocations having a $\langle 100 \rangle$ Burgers vector, observed experimentally in all bcc transition metals, to participate to the plastic deformation, using atomistic simulations (**Chapter 6**).

Literature review

As briefly prefaced in Introduction, a quantitative understanding of the mechanical properties of pure chromium (Cr), with a focus on its plastic deformation, is required for industrial applications mentioned. In the present context, the Cr coating needs to endure the mechanical strain imposed by the zirconium fuel rods it covers without initiation of serious deformation or cracking, otherwise oxidation would start broaching the fuel rod. Cr is a body-centered cubic (bcc) transition metal, whose plasticity has been the focus a very few experimental and numerical studies compared to the other six bcc transition metals presented in the periodic table of Tab. 1. Among them, Cr is the only one with an antiferromagnetic ground state below ambient [6], which needs to be addressed to rationalize its plastic deformation.

Table 1: Periodic table showing the body-centered cubic (bcc) transition metals in blue.

	III	IV	V	VI	VII	VIII	IX	X	XI
4	Sc	Ti	V	Cr	Mn	Fe	Co	Ni	Cu
5	Y	Zr	Nb	Mo	Tc	Ru	Rh	Pd	Ag
6	-	Hf	Ta	W	Re	Os	Ir	Pt	Au

The different mechanisms at stake and their corresponding temperature range are presented in Fig. 1a for Cr, showing their intricate combination and relative importance. A limiting property of Cr when looking at applications under extreme conditions is the dual observation of a high ductile-brittle transition temperature (Fig. 1b) with a lack of ductility below, and a weak strength at high temperature, both of which are very sensitive to multiple factors such as impurities, substitutional elements, or the microstructure of the sample [7]. For these applications, a good understanding of the physical origin of its particular mechanical properties is needed. The aim of the present review is to introduce the features and mechanisms at stake in the plastic deformation of bcc metals, both experimentally and using atomistic simulations, in order to compare the different bcc transition metals, and assess if Cr shows standard plasticity in this respect.

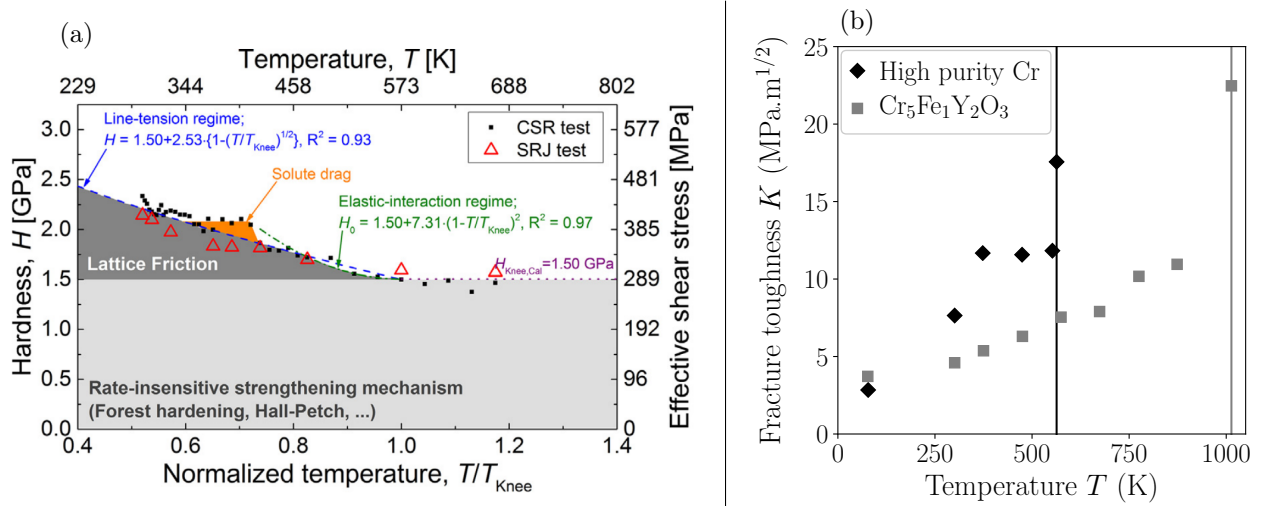


Figure 1: (a) Dependence of the deformation mechanisms of Cr as a function of temperature from hardness and shear stress measurements at constant indentation strain rate (CSR) and strain rate jump (SRJ) (reproduced from Choi *et al.* [8]). (b) Temperature evolution of the fracture toughness K for high-purity and alloyed polycrystalline samples showing the high ductile-brittle transition temperature of Cr [5].

This literature review focuses on the three following topics: properties of dislocations and features of plasticity common to all bcc transition metals; results of atomistic simulations on dislocations in bcc transition metals; particularities of Cr both in terms of magnetic order and experimental features of plasticity.

1. Plasticity of body-centered cubic transition metals

Plastic flow and strength of crystals are driven by the motion of dislocations in the crystal, the line-defects carrying elemental atomic shear deformation. Plasticity of bcc metals is mediated by the strong lattice friction screw dislocations experience when shearing the crystal. Some characteristic features of their plastic deformation are common to all bcc transition metals including Cr, which are the focus of this section.

1.1. Energetic description of dislocations

Dislocations are the line defects carrying plastic deformation at the atomic scale, defined by the amount of shear they induce to the crystal, the Burgers vector \vec{b} , and their line orientation \vec{l} tangent to the dislocation line. When the Burgers \vec{b} and line \vec{l} vectors are collinear, the dislocation has a screw character, and when both vectors are orthogonal, the dislocation has an edge character. Any other relative orientation of these two vectors defines a mixed dislocation of character θ , the angle between \vec{b} and \vec{l} .

Dislocations are responsible for a deformation of the crystal, described in the frame of elasticity theory by a strain and stress field decreasing as the inverse of the distance r to the dislocation line $1/r$ [9]. This field accounts for the long-range elastic distortion of the lattice. Close to its line, the deformation induced by a dislocation is too important to be accounted for by elasticity theory. One thus needs to define a region near the line to encapsulate these strong displacements, a core region of radius r_C leading to an energy contribution $E^{\text{core}}(r_C)$ which is independent of the surrounding microstructure. Outside this core region, elasticity theory allows for an accurate description of its energy E^{elas} as a long-range elastic contribution. This leads to the following partitioning of the total energy E^{tot} of the dislocation:

$$\begin{aligned} E^{\text{tot}}(\theta) &= E^{\text{core}}(r_C) + E^{\text{elas}}(\theta, r_C) \\ &= E^{\text{core}}(r_C) + \frac{b_i [K_{ij}(\theta)] b_j}{4\pi} \ln \left(\frac{R_\infty}{r_C} \right) = E^{\text{core}}(r_C) + e(\theta) \ln \left(\frac{R_\infty}{r_C} \right), \end{aligned} \quad (1)$$

where \bar{K} is the Stroh tensor, function of the character θ of the dislocation [10, 11] and the elastic constants of the material. R_∞ is the outer cutoff radius for elastic interactions, depending on the microstructure of interest, and r_C is the radius of the dislocation core, defining the region where elasticity is not valid, used to partition the dislocation energy in two contributions resulting in E^{tot} independent of the core radius. These two contributions to the dislocation energy have different physical meanings, which we focus on detailing how they relate to its macroscopic properties in the following. The elastic anisotropy is quantified by the ratio $A = C_{44}/C'$ between the two shear moduli $C' = (C_{11} - C_{12})/2$ and C_{44} , equal to 1 in the isotropic case of tungsten, and defines the shape of the character variation of the elastic energy of dislocations [12, 13]. Experimental elastic constants for all bcc transition metals are presented in Tab. 2, measured at 4.2 K.

Table 2: Lattice parameter a_0 (Å), elastic constants C_{ij} (GPa), elastic anisotropy ratio $A = 2C_{44}/(C_{11} - C_{12})$, and modified bulk to shear moduli ratio $m_B = (C_{11} + 2C_{12})/C_{44}$ for all bcc transition metals. Values are taken from various experimental references and were measured at approximately 4.2 K.

	a_0	C_{11}	C_{12}	C_{44}	A	m_B
V [14]	3.03	230	120	43	0.78	10.90
Nb [14, 15]	3.29	246	132	28	0.50	17.95
Ta [14]	3.30	262	156	83	1.56	6.94
Cr [16]	2.88	392	91	103	0.68	5.55
Mo [17]	3.14	458	168	111	0.77	7.16
W [17]	3.16	517	203	157	1.00	5.88
Fe [18]	2.87	233	135	116	2.38	4.34

In the frame of isotropic elasticity theory, *i.e.* with an elastic anisotropy ratio $A = 1$ and corresponding to equal elastic shear moduli $C' = (C_{11} - C_{12})/2$ and C_{44} , the elastic energy of a straight infinite dislocation of character θ is given by the following expression:

$$E_{\text{iso}}^{\text{elas}}(\theta, r_C) = \frac{\mu b^2}{4\pi} \left[\frac{\sin^2(\theta)}{1 - \nu} + \cos^2(\theta) \right] \ln \left(\frac{R_\infty}{r_C} \right), \quad (2)$$

with b the norm of the Burgers vector of the dislocation, μ the bulk modulus, and ν the Poisson's ratio of the isotropic material. Considering Eq. 2, we note that the elastic energy of a dislocation is proportional to the square of the norm of its Burgers vector, thus minimizing the energy of dislocations having a Burgers vector equal to the smallest periodicity vector of the lattice, which is $1/2\langle 111 \rangle$ for the bcc lattice. Another consequence is that the elastic energy is minimum for the screw orientation ($\theta = 0$), and maximum for the edge orientation ($\theta = 90^\circ$) since ν is positive and smaller than 1. We note from the elastic constants of Tab. 2 that this isotropic description only holds for bcc tungsten, which has an anisotropy ratio $A = 1$. For an accurate description of the elastic properties of dislocations in other bcc metals, elastic anisotropy is required.

Now considering anisotropic elasticity theory, the Stroh tensor $\bar{\bar{K}}$ of Eq. 1 do not have an analytical expression for all characters θ of the dislocation, and therefore needs to be evaluated numerically. This is done using the BABEL package [19] with the experimental anisotropic elastic constants measured at 4.2 K presented in Tab. 2. The anisotropic elastic energy of the $1/2\langle 111 \rangle$ dislocation as a function of its character θ is presented in Fig. 2 for all bcc transition metals, which is the basis for simple line energy models developed in the following to study for instance the formation of dislocation junctions, detailed in Chapter 5.

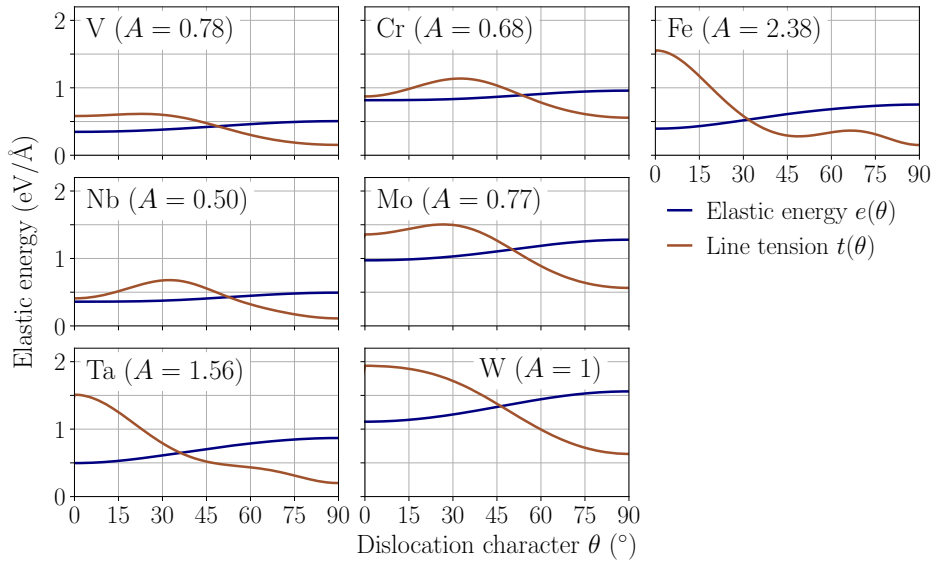


Figure 2: Logarithmic prefactor to the elastic energy (blue) and line tension (brown) of a straight infinite $1/2\langle 111 \rangle$ dislocation as a function of its character θ in the frame of anisotropic elasticity theory for all bcc transition metals. The core radius is set to $r_C = b = a_0\sqrt{3}/2$ the norm of the $1/2\langle 111 \rangle$ Burgers vector. Anisotropic elastic constants used are presented in Tab. 2.

For all bcc transition metals, the anisotropic elastic energy of the $1/2\langle 111 \rangle$ dislocation presented in Fig. 2 is minimum for the screw orientation and maximized for the edge orientation, as for the isotropic case (see tungsten for comparison). Another quantity of interest given by elasticity theory is the dislocation line tension T^{elas} , given by [12]:

$$T^{\text{elas}}(\theta) = \left[e(\theta) + \frac{\delta^2 e(\theta)}{\delta \theta^2} \right] \ln \left(\frac{R_\infty}{r_C} \right) = t(\theta) \ln \left(\frac{R_\infty}{r_C} \right), \quad (3)$$

which is plotted as function of the dislocation character θ for all bcc transition metals in Fig. 2 in brown. This line tension, homologous to a line energy, quantifies the ease of an initially straight dislocation line of

character θ to bow out under an applied stress, through the incorporation of the curvature of the elastic energy with the character. As the line tension shows a maximum for the screw orientation in the isotropic case, it will require a higher stress to induce a bowing of its line starting from an initially straight screw dislocation. This holds for metals having an elastic anisotropy characterized by a ratio $A > 1$ (Ta and Fe), for which the screw orientation of the $\frac{1}{2}\langle 111 \rangle$ dislocation minimizes its elastic energy, while maximizing its line tension. For metals having a ratio $A < 1$ (V, Nb, Cr and Mo), a mixed orientation of the dislocation minimizes its elastic energy and maximizes its line tension. However, as will be discussed in the following section, a dislocation line can only start to bend under an applied stress at a sufficiently high temperature, needed to completely wipe out the strong friction experienced by their screw orientation with the lattice.

Looking at elastic properties of Cr compared to other bcc transition metals, dislocations in Nb share similar properties due to these two metals having the smallest elastic anisotropy ratio. Due to the scarcity of experimental data on Cr, the study of other bcc transition metals with similar properties and for which experimental data is available can allow for comparison with the presented models. For example, experimental observation of anomalous slip has been reported in all bcc transition metals, including Cr, a mechanism believed to strongly depend on the elastic properties of the metal. Mostly studied in Nb, the obtained results can then be reasonably extended to Cr since they share similar elastic properties.

1.2. Dislocation glide in body-centered cubic metals

Two different mechanisms account for the motion of dislocations in the crystal, namely glide and climb. The first is a conservative mechanism where atoms in the vicinity of the dislocation line move to let the dislocation glide in a given crystallographic plane of normal \vec{n} satisfying $\vec{n} \perp \vec{b}$ and $\vec{n} \perp \vec{l}$. Therefore, as screw dislocations have collinear Burgers \vec{b} and line \vec{l} vectors, they can glide in different planes as long as they meet the previous orthogonality relation, whereas non-screw dislocations are constrained to glide in a single plane. The other mechanism, dislocation climb, is a non-conservative process, where dislocations move perpendicular to their glide planes, requiring atoms to be removed or added to allow their motion. Dislocation climb is assisted by diffusion processes, and operate at higher temperatures than dislocation glide. Only the glide mechanism for dislocation motion is discussed in the following as it is the focus of the present work.

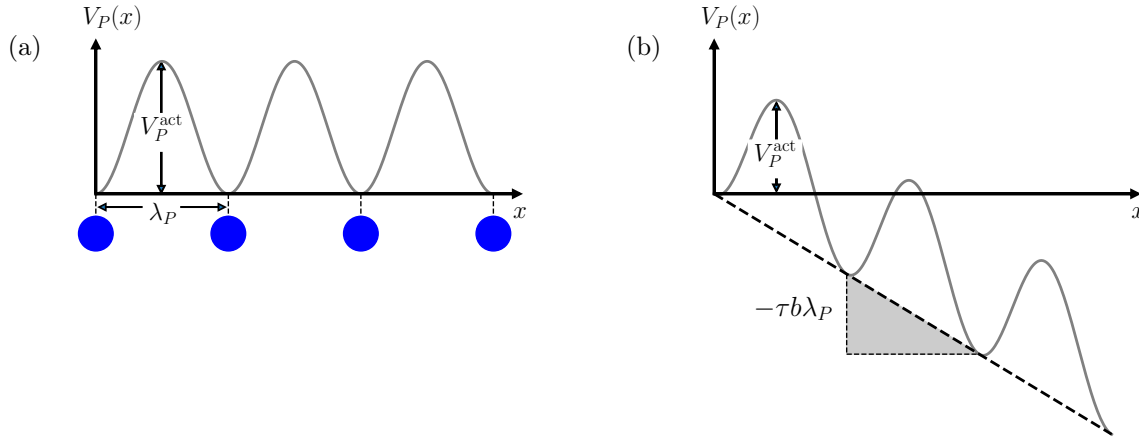


Figure 3: Sketch of the Peierls potential V_P opposing the motion of a dislocation in its glide plane: (a) in an unstressed crystal, and (b) under an applied resolved shear stress τ producing a Peach-Koehler force $F_{PK} = -\tau b \lambda_P$ on the dislocation.

When a dislocation moves inside a crystal, both contributions to its total energy vary, but only the core contribution depends on the position of the dislocation line with respect to the crystal lattice. Motion of dislocations through the lattice is therefore dictated by the variation of E^{core} as a function of the line position. This variation accounts for the lattice friction dislocations experience when shearing the lattice,

called the Peierls potential, and sketched in Fig. 3a. This friction potential has a periodicity dictated by the lattice, with minima corresponding to equilibrium configurations of the dislocation core, called Peierls valleys, separated from each other by a distance λ_P . When their habit crystal is subjected to an applied stress, the height V_P^{act} of the energy barrier opposing dislocation glide decreases by the amount of work produced by the force exerted on the moving dislocation, the Peach-Koehler force $\vec{F}_{\text{PK}} = (\vec{\sigma} \cdot \vec{b}) \times \vec{l}$, where $\vec{\sigma}$ is the stress tensor having a component τ resolved in the glide plane. The barrier ultimately vanishes at a threshold value τ_P of the applied stress at which dislocations start moving freely in the crystal without experiencing any lattice friction, the Peierls stress. A quantitative evaluation of the lattice friction experienced by dislocations when shearing the crystal can be computed through atomistic simulations of the Peierls potential opposing their glide, which is the focus of the next section.

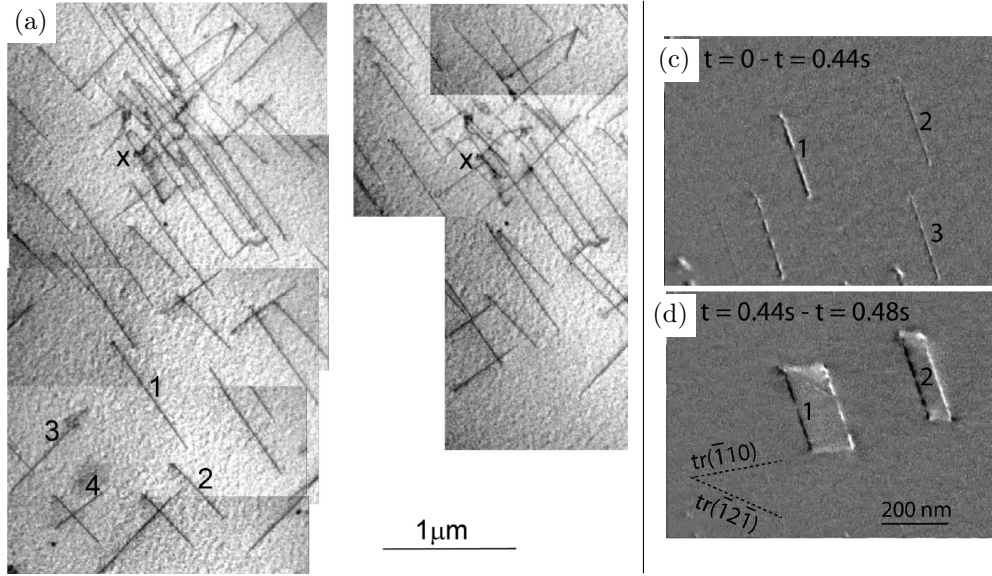


Figure 4: (a) Transmission electron microscope (TEM) observations of straight segments of screw dislocations having Burgers vectors $\vec{b}_1 = 1/2[111]$, $\vec{b}_2 = 1/2[\bar{1}\bar{1}1]$, $\vec{b}_3 = 1/2[1\bar{1}1]$ and $\vec{b}_4 = 1/2[\bar{1}11]$ at 300 K in tungsten at two different times (reproduced from Ref. [20]). (c)-(d) Differential images between snapshots recorded at three different times during *in situ* straining in a TEM in iron at room temperature, showing the slow glide of screw dislocations 1 and 2 in $(\bar{1}10)$ planes [21].

At low to ambient temperatures, the lattice friction experienced by screw dislocations is too important to allow for the bending of their lines as described by the line tension of Eq. 3, thus resulting in dislocations aligned along their screw orientations, stuck at the bottom of their Peierls valleys. *In situ* transmission electron microscopy (TEM) in strained bcc metals shows long dislocation lines aligned along their screw orientation [22, 23], like presented in Fig. 4a in tungsten at 300 K [20]. These dislocations are characterized by a Burgers vector corresponding to the smallest periodicity vector of the crystal lattice, which is $1/2\langle 111 \rangle$ for the bcc lattice [9]. Motion of these screw dislocations at low temperature is impeded by the strong lattice friction they experience compared to other line orientations. As a result, plasticity of bcc metals at low temperature is governed by glide of these screw dislocations in the close-packed crystallographic planes of the bcc lattice [24]. At low temperature, dislocation glide in $\{110\}$ planes dominates in most bcc metals [25] as shown in iron on Fig. 4b, but is also observed in $\{112\}$ [20, 26–28] and $\{123\}$ [20] planes at higher temperature, with a viscous rigid motion of their line as a whole, as shown in Fig. 4b in iron. The reported TEM observations were recorded *in situ* in a strained sample and presented in differential contrast images, *i.e.* through the subtraction of consecutive snapshots recorded at two different times during the test, the background and immobile dislocations are erased, and the resulting images show moving dislocations in positive bright contrast in their new positions, and in negative black contrast in their former positions.

When thermal agitation becomes non-negligible, crossing of the Peierls barrier can operate through the

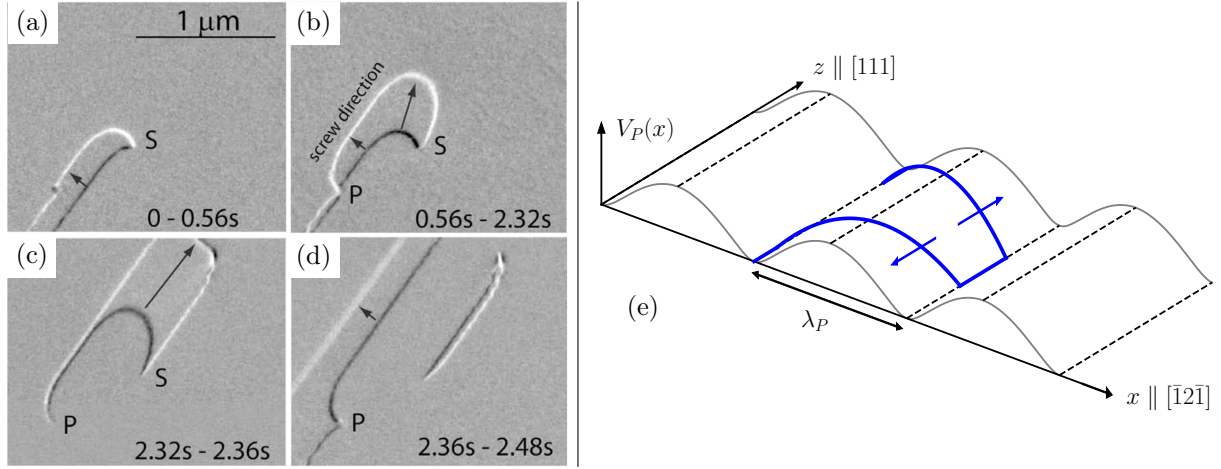


Figure 5: (a)-(d) Glide of a $\frac{1}{2}[111]$ dislocation at 300 K in iron imaged in TEM at different times showing the difficult motion of its screw component compared to its edge component (reproduced from Ref. [21]). (e) Sketch of the kink-pair nucleation mechanism showing a dislocation line in blue bowing to cross the Peierls barrier before the two kinks propagate along the line.

nucleation and migration of highly mobile short non-screw segments, or kink-pairs [22], along the dislocation line (Fig. 5e). In pure bcc metals, kinks glide along a dislocation line with a negligible lattice friction, and the motion of screw dislocations is therefore controlled by kink nucleation. The difficult motion of screw dislocations compared to other line orientations has been observed in TEM, like presented in iron on Fig. 5a-d [21]. The snapshots were recorded at different time steps under *in situ* straining conditions, showing the bowing of a dislocation line under stress, ultimately resulting in the alignment of its line and motion along its screw orientation. This confirms the limiting role of screw dislocations in the development of plastic deformation in bcc metals.

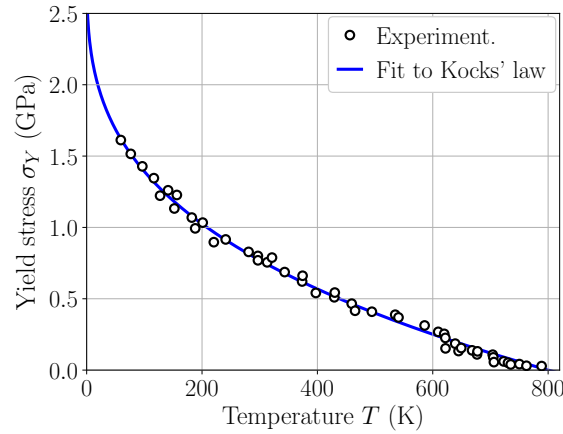


Figure 6: Experimental yield stress σ_Y of a tungsten single crystal tested under uniaxial tension as a function of temperature [29]. The solid blue line is our fit of the experimental data to Eq. 4, not presented in the original experimental work.

As a thermally activated process, dislocations require a decreasing applied stress to start moving as the temperature increases, before ultimately reaching zero at the athermal temperature of the Peierls mechanism T_{ath} , which approximately corresponds to the ductile-brittle transition of the material. The evolution of the yield stress σ_Y for a tungsten single crystal subjected to uniaxial tension with temperature is presented in

Fig. 6. The experimental data has been fitted to a law of the following form:

$$\sigma_Y(T) = \sigma_Y^0 \left[1 - \left(\frac{T}{T_{\text{ath}}} \right)^{1/q} \right]^{1/p}, \quad (4)$$

where σ_Y^0 is the estimated yield stress at 0 K, and p and q are adjustable parameters defining the shape of the temperature evolution of σ_Y . The above mobility law results from a model developed in this work, which will be presented in details in the following chapters. We see that the yield stress shows a very steep increase when the temperature approaches 0 K, where the lattice friction experienced by screw dislocations is the strongest, before slowly decreasing up to the athermal temperature T_{ath} of the Peierls mechanism. Above T_{ath} , *i.e.* in the absence of lattice friction, elasticity theory controls dislocation motion through the bowing of their lines under applied stress as described by the line tension. Below T_{ath} , *i.e.* in the temperature range where the lattice friction impedes glide of screw dislocations, unusual features are reported experimentally in the yield behavior of bcc metals, showing deviations from the predictions of the Schmid law, as opposed to face-centered cubic (fcc) metals for instance [25].

1.3. Non-Schmid effects and anomalous slip

According to the Schmid law, dislocation glide in a given slip plane occurs when the resolved shear stress in this plane exceeds a threshold value, the Peierls stress τ_P , necessary to overcome the lattice friction they experience. Hence, when the plane of maximum resolved shear stress (MRSSP) makes an angle χ with its $\{110\}$ slip plane, dislocation glide starts when the applied stress projected in the glide plane is higher than the Peierls stress τ_P . Then, the threshold stress necessary to activate dislocation glide for a uniaxial mechanical test is given by the following geometrical relation, the well-known Schmid law:

$$\sigma_Y(\chi) = \frac{2\tau_P}{\cos(\chi)} \quad (5)$$

The yield criterion given by the Schmid law is symmetrical with respect to the $\{110\}$ glide plane, one would thus expect to have a symmetrical yield behavior considering two similar crystals with orientations defined by $\chi < 0$ and $\chi > 0$. The most commonly used test to measure the yield strength of monocrystalline samples is the uniaxial mechanical loading, for which a vast majority of experimental data is available across a wide temperature range for all pure bcc transition metals. A sketch of such a mechanical loading is given in Fig. 7a defining the angles ζ between the loading axis \vec{t} and the $1/2[111]$ slip direction, and χ between the MRSSP

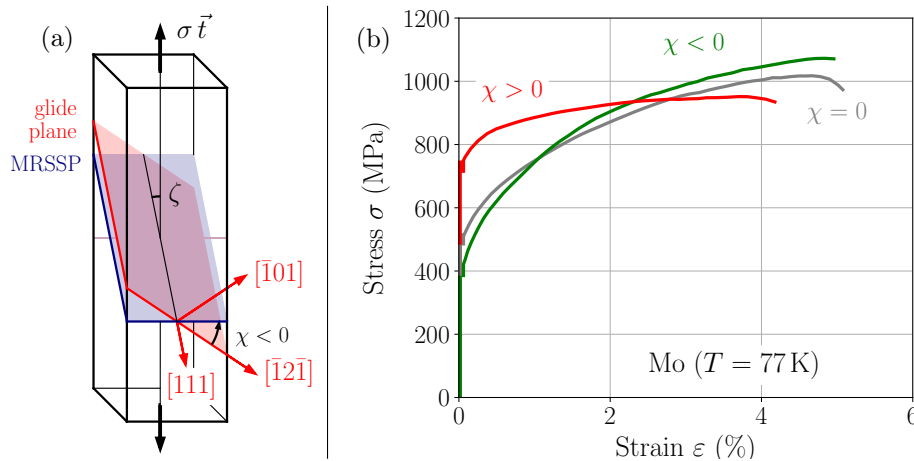


Figure 7: (a) Sketch of a uniaxial mechanical loading along an axis \vec{t} , showing the angles ζ and χ between the dislocation glide plane (in red) and the plane of maximum resolved shear stress (MRSSP, in blue). (b) Stress σ as a function of strain ϵ recorded upon application of a tensile load to single crystals of bcc Mo having different orientations at 77 K [30].

and the $(\bar{1}01)$ glide plane of the $1/2[111]$ screw dislocation. A typical stress/strain curve for such loading shows an elastic region with a linear variation of the stress σ as a function of strain ε , before reaching a yield point at which plastic deformation starts. An example is presented in Fig. 7b for three orientations of Mo single crystals tested under uniaxial tension at 77 K [30], showing the yield stress σ_Y (squares) at which dislocation glide can start propagate the plastic deformation. As opposed to the predictions of the Schmid law, the yield stress differs between the two $+30^\circ$ and -30° orientations of the MRSSP, with a lower tensile yield stress for $\chi < 0$ than $\chi > 0$. This effect is known as the twinning/antitwinning (T/AT) asymmetry, and has been reported experimentally in all pure bcc transition metals at low temperature [26, 30–35].

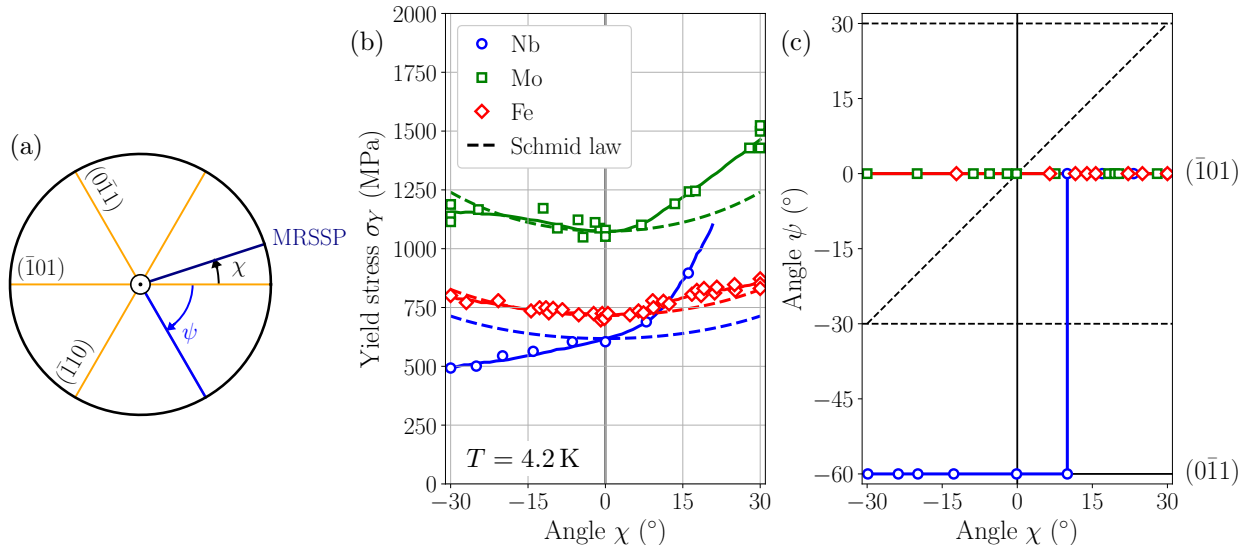


Figure 8: (a) Stereographic projection along the $[111]$ direction showing all $\{110\}$ planes contained in the (111) plane and the angle χ between the MRSSP and the $(\bar{1}01)$ glide plane. (b) Experimental variation of the yield stress in tension for Nb, Mo and Fe single crystals as a function of χ . (c) Angle ψ between the observed slip plane and $(\bar{1}01)$ as a function of the angle χ . Experimental data were measured at 4.2 K under uniaxial tension [30, 35, 36].

The variations of the yield stress σ_Y with the orientation χ of the MRSSP for Nb [36], Mo [30] and Fe [35] single crystals tested under uniaxial tension at 4.2 K are presented in Fig. 8b, with the predictions of the Schmid law indicated by colored dashed lines. All three metals show the same characteristic departure from the Schmid law, with a lower yield point in the twinning region $\chi < 0$, which is more pronounced in Nb and Mo than in Fe. The authors also evaluated the primary $1/2\langle 111 \rangle \{110\}$ slip system accounting for the plastic deformation of each sample with its orientation as the angle ψ the observed slip plane makes with the most highly stressed $(\bar{1}01)$ plane (Fig. 8a), which are presented in Fig. 8c for Nb, Mo and Fe. At 4.2 K, the primary glide plane in Mo and Fe is the maximum resolved shear stress plane $(\bar{1}01)$ across the whole range of χ orientations, *i.e.* $\psi(\chi) = 0$, whereas a change of glide plane from the expected $(\bar{1}01)$ to the low stressed $(0\bar{1}1)$ plane with $\psi = -60^\circ$ (Fig. 8a) is observed in Nb at $\chi \simeq 10^\circ$. Glide of dislocations in low stressed $\{110\}$ planes has also been observed in other bcc transition metals [31, 34, 37–40] except Fe, and is referred to as anomalous slip [25], which is the focus of Chapter 5.

At low temperature, bcc metals also exhibit an asymmetry between their tensile and compressive yield behaviors, with a generally lower yield stress in tension than in compression along the same loading axis [25, 42, 43], which is referred to as the tension/compression (T/C) asymmetry. Liu *et al.* [41] measured the yield stress of Mo single crystals with different orientations as a function of temperature under both uniaxial tension and compression, which are presented in Fig. 9 with corresponding fits to the law of Eq. 4. We note that the yield stress shows a significant T/AT asymmetry under uniaxial tension and compression, comparing red with green or blue with orange samples. This asymmetry holds in both tension and compression across

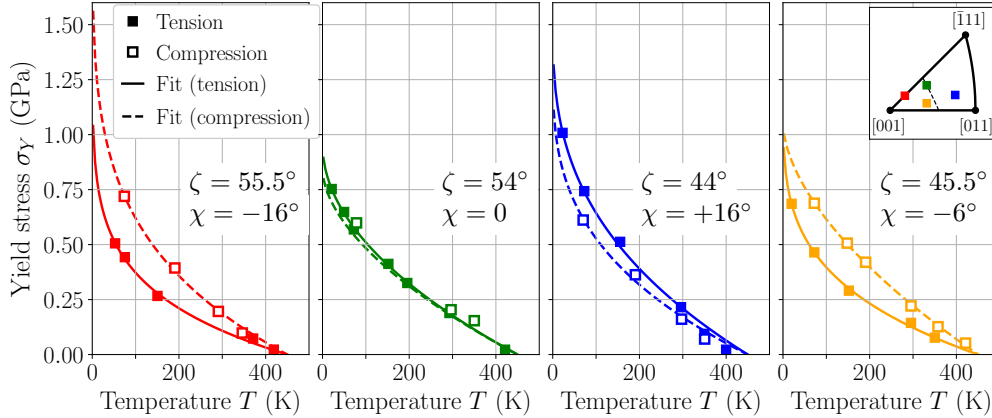


Figure 9: Experimental yield stress of Mo single crystals tested under uniaxial tension (filled symbols) and compression (open symbols) as a function of temperature considering four different crystal orientations shown in the stereographic projection of the right inset. Data are taken from Liu *et al.* [41] and were measured at a strain rate $\dot{\epsilon} = 3.3 \times 10^{-5} \text{ s}^{-1}$. Solid and dashed lines are our fit of the experimental data to Eq. 4 in tension and compression respectively.

the whole range of temperature, but becomes less pronounced as the temperature approaches $T_{\text{ath}} \simeq 450 \text{ K}$, at which the yield stress becomes zero regardless of the crystal orientation. The asymmetry between the tensile and compressive yield stress also progressively fades out with increasing temperature, with a lower tensile yield stress only for red and orange orientations, and a lower compressive yield stress for green and blue samples across the whole temperature range. A summary of the low temperature yield stress σ_Y and athermal temperature T_{ath} of the Peierls mechanism taken from various experimental references are listed in Tab. A.1 of Appendix A for all bcc transition metals under either tension or compression.

2. Atomistic study of dislocations in body-centered cubic metals

As discussed in the first section of this literature review, plasticity of bcc metals is mainly driven by glide of $1/2\langle 111 \rangle$ screw dislocations, which exhibit unusual properties directly linked to some of the surprising features of the macroscopic plastic behavior of bcc metals. A fine atomistic description of the core properties of these dislocations has helped understanding the elemental processes at the origin of such a behavior, a review of which is the focus of the present section.

2.1. *Ab initio* modeling of dislocations

Fine description of forces at the atomic scale is necessary to account for the mechanisms involved in the plastic deformation of bcc transition metals. Atomistic modeling of dislocations, whether with *ab initio* density functional theory (DFT) or semi-empirical interatomic potentials, have helped uncover some of their properties linked to the macroscopic plastic behavior of bcc metals, which are detailed in the following.

2.1.1. Core structure of the $1/2\langle 111 \rangle$ screw dislocation

The body-centered cubic (bcc) crystal lattice is made of a periodic stacking of three different $\{111\}$ atomic planes along a $\langle 111 \rangle$ direction with a three-fold helical symmetry (see Fig. 10). The projection of the bcc lattice along a $\langle 111 \rangle$ direction therefore shows three atomic layers spaced from each other by a distance equal to one third of the norm of the $1/2\langle 111 \rangle$ Burgers vector, *i.e.* $b/3 = a_0\sqrt{3}/6$ with a_0 the lattice parameter. On the $\{111\}$ projection, the three-fold high-symmetry positions of the screw dislocation match the center of a triangle formed by three adjacent $\langle 111 \rangle$ atomic columns and correspond to extrema of its core energy, either located in upward triangles with clockwise helicity of the three columns, or downward triangles with anticlockwise helicity. When a $1/2\langle 111 \rangle$ screw dislocation is inserted at the center of such triangles, it generates a helical displacement field of the lattice in the $\langle 111 \rangle$ direction, which either inverts the helicity of the triangle or brings the three atomic columns at the same height. The first case corresponds

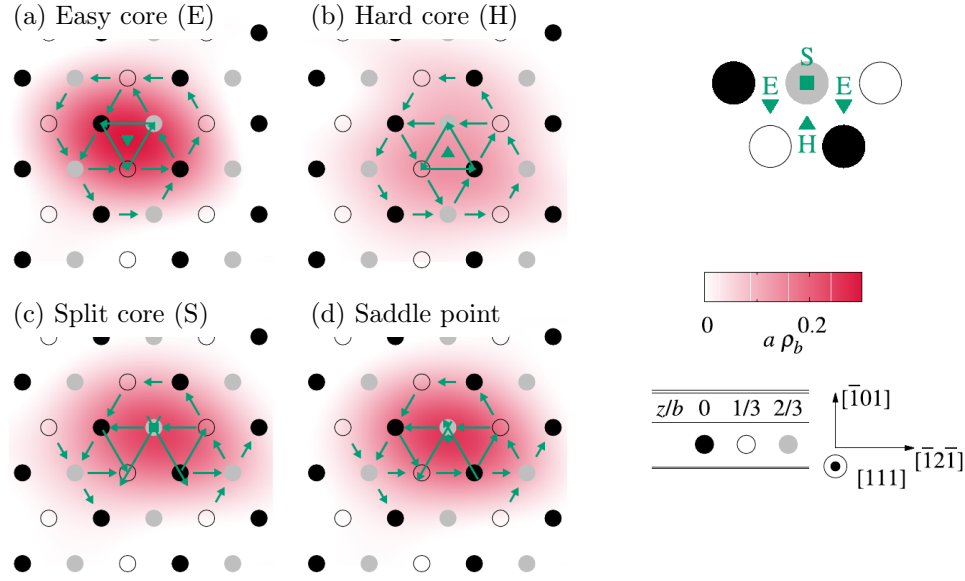


Figure 10: Differential displacement maps of a $1/2[111]$ screw dislocation core in bcc tungsten in its (a) easy, (b) hard, (c) split, and (d) saddle point configurations [44]. Atoms are represented in different colors depending on their heights along the $[111]$ direction. Positions of the dislocation are indicated by a green symbol, also sketched on the right panel. Arrows between two atomic columns have a size proportional to the differential displacement along $[111]$ between both columns, which is equal to $b/3$ when they join two columns. The color map is a projection of the Nye tensor, showing the dislocation density ρ_b normalized by the lattice parameter a (reproduced from Ref. [45]).

to the ground state of the screw dislocation core, called the easy core configuration, presented in Fig. 10a in tungsten [45]. The second configuration of the $1/2\langle 111 \rangle$ screw dislocation, presented in Fig. 10b in tungsten as well [45], is an energy maximum called the hard core configuration [44]. The core structure of the screw dislocation is visualized projected onto the (111) plane with differential displacement maps along the $[111]$ direction as first introduced by Vitek [46], showing the ground state easy configuration to have a compact and symmetrical structure. A third particular position of the $1/2\langle 111 \rangle$ screw dislocation is found when its core is located in the immediate vicinity of a $\langle 111 \rangle$ atomic column, called the split core configuration [47] and presented in Fig. 10d in bcc tungsten. This position does not respect the three-fold symmetry of the lattice and has three different variants depending on the direction the core approaches the $\langle 111 \rangle$ column.

This compact core is in contrast with the predictions of a broad range of interatomic potentials first used to model dislocations in pure bcc transition metals, predicting a degenerate ground state easy core [50–59], presented in Fig. 11b and c in bcc iron [49]. This degenerate structure was first thought to be the ground state of the $1/2\langle 111 \rangle$ screw dislocation core, but is in fact strongly dependent on the interatomic potential [49, 60–62]. This degenerate core structure leads to $1/2\langle 111 \rangle$ screw dislocations preferentially gliding in $\{112\}$ planes, which is in contradiction with the main experimental $\{110\}$ glide planes at low temperature. Since then, *ab initio* calculations have systematically demonstrated the non-degenerate compact core to be the true ground state of the $1/2\langle 111 \rangle$ screw dislocation in all pure bcc transition metals [44]. Early interatomic potentials having a compact easy core however predicted the split configuration as a metastable state [49]. In this case, the energy barrier between two adjacent easy configurations in a $\{110\}$ plane passes through this metastable state located halfway along the path, and shows a characteristic double-hump shape [49, 62, 63], each variant of the split core being associated with a different $\{110\}$ glide plane. *Ab initio* calculations have since then demonstrated that this split configuration corresponds to an energy maximum, resulting in single-hump energy barriers between two adjacent easy configurations [19, 44, 64]. Semi-empirical potentials have then been re-adjusted to predict a compact core structure for the $1/2\langle 111 \rangle$ screw dislocation, and the high energy of its split core configuration, using approximately the same form for the description of

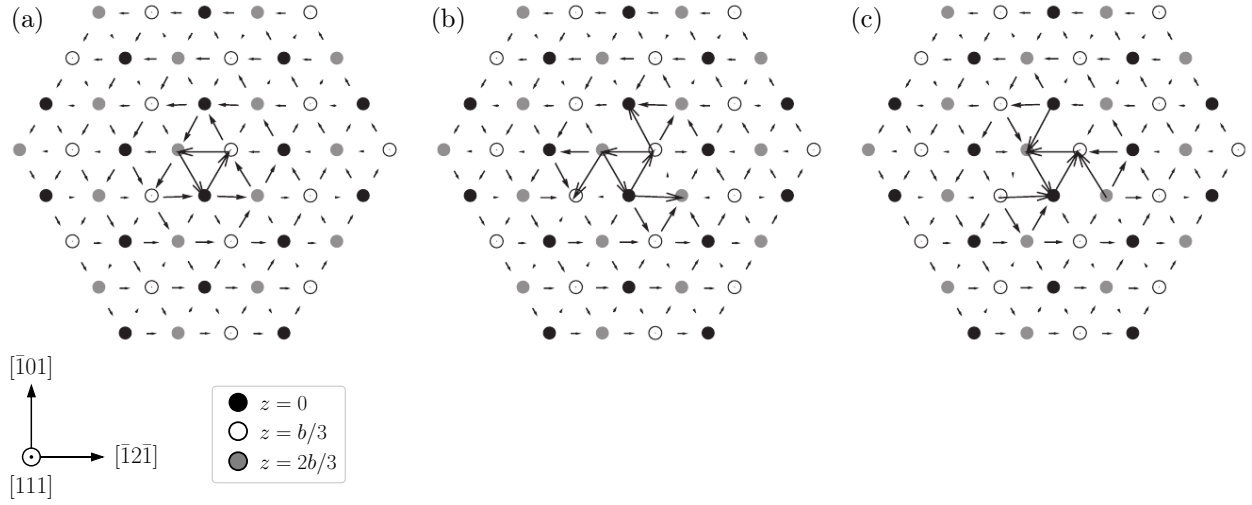


Figure 11: Differential displacement maps showing the core structure of the $\frac{1}{2}\langle 111 \rangle$ screw dislocation in bcc Fe in its (a) non-degenerate, and (b) and (c) two variants of its degenerate configuration obtained with the Dudarev-Derlet EAM potential [48] (reproduced from Ventelon *et al.* [49]). The same conventions as in Fig. 10 are adopted for the representation.

interactions between atoms [65, 66]. These interatomic potentials then allow for an accurate description of the properties of the $\frac{1}{2}\langle 111 \rangle$ screw dislocation in bcc transition metals, and modeling of their plasticity. It is however important to stress that prior to performing any simulation on dislocations using such semi-empirical potentials, one needs to carefully check its computed properties through comparison with *ab initio* calculations, to ensure no such artefact is predicted.

2.1.2. Peierls potential of the $\frac{1}{2}\langle 111 \rangle$ screw dislocation

Apart from the high-symmetry positions presented in Fig. 10, the screw dislocation can take any position in the $\{111\}$ plane orthogonal to its line [67, 68]. Its core energy then depends on its position on the $\{111\}$ plane, yielding a two-dimensional (2D) energy landscape showing minima near stable easy core positions, called Peierls valleys, separated by energy barriers which characterize the low-temperature glide of the $\frac{1}{2}\langle 111 \rangle$ screw dislocation in the crystal. The concept of a 2D Peierls potential was first introduced by Edagawa *et al.* [67, 68], and studied using a model potential, and has since then been evaluated using *ab initio* calculations in all bcc transition metals except Cr in the PhD work of Lucile Dezerald [44]. At equilibrium, the screw dislocation is in its ground state easy core configuration (Fig. 10a) and glides through a thermally-activated process towards an adjacent easy configuration, associated with an energy barrier called the Peierls barrier, presented in Fig. 12a [45]. The Peierls energy barrier shows a single hump, as opposed to the split potentials obtained using interatomic potentials predicting a metastable split core, and passes through a saddle point, presented in Fig. 10d. In addition to the Peierls barrier, the variation of the core energy along the path going from a high-energy hard to split core, presented in Fig. 12b, completes the definition of the 2D Peierls potential, presented for tungsten in Fig. 12c [44], which shows minima for the easy core, primary maxima for the hard core, and secondary maxima located at split core positions.

The Peierls potential is then a direct image of the lattice friction opposing $\frac{1}{2}\langle 111 \rangle$ screw dislocation glide. When a resolved shear stress τ is applied to the Peierls potential, the work of this stress lowers the energy barrier opposing dislocation glide, eventually canceling the Peierls energy barrier and allowing the dislocation to initiate its motion (see Fig. 3). At zero temperature, *i.e.* without thermal activation, this is the Peierls stress τ_P , which corresponds to the maximum slope of the Peierls potential in the $\{110\}$ glide plane of the dislocation:

$$\tau_P = \frac{1}{b} \max_x \left[\frac{\delta V_P(x, y)}{\delta x} \right], \quad (6)$$

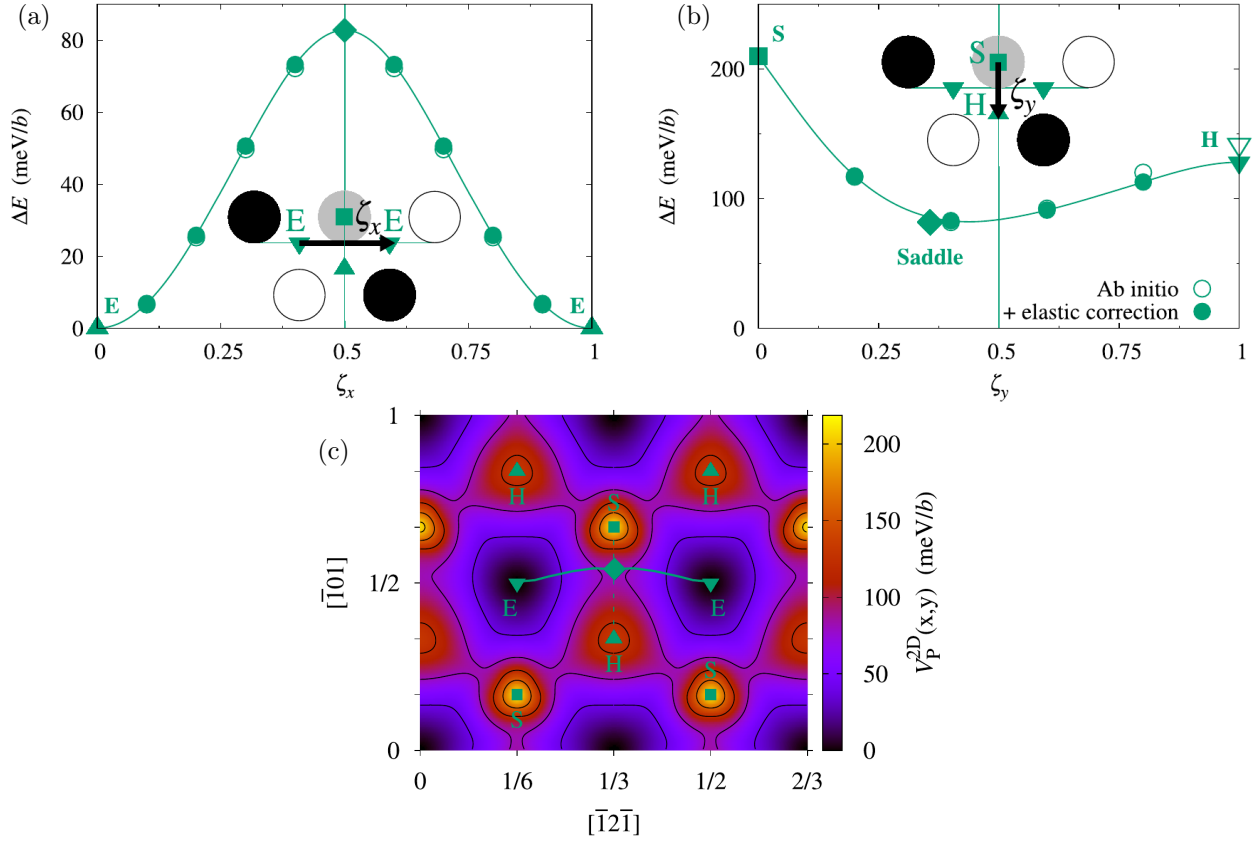


Figure 12: Variation of the $1/2[111]$ screw dislocation core energy in bcc tungsten along (a) the Peierls barrier between two easy configurations, and (b) between hard and split configurations [44]. Both paths are represented in insets, with the corresponding reaction coordinates ξ_x and ξ_y . (c) Two-dimensional (2D) Peierls potential showing the screw dislocation trajectory along the minimum energy paths between two easy configurations in solid line, and between hard and split configurations in dashed line [44]. The saddle point configuration presented in Fig. 10d is shown by a green diamond (reproduced from Ref. [45]).

where $b = a_0\sqrt{3}/2$ is the norm of the $1/2\langle 111 \rangle$ Burgers vector. To predict the plastic behavior of any bcc metal at 0 K under a given mechanical loading, one needs to evaluate the dependence of the Peierls stress on the orientation and sense of the applied stress. A review of *ab initio* calculations focused on explaining the plastic behavior of bcc metals under uniaxial mechanical loading is given in the following section.

2.1.3. Non-Schmid effects: screw dislocation trajectory and relaxation volume

As introduced in section 1, the plastic behavior of bcc metals deviates from the predictions of the Schmid law, both in terms of yield stress and slip activity (see Fig. 8). In particular, the yield stress σ_Y necessary to activate dislocation glide under uniaxial tension is lower when the MRSSP is on the twinning (T) region with $\chi < 0$, than in the antitwinning (AT) region with $\chi > 0$. This T/AT asymmetry has been demonstrated to be a consequence of the trajectory of the $1/2[111]$ screw dislocation in its $\{110\}$ glide plane using *ab initio* calculations by Dezerald *et al.* [69] in all bcc transition metals, except Cr. Indeed, as shown for tungsten in Fig. 12c and presented in more details in Fig. 13a, the trajectory, corresponding to the minimum energy path when the dislocation transits between neighboring equilibrium positions, deviates from the $\{110\}$ macroscopic glide plane towards the split core configuration, which crystallographically always lays in the twinning region, and away from the hard core configuration laying in the antitwinning region. This is also a consequence of the position of the saddle point configuration on the hard-split line of Fig. 12b, which is closer to the split configuration.

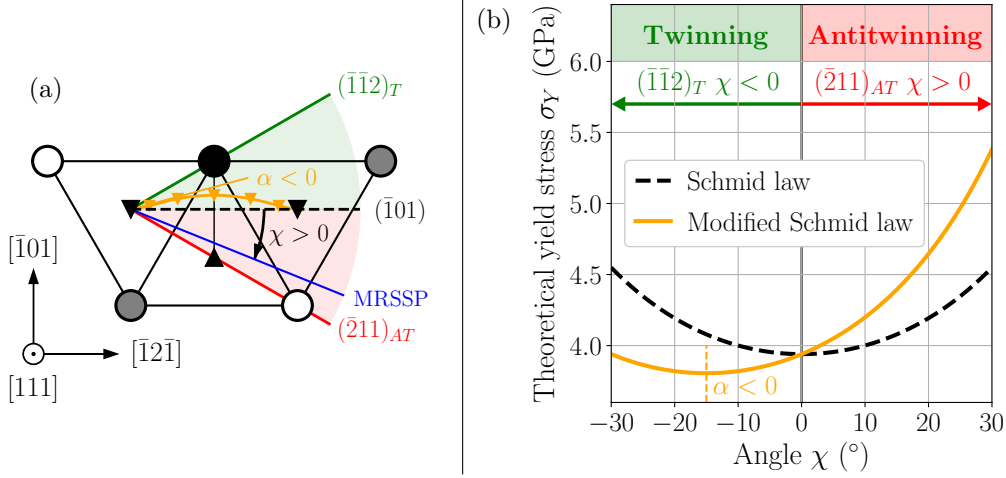


Figure 13: (a) Trajectory of a $1/2[111]$ screw dislocation in bcc tungsten upon crossing of the Peierls barrier between two adjacent easy configurations [45]. The angle α comes tangent to the dislocation trajectory at the inflexion point of the Peierls potential, and the MRSSP is located by its angle χ with the $(\bar{1}01)$ glide plane. (b) Variation of the yield stress σ_Y as a function of the angle χ according to the Schmid law (black dashed line), and including the deviated trajectory (solid orange line).

Therefore, the required stress to activate dislocation glide will be lower when the MRSSP comes tangent to this deviated trajectory, whose amplitude can be directly linked to the amplitude of the T/AT asymmetry through a modification of the Schmid law as follows [69]:

$$\sigma_Y(\chi) = \frac{2\tau_P \cos(\alpha)}{\cos(\chi - \alpha)}, \quad (7)$$

where α is the angle between the screw dislocation trajectory and its $\{110\}$ glide plane (see Fig. 13a). This modified Schmid law now states that a dislocation starts gliding when the stress resolved in the plane tangent to its trajectory exceeds the Peierls stress τ_P , instead of the stress resolved in its $\{110\}$ glide plane for the regular Schmid law (Eq. 5). The lowest yield stress is found for $\chi = \alpha < 0$ in the twinning region and is proportional to the amplitude of this deviation. The corresponding variation of the yield stress with the angle χ is presented in Fig. 13b for tungsten, showing a distinct T/AT asymmetry (orange solid line) with respect to $\chi = 0$ instead of the symmetrical variation predicted by the Schmid law (black dashed line). Values of the Peierls stresses and deviation angles obtained with *ab initio* calculations by Dezerald *et al.* [44, 69] are presented in Tab. 3. All bcc transition metals are presented, except Cr, for which no calculation has been performed because of the added complexity of its magnetic structure.

Table 3: Peierls stress τ_P (GPa) [44] and deviation angle α ($^\circ$) [69] in all bcc transition metals.

	V	Nb	Ta	Cr	Mo	W	Fe
τ_P	1.21	0.89	1.03	/	1.39	2.34	1.45
α	-10.6	-21.7	-7.1	/	-9.9	-10.9	-1.7

The α angle is negative in all bcc transition metals, systematically resulting in an easier twinning sense for $\chi < 0$. This deviation is the largest in Nb, followed by W, V, Mo and Ta with intermediate values, and the lowest in Fe where the trajectory of the $1/2\langle 111 \rangle$ screw dislocation between adjacent Peierls valleys is almost a straight line. This hierarchy between bcc metals is in good agreement with experiments presented in Fig. 8 for Nb, Mo and Fe under uniaxial tension at 4.2 K [30, 35, 36], where the T/AT asymmetry is the most pronounced in Nb, followed by Mo, and almost non-existent in Fe showing a symmetrical

variation of the yield stress with the angle χ . However, we note that the *ab initio* Peierls stresses are well overestimated with respect to the experimental values shown in Fig. 8, which are reported for all bcc transition metals in Tab. A.1 at different temperatures. This discrepancy with experiments is a well-known error of atomistic simulations, whether using *ab initio* calculations [44, 69–71] or semi-empirical potentials [72]. Several mechanisms have been proposed to explain this observation, among which influence of collective dislocation effects [73, 74] and quantum zero-point energy correction [65].

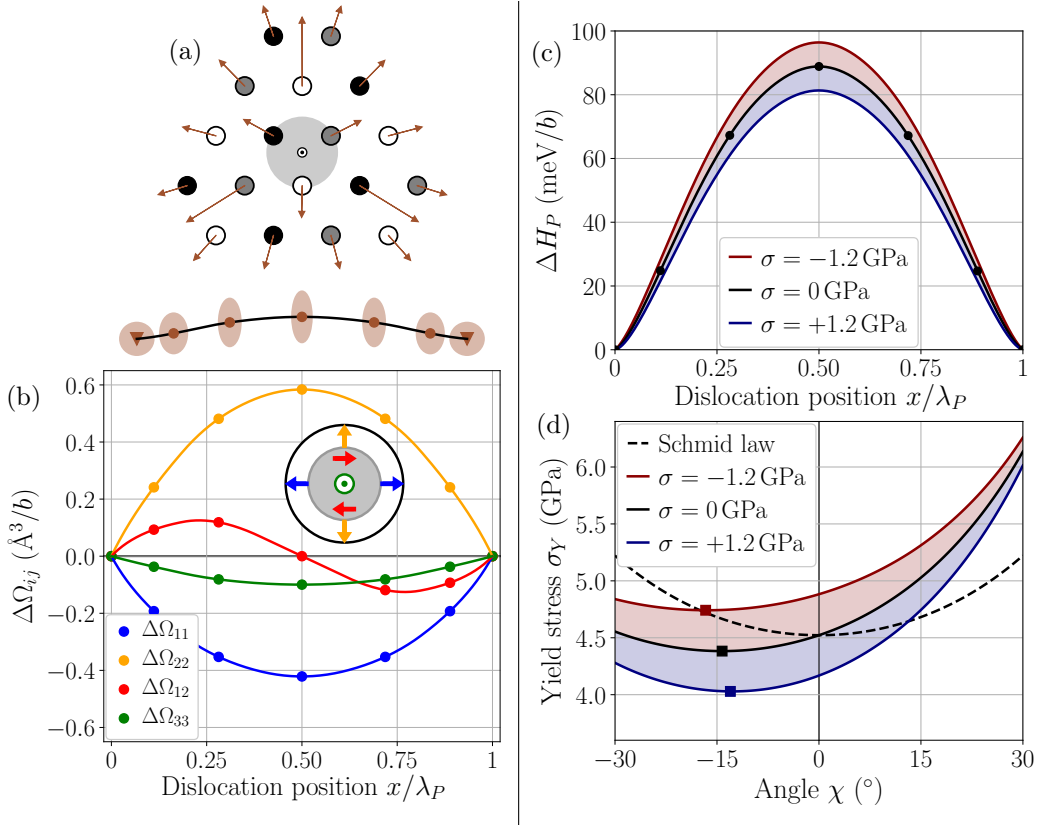


Figure 14: (a) Atomic displacements ($\times 50$) in the (111) plane perpendicular to the dislocation line induced in bcc tungsten by the core of the $1/2[111]$ screw dislocation in its easy core configuration. (b) Variation of the relaxation volume tensor upon crossing of the Peierls barrier as a function of the dislocation position along the glide direction. The shape of the inclusion is sketched in inset. Change in (c) Peierls enthalpy barrier ΔH_P and (d) yield stress σ_Y upon application of a non-glide stress $\sigma = \pm 1.2$ GPa perpendicular to the MRSSP. All figures are adapted from Clouet *et al.* [45].

Ab initio calculations have also shown that the $1/2\langle 111 \rangle$ screw dislocation induces a short-range dilatation field in the plane orthogonal to its line direction, in addition to the Volterra elastic field [75–77]. This additional field has been observed in all bcc transition metals using *ab initio* calculations, and is strongly metal-dependent [44]. It can be visualized in absolute displacements on Fig. 14a for bcc tungsten, showing an edge component of the displacement in the (111) plane perpendicular to the $1/2\langle 111 \rangle$ screw dislocation line in the vicinity of its core. This local dilatation of the lattice caused by the dislocation core is responsible for the dislocation formation volume, evidenced experimentally through an increase of the average lattice parameter with the dislocation density [78]. This core field can be modeled as a 2D Eshelby cylindrical inclusion [79–82] of surface S_0 and associated with an eigenstrain tensor $\bar{\bar{\epsilon}}^*$, the coupling of which with an applied stress is well described by its relaxation volume tensor $\bar{\bar{\Omega}} = S_0 \bar{\bar{\epsilon}}^*$ defined per unit length of dislocation line [45, 79]. When a $1/2\langle 111 \rangle$ screw dislocation lays in a Peierls valley, the three-fold symmetry of the bcc lattice in (111) planes imposes $\bar{\bar{\Omega}}$ to be diagonal. However, upon crossing of the Peierls barrier, the dilatation field loses its high-symmetry and develops non-diagonal components, the variations of which

are presented in Fig. 14b for tungsten [45]. Because of the variations and coupling of the dilatation field with an applied stress, the Peierls enthalpy barrier of the dislocation now becomes sensitive to non-glide stresses, *i.e.* components of the stress tensor which do not produce any net force on the gliding dislocation [45, 79]. This effect is exemplified on Fig. 14c and d for a ideal mechanical loading composed of a shear stress resolved in the MRSSP, and a tension/compression stress σ normal to the MRSSP. When the MRSSP is in tension (compression), *i.e.* $\sigma > 0$ ($\sigma < 0$), both the Peierls enthalpy barrier ΔH_P and the yield stress σ_Y necessary to overcome the barrier decrease (increase). This is a direct consequence of the expansion of the dilatation field in the direction orthogonal to the $\{110\}$ glide plane, *i.e.* $\Delta\Omega_{22} > 0$, and contraction in the glide plane, *i.e.* $\Delta\Omega_{11} < 0$, along the path between two adjacent Peierls valleys. The variation of the dislocation relaxation volume therefore allows to account for the asymmetrical tensile and compressive yield behaviors of bcc metals observed experimentally, with a generally lower yield stress in tension [25, 42, 83].

Ab initio evaluation of non-Schmid effects through the deviated trajectory and variations of the dilatation field of the $1/2\langle 111 \rangle$ screw dislocation was only done in tungsten [79], and has been extended to all bcc transition metals in this work, including Cr for which no *ab initio* data on the properties of dislocations was available. All these physical ingredients can then be integrated in models describing kink-pair nucleation, to account for non-Schmid effects in the prediction of the flow stress of bcc metals with temperature. This approach, based on *ab initio* calculations to provide the required parameters, is detailed in Chapter 2.

2.2. Dislocation-based plasticity using interatomic potentials

As discussed in the previous section, a broad picture of the atomic properties of dislocations in bcc metals can be obtained with the precision of *ab initio* calculations, however limiting the accessible system size to study of isolated straight infinite screw dislocations. To study processes involving long dislocation lines, like kink-pair nucleation and migration [85], interaction between multiple dislocations [74, 86] taking part in the plastic behavior of metals at the macroscopic scale, larger simulation cells are needed to capture these elemental mechanisms occurring at a larger characteristic scale. Common simulation tools for the study of large scale processes, keeping an atomistic resolution, goes through semi-empirical interatomic potentials describing interactions between the atoms of a given system. As stressed in the previous section,

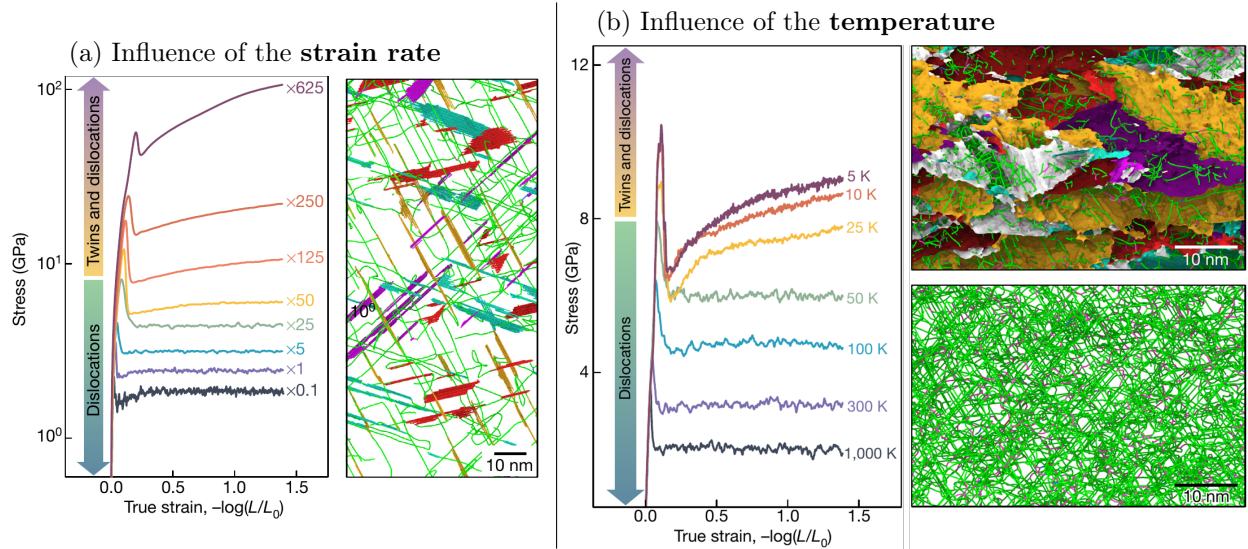


Figure 15: Simulated stress/strain response of a tantalum [001] single crystal to uniaxial compression using molecular dynamics straining simulations at different (a) strain rates taking $\dot{\epsilon} = 1.1 \times 10^7 \text{ s}^{-1}$ as a reference, and (b) temperatures ranging from 5 to 1000 K with $\dot{\epsilon} = 1.1 \times 10^7 \text{ s}^{-1}$. Snapshots of the simulations showing the obtained microstructures are presented on the right of each stress/strain plots, with $1/2\langle 111 \rangle$ and $\langle 100 \rangle$ dislocations represented by green and purple lines respectively, twins appearing as colored planes (reproduced from Zepeda-Ruiz *et al.* [84]).

one needs to carefully choose the potential for studying crystal plasticity to avoid artefacts such as the degenerate core structure of the $\frac{1}{2}\langle 111 \rangle$ screw dislocation in bcc metals. Semi-empirical potentials also allow to study dynamic processes through classical molecular dynamics (MD) simulations, including the effect of temperature or under dynamical straining conditions. Interatomic potentials suited for the study of plasticity have been the focus of many developments, ranging from embedded-atom method (EAM) [65, 66] to machine-learning potentials fitted to DFT data [87, 88]. Studying plasticity of bcc transition metals, one can rely on the modified EAM (MEAM) method [89], which includes the orientational dependence of interactions between atoms. This is not accounted for in standard EAM potentials, and an *a priori* important feature since atomic bonds in transition metals are known to have a strong orientational dependence.

Such interatomic potentials drastically cut computational times with respect to *ab initio* calculations, allowing one to run large-scale MD simulations in order to test the ability of direct atomistic calculations to study dislocation-based plasticity and compare with experiments. Example of MD straining simulations performed on a micrometer cube sample of roughly 400 million atoms are presented in Fig. 15 [84] at different strain rates and temperatures. The simulated stress/strain curves show the characteristic experimental features and reveal complex microstructural evolutions during the simulations. However, the time scales accessible to such atomistic simulations remains of the order of a few nanoseconds, resulting in extreme strain rates ($1.1 \times 10^7 \text{ s}^{-1}$ on Fig. 15 [84], compared to $\simeq 10^{-5} \text{ s}^{-1}$ in experiments on Fig. 9 [41]).

3. The case of chromium

3.1. Magnetic phases of chromium

As will be discussed in the following sections, Cr has an ordered magnetic ground state at low to ambient temperature, the impact of which on its plastic deformation and elasticity is discussed here.

3.1.1. Experimental observations

Neutron diffraction experiments on bulk bcc Cr [90] demonstrated the occurrence of complex magnetic orderings, first thought to be linked to the presence of magnetic domain walls and spirals. Later experiments using both neutron diffraction [91–93] and X-ray scattering [94, 95] established the magnetic ground state of

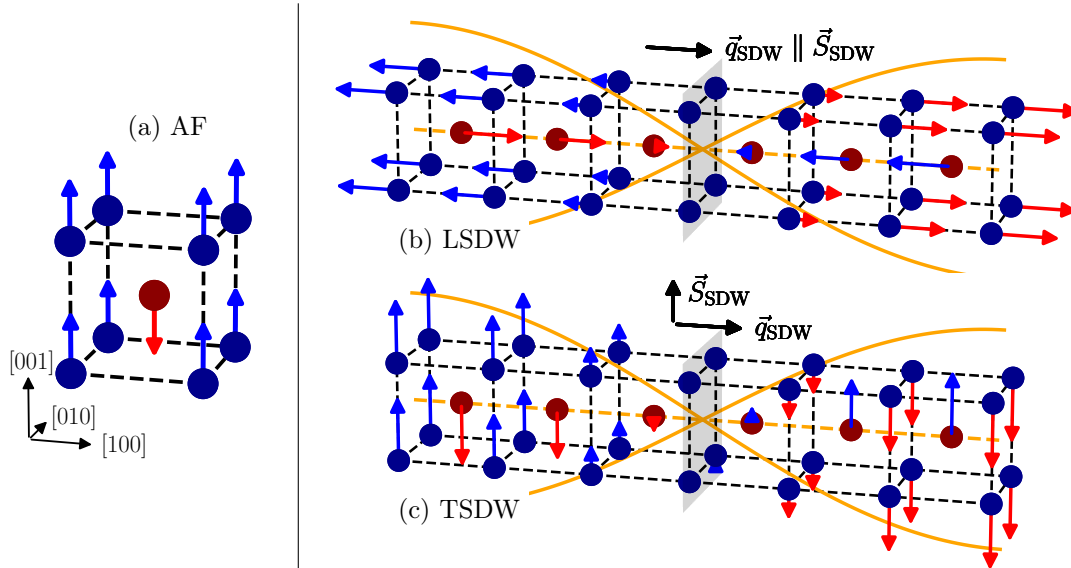


Figure 16: Sketches of the different bulk magnetic phases occurring in bcc Cr at low temperature: (a) antiferromagnetic (AF), (b) longitudinal SDW (LSDW), and (c) transverse SDW (TSDW). The arrows represent the directions and approximate magnitudes of the magnetic moments. The envelope of the magnetic moment modulation along the wave is shown in orange.

Cr at low temperature to be a spin-density wave (SDW), a quasi-sinusoidal modulation of spins magnitude along a $\langle 100 \rangle$ crystal direction with local antiferromagnetic (AF) order, but with incommensurate periodicity of about 20 lattice parameters with respect to the lattice [6]. This complex magnetic phase occurs in bcc Cr below its Néel temperature of 311 K [6, 96], above which the disordered paramagnetic (PM) phase becomes prominent. Below ambient, a magnetic transition has been observed around 120 K [6, 92, 93] corresponding to a change in the polarization of the SDW. At low temperature, the SDW has a longitudinal polarization, with magnetic moments oriented along its direction of propagation (Fig. 16b), before transitioning to a transverse wave, with spins orthogonal to its propagation vector (Fig. 16c) above 120 K, keeping the same incommensurate periodicity with the crystal lattice. This temperature is called the spin-flip transition T_{sf} , and occurs around 200 K below the Néel temperature T_N [6]. The magnetic structure of the SDW is sketched in Fig. 16, showing the longitudinal SDW (LSDW) in b, and transverse SDW (TSDW) in c. Regardless of its polarization, the SDW shares the same local magnetic order as the AF phase shown in Fig. 16a, where atoms located on the two different sub-lattices of the bcc lattice are represented in dark blue and red respectively, which coincide with two orientations of the magnetic moments, namely up \uparrow (blue) and down \downarrow (red) respectively. In the SDW phase, the sinusoidal modulation of the spin magnitudes is responsible for the introduction of a locally zero magnetic moment located halfway along the period of the wave (black shaded $\{100\}$ plane in Figs. 16b and c). On top of the modulation of the magnetic moments of atoms along the wave, the SDW is accompanied with a charge modulation, or charge-density wave (CDW), and also a perturbation of atomic positions, or strain wave [6]. These two waves are characterized by half the period of the SDW and a similar sinusoidal evolution. It has been shown experimentally, also using neutron diffraction, that these three waves are closely linked, the charge and strain waves being a direct consequence of the magnetic modulation [6, 97, 98].

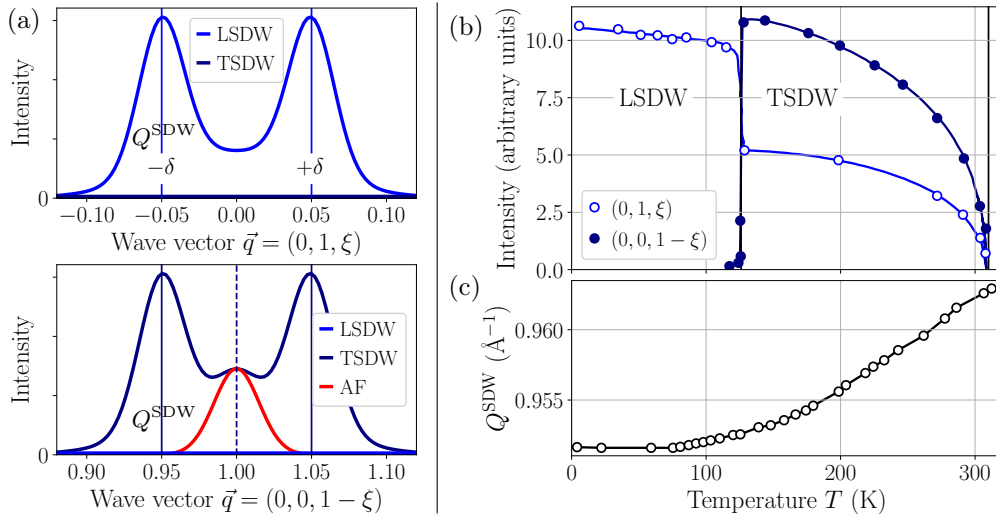


Figure 17: (a) Characteristic neutron scattering pattern for the three LSDW, TSDW and AF phases of bcc Cr for a neutron wave vector \vec{q} along $(0, 1, \xi)$ and $(0, 0, 1 - \xi)$, with δ the shift of the satellite peaks due to the incommensurate scattering of the SDW magnetic order. The temperature dependence of (b) the intensity of the LSDW and TSDW satellite peaks, and (c) the magnitude of the wave vector Q^{SDW} are reproduced from Werner *et al.* [99].

Characteristic patterns obtained through neutron diffraction are presented in Fig. 17a for the two polarizations of the SDW, and the AF order. Neutrons are scattered by the spin structure when their wave vector \vec{q} is orthogonal to the spin order \vec{S} of the sample. Hence, depending on the polarization of the SDW, different characteristic patterns are expected due to the change in orientation of the magnetic moments with respect to the constant wave vector \vec{q}_{SDW} of the SDW. Assuming \vec{q}_{SDW} to be along the $[001]$ direction, neutrons with wave vectors along $(0, 1, \xi)$ will then be scattered by the magnetic order of the sample by the longitudinal SDW only with $\vec{S}_{SDW} \parallel \vec{q}_{SDW}$, and $(0, 0, \xi)$ in the transverse state with $\vec{S}_{SDW} \perp \vec{q}_{SDW}$. If it was for the AF order, a single diffraction peak would appear in the neutron scattering, centered on the $(0, 0, 1)$

direction, since there is no modulation of the spins magnitude, with a commensurate magnetic order. Since the SDW has an incommensurate periodicity with respect to the lattice, neutron scattering patterns show satellite peaks located at $\xi = \pm\delta$. The relative intensity and presence of these two peaks can then be related to the different magnetic orderings inside the crystal. The temperature evolution of the intensity of the two characteristic peaks of the LSDW at $(0, 1, \pm\delta)$ and TSDW at $(0, 0, 1 \pm \delta)$ is presented in Fig. 17b up to the Néel temperature $T_N = 311$ K [99]. Below the spin-flip transition at $T_{sf} = 120$ K, only the LSDW phase is present, with no scattering along $(0, 0, \xi)$. Above T_{sf} the characteristic peak of the TSDW phase becomes prominent, with however a non-negligible peak corresponding to a remanent LSDW order. Both satellite peaks then vanish at the Néel temperature where the disordered PM phase prevails.

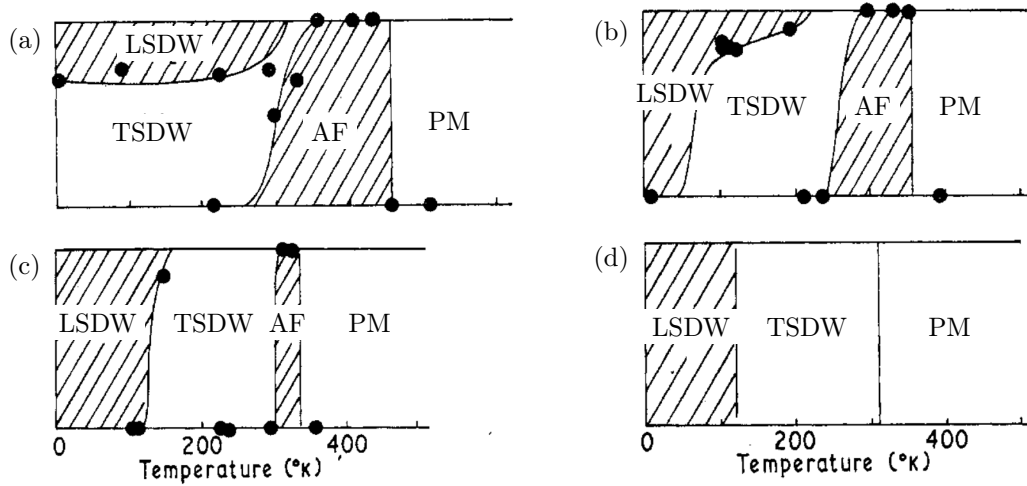


Figure 18: Stability and coexistence of the different ordered magnetic phases of bulk bcc Cr presented in Fig. 16, antiferromagnetic (AF), longitudinal SDW (LSDW), transverse SDW (TSDW) and disordered paramagnetic (PM) as a function of temperature in (a) powder sample, same sample after annealing at (b) 600° C and (c) 1000° C. The ideal case of a perfect monocrystalline sample is shown in (d) (reproduced from Bacon and Cowlam [100]).

Neutron diffraction performed at various temperatures by both Bacon and Cowlam [100] and Williams and Street [101] helped determine how these different magnetic phases coexist and in which proportions. Magnetic phase diagrams showing the relative proportion of the different phases as interpreted by the authors are presented in Fig. 18 considering four different samples. The case of a perfect bulk monocrystalline sample as discussed above is presented in d. The three other diagrams are obtained using the same coarse grain powder sample (with a grain size of approximately 100 μm), before and after annealing at different temperatures. The initial sample is strained due to the fabrication process, and shows a complex ordering of the three magnetic phases presented in Fig. 16 with the occurrence of a region where the simple AF phase prevails from 300 K to the Néel temperature of 450 K, higher by 150 K compared to the monocrystalline case. After annealing at 600° C in b, and then 1000° C in c, the phase diagram tends to the model case presented in d, with a reduced temperature range where the AF phase is present, and a decreasing Néel temperature. This study of Bacon and Cowlam [100] shows how the dislocation density present in a sample influences the occurrence and coexistence of different magnetic structures. Williams *et al.* [101–103] proposed a model based on the dislocation density present in the sample to account for the relative stability and coexistence of the different magnetic phases shown in Fig. 18, assuming the prominent magnetic order to be linked to the representative length scale allowed by the dislocation density.

With increasing temperature, magnetic fluctuations become more and more important, gradually leading to the disappearance of long-range magnetic order in the PM phase, which prevails above the Néel temperature T_N . As shown in Fig. 18, T_N depends on the deformation state of the sample, ranging from 311 K in a perfectly monocrystalline sample up to 450 K for an AF ground state in a strained sample [100, 101]. Neutron diffraction experiments [97, 98, 104] and X-ray photoelectron spectroscopy [105] in this disordered

PM phase demonstrated the persistence of atomic magnetic moment above the Néel transition. Grier *et al.* [98] measured short-range correlations between magnetic moments over 11 bcc unit cells up to a temperature of 700 K, well above T_N , showing magnetic order still exists, in a lesser extent, in this disordered PM phase. The corresponding magnetic scattering are presented in Fig. 19a at 4 different temperatures, from 200 K in the TSDW phase showing the two characteristic satellite peaks, up to 650 K in the disordered PM phase. A measure of the short-range magnetic order as a function of temperature is obtained through the evolution of the intensity and width of the peak in the magnetic scattering centered around $(0, 0, 1)$, corresponding to the AF commensurate order. Both peak intensity and widths as obtained through a Gaussian fit are reported on Fig. 19b, showing a decreasing but non-zero intensity up to approximately 700 K, and a widening of the peak with increasing temperature indicating the weakening magnetic correlations. Ziebeck *et al.* [104] confirmed the persistence of a magnetic moment in Cr far above T_N , with a decreasing characteristic wavelength of the magnetic correlations with increasing temperature. However, the average atomic magnetic moment was reported to be almost independent of temperature and magnetic order. The authors [6, 97, 98, 104] also linked the spin-flip transition between the two polarizations of the SDW and the disappearance of long-range order to magnetic excitations in both the spin magnitude and electronic density.

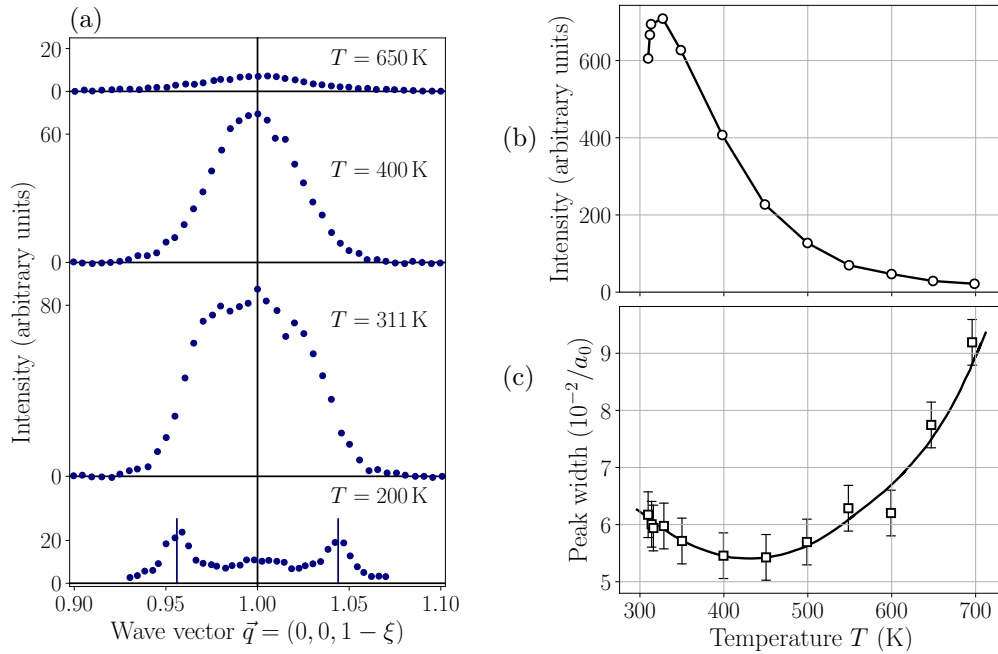


Figure 19: Intensity of the TSDW satellite $(0, 0, Q^{\text{SDW}})$ and AF commensurate $(0, 0, 1)$ neutron scattering peaks at different temperatures from 200 K to well above the Néel temperature of 311 K are presented in (a), with the corresponding peak intensity and width obtained from a fit to a Gaussian function shown in (b) and (c) respectively (reproduced from Grier *et al.* [98]).

3.1.2. Theoretical investigations

Since the experimental confirmation of the low temperature SDW magnetic ground state of bulk bcc Cr, many theoretical works have been focused on explaining the physical origin of such a complex structure. The first investigations of both Overhauser [107] and Lomer *et al.* [108] pointed out that the mechanism responsible of the stabilization of the SDW comes from particular features in the Fermi surface of Cr. The (100)-cut of the theoretical Fermi surface presented in Fig. 20 is composed of electron pockets located close to the center of the Brillouin zone, and hole pockets at the corners. The latter is slightly larger than the electron pocket, resulting in two so-called nesting vectors $\mathbf{Q}_{\pm} = 2\pi/a_0(1 \pm \delta, 0, 0)$ (with $a_0 = 2.884 \text{ \AA}$ [109] the lattice parameter) joining electron and hole pockets. Then, the difference in the size of these two pockets explains the incommensurate character of the SDW. These nesting vectors are linked to the wave vector \vec{q}

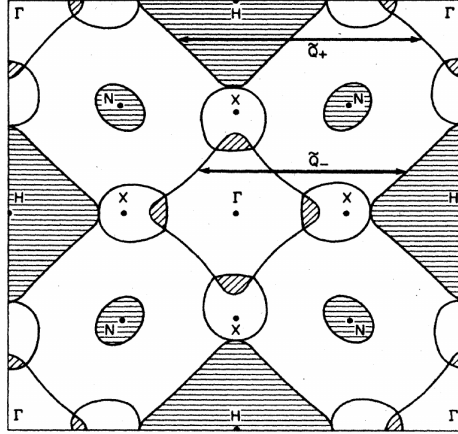


Figure 20: Cut of the Fermi surface of bulk bcc Cr in a (100) plane showing the nesting vectors \mathbf{Q}_+ and \mathbf{Q}_- linked to the wave vector of the SDW $\vec{q} = \mathbf{Q}_+ - \mathbf{Q}_-$ between electron and hole pockets shown by open and dashed surfaces respectively (reproduced from Laurent *et al.* [106]).

of the SDW by the relation $\vec{q} = \mathbf{Q}_+ - \mathbf{Q}_- = 2\pi/a_0(2\delta, 0, 0)$, corresponding to a periodicity of about $20a_0$ at 4.2 K, showing small variations with temperature, as presented in Fig. 17b [99].

The study of the stability of the SDW has then been the focus of great simulation efforts, using different electronic structure calculations to explain the origin of its stability. Due to the periodic boundary conditions in simulation cells used for the study of the SDW, it is impossible to consider the experimental incommensurate wave, but commensurate waves are studied instead. However, DFT calculations have systematically failed to reproduce the SDW magnetic phase as the ground state of bcc Cr at 0 K. All calculations performed either within the KKR scheme [110, 111] or using different approximations and exchange and correlation functionals within DFT [112–115] invariably found the AF phase to have a lower energy than the SDW. These discrepancies with experiments have been blamed on the impossibility to account for the incommensurability of the SDW [115], which could not be confirmed due to the inner limitations of these calculations. Another possible explanation is the influence of the polarization of the SDW on its stability. Soulaïrol *et al.* [113] performed DFT calculations using non-collinear magnetism and spin-orbit coupling, both necessary to account for the two polarizations, in order to investigate the influence of the polarization of the wave on its stability. Their study concluded that regardless of the approximations used, the energy difference between the transverse and longitudinal SDW falls within DFT accuracy, still having a higher energy than the AF phase, and therefore invalidating such hypothesis. However, the authors stress that the energy difference between the AF and SDW phases is very low, of a few meV/atom, whereas switching off magnetism to study the non-magnetic (NM) phase reveals an energy difference ten times higher with respect to the AF ground state [112–115]. Therefore, it appears that no standard DFT calculations can properly describe the electronic structure of Cr to effectively predict the incommensurate SDW as its low temperature ground state, nor explain its physical origin. Nevertheless, proper incorporation of electronic correlations in the frame of a Hubbard model showed the incommensurate SDW can arise spontaneously as a result of a strong spin-orbit coupling [116].

3.2. Elastic properties of chromium

The occurrence of different magnetic phases in bulk bcc Cr can impact other bulk properties of the material. The influence of the magnetic state on the elastic properties of Cr has been investigated in numerous experimental studies [16, 109, 117–120], mostly as a function of temperature. The three independent C_{11} , C_{12} , and C_{44} elastic constants of bcc Cr are presented in Fig. 21 as a function of temperature with experimental data of Palmer and Lee [109] measured on monocrystalline samples. The SDW magnetic phase has a tetragonal symmetry, corresponding to 6 independent elastic constants, where a regular bcc crystal requires

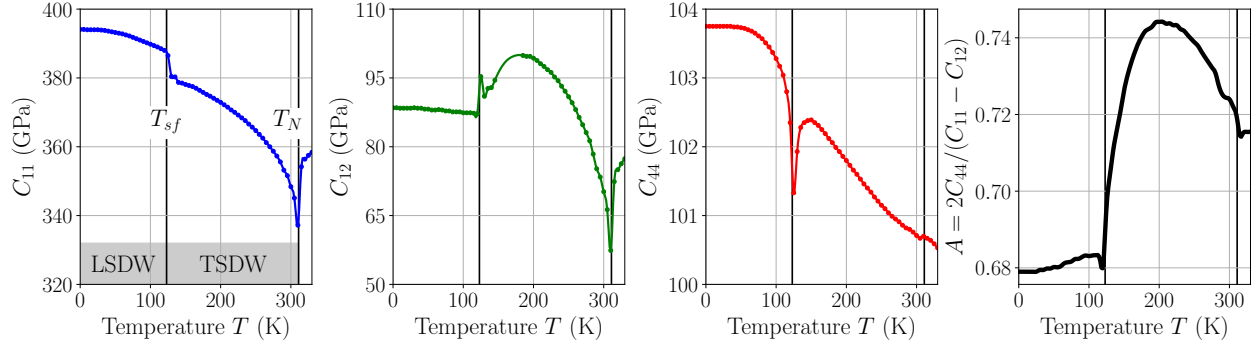


Figure 21: Elastic constants C_{ij} (in GPa) and anisotropy A of bulk bcc Cr from 0 K to above the Néel temperature $T_N = 311$ K, showing the spin flip transition at $T_{sf} = 123$ K from the longitudinal (LSDW) to the transverse (TSDW) polarizations of the SDW. Data are taken from Palmer and Lee [109] and were measured on monocrystalline samples.

3 independent constants. However, the tetragonal elastic anisotropy of the SDW is small, thus elastic constants are presented with cubic symmetry, an average of the three possible $\langle 100 \rangle$ orientations of the SDW contained in the test material. The two transition temperatures $T_{sf} = 123$ K and $T_N = 311$ K are marked by vertical lines, which are associated with an abrupt change in the elastic constants. This observation was also reported on experimental measurements of the specific heat [102] and electrical resistivity [103], *a priori* indicating a strong impact of magnetism on bulk properties. The dependence of the elastic properties of bcc Cr on its magnetic phase can then influence the elastic behavior of dislocations when investigating the plastic deformation of bcc Cr. In particular, the elastic anisotropy A shows a slight increase in the temperature range between T_{sf} and T_N , which has an impact on both the formation of dislocation junctions, and the ratio between elastic energies of dislocations having different Burgers vectors, discussed in the following.

3.3. Plasticity of chromium

As a bcc metal, the plastic deformation of Cr at low temperature is *a priori* governed by screw dislocations gliding in close-packed $\{110\}$ crystallographic planes. This motion is difficult and requires thermal activation to ease plastic deformation, a phenomenon responsible for the brittleness of Cr at low temperature [7, 8, 121]. Presence of $1/2\langle 111 \rangle$ screw dislocations have been observed by TEM in strained Cr polycrystals [13, 122, 123] at temperatures where its magnetic order prevails, below its Néel temperature T_N of 311 K. Analysis of slip traces confirmed that these dislocations glide in the expected $\{110\}$ planes [13, 122, 124], with glide in $\{112\}$ and $\{123\}$ planes also observed at higher temperatures [122, 125]. These features are common to plasticity of all bcc transition metals, showing that bcc Cr has *a priori* a standard plastic behavior. Among the seven pure bcc transition metals, Cr shows one the highest yield stress under uniaxial loading, ranging from 780 to 1 200 MPa [34, 126] (see Tab. A.1 in Appendix A). The ductile-brittle transition temperature of bcc Cr, corresponding approximately to the athermal temperature of the Peierls mechanism [42], is also high compared to other bcc metals, ranging from 400 to 600 K, or 0.18 to 0.28 T_{melt} in homologous temperature, depending on the loading conditions [8, 126].

Like all other bcc transition metals, dislocations responsible for their plastic deformation have a Burgers vector equal to the smallest periodicity vector of the bcc lattice, which is $1/2\langle 111 \rangle$, minimizing its elastic energy. A sketch of the bcc unit cell is presented in Fig. 24a showing this Burgers vector in orange. However, the magnetic ground state of bcc Cr is close to antiferromagnetic at low temperature, and the smallest $1/2\langle 111 \rangle$ Burgers vector does not correspond to a periodicity vector of the magnetic order. Hence, when the crystal is sheared by such dislocations, magnetic faults should be generated in their glide planes, possibly impeding the motion of these line-defects. These faults need to be closed by another topological defect, *a priori* pairing two $1/2\langle 111 \rangle$ dislocations separated by a magnetic fault, similar to a magnetic domain wall. This effect was predicted by Marcinkowski and Lipsitt [126] and should be responsible for a strengthening due to the added resistance of the magnetic fault $1/2\langle 111 \rangle$ dislocations are forced to drag behind them. To

quantify the magnitude of this effect, which is proportional to the energy of the created domains, the authors measured the yield stress slightly below and above the Néel temperature. The authors finally reported no such antiferromagnetic strengthening in this temperature range, probably because of the low energy of the magnetic domain walls close to the transition to the PM phase, linked to the disappearance of the long-range magnetic order.

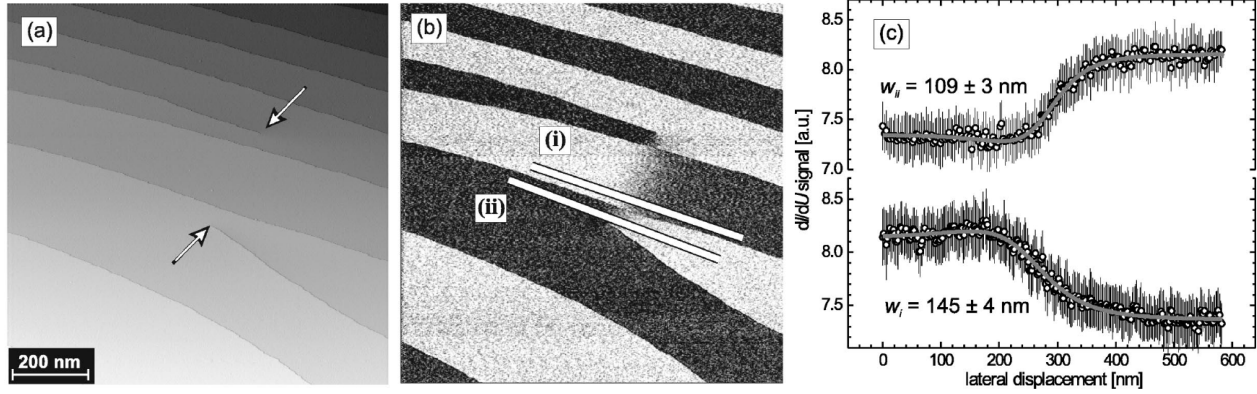


Figure 22: Observation of a Cr(100) surface with two screw dislocations (white arrows in a) in spin-polarized scanning tunneling microscopy. The topology of the surface is shown in (a), and (b) shows the contrast in magnetic signal dI/dU , a cut line of the surface is presented in (c) along the white lines in (b). The figure has been extracted from Ravlić *et al.* [127].

Regarding the disruption of the magnetic order, both Ravlić *et al.* [127] and Kleiber *et al.* [128] reported the existence of AF magnetic domains at Cr{100} surfaces separated by walls using spin-polarized scanning tunneling microscopy at room temperature, very close to the Néel temperature T_N . These walls are monoatomic steps with a height equal to one half of the lattice parameter a_0 . Some of them are not entirely closed, suggesting the presence of dislocations going through the {100} surfaces and bounding the magnetic fault defined by the domain walls. Given the height of the observed steps, these dislocations have *a priori* a $1/2\langle 111 \rangle$ Burgers vector, whose projection on a {100} surface would indeed give a step of $a_0/2$. The authors estimated the width of such walls to 120 nm at room temperature [127, 128], close to the disappearance of the long-range magnetic order, and hence where the energy of such domain walls should quickly fall to zero. An example of a magnetic fault bounded by two dislocations observed by Ravlić *et al.* [127] is presented in Fig. 22, showing two $1/2\langle 111 \rangle$ screw dislocations bounding a fault visualized by magnetic contrast.

In addition to these $1/2\langle 111 \rangle$ dislocations, TEM observations reveal the presence of dislocations having the slightly longer Burgers vector $\langle 100 \rangle$ (Fig. 24a) in magnetically ordered Cr [13, 122, 123]. Reid and Gilbert [13] reported a cross-slip event at room temperature incompatible with a $1/2\langle 111 \rangle$ dislocation. As intersections between the primary and the cross-slipped {110} planes were along $\langle 100 \rangle$ and not $\langle 111 \rangle$ directions, this observation clearly indicates slip activity of these $\langle 100 \rangle$ dislocations in bcc Cr, with an ability to cross-slip at ambient temperature. Presence of these $\langle 100 \rangle$ dislocations was also confirmed by Hale and Henderson Brown [123] through determination of the Burgers vectors of dislocations using extinction experiments ($\vec{g} \cdot \vec{b} = 0$ contrast). Although these $\langle 100 \rangle$ dislocations have a larger Burgers vector than $1/2\langle 111 \rangle$ dislocations, both have close elastic energy as a consequence of the anisotropy of the elastic constants of bcc Cr [129]. Its strong elastic anisotropy, with a ratio $A = 2C_{44}/(C_{11} - C_{12})$ smaller than 1 ($A \simeq 0.68$ using elastic constants measured at 4.2 K [109]), $\langle 100 \rangle$ and $1/2\langle 111 \rangle$ screw dislocations have in fact comparable elastic energies (see Fig. 23). As presented in Fig. 21, the elastic constants of bcc Cr show discontinuities at the spin-flip T_{sf} and Néel T_N temperatures, with *a priori* an effect on the elastic energy difference between the two Burgers vectors. The effect of temperature on their elastic energies is shown in Fig. 23b for this character only, with the corresponding ratio between the prefactors to the elastic energies $e_{screw}^{1/2\langle 111 \rangle}$ and $e_{screw}^{(100)}$ for both Burgers vectors. Looking at their close energies, regardless of the temperature, there is thus no valid physical argument to discard *a priori* these $\langle 100 \rangle$ dislocations when rationalizing plasticity of bcc Cr.

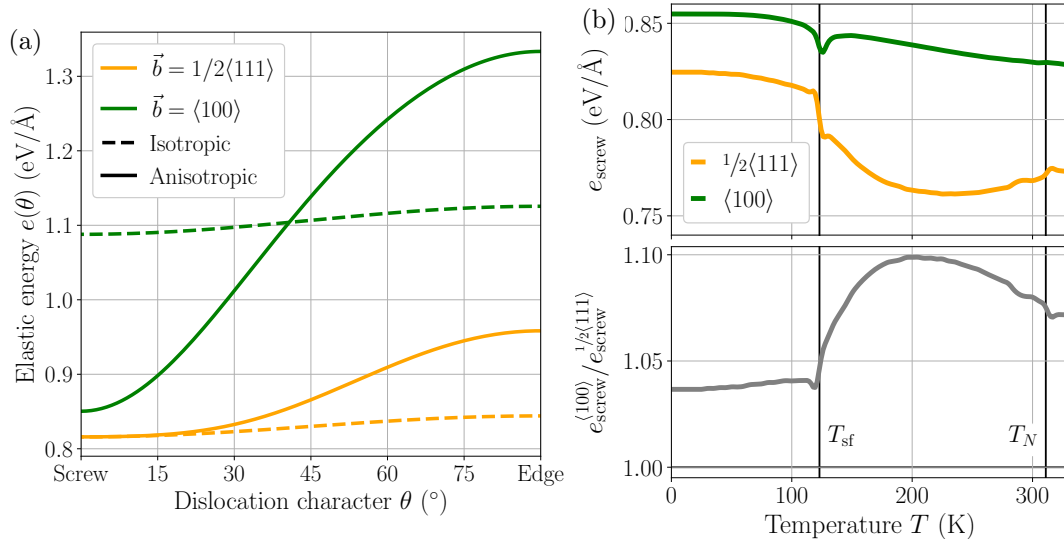


Figure 23: (a) Prefactor e to the elastic energy of $1/2\langle 111 \rangle$ and $\langle 100 \rangle$ dislocations as a function of their character θ using the elastic constants of Palmer and Lee at 4.2 K [109]. (b) Prefactor e_{screw} to the elastic energy of $1/2\langle 111 \rangle$ and $\langle 100 \rangle$ screw dislocations, and ratio between them, as a function of the temperature T using the elastic constants presented in Fig. 21.

Magnetic ordering of Cr at low temperature gives another argument in favor of these $\langle 100 \rangle$ dislocations: as $\langle 100 \rangle$ is a periodicity vector of the magnetic order below the Néel temperature, such dislocations can exist without generating magnetic faults, in contrast to $1/2\langle 111 \rangle$ dislocations (see Fig. 24a).

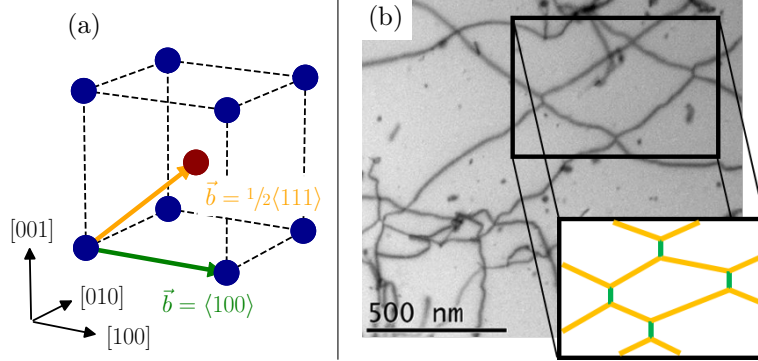


Figure 24: (a) Unit cell of the bcc lattice showing the two $1/2\langle 111 \rangle$ and $\langle 100 \rangle$ Burgers vectors. Atoms are represented in different colors according to the sign of their magnetic moments in bcc Cr (see Fig. 16). (b) Bright field STEM image showing a dislocation network lying in the $(0\bar{1}1)$ foil plane (adapted from Holzer *et al.* [34]).

The existence of such $\langle 100 \rangle$ dislocations have been observed in most bcc metals at the intersection between two $1/2\langle 111 \rangle$ dislocations, the sum of their Burgers vectors resulting in a $\langle 100 \rangle$ junction, a reaction driven by elasticity [9]. These junctions have been observed in Cr recently by TEM in compressed single crystals at 77 K by Holzer *et al.* [34], and is presented in Fig. 24b. Despite their presence, the authors did not report activity of $\langle 100 \rangle$ dislocations gliding in $\{110\}$ planes for the compression axis they investigated at 77 K. However, as opposed to the variety of experimental and theoretical works focused on its magnetic properties, very little is known about the plastic deformation of bcc Cr, and the comparison with other bcc transition metals still has to be addressed to conclude on whether it has a similar behavior or not. The recent study of Holzer *et al.* [34] coupled compression experiments with atomistic simulations using a non-magnetic bond-order potential developed by Lin *et al.* [130], which has also been used by Gröger and

Vitek [131] to study non-Schmid effects. These studies concluded on a standard low temperature plastic behavior compared to other bcc transition metals, however omitting the impact of magnetism, which should *a priori* have a non-negligible contribution to the plasticity of bcc Cr. A yield criterion for bcc Cr subjected to a uniaxial test has been developed by Gröger and Vitek [131] based on a modeling of $\frac{1}{2}\langle 111 \rangle$ dislocations using a non-magnetic bond-order potential (BOP). The authors report deviations from the Schmid law in terms of T/AT and tension/compression asymmetries, as observed in all other bcc transition metals using similar potentials. The same interatomic potential has also been used in the experimental work of Holzer *et al.* [34], focusing on explaining their observation of anomalous slip traces in specimens compressed at 77 K in terms of motion of dislocation networks such as presented in Fig. 24b.

In conclusion, the plastic deformation of bcc Cr has been the focus of very few experimental and simulation works compared to other bcc transition metals, therefore not allowing to conclude on the similitudes and differences existing between plasticity of Cr and other bcc transition metals. The experimental review presented in this section shows an *a priori* standard behavior of Cr, with motion of screw dislocations at low temperature. The impact of magnetism on the plastic deformation of bcc Cr still has to be addressed since most simulation works have been carried out without considering its AF order [34, 131], possibly having a strong impact on properties of dislocations. Indeed, both the disruption of the AF order by the $\frac{1}{2}\langle 111 \rangle$ Burgers vector and elastic properties of dislocations must be studied with a proper description of magnetism, since for instance a change in the elastic constants is observed depending on which magnetic phase is prevailing as shown in Fig. 21.

Summary of the Literature review:

- The plastic deformation of bcc metals is controlled by the motion of $\frac{1}{2}\langle 111 \rangle$ screw dislocations in the crystal due to the strong lattice friction they experience compared to other line orientations. Motion of screw dislocations is a thermally activated process operating through nucleation and migration of highly mobile non-screw segments along their line. Lattice friction experienced by dislocations vanishes at the athermal temperature of the Peierls mechanism.
 - The yield behavior of bcc metals at low temperature shows deviations from the Schmid law, with defined twinning/antitwinning and tension/compression asymmetries also affecting slip activity. Anomalous slip in low-stressed $\{110\}$ glide planes is also reported experimentally.
 - *Ab initio* calculations on the $\frac{1}{2}\langle 111 \rangle$ screw dislocation have demonstrated its compact core structure, and a mapping of its core energy as a function of its position in the (111) plane, the Peierls potential, quantifies the lattice friction it is subjected to when shearing the crystal. The trajectory and variations of the dislocation relaxation volume upon crossing of the Peierls barrier are linked to the twinning/antitwinning and tension/compression asymmetries observed experimentally.
 - Among all bcc transition metals, chromium is the only one with an ordered magnetic ground state close to AF order below ambient, with sinusoidal modulation of magnetic moments in the form of a SDW. Despite thorough theoretical investigations, the AF phase is predicted to have a lower energy than the SDW by *ab initio* DFT calculations.
 - Plasticity of chromium shows the characteristic features shared by all bcc metals, with a viscous glide of $\frac{1}{2}\langle 111 \rangle$, but also $\langle 100 \rangle$, dislocations, both in $\{110\}$ planes. The disruption of its AF order by the $\frac{1}{2}\langle 111 \rangle$ Burgers vector should generate magnetic faults upon shearing the crystal.
-

Aim of the present work: The aim of the present work is to gain insights on the properties and mobility of dislocations in chromium using atomistic simulations. Comparison of the obtained properties with other bcc transition metals will then help assess if chromium has a standard plastic behavior, for which the validity of the approach can be measured through comparison to experimental data. The following points will then be addressed in the present work:

- Quantify the influence of magnetism at both zero and finite temperature on the properties of dislocations in bcc chromium, including both $\frac{1}{2}\langle 111 \rangle$ and $\langle 100 \rangle$ Burgers vectors reported experimentally.
 - Develop a yield criterion based on *ab initio* properties of screw dislocations across all bcc transition metals, including non-Schmid effects. The ability of the model to compare with experimental data can then be used to assess the validity of the approach in chromium.
 - Investigate with atomistic simulations a new mechanism explaining anomalous slip based on *in situ* TEM observations in niobium. Such results can then be extended to other bcc transition metals where anomalous slip has been reported experimentally, including chromium.
 - Study the properties of $\langle 100 \rangle$ dislocations in all bcc transition metals using both *ab initio* calculations and interatomic potentials to get insights on their mobility, and conclude on whether chromium has a particularity explaining experimental observation and motion of such dislocations.
-

Methods

We give in this section a detailed review of all methods which were used in this work to obtain all results presented in the following chapters. References to the different techniques presented in this section will then be made accordingly in the following chapters without further details.

1. Energetic models

We begin this methods section by giving a review of the energetic models used to describe atomic systems of interest in the present work.

1.1. *Ab initio* density functional theory calculations

Ab initio or first principles calculations, are a class of simulation methods which include explicitly the electronic structure of atoms to evaluate the energy of a given system, based on the resolution of Schrödinger's equation, with no prior adjustment required. This section focuses on density functional theory (DFT), a first principles method to solve Schrödinger's equation under approximations detailed in the following.

1.1.1. Solving Schrödinger's equation

The aim of *ab initio* methods is to solve time-independent Schrödinger's equation:

$$\mathcal{H}\psi = E\psi, \quad (1)$$

where E and ψ are the total energy and the wave function of the system, and \mathcal{H} is the Hamiltonian, which is written as the sum of the following components:

$$\mathcal{H} = T_e + T_n + V_{ee} + V_{nn} + V_{en}, \quad (2)$$

where T_e and T_n are the kinetic energies of electrons and nuclei respectively, while V_{ij} are the potential energies corresponding to electron-electron (V_{ee}), nucleus-nucleus (V_{nn}), and electron-nucleus (V_{en}) Coulomb interactions. A common approximation for solving Schrödinger's equation in the frame of DFT is the Born-Oppenheimer approximation, under which nuclei are considered immobile or "frozen" due to their high mass compared to the one of electrons. Their kinetic energy T_n is then zero, and the interaction term V_{nn} is constant, equal to E_{nn} . Under this approximation, the system of N electrons at positions $\{\mathbf{r}_i\}_{i \in [1, N]}$ has the following Hamiltonian in reduced units:

$$\mathcal{H} = -\frac{1}{2} \sum_{i=1}^N \frac{\delta^2}{\delta \mathbf{r}^2} + \cancel{\mathcal{T}_n} + \sum_{i>j}^N \frac{1}{|\mathbf{r}_i - \mathbf{r}_j|} + E_{nn} + \sum_{i=1}^N v(\mathbf{r}_i), \quad (3)$$

where the first term of the above Hamiltonian is the kinetic energy T_e of the electrons, and the second and last terms are Coulomb interaction potentials acting between electrons V_{ee} , and electrons and nuclei V_{en} respectively. This is the complete form of the Hamiltonian of the Schrödinger's equation for any system under the Born-Oppenheimer adiabaticity approximation. An exact resolution of Schrödinger's equation for systems made of more than two electrons is not possible due to the Coulombian repulsion term V_{ee} . To be able to study more complex systems, some approximations are needed to solve Eq. 1, which are developed in the following sections in the frame of DFT calculations.

1.1.2. Density functional theory

Resolution of Schrödinger's equation in the frame of DFT, as introduced by Hohenberg and Kohn [132], states that the total energy E of the system is a functional of the electronic density $\rho(r)$, and its ground state energy is obtained by minimizing this functional. Since the kinetic energy of an interacting electron gas is unknown, Kohn and Sham [133] proposed a different formulation of the N -body problem (Eq. 3), which is replaced by a system of N independent particles interacting with an external potential V_{ext} , which

is a function of a single variable, the electronic density $\rho(r)$. The problem is then expressed as a system of N single-electron equations, with wave functions ψ_i , called Kohn-Sham states:

$$\mathcal{H}\psi_i = \epsilon_i\psi_i = -\frac{\Delta}{2}\psi_i + V_{\text{ext}}\psi_i, \quad (4)$$

with ϵ_i the eigenvalues of each independent single-electron system of wave function ψ_i . The electronic density $\rho(r)$ of the system is then obtained through a sum over all subsystems, as:

$$\rho(r) = \sum_{i=1}^N |\psi_i|^2, \quad (5)$$

The energy E of the N -independent particles system is expressed in functional form as:

$$E[\rho] = \int V_{\text{ext}}(r)\rho(r)dr + T_e[\rho] + V_H[\rho] + E_{\text{exc}}[\rho], \quad (6)$$

with V_{ext} the external potential energy (*e.g.* Coulomb electron-nuclei interactions), T_e the kinetic energy of the isolated electron, V_H the Coulomb interaction between electronic densities at two different positions r and r' , or the Hartree potential, given by:

$$V_H[\rho] = \frac{1}{2} \int \frac{\rho(r)\rho(r')}{|r - r'|} d^3r d^3r', \quad (7)$$

and E_{exc} is the exchange and correlation functional, which is unknown and needs to be approximated as will be discussed in the following section. To determine the ground state of the system, DFT calculations aim at minimizing Eq. 6 with respect to the electronic density ρ through a self-consistent scheme. A starting density ρ_0 is set, allowing for a new evaluation of the electronic density and energy of the system using Eqs. 5 and 6 respectively, and repeating this process until convergence of the energy E is reached, and the electronic density then corresponds to the ground state of the system. A convergence criterion on E thus needs to be chosen, under which the self-consistent step on the electronic density is stopped, which in this work is set to a 10^{-6} eV energy difference between two consecutive steps.

From the derivatives of the total energy with respect to atomic positions, the forces acting on each atom can be deduced when convergence on the energy is reached at the end of each electronic step. Minimization of these forces then allows to find the equilibrium structure of a system, which is achieved self-consistently as well, thus starting new electronic steps at each force evaluation until convergence is met. The stopping criterion for atomic relaxation is set on all forces acting on each atom of the system to be less than $5 \text{ eV}/\text{\AA}$ in all Cartesian directions. The stress on the simulation cell is then obtained through the derivative of the atomic forces when the equilibrium structure is found.

1.1.3. Exchange and correlation functional

Two types of exchange and correlation functionals to describe E_{exc} in Eq. 6 are widely used depending on the system and properties of interest:

- *Local density approximation (LDA)*: Assuming the electronic density ρ of the system to have very little variations in space, the exchange and correlation functional can be expressed as a local term:

$$E_{\text{exc}}^{\text{LDA}}[\rho] = \int \rho(r)\epsilon_{\text{exc}}(\rho(r)) dr, \quad (8)$$

where ϵ_{exc} is the exchange and correlation energy density of a uniform electron gas with electronic density ρ , which is evaluated using quantum Monte Carlo simulations. The effective Kohn-Sham potential of Eq. 6 can then be expressed as the sum between the external potential V_{ext} , the Hartree potential V_H and the exchange and correlation potential $\mu_{\text{exc}} = \delta E/\delta\rho$;

- *Generalized gradient approximation (GGA)*: Given that the electronic density is far from homogeneous in most systems, one can also choose to account for its variations in space by expressing the exchange and correlation energy as a function of the electronic density ρ and its gradient $\nabla\rho$ as:

$$E_{\text{exc}}^{\text{GGA}}[\rho] = \int \rho(r) \epsilon_{\text{exc}}(\rho(r), \nabla\rho(r)) dr \quad (9)$$

As opposed to the LDA, evaluation of the $\epsilon_{\text{exc}}(\rho(r), \nabla\rho(r))$ term in the frame of the GGA approximation has different formulations, among which the one of Perdew, Burke and Ernzerhof (PBE) [134] used for all *ab initio* calculations performed in this work.

The choice of the GGA over the LDA approximation strongly depends on the properties of interest, which is motivated here by a better agreement with experiments than the LDA in terms of the predicted lattice parameter and elastic constants of most body-centered cubic transition metals. Other forms for the exchange and correlation functionals are available, including hybrid formulations, and allowing for a better inclusion of electronic correlations, but coming at a higher computational cost.

1.1.4. Pseudo potential approximation

In an attempt to reduce the computational cost of DFT calculations for systems containing a high number of electrons, atoms are modeled with a so-called pseudo-potential (PP). These calculations only include a fraction of the total electrons of a given atomic species, namely valence electrons. Core electrons, strongly anchored to the nuclei, do not participate to the formation of chemical bonds, and hence can be neglected when one is interested in computing structural properties of a solid. Additionally, the potential created by core electrons has fast oscillations, resulting in a high computational cost to include them. The purpose of the PP approach is then to replace both nuclei and core electrons (contained in a sphere of radius r_c) by an approximated, softer potential, mimicking the potential they both exercise on valence electrons.

In practice, three different methods are commonly used for constructing a PP, namely:

- *Norm-conserving (NC)*: both eigenvalues and wave-functions outside the sphere of radius r_c are equal to the full-electron calculation, and the charge is equal inside the same sphere. This method ensures the norm of wave-function obtained is the same as would be obtained from a full-electron calculation;
- *Ultra-soft (US)*: same method as for the norm-conserving PPs, but the potential inside the sphere is even softer, and the condition on the charge is not enforced anymore;
- *Projector-augmented wave (PAW)*: the wave-function outside the core sphere is the same as the full-electron calculation, like for the two other methods. The pseudo wave-function inside the sphere is obtained from applying a linear transformation to the full-electron wave-function, so one can recover the full-electron wave-function at any time. This method is more robust than the two others, but can be more expensive.

All *ab initio* DFT calculations presented in this work are performed using the PAW method, including semi-core electrons, *i.e.* electrons which are not explicitly in the outer valence band are considered as valence

Table 1: Period, group and electronic configuration of the seven bcc transition metals. Core electrons are indicated between brackets, while valence electrons are outside the brackets. Semi-core electrons are indicated in red, with the corresponding number N of valence electrons included in the DFT calculations for each element.

Element	Period	Group	N	Electronic configuration
V	4	V	13	$[1s^2 2s^2 2p^6 3s^2 3p^6] 3d^3 4s^2$
Cr	4	VI	12	$[1s^2 2s^2 2p^6 3s^2 3p^6] 3d^5 4s^1$
Fe	4	VIII	16	$[1s^2 2s^2 2p^6 3s^2 3p^6] 3d^6 4s^2$
Nb	5	V	13	$[1s^2 2s^2 2p^6 3s^2 3p^6 3d^{10} 4s^2 4p^6] 4d^4 5s^1$
Mo	5	VI	12	$[1s^2 2s^2 2p^6 3s^2 3p^6 3d^{10} 4s^2 4p^6] 4d^5 5s^1$
Ta	6	V	11	$[1s^2 2s^2 2p^6 3s^2 3p^6 3d^{10} 4s^2 4p^6 4d^{10} 4f^{14} 5s^2 5p^6] 5d^3 6s^2$
W	6	VI	14	$[1s^2 2s^2 2p^6 3s^2 3p^6 3d^{10} 4s^2 4p^6 4d^{10} 4f^{14} 5s^2 5p^6] 5d^4 6s^2$

and thus included in the computation. The electronic structure and total number N of electrons included in the calculation are summarized in Tab. 1 for all bcc transition metals.

1.1.5. Plane wave basis

To decompose the Kohn-Sham wave functions ψ_i of each independent particle, different basis can be used. Most DFT calculations are performed using a plane wave basis set, like PWSCF and VASP [135] codes, or localized basis centered on each atom and describing its orbitals, which are used in the SIESTA code. Plane wave basis necessitate the use of a large number of functions to correctly describe the pseudo wave functions of valence electrons, but are easier to use than localized basis, which are less computationally costly but require a prior adjustment to ensure accurate results. All DFT calculations performed in the present work use the VASP code, with a plane wave basis, and simulation cells which are periodic in each direction. In principle, one needs an infinite basis to accurately evaluate the electronic wave functions. In practice, a finite number of plane waves is used by defining a cutoff kinetic energy below which all plane waves are used. Increasing this cutoff energy leads to higher accuracy, but can drastically increase the computational cost of DFT calculations. One thus needs to set a criterion for the desired accuracy by selecting a reasonable number of plane waves. This criterion also depends on the type of PP and the electrons included in the valence for the calculation. With semi-core electrons included, a higher cutoff energy needs to be set for the basis, since their potentials show faster oscillations. The cutoff energy for the plane wave basis is set to 600 eV in all calculations presented in this work, which assures very satisfactory convergence of the properties of interest, in terms of energy, forces and stresses.

1.1.6. Sampling of the Brillouin zone

Integrating the total energy of the system is performed in reciprocal space, sampled using a finite grid of \vec{k} -points at which the wave functions of the Kohn-Sham states are evaluated. Such a grid is set as to ensure that the \vec{k} -points density is constant in all simulation cells and in each Cartesian direction. In this work, the sampling grid is generated using the Monkhorst-Pack scheme [136] with a Methfessel-Paxton broadening with a smearing of width 0.1 eV. For metals, a precise evaluation of the Fermi level is required to have correct electronic properties of the system, which require a denser grid than for other materials. We also note that *ab initio* stresses require a higher \vec{k} -points density to reach a satisfactory convergence than the energy or forces, which is ensure by a sampling of 24 \vec{k} -points per lattice parameter length in all Cartesian directions. The sampling used for *ab initio* modeling of dislocations will be given in the following section.

1.1.7. Spin-polarized density functional theory

The total magnetic moment of a given atomic system has both a spin and an orbital component, the latter being negligible for the two magnetic bcc transition metals Cr and Fe we are interested in. Depending on the complexity of the magnetic order of interest, two different approaches can be used to describe the spin magnetism of a given electronic system: the collinear and non-collinear approaches.

In the collinear frame, only up \uparrow and down \downarrow states are allowed for the spin, the only degree of freedom being the magnitude of the magnetic moments $||\vec{m}_i||$. This simple description allows to model most of the bulk magnetic phases of a wide range of materials, having a ferromagnetic (FM) or an antiferromagnetic (AF) order. All spins are aligned along a randomly oriented quantization axis, defining whether a spin should be considered in its \uparrow or \downarrow state. Collinear magnetism in the frame of spin-polarized DFT is described by decomposing the total electronic density ρ into a up ρ_\uparrow and down ρ_\downarrow component, the energy of the system being a functional of both densities. The total magnetization of the system is then given as the difference between the two sub-densities. The collinear frame then limits a calculation to simple magnetic orderings.

On the other hand, in the non-collinear frame, a great variety of magnetic structures can be considered, allowing magnetic moments to have both a magnitude and orientational degree of freedom. Non-collinear magnetic configurations can be ground states of certain systems, or emerge as its temperature rises, and can also help describe the magnetic structure of domain walls in a wide range of materials. In non-collinear DFT calculations, the 3D spin vector is transformed into a two-dimensional spinor described by a 2×2

electronic density matrix whose non-diagonal components are responsible of non-collinear effects. All three types of spin-polarized DFT calculations are used in this work: non-magnetic, collinear and non-collinear calculations, depending on the magnetic structures of interest. The non-collinear frame also allows to define explicitly the quantization axis of the spins with respect to the crystal lattice, called spin-orbit coupling, which in this work is mostly neglected unless otherwise specified.

To explore the magnetic energy landscape of a system, it is useful to constrain local magnetic moments to have a target value. Such constrained calculations are performed by adding a penalty energy E_{penalty} to the total energy of the system [137], which is given by the following:

$$E_{\text{penalty}} = \sum_i \lambda (\vec{m}_i - \vec{m}_i^{\text{target}})^2, \quad (10)$$

with \vec{m}_i the magnetic moment of atom i with target value $\vec{m}_i^{\text{target}}$, and λ a Lagrange multiplier defining the constraint. In the above equation 10, the penalty on the total energy is written so as to constrain all atomic spins to a target vector, *i.e.* constraining all three Cartesian components and magnitude of the magnetic moments, in a non-collinear frame. In a similar way, only the magnitude $||\vec{m}_i||$ of selected atom i can be constrained, reducing the added computational cost due to the inclusion of non-collinear magnetism [138]. The penalty parameter λ is to be set by the user, which defines the strictness of the constraint, and needs to be increased incrementally so as to avoid issues in the self-consistent convergence of the calculation. In practice constrained magnetism calculations are very costly using *ab initio* calculations, but is easier in the tight binding approach, presented in the next section.

Summary of *ab initio* parameters: All DFT calculations presented in this work are performed using the VASP code [135]. A summary of the *ab initio* parameters used is given in Tab. 2, which were chosen as to ensure convergence of the properties of interest, derived from the energy and stresses measured in these calculations. Semi-core electrons are included in the PPs chosen to model all bcc transition metals (see Tab. 1), which are particularly important for a correct evaluation of magnetic properties.

Table 2: Parameters used for all *ab initio* DFT calculations presented in this work.

Parameter	Value
Pseudo-potentials	PAW with semi-core electrons (see Tab. 1)
Exchange-correlation functional	GGA-PBE
Plane-wave basis cutoff energy	600 eV
k -point sampling method	Monkhorst-Pack
Smearing function and width	Methfessel-Paxton with $\sigma = 0.1$ eV
k -point mesh	24 k -points per lattice parameter unit length
Convergence criterion for electronic density	Energy change less than 10^{-6} eV between two consecutive electronic steps
Atomic relaxation stopping criterion	All forces are less than 5 eV/Å in all Cartesian directions

1.2. Tight-binding formalism

In the tight-binding (TB) formalism, any wave-function is described as a linear combination of pseudo-atomic orbitals $\psi_{i\lambda}(\vec{r})$ in a localized basis, so that any wave-function $\Psi(\vec{r})$ is decomposed on this basis as:

$$\Psi(\vec{r}) = \sum_{i,\lambda} a_{i\lambda} \psi_{i\lambda}(\vec{r}) \quad \leftrightarrow \quad |\Psi\rangle = \sum_{i,\lambda} a_{i\lambda} |i\lambda\rangle, \quad (11)$$

where indices i and λ refer to atom i and orbital λ , and $a_{i\lambda}$ are the coefficients of the pseudo-atomic orbitals decomposition. The number and type of orbitals taken into account depend on the electronic structure

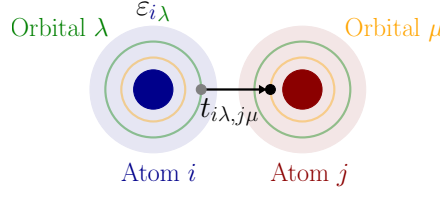


Figure 1: Schematic representation of the tight binding approach showing two atoms i and j with on-site energies ε , and orbitals λ and μ , from which an electron can hop according to the t parameter.

of the described material, which is a *spd*-type of basis set in the model for 3d transition metals used in this study [139]: $4s$, $3p_x$, $3p_y$, $3p_z$, $3d_{xy}$, $3d_{yz}$, $3d_{xz}$, $3d_{x^2-y^2}$ and $3d_{z^2}$. The unsolvable N -body quantum problem described by the Schrödinger's equation is replaced by a single electron interacting with an effective potential accounting for electron-electron interactions, which is approximated in the TB formalism by the sum of the potentials produced by each atom on the electron (see sketch in Fig. 1). The TB Hamiltonian then has the following form under these approximations:

$$\mathcal{H}_{\text{at}} = \sum_{i\lambda} \varepsilon_{i\lambda}(\rho_i) [c_{i\lambda}^\dagger c_{i\lambda}] + \sum_{ij,\lambda\mu} \left(t_{i\lambda,j\mu}(\vec{r}_{ij}) [c_{i\lambda}^\dagger c_{j\mu}] + S_{i\lambda,j\mu}(\vec{r}_{ij}) \right), \quad (12)$$

where indices i, j refer to different atomic sites, and λ, μ atomic orbitals, as sketched in Fig. 1. $c_{i\lambda}$ and $c_{i\lambda}^\dagger$ are the creation and annihilation operators referring to the electron located on the λ -orbital of atom i . With these notations, $\varepsilon_{i\lambda}(\rho_i)$ is the on-site parameter describing the electron staying on the λ -orbital of atom i , and function of the atomic density ρ_i surrounding atom i . The second term, $t_{i\lambda,j\mu}(\vec{r}_{ij})$, is the hopping interaction which describes when the electron jumps from orbital λ on atom i to orbital μ on atom j , and is a function of the distance \vec{r}_{ij} between atoms i and j . The last term, $S_{i\lambda,j\mu}$, is the overlap integral between orbital λ on atom i and orbital μ on atom j . The on-site $\varepsilon_{i\lambda}$, hopping $t_{i\lambda,j\mu}$ and overlap integrals $S_{i\lambda,j\mu}$ parameters of the TB Hamiltonian of Eq. 12 are then adjusted to reproduce chosen properties of the material.

This contribution \mathcal{H}_{at} to the TB Hamiltonian corresponds to the non-magnetic part. Magnetism is then readily included in the TB approach using the Stoner formalism [140] with an additional term $\mathcal{H}_{\text{Stoner}}$, which induces a shift in the on-site parameters $\varepsilon_{i\lambda}$ of the non-magnetic Hamiltonian \mathcal{H}_{at} of Eq. 12, given by the following in the collinear magnetism approximation:

$$\begin{aligned} \varepsilon_{i\lambda}^\uparrow &= \varepsilon_{i\lambda} - \frac{I_\lambda}{2} m_i^\lambda \\ \varepsilon_{i\lambda}^\downarrow &= \varepsilon_{i\lambda} + \frac{I_\lambda}{2} m_i^\lambda, \end{aligned} \quad (13)$$

where superscripts \uparrow and \downarrow refer to up and down magnetic moments respectively, and m_i^λ is the projection of the magnetic moment \vec{m}_i of atom i on orbital λ . I_λ is the Stoner parameter of orbital λ . Non-collinear magnetism can also be described within the Stoner formalism, inducing a rotation of the collinear Hamiltonian to align the direction of the spin \vec{m}_i with a defined quantization axis. The total Hamiltonian \mathcal{H}_{TB} is:

$$\mathcal{H}_{\text{TB}} = \mathcal{H}_{\text{at}} + \mathcal{H}_{\text{Stoner}} + \mathcal{H}_{\text{SO}}, \quad (14)$$

where \mathcal{H}_{at} describes non-magnetic inter and intra atomic interactions between atoms and orbitals, given by Eq. 12, $\mathcal{H}_{\text{Stoner}}$ is the magnetic Stoner Hamiltonian describing interactions between magnetic moments of atoms, and \mathcal{H}_{SO} is the spin-orbit coupling. Parametrization of such a TB model for all transition metals has been proposed by Barreteau *et al.* [141] including non-collinear magnetism, which has been used to study various bulk properties and interfaces of iron-chromium by Soulaïrol *et al.* [113, 142], which will be used in this work for bcc Cr. Constraining magnetic moments within the TB formalism is performed with a penalty energy similar to the one introduced in section 1.1.7, which is added to the on-site energy of each atom, and is less demanding for the self-consistency to convergence than for *ab initio* calculations.

Validation of the TB model of chromium: Comparison between TB results and *ab initio* bulk properties of bcc chromium is presented in Tab. 3, showing a very good agreement between the two methods, like reported in previous studies [113, 142]. All calculations using the TB model are performed with the DYNAMOL code [143]. More complex properties computed with the TB model are presented in Appendix B, which are out of the reach of *ab initio* calculations.

Table 3: Properties of the bulk AF phase of bcc chromium: equilibrium lattice parameter a_0 , magnetic moment m_0 , elastic constants C_{ij} , and relative stability of the spin-density wave (SDW) and non-magnetic (NM) phases obtained using *ab initio* and TB calculations, and compared to experimental data measured at 4.2 K.

	<i>ab initio</i>	TB	Expt. [6]
a_0 (Å)	2.87	2.89	2.88
m_0 (μ_B)	1.10	1.27	0.50
C_{11} (GPa)	432	432	394
C_{12} (GPa)	63	64	89
C_{44} (GPa)	96	92	104
ΔE^{NM} (meV/atom)	12.5	12.8	/
ΔE^{SDW} (meV/atom)	10.4	12.3	/

1.3. Generalized Heisenberg and effective interaction models

Lattice-based effective interaction models aim at describing the energetics of a system using pair interactions between neighboring sites which depend on the quantity of interest (*e.g.* chemical species, occupation). In this work, such model aims at describing magnetic properties of chromium. In this respect, each of the N atomic sites i composing the system is given a magnetic moment \vec{m}_i . This class of interaction models includes the Ising model, which is the simplest, and only allows for spins to have a magnitude $\pm m_0$:

$$E_{\text{Ising}}^{\text{mag}}(\{m_i\}_{i \in [1, N]}) = \sum_{i=1}^N \left[\sum_{j \in 1\text{NN}(i)} J_1(m_i, m_j) + \sum_{j \in 2\text{NN}(i)} J_2(m_i, m_j) \right], \quad (15)$$

where each magnetic moment m_i is a scalar equal to $\pm m_0$. The parameters J_1 and J_2 , called exchange coupling, describe the pair interaction between the two neighboring sites i and j , where in the above Eq. 15, site j belongs to the first nearest neighbors (1NN), or second nearest neighbors (2NN) of site i . In this work, exchange coupling between atomic sites are considered up to 2NN neighbors only, which is sufficient

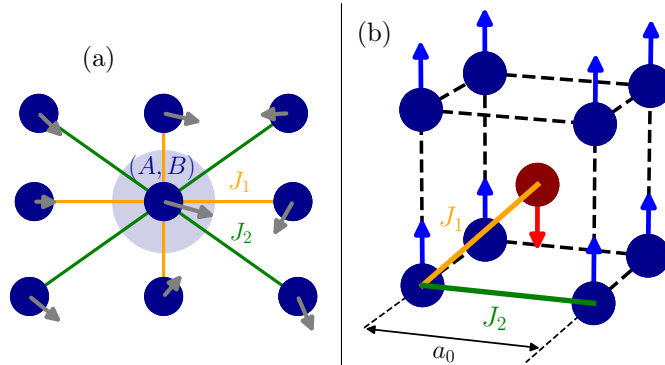


Figure 2: Sketch of the generalized Heisenberg (HL) model on (a) a two-dimensional square lattice and (b) the bcc lattice with antiferromagnetic order, showing exchange coupling between nearest neighbors J_1 and next nearest neighbors J_2 , and Landau parameters (A, B) controlling the magnitude of the atomic spins.

to have a satisfactory agreement with reference data on which the parameters of the model are adjusted. We stress that exchange coupling can however be extended over the 2NN shell. In the frame of the Heisenberg model, magnetic moments are described by vectors \vec{m}_i , and allows for variation of their orientations:

$$E_{\text{Heisenberg}}^{\text{mag}}(\{\vec{m}_i\}_{i \in [1, N]}) = \sum_{i=1}^N \left[\sum_{j \in 1\text{NN}(i)} J_1(\vec{m}_i \cdot \vec{m}_j) + \sum_{j \in 2\text{NN}(i)} J_2(\vec{m}_i \cdot \vec{m}_j) \right] \quad (16)$$

In the frame of the generalized Heisenberg, or Heisenberg-Landau (HL) model, the magnetic energy is [144]:

$$E_{\text{HL}}^{\text{mag}}(\{\vec{m}_i\}_{i \in [1, N]}) = \sum_{i=1}^N \left[A \|\vec{m}_i\|^2 + B \|\vec{m}_i\|^4 + \sum_{j \in 1\text{NN}(i)} J_1(\vec{m}_i \cdot \vec{m}_j) + \sum_{j \in 2\text{NN}(i)} J_2(\vec{m}_i \cdot \vec{m}_j) \right], \quad (17)$$

where A and B are the Landau parameters which control the magnitude of the on-site magnetic moments, and the J_{ij} parameters are the Heisenberg pair exchange coupling between atoms i and j . On a fixed lattice, the J_{ij} exchange parameters are defined for a shell of nearest neighboring sites j of atom i . In the models developed for this work, only the first and second nearest neighbors of each atomic sites are considered. For the bcc lattice, sketched in Fig. 2b, first nearest neighbors (1NN) of a given atomic site are spaced from it by all 8 possible $1/2\langle 111 \rangle$ vectors, at a distance $a_0\sqrt{3}/2$ with a_0 the lattice parameter, and second nearest neighbors (2NN) by each of the 6 $\langle 100 \rangle$ vectors, at a distance a_0 . The exchange coupling between neighboring sites allows for the orientational degree of freedom for magnetic moments \vec{m}_i . The total magnetic energy of a system given by Eq. 17 is thus the sum between two components, controlling the magnitude and orientations of the spins. The parameters of the HL model of bcc chromium developed in this work are obtained through a fit to *ab initio* data, detailed in Chapter 3. Such simple models then allow to study finite temperature magnetic excitations using a Metropolis Monte Carlo algorithm to access equilibrium properties predicted by the model as a function of temperature. This method is described in details in section 2.1.1. If one is interested in computing the dynamics of a spin system, *i.e.* including a time dependence on the relaxation of the system, spin-dynamics simulations can be performed using such generalized Heisenberg Hamiltonian, or using any other energetic model, such as a tight-binding approach [143, 145] or *ab initio* calculations [146–148]. Similar effective magnetic interaction model was previously developed for iron-chromium alloys [144, 149], and has also successfully described other magnetic properties such as point defects and phase diagrams of various binary magnetic alloys [150–155].

1.4. Empirical interatomic potentials

The high computational cost of *ab initio* DFT calculations restrict their use to systems of a few hundreds of atoms at most. Going up in both system sizes and accessible time scales keeping an atomistic resolution requires the use of different approaches, such as the TB method (section 1.2) or effective interaction models (section 1.3). Another approach consists in the use of empirical interatomic potentials, which are briefly introduced in the present section. These empirical potentials rely on the description of interactions between atoms by analytical functions whose form is chosen to suit the system of interest, and which can have a physical justification. With the use of such analytical formulation of the energy of the system, the required computational cost is drastically cut with respect to *ab initio* calculations, since electrons are not included explicitly. Construction of an interatomic potential then comes to the adjustment of the parameters of these analytical functions, whether to reproduce experimental properties of the material, or to fit their parameters to other energetic models, like *ab initio* calculations. Once the potential is accurately constructed and its ability to reproduce the desired properties tested, it can be used to study a wide range of atomic scale physical phenomena necessitating larger system sizes. One approach to construct such empirical potential, which is particularly common for the description of metals, is the embedded-atom method (EAM), composed of pairwise interactions between atoms, and a many-body term, having the following form:

$$V = \sum_{i>j} \phi(r_{ij}) + \sum_i F(\rho_i), \quad (18)$$

where $\phi(r_{ij})$ is the pair potential between atoms i and j separated by a distance r_{ij} , and $F(\rho_i)$ corresponds to the energy required for embedding the atom i at a given location with electronic density ρ_i . It is expressed as a superposition of the atomic electronic densities ρ^{atomic} surrounding atom i :

$$\rho_i = \sum_{k=1}^N \rho_j^{\text{atomic}}(r_{ij}) \quad (19)$$

Functions describing both terms appearing in Eq. 18 are then fitted to a set of reference data or adjusted to reproduce experimental properties of the material of interest. Semi-empirical interatomic potentials used in the present work were chosen as to give a good agreement in the predicted elastic properties with respect to both *ab initio* calculations and experiments, but also a non-degenerate core structure of the $1/2\langle 111 \rangle$ screw dislocation and a single hump Peierls energy barrier between two equilibrium easy core configurations, as detailed in the Literature review (see section 2). Considering EAM potentials, interactions between atoms are described solely as a function of the distance between them. However, atomic bonds in transition metals are known to have a strong angular dependence, which is thus required for a better description of interactions between atoms. This dependence is readily included in the frame of the modified EAM (MEAM) method in the atomic electronic densities ρ_i of Eq. 19, without changing the other terms appearing in Eq. 18. Using these potentials however yields higher computational costs than standard EAM potentials. Empirical potentials are used in this study for bcc transition metals listed in Tab. 4 with the corresponding choice of parameters and validation on the predicted elastic properties with respect to experiments. Atomic relaxations are performed using a molecular statics relaxation step at 0 K using the FIRE algorithm [156] with a threshold criterion of 5 meV/Å set on all atomic forces in each Cartesian direction.

Summary of interatomic potentials: All calculations using semi-empirical interatomic potentials presented in this work, whether molecular statics or dynamics, are performed with the LAMMPS code [157], with the potentials given in Tab. 4 used to describe interactions between atoms.

Table 4: Interatomic potentials used in this work with computed lattice parameter a_0 (Å), elastic constants C_{ij} (GPa), and elastic anisotropy $A = 2C_{44}/(C_{11} - C_{12})$ compared to experimental values measured at 4.2 K and taken from various references, and results of *ab initio* DFT calculations performed in this work with the parameters given in section 1.1.2.

Element	Type	Reference	a_0	C_{11}	C_{12}	C_{44}	A
Niobium (Nb)	EAM	Fellinger <i>et al.</i> [158]	3.31	233	124	32	0.59
	MEAM	Yang and Qi [159]	3.32	249	135	21	0.37
	<i>ab initio</i>	This work	3.31	255	138	20	0.34
	Expt.	Caroll <i>et al.</i> [15]	3.29	246	132	28	0.49
Tantalum (Ta)	MEAM	Park <i>et al.</i> [89]	3.32	287	172	94	1.63
	<i>ab initio</i>	This work	3.32	269	169	76	1.53
	Expt.	Bolef <i>et al.</i> [14]	3.30	262	156	83	1.57
Molybdenum (Mo)	EAM	Ackland <i>et al.</i> [160]	3.15	465	162	109	0.72
	MEAM	Park <i>et al.</i> [89]	3.17	423	143	95	0.68
	<i>ab initio</i>	This work	3.16	485	170	100	0.64
	Expt.	Bolef <i>et al.</i> [17]	3.14	458	168	111	0.77
Tungsten (W)	EAM	Marinica <i>et al.</i> [66]	3.14	523	202	161	1.00
	MEAM	Park <i>et al.</i> [89]	3.19	524	205	161	1.01
	<i>ab initio</i>	This work	3.19	517	217	141	0.94
	Expt.	Bolef <i>et al.</i> [14]	3.16	517	203	157	1.00

2. Finite temperature simulations

We now detail two different methods for performing simulations including various degrees of freedom allowed at finite temperature, namely a Metropolis Monte Carlo sampling, and molecular dynamics simulations.

2.1. Magnetic excitations

The methods presented in the present section aim at performing efficient sampling of finite temperature excitations predicted by a given energetic model, with a focus on magnetic excitations in bcc Cr.

2.1.1. Metropolis Monte Carlo sampling

Monte Carlo simulations encapsulate a range of methods based on the stochastic evolution of a system, the energy of which is given by any energetic model, like those described above. By attributing a success probability to a given event, associated with a change δE in the energy of the system, it is then accepted or rejected based on the comparison of the statistical probability associated to δE with a randomly generated number. Here, the system of interest is a given number of N atoms, arranged on a rigid lattice and associated with a magnetic moment $\vec{m}_{i \in [1, N]}$. The purpose of Monte Carlo simulations is to explore finite temperature magnetic excitations in a system, to find its equilibrium magnetic states at different simulated temperatures, based on the following Metropolis algorithm:

- The energy E_i of the current state of the system is calculated.
- One out of the N spins is chosen and a random change of its three Cartesian components is performed. The energy E_f of the new system is then re-evaluated after the transition.
- The energy difference $\delta E = E_f - E_i$ associated with the transition is calculated.
- The transition is accepted:
 - if $\delta E \leq 0$, *i.e.* if the energy of the system decreases;
 - or $\delta E > 0$ and $\exp\left[-\frac{\delta E}{k_B T}\right] < \text{rand}$, with rand a randomly generated number between 0 and 1,
 and the system is updated accordingly.
- If the transition is rejected, the system is brought back to its initial state at the beginning of the step.

Monte Carlo steps are then performed until the equilibrium state of the magnetic system at the simulated temperature T is reached. To have a good sampling of the energy landscape at T and ensure that even rare magnetic transitions are allowed to occur, a sufficiently large number of Monte Carlo thermalization steps needs to be performed at each temperature, which is the case for approximately 10^8 steps, in all simulations presented in this work. Stable configurations of a magnetic system at zero temperature are found with the same Metropolis Monte Carlo algorithm, with $T = 0$. More accurate minimization methods would need to be implemented to properly quench the system at 0 K, which was not done for the present work. We now focus on how to extract thermodynamics properties from these simulations.

2.1.2. Thermodynamics using Metropolis Monte Carlo sampling

From the Monte Carlo sampling with temperature, one can access thermodynamical equilibrium properties of the system through ensemble average of its magnetic energy E^{mag} . The magnetic heat capacity C_P^{mag} is then obtained from the derivative of E^{mag} with respect to the temperature T as:

$$C_P^{\text{mag}}(T) = \frac{\partial E^{\text{mag}}}{\partial T} \quad (20)$$

From the magnetic heat capacity C_P^{mag} , the magnetic entropy S^{mag} of the system is given by:

$$S^{\text{mag}}(T) = \int_0^T \frac{C_P^{\text{mag}}(T')}{T'} dT' \quad (21)$$

The magnetic free energy of the system is then $F^{\text{mag}}(T) = E^{\text{mag}}(T) - TS^{\text{mag}}(T)$. An alternate way to access the magnetic free energy F^{mag} of the system is through a thermodynamical integration over the temperature range covered by the simulation, where the magnetic energy E^{mag} is sampled. The use of this method thus requires a reference point at which the value of F^{mag} is known. This reference is set at a temperature T_{ref} , whose choice depends on the system of interest. The magnetic free energy F^{mag} of the system is given by:

$$Z = \exp\left(-\frac{F^{\text{mag}}}{k_B T}\right) \rightarrow \ln Z = -\frac{F^{\text{mag}}}{k_B T}, \quad (22)$$

with Z the partition function of the system. Using the expression of the internal magnetic energy E^{mag} as a function of this partition function Z , we have:

$$E^{\text{mag}} = k_B T^2 \frac{\partial \ln Z}{\partial T} = -k_B T^2 \left(\frac{1}{T} \frac{\partial F^{\text{mag}}}{\partial T} - \frac{F^{\text{mag}}}{T^2} \right) = F^{\text{mag}} - T \frac{\partial F^{\text{mag}}}{\partial T} \quad (23)$$

It is then convenient to work with the inverse temperature $\beta = 1/k_B T$ to express thermodynamical quantities of interest. Performing the change of variable $\beta \leftrightarrow 1/k_B T$, the above equation becomes:

$$\begin{aligned} E^{\text{mag}} &= F^{\text{mag}} - T \frac{\partial F^{\text{mag}}}{\partial \beta} \times \frac{\partial \beta}{\partial T} = F^{\text{mag}} - T \frac{\partial F^{\text{mag}}}{\partial \beta} \left(-\frac{1}{k_B T^2} \right) \\ &= F^{\text{mag}} + \beta \frac{\partial F^{\text{mag}}}{\partial \beta} = \frac{\partial}{\partial \beta} [\beta F^{\text{mag}}] \end{aligned} \quad (24)$$

Integration of the above equation between β and β_{ref} gives the following:

$$\beta F^{\text{mag}}(\beta) - \beta_{\text{ref}} F^{\text{mag}}(\beta_{\text{ref}}) = \int_{\beta'=\beta_{\text{ref}}}^{\beta} E^{\text{mag}}(\beta') d\beta' \quad (25)$$

We now focus on performing this thermodynamical integration for a system containing a defect (*e.g.* magnetic fault, point defects, dislocation core). The magnetic excess energy ΔE^{mag} and free energy ΔF^{mag} associated with the defect are defined as:

$$\begin{aligned} \Delta E^{\text{mag}}(\beta) &= E_{\text{fault}}^{\text{mag}}(\beta) - E_{\text{bulk}}^{\text{mag}}(\beta) \\ \Delta F^{\text{mag}}(\beta) &= F_{\text{fault}}^{\text{mag}}(\beta) - F_{\text{bulk}}^{\text{mag}}(\beta) \end{aligned} \quad (26)$$

where $E_{\text{fault}}^{\text{mag}}$ and $E_{\text{bulk}}^{\text{mag}}$ refers to the energy of the simulation cell containing the defect, and the perfect bulk crystal respectively. Applying Eq. 25 to these excess magnetic energies, we obtain:

$$\beta \Delta F^{\text{mag}}(\beta) - \beta_{\text{ref}} \Delta F^{\text{mag}}(\beta_{\text{ref}}) = \int_{\beta'=\beta_{\text{ref}}}^{\beta} \Delta E^{\text{mag}}(\beta') d\beta' \quad (27)$$

As will be detailed in Chapter 3, two main defects are studied in Cr using this method, which are an infinite magnetic fault caused by a ferromagnetic frustration due to a $1/2\langle 111 \rangle$ shear, and the magnetic contribution to the core energy of a $1/2\langle 111 \rangle$ screw dislocation. In both cases, we find that $\Delta F^{\text{mag}}(\beta_{\text{ref}}) = 0$ setting the reference $T_{\text{ref}} = 5T_N/4$, where the system is in the disordered paramagnetic (PM) phase. We then checked that the excess magnetic energy contained in a faulted simulation cell is zero at this temperature, *i.e.* the system has the same energy whether a defect is present or not. In this case, the magnetic free energy ΔF^{mag} of these two defects can be expressed as:

$$\Delta F^{\text{mag}}(\beta) = \frac{1}{\beta} \int_{\beta'=\beta_{\text{ref}}}^{\beta} \Delta E^{\text{mag}}(\beta') d\beta' \quad \leftrightarrow \quad \Delta F^{\text{mag}}(T) = T \int_{t=T}^{T_{\text{ref}}} \frac{\Delta E^{\text{mag}}(t)}{t^2} dt \quad (28)$$

The convergence of these thermodynamical properties was checked by comparing values obtained upon heating the system from 0 K, and cooling down to 0 K. All simulation cells contain approximately 14 000 atoms to allow for magnetic fluctuations to occur without boundary effects in the simulated volume.

2.1.3. Including quantum statistics

In the frame of classical physics, the energy distribution of magnetic excitations described by Hamiltonian 17 is assumed continuous, thus allowing for fluctuations in the magnitude and angle of the spins even at very low temperatures, as soon as thermal energy is sufficient to explore higher energy configurations. However, this yields non-physical results as the magnetic heat capacity C_P^{mag} evaluated from Eq. 20 does not converge to zero at 0 K, where the magnetic entropy S^{mag} given by Eq. 21 thus diverges [161]. Therefore, a correct evaluation of the magnetic free energy cannot be obtained through thermodynamical integration since the value of F^{mag} is not known at 0 K, where it should enforce $F^{\text{mag}}(0 \text{ K}) = E^{\text{mag}}(0 \text{ K})$. Considering discrete energy levels, these low temperature thermal excitations are no longer permitted, accounted for by evaluating the thermal energy using quantum statistics. Magnetic fluctuations operate through excitation modes of the spin structure in the form of elementary spin spirals (Fig. 3a) called magnons, similar to phonons when looking at the vibration modes of a crystal. Thermal energy given to the system allows for excitation of these magnons, corresponding to a disorientation of the spins with respect to the 0 K ground state of the system. These modes are composed of elementary spin spirals, *i.e.* non-collinear magnetic structures which propagate a rotation of magnetic moments of fixed magnitude. The magnon spectrum of bcc Cr, *i.e.* the energy of spin spirals as a function of the wave-vector \vec{q} over the Brillouin zone, obtained using the TB model is presented in Fig. 3b, with the corresponding density of states (mDOS) obtained through integration of the spectrum over the entire Brillouin zone presented in Fig. 3c. Accounting for the quantization of magnon modes in the Metropolis algorithm allows for a quantum description of low temperature energetics.

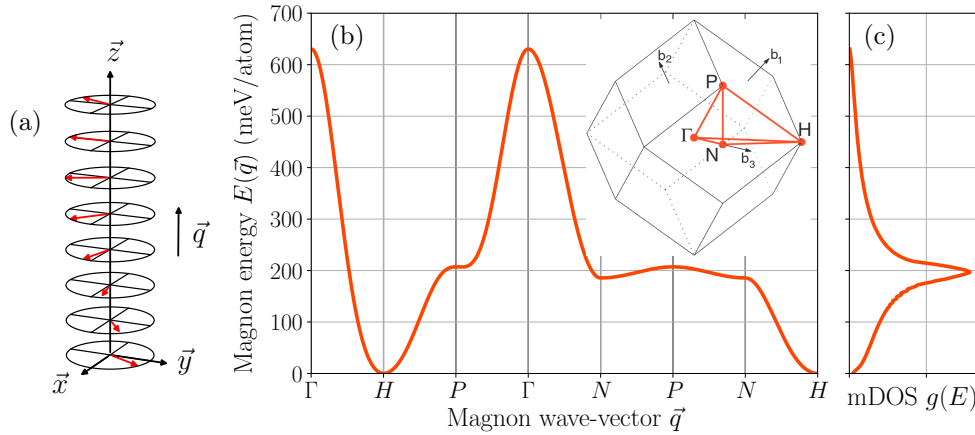


Figure 3: (a) Schematic representation of a spin spiral of wave-vector \vec{q} along the z axis. (b) Magnon spectrum of bcc chromium along the high-symmetry path $\Gamma - H - P - \Gamma - N - P - N - \Gamma$ of the Brillouin zone of the bcc lattice. (c) Magnon density of states (mDOS) $g(E)$, obtained through integration of the magnon spectrum over the Brillouin zone. The Brillouin zone of the bcc lattice, with special points $\Gamma = (0, 0, 0)$, $H = (1, -1, 1)$, $P = (1/2, 1/2, 1/2)$ and $N = (0, 0, 1)$, is shown in inset on (b) [162].

As detailed in section 2.1.1, the acceptance probability $p(\delta E)$ of a magnetic transition of energy δE is:

$$p(\delta E) = \begin{cases} 1, & \text{if } \delta E \leq 0 \\ \exp \left[-\frac{\delta E}{\eta(T)} \right], & \text{if } \delta E > 0 \end{cases} \quad (29)$$

where $\eta(T) = k_B T$ using the classical Boltzmann distribution in the Metropolis algorithm. To have a proper sampling of the thermodynamical properties of the system, quantum statistics must be included, *i.e.* with a Bose-Einstein distribution, for which the quantum scaling factor $\eta(T)$ of the Metropolis algorithm is [161]:

$$\eta_Q(T) = \int_0^\infty \frac{E}{\exp \left(\frac{E}{k_B T} \right) - 1} g(E, T) dE, \quad (30)$$

with E the energy of a magnon of wave-vector \vec{q} (see Fig. 3b), and $g(E, T)$ is the magnon density of states (mDOS) (see Fig. 3c) at the temperature T and the energy E . Given that the mDOS is zero above a certain maximum energy (approximately 625 meV/atom in Fig. 3b), one can perform the above integral from 0 to E_C , where E_C is the highest energy contributing to the mDOS at T , *i.e.* the maximum energy on Fig. 3b. One sees that the key to construct such quantum statistics from Eq. 30 is the knowledge of the temperature dependent mDOS, $g(E, T)$. Following the method introduced by Woo *et al.* [163] and Bergqvist *et al.* [161], the temperature dependence of the mDOS is evaluated by rescaling the upper limit in energy E_C of the mDOS at 0 K, resulting in the following expression at temperature T :

$$E_C(T) = E_C(T = 0 \text{ K}) \times \left(1 - \frac{T}{T_N}\right)^\beta, \quad (31)$$

with T_N the Néel temperature, identical whether classical or quantum statistics is employed, and $\beta \simeq 0.375$ is the critical exponent of the 3D Heisenberg model [164], which only depends on the dimensionality of the Heisenberg model and is the same regardless of the structure of the system of interest. This implies that the temperature dependent mDOS is rescaled upon temperature, keeping the same shape with this rescaled cutoff magnon energy, as presented in Fig. 4a at different temperatures, with the following expression:

$$g(E, T) = \frac{g\left(E \times \frac{E_C(T)}{E_C(T = 0 \text{ K})}, T = 0 \text{ K}\right)}{\int_{e=0}^{E_C} g\left(e \times \frac{E_C(T)}{E_C(T = 0 \text{ K})}, T = 0 \text{ K}\right) de} \quad (32)$$

This model assumes that above T_N , *i.e.* when long-range magnetic order vanishes, the cutoff energy E_C becomes zero and the statistics thus sharply switches from quantum to classical. Hence, such approximation is expected to be valid at low temperatures only, well below T_N . This method is applied with the magnon spectrum obtained with one of the presented energetic models, from which the mDOS at 0 K is obtained by integrating the energy of the magnons over the entire Brillouin zone. The scaling factor η of the Metropolis algorithm is then interpolated at the transition from classical to quantum statistics:

$$\eta(T) = \begin{cases} \eta_Q(T) \text{ (Eq. 30)}, & \text{if } T < T_N \\ k_B T, & \text{if } T \geq T_N \end{cases} \quad (33)$$

correctly accounting for low temperature thermal excitations below the Néel temperature T_N through quantum statistics, and using a classical Boltzmann distribution above. We note that a more accurate evaluation

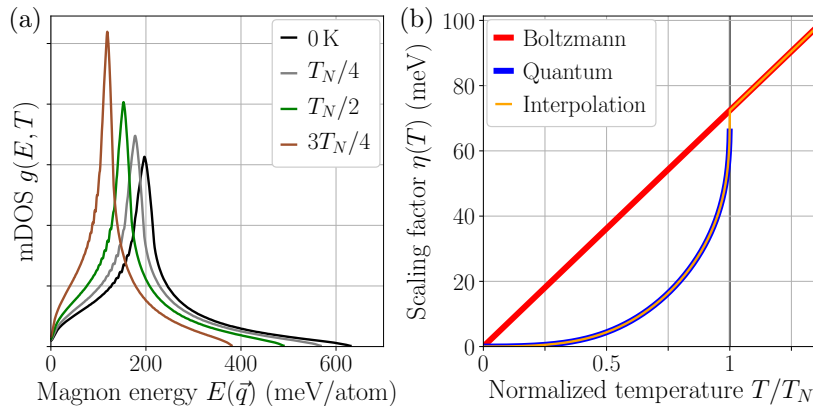


Figure 4: (a) Temperature dependent magnon density of state (mDOS) $g(E, T)$ in the approximation of Eq. 31 at different temperatures below T_N obtained using the TB model. (b) Scaling factor $\eta(T)$ of the Metropolis algorithm using classical Boltzmann statistics, $\eta(T) = k_B T$, and approximate quantum statistics, $\eta(T) = \eta_Q(T)$ (Eq. 30), as a function of temperature.

of the temperature dependent mDOS can be obtained through evaluation of the dynamical structure factor $S(\vec{q}, E)$ [146–148], including temperature effects originating from magnon-magnon interactions and magnetic damping. However, this approach is much more computationally expensive and yields a similar scaling factor at low temperature as the quantum approximation introduced in this section. Thus, finite temperature magnetic excitations in bcc chromium will be studied using the statistics of Eq. 33. When studying magnetic properties of a $1/2\langle 111 \rangle$ screw dislocation dipole in bcc Cr in a simulation cell containing 546 atoms using the TB model (see Appendix B), we realized that the computational cost of these simulations was already high for this rather small system size. Hence, finite temperature magnetic excitations will not be studied using the TB model, requiring the use of much larger systems and number of simulations to sample finite temperature magnetic excitations. This study will be performed using a generalized Heisenberg-Landau model (see section 1.3), drastically cutting computational cost, and thus allowing for the treatment of finite temperature magnetic excitations, which is the focus of Chapter 3.

2.2. Molecular dynamics simulations

Molecular dynamics simulations aim at computing equilibrium and dynamical properties of many-body atomic systems through integration of Newton’s classical equations of motion for nuclei, which obey classical mechanics. Such equations are written for each atom i as:

$$m_i^{\text{atom}} \frac{d\vec{v}_i}{dt} = \vec{F}_i = -\vec{\nabla} V_i, \quad (34)$$

with m_i^{atom} the mass of atom i , \vec{v}_i its velocity, and \vec{F}_i the sum of the forces acting on atom i , derived as the gradient of its potential energy with respect to its position given by the energetic model chosen to describe interactions between atoms (see section 1). Such molecular dynamics simulations will only be used in the present work for the simulation of dynamical properties of a dislocation microstructure using interatomic potentials to model interactions between atoms. However, other energetic models could be used in the same framework for performing molecular dynamics simulations. The dynamic evolution of the system is then evaluated by integrating the equations of motion of Eq. 34 at each time step Δt , and for each atom i of the system using a velocity-Verlet algorithm:

$$\begin{cases} \vec{r}_i(t + \Delta t) = \vec{r}_i(t) + \vec{v}_i \Delta t + \frac{\vec{F}_i(\vec{r}_i(t))}{2m_i^{\text{atom}}} \Delta t^2 + \mathcal{O}(\Delta t^3) \\ \vec{v}_i(t + \Delta t) = \vec{v}_i(t) + \frac{\vec{F}_i(\vec{r}_i(t)) + \vec{F}_i(\vec{r}_i(t + \Delta t))}{2m_i^{\text{atom}}} \Delta t + \mathcal{O}(\Delta t^3) \end{cases} \quad (35)$$

with $\vec{r}_i(t)$ and $\vec{r}_i(t + \Delta t)$ the initial and updated positions of atom i respectively. Such dynamical simulations are performed at a given temperature T adding thermal energy to atoms of a system previously relaxed with a molecular statics relaxation at 0 K. The NVE ensemble, *i.e.* constant number of particles N volume V and energy E , is used to integrate the equations of motion in molecular dynamics simulations with a time step $\Delta t = 2$ fs, and initializing the temperature of the system twice higher than its target value, without the use of a thermostat, which is then equilibrated with an initial thermalization stage.

3. Atomistic modeling of dislocations and plasticity of body-centered cubic metals

We now detail the modeling of dislocations using the energetic models introduced in the previous section, with a focus on *ab initio* DFT calculations and interatomic potentials.

3.1. Ab initio modeling of dislocations

To accurately account for the fine atomistic properties of dislocations, one needs to rely on a precise description of the interatomic forces, allowing for the description of the core structure and mobility of dislocations in a crystal. Modeling of dislocations using *ab initio* calculations relies on DFT calculations,

which are computationally costly and can therefore reasonably handle systems of a few hundreds of atoms at most. In this respect, *ab initio* calculations have been mainly restricted to the study of straight infinite dislocations, minimizing the length of the simulation cell in its line direction. In the plane orthogonal to the line direction, dislocations are responsible of an elastic strain field which needs to be handled carefully given that this field varies as the logarithm of the distance to the line position, and therefore does not fade out at the short distances handled in *ab initio* calculations. Additionally, it is not possible to model a single isolated dislocation in simulation cells with full periodic boundary conditions for topological reasons, since the displacement discontinuity induced by the dislocation needs to be closed by another defect. To overcome this constraint, different approaches have been developed, among which the dipolar arrangement, where dislocations are introduced pairwise in the simulation cell, with opposite Burgers vectors, therefore allowing for the use of full periodic boundary conditions, resulting in an infinite periodic array of dislocations [19, 64]. Such *ab initio* calculations of dislocations have uncovered some of their properties linked to the macroscopic plastic behavior of bcc metals, which are detailed in the following.

3.1.1. Simulation setup for dislocation modeling

Simulation cells used for modeling $1/2\langle 111 \rangle$ screw dislocations using a dipolar arrangement have Cartesian directions chosen so that the $\{110\}$ glide plane of the dislocations is oriented with its normal along $Y \parallel \vec{u}_2 = [\bar{1}01]$, the glide direction is along $X \parallel \vec{u}_1 = [\bar{1}2\bar{1}]$, and the dislocation line is along the $Z \parallel \vec{u}_3 = [111]$ axis.

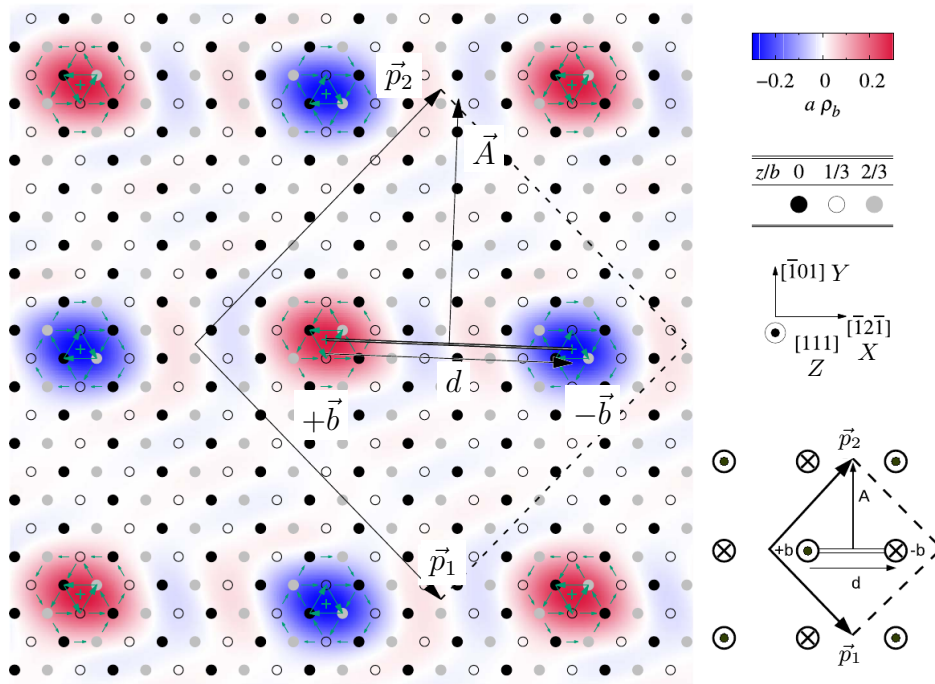


Figure 5: Simulation cell used to model a $1/2[111]$ screw dislocation dipole in bcc metals, with periodicity vectors \vec{p}_1 and \vec{p}_2 in the (111) plane orthogonal to the dislocation line. The cell contains a periodic array of opposite sign screw dislocations with quadrupolar arrangement, separated from each other by a distance d and a cut vector \vec{A} showing the discontinuity surface indicated by double black lines. The atomic structure of the dislocation is represented using differential displacement and Nye tensor maps. Atoms are represented by different colors depending on their height along the $[111]$ direction in the perfect crystal. Arrows between atoms are proportional to the differential displacement between them due to the presence of the dislocation. The color map is a measure of the dislocation density ρ_b normalized by the lattice parameter a (reproduced from Ref. [45]).

In this Cartesian basis, the periodicity vectors $(\vec{p}_1, \vec{p}_2, \vec{p}_3)$ of the simulation cell are expressed as:

$$\begin{aligned}\vec{p}_1 &= \lambda_1 \vec{u}_1 - \lambda_2 \vec{u}_2 + \lambda_3 \vec{u}_3 \\ \vec{p}_2 &= \lambda_1 \vec{u}_1 + \lambda_2 \vec{u}_2 + \lambda_3 \vec{u}_3 \\ \vec{p}_3 &= n_3 \vec{u}_3\end{aligned}\tag{36}$$

with the λ_i parameters defining the geometry of the simulation cell, given in Tab. 5 for different cell sizes. The smallest simulation cell contains 135 atoms per unit b length in the direction Z of the dislocation line, which is represented in Fig. 5. According to linear elasticity theory, the energy variation associated with a homogeneous strain $\bar{\varepsilon}$ in the periodic simulation cell is given by the following when the core field of the dislocation is neglected:

$$\Delta E(\bar{\varepsilon}) = \frac{1}{2} S C_{ijkl} \varepsilon_{ij} \varepsilon_{kl} + C_{ijkl} b_i A_j \varepsilon_{kl},\tag{37}$$

with C_{ijkl} the elastic constants of the perfect crystal, and S the surface of the simulation cell in the plane orthogonal to the dislocation line, oriented by vector \vec{l} . The resulting stress σ_{ij} generated in the simulation cell is obtained through derivation of the above expression with respect to the strain ε_{ij} [75]:

$$\sigma_{ij}(\bar{\varepsilon}) = \frac{1}{S} \frac{\partial \Delta E}{\partial \varepsilon_{ij}} = C_{ijkl} (\varepsilon_{kl} - \varepsilon_{kl}^0)\tag{38}$$

where the plastic strain ε_{kl}^0 is given by the following:

$$\varepsilon_{kl}^0 = -\frac{b_k A_l + b_l A_k}{2S}\tag{39}$$

Let \vec{d} be the vector joining the two $+\vec{b}$ and $-\vec{b}$ dislocations of the dipole, one can then define the cut vector of the surface sheared by the dislocation dipole as $\vec{A} = \vec{d} \wedge \vec{l}$, thus related to the relative position of the two dislocations. All notations are presented in Fig. 5 [45]. Dislocations are introduced in the simulation cell using anisotropic elasticity theory and taking full account of periodicity in all three Cartesian directions using the BABEL package [165], and applying an homogeneous strain to the periodicity vectors of the cell to cancel the plastic strain generated by the dislocation dipole given by Eq. 39 [19, 64]. According to the same relation, one also sees that if the relative positions of the dislocations varies, *i.e.* if the cut vector \vec{A} varies, this would generate a stress in the simulation cell containing the dipole, whose *ab initio* evaluation can be used to extract the relative position of the dislocations, which is detailed in the next section.

Simulation cells have periodic boundary conditions in all three Cartesian directions, and the dislocation dipoles are arranged in quadrupolar arrays in order to minimize the elastic interactions with their periodic images [19, 64] (see Fig. 5). In this setup, the two dislocations of a dipole are separated from each other by a vector $(\vec{p}_1 + \vec{p}_2)/2$ when aligned horizontally along the $X \parallel [12\bar{1}]$ axis, and $(\vec{p}_1 - \vec{p}_2)/2$ when aligned vertically along the $Y \parallel [\bar{1}01]$ axis. These two setups are geometrically equivalent and both assure the maximum separation distance between dislocations and their periodic images permitted in such tri-periodic *ab initio* simulation cells. Periodicity vectors of the simulation cells are kept fixed during all atomic relaxations. The k -points grid used for the 135-atom per b simulation cell (see Fig. 5) is $3 \times 3 \times 28$, roughly corresponding

Table 5: Parameters λ_i defining the periodicity vectors of the supercells used for the study of the $1/2\langle 111 \rangle$ screw dislocation (Eq. 36) corresponding to a number of atoms N for a $1b$ -high simulation cell.

N	λ_1	λ_2	λ_3
135	5/2	9/2	0
187	17/6	11/2	2/3
209	19/6	11/2	1/3
273	7/2	13/2	0

to a density of 24 k -points in each Cartesian direction.

Through *ab initio* calculation on such simulation cells, one can access the excess energy associated with the dislocation dipole introduced in the cell. This excess energy can be decomposed in the following partition:

$$\begin{aligned}\Delta E &= E^{\text{tot}} - E^{\text{bulk}} = 2E^{\text{core}}(r_C) + E^{\text{elas}}(\theta, r_C) + E^{\text{inter}} \\ &= 2E^{\text{core}}(r_C) + \frac{b_i K_{ij}(\theta) b_j}{4\pi} \ln\left(\frac{d}{r_C}\right) + E^{\text{inter}},\end{aligned}\quad (40)$$

with E^{bulk} the energy of the perfect crystal without dislocations, E^{core} the core energy of the dislocation, counted twice since dislocations are introduced in dipoles. The core region is defined by a radius r_C , inside which the energy of the dislocation is entirely described by E^{core} . Outside the core region, the energy of the dipole is accounted for by elasticity theory, with E^{elas} the elastic energy of the dipole, and E^{inter} the interaction energy of the dipole with its periodic images. These two contributions can be evaluated exactly using anisotropic elasticity theory, allowing to extract the core energy E^{core} of the dislocations, and most importantly its variation with the position of the dislocation, which describes the lattice friction experienced by the dislocation and thus governs its mobility. The *ab initio* evaluation of this lattice friction, or Peierls potential, in bcc transition metals is the focus of the next section.

3.1.2. Peierls potential and mobility of dislocations

Calculation of the Peierls energy barrier consists in finding the saddle point energy and configuration of the dislocation core along the path joining two adjacent equilibrium configurations. Minimum energy path between two stable dislocation configurations are found using the nudged elastic band (NEB) method [166] as implemented in VASP in simulation cells with fixed periodicity vectors, using 5 intermediate images between the initial and final states and a spring constant of 5 eV/Å between them. Such calculations yield the variation of the energy of the system upon crossing the Peierls energy barrier ΔE as a function of the reaction coordinate ξ , a measure of the position of the different images along the path. A sketch of the

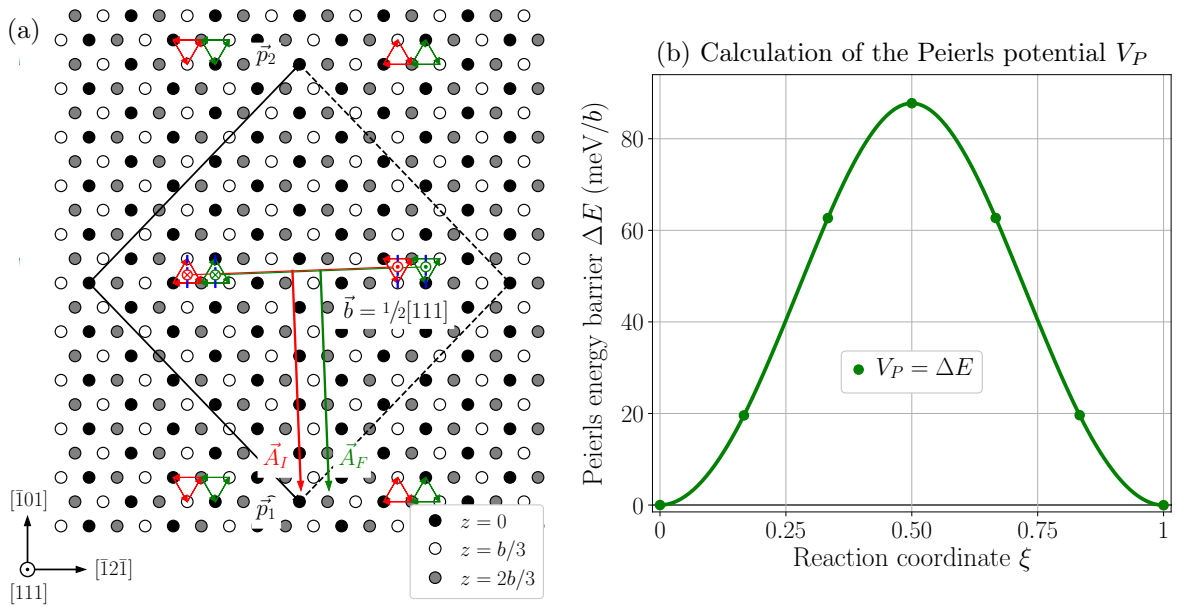


Figure 6: (a) Dislocation setup used for the calculation of the *ab initio* Peierls potential of $1/2\langle 111 \rangle$ screw dislocations using the 135 atom supercell. Initial and final positions of the dipole are shown in red and green respectively, and the position of the quadrupolar arrangement indicated by dashed blue lines. (b) Peierls energy barrier ΔE and potential V_P in bcc tungsten as a function of the reaction coordinate ξ along the NEB path between the red and green configurations shown in (a). The present setup will be referenced in the following as "both".

3.1.3. Dislocation core dilatation field and eigenstrain model

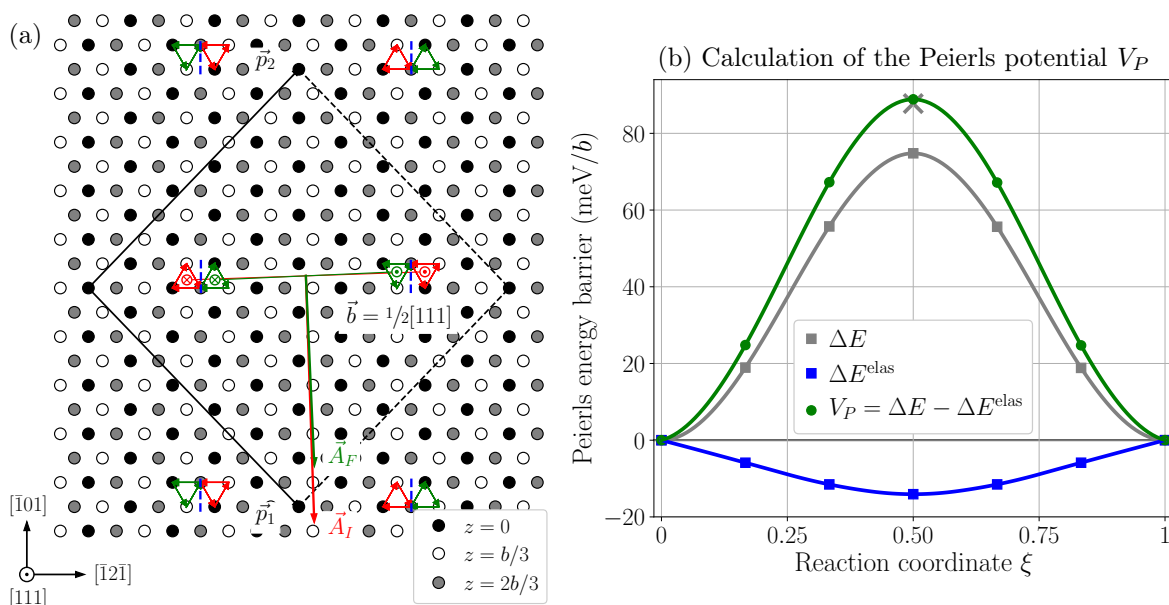
$$\Delta E(\bar{\varepsilon}) = \frac{1}{2} S C_{ijkl} \varepsilon_{ij} \varepsilon_{kl} + C_{ijkl} (b_i A_j - 2\Omega_{ij}) \varepsilon_{kl}, \quad (41)$$
$$\sigma_{ij}(\bar{\bar{\epsilon}}) = C_{ijkl} \left(\varepsilon_{kl} + \frac{b_k A_l - 2\Omega_{kl}}{S} \right) \quad (42)$$


Figure 7: (a) Dislocation setup used for *ab initio* calculation of the Peierls potential V_P , trajectory and relaxation volume $\bar{\Omega}$ of the $1/2\langle 111 \rangle$ screw dislocation in bcc metals. The position of the quadrupolar arrangement, located halfway between initial and final configurations, is indicated by dashed blue lines. (b) Peierls energy barrier ΔE , variation of the elastic energy of the dipole ΔE^{elas} , and Peierls potential $V_P = \Delta E - \Delta E^{\text{elas}}$ as a function of the reaction coordinate ξ in bcc tungsten. The present setup will be referenced in the following as "*stress*". The height of the barrier of Fig. 6b obtained using the setup *both* is indicated by a grey cross at $\xi = 0.5$ in (b).

One sees from Eqs. 41 and 42 that if the cut vector \vec{A} of the dipole, *i.e.* in the relative position of the two dislocations of the dipole, or the relaxation volume of the dislocation core changes, stress variations are generated in the simulation cell. These variations are recorded along a NEB path between configurations where both dislocations of the dipole move in opposite direction in a simulation cell with fixed periodicity vectors, sketched in Fig. 7a. There are two main differences between the present setup, called *stress*, and the setup *both* presented in Fig. 6: the two dislocations move in opposite directions, thus yielding stress variations and a change in the elastic energy of the dipole; the initial and final positions of the dipole do not match a quadrupolar arrangement, which instead is located halfway between the initial and final states of the path (dashed blue vertical lines in Fig. 7a). These stress variations $\Delta\bar{\sigma}$ are expressed as [79]:

$$\Delta\sigma_{ij}(\xi) = \frac{C_{ijkl}}{hS} [b_k \Delta A_l(\xi) - 2h \Delta\Omega_{kl}(\xi)], \quad (43)$$

with ξ the reaction coordinate along the NEB path, \bar{C} the elastic constant tensor, $\vec{b} = a_0\sqrt{3}/2\vec{e}_z$ the Burgers vector of the dislocations, S the projected surface of the simulation cell in the $\{111\}$ plane, h the corresponding cell height along the $[111]$ direction, $\Delta\bar{\Omega}$ the variation of the dislocation relaxation volume tensor, and $\Delta\vec{A}$ is the variation of the dipole cut vector. If the trajectory of the $+\vec{b}$ dislocation is defined by the displacement vector $\vec{r}(\xi) = (x(\xi), y(\xi), 0)$ with $x(0) = 0$ and $y(0) = 0$, then $\Delta\vec{A}(\xi) = 2b(y(\xi), -x(\xi), 0)$, where $\vec{r}(\xi) = (x(\xi), y(\xi), 0)$ is the displacement vector of the $+\vec{b}$ dislocation. Knowing, from *ab initio* NEB calculation, the stress variation along the minimum energy path, one thus obtains the dislocation trajectory and the variation of its relaxation volume along this path. Using the form of the elastic constant tensor in the frame of the $1/2\langle 111 \rangle$ dislocation then gives:

$$\begin{bmatrix} \Delta\sigma_{11} \\ \Delta\sigma_{22} \\ \Delta\sigma_{33} \\ \Delta\sigma_{32} \\ \Delta\sigma_{31} \\ \Delta\sigma_{12} \end{bmatrix} = \frac{2}{hS} \begin{bmatrix} C_{11} & C_{12} & C_{13} & 0 & C_{15} & 0 \\ C_{12} & C_{11} & C_{13} & 0 & -C_{15} & 0 \\ C_{13} & C_{13} & C_{33} & 0 & 0 & 0 \\ 0 & 0 & 0 & C_{44} & 0 & -C_{15} \\ C_{15} & -C_{15} & 0 & 0 & C_{44} & 0 \\ 0 & 0 & 0 & -C_{15} & 0 & C_{66} \end{bmatrix} \begin{bmatrix} -\Delta\Omega_{11} \\ -\Delta\Omega_{22} \\ -\Delta\Omega_{33} \\ +2b^2x \\ -2b^2y \\ -2\Delta\Omega_{12} \end{bmatrix}, \quad (44)$$

which gives the following set of 6 equations:

$$\begin{cases} hS\Delta\sigma_{11}(\xi) = -2C_{11}\Delta\Omega_{11}(\xi) - 2C_{12}\Delta\Omega_{22}(\xi) - 2C_{13}\Delta\Omega_{33} - 4C_{15}b^2y(\xi) \\ hS\Delta\sigma_{22}(\xi) = -2C_{12}\Delta\Omega_{11}(\xi) - 2C_{11}\Delta\Omega_{22}(\xi) - 2C_{13}\Delta\Omega_{33}(\xi) + 4C_{15}b^2y(\xi) \\ hS\Delta\sigma_{33}(\xi) = -2C_{13}(\Delta\Omega_{11}(\xi) + \Delta\Omega_{22}(\xi)) - 2C_{33}\Delta\Omega_{33}(\xi) \\ hS\Delta\sigma_{32}(\xi) = +4C_{44}b^2x(\xi) + 4C_{15}\Delta\Omega_{12}(\xi) \\ hS\Delta\sigma_{31}(\xi) = -2C_{15}(\Delta\Omega_{11}(\xi) - \Delta\Omega_{22}(\xi)) - 4C_{44}b^2y(\xi) \\ hS\Delta\sigma_{12}(\xi) = -4C_{15}b^2x(\xi) - 4C_{66}\Delta\Omega_{12}(\xi) \end{cases} \quad (45)$$

We now only consider the two equations of the system involving the dislocation position $x(\xi)$. Given that dislocations have glided across one Peierls valley in their final positions, *i.e.* $x(\xi = 1) = \lambda_P$, and since both initial and final configurations of the NEB path correspond to the dislocation ground state easy core configuration and are equivalent, one expects $\Delta\Omega_{ij}(\xi = 1) = 0$. As a result, one should thus have:

$$\begin{cases} +4C_{44}b^2\lambda_P = hS\Delta\sigma_{32}(\xi = 1) \\ -4C_{15}b^2\lambda_P = hS\Delta\sigma_{12}(\xi = 1) \end{cases} \quad (46)$$

When extracting the dislocation trajectory and relaxation volume with Eq. 43 from the stress variations recorded along the *stress* NEB path (Fig. 7a), we found that these quantities are very sensitive to the values of the elastic constants. Using the elastic constants calculated in the perfect crystal, the symmetry of the trajectory and relaxation volume along the path are not fully respected. Indeed, the initial $x(\xi = 0)$ and final $x(\xi = 1)$ positions of the dislocations do not fall exactly in the bottom of a Peierls valley, *i.e.* the easy

core configuration, and some components of the relaxation volume are not symmetrical with respect to the middle of the trajectory. This inconsistency can be fixed by slightly adjusting the elastic constants, which appears legitimate since the shearing of the crystal by the dislocation dipole induces a change of elastic constants because of anharmonicity. The elastic constants C_{44} and C_{15} are modified to enforce relation 46, using the stress differences $\Delta\sigma_{32}(\xi = 1)$ and $\Delta\sigma_{12}(\xi = 1)$ between the initial and final configurations given by *ab initio* calculations. Results of this adjustment are presented in Appendix D.

To obtain the Peierls potential V_P , the energy barrier $\Delta E(\xi)$ obtained from the NEB calculation presented in Fig. 7 needs to be corrected for the variation in the elastic energy of the dipole ΔE^{elas} caused by the change in the distance between dislocations upon crossing of the Peierls barrier. The elastic energy of the dipole is evaluated using anisotropic elasticity theory along the trajectory $(x(\xi), y(\xi))$ of the dislocation in the plane orthogonal to its line, extracted from the stress variations recorded along the NEB path with the reaction coordinate ξ . The elastic energy of the dipole is evaluated using the modified elastic constants obtained after performing the adjustment described above to enforce the symmetry of the path. This energy variation is subtracted from the NEB energy barrier to obtain the Peierls potential as $V_P = \Delta E - \Delta E^{\text{elas}}$. The height of the barrier obtained using setup *both* is reported on Fig. 7b, *i.e.* with a negligible variation in elastic energy, which is in perfect agreement with the corrected barrier using setup *stress*. This proves the validity of the method for evaluation of the elastic energy and effective correction of the Peierls energy barrier.

Using the variations of the relaxation volume $\Delta\bar{\bar{\Omega}}$ and the trajectory (x, y) of the dislocation extracted from *ab initio* calculations, it is then possible to model the effect of an applied stress $\bar{\bar{\Sigma}}$ on the 2D energy landscape given by the Peierls potential V_P , following the model of Kraych *et al.* [79]. Two assumptions are made for such modeling. The effect of the applied stress on V_P is modeled assuming this stress only tilts the Peierls potential by the amount of work produced by the Peach-Koehler force on the moving dislocation, but does not affect the potential itself. The validity of this first assumption was tested in the case of tungsten [45, 79] by evaluating the Peierls enthalpy barrier $\Delta H_P(\tau)$ opposing $1/2\langle 111 \rangle$ screw dislocation glide under an applied stress τ . Once the contribution of the Peach-Koehler force was removed from the obtained enthalpy barriers, the Peierls potential is retrieved, showing it is indeed independent of the applied stress. This result was also reported in other bcc transition metals using *ab initio* calculations [69] with a similar definition of the dislocation position, extracted from stress variations recorded along the NEB path. This gives the following expression of the 2D enthalpy barrier ΔH_P^{2D} of the dislocation [45, 79]:

$$\Delta H_P^{2D}(x, y, \bar{\bar{\Sigma}}) = V_P^{2D}(x, y) - \Sigma_{yz} b x(\bar{\bar{\Sigma}}) + \Sigma_{xz} b y(\bar{\bar{\Sigma}}) - \sum_{ij} \Sigma_{ij} \Delta\Omega_{ij}^{2D}(x, y, \bar{\bar{\Sigma}}), \quad (47)$$

with x and y the position of the dislocation in directions parallel and orthogonal to the glide plane respectively (*i.e.* $x \parallel [12\bar{1}]$ and $y \parallel [\bar{1}01]$ in the case of the $1/2[111]$ screw dislocation gliding in the $(\bar{1}01)$ plane presented in Fig. 7a). The two Σ_{xz} and Σ_{yz} are the components of the applied stress that produces a Peach-Koehler force on the dislocation. The other assumption is that both the trajectory (x, y) and the variations of the relaxation volume tensor $\Delta\bar{\bar{\Omega}}$ of the dislocation are also independent of the applied stress $\bar{\bar{\Sigma}}$, which has been demonstrated by *ab initio* calculations in tungsten [79]. Using this result, one can reduce the 2D enthalpy of Eq. 47 to a 1D function of the dislocation position x as:

$$\begin{aligned} \Delta H_P^{2D}(x, y, \bar{\bar{\Sigma}}) &= \Delta H_P^{1D}(x, \bar{y}(x), \bar{\bar{\Sigma}}) \\ &= V_P^{1D}(x) - \Sigma_{yz} b x + \Sigma_{xz} b \bar{y}(x) - \sum_{ij} \Sigma_{ij} \Delta\Omega_{ij}^{1D}(x), \end{aligned} \quad (48)$$

with $\bar{y}(x)$ the trajectory of the dislocation in the plane orthogonal to its line. The Peierls potential under zero applied stress $V_P^{1D}(x) = V_P^{2D}(x, \bar{y}(x))$ is presented in Fig. 7b in the case of a $1/2\langle 111 \rangle$ screw dislocation gliding in a $\{110\}$ plane in tungsten. The yield stress is then defined as the stress at which the energy of the saddle point of the enthalpy barrier given by Eq. 48 vanishes, thus allowing the dislocation to move freely since no energy barrier opposes its motion. This method can be applied to any mechanical loading of stress tensor $\bar{\bar{\Sigma}}$, to predict the yield stress as a function of the orientation of the loading axis.

3.2. Interatomic potentials and molecular dynamics simulation of dislocations

As discussed above in section 1.4, the use of semi-empirical interatomic potentials allows for considering systems containing a larger number of atoms than *ab initio* calculations. Studying dislocation-based plasticity using such methods allows to account for more complex mechanisms than the straight infinite dislocations *ab initio* calculations are limited to, such as interaction between different dislocations having more complex shapes, *e.g.* dislocation loops for instance. For these simulations too, a dislocation microstructure is introduced in a simulation cell using anisotropic elasticity theory. The obtained system is then relaxed at zero temperature with a molecular statics step, and dynamic conditions can then be applied to the system (*e.g.* temperature, stress, strain). An example of a dynamic straining simulation to study glide of a $1/2[111]$ screw dislocation is presented in Fig. 8.

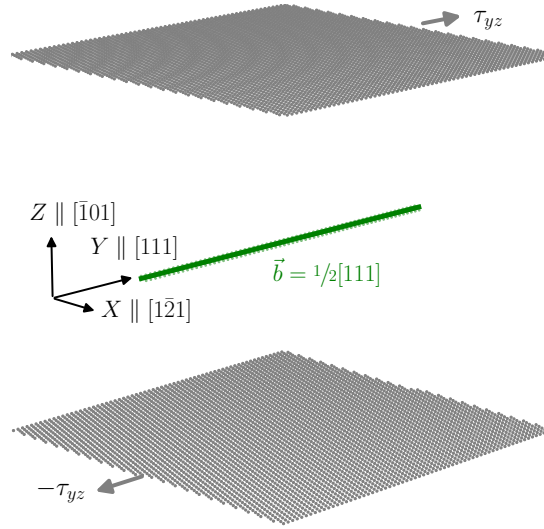


Figure 8: Sketch of the simulation setup used for the study of $1/2[111]$ screw dislocation glide under a resolved shear stress τ_{yz} in straining molecular dynamics simulations with flexible boundary conditions [167] and periodicity in X and Y directions.

Using the flexible boundary conditions introduced by Rodney [167], the application of a stress necessitates free surfaces, whose average displacement or force is controlled to induce a strain or a stress to the system. In this respect, dynamic straining conditions are applied by constraining the positions of atoms located in the top and bottom layers of the simulation cells along a direction with non-periodic boundary conditions, represented in grey on Fig. 8. These atoms are either forced to follow a constant strain rate $\dot{\epsilon}$ by displacing their center of gravity by a controlled amount at each time step of the molecular dynamics simulation, or a constant stress τ_{xz} by constraining the average forces applied on these two layers. In Fig. 8, periodic boundary conditions are applied along the X and Y Cartesian directions of the simulation cell, with free surfaces in the Z direction. In this case, if a force is applied on atoms of the top and bottom layers along the X (respectively Y) direction, the resulting stress has a component τ_{xz} (respectively τ_{yz}). A strain develops in the simulation cell as a result of the applied stress, which is evaluated at each time step through the average displacement of atoms located in the top and bottom layers. Now considering constant strain rate conditions, an average displacement imposed on the two layers oriented by Z along the X (respectively Y) direction results in a strain ϵ_{xz} (respectively ϵ_{yz}). Since a displacement is imposed at each time step Δt of the simulation, the corresponding strain rate is then $\dot{\epsilon} = \epsilon(t + \Delta t) - \epsilon(t) / \Delta t$. This controlled strain induces a stress on the system which is evaluated at each time step from the average force generated on the top and bottom layers of the simulation cell.

Due to the limited time scale accessible to molecular dynamics simulations, of the order of a few nanoseconds at a reasonable computational cost, simulated strain rates $\dot{\epsilon}$ are several orders of magnitude higher

than experimental conditions (see Literature review, section 2.2). In this work, straining simulations are performed under constant strain rate conditions, imposed by controlling the average displacement of atoms located in the upper and lower layers of the simulation cell, with flexible boundary conditions [167]. The geometry of the cell, indicating periodic and non-periodic directions, dislocation setup, and simulation parameters used for molecular statics or dynamics simulations will be detailed before each calculation presented in the following as they strongly depend on the system of interest.

Summary of the Methods:

- *Ab initio* calculations allow for an accurate description of a many-body system in the frame of density functional theory, which will be used to study bulk properties of bcc Cr (elastic, magnetic), and straight infinite dislocations in bcc transition metals.
 - The tight-binding method reduces computational costs with respect to DFT, keeping an explicit inclusion of electrons in calculations. This allows for an accurate evaluation of the properties of bulk Cr and the study of more complex properties linked to its magnetic properties and plasticity.
 - Effective interaction models parametrized on *ab initio* calculations allow for exploration of magnetic configurations on a fixed lattice through a Metropolis Monte Carlo sampling, which will be used to study finite temperature magnetic excitations in bcc Cr and their effect on its plasticity.
 - *Ab initio* modeling of dislocations, which is limited to infinite straight lines due to the high computational cost of such calculations, has helped uncover some of the key properties of $\frac{1}{2}\langle 111 \rangle$ screw dislocations in bcc transition metals, which can be linked to their macroscopic mechanical behavior.
 - To overcome the limited system sizes accessible to *ab initio* calculations, interatomic potentials can be used, allowing for the study of multiple dislocation processes, or performing dynamic straining simulations at finite temperature, but neglecting all electronic effects, including magnetic contributions.
-

Chapter 1: Bulk properties of bcc chromium

Among the seven bcc transition metals, Cr is the only one with a magnetic ground state close to antiferromagnetism at low temperature. It is therefore of importance to have a good understanding of its different magnetic phases before moving on to the study of plasticity in bcc Cr. Indeed, the interplay between magnetism and defects controlling plastic deformation can have an impact on the mechanical properties of Cr. The focus of this chapter is to quantify the impact of magnetism on the bulk properties of bcc Cr, in terms of the relative stability of its different magnetic phases, and their elastic behaviors. Generalized stacking faults are then presented, as an introductory step towards the study of dislocations.

1. Magnetic phases

1.1. Stability of the different magnetic phases

In our *ab initio* modeling of bulk bcc Cr, we considered the three non-magnetic (NM), antiferromagnetic (AF), and SDW phases. Before getting into the detailed competition between ordered magnetic phases, it is worth noting that the NM phase, *i.e.* where all magnetic moments are zero, is found to have the highest energy among the three considered magnetic phases (see Tab. 1). However, as discussed in the Literature review (see section 3.1.2), DFT calculations fail to reproduce the experimental SDW magnetic ground state of Cr [112–115, 142], and invariably predict the AF phase to have a lower energy at 0 K. This was reported in various theoretical works using different exchange and correlation functionals and DFT approximations. Indeed, all Vanhoof *et al.* [114] using LDA + U, Soulaire *et al.* [113] using both LDA, GGA, and mixed LDA-GGA functionals, and Cottenier *et al.* [112] using the FLAPW method with GGA functional, found the SDW to have a higher energy than the AF phase.

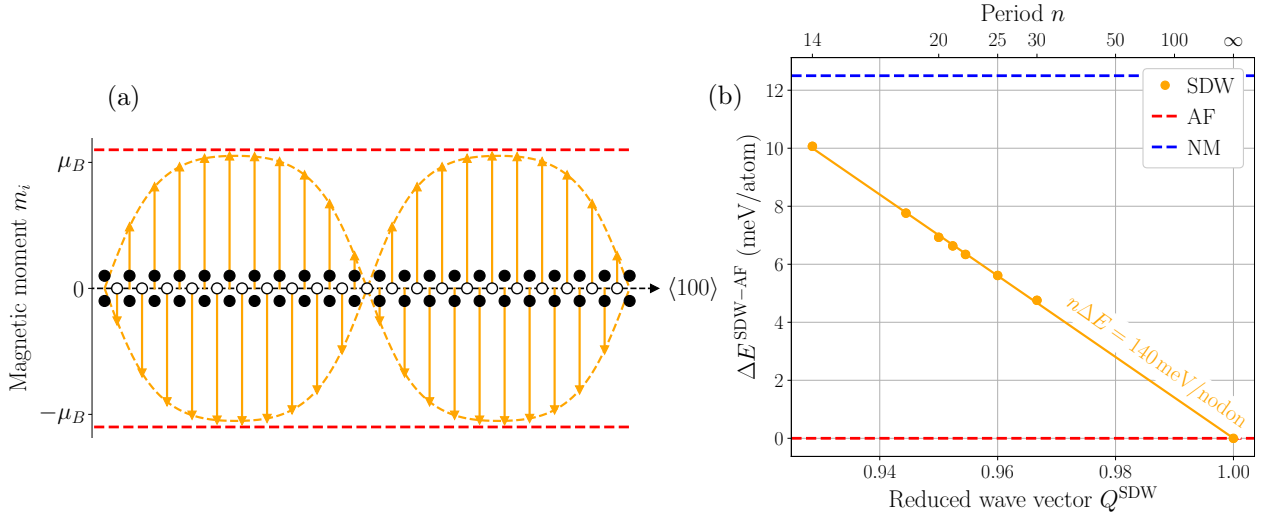


Figure 1: (a) Structure of a spin-density wave of period $n = 20 a_0$ along a $\langle 100 \rangle$ crystal axis, *i.e.* amplitude of the magnetic moments m_i along the propagation direction. (b) Energy difference between the SDW and AF phases $\Delta E^{\text{SDW-AF}}$ as function of the reduced wave vector $Q = 1 - 1/n$ of the SDW with $\vec{q} = Q \times 2\pi/a_0\langle 100 \rangle$.

Through neutron and coherent X-ray diffraction experiments, no evidence of the occurrence of bulk non-collinear magnetic structures have been found. These observations also confirmed the collinearity of the SDW magnetic ground state of bcc Cr at low temperature [6, 95]. Hence, all three considered bulk magnetic phases are modeled within the collinear magnetism approximation, the SDW corresponding to a modulation of the magnitude of the spins with a locally AF order. However, we found that stable non-collinear magnetic structures can arise from thermal excitations, which will be evaluated *ab initio* and discussed in a following chapter focused on the study of magnetism at finite temperature. Due to the finite size limitation of DFT simulation cells, we were not able to consider the incommensurate state of the SDW, but instead modeled commensurate structures of period $n a_0$, equal to an integer n multiple of the lattice parameter a_0 in a $\langle 100 \rangle$

direction of the lattice. The wave-vector of such waves is defined as $\vec{q} = 2\pi/a_0 \times [1 - 1/n, 0, 0]$. To be able to distinguish between the longitudinal and transverse polarizations of the SDW, spin-orbit coupling, and hence non-collinear magnetism, are needed. However, Soulaire *et al.* [113, 142] showed that the energy difference between the two polarizations of the wave is not relevant within the accuracy of standard DFT calculations, motivating our choice to neglect these different polarizations and to use collinear magnetism approximation. The energy difference between the SDW and AF phases is presented in Fig. 1b as a function of the wave-vector and period of the wave.

Our calculations lead to a higher energy for the SDW than the AF phase for any period n of the wave, in good agreement with previous *ab initio* studies, but in contradiction with experiments. Its excess energy per atom ΔE varies linearly with the magnitude of the wave-vector $1/n$. This discrepancy with experiments is often attributed to the inner limitations of DFT calculations [115], in particular its inability to give a good reproduction of the Fermi surface of Cr. However, Vanhoof *et al.* [114] offer another possible explanation in the form of a nodon model. Their approach to the problem suggests that the stabilization of the SDW comes from the perturbation of the AF order by the introduction of nodes along $\langle 100 \rangle$ lattice directions, corresponding to locally zero magnetic moments, and their associated entropy. The linear variation of the energy difference between the SDW and AF phases as a function of \vec{q} corresponds to a nodon excitation energy of 140 meV/nodon, very close to the value of 152 meV/nodon reported by the authors [114]. However, this energy can only be defined for a surface unit of $\{100\}$ planes perpendicular to the propagation of the SDW. Therefore, a more accurate representation of the nodon would be as a fault energy expressed in surface unit, resulting in $\gamma = \Delta E/a_0^2 = 17.1 \text{ meV}/\text{\AA}^2$, with $\Delta E = 140 \text{ meV/nodon}$ and a_0^2 the surface of a $\{100\}$ plane. As the nodon energy actually depends on the surface perpendicular to the propagation of the wave, this excitation energy of a nodon is not bounded, and the contribution of its entropy cannot account for the stabilization of the SDW through the mechanism proposed by Vanhoof *et al.* [114].

Table 1: Bulk properties of the three NM, AF and SDW phases: lattice parameter a_0 , bulk modulus B , shear moduli $C' = (C_{11} - C_{12})/2$ and C_{44} , elastic anisotropy ratio $A = C_{44}/C'$, energy difference ΔE with respect to the AF ground state, and bulk magnetic moment m_0 . Experimental data presented in the last row are taken from Palmer and Lee [109] and were measured at a temperature of 4.2 K, corresponding to an incommensurate SDW magnetic ground state.

Magnetic phase	a_0 (Å)	B (GPa)	C' (GPa)	C_{44} (GPa)	A	ΔE (meV/atom)	m_0 (μ_B)
NM	2.847	262	166	98	0.59	12.5	0
AF	2.865	186	185	96	0.52	0	1.10
SDW ($n = 20 a_0$)	2.857	198	187	101	0.54	6.4	1.05
Experiments	2.884	190	153	104	0.68	/	0.50

The variation of the magnetic moments m_i of atoms located at positions \vec{R}_i along the $\langle 100 \rangle$ propagation direction of the SDW takes the form of a Fourier series with only two harmonics [6]:

$$m_i = M_1 \sin(\vec{q} \cdot \vec{R}_i) + M_3 \sin(3\vec{q} \cdot \vec{R}_i), \quad (1)$$

with M_1 and M_3 the amplitudes of these two harmonics, the ratio M_3/M_1 determining the shape of the wave. For a SDW of period $n = 20 a_0$, we found $M_1 = 1.18 \mu_B$ and $M_3 = 0.15 \mu_B$, resulting in $M_3/M_1 = 0.12$, comparing very well to other DFT studies [113, 114], but poorly with the experimental value of 0.02 measured for the incommensurate wave at low temperature [6, 168]. The magnetic moment modulation induced by a SDW of different periods with the shape parameter M_3/M_1 are presented in Fig. 2b, showing very little variation upon increasing the period n of the wave. This gives a peak amplitude of $1.05 \mu_B$, which is very close to the $1.1 \mu_B$ found in the AF phase. However, these values are drastically overestimated with respect to the experimental value of $0.5 \mu_B$ measured at 4.2 K [6]. This discrepancy is a well-known artefact of the GGA-PBE exchange and correlation functional, also reported in previous theoretical works [113–115]. The equilibrium bulk lattice parameters a_0 of the three magnetic phases is found lower than the experimental

value of 2.884 \AA at 4.2 K , with however a better agreement found for the AF and SDW than the NM phase (Tab. 1). A better agreement with the experimental bulk magnetic moment is found using the LDA functional, at the cost of a less accurate evaluation of the lattice parameter [113].

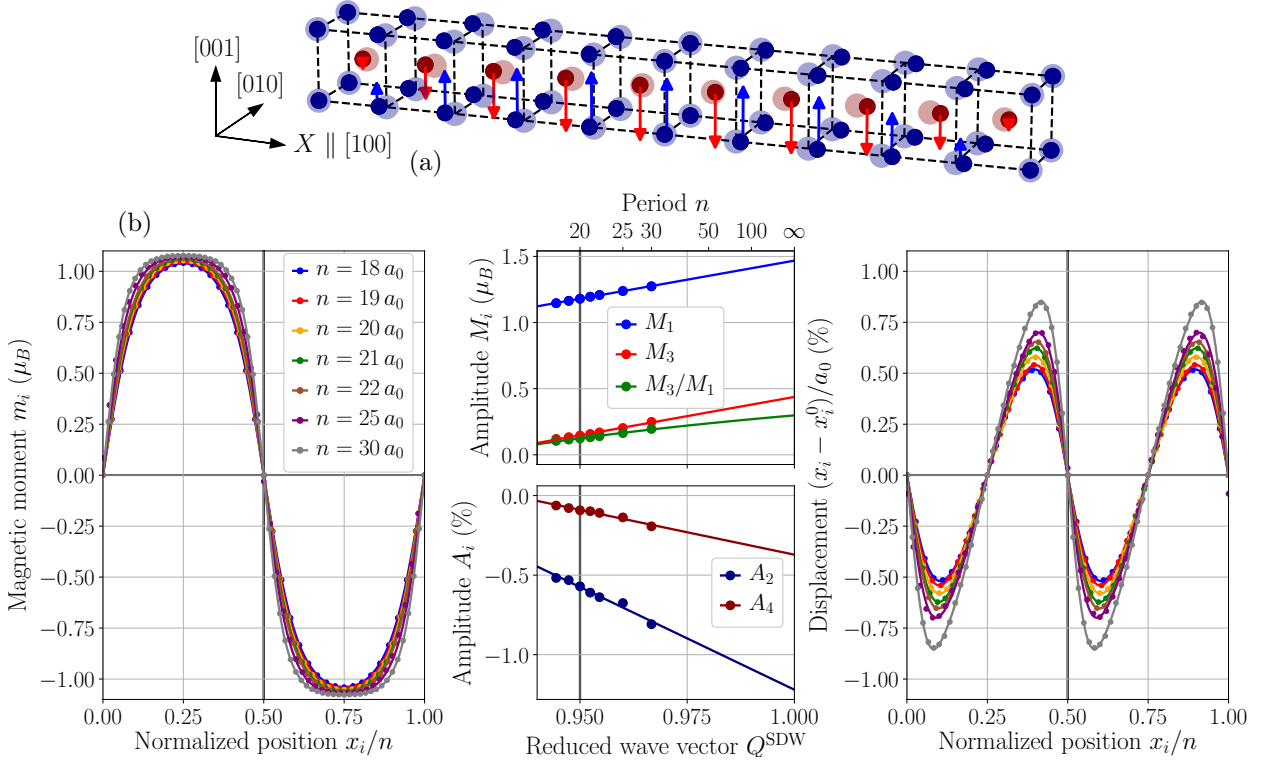


Figure 2: (a) Strain wave along the propagation of a SDW in the first half of its period $20 a_0$. Atoms are represented by shaded and full circles in their initial and relaxed positions respectively, with displacements magnified by a factor 25. (b) Shapes of the SDW (left panel) and strain wave (right panel) for different periods of the SDW. The amplitudes of the Fourier series coefficient are displayed in the center panel as a function of the reduced wave vector $Q^{\text{SDW}} = 1 - 1/n$ of the SDW.

As introduced in the Literature review (see section 3.1.1), the SDW comes with a charge modulation, or charge-density wave (CDW), and a perturbation of the atomic positions in the $\{100\}$ planes orthogonal to the propagation of the SDW, or strain wave [6, 169]. These two additional waves share half the periodicity and wave vector of the SDW, and can also be described using different Fourier series. However, as reported by Soulaïrol *et al.* [113] using various *ab initio* methods, the amplitude of the CDW is too small compared to the precision of the calculations, which we also report regardless of the SDW period. As for the strain wave, it is described with the following Fourier series using the first two harmonics:

$$x_i = x_i^0 + A_2 \sin(2\vec{q} \cdot \vec{R}_i) + A_4 \sin(4\vec{q} \cdot \vec{R}_i), \quad (2)$$

where x_i and x_i^0 are the relaxed and bulk positions of atom i respectively, located at \vec{R}_i along the propagation of the SDW of wave vector \vec{q} . The strain wave then generates atomic displacements given by:

$$\frac{x_i - x_i^0}{a_0} = \frac{A_2}{a_0} \sin(2\vec{q} \cdot \vec{R}_i) + \frac{A_4}{a_0} \sin(4\vec{q} \cdot \vec{R}_i), \quad (3)$$

whose amplitude can be measured experimentally [6]. The existence of such perturbation waves has been reported in various experimental works using both neutron and coherent X-ray diffraction techniques, resulting in an experimental value for A_2/a_0 ranging from -0.10 to -0.35% [168–172]. This compares well with the -0.57% we find for a SDW of period $20 a_0$, close to the experimental periodicity of the SDW (see

vertical line in the middle panel of Fig. 2). We also plot on Fig. 2 the profiles of both magnetic moments m_i and atomic displacements $x_i - x_i^0$ for different periods of the SDW ranging between 18 and $30 a_0$. As the period of the SDW increases, the modulation of magnetic moments along the wave tends to a profile close to a magnetic domain wall, confirming our description of the nodon as a surface fault. Now looking at the strain wave, the peak amplitude of the perturbation increases with the period of the SDW, maintaining a similar shape. In the first theoretical works on the stability of the SDW using *ab initio* calculations, it was thought that the strain wave would stabilize the SDW, reversing the energy difference with the AF ground state [111, 173]. However, Soulaire *et al.* [113] later reported a very small energy gain induced by the presence of the strain wave along the SDW of -0.5 meV/atom, or approximately 4% of the energy difference between the SDW and AF phases, therefore invalidating this hypothesis. In our study, we find an even smaller energy gain of -0.12 meV/atom, regardless of the period of the SDW, confirming these results.

1.2. Elastic properties of the magnetic phases

The elastic properties of the three considered NM, AF and SDW phases are then evaluated, and results are presented in Tab. 1. To do so, three different deformations are applied to a crystal unit-cell corresponding to a hydrostatic pressure, a tetragonal and a trigonal perturbation, and the resulting energy variations fitted to a polynomial equation of state [174]. The SDW structure has a tetragonal symmetry, corresponding to 6 independent elastic constants, while the NM and AF phases have a cubic symmetry, and thus 3 independent constants. However, the anisotropy of the SDW is very small, with a maximum discrepancy of 6 GPa between C_{11} and C_{22} . The presented results in cubic symmetry are obtained by averaging over the three [100], [010] and [001] possible wave directions of the SDW with periodicity $n = 20 a_0$. We note that the obtained values for the AF and SDW phases are closer to experimental data at 4.2 K of Palmer and Lee [109] than the NM phase, in particular regarding the bulk modulus B . This is a consequence of the high sensitivity of magnetism to volume variation, highlighting its significant impact on the elastic properties of bcc Cr at low temperature.

The elastic properties of the SDW and AF phases are very close, the discrepancy with experiments coming from an overestimation of C' . Most importantly, both C' and C_{44} shear moduli of these two magnetic phases are identical within DFT accuracy. This is also true of the elastic anisotropy A , which have an influence on some important elastic properties of dislocations, such as the formation of junctions or the relative stability between different Burgers vectors, which will be discussed in the following. Both observations are of upmost importance in our case as screw dislocations do not induce a variation of volume, and their elastic behaviors is governed by these two shear moduli, *a priori* resulting in similar elastic properties of screw dislocations in these two magnetic phases.

In the following, the AF phase will be used as an approximate of the experimental SDW ground state of bcc Cr, based on their close magnetic order and elastic properties. This choice is motivated by the impossibility to introduce both a SDW and structural defects relevant in the plastic deformation of Cr, such as a stacking fault or a dislocation, in a simulation cell containing a reasonable number of atoms. Besides, as shown in Fig. 18 of the Literature review, both Bacon and Cowlam [100] and Williams and Street [101] have observed that the AF phase may be stabilized above 200 K in strained samples containing dislocations, with an increased Néel temperature of 450 K. It appears therefore fully legitimate to study the plastic deformation of bcc Cr in this approximate AF phase.

2. Generalized stacking faults

As an introductory step before studying dislocations in a crystal, calculations of generalized stacking faults (GSF) [175] may give useful information on the relative ease to shear a given crystal in different planes (*i.e.* glide plane), and along different directions (*i.e.* Burgers vector). A GSF maps the excess energy γ_{GSF} (per surface unit) associated with the rigid shearing of an initially perfect crystal in two halves by a fault vector \vec{f} laying in the crystallographic fault plane, also called a γ -surface.

2.1. Simulation setup

Simulation cells for the study of the GSFs contain a periodic stacking of the crystallographic planes of interest. To maximize the separation distance d_{fault} between two periodic images of the fault, the rigid shear displacement vector \vec{f} is also applied to the periodicity vector normal to the fault plane \vec{u}_3 , as sketched in Fig. 3. This way, only one fault is contained per simulation cell and free surfaces are avoided. The atoms are then allowed to relax only in the direction perpendicular to the fault plane to maintain the fault during relaxation [64]. The GSF energy γ_{GSF} per unit surface is given by:

$$\gamma_{\text{GSF}}(\vec{f}) = \frac{E_{\text{fault}}(\vec{f}) - E_{\text{bulk}}}{S_{\text{GSF}}}, \quad (4)$$

where $E_{\text{bulk}} = E_{\text{fault}}(\vec{f} = \vec{0})$ is the energy of the perfect bulk crystal (Fig. 3a), and E_{fault} is the energy of the crystal sheared by a vector \vec{f} in a plane of surface S_{GSF} (Fig. 3c).

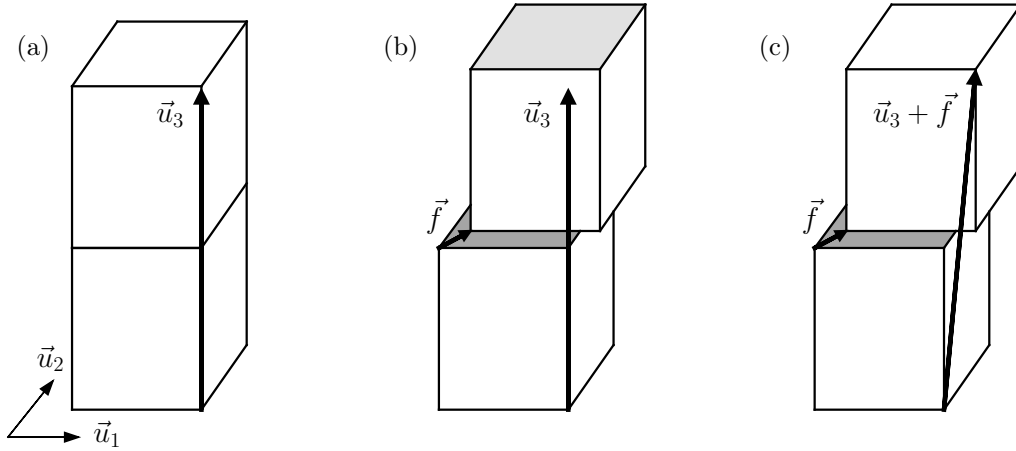


Figure 3: Sketch of the simulation setup used for the calculation of GSF energies showing (a) the bulk structure, and the crystal sheared by a fault vector \vec{f} using (b) free surfaces, and (c) periodic boundary conditions.

As detailed in the Literature review, dislocations in Cr have a Burgers vector corresponding to the smallest periodicity vectors of the bcc lattice, namely $\frac{1}{2}\langle 111 \rangle$ or $\langle 100 \rangle$. As to get insights on the ease to shear a given glide plane by one of these Burgers vectors, they need to be contained in the fault plane. These dislocations mainly move in $\{110\}$ planes across the temperature range where the Peierls mechanism prevails, but also occasionally in $\{112\}$ and $\{123\}$ planes [176], which has also been observed in Cr [13, 122]. As $\{110\}$ is the main glide plane family, the whole γ -surface is calculated only for these planes in both the NM and AF phases of bcc Cr, and only in the NM phase for $\{112\}$ and $\{123\}$ planes. As dislocations with $\langle 100 \rangle$ Burgers vectors can theoretically glide in $\{100\}$ planes, although it is not observed experimentally,

Table 2: Geometry of the simulation cells used for the calculation of the $\{110\}$, $\{112\}$, $\{123\}$ and $\{100\}$ γ -surfaces: periodicity vectors (\vec{X} , \vec{Y} , \vec{Z}), number of stacked planes n_Z and distance d_{GSF} between two periodic images of the faults.

Fault plane	\vec{X}	\vec{Y}	\vec{Z}	n_Z	d_{fault}
$\{110\}$	$[\bar{1}1\bar{2}]$	$[111]$	$[\bar{1}10]$	12	$6a_0\sqrt{2}$
$\{112\}$	$[\bar{1}10]$	$[111]$	$[\bar{1}1\bar{2}]$	24	$4a_0\sqrt{6}$
$\{123\}$	$[\bar{5}41]$	$[111]$	$[\bar{1}23]$	28	$2a_0\sqrt{14}$
$\{100\}$	$[100]$	$[010]$	$[001]$	40	$20a_0$

the $\{100\}$ γ -surface is also studied in the NM phase. Projections of the γ -surfaces along the $\frac{1}{2}\langle 111 \rangle$ or $\langle 100 \rangle$ lines, or γ -lines, are calculated in both magnetic phases as they represent the most useful quantity. The convergence of the GSF with respect to the number of stacked planes was checked, which is assured by the geometry of the cells given in Tab. 2. A grid of 10 fault vectors \vec{f} per direction and a Fourier series interpolation is then used for the construction of the γ -surfaces.

2.2. Complete γ -surfaces in the NM phase

Dislocations with $\frac{1}{2}\langle 111 \rangle$ Burgers vectors in bcc metals glide preferentially in one of the three families of crystallographic planes with the largest interplanar distance, namely $\{110\}$, $\{112\}$, and $\{123\}$ by order of increasing distance, with a prevalence for $\{110\}$ planes [176], which has also been observed experimentally in bcc Cr [13, 34, 123, 124]. The γ -surface in all four $\{110\}$, $\{112\}$, $\{123\}$ and $\{100\}$ planes in the NM phase of bcc Cr are presented in Fig. 4. The three $\{112\}$, $\{123\}$ and $\{100\}$ γ -surfaces show very high extrema compared to $\{110\}$ planes (Fig. 4a), with a pronounced twinning/antitwinning (T/AT) asymmetry in $\{112\}$ and $\{123\}$ planes, which will be discussed later. Overall, no stable energy minimum is found in all 4 presented γ -surfaces, except for the unfaulted crystal recovered upon shearing by a periodicity vector of the lattice. The minimum energy paths for $\vec{b} = \frac{1}{2}\langle 111 \rangle$ shear correspond to a fault vector \vec{f} always collinear to the Burgers vector \vec{b} in all three $\{110\}$, $\{112\}$ and $\{123\}$ planes. No edge component is thus expected to develop from the possible spreading of the $\frac{1}{2}\langle 111 \rangle$ screw dislocation core. This is also the case for a $\vec{b} = \langle 100 \rangle$ Burgers vector shearing a $\{100\}$ plane (see the green arrow in Fig. 4d), but not for a $\{110\}$

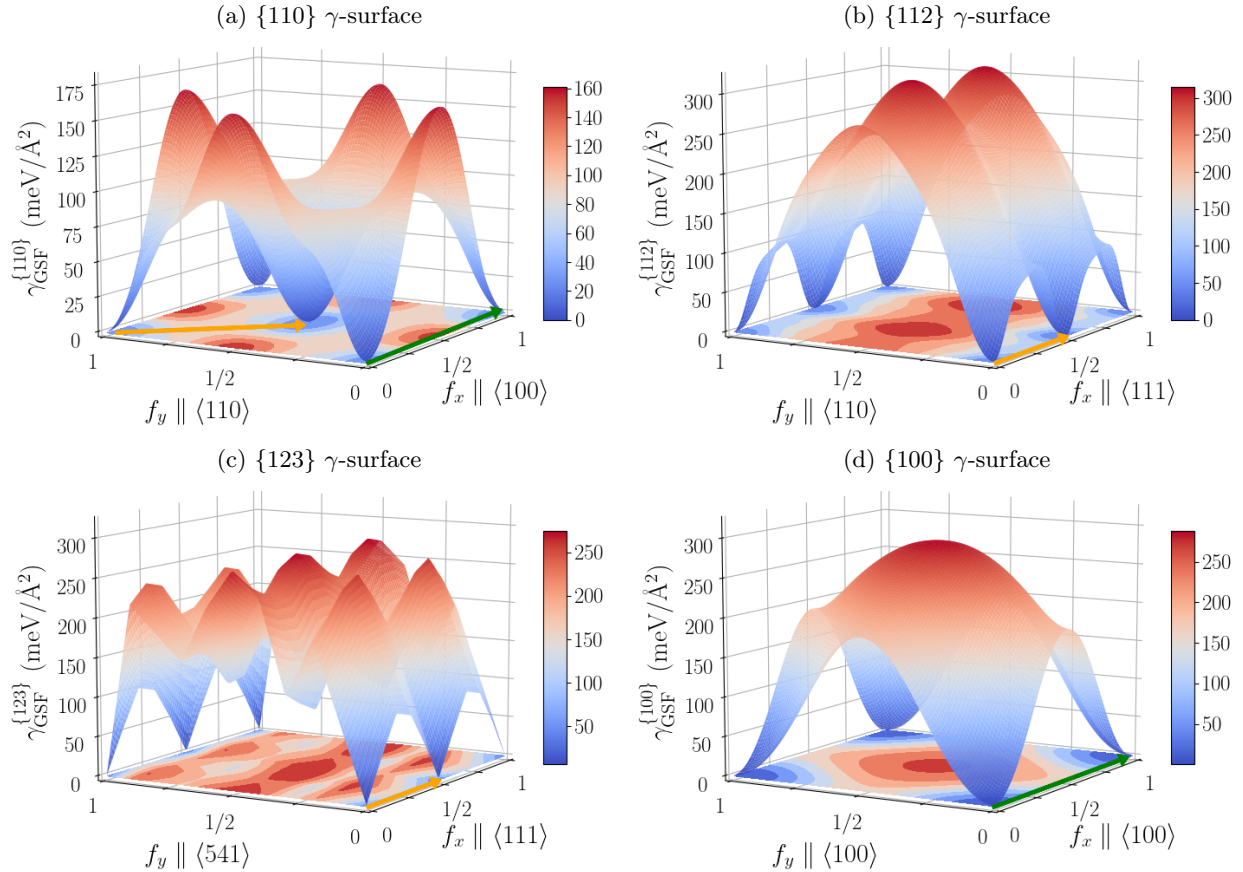


Figure 4: Generalized stacking fault energy γ_{GSF} in the NM phase of bcc chromium over (a) $\{110\}$ (b) $\{112\}$, (c) $\{123\}$, and (d) $\{100\}$ fault planes. The orange in (a), (b) and (c), and green arrows in (a) and (d) show a $\frac{1}{2}\langle 111 \rangle$ and $\langle 100 \rangle$ Burgers vector respectively.

plane. Indeed, the path for which the fault vector stays collinear to the Burgers vector upon shearing of the lattice (green arrow in Fig. 4a) corresponds to a maximum energy path of the $\{110\}$ γ -surface. A possible edge component may therefore develop when a $\langle 100 \rangle$ screw dislocation starts shearing the crystal, with the associated spreading of its core. We will discuss in the following the core structure of this $\langle 100 \rangle$ dislocation in bcc transition metals, and how this possible spreading was discarded using both *ab initio* calculations and semi-empirical interatomic potentials. We also note that shear is easier along a $\langle 111 \rangle$ than a $\langle 100 \rangle$ direction in $\{110\}$ planes, indicating an *a priori* easier glide of $1/2\langle 111 \rangle$ dislocations than $\langle 100 \rangle$ in these planes.

2.3. $\langle 111 \rangle$ slip mode in the NM and AF phases

The complete $\{110\}$ γ -surface in the AF phase is presented in Fig. 5. The shape of the two γ -surfaces is almost identical in the two NM and AF phases (see Fig. 4a for comparison), except for the introduction of a stable fault for a vector $\vec{f} = \vec{b} = 1/2\langle 111 \rangle$ in the AF phase (orange arrow in Figs. 4a and 5). This vector corresponds to the smallest periodicity vector of the bcc lattice, hence there is no excess fault energy in the NM phase as the perfect crystal is recovered upon shearing by $\vec{b} = 1/2\langle 111 \rangle$. However, this vector breaks the AF order of bcc Cr, thus leading to the generation of a fault in the AF phase. This fault corresponds to a local minimum in the GSF energy, which is better visualized on the $\langle 111 \rangle$ γ -line, defined as the projection of the γ -surface in the $\langle 111 \rangle$ direction, presented in Fig. 6a. Are also presented the $\langle 111 \rangle$ γ -lines for the $\{112\}$ and $\{123\}$ fault planes in both the NM and AF phases (Fig. 6b and c respectively).

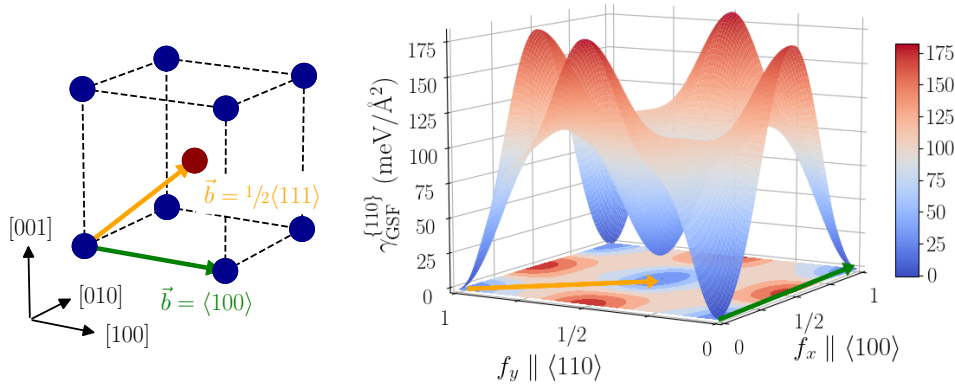


Figure 5: Generalized stacking fault energy γ_{GSF} over a $\{110\}$ plane, or $\{110\}$ γ -surface, in the AF phase of bcc Cr. The orange and green arrows show a $1/2\langle 111 \rangle$ and $\langle 100 \rangle$ Burgers vector respectively. The γ -surface in the AF phase shows a stable magnetic fault at the Burgers vector $\vec{b} = 1/2\langle 111 \rangle$ (orange arrow).

To rationalize all presented GSF energy profiles and surfaces, we evaluate the shear stress τ_{GSF} associated with the rigid shearing of the crystal by a fault vector $\langle hkl \rangle$ in a given plane as:

$$\tau_{\text{GSF}} = \max_{f \in \gamma_{\langle hkl \rangle}} \left[\frac{\partial \gamma_{\text{GSF}}(f)}{\partial f} \right] \quad (5)$$

All extracted quantities are presented in Tab. 3 for the $\langle 111 \rangle$ slip mode in the NM and AF phases of bcc Cr. The two $\langle 111 \rangle$ γ -lines in $\{112\}$ and $\{123\}$ planes exhibit the well-known twinning/antitwinning (T/AT) asymmetry, showing an easier shearing sense along the same displacement vector [64]. This corresponds to a lower maximal slope of the $\langle 111 \rangle$ γ -line in the twinning direction (indicated by a black arrow in Fig. 6b) than the antitwinning direction for $\{112\}$ and $\{123\}$ planes (see Tab. 3). Due to the magnetic fault located at the middle of the three γ -lines for the fault vector $\vec{f} = \vec{b} = 1/2\langle 111 \rangle$, the two extrema in the slope of the GSF energy profiles differ in the two $\vec{f} \in [0, 1/2\langle 111 \rangle[$ and $\vec{f} \in]1/2\langle 111 \rangle, \langle 111 \rangle]$ halves, yielding two different values for the stress necessary to shear the lattice. The shear stress is lower starting from $\vec{f} = 1/2\langle 111 \rangle$ towards the perfect crystal at $\vec{f} = \vec{0}$ or $\langle 111 \rangle$, *i.e.* after the magnetic fault has already been generated by a first $1/2\langle 111 \rangle$ shear displacement, than starting from $\vec{f} = \vec{0}$ or $\langle 111 \rangle$ towards the position of the magnetic fault. This is due to the added stress needed to introduce the magnetic fault in the crystal.

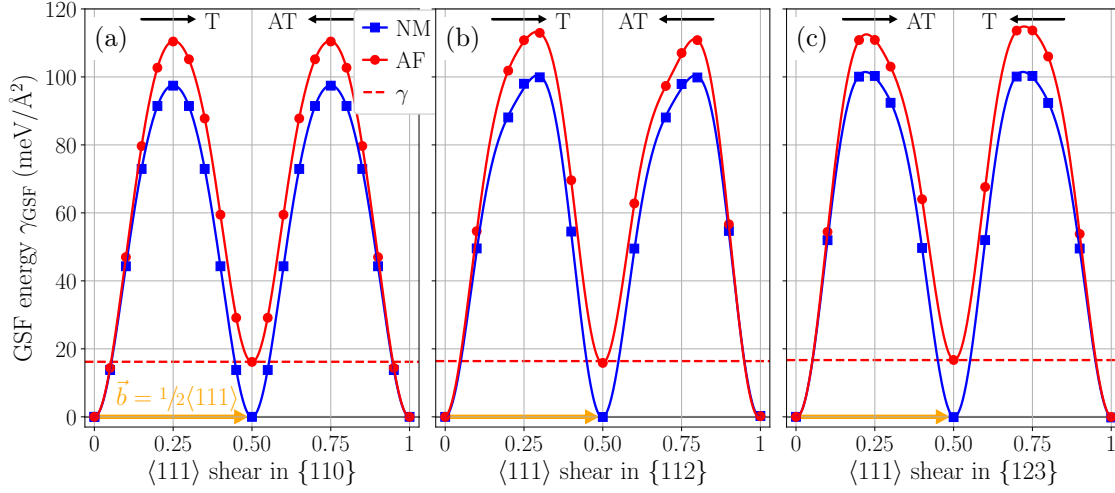


Figure 6: Generalized stacking fault energy along a $\langle 111 \rangle$ direction, or $\langle 111 \rangle$ γ -line, in a (a) $\{110\}$, (b) $\{112\}$, and (c) $\{123\}$ fault plane in the NM (blue squares) and AF (red circles) phases. Orange arrows show the Burgers vector $\vec{b} = 1/2\langle 111 \rangle$ for which a magnetic fault of energy γ is created. Symbols are *ab initio* results and lines their interpolations with Fourier series.

Table 3: Height γ_{GSF} (meV/Å²) of the different $\langle 111 \rangle$ γ -lines presented in Fig. 6, and the resulting shear stress τ_{GSF} (GPa) for the twinning/antitwinning sense in the NM and AF phases of bcc Cr. Values in the AF phase indicated in italic are obtained for a shearing of the lattice starting from a magnetic fault already present in the crystal after shearing by $1/2\langle 111 \rangle$.

Fault plane	γ_{GSF}		τ_{GSF}	
	NM	AF	NM	AF
$\{110\}$	98	111	0.81 / 0.81	0.88 (0.81) / 0.88 (0.81)
$\{112\}$	100	113	0.85 / 1.04	0.94 (0.80) / 1.14 (1.00)
$\{123\}$	101	115	0.88 / 1.01	0.97 (0.81) / 1.08 (0.97)

These magnetic faults are introduced in the crystal upon shearing by a fault vector equal to $\vec{b} = 1/2\langle 111 \rangle$, with very close energies per unit surface $\gamma_{\{110\}} = 16.2$, $\gamma_{\{112\}} = 16.4$ and $\gamma_{\{123\}} = 16.7$ meV/Å² in the three planes. These energies are obtained after full relaxation in all three Cartesian directions to check the stability of the fault. The shearing of the crystal by a $1/2\langle 111 \rangle$ Burgers vector results in two parallel magnetic moments forced to face each other, leading to a magnetic frustration partially resolved by reducing the amplitude of the magnetic moments in the vicinity of the fault plane. This is equivalent to the creation of a magnetic domain wall separating two half crystals of reverse magnetization. These magnetic fault energies are very close to the $\{100\}$ nodon surface energy of 17.1 meV/Å² found in the previous section, indicating the same process is involved in both cases. The structure of these magnetic faults are presented in Fig. 7 for all three $\{110\}$, $\{112\}$ and $\{123\}$ planes. We also evaluated the convergence of the magnetic fault surface energy with respect to the separation distance between periodic images of the fault for $\{110\}$ and $\{112\}$ planes. We report a very good convergence of the resulting fault energies with respect to the size of the simulation cell for the values of Tab. 2. However, we chose to present in Fig. 7 the structure of the magnetic faults in the two $\{110\}$ and $\{112\}$ planes obtained using larger cells, with 20 $\{110\}$ and 60 $\{112\}$ stacked planes respectively, to better visualize its magnetic structure.

The obtained profiles of the magnetic moments along the direction orthogonal to the fault plane is fitted to a standard domain wall profile of the form:

$$m(z) = m_0 \tanh\left(\frac{z - z_0}{w/2}\right) \quad (6)$$

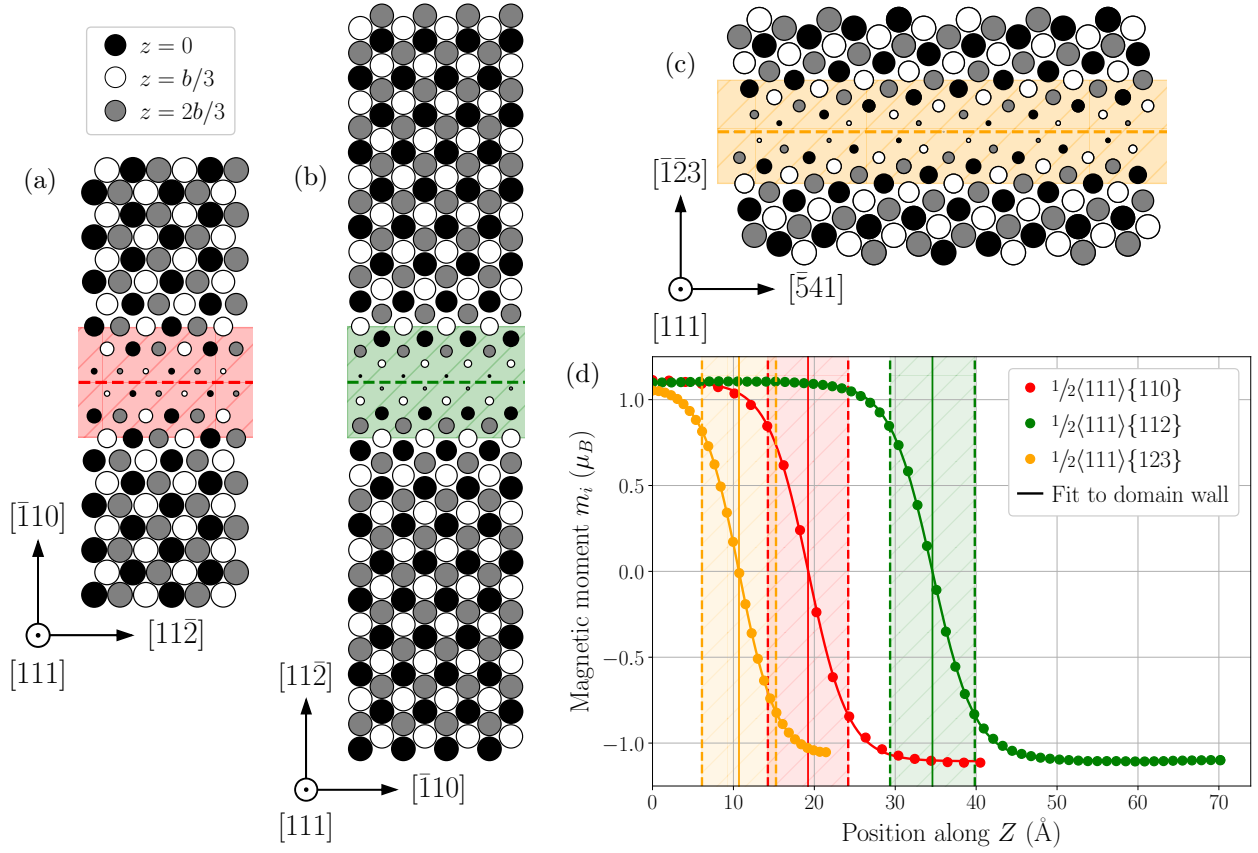


Figure 7: Structure of the stable collinear magnetic faults generated by a fault vector $\vec{f} = \vec{b} = \frac{1}{2}\langle 111 \rangle$ in a (a) {110}, (b) {112}, and (c) {123} plane projected in the [111] plane. Atoms are represented in different colors depending on their height along the [111] direction in the initial perfect crystal, with a size proportional to their magnetic moments. (d) Profiles of the magnetic domain walls created by the fault in the three {110}, {112} and {123} planes. The width of the walls are shaded.

where $m_0 = 1.1 \mu_B$ is the bulk magnetic moment, z_0 is the position of the fault plane, and w is the width of the domain wall. Results are shown on Fig. 7d in all three planes. We find an almost identical domain width in all three fault planes, more precisely $w_{\{110\}} = 9.9 \text{ \AA}$, $w_{\{112\}} = 10.5 \text{ \AA}$ and $w_{\{123\}} = 9.2 \text{ \AA}$, indicating the structure of the magnetic fault does not depend on the crystallographic plane. This correlates well with the identical magnetic fault energy per unit surface γ found on Fig. 6. Another possibility to partially resolve such magnetic frustration would have been to induce a disorientation of magnetic moments while conserving their bulk amplitude. We checked that this possibility could not arise naturally from the relaxation of the same magnetic structure by including both non-collinear magnetism and spin-orbit coupling. The magnetic moments were all initialized along the X direction of the simulation cell (perpendicular to the normal of the fault plane Z), except for the two closest planes from the fault plane, where magnetic moments were initialized along Z to introduce a non-collinear perturbation. This initially non-collinear perturbation was found to relax to the identical structure as in the collinear case. However, when studying magnetic excitations at finite temperatures in Chapter 3, we will show that stable non-collinear magnetic structures do indeed exist. But to be able to stabilize them in *ab initio* calculations, one needs to initialize the system with a magnetic configuration close to its equilibrium configuration, which will be allowed later with the generalized Heisenberg model developed for the study of finite temperature magnetic excitations.

Another possibility would be that the SDW order does not allow for the presence of such magnetic faults. Depending on the relative position between the location of the fault plane and the node of the wave, the

situation might indeed differ. If the structure is sheared in the $\{100\}$ plane where all magnetic moments are zero, *i.e.* in a node, then the magnetic fault would have zero energy since a fault cannot be defined given that the AF order is not broken. However, this is not possible since the Burgers vector $\frac{1}{2}\langle 111 \rangle$ does not belong to $\{100\}$ planes, thus the SDW magnetic order will necessarily be disrupted in the same way as the AF order, responsible for the generation of similar magnetic faults. This further comforts us in the approximation of the experimental SDW ground state by the AF phase.

Except for the excess energy associated with the creation of the magnetic fault at the center of the presented γ -lines of Fig. 6, their shapes are very similar in the NM and AF phases of bcc Cr, in all three considered fault planes. This indicates a small impact of magnetism on the relative ease to shear the three $\{110\}$, $\{112\}$ and $\{123\}$ planes. Moreover, regardless of the magnetic phase, the height and slope of the $\langle 111 \rangle$ γ -line are similar in all three planes, with a shear stress of 0.81, 0.85 and 0.88 GPa respectively in the easiest shearing direction for all three planes in the NM phase (see Tab. 3). Hence, no particular slip system appears to be easier to activate than any other, and most particularly, $\{110\}$ does not seem to be the easiest one to shear even if it is the main experimental slip plane. This shows that a fine atomistic description of the structure and mobility of dislocations is probably required to get a good understanding of the mechanisms involved in the plastic deformation of bcc Cr.

2.4. $\langle 100 \rangle$ slip mode in the NM and AF phases

Since there is experimental evidence of the mobility of dislocations with $\langle 100 \rangle$ Burgers vector in Cr, it is also of interest to calculate the γ -surfaces of planes containing $\langle 100 \rangle$ slip directions, which are $\{110\}$ and $\{100\}$ planes. Projections of the $\langle 100 \rangle$ γ -line in these two planes are presented in Fig. 8 in the NM and AF phases, and in the SDW phase only for $\{100\}$ planes as the fault plane is orthogonal to its propagation vector. In the SDW phase, as the magnetic moments of atoms laying in a given $\{100\}$ plane depend on its position along the propagation of the SDW (see Fig. 1a), the perturbation induced along the $\langle 100 \rangle$ γ -line *a priori* depends on the location of the fault plane with respect to the nodes of the SDW. In this respect, the GSF energies were calculated for a fault plane matching both a zero and maximum magnetic moment $\{100\}$ plane. We find that both magnetic and atomic relaxed configurations are identical in these two cases, the node remaining in its initial plane and with the same GSF energy along the $\langle 100 \rangle$ γ -line. Results presented for the SDW phase in Fig. 8b are plotted for a fault plane located on a node of the wave. The resulting

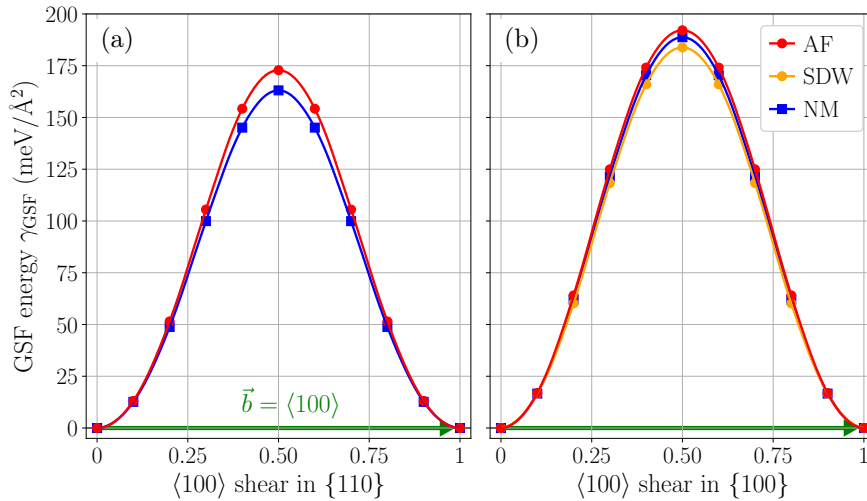


Figure 8: Generalized stacking fault energy along a $\langle 100 \rangle$ direction, or $\langle 100 \rangle$ γ -line, in a (a) $\{110\}$, and (b) $\{100\}$ fault plane in the NM (blue squares), AF (red circles), and SDW (orange circles only in b) phases. For the SDW phase, the fault plane is located at a node of the wave (*i.e.* where the local magnetic moment is zero). The green arrows represent the Burgers vector $\vec{b} = \langle 100 \rangle$. Symbols are *ab initio* results and lines their interpolations with Fourier series.

γ -line in the $\{110\}$ plane has a lowest energy maximum than in $\{100\}$ planes in both the NM and AF phases, indicating an *a priori* easier glide of $\langle 100 \rangle$ dislocations in $\{110\}$ planes, which is also observed experimentally [13]. Also, no magnetic fault is generated upon shearing by a $\langle 100 \rangle$ Burgers vector, as could be expected from the AF order of bcc Cr. However, as was also observed along $\langle 111 \rangle$ directions (Fig. 6), shearing by any fault vector induces a minor frustration of the magnetic moments of the atoms, resulting in higher fault energies in the AF than in the NM phase. The quantities extracted from the $\langle 100 \rangle$ γ -lines of Fig. 8 are presented in Tab. 4, showing a close but still higher stress is required for $\langle 100 \rangle$ than for $1/2\langle 111 \rangle$ shear, with close values in both magnetic phases.

Table 4: Height γ_{GSF} (meV/Å²) of the different $\langle 100 \rangle$ γ -lines presented in Fig. 8, and the resulting shear stress τ_{GSF} (GPa) for the twinning/antitwining sense in the NM, AF and SDW phases of bcc Cr.

Fault plane	γ_{GSF}			τ_{GSF}		
	NM	AF	SDW	NM	AF	SDW
$\{110\}$	163	173	/	1.17 / 1.17	1.23 / 1.23	/
$\{100\}$	189	192	184	1.36 / 1.36	1.39 / 1.39	1.33 / 1.33

Conclusions of Chapter 1:

- The magnetically ordered AF and SDW phases are more stable than the NM phase, with properties closer to experimental data.
 - The DFT magnetic ground state is found to be the AF phase, in contradiction with the experimentally observed SDW. The energy difference between the two phases decreases linearly with the wave-vector of the SDW.
 - Computed elastic properties show that the AF and SDW phases share almost identical elastic behaviors. Adding their close magnetic order, the AF phase appears as a legitimate approximate of the true magnetic ground state of bcc Cr at low temperature.
 - The study of the GSFs along $\langle 111 \rangle$ crystal directions show the generation of a stable magnetic fault due to the breaking of the AF order by the fault vector $\vec{f} = \vec{b} = 1/2\langle 111 \rangle$ in the three close-packed $\{110\}$, $\{112\}$ and $\{123\}$ planes. The structure and energy of this collinear fault is identical in the three investigated planes, with the partial recovery of the magnetic frustration leading to a structure similar to a magnetic domain wall.
 - Apart from this magnetic fault, the γ -surfaces are very similar in the NM and AF phases.
 - The $\langle 100 \rangle$ slip mode shows a lower maximum fault energy in $\{110\}$ than in $\{100\}$ planes, indicating an *a priori* easier glide of $\langle 100 \rangle$ dislocations in $\{110\}$ planes.
-

Chapter 2: Dislocations and plasticity in bcc chromium

Now that we have a good understanding of the bulk magnetic properties of Cr, we can study the properties of dislocations in the crystal, the linear defect controlling the plastic deformation of bcc transition metals. As stressed at the end of the previous chapter, generalized stacking faults are only a first step towards rationalizing the plastic behavior of bcc Cr, particularly regarding the preferred slip system. To get an accurate representation of the atomistic mechanisms at stake, one needs to account for a fine description of the core structure and mobility of dislocations in the crystal. This is the focus of the present chapter using the *ab initio* modeling of Cr presented in the Methods section, including the influence of magnetism detailed in the previous chapter.

1. Core properties of the $\frac{1}{2}\langle 111 \rangle$ screw dislocation

1.1. Impact of magnetism on the core structure of the $\frac{1}{2}\langle 111 \rangle$ screw dislocation

The core structure of the $\frac{1}{2}\langle 111 \rangle$ screw dislocation obtained after atomic relaxation can be visualized using differential displacement maps along the $\langle 111 \rangle$ direction (*i.e.* parallel to the dislocation line) as proposed by Vitek [46]. The relaxed dislocation core is presented in Fig. 1 for the NM phase of bcc Cr. The core is presented in two configurations, the ground state easy core (Fig. 1a), and the unstable maximum hard core (Fig. 1b), located at the same position but with an opposite Burgers vector. Differential displacement maps presented in the upper row show a compact core structure for both configurations, as reported in all other bcc transition metals using *ab initio* DFT calculations [64]. The easy core shows reversed helicity in the three $\langle 111 \rangle$ atomic columns in the vicinity of the dislocation core, whereas the hard core constrains these same three columns to the same height, since it induces the opposite displacement along $[111]$ due to its opposite Burgers vector. The latter corresponds to an unstable maximum in the configuration space of the $\frac{1}{2}\langle 111 \rangle$ screw dislocation core. To be able to relax the hard core configuration, the three mentioned atomic columns are constrained in the Z direction, while other atoms are allowed to relax

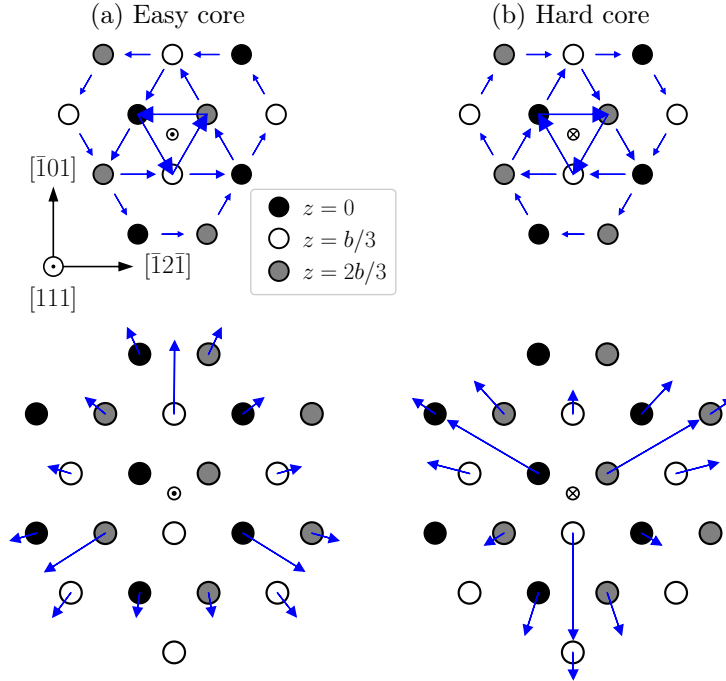


Figure 1: (Upper row) Differential displacement map showing the core structure of the $\vec{b} = \frac{1}{2}\langle 111 \rangle$ screw dislocation in the NM phase of bcc Cr in its (a) easy and (b) hard configurations. An arrow joining two atoms corresponds to a differential displacement of $b/3$ along $[111]$. (Lower row) Absolute displacement in the (111) plane after subtraction of the Volterra elastic field (magnified by a factor 35). Atoms are represented in different colors according to their height along the $[111]$ direction.

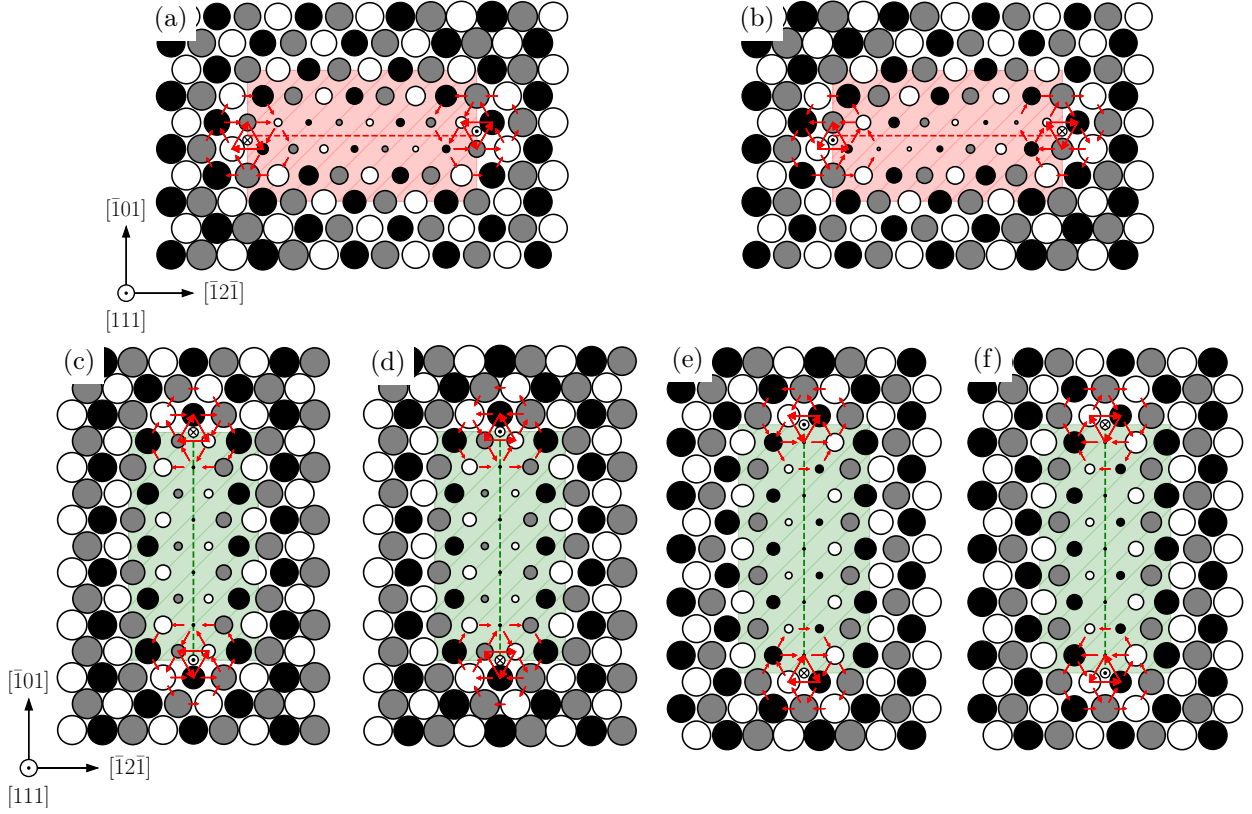


Figure 2: Differential displacement map along the $[111]$ direction showing the core structure of the $\vec{b} = 1/2\langle 111 \rangle$ screw dislocation in the AF phase of bcc Cr with a magnetic fault lying in the $(\bar{1}01)$ plane in its (a) easy and (b) hard configurations, and in the $(\bar{1}2\bar{1})$ plane in its (c) easy and (d) hard configurations for the up triangles; (e) and (f) for the down triangles. Atoms are represented with a diameter proportional to their magnetic moments. Two touching circles corresponds to the bulk value of $1.1 \mu_B$, and the smallest circles correspond to zero magnetic moment.

in all three Cartesian directions. As shown in the lower panels of Fig. 1, the screw dislocation induces a dilatation field of the crystal in the vicinity of its core, here visualized in absolute displacements in the (111) plane orthogonal to the dislocation line, which has also been reported for all bcc transition metals [44].

Differential displacement maps of the two easy and hard core configurations of the $1/2\langle 111 \rangle$ screw dislocation core in the AF phase are presented in Fig. 2. The core structure of the $1/2\langle 111 \rangle$ screw dislocation is identical in the two NM and AF phases, in both its easy and hard configurations. The only notable difference between the two phases is the presence of a magnetic fault bounded by the two dislocations of a same dipole. This is due to their Burgers vector not being a periodicity vector of the AF order of bcc Cr. This fault is located in the region of the initially perfect bulk crystal which has been sheared by the Burgers vector to create the dislocation dipole. This shearing introduces a magnetic frustration in the system by forcing two same-sign spins to face each other in the two planes located above and below the cut surface of the dislocation dipole. This frustration is partially resolved upon relaxation by reducing the magnitude of the magnetic moments of atoms near the sheared region. To better visualize the structure of this magnetic fault, the same representation as for the infinite magnetic fault is adopted (see Fig. 7 in Chapter 1), with a diameter proportional to their magnetic moments, and the differential displacement map is superimposed on top of it (Fig. 2). The calculation has been performed for a magnetic fault located in both a $\{110\}$ and a $\{112\}$ plane, depending on the initial choice for the vector joining the two dislocations of the dipole, *i.e.* $(\vec{p}_1 + \vec{p}_2)/2$ and $(\vec{p}_1 - \vec{p}_2)/2$ respectively, in the same simulation cell containing 135 atom per b (see Methods,

section 3.1.1 for more details about the simulation setup).

The center of a $1/2\langle 111 \rangle$ screw dislocation core, whether in its easy or hard configuration, is located at the center of gravity of triangles formed by three adjacent atomic columns along a $\langle 111 \rangle$ direction (Fig. 1). Dislocations with $+\vec{b}$ Burgers vector in their easy configuration are located at the center of triangles pointing down, and $-\vec{b}$ dislocations of triangles pointing up. As a result, the length of the vector joining two dislocation cores varies by a small amount $\pm\delta = a_0\sqrt{2}/6$ if it links two triangles pointing up and down or down and up, and also on the core configuration (*i.e.* easy or hard). This is not relevant in the NM and AF phases when the fault lies in a $\{110\}$ plane, but it slightly changes the structure and length of the magnetic fault when located in a $\{112\}$ plane (Fig. 2c-f). As can be seen by comparing these faults with the ones obtained at the local minima of the $\langle 111 \rangle$ γ -lines of Fig. 7 in Chapter 1, the structure of the infinite fault is identical as the one observed for a dislocation dipole laying in a $\{110\}$ plane, but slightly differs for a $\{112\}$ plane. In the GSF, the magnetic fault lays between two adjacent $\{112\}$ planes, hence no magnetic moment is strictly zero. In the two configurations of the $\{112\}$ dislocation dipole (up and down triangles), the fault is located on a $\{112\}$ atomic plane, reducing the magnetic moments of atoms in that plane to exactly zero. Besides this effect, the structure of the magnetic fault is almost identical for both the easy and hard core configurations, regardless of the orientation of its plane or the dislocation setup. We now focus on quantifying the energetics of the dislocation core in the following section.

1.2. Core energy of the $1/2\langle 111 \rangle$ screw dislocation

The total energy E^{tot} of a simulation cell containing a dislocation dipole can be partitioned as:

$$E^{\text{tot}} = E^{\text{bulk}} + E^{\text{elas}} + 2E_c + E^{\text{fault}} \quad (1)$$

where E^{bulk} is the energy of the perfect crystal without dislocations, E^{elas} is the elastic energy of the dislocation dipole containing the self energy of dislocations and interactions between dislocations and their periodic images, E_c is the core energy, and E^{fault} is the energy of the magnetic fault. All contributions to the total energy are normalized by the length of the simulation cell along the Z axis to account for the different heights of the cells in the NM and AF phases. The elastic energy E^{elas} of the dipole is evaluated with anisotropic elasticity using the BABEL package [165] with a core radius $r_c = a_0\sqrt{3}/2$.

As shown in Eq. 1, the energy of the magnetic fault generated in the AF phase needs to be subtracted before being able to correctly evaluate the core energy of the dislocations in the simulation cell. The

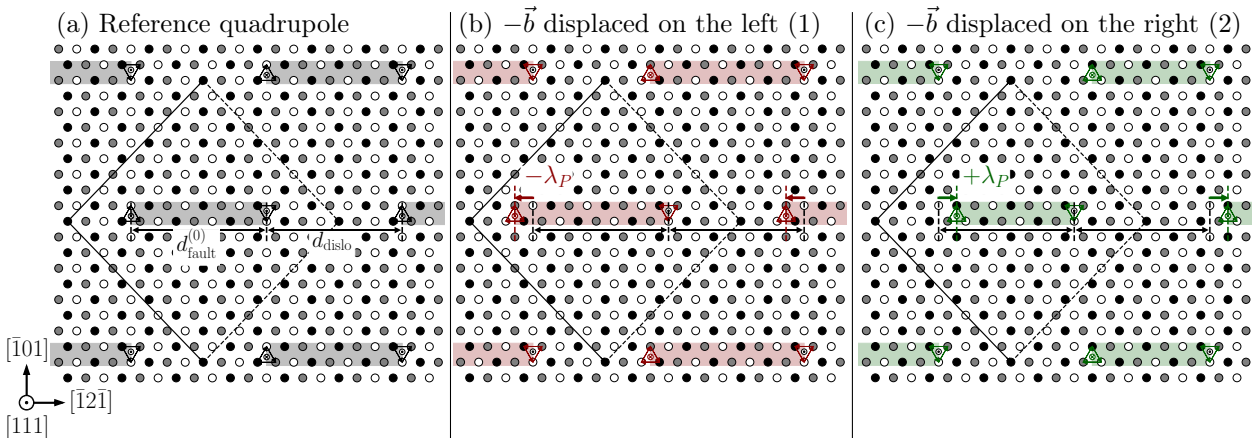


Figure 3: Sketch of the dislocation arrangement used for the evaluation of the magnetic fault energy separating two $1/2\langle 111 \rangle$ screw dislocations of the same dipole: the $-\vec{b}$ dislocation is moved by the distance $\lambda_P = a_0\sqrt{2}/3$ between two Peierls valleys on the left in position (1), and on the right in position (2), keeping the same distance in both position with the $+\vec{b}$ dislocation.

fault is assumed to have an energy proportional to the distance d between the two dislocations of the dipole, $E^{\text{fault}} = \gamma d$ with γ its energy per surface unit. The energy of the magnetic fault bounded by two dislocations should be the same as the one generated by the rigid shearing of the crystal in the fault plane shown in the GSFs of Chapter 1, which we propose to check with the method sketched in Fig. 3. Upon moving one of the two dislocations of the dipole on the left or the right by a distance $\lambda_P = a_0\sqrt{2/3}$ separating two adjacent Peierls valleys starting from the quadrupolar dislocation setup and keeping the other fixed, the elastic energy of the dipole is equal in these two positions (Figs. 3b and c) as the distance between periodic images of the dislocations stays the same. As the core energy also stays the same, the energy difference between configurations (1) and (2) is therefore only due to the change in length of the magnetic fault, *i.e.* $\pm\lambda_P$ with respect to the quadrupolar arrangement. The surface energy γ of the magnetic fault bounded by the two $1/2\langle 111 \rangle$ screw dislocations can then be obtained directly as:

$$\gamma = \frac{E_{(1)}^{\text{tot}} - E_{(2)}^{\text{tot}}}{4b\lambda_P} \quad (2)$$

This calculation is done for a magnetic fault laying in a $\{110\}$ plane only, as the surface energy of the infinite fault found with the GSFs was independent of the plane. This leads to $\gamma = 16.3 \text{ meV}/\text{\AA}^2$, in perfect agreement with the $\gamma_{\{110\}} = 16.2 \text{ meV}/\text{\AA}^2$ found in the GSF, the small difference between the two probably due to boundary effects near the dislocation cores. This result shows that whether the magnetic fault arises from a rigid shearing of the crystal or by the introduction of dislocations, the same phenomenon is involved, at least in $\{110\}$ fault planes. As almost identical values of the fault energy were also found in $\{112\}$ and $\{123\}$ planes, we can reasonably assume that this result can be extended to all three planes, and $\gamma = 16.3 \text{ meV}/\text{\AA}^2$ will be used in the following for a dislocation dipole in Eq. 1 regardless of the fault plane.

We then check the convergence of the dislocation core energies with respect to the size of the simulation cell, *i.e.* the distance between two dislocations of a same dipole and between their periodic images, using the geometries given in Tab. 5 of the Methods. The results are presented in Fig. 4 for the NM and AF phases, with a magnetic fault lying in both a $\{110\}$ and a $\{112\}$ plane. We stress that in the absence of the magnetic fault, the dislocation setup is the same in both magnetic phases. We found that the calculated core energies are almost independent of the cell size in both magnetic phases, showing the convergence of the presented results with the geometry, and of the fault plane in the AF phase. This shows the relevance of the energy partition of Eq. 1, with a good evaluation of the elastic and magnetic contributions, leading to a core energy almost independent on dislocation environment. Like in other bcc transition metals [44],

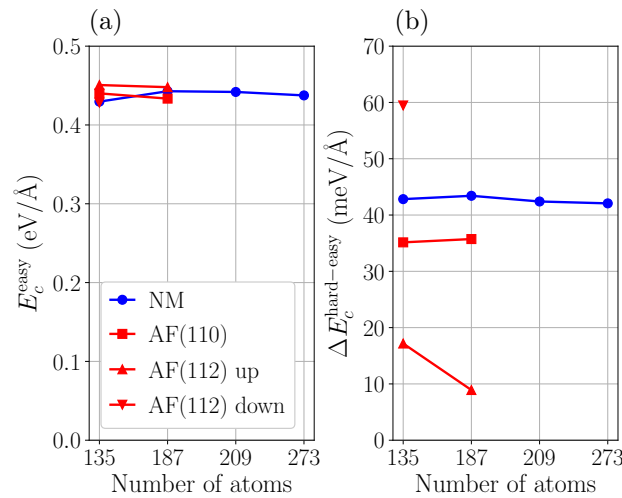


Figure 4: Convergence of the $1/2\langle 111 \rangle$ screw dislocation core energy E_c with respect to the size of the simulation cell in (a) its easy configuration, and (b) the energy difference between the hard and easy configurations, in both NM and AF phases.

the energy of the hard core configuration is higher than that of the easy core in both magnetic phases. This energy difference shows larger variations in the AF phase when the magnetic fault lies in a $\{112\}$ plane, also depending on the dislocation position located in either up or down triangles (Fig. 4b). Since the elastic energy of the dipole is the same in its easy and hard core configurations, this perturbation necessarily arises from the approximate evaluation of the magnetic fault contribution. This is further confirmed by our observation that the structure of the $\{112\}$ magnetic fault when bounded by dislocations slightly differs from the infinite fault obtained in the GSF (see Chapter 1, Fig. 7b). Therefore, the dislocation setup with the magnetic fault laying in a $\{110\}$ plane will be preferred in following calculations such as the Peierls energy barrier.

When comparing the core properties of the $1/2\langle 111 \rangle$ screw dislocation, *i.e.* both structure and energetics, obtained in the NM and AF phases, one sees that once the contribution of the magnetic fault in the AF phase has been removed, magnetism has only a marginal impact. Indeed, the structure of the core is identical in the two magnetic phases, in both configurations, with close core energies except a slightly smaller difference between hard and easy configurations in the AF than in the NM phase, 35 instead of 43 meV/Å.

1.3. Consequence of the magnetic fault in the AF phase

Considering the previous results on the core structure and energy of $1/2\langle 111 \rangle$ screw dislocations, the main impact of magnetism on their properties is the generation of a magnetic fault in the glide plane. This fault necessarily exerts a force on the dislocation, resulting in a back-stress given by $\tau = \gamma/b \simeq 1$ GPa, too high to allow for the existence of isolated $1/2\langle 111 \rangle$ dislocations carrying magnetic faults in the AF phase. No such magnetic fault has been observed in bcc Cr strained under its Néel temperature [13, 122], possibly in agreement with its high energy cost. Such magnetic faults bounded by one or two dislocations have been observed at room temperature both ending up at a $\{100\}$ surface [127, 128] (see Fig. 22 in the Literature review). When studying magnetic excitations at finite temperatures in the next chapter, a different structure for these magnetic faults is found including non-collinear magnetism, which however cannot be considered as a fault since its energy does not converge with the separation distance between faults.

This magnetic fault therefore needs to be closed by another topological defect, *e.g.* another $1/2\langle 111 \rangle$ dislocation, possibly constraining them to coexist and move pairwise and thus leading to a superdislocation of total $\langle 111 \rangle$ Burgers vector dissociated in two $1/2\langle 111 \rangle$ dislocations separated by a magnetic fault. This follows the reaction $1/2[111] + \text{MF} + 1/2[111] \rightarrow [111]$, with MF the magnetic fault, where the dissociated configuration is energetically more favorable than the single $\langle 111 \rangle$ dislocation. If there was no magnetic fault as in the NM and disordered PM magnetic phases, the two partial dislocations would glide apart at an infinite equilibrium distance, whereas the magnetic fault in the AF phase prevents this infinite separation. The equilibrium dissociation distance between two $1/2\langle 111 \rangle$ partial dislocations can be evaluated using elasticity theory, with the following expression for the energy variation arising from the dissociation:

$$\Delta E^{\text{diss}}(d) = -b_i^{(1)} K_{ij} b_j^{(2)} \ln \left(\frac{d}{r_c} \right) + \gamma d, \quad (3)$$

where d is the dissociation distance between the two partial dislocations $\vec{b}^{(1)} = \vec{b}^{(2)} = 1/2\langle 111 \rangle$, K is the Stroh tensor in the reference frame of the $\langle 111 \rangle$ dislocation, and r_c is the core radius. The equilibrium dissociation distance d_{eq} is found by minimizing the above Eq. 3 with respect to d , and using the analytical expression of the Stroh tensor for the $\langle 111 \rangle$ screw orientation [177, 178]:

$$d_{\text{eq}} = \frac{b_i^{(1)} K_{ij} b_j^{(2)}}{\gamma} = \frac{b^2 \sqrt{C' C_{44}}}{2\pi\gamma}, \quad (4)$$

with $b = a_0\sqrt{3}/2$ the norm of the partial Burgers vectors. With the elastic constants of the AF phase calculated at 0 K presented in Tab. 1 of Chapter 1 and $\gamma = 16.3$ meV/Å², we find $d_{\text{eq}} = 55$ Å as the equilibrium dissociation distance of the $\langle 111 \rangle$ screw superdislocation. Depending on the dislocation character, this

distance ranges from 54 to 59 Å, a small variation due to the strong elastic anisotropy of Cr.

This dissociation distance is small, thus potentially explaining why no TEM observation has reported the presence of such $\langle 111 \rangle$ dislocations at low temperature. Also, identification of Burgers vectors in TEM observations usually relies on an extinction criterion, *i.e.* with $\vec{g} \cdot \vec{b} = 0$ contrast, based on the orientation of the Burgers vectors, which therefore cannot help distinguish between $1/2\langle 111 \rangle$ and $\langle 111 \rangle$ dislocations. Marcinkowski and Lipsitt [126] proposed that as a result of $1/2\langle 111 \rangle$ dislocations dragging magnetic faults when gliding, an antiferromagnetic strengthening should occur, the amplitude of which is proportional to the surface energy of the fault. However, they report no evidence for such a strengthening in the temperature range they investigated, near the Néel temperature close to ambient, *a priori* owing to the weak energy of the fault at these temperatures. Holzer *et al.* [34] observed dislocation networks formed by intersecting dislocations with two different $1/2\langle 111 \rangle$ Burgers vectors, whose sum results in the formation of $\langle 100 \rangle$ junctions. If these reacting segments had a $\langle 111 \rangle$ Burgers vector instead, the resulting junction would be $\langle 200 \rangle$, which is highly unstable and would dissociate, which is not observed, thus confirming the $1/2\langle 111 \rangle$ Burgers vectors of these dislocations. It is worth mentioning that in the TEM observations of Holzer *et al.*, these $1/2\langle 111 \rangle$ dislocations possibly appear by pairs with equal Burgers vector. In this respect, the measured dissociation distance between two dislocations would be roughly 200 nm, much larger than calculated at 0 K, which would indicate a much lower magnetic fault energy at temperatures as low as 77 K. Results of a more detailed study on the consequences of this fault on the motion of dislocations at finite temperatures are presented in the next chapter, also considering the disordered PM phase.

1.4. Peierls potential and lattice friction

We now evaluate the Peierls energy barrier opposing $1/2\langle 111 \rangle$ screw dislocation glide in $\{110\}$ planes, *i.e.* the variation of its core energy across the path between two adjacent easy configurations or Peierls valleys. Two different dislocation setups to calculate the Peierls barrier are used in this study. First using setup *both* presented in section 3.1.2 of the Methods, where the two dislocations of the dipole are moved in the same direction along X from their initial ground state easy core configuration to the next nearest, the dipole keeping a quadrupolar arrangement. This way, the elastic and magnetic fault energies remains constant upon crossing of the barrier as the distance between the two dislocations of the dipole is unchanged. However, we are also interested in evaluating the dislocation trajectory and variations of its relaxation volume, which requires a different setup where the stress variations caused by the moving dislocations can be

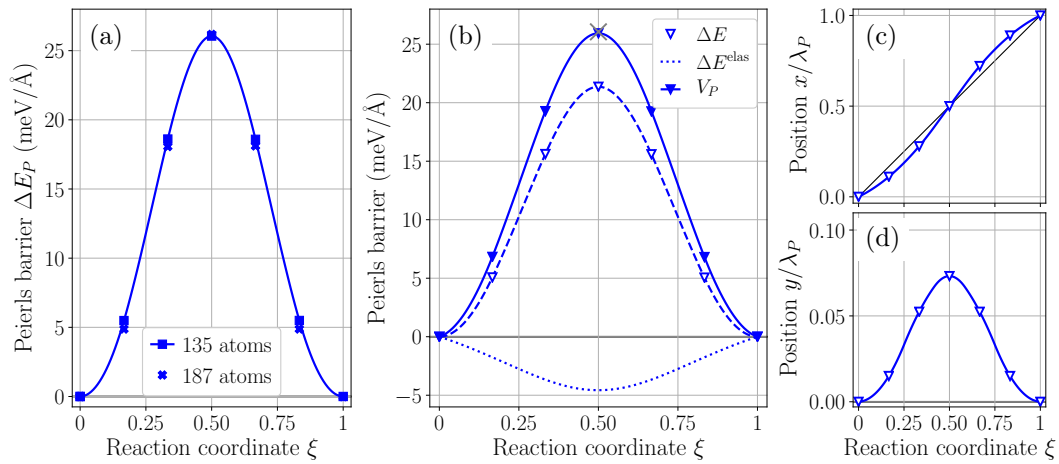


Figure 5: Peierls energy barrier opposing $1/2\langle 111 \rangle$ screw dislocation glide in a $\{110\}$ plane obtained in the NM phase with the dislocation setup where (a) both dislocations glide in the same direction, and (b) in opposite directions. We show in (b) the NEB energy barrier ΔE (dashed line), the variation of the elastic energy ΔE^{elas} (dotted line), and the corrected Peierls potential $V_P = \Delta E - \Delta E^{\text{elas}}$ (solid line) as a function of the reaction coordinate ξ . The grey cross at $\xi = 0.5$ shows the height of the Peierls barrier obtained in (a). (c) and (d) show the dislocation position along the X and Y axis respectively.

recorded, referred to as *stress* (see Methods, section 3.1.3 for details about the setup). The calculation is performed using the 135-atom simulation cell of height $1b$ and $2b$ in the NM and AF phases respectively, with a magnetic fault located in the $\{110\}$ glide plane as explained in the previous section. Results using both setups are presented in Figs. 5 and 8 in the NM and AF phases respectively.

The obtained Peierls barrier using the dislocation setup *both* is presented in Fig. 5a in the NM phase, in the 135 and 187-atom simulation cell, for which we note a very satisfactory convergence with the size of the simulation cell. Differential and absolute displacements maps showing the core structure of the dislocation at the saddle point of the Peierls barrier are presented in Fig. 6 in the NM phase. This configuration differs from the hard core presented in Fig. 1b. Indeed, the dislocation drifts away from the center of gravity of the triangle corresponding to the hard core when crossing the barrier, hence the saddle energy of the Peierls barrier ($25 \text{ meV}/\text{\AA}$ in the NM phase) is lower than the energy difference between the easy and hard core configurations ($43 \text{ meV}/\text{\AA}$ in the NM phase).

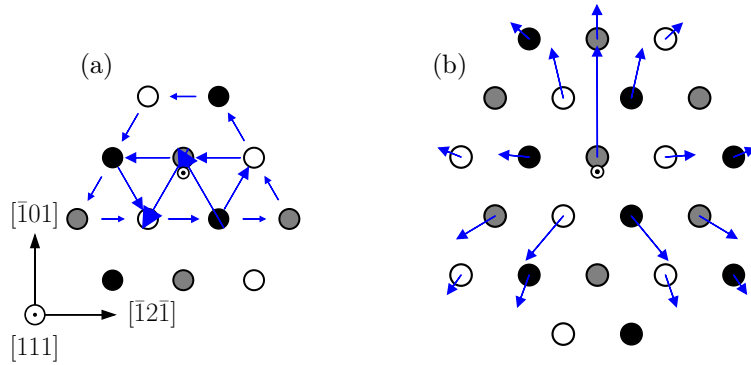


Figure 6: Saddle point configuration of the $1/2[111]$ screw dislocation in the NM phase shown through (a) differential displacements along the $[111]$ direction, and (b) absolute displacements in the (111) plane (magnified by a factor 35).

Using the *stress* dislocation setup, where the two dislocations glide in opposite directions, the NEB energy barrier ΔE needs to be corrected from the variation of elastic energy ΔE^{elas} caused by the change in the distance between the two dislocations of the dipole along the path. This process is illustrated in Fig. 5b in the NM phase. Using the dislocation position (x, y) (Fig. 5c and d) extracted from the stress variations recorded along the path, the elastic energy variation is evaluated with anisotropic elasticity theory (dotted line in Fig. 5b). This energy variation ΔE^{elas} is symmetrical with respect to the saddle point, as expected from the symmetrical dislocation setup used, and accounts for about one fifth of the total energy barrier observed in the NEB calculation. The Peierls potential V_P (solid line) is then obtained after correcting the NEB barrier by this change in elastic energy. We find a very good agreement in the height of the Peierls barrier with setup *both* (Fig. 5a), where both dislocations glide in the same direction, illustrating the correctness of the elastic energy calculation and the ability of the approach to lead to a good evaluation of the Peierls potential, despite these energy variations. The main benefit of these NEB calculations is that they allowed for the determination of the dislocation position upon crossing of the Peierls barrier. Fig. 5c shows that the position x differs from a simple proportionality relation $x = \xi \lambda_P$ with the reaction coordinate ξ . Most importantly, with a position $y > 0$ in the glide plane, the $1/2[111]$ screw dislocation deviates from its macroscopic $\{110\}$ glide plane, one of the features responsible for non-Schmid effects in bcc metals [69] and observed here in Cr, at least in the NM phase.

The results in the AF phase using setup *both* is presented in Fig. 8a in the 135-atom supercell. We note that the Peierls energy barrier has the same shape as in the NM phase, with a lower maximum in the AF phase (23.1 and $26.1 \text{ meV}/\text{\AA}$ in the AF and NM phases respectively). The dislocation core has the same structure in both phases along the minimum energy path, indicating that the magnetic fault *a priori* does not disrupt its structure upon crossing of the Peierls barrier. However, due to the magnetic fault, the energy

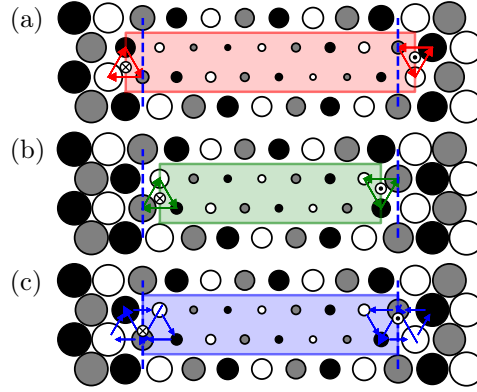


Figure 7: Differential displacement maps showing the dislocation dipole in the AF phase with a fault laying in the $(\bar{1}01)$ plane in the (a) initial and (b) final configurations for the calculation of the Peierls potential. The colored rectangles show the range of the magnetic fault bounded by the two dislocations of the dipole. The saddle configuration located in the middle is shown in (c). Atoms are represented with different colors and diameters according to their heights and magnetic moments respectively.

of the initial and final states of the NEB calculation differs using setup *stress* in the AF phase, leading to a negative slope on the energy barrier (curve $I \rightarrow F$ on Fig. 8b) as the dislocations erase part of the magnetic fault when gliding (Fig. 7). With a surface energy $\gamma = 16.3 \text{ meV}/\text{\AA}^2$ for the magnetic fault, one thus expects an energy variation $\Delta E^{\text{mag}} = \lambda_P \gamma = 38.1 \text{ meV}/\text{\AA}$ per unit length of dislocation line between I and F states. Direct *ab initio* calculations lead to an energy difference in good agreement (Fig. 8b), only slightly smaller due to the perturbation of the magnetic fault by the dislocation core. To remove this magnetic contribution from the energy barrier, we consider the same NEB calculation, but read along the reversed path $F \rightarrow I$ where the width of the fault is increased by dislocation glide, leading to a positive slope on the energy barrier (curve $F \rightarrow I$ on Fig. 8b). Because of the symmetry of the bcc lattice and of the simulation setup with the quadrupolar position located at the middle of the path, the two paths $I \rightarrow F$ and $F \rightarrow I$ lead to the same variation of both the Peierls (*i.e.* core) and elastic energies. The average of the

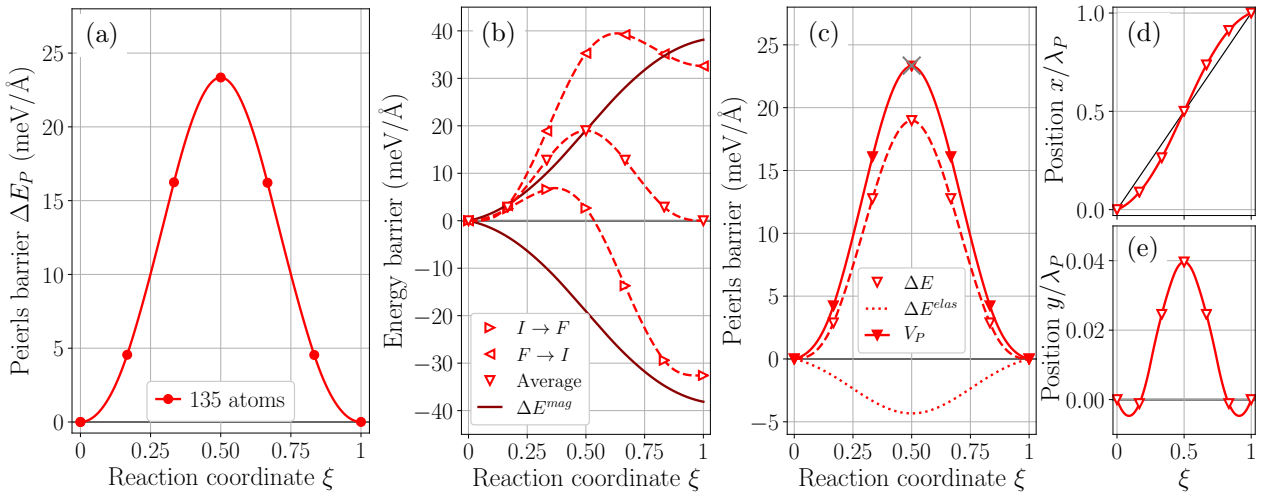


Figure 8: (a) Peierls energy barrier of the $1/2\langle 111 \rangle$ screw dislocation gliding in a $\{110\}$ plane in the AF phase using setup *both* (b) Energy barriers following the two paths $I \rightarrow F$ and $F \rightarrow I$, with the change in the magnetic fault energy $\Delta E^{\text{mag}} = \gamma x(\xi)$ as a function of the reaction coordinate ξ when dislocations glide in opposite directions. (c) Peierls potential V_P obtained after averaging the paths $I \rightarrow F$ and $F \rightarrow I$. The grey cross at $\xi = 0.5$ shows the height of the Peierls barrier obtained in (a). (d) and (e) show the position of the dislocation projected along the X and Y axis respectively.

two energy barriers $[\Delta E(\xi) + \Delta E(1 - \xi)]/2$ therefore cancels the contribution of the magnetic fault while keeping unchanged all other energy contributions. The same symmetrization procedure, which is sketched on Fig. 7, is also applied to the stress variations to extract the dislocation position along the path. The elastic energy variation is then removed from the averaged energy barrier to obtain the Peierls potential V_P (Fig. 8c) following the same method as in the NM phase. A very good agreement between the height of the Peierls barriers obtained with the two dislocation setups is found (grey cross and solid red line in Fig. 8c).

1.5. Dislocation trajectory and relaxation volume

From the NEB calculation of the Peierls potential using setup *stress*, where both dislocations glide in opposite directions, the stress variations recorded along the path give the dislocation position (x, y) in its glide plane, and also the variations of its relaxation volume tensor $\Delta\Omega_{ij}$ when gliding [45, 79]. These two quantities obtained in both NM and AF phases are compared in Fig. 9. As previously reported in all other bcc transition metals [69], the $1/2\langle 111 \rangle$ screw dislocation does not have a straight trajectory gliding from one Peierls valley to the next nearest in a $\{110\}$ plane. As presented on Fig. 9b, the screw dislocation leaves its average macroscopic $(\bar{1}01)$ glide plane to move towards the split core configuration [44], located on the black atom at the middle of its trajectory. This can be described by a deviation angle α^* , defined by the tangent to the dislocation trajectory at the position x^* corresponding to the maximum slope of the Peierls potential $V_P(x)$ shown in Fig. 9a. This gives a deviation angle α^* of -13.5° and -7.0° in the NM and AF phases of bcc Cr respectively, therefore more pronounced in the NM phase in which one thus expects the twinning/antitwinning (T/AT) asymmetry to be more important in this NM phase. This point will be exemplified later when comparing the predicted yield properties in both magnetic phases.

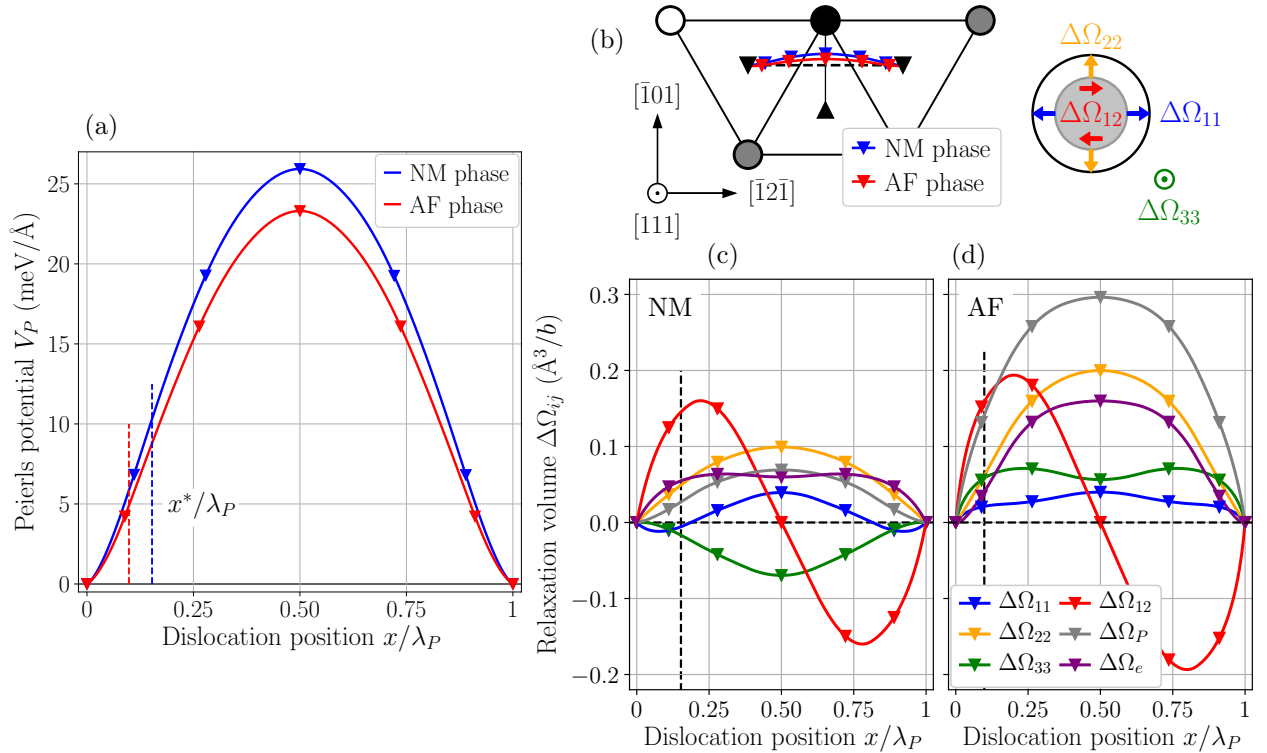


Figure 9: (a) Peierls potential V_P in the NM (blue) and AF (red) magnetic phases of bcc Cr as a function of the dislocation position along $X \parallel [\bar{1}2\bar{1}]$. (b) Trajectory of the $1/2[111]$ screw dislocation in its (111) glide plane as extracted from the stress variations recorded along the *stress* NEB path. Variations of the non-zero components of the relaxation volume tensor of the $1/2[111]$ screw dislocation, sketched in the (111) plane in (b), are presented in the (c) NM and (d) AF phases.

Now that the position of the $1/2\langle 111 \rangle$ screw dislocation is precisely known, we can effectively evaluate the Peierls stress τ_P necessary to overcome the energy barriers presented in Fig. 9a, given by:

$$\tau_P = \frac{1}{b} \max_x \left[\frac{\partial V_P(x)}{\partial x} \right], \quad (5)$$

with $b = a_0\sqrt{3}/2$ the norm of the $1/2\langle 111 \rangle$ Burgers vector. We obtain a Peierls stress of 2.3 and 2.0 GPa for $1/2\langle 111 \rangle$ screw dislocation glide in $\{110\}$ planes in the NM and AF phases respectively, indicating an easier glide in the AF phase. The other important quantity extracted from the presented NEB calculation is the variation of the relaxation volume tensor of the $1/2\langle 111 \rangle$ screw dislocation in its $\{111\}$ glide plane, *i.e.* the variations of the dilatation field induced by the dislocation in the vicinity of its core. In the frame of the simulation cell, this tensor has the following form [79]:

$$\bar{\bar{\Omega}}_{1/2\langle 111 \rangle} = \begin{bmatrix} \Omega_{11} & \Omega_{12} & 0 \\ \Omega_{12} & \Omega_{22} & 0 \\ 0 & 0 & \Omega_{33} \end{bmatrix}, \quad (6)$$

where the Ω_{32} and Ω_{13} are negligible compared to the other components of the tensor. There is no symmetry argument imposing the nullity of these components, but as reported in the case of bcc tungsten [45, 79], post-processing of the two $I \rightarrow F$ and $F \rightarrow I$ paths show that this is the case also in both magnetic phases of bcc Cr. The variations of this relaxation volume tensor as extracted from the stress variations along the path are presented in Fig. 9c and d as a function of the dislocation position x in the NM and AF phases respectively. Both the dislocation trajectory and variations of its relaxation volume are obtained after performing an adjustment of the elastic constants to enforce the symmetry of the dislocation trajectory, as introduced in the Methods (see section 3.1.3 and Appendix D), with the elastic constants presented in Tab. 1. This adjustment appears legitimate, given that the shearing of the crystal by the dislocation dipole induces a change in elastic constants due to anharmonic effects. To check the validity of this approach, the elastic constants of a dislocated cell were calculated *ab initio* and compared to the values obtained for the perfect bulk crystal. Calculations were performed only for the NM phase, and the results are also presented in Tab. 1, with the adjusted elastic constants chosen to assure the screw dislocation is at the bottom of a Peierls valley in both its initial and final positions. These elastic constants slightly differ from the one of the bulk crystal, and the difference is of the same order as the values obtained through the fitting procedure to enforce the symmetry of the dislocation trajectory.

Table 1: Elastic constants of Cr (in GPa) for the perfect bcc unit cell rotated in the frame of the $1/2\langle 111 \rangle$ screw dislocation (Perfect crystal), of the simulation cell containing the dislocation dipole (Dislocated crystal), and the adjusted values used to extract the screw dislocation trajectory and variations of the relaxation volume (Fit).

NM phase	C_{11}	C_{12}	C_{13}	C_{15}	C_{33}	C_{44}	C_{66}
Perfect crystal	420	164	191	38	394	155	128
Dislocated crystal	416	174	195	33	382	135	118
Fit	420	164	191	32	394	138	128
AF phase	C_{11}	C_{12}	C_{13}	C_{15}	C_{33}	C_{44}	C_{66}
Perfect crystal	338	86	117	45	306	157	126
Fit	338	86	117	35	306	140	126

As also reported in tungsten [45, 79], the dilatation field induced by the $1/2\langle 111 \rangle$ screw dislocation core does not remain isotropic upon crossing of the Peierls barrier, but develops an elliptical shape. This shape is defined by its ellipticity $\Delta\Omega_e = \Delta\Omega_{22} - \Delta\Omega_{11}$, and the tilt of the core deformation $2\Delta\Omega_{12}$. The core dilatation field has a similar tilt component in both magnetic phases (red lines in Fig. 9c and d), but the ellipticity $\Delta\Omega_e$ (purple lines) is higher in the AF than in the NM phase, indicating *a priori* a more

pronounced tension/compression asymmetry in this AF phase. Another important feature of this dilatation field is carried by the non-negligible trace of the tensor $\Delta\Omega_P = \Delta\Omega_{11} + \Delta\Omega_{22} + \Delta\Omega_{33}$ (grey lines), which represents the coupling between the dislocation core and an applied pressure. As a consequence of this last point, the yield stress will become sensitive to applied pressure, which is not the case in bcc tungsten. Another major difference from what was reported in tungsten is the non-negligible $\Delta\Omega_{33}$ component of the tensor, which should result in a coupling between the core and stresses applied parallel to the dislocation line.

Now that we have a precise knowledge of the dislocation trajectory and variations of its relaxation volume tensor upon crossing of the Peierls barrier in $\{110\}$ planes, it becomes possible to study in more details the yield properties of bcc Cr mediated by $1/2\langle 111 \rangle$ screw dislocation glide, taking full account of the well-known non-Schmid effects observed experimentally in all bcc transition metals, including Cr [34].

2. Non-Schmid effects and $\langle 111 \rangle \{110\}$ slip activity

2.1. Derivation of a yield criterion for uniaxial loading

With all core properties extracted from *ab initio* calculations, one can now write the Peierls enthalpy of the screw dislocation gliding under an applied stress $\bar{\Sigma}$ as:

$$\Delta H_P(x) = V_P(x) - \Sigma_{yz} b x + \Sigma_{xz} b y(x) - \sum_{ij} \Sigma_{ij} \Delta\Omega_{ij}(x), \quad (7)$$

where $y(x)$ and $\Delta\bar{\Omega}(x)$ are parameterizations of the dislocation trajectory and of its relaxation volume along the minimum energy path for $\{110\}$ glide given in the previous section. The yield stress at 0 K for any mechanical loading is defined as the stress at which the function $\Delta H_P(x)$ ceases to have a saddle point. In this section, we illustrate the approach by considering a uniaxial mechanical loading, *i.e.* a tension or compression test, and develop an analytical generalized yield criterion based on the *ab initio* data obtained in the previous section using the method of Kraych *et al.* [79] detailed in Methods, section 3.1.3. The choice

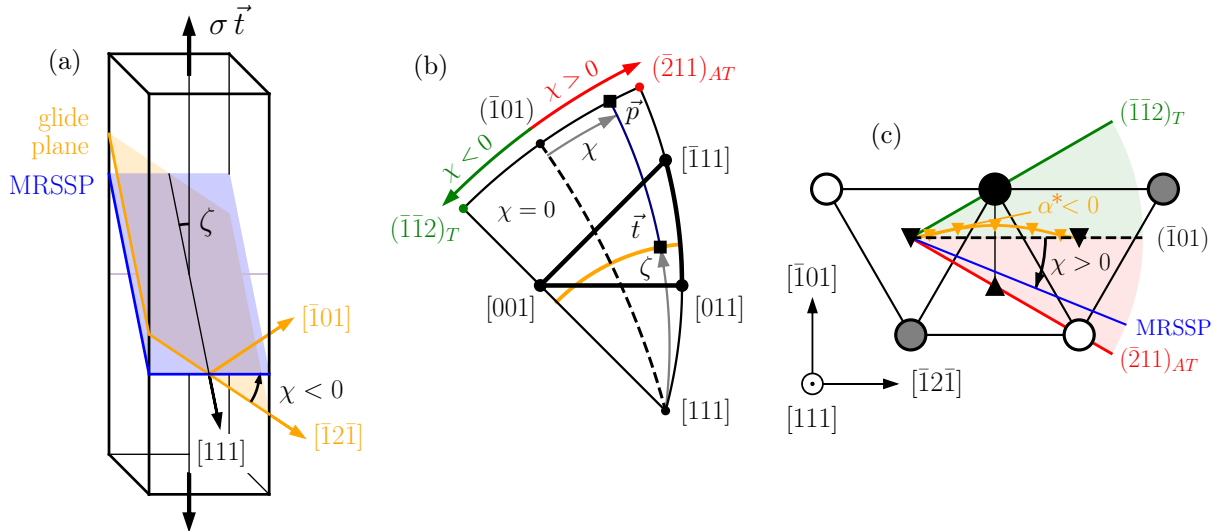


Figure 10: (a) Schematic representation of a single crystal under uniaxial loading along an axis \vec{t} , showing the $(\bar{1}01)$ glide plane of the $1/2[111]$ screw dislocation and the MRSSP, defining the angles ζ and χ . (b) Angles ζ and χ defining the orientation of \vec{t} represented in the irreducible region of the stereographic projection for the $[111](\bar{1}01)$ slip system with $\zeta \in [0, 90^\circ]$ and $\chi \in [-30^\circ, +30^\circ]$. The thick black triangle delimited by $[001]$, $[011]$ and $[\bar{1}11]$ corner axis is the standard stereographic triangle where the $[111](\bar{1}01)$ slip system has the highest Schmid factor. (c) Projection of the MRSSP in the frame of the $1/2[111]$ screw dislocation gliding in the $(\bar{1}01)$ plane. The trajectory of the dislocation in the NM phase is represented by an orange line between two neighboring easy configurations, showing the deviation angle α^* .

to focus on a uniaxial mechanical loading is motivated by the variety of experimental data available at low temperature for all bcc transition metals, and hence the possibility to compare the results of the yield criterion with experiments. However, we stress that the model described here can be applied to any other loading.

Under a uniaxial mechanical loading of magnitude σ applied along an axis \vec{t} , the stress tensor $\bar{\bar{\Sigma}}$ is given by the following, with the tensile axis expressed in the frame of the gliding dislocation [79, 179]:

$$\bar{\bar{\Sigma}}(\sigma, \zeta, \chi) = \sigma(\vec{t} \otimes \vec{t}) = \sigma \begin{bmatrix} \sin^2 \zeta \sin^2 \chi & 1/2 \sin^2 \zeta \sin 2\chi & 1/2 \sin 2\zeta \sin \chi \\ & \sin^2 \zeta \cos^2 \chi & 1/2 \sin 2\zeta \cos \chi \\ & & \cos^2 \zeta \end{bmatrix}, \quad (8)$$

with ζ the angle between the slip direction (or Burgers vector \vec{b}) of the gliding dislocation and \vec{t} , and χ the angle between the normal \vec{n} to the glide plane and the plane of maximum resolved shear stress (MRSSP). A sketch of a sample subjected to a uniaxial loading, showing the angles ζ and χ , with the corresponding projection in both stereographic space and in the frame of the gliding $1/2[111]$ screw dislocation is presented in Fig. 10. As written in Eq. 7, two distinct contributions of the stress tensor appear in the enthalpy barrier except from the Peierls potential V_P . These contributions originate from the coupling between components Σ_{yz} and Σ_{xz} with the dislocation trajectory $(x, y(x))$ in its glide plane, producing a Peach-Koehler force on the moving dislocation, and non-glide stresses Σ_{ij} , *i.e.* which do not produce a net force on the dislocation, with the variations of its relaxation volume tensor $\Delta\Omega_{ij}$. To have a physical understanding of the contribution of the relaxation volumes to the yield stress, it is helpful to define the quantities [45, 79, 180, 181]

$$\begin{aligned} \Delta\Omega_P &= \text{Tr} \Delta\bar{\bar{\Omega}} = \Delta\Omega_{11} + \Delta\Omega_{22} + \Delta\Omega_{33} \\ \Delta\Omega_e &= \Delta\Omega_{22} - \Delta\Omega_{11} \end{aligned} \quad (9)$$

where $\Delta\Omega_P$ represents the coupling with pressure, and $\Delta\Omega_e$ is the ellipticity of the dislocation core field. Injecting the stress tensor 8 in Eq. 7 the dislocation enthalpy ΔH_P per unit length can be written as:

$$\begin{aligned} \Delta H_P(x) &= V_P(x) - \frac{1}{2} \sigma b \sin(2\zeta) [-y(x) \sin(\chi) + x \cos(\chi)] \\ &\quad - \frac{1}{2} \sigma \sin^2(\zeta) [\Delta\Omega_P(x) + \Delta\Omega_e(x) \cos(2\chi) + 2\Delta\Omega_{12}(x) \sin(2\chi)] \\ &\quad + \frac{1}{2} \sigma [1 - 3 \cos^2(\zeta)] \Delta\Omega_{33}(x) \end{aligned} \quad (10)$$

The yield stress σ_Y necessary to overcome the above Peierls enthalpy barrier ΔH_P is found at the unstable position x^* of the dislocation meeting the following conditions:

$$\left. \frac{\partial \Delta H_P}{\partial x} \right|_{x^*} = 0 \text{ and } \left. \frac{\partial^2 \Delta H_P}{\partial x^2} \right|_{x^*} = 0, \quad (11)$$

corresponding to the inflexion point of $\Delta H_P(x)$, assuming both the dislocation trajectory and variations of its relaxation volume tensor is unchanged upon application of a stress [79] (see Methods, section 3.1.3 for more details). The following expression for the yield stress σ_Y^T under uniaxial tension is then found:

$$\sigma_Y^T(\zeta, \chi) = \frac{2\tau_P}{\sin(2\zeta) \frac{\cos(\chi - \alpha^*)}{\cos(\alpha^*)} + \beta(\zeta, \chi)} \quad (12)$$

In the above criterion, β is a function of the angles ζ and χ incorporating all the contributions of the core dilatation. It only depends on the derivatives of the variations of the relaxation volume with respect to the position x at the inflexion point x^* of the Peierls potential as follows:

$$\beta(\zeta, \chi) = \sin^2(\zeta) \left[\frac{\Delta\Omega_e'^*}{b} \cos(2\chi) + \frac{2\Delta\Omega_{12}'}{b} \sin(2\chi) + \frac{\Delta\Omega_P'}{b} \right] - [1 - 3 \cos^2(\zeta)] \frac{\Delta\Omega_{33}'}{b} \quad (13)$$

Superscripts ' and * indicate the first derivative with respect to x and its value at x^* respectively. Parameters of the yield criterion in tension are listed in Tab. 2 for the NM and AF phases of bcc Cr. The yield criterion for compression is found by substituting $\chi \rightarrow -\chi$, $\alpha^* \rightarrow -\alpha^*$ and $\beta \rightarrow -\beta$ in Eq. 12, resulting in the following expression:

$$\sigma_Y^C(\zeta, \chi) = \frac{2\tau_P}{\sin(2\zeta) \frac{\cos(\chi + \alpha^*)}{\cos(\alpha^*)} - \beta(\zeta, \chi)} \quad (14)$$

Comparing Eqs. 12 and 14, when the effect of the relaxation volume is neglected, *i.e.* $\beta(\zeta, \chi) = 0$, the difference between tensile and compressive yield stresses is carried by the changing sign of the deviation angle α^* , reversing the "soft" twinning sense upon changing the sign of the applied stress σ . This effect is captured by the modified Schmid law introduced by Dezerald *et al.* [69], having the following expression:

$$\sigma_Y^{\text{mSchmid}}(\chi) = \frac{2\tau_P \cos(\alpha)}{\cos(\chi - \alpha)}, \quad (15)$$

where α is the angle between the tangent to the dislocation trajectory at the bottom of a Peierls valley and the $\{110\}$ glide plane. As a consequence of this deviation angle, the yield stress is lower when the MRSSP comes tangent to the dislocation trajectory instead of the $\{110\}$ glide plane of the $1/2\langle 111 \rangle$ screw dislocation, resulting in a lower yield stress for negative χ orientation of the loading axis, or the twinning region. The complex dependence of the β function on ζ and χ makes it more difficult to compare qualitatively the two criteria, which will be discussed in the following section. It is also of interest to consider the absence of non-Schmid effects, *i.e.* considering both the dislocation trajectory to be straight between two adjacent Peierls valleys ($y(x) = 0$ and thus $\alpha^* = 0$) and the relaxation volume to be constant along this trajectory ($\Delta\Omega_{ij} = 0$ and thus $\beta(\zeta, \chi) = 0$). The yield criterion in either tension or compression is then:

$$\sigma_Y^{\text{Schmid}}(\zeta, \chi) = \frac{2\tau_P}{\sin(2\zeta) \cos(\chi)} = \frac{\tau_P}{\text{SF}(\zeta, \chi)}, \quad (16)$$

where $\text{SF}(\zeta, \chi) = \sin(2\zeta) \cos(\chi)/2$ is the Schmid factor of the slip system. This expression results in the Schmid law, and is equivalent to Eqs. 12 and 14 with $\alpha^* = 0$ and $\beta(\zeta, \chi) = 0$.

Table 2: Parameters of the yield criterion for $\langle 111 \rangle \{110\}$ slip in the NM and AF phases of bcc Cr: Peierls stress τ_P (GPa), position x^* of the inflexion point of the Peierls potential normalized by the distance λ_P between Peierls valleys, deviation angle α^* ($^\circ$) of the dislocation trajectory at x^* , and derivatives $\Delta\Omega'_{ij}$ of the relaxation volume with respect to x at x^* .

	τ_P	x^*/λ_P	α^*	$\Delta\Omega'_{11}$	$\Delta\Omega'_{22}$	$\Delta\Omega'_{33}$	$\Delta\Omega'_{12}$	$\Delta\Omega'_P$	$\Delta\Omega'_e$
NM phase	2.32	0.153	-13.5	+0.025	+0.050	-0.034	+0.067	+0.041	+0.025
AF phase	1.98	0.099	-7.0	-0.013	+0.116	+0.041	+0.119	+0.171	+0.103

The proposed generalized yield criterion differs from that first introduced by Vitek and co-authors [182–188] and used in various simulation works [189, 190]. As previously discussed [79], Vitek's criterion considers a mechanical loading made of a superposition of a shear stress τ in the MRSSP and a non-glide tensile or compressive stress σ normal to the dislocation line, leading to:

$$\bar{\Sigma}(\sigma, \tau, \chi) = \begin{bmatrix} -\sigma \cos(2\chi) & -\sigma \sin(2\chi) & \tau \sin(\chi) \\ \sigma \cos(2\chi) & -\tau \cos(\chi) & 0 \end{bmatrix}, \quad (17)$$

where the two stresses τ and σ are independent. Using this stress tensor in Eq. 7, the obtained criterion is equivalent to the one presented here in Eqs. 12 and 14, only when the components $\Delta\Omega_{33}$ and $\Delta\Omega_P$ of the relaxation volume can be neglected [79]. As shown in the previous section, such an approximation is

however not valid for bcc Cr. This is also the case for other bcc transition metals as will be discussed in Chapter 4, thus motivating the use of more general criteria incorporating all contributions.

With the inclusion of non-Schmid effects, we are now able to consider all possible $\langle 111 \rangle \{110\}$ slip systems in the evaluation of the yield stress as a function of the orientation of the loading axis. All twelve $\langle 111 \rangle \{110\}$ slip systems, defined by four different $\langle 111 \rangle$ slip directions, and three $\{110\}$ glide planes, are presented on a stereographic projection of the bcc lattice in Fig. 11. In each region delimited by a $\langle 100 \rangle$, $\langle 110 \rangle$ and $\langle 111 \rangle$ orientation, a single $\langle 111 \rangle \{110\}$ slip system has a maximum Schmid factor, and hence necessitates the lowest yield stress according to the Schmid law (Eq. 16). This defines the standard stereographic triangle for this system, which are represented in different colors on Fig. 11, showing the projection of the loading axis \vec{t} in stereographic projection. We will see in the following how the inclusion of non-Schmid effects changes the predicted slip activity and the distribution of the yield stress among all slip systems.

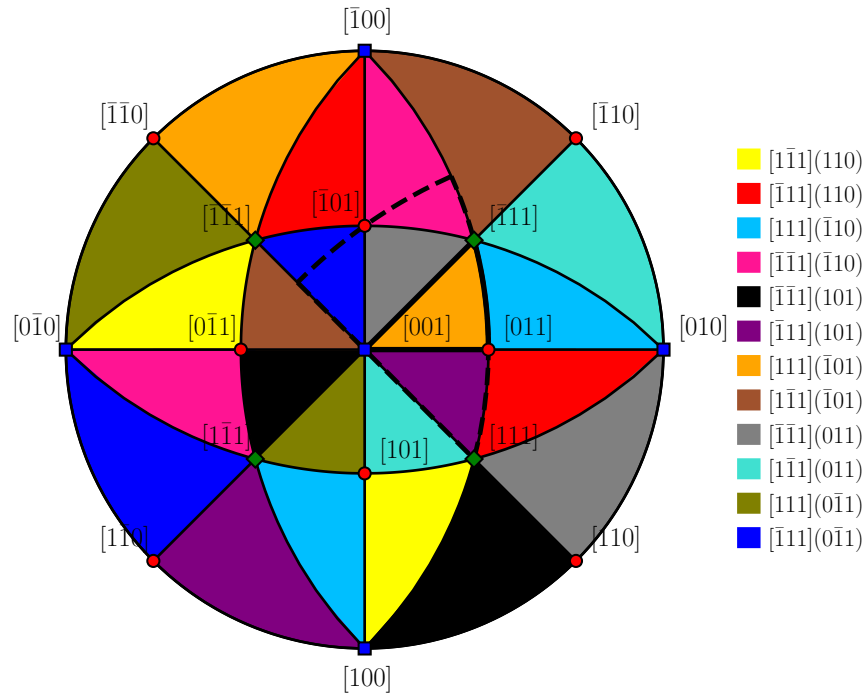


Figure 11: Stereographic projection of the bcc lattice showing in different colors the regions where each individual $\langle 111 \rangle \{110\}$ slip system has the highest Schmid factor. The thick black dashed triangle corresponds to the minimum irreducible zone of the $[111](101)$ slip system (orange), with $\zeta \in [0, 90^\circ]$ and $\chi \in [-30^\circ, +30^\circ]$ as presented in Fig. 10b.

2.2. Deviations from the Schmid law

As presented in Fig. 11, 8 different $\langle 111 \rangle \{110\}$ slip systems are equivalent for a tension or compression axis corresponding to any $\langle 100 \rangle$ orientation (blue squares), 4 for a $\langle 110 \rangle$ axis (red circles), and 6 for a $\langle 111 \rangle$ axis (green diamonds). Among these equivalent slip systems at each corner orientation, all make the same angle ζ with the loading axis, but only half share the same positive χ angle, while the other half share the negative $-\chi$. Therefore, only half of them are sheared in the twinning sense, and the other half in the antitwining sense. This is of no consequence considering the symmetrical variation of the Schmid law with the orientation χ of the MRSSP with respect to the $\{110\}$ glide plane (Eq. 16), but with the deviation angle α^* , positive and negative χ are no longer equivalent and systems with $\chi < 0$ ($\chi > 0$) are easier to activate in tension (compression). This results in a splitting of the slip systems in a twinned and antitwinned group. Therefore, an accurate picture of the orientation dependence of the yield stress cannot be obtained considering only a single slip system, but needs to account for all possible slip systems. This also results in

a reduction of the minimum symmetry-equivalent region of the stereographic space from $1/48$ of the whole sphere, *i.e.* a single triangle, like predicted by the Schmid law, to $1/24$ of the sphere, *i.e.* two adjacent triangles. The distribution of the primary $\langle 111 \rangle \{110\}$ slip system, *i.e.* requiring the lowest yield stress, is presented in the first rows of Figs. 12 and 13 for the NM and AF phases of bcc Cr respectively, with the corresponding variations of the yield stress across the stereographic projection of Fig. 10b presented in the second row. This is done both according to the Schmid law, and including non-Schmid effects in tension and compression using Eqs. 12 and 14.

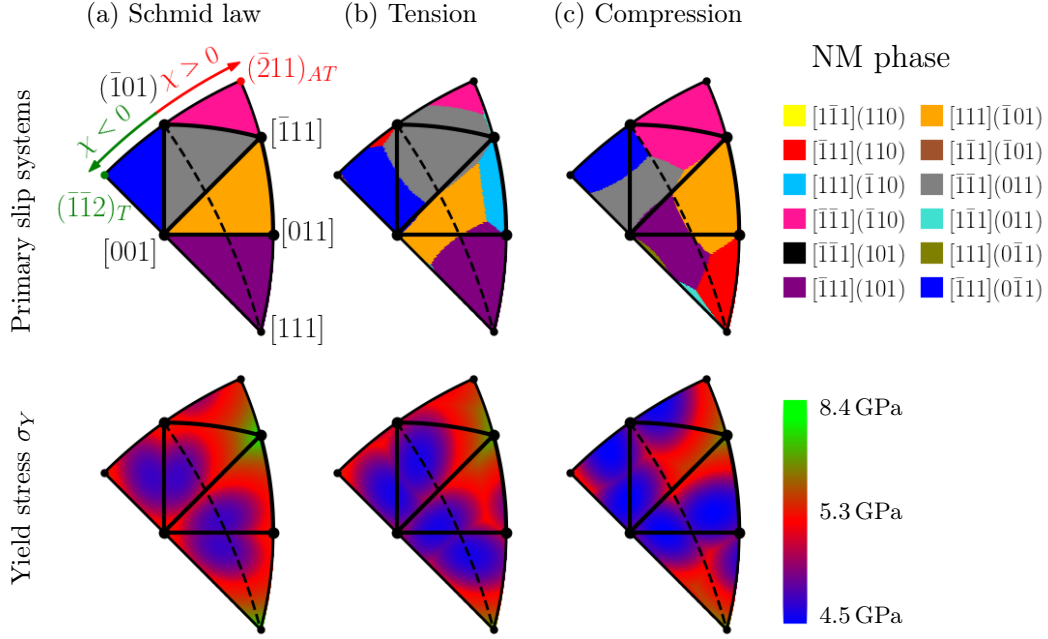


Figure 12: Primary $\langle 111 \rangle \{110\}$ slip systems (first row) and corresponding yield stress σ_Y (second row) for the NM phase of bcc Cr under uniaxial loading at 0 K as a function of the orientation of the loading axis in the stereographic projection: (a) according to the Schmid law, and the yield criterion of Eqs. 12 and 14 in (b) tension and (c) compression respectively.

According to the Schmid law, only a single primary slip system dominates in each stereographic triangle, and the variations of the yield stress follow the distribution of its Schmid factor, *i.e.* with a lower yield stress near the $[001]$ - $[011]$ edge and the $\chi = 0$ line, and maximum yield stress near the $[\bar{1}11]$ axis. Hence, the predicted slip activity is identical in the NM and AF phases, with a lower yield stress in the AF phase due to the lower Peierls stress τ_P in this phase. Now including non-Schmid effects, multiple primary slip systems appear within the $[001]$ - $[011]$ - $[\bar{1}11]$ standard stereographic triangle, with different distributions in tension and compression, and in the two magnetic phases. The region where the expected $[111](\bar{1}01)$ primary slip system is activated (orange) is shifted towards $\chi < 0$ in tension, and $\chi > 0$ in compression, responsible for the emergence of other primary slip systems close to the edges of the standard triangle, namely $[111](\bar{1}10)$ (sky blue) in tension and $[\bar{1}11](101)$ (purple) in tension. The predicted slip activity differs in the two magnetic phases, following the same trends. Indeed, the T/AT asymmetry in the yield stress is more pronounced in the NM phase, caused by a deviation angle α^* twice higher than in the AF phase, whereas the tension/compression asymmetry is more pronounced in the AF phase due to the higher ellipticity component of $\Delta\bar{\Omega}$ in this phase.

Competition between the different $\langle 111 \rangle \{110\}$ slip systems is better visualized in Fig. 14, showing profiles of the yield stress for all systems with the angle χ between the MRSSP and the $\{110\}$ glide plane for a fixed ζ angle between the tensile axis and the $\langle 111 \rangle$ slip direction. To emphasize on the sensitivity of the yield stress on the angle ζ , the $\sigma_Y = f(\chi)$ curves are plotted for three different values of 48 , 51 and 54° . To

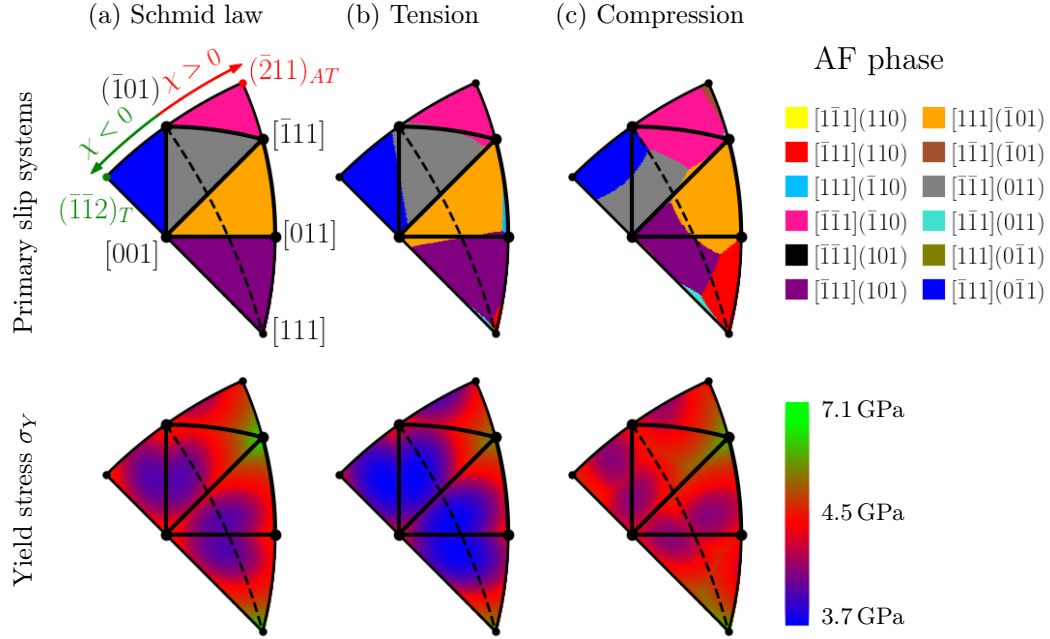


Figure 13: Primary $\langle 111 \rangle \{110\}$ slip systems (first row) and corresponding yield stress σ_Y (second row) for the AF phase of bcc Cr under uniaxial loading at 0 K as a function of the orientation of the loading axis in the stereographic projection: (a) according to the Schmid law, and the yield criterion of Eqs. 12 and 14 in (b) tension and (c) compression respectively.

relate to the experimental measurement of slip activity, $\psi = f(\chi)$ plots for these three ζ angles are presented in the second row of Fig. 14. Slip activity, or active glide planes, is determined experimentally through the identification of slip traces dislocations leave on the surfaces of a deformed sample, making an angle ψ with the expected $(\bar{1}01)$ plane according to the Schmid law. The yield stress profiles highlight the departure from the Schmid law, each slip system showing a clear T/AT asymmetry in both tension and compression, and the competition between slip systems. Apart from the primary slip systems, which are reported in the second row of Fig. 14, the competition between slip systems requiring a higher yield stress also show strong deviations from the Schmid law, with a change in the difference between their yield stresses. According to the Schmid law, only the expected $[111](\bar{1}01)$ slip system is predicted in the range of loading orientations comprised in the standard stereographic triangle, resulting in $\psi(\chi) = 0$ for all χ angles. This is almost the case in tension in both magnetic phases, except near $\chi = +30^\circ$ in the NM phase where the $[111](\bar{1}10)$ slip system, with $\psi = +60^\circ$, is predicted to require a lower yield stress. The $\psi = f(\chi)$ curves under compression are almost identical in both magnetic phases, showing a wide range of negative χ angles where the $[\bar{1}11](101)$ slip system having $\psi = +90^\circ$ is predicted.

Non-Schmid effects also manifest themselves through a strong asymmetry between tension and compression, both in terms of slip activity and yield stress variations, as exemplified in Figs. 12, 13 and 14. The tension/compression (T/C) asymmetry in yield stresses is best studied as a function of the loading axis in terms of a strength differential (SD) introduced by Gröger *et al.* [183, 184]:

$$SD = \frac{\sigma_T - \sigma_C}{(\sigma_T + \sigma_C)/2}, \quad (18)$$

with σ_T and σ_C the absolute values of the yield stress in tension and compression given by Eqs. 12 and 14 respectively, for the same orientation of the loading axis. Level plots of the SD are presented in Fig. 15, considering only the primary expected slip system $[111](\bar{1}01)$ in the left column, and the primary slip system among all $\langle 111 \rangle \{110\}$ slip systems in the right column, in order to stress the importance of accounting for all systems when describing the T/C asymmetry [181]. When only the expected $[111](\bar{1}01)$ slip system is

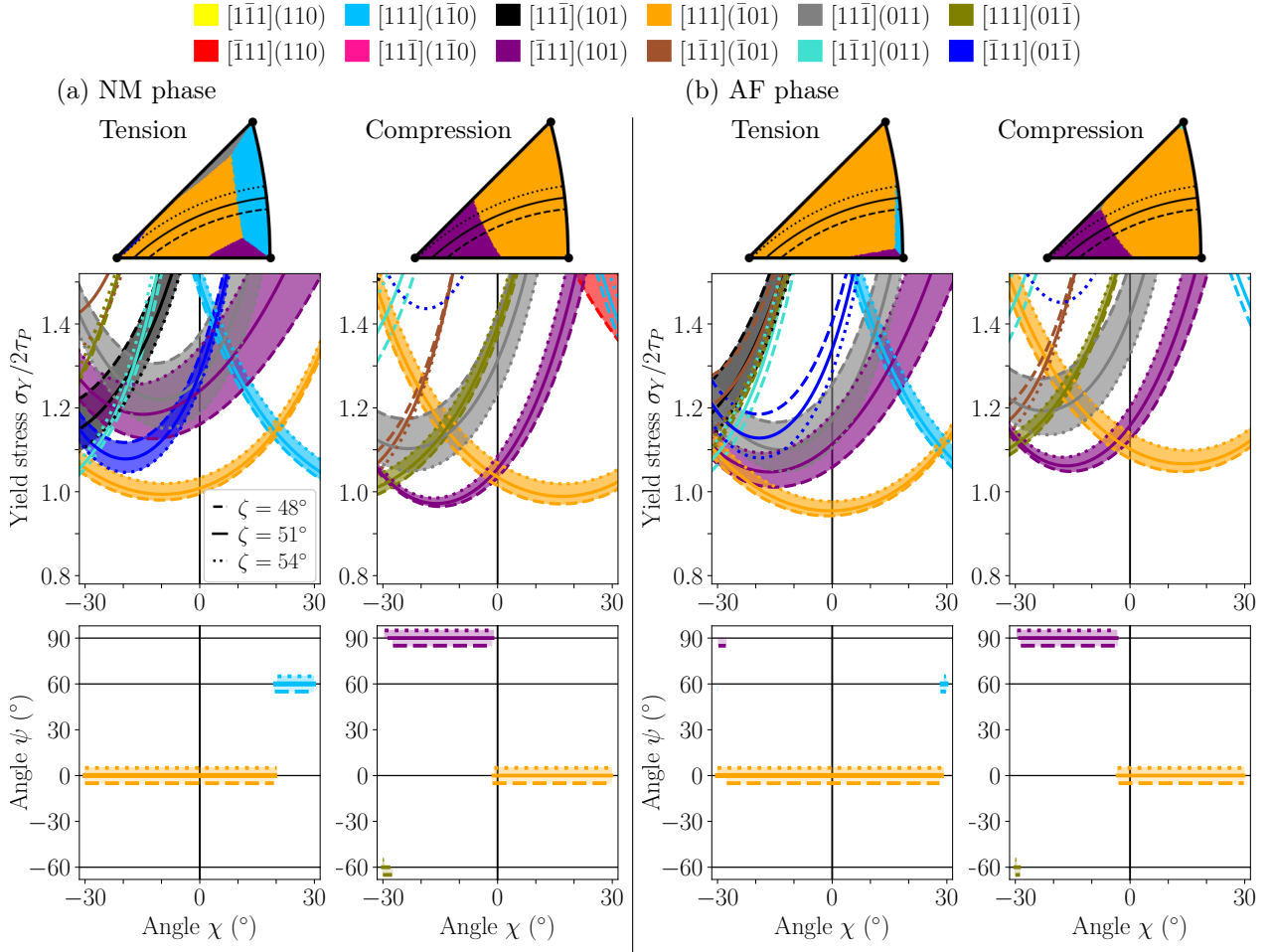


Figure 14: (Middle row) Normalized yield stress $\sigma_Y/2\tau_P$ under uniaxial tension and compression for each $\langle 111 \rangle \{110\}$ slip system as a function of the angle χ in the (a) NM and (b) AF phases of bcc Cr along the $\zeta \in \{48^\circ, 51^\circ, 54^\circ\}$ lines shown in black in the stereographic triangles of the upper row. (Lower row) Corresponding angle ψ between the $(\bar{1}01)$ and the predicted primary $\{110\}$ slip plane. Profiles for the three ζ -lines are shifted up and down for clarity.

considered, a non-negligible range of loading orientations show a lower yield stress in compression than in tension in the NM phase, *i.e.* $SD > 0$ in red. This is a direct consequence of the T/AT asymmetry of the $[111](\bar{1}01)$ slip system, showing a reversing of the easier twinning sense from $\chi < 0$ in tension to $\chi > 0$ in compression. The yield stress is therefore lower in compression near the $[011]-[\bar{1}\bar{1}1]$ edge of the standard stereographic triangle, and the opposite near the $[001]$ corner axis. This effect is more pronounced in favor of compression in the NM phase, and of tension in the AF phase. However, this reasoning is too simplistic as active slip systems differ inside the standard stereographic triangle when non-Schmid effects are taken into account, as shown in Figs. 12 and 13. For this reason, it is necessary to consider all possible $\langle 111 \rangle \{110\}$ slip systems to have a correct representation of the T/C asymmetry. Also, two adjacent triangles are plotted to account for the reduction of the minimum symmetry-equivalent region of the stereographic projection caused by the inclusion of non-Schmid effects. When all possible slip systems are accounted for, the distribution of the SD changes, showing a larger range of orientations where compression is easier than tension in the NM phase, and the opposite in the AF phase. In this AF phase, the predicted yield stress is lower in tension than in compression for any orientation of the loading axis, whereas a large part of the stereographic projection shows a lower compressive yield stress in the NM phase.

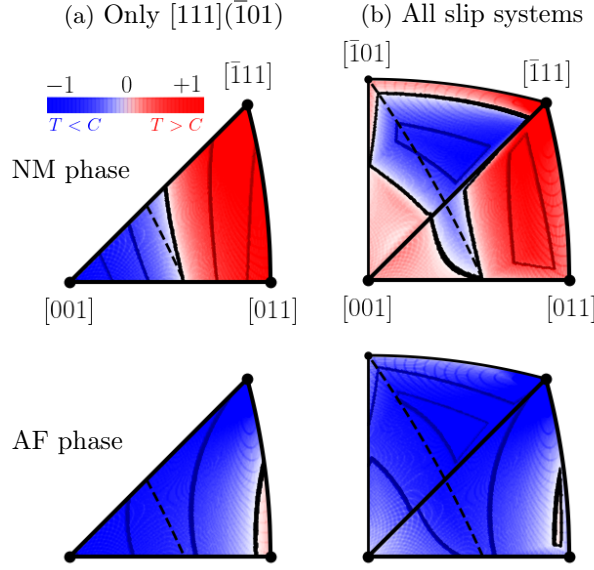


Figure 15: Level plots of the strength differential (SD) of Eq. 18 for single crystals of bcc Cr in the NM (first row) and AF (second row) magnetic phases under uniaxial loading considering (a) only the $[111](\bar{1}01)$ slip system, and (b) all $\langle 111 \rangle \{110\}$ slip systems. Levels are indicated by dark lines every 0.1 step.

Due to a lack of experimental data on bcc Cr to compare the predictions of the presented yield criterion to, the ability of the model to reproduce the experimental features of non-Schmid effects will be tested in Chapter 4 considering the other bcc transition metals, for which more experimental data are available. Inclusion of temperature effects through *ab initio* calculations is now the focus of the following section.

3. Thermal activation and mobility law

As detailed in the Literature review (see section 1.2), a line tension model is able to capture the physics of dislocation glide through nucleation of kink-pairs along its line, the mechanism responsible for the thermally activated motion of dislocations at finite temperature. Parameters of such a line tension model can be extracted from direct *ab initio* calculations using the methodology introduced in Refs. [85, 191], allowing for evaluation of the effect of temperature on the yield stress of bcc metals using a multiscale approach, rather than large supercells containing a kinked dislocation, out of the reach of DFT calculations.

3.1. Line tension model for kink-pair mechanism

In the frame of the line tension (LT) approximation, a dislocation is modeled as an elastic line, whose ease to bend is quantified by its line tension Γ . The shape of the dislocation is represented by a one dimensional function $x(z)$, defining its position x in the glide plane as a function of the coordinate z along its line. The dislocation enthalpy H_{LT} under an applied stress $\bar{\Sigma}$ in its continuous formulation is given by [85]:

$$H_{LT}[x(z), \bar{\Sigma}] = \int dz \left[\Delta H_P[x(z), \bar{\Sigma}] + \frac{\Gamma}{2} \left(\frac{\delta x}{\delta z} \right)^2 \right], \quad (19)$$

with ΔH_P the enthalpy of the straight dislocation under a stress $\bar{\Sigma}$, given by Eq. 10 whether non-Schmid effects are included or not. The line tension Γ is assumed to be isotropic, *i.e.* identical regardless of the direction of the bowing of the line, and independent of the applied stress. Γ can be extracted with direct *ab initio* calculations using the approach of Provile *et al.* [85, 191], emulating the bow out of the dislocation line in a simulation cell only $2b$ -high, which is sketched in Fig. 16. Upon crossing of the Peierls barrier by the $\frac{1}{2}[111]$ screw dislocation, only the three $[111]$ atomic columns represented in colors on Fig. 16a

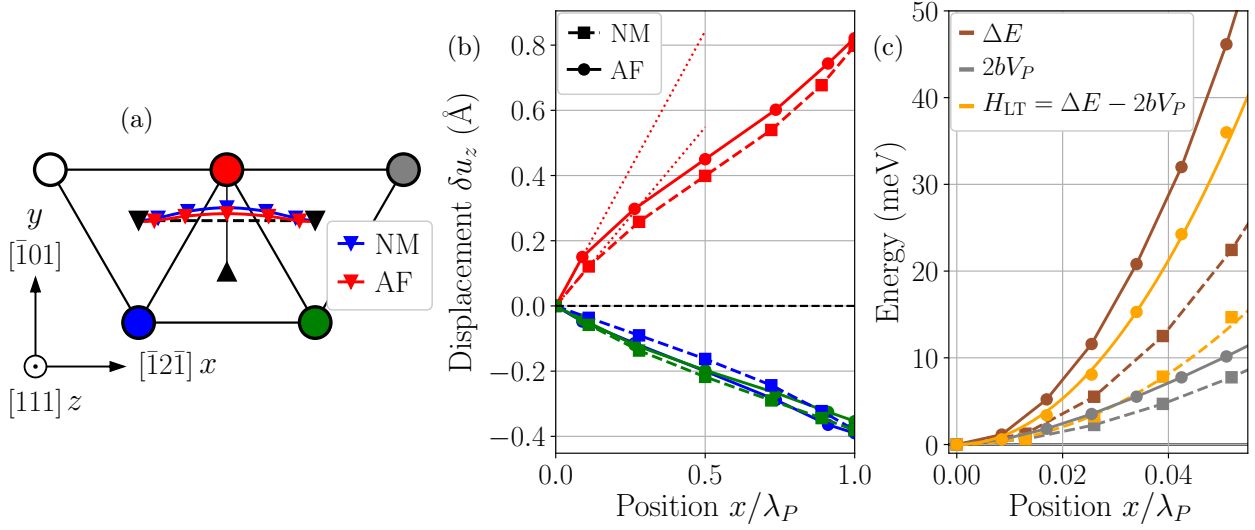


Figure 16: (a) Trajectory of the $1/2[111]$ screw dislocation in the NM and AF phases showing in colors the three most displaced atomic columns in the $[111]$ direction. (b) Displacement δu_z of the three $[111]$ atomic columns shown in (a) along $[111]$ as a function of the dislocation position x projected along the $[\bar{1}2\bar{1}]$ direction. (c) Total energy difference ΔE (brown), change in Peierls energy $2bV_P$ (grey), and resulting line tension energy $H_{LT} = \Delta E - 2bV_P$ (orange) of a kinked $1/2[111]$ screw dislocation in the NM (dashed squares) and AF (solid circles) phases as a function of its position x .

move along the $z \parallel [111]$ direction to let the dislocation glide in the $(\bar{1}01)$ plane. Starting from a relaxed dislocation dipole in a quadrupolar arrangement, a bow out of the line is induced by constraining the height of these three columns to mimic their displacements as recorded upon crossing of the Peierls barrier only in the top $1b$ -high layer of the cell, while keeping the other layer fixed, with the dislocation located at the bottom of its Peierls valley. To avoid variation of the elastic energy of the dipole, both dislocations are displaced synchronously in the same direction, with the magnetic fault in the AF phase located in the $(\bar{1}01)$ glide plane. According to the LT model, the energy of such a kinked dislocation dipole is given by [65, 191]:

$$H_{LT}(X_1, X_2) = 2b[V_P(X_1) + V_P(X_2)] + \frac{2\Gamma}{b}(X_2 - X_1)^2, \quad (20)$$

where X_1 and X_2 are the positions of the two $1b$ -long segments of the line contained in the simulation cell, in their glide plane. Given that the dislocation lays at the bottom of a Peierls valley in the bottom layer, *i.e.* $V_P(X_1) = 0$, the energy difference ΔE with respect to the straight relaxed dislocation dipole is:

$$\Delta E - 2bV_P(X_2) = \frac{2\Gamma}{b}(X_2 - X_1)^2, \quad (21)$$

which can be fitted to a quadratic function of the difference in the dislocation positions $X_2 - X_1$ to extract the line tension Γ . The fitted curves to the *ab initio* data are presented in Fig. 16c, resulting in a line tension Γ of 1.26 and 3.01 eV/Å in the NM and AF phases of bcc Cr. Now that the two parameters entering the LT model (the line tension Γ and the Peierls enthalpy ΔH_P) have been computed *ab initio*, the kink-pair nucleation enthalpy is found by searching for the critical profile $x(z)$ of the dislocation line crossing one Peierls valley as the saddle point of Eq. 19. The critical profiles normalized by the distance λ_P between Peierls valleys obtained for different magnitudes of the applied stress σ are presented in Fig. 17a, with the corresponding nucleation enthalpies ΔH_{kp} in Fig. 17b in the NM and AF phases of bcc Cr. Results presented in Fig. 17 were obtained using a simple Peierls potential without including non-Schmid effects, *i.e.* with $y(x) = 0$ and $\Delta\Omega_{ij} = 0$ in Eq. 10, hence only the glide stress Σ_{yz} needs to be accounted for. Non-Schmid effects will be incorporated later, and their impact discussed.

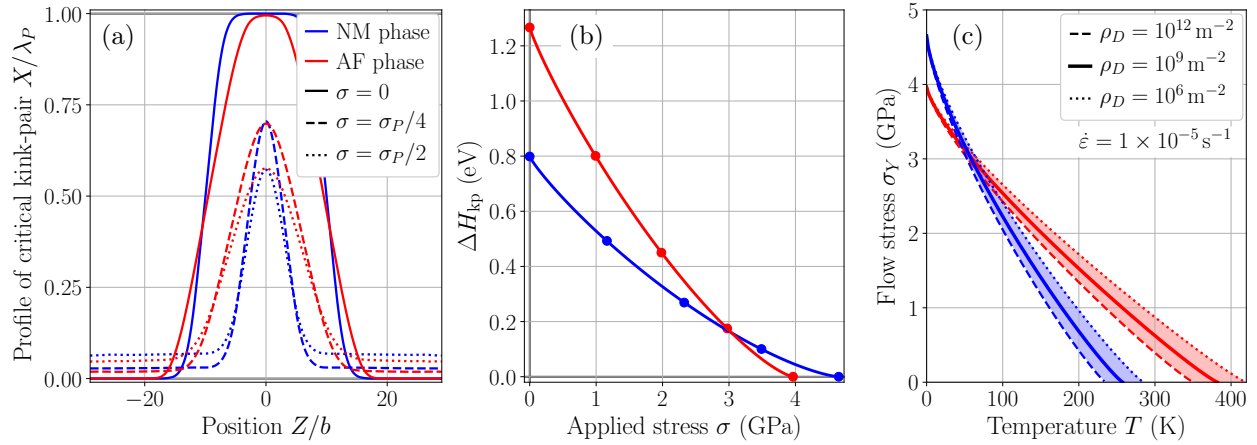


Figure 17: Results of the line tension model adjusted on *ab initio* calculations in the NM and AF phases of bcc Cr: (a) line profiles of a $1/2\langle 111 \rangle$ screw dislocation with a critical kink-pair at different applied stresses σ ; (b) kink-pair nucleation enthalpy ΔH_{kp} as a function of the applied stress σ (symbols) fitted to a Kocks' law (solid lines); (c) yield stress σ_Y as a function of the temperature T considering a strain rate $\dot{\epsilon} = 1 \times 10^{-5} \text{ s}^{-1}$ and different dislocation densities $\rho_D \in \{10^6, 10^9, 10^{12}\} \text{ m}^{-2}$.

The line tension can also be evaluated in the frame of elasticity theory as [12]:

$$\Gamma^{\text{elas}} = T^{\text{elas}}(\theta = 0) = \left[e + \frac{\partial^2 e}{\partial \theta^2} \right] \Big|_{\theta=0} \ln \left(\frac{w_{kp}}{r_C} \right), \quad (22)$$

where e is the prelogarithmic factor to the elastic energy of a straight infinite dislocation of character θ , w_{kp} is the kink-pair width, and r_C is the core cutoff radius, set to the norm $a_0\sqrt{3}/2$ of the Burgers vector. The prelogarithmic factors to the anisotropic elastic energy e and line tension t of a $1/2\langle 111 \rangle$ dislocation computed numerically with the BABEL package [75–77] and the *ab initio* elastic constants of the two NM and AF phases are presented in Fig. 18a as a function of the dislocation character θ . The width w_{kp} of the kink-pair is evaluated under a small but non-zero stress $\sigma = 40 \text{ MPa}$, a typical value of the athermal

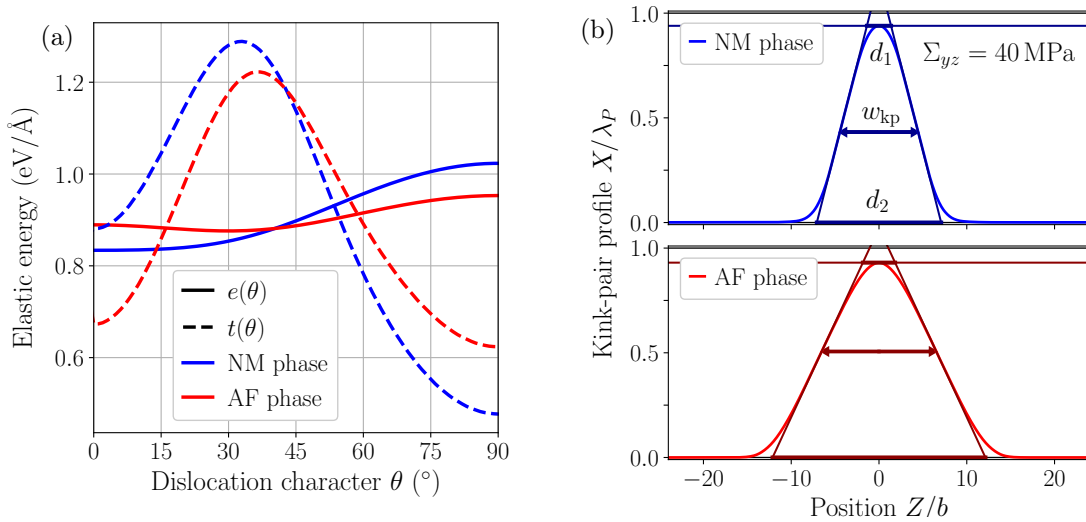


Figure 18: (a) Logarithmic prefactor to the anisotropic elastic energy e (solid lines) and line tension t (dashed lines) of the $1/2\langle 111 \rangle$ dislocation in the NM and AF phases of bcc Cr as a function of its character θ . (b) Profiles of the dislocation line with a critical kink-pair at a stress $\sigma_{yz} = 40 \text{ MPa}$ computed with the LT model in the NM and AF phases using a line tension Γ of 1.26 and 3.01 eV/Å respectively in the two phases as obtained with *ab initio* calculations.

stress [191], resulting in widths $w_{\text{kp}}^{\text{NM}} = 20.9 \text{ \AA} = 8.5b$ and $w_{\text{kp}}^{\text{AF}} = 34.6 \text{ \AA} = 14.0b$ in the two magnetic phases. Using Eq. 22 with an equal kink-pair width $w_{\text{kp}} = 10b$ in both magnetic phases, we obtain a line tension Γ^{elas} of 2.03 and 1.55 eV/ \AA in the NM and AF phases respectively. These close values obtained with elasticity theory originate from the similar elastic properties of the NM and AF phases of bcc Cr. However, the LT model with *ab initio* parameterization gives a much larger line tension in the AF than in the NM phase, showing a fine atomistic description of the dislocation core and mobility is needed to account for these effects, which was also reported systematically among all bcc metals by Dezerald *et al.* [191]. This difference between the two magnetic phases of Cr, despite their close elastic properties, may be due to the magnetic fault bounded by the two $1/2\langle 111 \rangle$ screw dislocations, possibly impeding the formation of a kink along the line due to the added back stress. In the following, we use the *ab initio* line tensions Γ in all simulations, starting from the nucleation enthalpy of a kink under an applied stress.

The resulting nucleation enthalpy ΔH_{kp} as a function of the magnitude σ of the applied stress can then be fitted to a Kocks' law of the form [192] (see Fig. 17b):

$$\Delta H_{\text{kp}}(\sigma) = \Delta E_{\text{kp}} \left[1 - \left(\frac{\sigma}{2\tau_P} \right)^p \right]^q, \quad (23)$$

with ΔE_{kp} the kink-pair formation energy under zero stress, τ_P the Peierls stress in $\{110\}$ planes, and p and q are adjustable parameters defining the shape of the stress variation of ΔH_{kp} . We obtain a formation energy ΔE_{kp} of 0.80 and 1.27 eV for a pair of two isolated kinks in the NM and AF phases respectively. It has been proposed that this formation energy can be approximated by $\Delta E_{\text{kp}} = 4\sqrt{2}/\pi \times \lambda_P \sqrt{\Gamma V_P^{\text{act}}}$ [191], with V_P^{act} the height of the Peierls potential. This results in 0.73 and 1.12 eV in the NM and AF phases respectively, in very good agreement with the values obtained by minimization of Eq. 19, showing ΔE_{kp} is equally sensitive to both the line tension and the Peierls potential. All extracted quantities entering the LT model are listed in Tab. 3, with values of p and q obtained for the simple Peierls enthalpy $\Delta H_P(x) = V_P(x)$. Non-Schmid effects can then be included using the full Peierls enthalpy of Eq. 10 in Eq. 19, and the resulting kink-pair nucleation enthalpy can still be fitted to a Kocks' law, whose parameters now depend on the mechanical loading under consideration. This results in the following for a uniaxial loading:

$$\Delta H_{\text{kp}}(\sigma, \zeta, \chi) = \Delta E_{\text{kp}} \left[1 - \left(\frac{\sigma}{\sigma_Y^0(\zeta, \chi)} \right)^{p(\zeta, \chi)} \right]^{q(\zeta, \chi)}, \quad (24)$$

with the dependence of the yield stress σ_Y^0 on the orientation of the loading axis (ζ, χ) under a uniaxial tension or compression given by the yield criteria of Eqs. 12 or 14. This will be used in the following section to construct a mobility law for $1/2\langle 111 \rangle$ screw dislocations gliding in $\{110\}$ planes including both non-Schmid effects and the influence of temperature in the NM and AF phases of bcc Cr.

Table 3: Parameters of the mobility law for the NM and AF phases of bcc Cr: Peierls stress τ_P (GPa), line tension Γ (eV/ \AA), kink-pair formation energy ΔE_{kp} (eV), and parameters p and q of the Kocks' law in Eq. 23.

	τ_P	Γ	ΔE_{kp}	p	q
NM phase	2.32	1.26	0.80	0.88	1.39
AF phase	1.98	3.01	1.27	0.89	1.33

3.2. Flow stress at finite temperature and mobility law

Assuming dislocation glide is governed by nucleation of kinks along its line, the dislocation velocity v_{gl} is then given by the following thermally activated law:

$$v_{\text{gl}} = \nu_D \frac{l_D}{b} \lambda_P \exp \left[-\frac{\Delta G_{\text{kp}}}{k_B T} \right]. \quad (25)$$

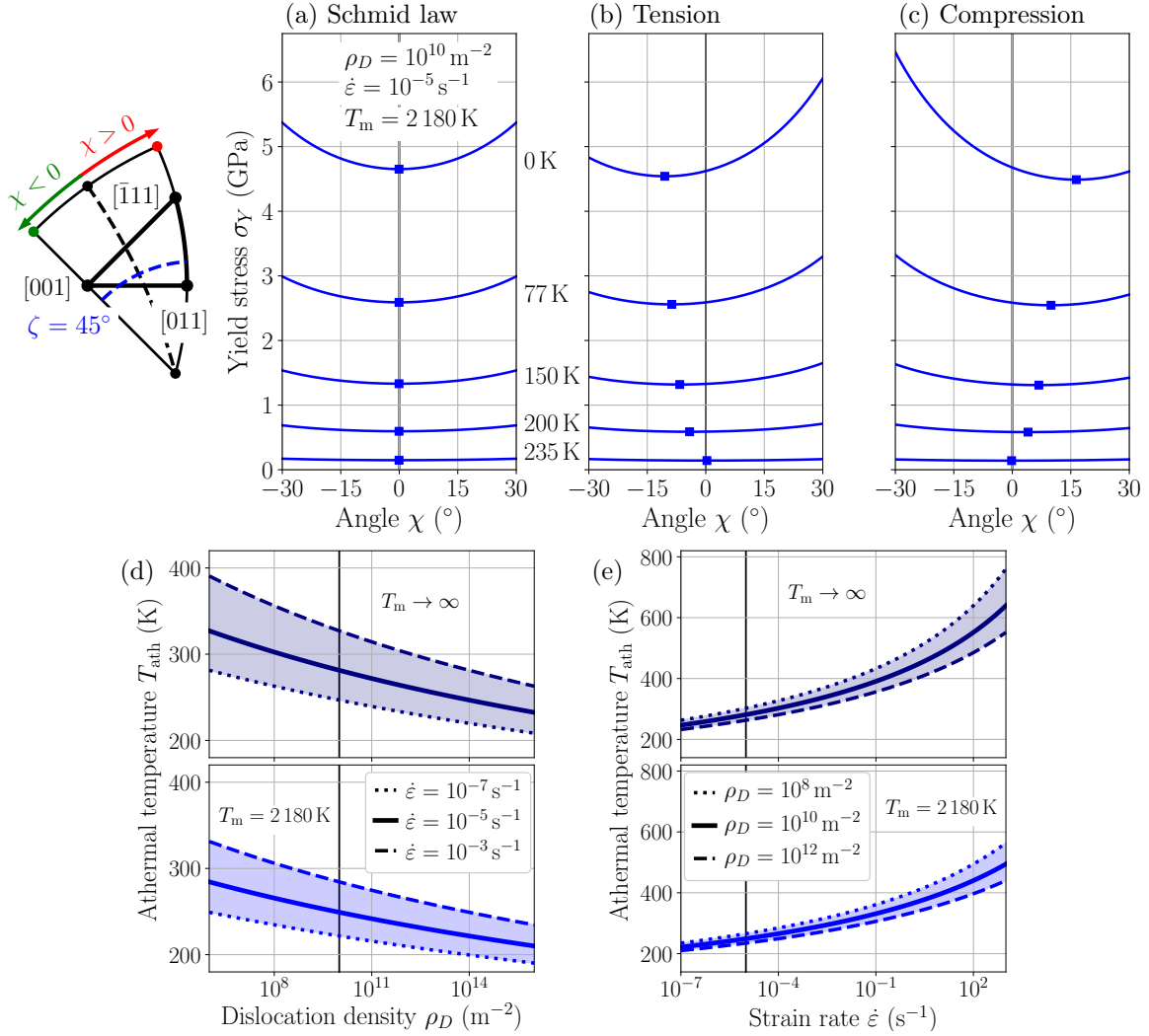


Figure 19: Yield stress σ_Y of the $[111](\bar{1}01)$ slip system in the NM phase at different temperatures as a function of the angle χ for $\zeta = 45^\circ$ (a) according to the Schmid law, and including non-Schmid effects in (b) tension, and (c) compression. Parameters of the model are the same as in Fig. 17. The athermal temperature T_{ath} predicted from Eq. 30 is presented as a function of (d) dislocation density ρ_D , and (e) strain rate $\dot{\epsilon}$. Vertical lines indicate the parameters used in (a)-(c) and Fig. 17.

In the above expression 25, ν_D is an attempt frequency for the nucleation event of a kink, ultimately leading to the motion of the dislocation, and taken equal to the Debye frequency ($\nu_D = 82 \text{ THz}$ for Cr [174]). The ratio l_D/b between the length of the dislocation line l_D and the norm of its Burgers vector b is the number of possible nucleation sites for the kink pair. The characteristic length of the line chosen for the model is estimated by $l_D = 1/\sqrt{\rho_D}$, with ρ_D the dislocation density [45], a measure of the average distance between dislocations contained in the microstructure. As expressed in Eq. 25, thermal fluctuations are not taken into account. After nucleating, a kink-pair has a non-negligible probability to cancel out instead of migrating along the dislocation line, which lowers the dislocation velocity. This effect can be described in the frame of classical nucleation theory through the introduction of the Zeldovitch factor Z in the above expression, accounting for this non-zero probability for kink-pair cancellation. This factor can be evaluated numerically using the LT model as formulated here, which is done in the work of Hachet *et al.* on bcc tungsten [193], or approximated using the kink diffusive glide mechanism introduced by Hirth and Lothe [9]. Fluctuations are neglected in the present work, but yield lower dislocation velocities than with Eq. 25.

The kink-pair formation free energy $\Delta G_{kp} = \Delta H_{kp} - TS_{kp}$ has both an enthalpic contribution given by Eq. 24, and an entropic contribution, which is unknown. Computational methods to evaluate the entropic contribution, either based on a harmonic approximation [65] or using thermodynamical integration [194], are however too expensive using *ab initio* calculations. To study the potential effect of this entropic contribution, a simple Meyer-Neldel compensation rule [195] is used, assuming the nucleation entropy S_{kp} proportional to the nucleation enthalpy, *i.e.* $S_{kp} = \Delta H_{kp}/T_m$. The parameter T_m is homogeneous to a temperature, which is observed experimentally to be close to the melting point of the material, set to $T_m = 2180$ K for Cr [174]. Under this approximation, neglecting entropic contributions is equivalent to considering the $T_m \rightarrow \infty$ limit, which will be considered first in the following.

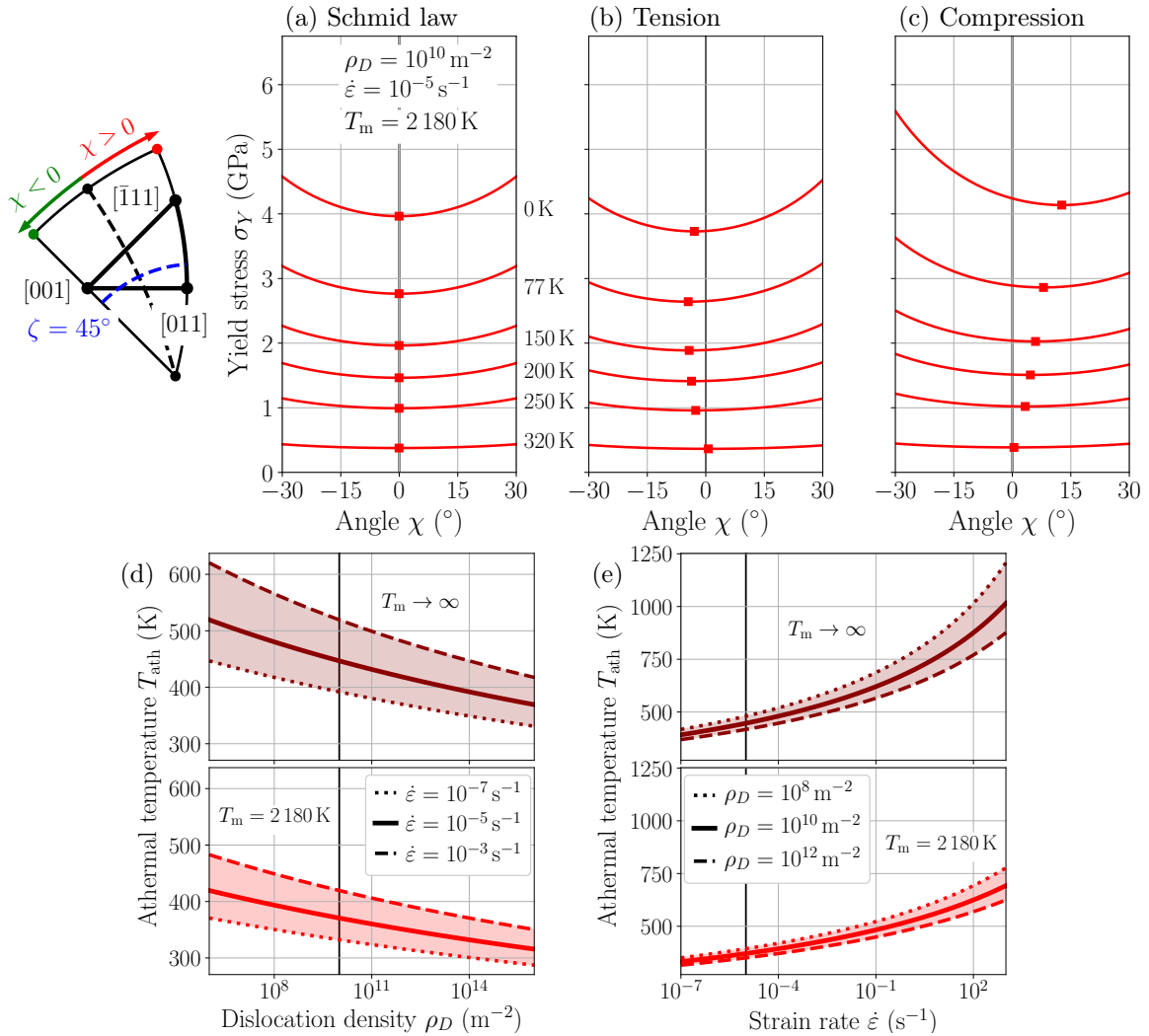


Figure 20: Yield stress σ_Y of the [111]($\bar{1}$ 01) slip system in the AF phase at different temperatures as a function of the angle χ for $\zeta = 45^\circ$ (a) according to the Schmid law, and including non-Schmid effects in (b) tension, and (c) compression. Parameters of the model are the same as in Fig. 17. The athermal temperature T_{ath} predicted from Eq. 30 is presented as a function of (d) dislocation density ρ_D , and (e) strain rate $\dot{\epsilon}$. Vertical lines indicate the parameters used in (a)-(c) and Fig. 17.

Entering the expression for the nucleation enthalpy ΔH_{kp} incorporating non-Schmid effects, and using the Meyer-Neldel compensation rule to evaluate the entropic contribution, the nucleation free energy is then:

$$\Delta G_{kp}(\sigma, \zeta, \chi, T) = \Delta E_{kp} \left[1 - \left(\frac{\sigma}{\sigma_Y^0(\zeta, \chi)} \right)^{p(\zeta, \chi)} \right]^{q(\zeta, \chi)} \left(1 - \frac{T}{T_m} \right) \quad (26)$$

From the dislocation velocity v_{gl} given by Eq. 25, one can deduce the rate of plastic deformation $\dot{\epsilon}$ associated to a density ρ_D of mobile dislocations using Orowan's law, stating:

$$\dot{\epsilon} = \rho_D b v_{gl}, \quad (27)$$

which can be inverted to obtain an expression of the yield stress σ_Y necessary to activate a slip system at a given temperature and strain rate. Considering the case of a uniaxial loading, one can use the yield criteria developed at 0 K of Eqs. 12 and 14, which results in the following mobility law in tension:

$$\begin{aligned} \sigma_Y(T, \zeta, \chi) &= \sigma_Y^0(\zeta, \chi) \left(1 - \left[\frac{k_B T}{\Delta E_{kp}} \frac{T_m}{T - T_m} \ln \left(\frac{\dot{\epsilon}}{\nu_D \lambda_P \sqrt{\rho_D}} \right) \right]^{1/q(\zeta, \chi)} \right)^{1/p(\zeta, \chi)} \\ &= \frac{2\tau_P \left(1 - \left[\frac{k_B T}{\Delta E_{kp}} \frac{T_m}{T - T_m} \ln \left(\frac{\dot{\epsilon}}{\nu_D \lambda_P \sqrt{\rho_D}} \right) \right]^{1/q(\zeta, \chi)} \right)^{1/p(\zeta, \chi)}}{\sin(2\zeta) \frac{\cos(\chi - \alpha^*)}{\cos(\alpha^*)} + \beta(\zeta, \chi)}, \end{aligned} \quad (28)$$

and in compression by applying the transformations $\chi \rightarrow -\chi$, $\alpha^* \rightarrow -\alpha^*$ and $\beta \rightarrow -\beta$, resulting in a similar form to the 0 K yield criterion. Neglecting entropic effects, the athermal temperature of the Peierls mechanism T_{ath} at which the yield stress given by the above law vanishes, is given by:

$$T_{ath}^0 = \frac{\Delta E_{kp}}{k_B \ln \left[\frac{\nu_D \lambda_P \sqrt{\rho_D}}{\dot{\epsilon}} \right]}, \quad (29)$$

while incorporating entropic effects through the Meyer-Neldel compensation rule gives:

$$T_{ath} = \frac{T_{ath}^0}{1 + \frac{T_{ath}^0}{T_m}} = \frac{T_m \Delta E_{kp}}{\Delta E_{kp} + T_m k_B \ln \left[\frac{\nu_D \lambda_P \sqrt{\rho_D}}{\dot{\epsilon}} \right]}, \quad (30)$$

equivalent to Eq. 29 in the limit $T_m \rightarrow \infty$. Entropic effects yield lower energy barriers for kink nucleation, hence allowing for easier dislocation glide at finite temperature, with a lower athermal temperature T_{ath} . It is important to note that, regardless of the entropic effects, this critical temperature neither depends on the orientation of the loading axis nor on the considered slip system, defining the athermal limit above which dislocation glide is no longer a thermally activated process. The temperature dependence of the yield stress for $\langle 111 \rangle \{110\}$ slip in the NM and AF phases of bcc Cr are presented in Fig. 17c without the inclusion of non-Schmid effects, with the corresponding athermal temperatures for different dislocation densities at a fixed strain rate. Given that the kink-pair formation energy ΔE_{kp} is higher in the AF than in the NM phase (Tab. 3), the athermal temperature under the same conditions $(\rho_D, \dot{\epsilon})$ is higher in the AF than in the NM phase. As the 0 K Peierls stress is higher in the NM phase, this results in a crossing of the yield stress temperature variation at which $\langle 111 \rangle \{110\}$ slip becomes more difficult in the AF phase, before fading out first in the NM phase.

Apart from the parameters derived from *ab initio* calculations, the choice is left regarding the dislocation density ρ_D and the strain rate $\dot{\epsilon}$. For the choice of ρ_D , we rely on the model developed by Williams *et al.* [101, 102], based on the dislocation density present in a given sample to account for both the shift in the Néel temperature and the domains of coexistence between the different magnetic phases of bcc Cr they observed. Using this model, the authors evaluated a dislocation density ρ_D in annealed samples ranging

from 10^8 to 10^{11} m^{-2} , depending on the annealing temperature and time. As for the strain rate, the value $\dot{\epsilon} = 1 \times 10^{-5} \text{ s}^{-1}$ was chosen to match experiments of both Holzer *et al.* [34] for compression tests on monocrystalline samples at 77 K, and Marcinkowski and Lipsitt [126] for tensile tests on a polycrystal of pure Cr at various temperatures. Now including non-Schmid effects according to the mobility law of Eq. 28, with $\rho_D = 10^{10} \text{ m}^{-2}$ and $\dot{\epsilon} = 10^{-5} \text{ s}^{-1}$, the yield stress for the $[111](\bar{1}01)$ slip system as a function of the orientation χ of the MRSSP at $\zeta = 45^\circ$ is plotted at different temperatures ranging from 0 K to the critical athermal temperature in the NM and AF phases of bcc Cr in Figs. 19 and 20 respectively. The dependence of the athermal temperature on the dislocation density ρ_D and the strain rate $\dot{\epsilon}$, both neglecting and incorporating entropic effects, are presented in d and e respectively on both figures for the NM and AF phases. We note that T_{ath} is only sensitive to these two parameters, as given by Eq. 30, and does not depend on the considered slip system or the inclusion of non-Schmid effects. A notable feature of the temperature dependence of the yield stress as presented in Figs. 19 and 20 is that deviations from the Schmid law, both in terms of T/AT and tension/compression asymmetries, become less pronounced with increasing temperature. The strong deviations reported at 0 K in section 2.2 progressively fade out as the temperature approaches the critical athermal temperature of the Peierls mechanism, where the Schmid law is recovered. Such a conclusion was also reported using a model 2D Peierls potential coupled with a LT model in the work of Edagawa *et al.* [67, 68]. The temperature dependence of non-Schmid effects has been observed experimentally in other bcc metals, in particular in molybdenum [41], but has not been characterized in Cr.

Marcinkowski and Lipsitt [126] measured an athermal temperature $T_{\text{ath}} \simeq 420 \text{ K}$ in polycrystalline sample at a strain rate $\dot{\epsilon} \simeq 10^{-5} \text{ s}^{-1}$. Under the same conditions, we find T_{ath} ranging from 393 and 359 K in the AF phase, and 265 and 241 K in the NM phase for a dislocation density comprised between 10^8 to 10^{11} m^{-2} . A better agreement is found considering the AF phase, due to the higher kink-pair formation energy ΔE_{kp} . The sensitivity of this critical temperature on the Meyer-Neldel parameter T_m shows the strong impact of entropic contributions on the yield stress of bcc metals at high temperatures. Accounting for the vibrational entropy in kink-pair nucleation appears therefore necessary both at low temperatures, to resolve the discrepancy between experimental and theoretical Peierls stresses [65], and high temperatures with the need for precise approaches for the evaluation of the vibrational entropy based on thermodynamical integration [194]. In the particular case of Cr, one needs to keep in mind that the athermal limit of the Peierls mechanism is close to the Néel temperature T_N , ranging from 300 to 450 K [6, 100, 101], where long-range magnetic order vanishes, hence raising the question of the influence of magnetism on its plastic deformation in the high temperature disordered PM phase, prominent above T_N .

Conclusions of Chapter 2:

- The $1/2\langle 111 \rangle$ screw dislocation has an identical compact core structure in both the NM and AF phases of chromium, like reported in all other bcc transition metals using *ab initio* calculations.
- The magnetic fault bounded by two $1/2\langle 111 \rangle$ dislocations has the same structure as the infinite fault obtained in the GSF calculations, with exactly the same surface energy $\gamma = 16.3 \text{ meV}/\text{\AA}^2$. Due to its high energy, the magnetic fault *a priori* constrains $1/2\langle 111 \rangle$ dislocations to coexist and move pairwise, creating $\langle 111 \rangle$ superdislocations dissociated in two partial dislocations separated by a magnetic fault with an equilibrium length of approximately 6 nm at 0 K.
- Apart from the magnetic fault, the core structure of the $1/2\langle 111 \rangle$ screw dislocation is identical in both magnetic phases, with similar Peierls energy barriers and stresses.
- The trajectory of the $1/2\langle 111 \rangle$ screw dislocation in a $\{110\}$ glide plane deviates towards the split core position upon crossing of the Peierls barrier, with a deviation more pronounced in the NM phase. Variations of the screw dislocation relaxation volume show the same trends in both magnetic phases, with a more pronounced tension/compression asymmetry in the AF phase.
- Using the properties of the $1/2\langle 111 \rangle$ screw dislocations evaluated *ab initio*, a yield criterion incorporating non-Schmid effects is derived and applied to the case of a uniaxial mechanical loading. The

model reproduces the experimental features of the deviations from the Schmid law observed in bcc metals, namely a twinning/antitwinning and tension/compression asymmetry, with similar qualitative behaviors in both magnetic phases of bcc Cr.

- Through a line tension model describing the kink-pair nucleation mechanism, with parameters extracted from *ab initio* calculations, the thermally activated glide of screw dislocations is accounted for in the generalized yield criterion and applied to uniaxial loading of bcc Cr. Non-Schmid effects at finite temperature show the same characteristic features as at 0 K, before progressively vanishing when the temperature approaches the athermal temperature of the Peierls mechanism.
 - All these results *a priori* indicate that $1/2\langle 111 \rangle$ screw dislocations in Cr have a behavior similar to all other bcc transition metals, except for the presence of a magnetic fault in the AF phase.
-

Chapter 3: Magnetic excitations and plasticity of chromium

From bulk properties of the different magnetic phases of bcc Cr below its Néel temperature to the study of $1/2\langle 111 \rangle$ screw dislocations in the NM and AF phases, we showed in the two previous chapters that the main impact of magnetism is the generation of a magnetic fault due to the disruption of the magnetic order by the Burgers vector of these dislocations. The influence of such a magnetic fault, and generally the impact of magnetism on the plasticity of bcc Cr has been discussed at zero temperature in the two previous chapters, which is extended to finite temperatures in the present chapter, in an attempt to qualify the influence of magnetism on the plasticity of bcc Cr above and below its Néel temperature.

1. Finite temperature and magnetic excitations

Three different energetic models are considered for the study of the magnetic properties of bcc Cr, all detailed in Methods: spin-polarized *ab initio* DFT calculations, a tight-binding (TB) model developed for transition metals [141] and tested previously on bcc Cr [113, 196], and a magnetic interaction model in the frame of a generalized Heisenberg model, or Heisenberg-Landau model (HL). We now focus on finite temperature effects on the magnetic properties of bcc Cr, which is performed using the HL model. To ensure both a good evaluation of the zero temperature properties, which was checked using *ab initio* calculations in the two previous chapters, and a satisfactory agreement with experimental data at higher temperature, a careful fitting procedure of the HL model is required, which is detailed in the following.

1.1. Parametrization of a generalized Heisenberg model for chromium

Let us consider a magnetic system of N atoms located at fixed positions \vec{R}_i , each site having a magnetic moment \vec{m}_i . The Hamiltonian of the system in the frame of the HL model has the following form [144]:

$$E^{\text{mag}}(\{\vec{m}_i\}) = \sum_{i=1}^N \left[A|\vec{m}_i|^2 + B|\vec{m}_i|^4 + \sum_{j \in 1\text{NN}(i)} J_1 \vec{m}_i \cdot \vec{m}_j + \sum_{j \in 2\text{NN}(i)} J_2 \vec{m}_i \cdot \vec{m}_j \right] \quad (1)$$

In the above Hamiltonian, A and B are the Landau parameters, controlling longitudinal magnetic excitations, *i.e.* the magnitude of the magnetic moments. J_1 and J_2 are the Heisenberg exchange parameters, controlling transverse excitations, *i.e.* the relative orientations of magnetic moments. These exchange parameters are defined for a shell of nearest neighbors (NN), namely J_1 couples first NN (1NN) and J_2 second NN (2NN) atomic sites, as sketched in Fig. 1a for the bcc lattice having an AF order. As written in Eq. 1, such a Hamiltonian includes up to 2NN interactions. The phase diagram of the Ising model, equivalent to

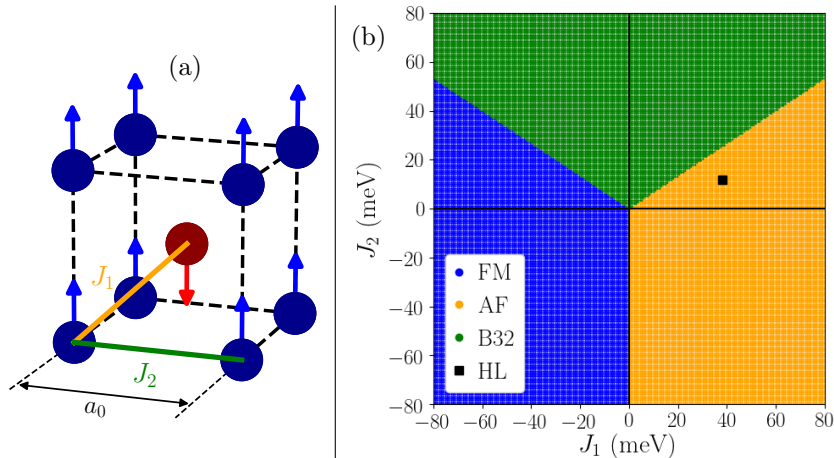


Figure 1: (a) Sketch of the bcc lattice showing the exchange coupling J_i up to second nearest neighbor interactions. (b) Phase diagram of the Ising model including up to second nearest neighbor (2NN) interactions [197].

the HL model assuming constant magnitude for all magnetic moments and only collinear phases, is presented in Fig. 1b in the (J_1, J_2) plane. In this approximation, the 2NN model has three possible collinear magnetic ground states, depending on the exchange parameters: ferromagnetic (FM), antiferromagnetic (AF) and B32 order [197]. The relative stability of these three phases thus depends on the amplitudes and signs of the exchange parameters of the model. In this respect, positive exchange coupling corresponds to FM interactions, and negative exchange to AF interactions between neighboring sites.

We know that bcc Cr has an AF magnetic ground state at 0 K according to *ab initio* calculations, which is also predicted by the TB model [113]. Therefore, the parameters (A, B, J_1, J_2) of the HL model must be chosen as to ensure the AF order has the lowest energy among the three phases appearing on Fig. 1b. To ensure a good reproduction of the 0 K *ab initio* properties, these parameters are extracted from a fit of Eq. 1 to reference DFT energies of these three possible collinear ground states of the model to ensure the correct hierarchy between them. As collinear phases, the only variables are the lattice parameter a_0 , defining distances between neighboring atoms, and the magnetic moment m_0 . The results of the fit to DFT data at three different values of a_0 are presented in Fig. 2 for the AF, FM and B32 phases as a function of m_0 , which are all considered in the fit since they represent three possible collinear ground states of the 2NN HL model (see Fig. 1b). Inclusion of the B32 phase necessitates the use a $2 \times 2 \times 2$ bcc unit cell. One sees that apart from the AF phase, neither the FM or B32 phase is stable according to *ab initio* calculations, regardless of the lattice parameter or magnetic moment, which was also reported in previous studies [110]. To construct the DFT database including these highly unstable phases, we thus used constrained spin-polarized calculations, which are detailed in Methods (see section 1.1.7). Different lattice parameters were included in the fit to evaluate the distance dependence of the parameters of the model. This is motivated by the interest in computing the energy of simulation cells containing dislocations, which induce a local distortion of the lattice in the vicinity of their cores, and thus non homogeneous distances between atoms. The resulting parameters (A, B, J_1, J_2) of the model as obtained from the fitted curves of Fig. 2 are presented in Fig. 3a

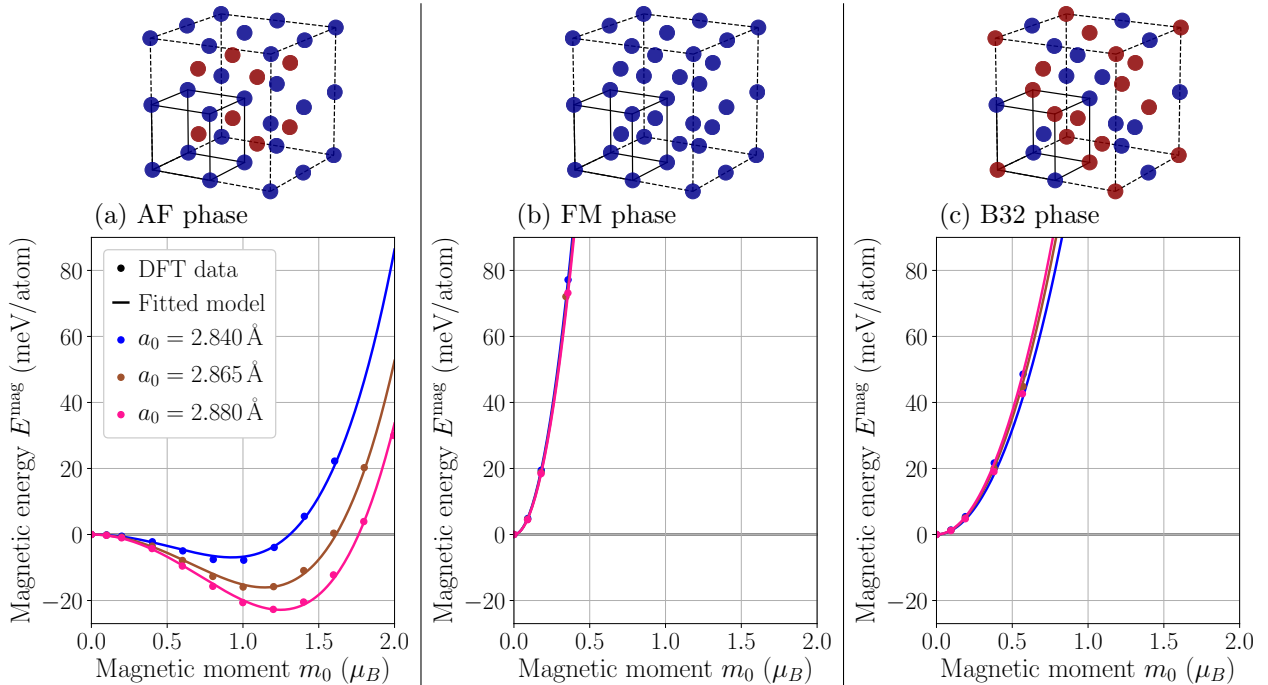


Figure 2: (a) AF, (b) FM, and (c) B32 magnetic phases included in the fitting procedure of the HL model, with corresponding magnetic energy E^{mag} obtained with *ab initio* DFT (circles) and the HL model (solid lines) as a function of the magnetic moment m_0 at three different lattice parameters a_0 . Atoms in red (blue) have a positive (negative) magnetic moment.

as a function of the lattice parameter a_0 .

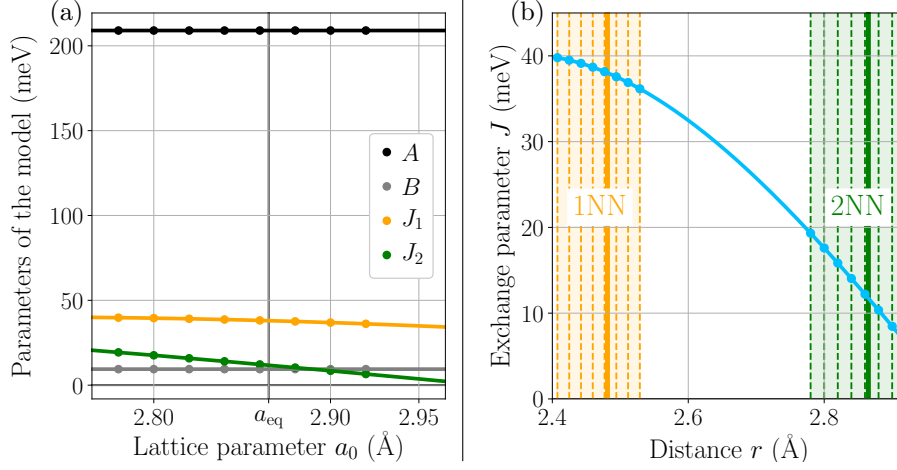


Figure 3: (a) Variations of the parameters (A, B, J_1, J_2) of the HL model with the lattice parameter a_0 adjusted to the DFT energies of the three collinear phases of Fig. 2. (b) Global exchange coupling parameter J appearing in Eq. 2 as a function of the distance r between neighboring atoms. The values of J_1 and J_2 are reported using circles.

The variation with the lattice parameter a_0 of the Landau parameters A and B , and the Heisenberg exchange couplings J_1 and J_2 for 1NN and 2NN interactions are presented in Fig. 3a. We note that both A and B have the same value over the whole range of a_0 included in the fit, whereas the amplitude of the exchange parameters J_1 and J_2 decrease with increasing lattice parameters, with positive values across the whole range. However, in the AF phase, 1NN interactions occur between two opposite sign spins, resulting in a negative AF coupling between them, and 2NN interactions couple magnetic moments pointing in the same direction, resulting in a positive FM coupling between them. The constant values for A and B result from a choice in the fitting procedure to impose this constraint. Indeed, this is motivated by the fact that these Landau parameters control the on-site magnetic energy, which is assumed to be independent on the lattice parameter a_0 . The inclusion of the distance dependence of the exchange coupling allows for considering a system of N atoms located at positions \vec{R}_i , which can now differ from the perfect crystal. The Hamiltonian of the HL model of Eq. 1 thus becomes:

$$E(\{\vec{m}_i\}, \{\vec{R}_{ij}\}) = \sum_{i=1}^N \left[A|\vec{m}_i|^2 + B|\vec{m}_i|^4 + \sum_{j \in \text{NN}(i)} \left(J(|\vec{R}_{ij}|) \vec{m}_i \cdot \vec{m}_j \right) \right] \quad (2)$$

$$\text{with } J(|\vec{R}_{ij}|) = \sum_{n=0}^3 j_n \times |\vec{R}_{ij}|^n$$

where the exchange parameters (J_1, J_2) are replaced by a global function J of the distance $|\vec{R}_{ij}|$ between the two neighboring atomic sites i and j . This function encapsulates both 1NN and 2NN interactions, and allows to include a distance dependence of the exchange coupling. A polynomial function of the interatomic distance is chosen for J , which we checked gives the best agreement with the parameters obtained from the fit to the energy of the three AF, FM and B32 phases as a function of both the lattice parameter a_0 and the magnetic moment m_0 . However, a range of distances r is not covered by the fit (between the orange and green shaded zones in Fig. 3b), in which the variation of the exchange parameter J with r is a direct consequence of the polynomial form chosen. A more physical expression can be obtained in the frame of the RKKY theory [198], for which indirect exchange coupling is expressed as:

$$J_{\text{RKKY}}(r) = J_0 \times \frac{2kr \cos(2kr) - \sin(2kr)}{r^\alpha}, \quad (3)$$

where k is the Fermi wave-vector, J_0 defines the amplitude of the exchange coupling, and the exponent α its decay with increasing distance r . Results obtained from a fit to the RKKY relation 3 are plotted with dashed lines on Fig. 4e, for which a less satisfactory agreement is found with respect to DFT data, however offering a physical meaning for the choice of the function. Nevertheless, we note that this formulation also yields a decay in the magnitude of the exchange parameter J , in agreement with the polynomial form in the range of distances not covered by the DFT data. A polynomial function was thus chosen for all following presented results. This choice is also motivated by the good agreement found with *ab initio* calculations in terms of the excess magnetic energy obtained along the $\langle 111 \rangle$ γ -line in $\{110\}$ and $\{112\}$ planes, detailed in section 1.3.

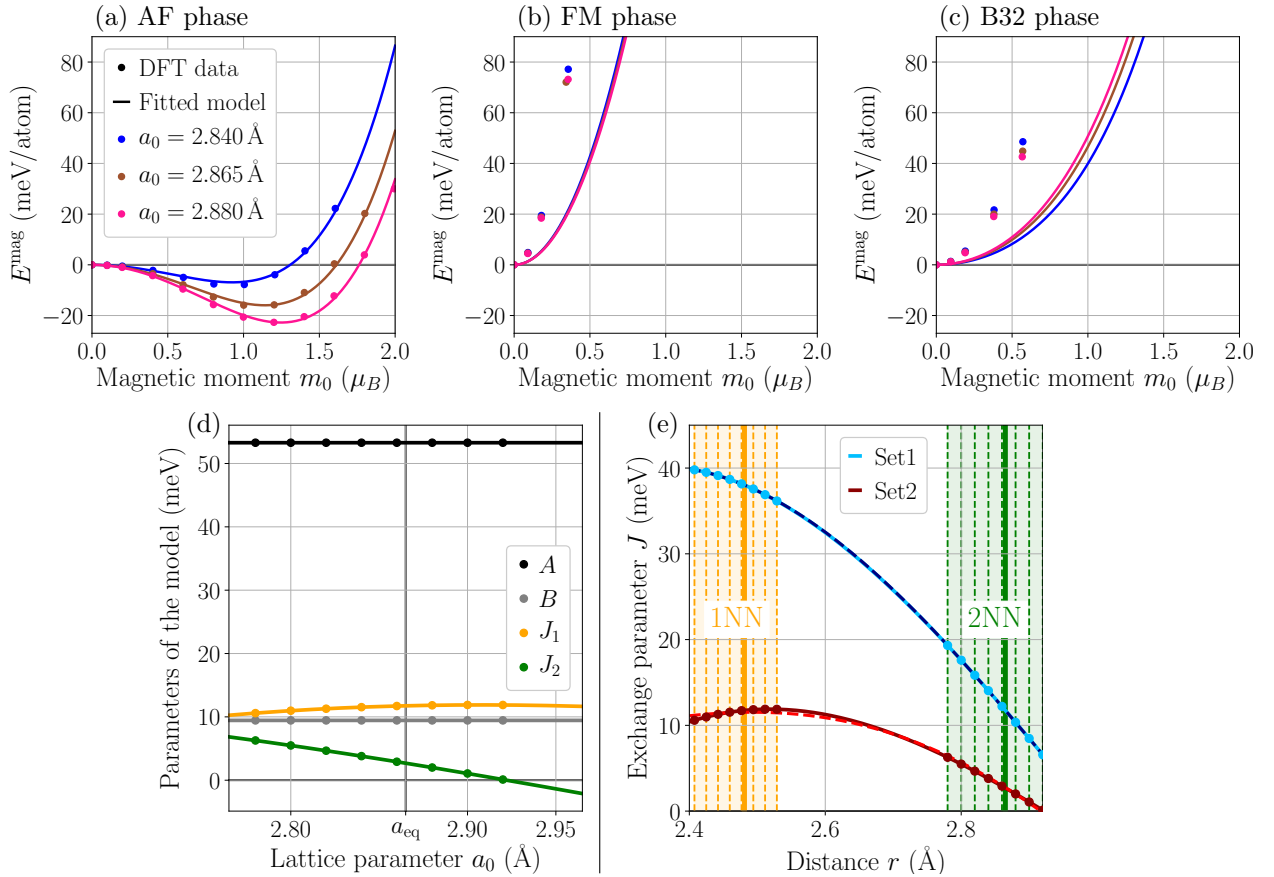


Figure 4: Fitting of the Set2 parameters of the HL model on the DFT energies of the (a) AF, (b) FM, and (c) B32 magnetic phases. (d) Variation of the parameters (A, B, J_1, J_2) with the lattice parameter a_0 . (e) Global exchange coupling J with respect to the interatomic distance r using Set1 and Set2 parameters. Results of a fit to Eq. 3 are plotted in dashed lines.

The aim of the developed HL model is to study finite temperature magnetic excitations. In this respect, a good reproduction of the Néel temperature T_N of bcc Cr must be ensured by the model. Its evaluation is the focus of section 1.4, with details about the simulation and algorithm for the Monte Carlo simulations given in Methods (see section 2.1.1). As obtained from a fit to DFT data, ensuring a good reproduction of the 0 K magnetic properties (Fig. 2), a Néel temperature $T_N = 1050$ K is predicted by the model, overestimated with respect to experiments reporting T_N between 300 and 450 K depending on the sample [6, 100, 101]. To lower the predicted T_N , we deteriorated the agreement for the two high-energy FM and B32 phases included in the fit by lowering by the same factor the energies predicted by the model compared to reference DFT values. Otherwise, the same DFT database as in Fig. 2 is used, without degrading the properties of the AF phase, the ground state of the model. The resulting fitted energy and parameters obtained for

this new set of parameters are presented in Fig. 4. These parameters will be referred to as "Set2" in the following, the original parameters being referred to as "Set1". Lowering the energy of the unstable FM and B32 phases results in a lower energy barrier associated with the loss of long-range magnetic order, *i.e.* when transitioning to the high-temperature paramagnetic (PM) phase above T_N . These new Set2 parameters result in a lower predicted $T_N = 384$ K, in the range of experimental values. However, such readjustment degrades properties of the model associated with the high-energy FM phase and some magnetic excitation modes, which will be discussed in the following section.

The energies of the three collinear AF, FM and B32 phases predicted by these new Set2 parameters (Fig. 4a-c) show a perfect agreement for the AF ground state of the model, and lower energies than Set1 for the two unstable FM and B32 phases, whose energies were lowered by a factor 1/4 with respect to DFT data to reduce the predicted T_N as discussed above. The values for the two sets of parameters of the HL model are presented in Tab. 1 at the equilibrium 0 K *ab initio* lattice parameter $a_0 = 2.865$ Å of the AF phase. We note that Set1 parameters have higher amplitudes than Set2, a consequence of the fitting procedure adopted for Set2, except for B which is the same for both sets. The variation of the exchange coupling J for the two sets (Fig. 4e) shows a different variation across the range of 1NN, 2NN and the blank region in between. The ability of these models to reproduce predicted 0 K *ab initio* properties is discussed in section 1.3.

Table 1: Values of the two Set1 and Set2 parameters of the HL model for $a_0 = 2.865$ Å, the 0 K equilibrium lattice parameter of the AF phase obtained from *ab initio* calculations. The experimental Néel temperature T_N is 311 K [6].

	A	B	J_1	J_2	j_0	j_1	j_2	j_3	T_N
HL (Set1)	209.0	9.4	38.0	11.8	-1.75	1.94	-0.67	0.07	1 050
HL (Set2)	53.3	9.4	11.7	2.7	-1.63	1.71	-0.58	0.06	384

At finite temperature, magnetic excitations allow for the exploration of higher energy magnetic structures, whether operating through modulation of the amplitude of magnetic moments, referred to as longitudinal excitations, or by inducing a disorientation of the spins with respect to each other. The latter corresponds to transverse excitations described by the Heisenberg exchange coupling parameter J , operating through the exploration of non-collinear magnetic structures defined by a disorientation of the spins called magnons (see section 2.1.3 in Methods), discussed in the next section.

1.2. Spin spirals and transverse magnetic excitations

At finite temperature, magnetic fluctuations operate through excitation modes of the spin structure in the form of elementary spin spiral called magnons. A spin-spiral of wave-vector \vec{q} defines the angle Φ the magnetic moment of an atom located at the position \vec{R}_i makes in the plane orthogonal to the propagation of the spiral, in the following form:

$$\Phi(\vec{R}_i) = \Phi_0 + \vec{q} \cdot \vec{R}_i \quad (4)$$

As introduced in Methods (section 2.1.3), the magnitude of the spins along the propagation of these spirals remains constant. In bulk bcc Cr, these non-collinear structures are known to be highly unstable for any wave vector [110, 113]. A direct *ab initio* evaluation of their energy over the whole Brillouin zone would thus be very costly, since one needs to account for both non-collinear magnetism and spin-orbit coupling, in constrained magnetism calculations. A few *ab initio* points were however evaluated for small disorientation of the AF order. Such constrained calculations are less costly in the TB formalism [141], thus allowing for direct evaluation of the magnon spectrum, *i.e.* the energy of spirals of wave-vectors \vec{q} spanning the entire Brillouin zone. Given the very good agreement of the TB model with *ab initio* data (see Methods, section 1.2), the TB magnon spectrum will serve as a reference to test the validity of the HL model in the following.

Using the HL model, the energy $E(\vec{q}, m_0)$ of a spin spiral of wave-vector \vec{q} and a constant magnetic moment m_0 has an analytical expression [199], given by:

$$E(\vec{q}, m_0) = A m_0^2 + B m_0^4 + \sum_{k \in i\text{NN}} \sum_{j \in k\text{NN}} J(|\vec{R}_k - \vec{R}_j|) m_0^2 \left[1 - e^{i\vec{q} \cdot (\vec{R}_k - \vec{R}_j)} \right], \quad (5)$$

corresponding to a sum over the shells of nearest neighbor interactions (NN) included in the model (Eq. 1). This results in the following expression considering the two 1NN and 2NN nearest neighboring shells:

$$E(\vec{q}, m_0) = A m_0^2 + B m_0^4 - 8J_1 m_0^2 \left(1 - \cos\left(\frac{a_0 q_x}{2}\right) \times \cos\left(\frac{a_0 q_y}{2}\right) \times \cos\left(\frac{a_0 q_z}{2}\right) \right) - 2J_2 m_0^2 ([1 - \cos(a_0 q_x)] + [1 - \cos(a_0 q_y)] + [1 - \cos(a_0 q_z)]) \quad (6)$$

The magnon spectrum of bcc Cr across the Brillouin zone is presented in Fig. 5a at the equilibrium *ab initio* lattice parameter $a_0 = 2.865 \text{ \AA}$ and magnetic moment $m_0 = 1.1 \mu_B$, obtained with Eq. 6 for the HL model and compared to TB calculations and a few DFT data. The special points Γ and H of the Brillouin zone correspond to the FM and AF phases respectively, which are the two extrema of the magnon spectrum. The magnon density of states (mDOS) $g(E)$, shown in b, is obtained through integration of the spectrum over the entire Brillouin zone. The magnon energies are plotted with respect to the AF ground state of the model, *i.e.* $E(\vec{q}, m_0) - E_{\text{AF}}^{\text{mag}}(m_0)$, to highlight the excitation energy they represent.

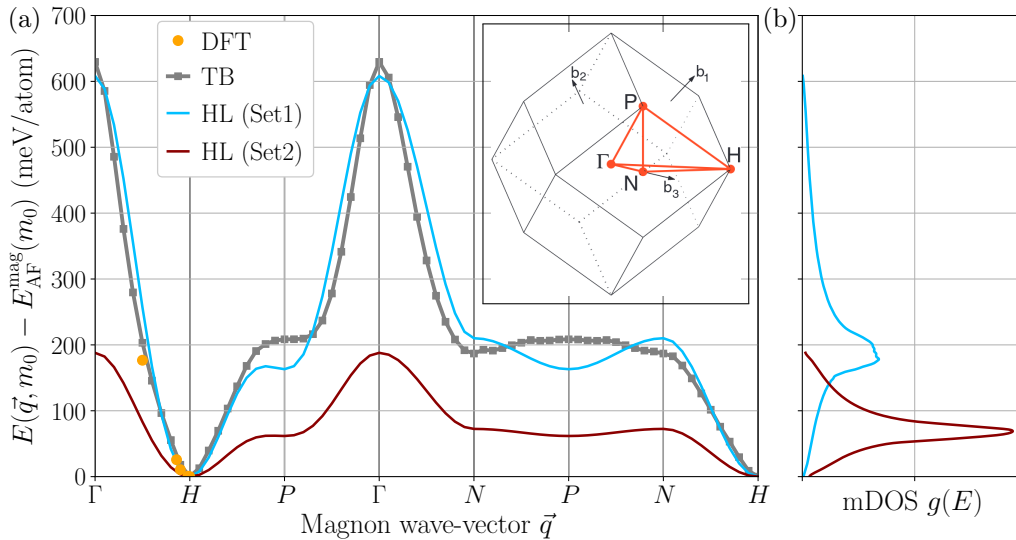


Figure 5: (a) Magnon spectrum of bcc Cr $E(\vec{q}, m_0) - E_{\text{AF}}^{\text{mag}}(m_0)$ obtained with constrained *ab initio* DFT calculations (orange dots), the TB model (thick grey lines), and with Eq. 6 for the HL model with Set1 (blue) and Set2 (red). Energies are obtained at the equilibrium *ab initio* lattice parameter $a_0 = 2.865 \text{ \AA}$ and magnetic moment $m_0 = 1.1 \mu_B$ of the AF phase, along the high-symmetry path $\Gamma - H - P - \Gamma - N - P - N - \Gamma$ of the Brillouin zone (see inset [162]), with $\Gamma = (0, 0, 0)$ (FM phase), $H = (1, -1, 1)$ (AF phase), $P = (1/2, 1/2, 1/2)$ and $N = (0, 0, 1)$. (b) Magnon density of states (mDOS) $g(E)$ of the HL model with Set1 and Set2 parameters.

The TB spectrum shows a very good agreement with the few *ab initio* data calculated near the H -point, showing spirals having intermediate energies located between Γ and H . The results of the HL model using Set1 (blue) are in good agreement with the TB calculation, which is very satisfactory since the parameters of the HL model were adjusted on energetics of collinear magnetic phases only. Only the cusp near P is not obtained in the TB spectrum. The second set of parameters, Set2 (red), predicts a lower energy for these non-collinear magnetic excitations, with however the same variation with \vec{q} as obtained with Set1. Since the paramagnetic (PM) phase of bcc Cr above the Néel temperature is mostly characterized by an orientational disorder between magnetic moments (see Literature review, section 3.1.1), an accurate picture of these spirals is required to have a good description of magnetic excitations occurring at finite temperatures.

1.3. Validation of the HL models

Before moving on to magnetic properties at finite temperatures, we test in the present section the ability of the HL models to reproduce the 0 K magnetic properties of bcc Cr obtained using *ab initio* calculations. The surface energy of infinite $\{110\}$ and $\{112\}$ magnetic faults, obtained by shearing the crystal by a fault vector $\frac{1}{2}\langle 111 \rangle$ in these two planes are presented in Tab. 2 obtained with DFT and the HL model with the two sets of parameters. We find a very good agreement of the magnetic fault energy γ between *ab initio* calculations and Set1 parameters of the HL model, and a less satisfactory agreement with parameters Set2, a direct consequence of the fitting procedure used to construct it. Indeed, such magnetic faults originates from a ferromagnetic frustration in the two planes located in the direct vicinity of the fault plane, where spins of the same direction are forced to face each other. Since the energy of this highly unstable FM phase has been lowered in the fitting of Set2 parameters, the energy of the magnetic fault is thus lower.

Table 2: Computed properties of the HL model compared to DFT: bulk magnetic moment m_0 , energy of the NM and SDW (of period $20a_0$) phases with respect to the AF phase, surface energy γ of the magnetic fault in $\{110\}$ and $\{112\}$ planes,

	DFT	HL (Set1)	HL (Set2)
m_0 (μ_B)	1.10	1.14	1.14
ΔE_{NM} (meV/atom)	12.5	12.5	12.5
ΔE_{SDW} (meV/atom)	10.4	8.6	4.8
$\gamma_{\{110\}}$ (meV/ \AA^2)	16.2	15.1	8.7
$\gamma_{\{112\}}$ (meV/ \AA^2)	16.4	15.1	8.7

To test the validity of the polynomial function chosen to interpolate the distance variation of the exchange coupling $J(r)$ of the HL model (see Fig. 4e), we also considered the variation of the GSF magnetic energy $\gamma_{\text{GSF}}^{\text{mag}}$ along the $\langle 111 \rangle$ γ -lines in the two $\{110\}$ and $\{112\}$ planes, presented in Fig. 6. This magnetic energy is defined as the total excess energy of the system in the AF phase, at its equilibrium lattice parameter $a_0 = 2.865 \text{ \AA}$, from which the energy of the identical structure in the NM phase is subtracted without relaxing the system. For a $\frac{1}{2}\langle 111 \rangle$ fault vector, the perfect crystal is recovered, and the GSF magnetic energy corresponds to the surface energy of the infinite magnetic fault also presented in Tab. 2. Between

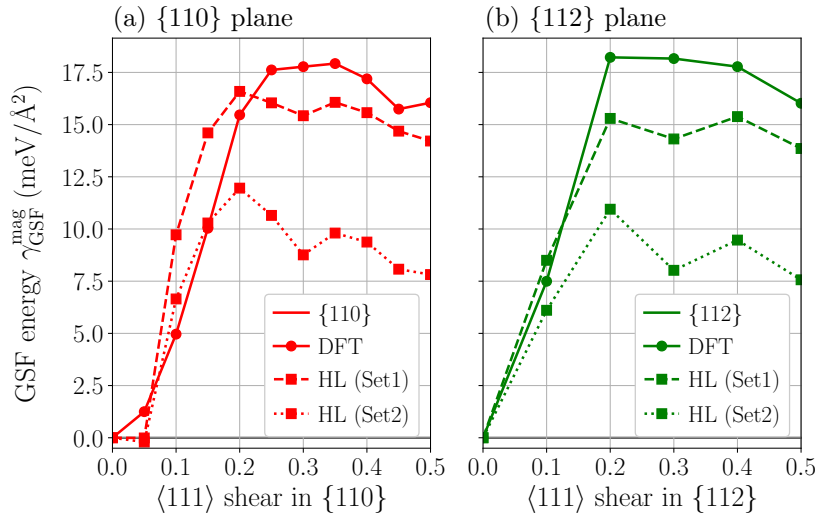


Figure 6: Magnetic contribution to the GSF energy $\gamma_{\text{GSF}}^{\text{mag}}$ along the first half of the $\langle 111 \rangle$ γ -line in a (a) $\{110\}$, and (b) $\{112\}$ plane in the AF phase obtained with *ab initio* DFT calculations (solid circles), and the HL model with Set1 (dashed squares) and Set2 (dotted squares) at the equilibrium lattice parameter $a_0 = 2.865 \text{ \AA}$ of the AF phase.

the two perfect crystals at 0 and $1/2\langle 111 \rangle$, the rigid shearing along the two γ -lines yields positions which do not correspond to bulk atomic sites, thus allowing to test the validity of the interpolated $J(r)$ function. We see that the magnetic GSF profiles in both $\{110\}$ and $\{112\}$ planes obtained with Set1 of the HL model is in good agreement with DFT data, with similar variations but lower energies obtained using Set2. Now that the predictions of the model are validated with respect to 0 K *ab initio* calculations, we can move on to magnetic properties at finite temperatures using these HL models, starting with bulk thermodynamical properties and energetics in the following section.

1.4. Thermodynamical magnetic properties of bulk bcc chromium

Evaluation of the equilibrium magnetic properties of bulk bcc Cr with temperature is the focus of the present section. Thermodynamical quantities are obtained as detailed in Methods (section 2.1.2) upon sampling of the magnetic energy of the system with temperature using a Metropolis Monte Carlo algorithm. This method gives access to the average of the magnetic energy E^{mag} of the system with temperature, from which other properties can then be derived. When the Boltzmann statistics is used in the Metropolis algorithm, *i.e.* with a scaling factor $\eta(T) = k_B T$ used in the acceptance probability $p(E) = \exp[-E/\eta(T)]$, the magnetic heat capacity C_P^{mag} does not converge to zero at temperatures near 0 K, resulting in a non-zero magnetic entropy at zero temperature. To overcome this issue, quantum statistics must be included at low temperature using a Bose-Einstein distribution, which is done following the approximation of Woo *et al.* [161, 163]. The resulting scaling factor is presented as a function of temperature in Fig. 7 for the two sets of parameters of the HL model. This quantum statistics encapsulates the quantization of magnetic excitations at low temperature, operating through excitation of magnons (see the magnon spectrum in Fig. 5b). The scaling factor η is evaluated through integration of the magnon DOS (mDOS) at a given temperature following the method of Woo *et al.* [163], which consists in a temperature dependent rescaling of the upper

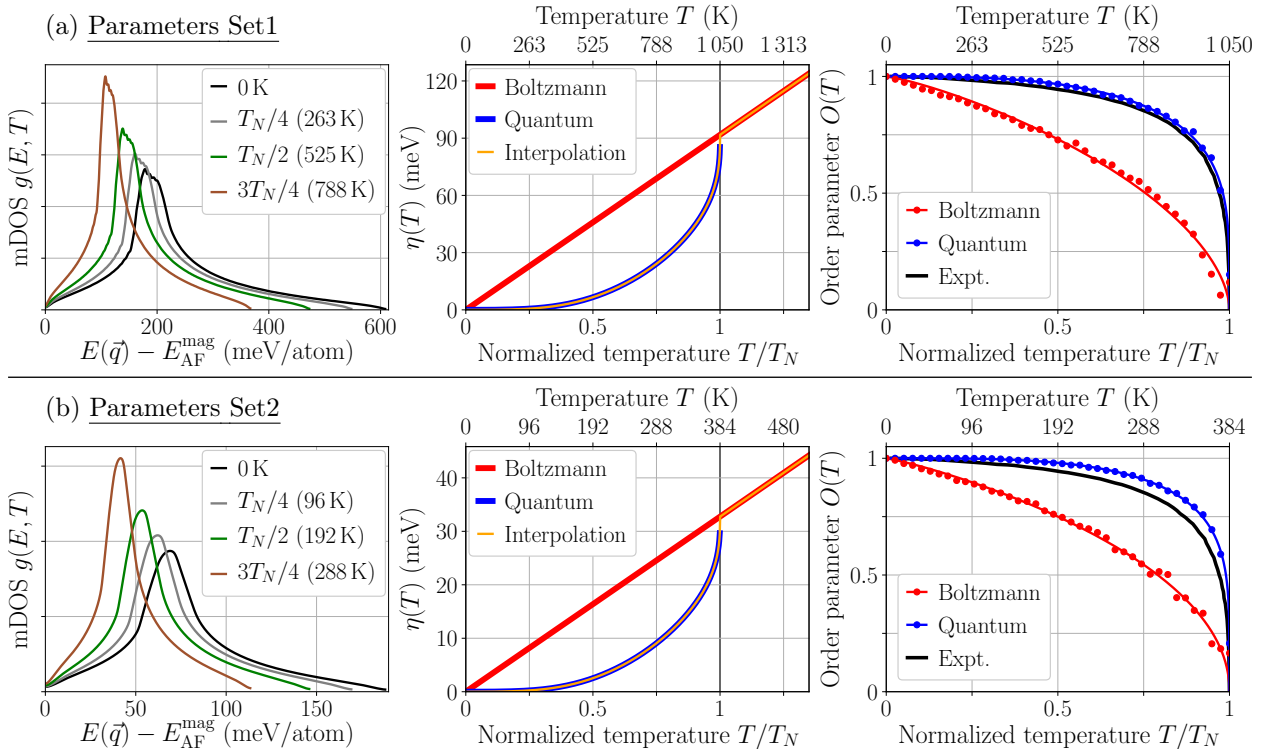


Figure 7: Temperature dependent mDOS $g(E, T)$, scaling factor of the Metropolis algorithm $\eta(T)$ within the classical Boltzmann (red) quantum statistics (blue), and long-range magnetic order O (Eq. 7) as a function of temperature using both statistics, and compared to experiments [6]. Results are presented for (a) Set1 and (b) Set2 parameters of the HL model.

limit in energy of the mDOS. The resulting mDOS are presented on the left column of Fig. 7 at different temperatures below T_N (see Methods, section 2.1.3 for more details about the approximation). This yields a zero scaling factor η close to 0 K, and the recovery of a classical Boltzmann distribution above T_N .

A first step to construct such an appropriate quantum statistics is to evaluate the Néel temperature T_N predicted by the HL model, in order to perform integration of the mDOS up to T_N (see Methods, section 2.1.3). Since both classical and quantum statistics converge at T_N , its value does not depend on the statistics, and can be evaluated properly using a classical Boltzmann distribution. The value of T_N is defined as the temperature from which long-range magnetic order vanishes completely. The magnitude of this long-range order is measured using an order parameter O defined as the sum of the average magnetizations over the two sub-lattices S_1 and S_2 of the AF order, *i.e.* with spins \uparrow and \downarrow respectively, as:

$$O = \frac{1}{m_0} \left[\frac{\|\sum_{i \in S_1} \vec{m}_i\|}{N/2} + \frac{\|\sum_{j \in S_2} \vec{m}_j\|}{N/2} \right], \quad (7)$$

with m_0 the 0 K bulk magnetic moment of the AF phase, and N the number of atoms contained in the simulation cell. When the system is in its AF ground state, the order parameter is equal to 1, with all magnetic moments of magnitude m_0 and opposite signs on each sub-lattice. The temperature evolution of the order parameter obtained using the classical and quantum statistics is presented in Fig. 7 for the two Set1 and Set2 parameters of the HL model, and compared with experimental data [6], with Néel temperatures T_N of 1050 and 384 K respectively (see section 1.1). As a reference, the experimental T_N measured on a perfect single crystal of bcc Cr is 311 K [6]. We note that the temperature dependence of the long range magnetic order (right on Fig. 7) obtained using the classical Boltzmann distribution is not in agreement with experiments, rapidly decreasing at temperatures close to 0 K. Indeed, as the thermal energy given to the system is non-zero close to 0 K, the magnetization of the system falls at temperatures where quantum effects should prevent the system to evolve. This quantization effect results in the small decrease slope close to 0 K reported experimentally, which is well reproduced using the quantum scaling factor in the Metropolis algorithm. The magnetic energy E^{mag} , free energy F^{mag} , entropy S^{mag} and heat capacity C_P^{mag} of bulk bcc Cr as a function of temperature obtained with the two statistics are presented in Fig. 8, highlighting the importance of including quantum effects to correctly evaluate the magnetic properties with temperature, most particularly for the magnetic heat capacity C_P^{mag} , entropy S^{mag} and free energy F^{mag} .

As presented in Fig. 7, the order parameter O (Eq. 7) falls to zero at the Néel temperature T_N . This parameter is a measure of long range magnetic order, which vanishes completely at T_N , with a temperature

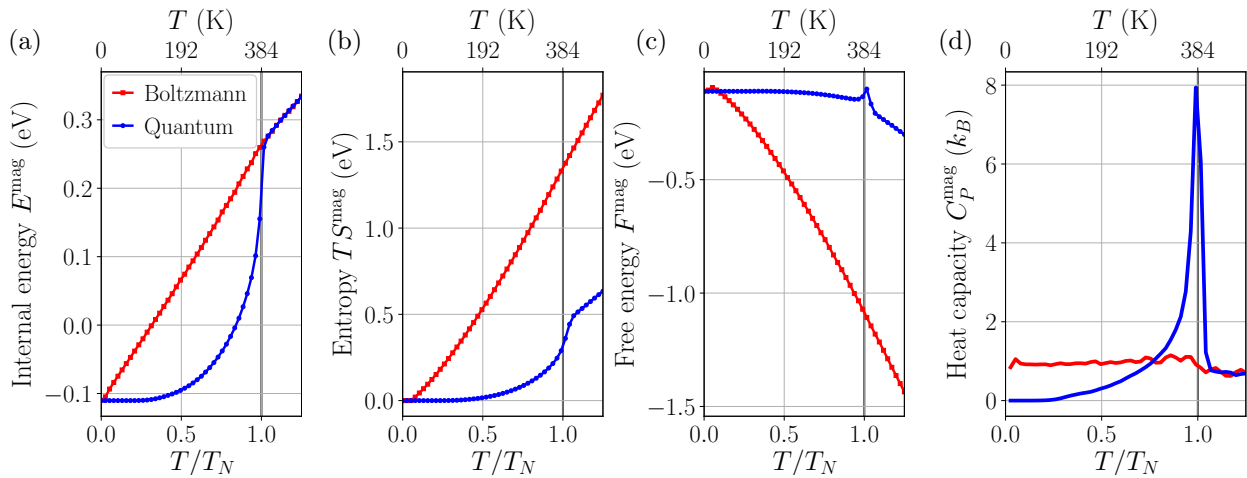


Figure 8: Temperature evolution of the magnetic (a) internal energy E^{mag} , (b) entropy TS^{mag} , (c) free energy F^{mag} , and (d) heat capacity C_P^{mag} of bulk bcc Cr with $a_0 = 2.865 \text{ \AA}$ using the Boltzmann (red) and quantum (blue) statistics with Set2.

evolution in very good agreement with experimental data using quantum statistics. Some experimental works qualify the magnetic disorder of the PM phase as an orientational disorder rather than a collapse of the magnitude of atomic magnetic moments [105]. The temperature variation of the average magnetic moment obtained with the HL model (Set2) is presented in Fig. 9a, showing its decrease from its 0 K value m_0 up to T_N , and which starts increasing above. To fully qualify the magnetic properties of the PM phase, another important quantity is the remaining magnetic short range order (MSRO), which is measured as the average correlations between magnetic moments of neighboring atoms:

$$\text{MSRO}_{n\text{NN}} = \langle \vec{m}_i \cdot \vec{m}_j \rangle = \frac{1}{m_0^2} \left[\frac{1}{N} \sum_{i=1}^N \frac{1}{Z_n} \sum_{j \in n\text{NN}(i)} \vec{m}_i \cdot \vec{m}_j \right] \quad (8)$$

where $n\text{NN}$ is the n th shell of nearest neighbors containing Z_n sites. The correlation between two magnetic moments is calculated as the scalar product between them. The temperature variation of the average MSRO between first nearest (1NN) and second nearest (2NN) neighbors are presented in Fig. 9b with the long range order parameter O . As discussed in the Literature review (see section 3.1.1), remaining MSRO has been observed experimentally up to approximately 11 bcc unit-cells at 700 K (*i.e.* $2.25 \times T_N$) by Grier *et al.* [98]. Other references, using similar neutron scattering experiments, showed persistence of magnetic order in the PM phase up to lower temperatures of approximately 500 K (*i.e.* $1.6 \times T_N$) [99, 200]. Results presented in Fig. 9b show the disappearance of long range order at T_N , with a remaining MSRO above T_N , in qualitative agreement with experiments, with a stronger correlation between 1NN than 2NN neighbors.

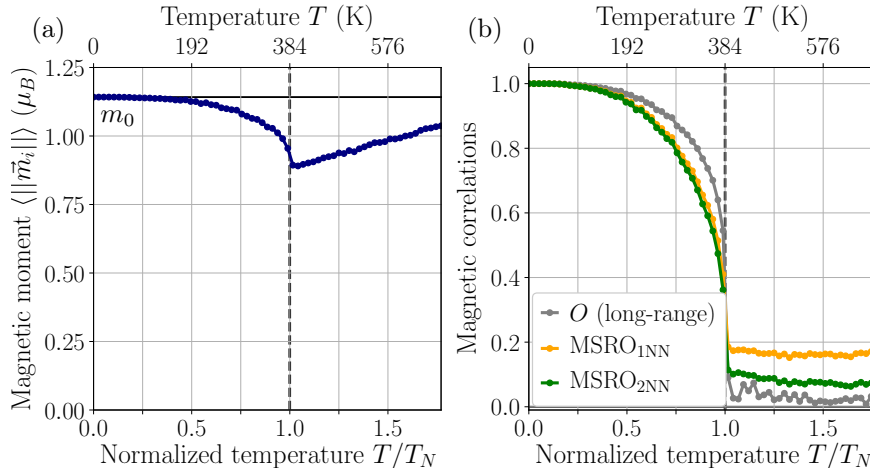


Figure 9: (a) Average magnetic moment $\langle ||\vec{m}_i|| \rangle$ as a function of temperature. (b) Magnetic correlations measured using the order parameter of Eq. 7 (grey), and the average magnetic short range order (MSRO) between first ($\text{MSRO}_{1\text{NN}}$) and second ($\text{MSRO}_{2\text{NN}}$) nearest neighbors. All presented results are obtained using Set2 parameters for the HL model.

2. Magnetism and plasticity of chromium at finite temperature

At zero temperature, both generalized stacking fault (GSF) calculations and the study of $1/2\langle 111 \rangle$ screw dislocations revealed the generation of magnetic faults when the crystal is sheared by the Burgers vector of dislocations in the AF phase. From these results, this magnetic fault appears as the only major impact of magnetism on the plasticity of bcc Cr, its energy being the main controlling parameter. In the present section, the temperature evolution of the magnetic fault generated by $1/2\langle 111 \rangle$ shear is studied using the HL model. As discussed above, the two Set1 and Set2 parameters are suited for studying different properties: Set1 gives better 0 K energies with respect to *ab initio* calculations, while Set2 gives a satisfactory reproduction of the experimental value of T_N , with less satisfactory 0 K properties. The next section focuses on the study of the magnetic fault generated upon shearing by $1/2\langle 111 \rangle$ at finite temperatures using the statistics presented here. All results are obtained using Set2 for the HL model unless otherwise specified.

2.1. Infinite magnetic faults

As presented in Chapter 1, the rigid shearing of the crystal by a fault vector equal to the $1/2\langle 111 \rangle$ Burgers vector results in the generation of magnetic faults, with a surface energy $\gamma = 16.3 \text{ meV}/\text{\AA}^2$ at 0 K, regardless of the fault plane (see Appendix B for a more extended study of the orientation dependence of the fault energy using the TB model). The structure and energy of this magnetic fault is the same when generated by the introduction of $1/2\langle 111 \rangle$ dislocations in the crystal. A discussed possible consequence of this magnetic fault on the plasticity of bcc Cr is the pairing of $1/2\langle 111 \rangle$ dislocations, resulting in $\langle 111 \rangle$ superdislocations dissociated in two partials separated by a magnetic fault. This phenomenon was predicted by Marcinkowski and Lipsitt [126], which should be responsible for a magnetic strengthening below the Néel temperature, the magnitude of this effect being controlled by the energy of the fault. The authors reported no evidence of such strengthening close to the Néel temperature, therefore indicating the weak energy of the fault near the disappearance of long-range magnetic order. However, from the magnetic fault energy calculated at 0 K, we reported an equilibrium dissociation distance of about 6 nm, which should bear consequences on the plasticity of bcc Cr, assuming a non-negligible energy up to the Néel temperature. We now focus on the temperature evolution of such faults, to check if the results obtained at 0 K hold with temperature.

At finite temperature, one needs to account for the entropic contribution S^{mag} to the total energy of the system, which is described by its free energy $F^{\text{mag}} = E^{\text{mag}} - TS^{\text{mag}}$, with E^{mag} the internal energy. We only focus on the magnetic part of such free energy calculations since it is the only accessible quantity through the HL model. The free energy of a magnetic fault ΔF^{mag} is evaluated through a thermodynamical integration over the temperature range where the magnetic energy ΔE^{mag} of the fault is sampled. To do so, the value at a reference point needs to be known, which we checked is the case above the Néel temperature T_N in the PM phase, at approximately $5T_N/4$, where the energy of the fault is zero since long-range magnetic order has vanished. More details about the evaluation of ΔF^{mag} are given in Methods, section 2.1.2. The magnetic energy of the infinite fault is evaluated as the excess energy of the crystal when sheared by a fault vector $1/2\langle 111 \rangle$ contained in the fault plane with respect to the perfect crystal, in the same way as the 0 K

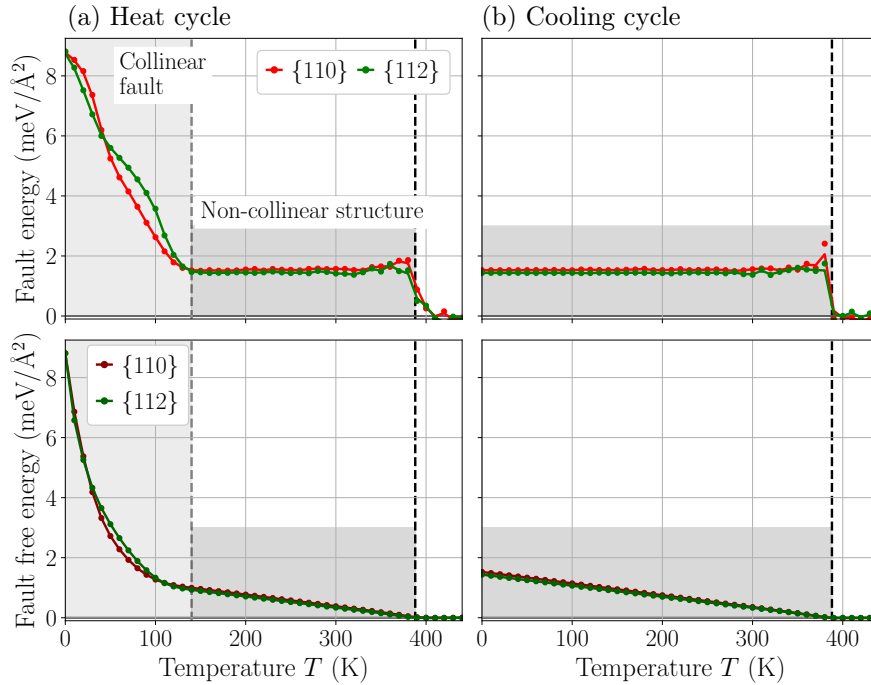


Figure 10: Magnetic fault energy ΔE^{mag} (first row) and free energy ΔF^{mag} (second row) of the two infinite $\{110\}$ (red) and $\{112\}$ (green) magnetic faults as a function of temperature upon (a) heating the system from 0 K, and (b) cooling to 0 K.

GSF presented in Chapter 1. The crystal is sheared by a vector $1/2\langle 111 \rangle$ in the fault plane, which is also applied to the periodicity vectors of the simulation cell to maximize the distance between periodic images of the fault (see Chapter 1, section 2.1). The resulting magnetic fault internal and free energies of an infinite magnetic fault contained in a $\{110\}$ and a $\{112\}$ plane are presented in Fig. 10. The heat cycle is shown in a, where temperature is increased starting from 0 K and initializing all magnetic moments to the AF ground state of the model in all three Cartesian directions, *i.e.* $m_i^x = m_i^y = m_i^z = m_0/\sqrt{3}$, where m_0 is the 0 K bulk magnetic moment. Similarly, the cooling cycle is presented in Fig. 10b, where the system is initialized in its disordered PM phase at temperature $5T_N/4$ before being gradually cooled down to 0 K. The simulation cell has periodicity vectors corresponding to $X = 8 \times [\bar{1}2\bar{1}]$, $Y = 11 \times [111]$ and $Z = 13 \times [\bar{1}01]$ for the $\{110\}$ magnetic fault (shown in red), and reversing X and Z for the $\{112\}$ magnetic fault (shown in green).

Upon heating the system, the energy of the magnetic fault (upper panel in Fig. 10a) starts at the 0 K value reported in Tab. 1 for the two $\{110\}$ (red) and $\{112\}$ (green) planes, before starting decreasing up to approximately 140 K, from which the energy of both faults stays constant, with a smaller fault energy, before ultimately vanishing at the Néel temperature $T_N \simeq 380$ K, where the disappearance of long-range magnetic order do not allow for a magnetic fault to exist anymore. The situation is slightly different when the system is cooled starting from temperatures above T_N , showing a constant magnetic energy as soon as magnetic order is recovered, down to 0 K. The energy of this structure arising at T_N is equal to the one found upon heating the same system in the temperature range between 140 K (*i.e.* $\simeq T_N/3$) and T_N , lower than the collinear fault found below 140 K upon heating the system from the AF structure. However, the atomic structure of the system is identical in the faulted and the perfect crystal. Such a magnetic structure with non-zero excess energy with respect to the AF ground state is thus stabilized upon cooling the system due to the constrain imposed by the periodicity vectors of the simulation cell, which are sheared by the same amount as the fault plane, thus forcing two spins with the same sign to face each other. We will discuss below the structure of the two different configurations of the magnetic structures evidenced from Fig. 10.

The free energy ΔF^{mag} of the faults is given by Eq. 9, obtained through integration of their magnetic energies ΔE^{mag} , whose detailed derivation is given in Methods (see section 2.1.2):

$$\Delta F^{\text{mag}}(\beta) = \frac{1}{\beta} \int_{\beta'=\beta_{\text{ref}}}^{\beta} \Delta E^{\text{mag}}(\beta') d\beta', \quad (9)$$

with $\beta = 1/k_B T$ the inverse temperature. In the above equation, the reference is taken at $5T_N/4$ to ensure both the magnetic energy ΔE^{mag} and free energy ΔF^{mag} of the fault are equal to zero (see Fig. 10). If one considers the free energy of a magnetic fault whose energy is constant up to the Néel temperature T_N , its integration using Eq. 9 gives a linearly decreasing free energy with temperature, like reported in Fig. 10:

$$\Delta E^{\text{mag}}(T) = \text{cte} \rightarrow \Delta F^{\text{mag}}(T) = \text{cte} \times \left(1 - \frac{T}{T_N}\right), \quad (10)$$

assuming the fault energy vanishes at T_N . Details about this model variation and other free energy profiles for different model temperature evolution of the magnetic fault energy are presented in Appendix C. The resulting magnetic fault free energy in both $\{110\}$ and $\{112\}$ planes are presented in the two lower panels of Fig. 10. Upon cooling the system, the magnetic free energies show this characteristic linearly decreasing temperature evolution, as soon as magnetic order is retrieved at T_N with the non-collinear structure of the system, before vanishing at T_N . When the system is heated starting from 0 K, the transition between the two structures yields a change in the shape of the free energy, starting with a steep decrease before 140 K, and a linear decrease in $1 - T/T_N$ above, matching the cooling cycle. We now describe these two magnetic structures evidenced by the HL model in the thermal cycles of Fig. 10, presented in Fig. 11.

We first consider the collinear structure (upper row in Fig. 11), which corresponds to the configuration of the fault found below 140 K upon heating. The variation of the magnetic moments \vec{m}_i along the direction orthogonal to the fault plane shows all three Cartesian components of the spins decrease down to zero in

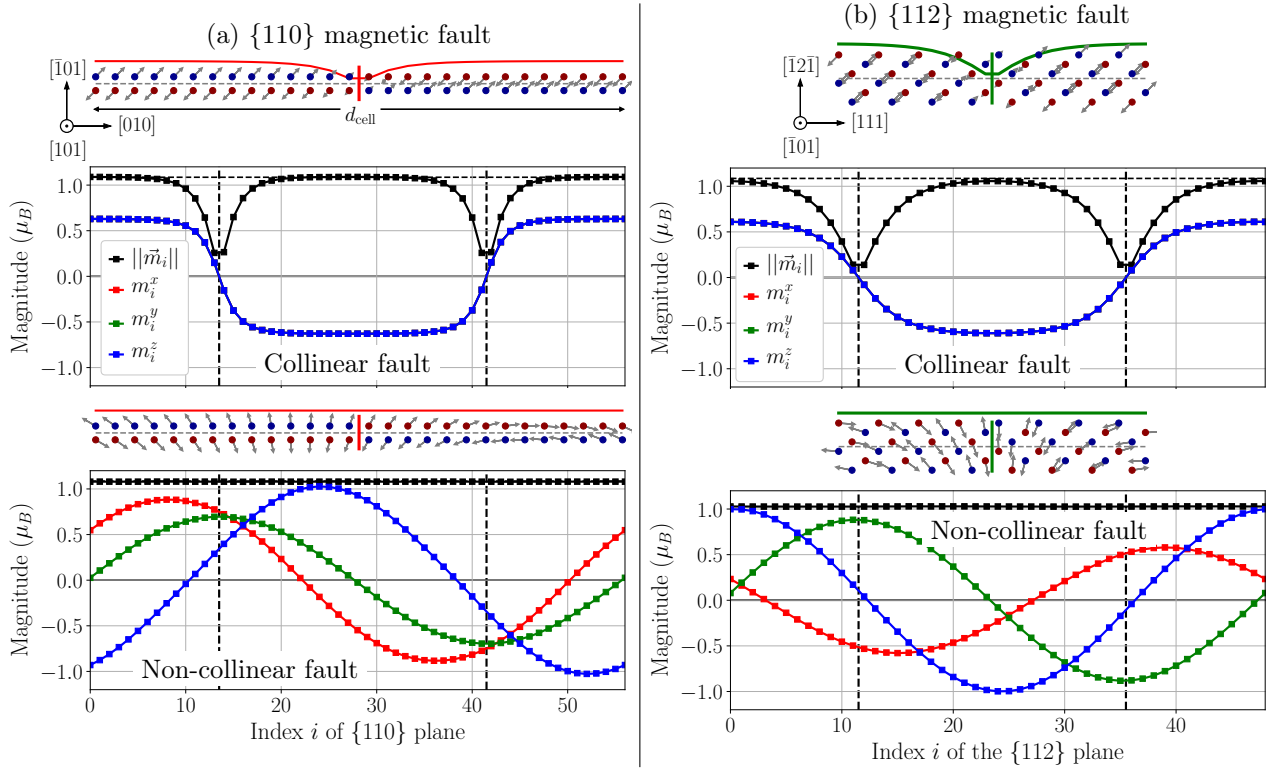


Figure 11: Structures of the collinear and non-collinear configurations of the (a) $\{110\}$, and (b) $\{112\}$ magnetic faults obtained after relaxation using *ab initio* calculations, with the profiles of the three Cartesian components of the spins along the normal to the fault plane. The relaxed magnetic structures obtained with the HL model are identical.

the vicinity of the fault for both $\{110\}$ and $\{112\}$ planes (indicated by black vertical dashed lines), with $m_i^x = m_i^y = m_i^z$. The fault is thus confined in the vicinity of the sheared plane, with an identical structure up to approximately 140 K, when heating the system. Now considering the configuration found above 140 K to T_N upon heating, or below T_N upon cooling, one sees it shows a non-collinear structure (lower panels in Fig. 11). Instead of a localized magnetic fault, characterized by a reduction in the magnitude of the spins, a structure similar to a spin spiral arises. In this configuration, the perturbation spreads over the entire simulation cell, with a spiral of periodicity dictated by the separation distance d_{cell} . With the inclusion of non-collinear magnetism, another possibility to resolve the magnetic frustration is indeed to induce a disorientation of magnetic moments, keeping a constant magnitude, in the direction orthogonal to the fault plane, keeping a local AF order in each stacked $\{110\}$, or $\{112\}$, plane. The energy cost associated with such disorientational perturbation is less than a local reduction of the amplitude of the magnetic moments due to the ferromagnetic frustration of the magnetic moments in the vicinity of the fault plane, which thus corresponds to the true magnetic ground state of the system. Another indication of the properties of this non-collinear structure is the multiplicity of possible spiral-like profiles having the same energy but different magnetic structures, two of which are presented in Fig. 12 for both $\{110\}$ and $\{112\}$ infinite faults. Similar to a propagating wave, the nodes of the spiral are not bounded to any topological defect, nor are stabilized by the $\frac{1}{2}\langle 111 \rangle$ fault vector since these structures arise upon cooling the system starting from a random initial configuration in the PM phase, above T_N . They are thus allowed to take any orientation in the volume of the simulation cell, all energetically equivalent, with a relative disorientation between adjacent planes defined by the separation distance d_{cell} .

The stability and relative energy of the two collinear and non-collinear configurations of this magnetic structure evidenced using the HL model is evaluated with *ab initio* calculations. In this respect, non-collinear

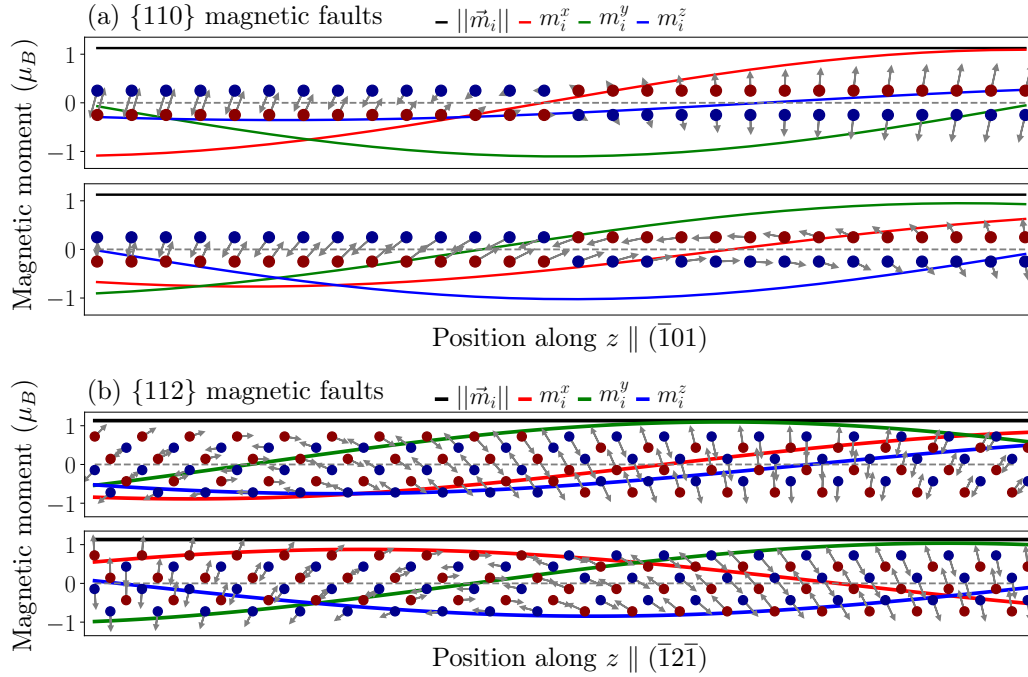


Figure 12: Two different equal energy configurations of the non-collinear structure arising from a rigid shearing by a $1/2\langle 111 \rangle$ vector in (a) $\{110\}$ and (b) $\{112\}$ planes located at the middle of the cell, obtained by minimization of the HL model (Set1) starting with an initially random structure. The definition of the axis is the same as in Fig. 11.

magnetism needs to be included, along with spin-orbit coupling to also incorporate the dependence of the magnetic moments on crystallographic directions. We initialized the calculations with the relaxed structures obtained with the HL model. The *ab initio* relaxed structures are presented in Fig. 11 for the two infinite $\{110\}$ and $\{112\}$ magnetic faults, both found identical to the predictions of the HL model. The two simulation cells contain 28 stacked $\{110\}$ and 24 $\{112\}$ planes respectively, which correspond to a separation distance between periodic images of the fault $d_{\text{cell}}^{\{110\}} = 28 \times a_0 \sqrt{2}/2 \simeq 56.7 \text{ \AA}$ and $d_{\text{cell}}^{\{112\}} = 24 \times a_0 \sqrt{6}/6 \simeq 28.1 \text{ \AA}$.

We now study the energy of both collinear and non-collinear magnetic structures arising from the rigid $1/2\langle 111 \rangle$ shearing with respect to the separation distance d_{cell} at 0 K, for the two $\{110\}$ and $\{112\}$ planes, using the HL model with parameters Set1, and compared to *ab initio* data. The results of this convergence study are presented in Fig. 13. As opposed to the collinear fault, whose energy γ_{fault} converges to a constant non-zero value equal in both fault planes, the surface energy of the non-collinear structure tends to zero for an infinite separation distance between periodic images of the fault, in both $\{110\}$ and $\{112\}$ planes. The slope of this decreasing excess energy is the same in both planes, equal to 221 meV/\AA using the HL model, indicating a similar phenomenon takes place in both cases, as for the collinear structure. Hence, a description of this non-collinear structure as a fault does not hold since convergence of its energy cannot be achieved by increasing the separation distance d_{cell} . These non-collinear structures are similar to a spin spiral as presented in Fig. 5, defined by a relative disorientation of the magnetic moments keeping a constant magnitude along the propagation direction of the spiral. When the fault planes are spaced from each other by an infinite distance, this relative disorientation between magnetic moments tends to zero, where the AF order is retrieved, and the energy of this structure thus falls to zero.

A more accurate description of this non-collinear structure would be similar to an elastic perturbation, which is not located in a defined region but instead spreads over the entire volume of the cell, and whose energy therefore decreases with increasing separation distance, since a larger volume is available to accom-

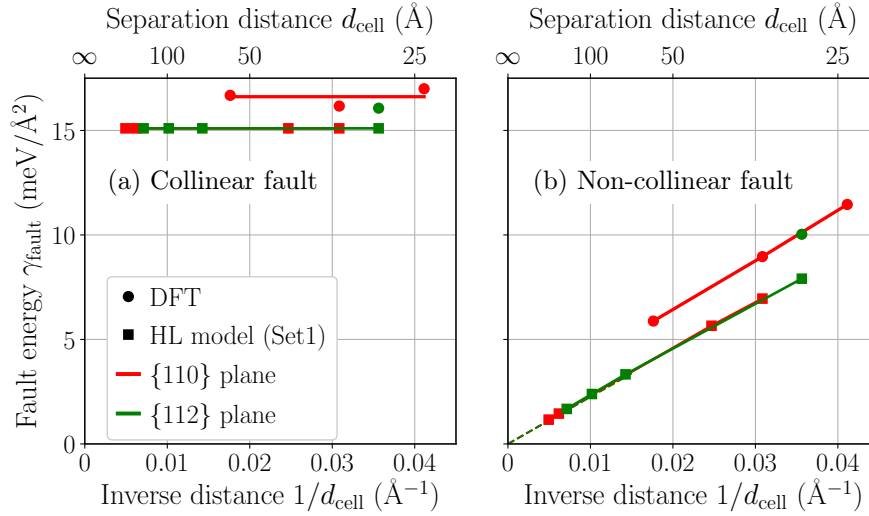


Figure 13: Energy γ_{fault} of the (a) collinear, and (b) non-collinear structures as a function of the separation distance d_{cell} between $\{110\}$ (red) and $\{112\}$ (green) fault planes obtained with *ab initio* (circles) and the HL model with Set1 (squares).

moderate the perturbation. In this respect, the temperature evolution of the excess energy contained in the crystal after a rigid $1/2\langle 111 \rangle$ shearing, presented in Fig. 10 reveals that the magnetic fault vanishes below the Néel temperature T_N . Indeed, as demonstrated at 0 K on Fig. 13, the energy of the non-collinear structure arising after this transition temperature depends on the separation distance d_{cell} between periodic images of the fault, and therefore the size of the simulation cell. Another important consequence of this structure is that upon cooling the system from the disordered PM phase down to lower temperatures, no magnetic fault can be retrieved. This was to be expected since the structure of the faulted crystal is identical to the bulk.

2.2. Magnetic fault bounded by two $1/2\langle 111 \rangle$ screw dislocations

We now study the temperature evolution of the magnetic fault when generated by a $1/2\langle 111 \rangle$ screw dislocation dipole. Quantification of its energy will be the focus of the next section when studying the magnetic contribution to the core energy of these dislocations. When studying the magnetic fault generated by the introduction of $1/2\langle 111 \rangle$ dislocations at 0 K in the previous chapter, we found that both its structure and energy are very similar to the case of the infinite fault, in both $\{110\}$ and $\{112\}$ planes. This observation has been further enforced by the TB study presented in Appendix B considering any possible orientation of the habit plane of the magnetic fault. However, both these *ab initio* and TB calculations were performed in the collinear magnetism approximation. These collinear calculations thus not allow the system to develop a non-collinear structure as an alternative possibility to the creation of a magnetic fault, and which was found to arise in the previous section 2.1, and whose structure is however not compatible with a fault. We now focus on the finite temperature properties of such magnetic faults when generated by $1/2\langle 111 \rangle$ screw dislocations, in a similar way as the 0 K calculations presented in the previous chapter.

The simulation cell used for this study is similar to supercells used in *ab initio* calculations and presented in the Methods, with periodicity vectors $\vec{p}_1 = 21/2 [\bar{1}2\bar{1}] - 39/2 [\bar{1}01]$, $\vec{p}_2 = 21/2 [\bar{1}2\bar{1}] + 39/2 [\bar{1}01]$, and $\vec{p}_3 = 6 \times 1/2[111]$, containing 14 742 atoms. As in the 0 K calculations presented in the previous chapter, the $1/2\langle 111 \rangle$ screw dislocation dipole is introduced in a quadrupolar arrangement using anisotropic elasticity theory, with the magnetic fault bounded by the two dislocations laying in the $(\bar{1}01)$ plane, which in the present simulation cell results in a distance $d = 73.7 \text{ Å}$ between the two dislocations. We chose to use a $6b$ -high supercell ($n_3 = 6$), which is sufficiently large to allow for magnetic fluctuations in each direction of the cell without periodic boundary effects. The structure of the magnetic fault bounded by the two $1/2\langle 111 \rangle$ screw dislocations of the dipole is presented in Fig. 14 at three different temperatures, recorded

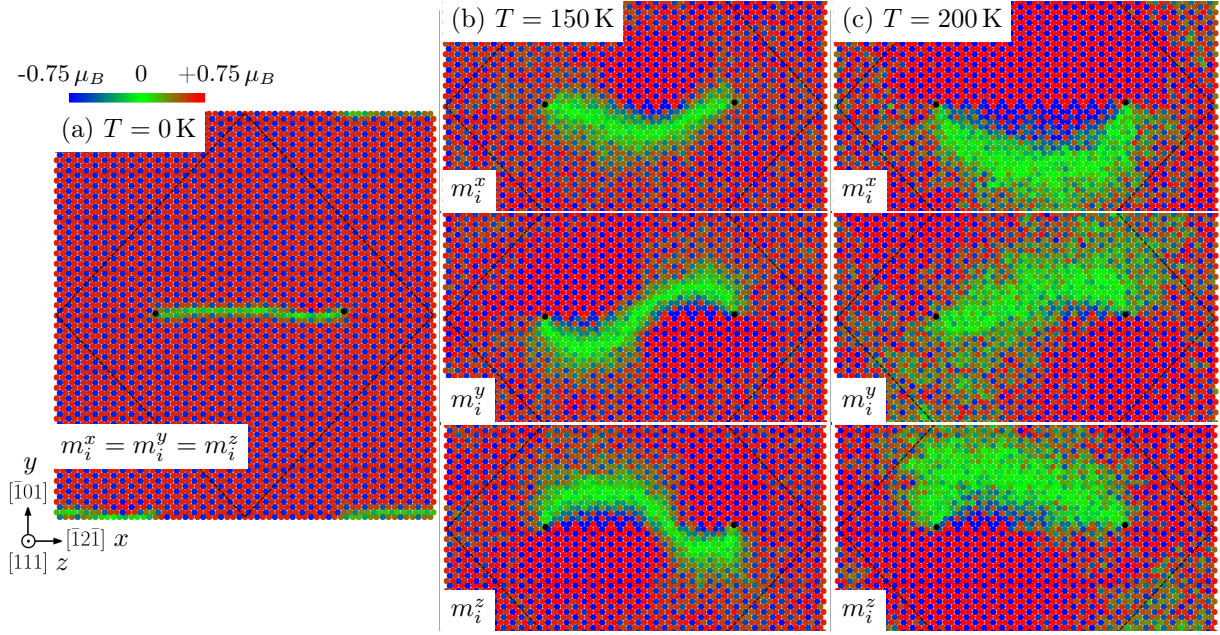


Figure 14: Evolution of the magnetic fault bounded by two $1/2[111]$ screw dislocations (black dots) upon heating from the 0 K collinear configuration in (a) to (b) 150 K ($\simeq 2T_N/5$) and (c) 200 K ($\simeq T_N/2$). The colors correspond to the projections m_i^x , m_i^y , and m_i^z of the magnetic moments along the x , y , and z axis respectively, according to the legend in the upper left of (a).

upon heating the system starting from 0 K and initializing all magnetic moments to their AF configurations, with $m_i^x = m_i^y = m_i^z = m_0/\sqrt{3}$ to better visualize the different variations of the three Cartesian components of the spins recorded upon heating and cooling the system. All configurations are presented in the plane orthogonal to the direction Z of the dislocation line at $z = h/2$, with h the height of the simulation cell. The magnetic structure of the system is however identical in each $1b$ -slice along Z .

The collinear structure of the magnetic fault in the $(\bar{1}01)$ plane at 0 K (Fig. 14a) is the same as obtained in *ab initio* calculations, with a reduction of the magnitude of the magnetic moments in the vicinity of the fault plane in the region bounded by the two $1/2[111]$ dislocations to accommodate the magnetic frustration. As the temperature is increased (Fig. 14b), this linear fault starts to fluctuate in space, developing different components along the three Cartesian directions. Through magnetic excitations, the fault caused by the dislocations is allowed to take a non-collinear structure where the frustration is partially resolved by inducing a disorientation of the spins in the region bounded by the two $1/2[111]$ screw dislocations, similar to the case of the infinite fault presented in the previous section. In this configuration, the magnitude of the spins is constant over the whole simulation cell, except in the direct vicinity of the dislocation cores where the strong lattice distortion causes a local reduction of the magnetic moments. The non-collinear magnetic structure obtained upon cooling the system from the high-temperature PM phase above T_N down to 0 K is presented in Fig. 15. Profiles of the magnetic moments along the thick black dashed lines reveal the structure of the fault in directions orthogonal and contained in the plane defined by the two $1/2[111]$ screw dislocations of the dipole, showing a similar but more complex structure as obtained for the infinite structures in the previous section. Indeed, the three components of the spins in the infinite non-collinear structure show a sinusoidal modulation in the direction orthogonal to the fault plane (see Fig. 11), which does not hold for the bounded magnetic fault presented here, especially for the m_i^z component as shown in the upper panel of Fig. 15c. Another important feature of this structure, which is better visualized on the spin maps of Fig. 15a and b, is that this non-collinear structure is not contained in the plane defined by the relative positions of the two dislocations, contrary to the collinear fault, but instead spreads over the entire simulation cell. The stability and energy of this configuration was not checked using *ab initio* calculations

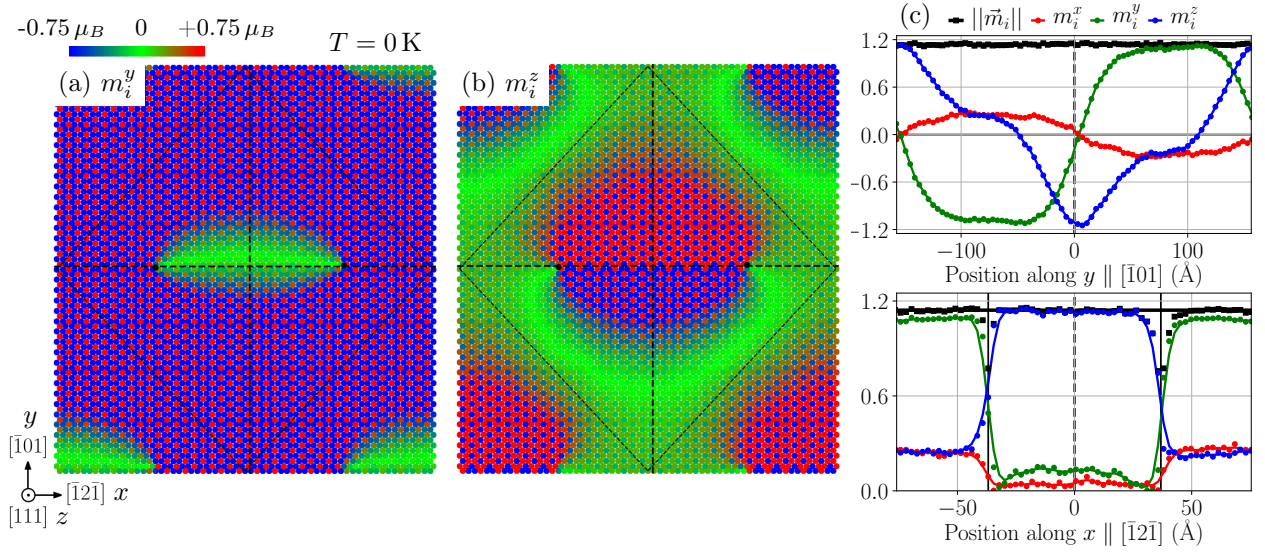


Figure 15: Non-collinear structure bounded by two $1/2[111]$ screw dislocations (black dots) projected along (a) \bar{y} and (b) \bar{z} . (c) Profile of the magnetic moments along the x and y dashed lines in (a) and (b). The structure is presented at 0 K, obtained upon cooling the system starting from initially random spins in the PM phase.

since the computational cost needed to include both non-collinear magnetism and spin-orbit coupling in a simulation cell containing at least 270 atoms would be drastically high. We are still confident in the validity of the presented results using the HL model, since it has proven its ability to predict correct energetics in the case of the infinite magnetic structures.

The magnetic structure obtained upon cooling from the high-temperature PM phase to 0 K are presented in Fig. 16 for two different distances d between the two bounding $1/2[111]$ screw dislocations of the dipole, in the same simulation cell as in Figs. 14 and 15. These two non-collinear structures are almost identical, also similar to the one of Fig. 15 obtained with a larger distance $d = 73.7 \text{ \AA}$, except the magnetic fault covers a narrower region. As the distance d is reduced, the structure of the fault between the two dislocations tends to the form of a domain wall, with a modulation of magnetic moments showing a sharper transition near their positions (indicated by black dots). Similar to the case of the infinite faults in the previous section, the magnetic structure bounded by two $1/2[111]$ screw dislocations has a collinear structure below a temperature of approximately 150 K in the simulations presented in this section. Above 150 K and up to T_N upon heating the system, a non-collinear structure is stabilized, which is also found upon cooling from the PM phase above T_N when long range magnetic order is retrieved. We will focus in the next section on quantifying the energetics of the magnetic structure contained in the dislocated simulation cell, in particular regarding the nature of the non-collinear perturbation arising upon cooling.

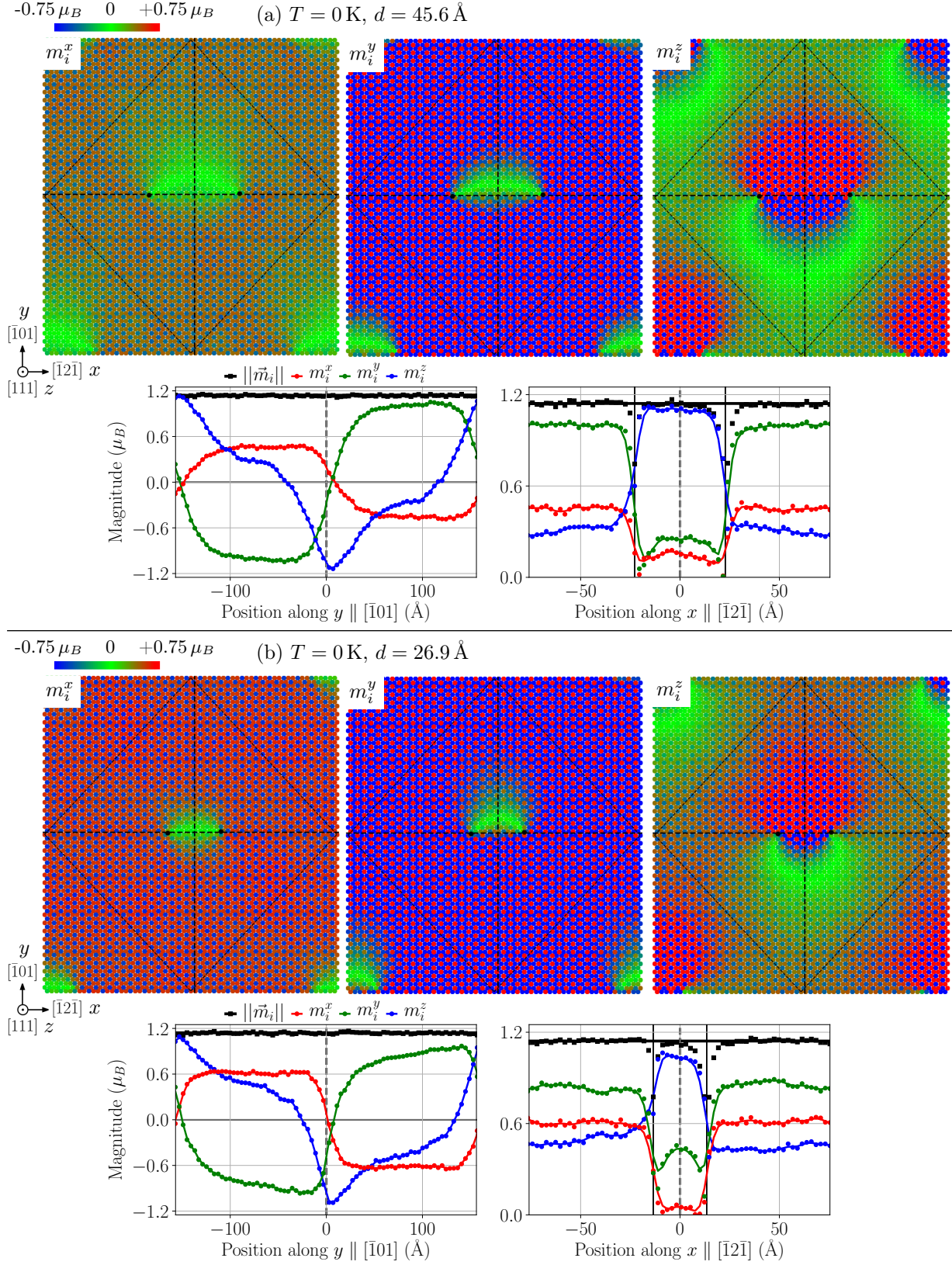


Figure 16: Structure of the non-collinear magnetic fault at 0K bounded by two $\frac{1}{2}[111]$ screw dislocations separated by a distance (a) $d = 45.6$ and (b) $d = 26.9 \text{ \AA}$ projected along the three Cartesian directions. The profiles of the magnetic moments along the constant x and y black dashed lines shown on the each spin map is presented below.

Experimentally, signatures of the existence of magnetic faults have been reported in the works of Ravlić *et al.* [127], Lagoute *et al.* [201] and Kleiber *et al.* [128, 202] using spin-polarized STM at $\{100\}$ surfaces at room temperature. The authors observe the emergence of pairs of $1/2\langle 111 \rangle$ screw dislocations at $\{100\}$ surfaces, responsible for monoatomic steps of height $a_0/2$ (*i.e.* the projection of $\vec{b} = 1/2\langle 111 \rangle$ along a $\langle 100 \rangle$ direction), with a_0 the lattice parameter. Magnetic contrast imaged in the region close to these dislocations show the presence of magnetic domain walls bounded by two dislocations, of width of a few hundred nanometers. When going through all experimental works mentioned above, it appears that depending on the sample and observation conditions, the fault is not necessary visible through the magnetic contrast. Since spin-polarized STM is only sensitive to the projection of the surface magnetization onto the tip magnetization, it may be a consequence of the non-collinear configuration of the magnetic structure bounded by $1/2\langle 111 \rangle$ dislocations shown in Fig. 15. Indeed, different contrasts can be obtained depending on the relative orientation between the direction resolved in the spin images and the direction of the non-collinear perturbation. To properly model these systems in similar conditions, we would need to introduce $1/2\langle 111 \rangle$ dislocations going through surfaces, after evaluating the ability of the HL model to give an accurate description of surface magnetism, which was not checked in this work. Occurrence of AF magnetic domains a few micrometers large were also observed with X-ray diffraction in bulk single crystals at temperatures near the spin-flip transition T_{sf} by Evans *et al.* [203]. However, upon cooling the sample through T_{sf} , the authors reported that these domains disappear below T_{sf} , where the magnetic order of Cr changes from transverse to longitudinal SDW.

2.3. Magnetic energy of the $1/2\langle 111 \rangle$ screw dislocation core

We now study the evolution of the magnetic contribution to the core energy of $1/2\langle 111 \rangle$ screw dislocations with temperature. In a similar way as the total energy of a simulation cell containing a dislocation dipole was partitioned in the previous chapter to evaluate the core energy at 0 K, the total magnetic energy of a simulation cell containing a dislocation dipole is partitioned as:

$$E_{\text{tot}}^{\text{mag}} = E_{\text{bulk}}^{\text{mag}} + E_{\text{fault}}^{\text{mag}} + 2E_{\text{core}}^{\text{mag}} + E_{\text{elas}}^{\text{mag}}, \quad (11)$$

where the magnetic elastic energy $E_{\text{elas}}^{\text{mag}}$ is not considered, given the magnetic contribution to the elastic constants in the frame of a HL model is negligible [118, 204] and atomic relaxation is not allowed here. Assuming the magnetic fault energy to be proportional to its surface $S = d \times h$, with h the height of the simulation cell in the $\langle 111 \rangle$ direction and d the distance between the two dislocations of the dipole, we have $E_{\text{fault}}^{\text{mag}} = S\gamma_{\text{fault}}$. The total excess magnetic energy contained in the simulation cell at temperature T is:

$$\begin{aligned} \Delta E^{\text{mag}}(d, T) &= E_{\text{tot}}^{\text{mag}} - E_{\text{bulk}}^{\text{mag}} \\ &= d \times \gamma_{\text{fault}}(T) + 2E_{\text{core}}^{\text{mag}}(T), \end{aligned} \quad (12)$$

with all energies normalized by the height h of the simulation cell in the Z direction parallel to the dislocation line. The magnetic energy of the bulk $E_{\text{bulk}}^{\text{mag}}$ is evaluated in the same simulation cell as presented in Figs. 14 and 15, before introducing the $1/2\langle 111 \rangle$ screw dislocation dipole. The above partition of the excess magnetic energy ΔE^{mag} is expressed as a linear function of the distance d between the two dislocations of the dipole, with a slope corresponding to the surface energy of the fault γ_{fault} . Taking advantage of Eq. 12 using the same simulation cell as in the previous section 2.2, the distance d is varied to reduce the range of the magnetic fault, allowing for the evaluation of the magnetic energy of the system as a function of both d and the temperature T . All dislocated simulation cells are constructed using anisotropic elasticity theory, similar to the other calculations presented. The variation of the excess energy ΔE^{mag} as a function of the distance d at various temperatures is presented in Fig. 17a and b upon heating and cooling the system respectively. A fit of the energies ΔE^{mag} of these different systems to Eq. 12 at a given temperature T then allows to simultaneously extract the magnetic contribution to the core energy of the dislocations $E_{\text{core}}^{\text{mag}}$, and the magnetic fault energy γ_{fault} at this temperature T . The linear fits are very satisfactory above a certain distance marked by a vertical black dashed line, below which the excess magnetic energy does not behave linearly, probably due to finite size effects for short separation distances. The magnetic energies of interest are therefore obtained from fitting to the excess energies obtained for larger distances d . This demonstrates

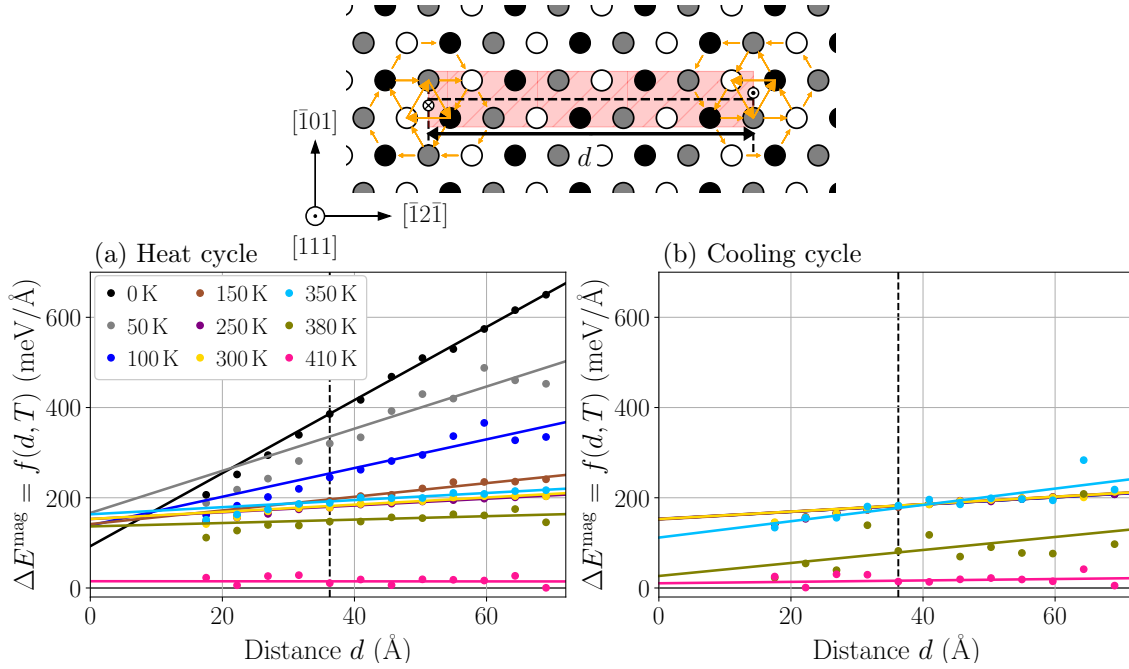


Figure 17: Excess magnetic energy ΔE^{mag} of the simulation cell containing a $1/2\langle 111 \rangle$ screw dislocation dipole as a function of the distance d between the two dislocations at various temperatures recorded upon (a) heating, and (b) cooling the system.

the validity of the proposed decomposition of the total energy of the system, at least up to temperatures close to T_N where fluctuations deteriorate this linear variation. This allows for a separate definition of the contributions of the fault and dislocation cores to the total energy of the system, verifying the magnetic contribution to the core energy of the dislocations is independent on their environment (see Fig. 18). When the system is heated starting from 0 K, the slope of the linear variations of the excess magnetic energy decreases up to approximately 150 K, from which it stays relatively constant up to the Néel temperature T_N (384 K), before finally vanishing above. Across the temperature range where magnetic order prevails, the value at the origin remains almost constant, which according to the energy partition of Eq. 12 is a measure of the magnetic contribution to the core energy of the dislocations. Now considering the cooling cycle (Fig. 17b), we see that below T_N , the linear variation of ΔE^{mag} is almost independent of the temperature, showing some fluctuations as the temperature increases, indicating a constant excess energy, which suddenly drops to zero at T_N where long-range magnetic order vanishes.

The slope and value for $d = 0$ obtained from Fig. 17b at each temperature T gives the energy γ_{fault} of the magnetic fault, and the magnetic core energy $E_{\text{core}}^{\text{mag}}$ respectively, which are presented in Fig. 18 as a function of T , upon both heating and cooling the system. The magnetic energy and free energy of the fault (second column in Fig. 18) show a similar temperature dependence as the infinite fault presented in the previous section. Upon heating the system starting from 0 K, a collinear magnetic fault is found between the two dislocations contained in the simulation cell, whose structure is presented in Fig. 14a. This structure is stable up to approximately 180 K, with a linearly decreasing energy with temperature. From 180 K to the Néel temperature, the non-collinear magnetic structure is stabilized by thermal fluctuations, with a constant energy lower than the collinear fault. This non-collinear perturbation spread over the entire simulation cell thus represents the true magnetic ground state of the system. However, similarly to the case of the infinite fault presented in the previous section, this structure may not be considered as a fault if its energy depends on the volume of the simulation cell. To check this possibility, the same calculations need to be performed for different cell sizes, which was not done at this point. This non-collinear structure also arises spontaneously upon cooling the system, with a constant magnetic energy across the whole range of

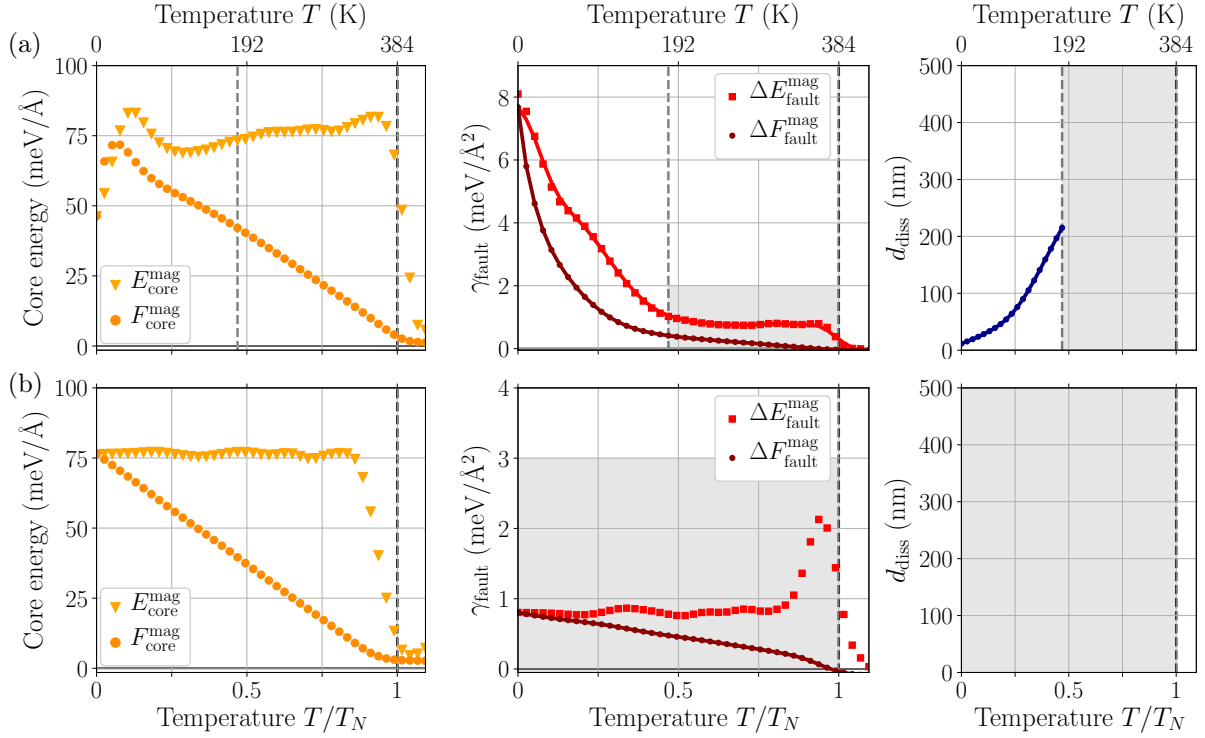


Figure 18: (Left) Magnetic energy (triangles) and free energy (circles) of a $1/2\langle 111 \rangle$ screw dislocation core as a function of temperature. (Middle) Surface fault energy (squares) and free energy (circles) of the magnetic fault separating the two $1/2\langle 111 \rangle$ screw dislocations as a function of temperature. (Right) Dissociation distance d_{diss} of the $\langle 111 \rangle$ screw superdislocation as a function of temperature. Simulations are performed with parameters Set2, upon (a) heating, and (b) cooling the system.

temperatures scanned except near the Néel temperature T_N where fluctuations in the energy do not allow for a proper separation of the two contributions to the magnetic energy. Upon cooling through T_N , the slope of the total excess magnetic energy of the system given by Eq. 12 shows a sudden increase, before falling and then remaining constant down to 0 K with the same value as found upon heating the system between 180 K and T_N . Similar magnetic energy profiles with temperature, showing an increased energy near the disappearance of long-range magnetic order has been previously reported in the case of domain walls in different systems [205]. Considering the magnetic contribution to the $1/2\langle 111 \rangle$ screw dislocation core (first column in Fig. 18), similar temperature variations are found upon heating and cooling the system, with almost constant energy across the whole range of temperature below T_N , except near 0 K upon the heat cycle where this contribution falls. Due to the steep decrease of the magnetic fault energy, separation of the two contributions is difficult in this temperature range, yielding the decrease of the magnetic core energy to the $1/2\langle 111 \rangle$ screw dislocation. This similar temperature dependence found whether heating or cooling shows that contrary to the fault, the core energy of the dislocations does not depend on the magnetic structure of the system. Similarly to the fault, the magnetic contribution to the core energy vanishes when long-range magnetic order disappears at T_N . This yields a linearly decreasing free energy with increasing temperature.

We stress that, similarly to the case of infinite magnetic faults of the previous section, the presented magnetic energy and free energy of the fault obtained upon cooling the system may also depend on the size of the simulation cell since the cooling cycle yields the non-collinear structure presented in Figs. 15 and 16. To check if a non-collinear fault can be defined when bounded by two $1/2\langle 111 \rangle$ dislocations, contrary to the infinite structure, the same calculation must be performed in simulation cells with different sizes. This is to check that the magnetic energy of the fault and of the dislocation core are identical for the same separation distance d between the two $1/2\langle 111 \rangle$ screw dislocations, but contained in a simulation cell of different size.

This study is not completed at the time, but preliminary results tend to show the situation is the same as in the case of the infinite magnetic fault, *i.e.* convergence of the magnetic fault energy cannot be achieved by increasing the size of the simulation cell. Thus, across the temperature range where the non-collinear structure arises, *i.e.* upon the whole cooling cycle and above a given temperature below T_N ($\simeq 180$ K in the present simulations) upon heating the system (black shaded regions in Fig. 18), a magnetic fault cannot be defined properly. Further discussion about the dissociation of possible $\langle 111 \rangle$ superdislocations, which require the existence of such faults, are therefore only valid upon heating up to a temperature below T_N , which is approximately 180 K in the presented calculations.

Using the free energy γ_{fault} of the magnetic fault bounded by the two $1/2\langle 111 \rangle$ screw dislocations (Fig. 18), the equilibrium dissociation distance of the $\langle 111 \rangle$ screw superdislocation is evaluated with anisotropic elasticity theory using the 0 K elastic constants, similar to the evaluation at 0 K presented in Chapter 1:

$$d_{\text{diss}}(T) = \frac{b_i^{(1)} K_{ij} b_j^{(2)}}{\gamma_{\text{fault}}(T)} = \frac{b^2 \sqrt{C' C_{44}}}{2\pi \gamma_{\text{fault}}(T)}, \quad (13)$$

which is presented in the third column of Fig. 18 as a function of the temperature T upon heating the system up to 180 K, since heating above this temperature stabilizes the non-collinear structure which *a priori* cannot be defined as a fault. Such dissociation distance cannot be neither properly defined across the whole cooling cycle since no magnetic fault exist. Considering only the heating cycle, up to approximately 180 K (or $T_N/2$) where a magnetic fault can be properly defined, its decreasing free energy with temperature yields a dissociation distance d_{diss} rapidly increasing up to a few hundreds of nanometers. In the temperature range between 180 K and T_N , since the magnetic fault has already vanished, the two $1/2\langle 111 \rangle$ dislocations are free to move without a magnetic fault forcing them to coexist and move pairwise. This holds across the whole cooling cycle, where the non-collinear magnetic structure is stabilized as soon as long range magnetic order is retrieved at T_N , down to 0 K. In this case, the two dislocations are also free to move independently, nevertheless bounding a non-collinear magnetic structure as shown in Fig. 15.

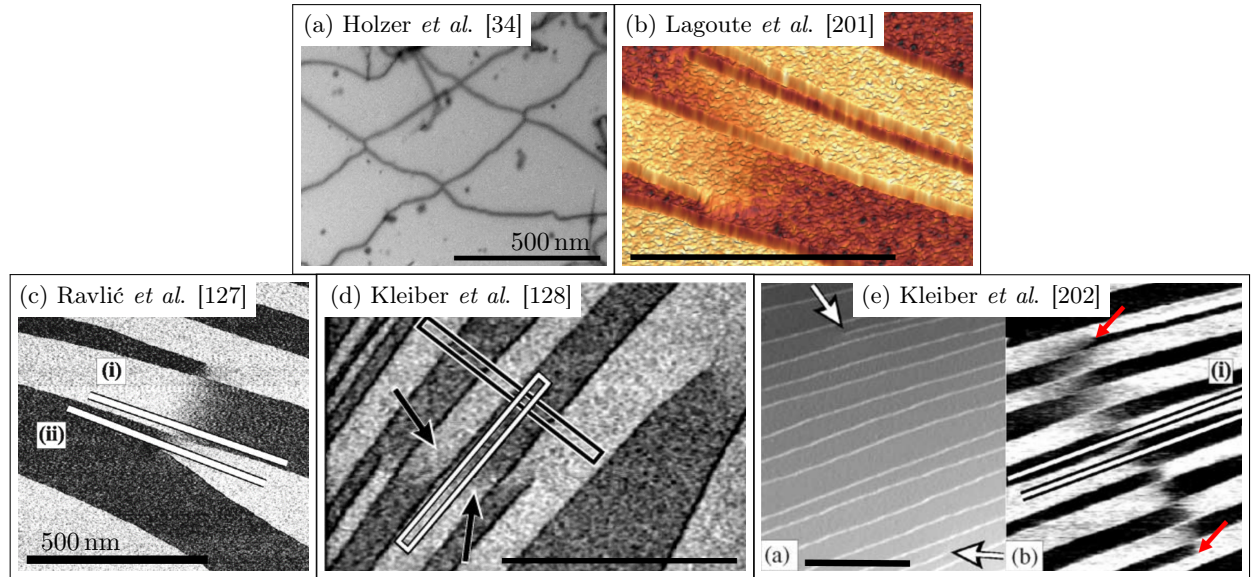


Figure 19: Experimental observations of the possible signature of a magnetic fault bounded by two $1/2\langle 111 \rangle$ dislocations: (a) TEM image of Holzer *et al.* [34] showing two pairs of screw dislocations intersecting to form $\langle 100 \rangle$ junctions in a single crystal compressed at 77 K; (b) to (e) spin-polarized STM magnetic contrast images of various experimental works [127, 128, 201, 202] showing a magnetic fault bounded by two $1/2\langle 111 \rangle$ screw dislocations emerging from $\{100\}$ surfaces at room temperature. Horizontal thick black lines in all figures correspond to 500 nm. Arrows show the positions of the dislocations at the surface.

All existing experimental evidence of such a magnetic fault are presented in Fig. 19. In the TEM observation of Holzer *et al.* [34] at 77 K shown in (a), two pairs of $1/2\langle 111 \rangle$ screw dislocations with the same Burgers vector intersect to form a network of $\langle 100 \rangle$ junctions, such dislocations being spaced from each other from an approximate distance of 200 nm, which could be due to dissociated pairs of these dislocations. However, even if the sample was deformed at 77 K, which is below the temperature of disappearance of the magnetic fault ($\simeq T_N/2$), the analysis and imaging were performed at room temperature in the electron microscope. It is therefore probable that the magnetic structure is arranged in the non-collinear structure where the two dislocations are then free to move independently. Spin-polarized STM magnetic contrast images recorded at $\{100\}$ surfaces of Lagoute *et al.* [201], Ravlić *et al.* [127] and Kleiber *et al.* [128, 202] at room temperature (Fig. 19b to e) show the magnetic structure bounded by two $1/2\langle 111 \rangle$ screw dislocations with opposite Burgers vectors emerging at the $\{100\}$ surface of the sample, and separated by a distance ranging from 250 nm to $1\text{ }\mu\text{m}$. The variation in the magnetic contrast clearly shows signature of a magnetic frustration between the two dislocations, extending over an approximate domain size of the order of a few hundreds of nanometers. These experimental observations were recorded at room temperature, which is very close to the Néel temperature T_N . However, our results show that the magnetic fault generated by $1/2\langle 111 \rangle$ dislocations has must probably already disappeared at this temperature. In this respect, since there is still evidence of a modulation of magnetic moments in the region between the two dislocations, the recorded magnetic contrast are possibly imaging the non-collinear structure of Fig. 15, in a temperature range where the two bounding dislocations are already free to move. If the existence of these dissociated $\langle 111 \rangle$ superdislocations is to be confirmed, a careful experimental procedure is required to ensure they are visible. In the light of the presented results, *post mortem* imaging at room temperature of the dislocation microstructure present in a deformed sample should not allow for their observation. To do so, *in situ* TEM straining observations of samples deformed below $T_N/2$ is required, *e.g.* at 77 K, to ensure dislocation sources have emitted paired dislocations separated by a magnetic fault of finite energy.

Conclusions of Chapter 3:

- Through formulation of the magnetic energy of in the frame of a Heisenberg-Landau model parametrized for bcc Cr, a Metropolis Monte Carlo algorithm allows for the exploration of different types of magnetic structures when thermal energy is given to the system operating through longitudinal (amplitude) and transverse (orientation) magnetic excitations.
- Two sets of parameters are determined for the Heisenberg-Landau model through a fit to DFT data. This model yields a satisfactory picture of the 0 K properties of bcc Cr, with better energetics using Set1, and a good estimate of the Néel temperature T_N using Set2. The bulk thermodynamical properties obtained using the quantum statistics gives a good agreement with experimental magnetization curve of bcc Cr up to the Néel temperature where long-range magnetic order vanishes in the PM phase.
- The energy of the magnetic fault caused by shearing of a $1/2\langle 111 \rangle$ vector decreases upon heating the system to a temperature below T_N , where its structure takes a non-collinear configuration to partially accommodate the magnetic frustration caused by the fault vector.
- Upon cooling a crystal rigidly sheared by a $1/2\langle 111 \rangle$ vector, a non-collinear magnetic structure similar to a spin spiral with a lower energy than the magnetic fault appears. With an energy reaching zero for infinite separation distance between fault planes, this structure cannot be considered as a fault, but is the true magnetic ground state of the system. Magnetic faults caused by $1/2\langle 111 \rangle$ shear therefore only exist in a collinear structure found upon heating, with a free energy falling to zero before T_N .
- Upon heating the system in the temperature range where the magnetic fault still exists, the dissociation distance of possible $\langle 111 \rangle$ superdislocations rapidly stretches up to a few hundreds of nanometers. Both the magnetic fault and the dislocation core internal and free energies decrease with increasing temperature. These magnetic faults vanish below T_N , and a non-collinear spiral-like structure bounded by two $1/2\langle 111 \rangle$ dislocations is stabilized.

- These results showed the magnetic internal and free energies of both the fault and the dislocation core vanish at the Néel temperature T_N , which enforces the conclusion that above T_N , $1/2\langle 111 \rangle$ dislocations should glide freely without dragging magnetic faults behind them. As a result, the study of plasticity in the disordered PM phase of bcc Cr can be reasonably approximated by the NM phase.
-

Chapter 4 - Non-Schmid effects across bcc transition metals

We now extend the generalized yield criterion presented in Chapter 2 for bcc Cr to all bcc transition metals, based on *ab initio* evaluation of the properties of the $\frac{1}{2}\langle 111 \rangle$ screw dislocation gliding in $\{110\}$ planes. Such a systematic study across bcc transition metals allows quantifying similarities and differences between different metals, and in particular to conclude on whether Cr shows a similar yield behavior compared to other bcc metals. We also test the ability of the presented model to predict the plastic behavior of these metals by directly comparing the results of this "*ab initio*" yield criterion to experiments.

1. Core properties and mobility of $\frac{1}{2}\langle 111 \rangle$ screw dislocations

We present in this section the core properties of the $\frac{1}{2}\langle 111 \rangle$ screw dislocation gliding in a $\{110\}$ plane in all bcc transition metals. The following results are obtained using the *stress* dislocation setup (see Methods, section 3.1.3, Fig. 7) for the simultaneous evaluation of the Peierls potential V_P , dislocation trajectory (x, y) and variations of its relaxation volume tensor $\Delta\bar{\Omega}$ in the $\{111\}$ plane orthogonal to the dislocation line. The simulation cell is the same as for the NM phase of Cr presented in Chapter 2, with 135 atoms per b in the direction of the line. The $\frac{1}{2}\langle 111 \rangle$ screw dislocation dipole is introduced in the cell using anisotropic elasticity theory using the 0 K *ab initio* elastic constants presented in Tab. D.1 of Appendix D.

1.1. Peierls potential

The Peierls potentials V_P after elastic correction are presented in Fig. 1 as a function of the dislocation position x along the glide direction $[\bar{1}2\bar{1}]$. The height of the barriers obtained using setup *both* (see Methods, Fig. 6) where both dislocations of the dipole glide in the same direction, hence with negligible elastic energy variation, are indicated by grey crosses at $x = \lambda_P/2$. We note a very good agreement between both setups, highlighting the validity of the elastic correction, necessary for the setup *stress*. The obtained potentials are smooth with respect to the dislocation position and allow for the determination of the Peierls stress τ_P

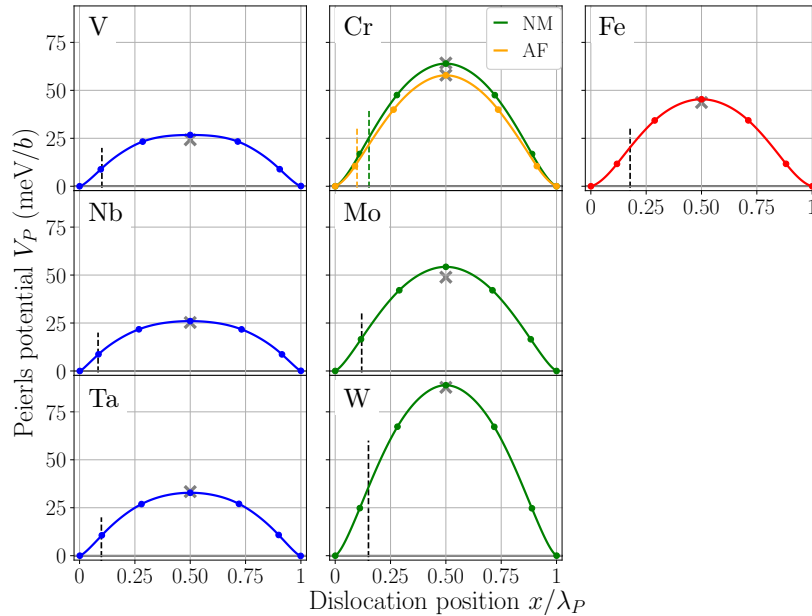


Figure 1: Peierls potential V_P of the $\frac{1}{2}\langle 111 \rangle$ screw dislocation gliding in a $\{110\}$ plane as a function of its position x for all bcc transition metals obtained after performing the elastic energy correction using the setup *stress*. Grey crosses located at $x = \lambda_P/2$ indicate the heights of the Peierls barriers obtained using the dislocation setup *both*. Vertical dashed lines indicate the position of the inflexion point x^*/λ_P of the Peierls potential.

necessary to overcome the Peierls barrier $V_P(x)$, with:

$$\tau_P = \frac{1}{b} \max_x \left. \frac{\partial V_P}{\partial x} \right|_x \quad (1)$$

The values of τ_P are presented in Tab. 1, which compare very well with previous studies using different *ab initio* parameters, dislocation setup and definition of the dislocation position [191]. In particular, the same hierarchy of the Peierls stresses between different bcc transition metals is found. We also note that all Peierls potentials are sharp close to the bottom of the Peierls valleys, *i.e.* near $x = 0$ and λ_P , and form cusps, in contrast with the sinusoidal shape assumed in simple models [206].

1.2. Dislocation trajectory and relaxation volume

The trajectory of a $1/2[111]$ screw dislocation in the (111) plane is presented in Fig. 2. They display the same distinctive departure from their macroscopic $(\bar{1}01)$ glide plane, as previously reported by Dezerald *et al.* [44, 69] in all bcc transition metals using *ab initio* calculations, and also reported in Cr considering both its NM and AF phases in Chapter 2 [180]. The deviation is quantified by the angle α^* that the trajectory makes with the $(\bar{1}01)$ plane at the inflexion point x^* of the Peierls potential [45, 180] (see Tab. 1). It can be directly linked to the twinning/antitwining (T/AT) asymmetry characteristic of bcc metals [69]. A good agreement is again found with previous calculations, with the same hierarchy between bcc metals, except for Ta which was previously found to have a less deviated trajectory [69]. Among all bcc transition metals, Nb has the most deviated trajectory, causing the most pronounced T/AT asymmetry, a feature also reported experimentally [36]. The less deviated trajectory, with almost zero deviation angle α^* , is found for Fe, which yields an almost negligible T/AT asymmetry, also observed in experiments [35]. Comparison with available experimental data on the yield properties of bcc metals will be presented in a following section.

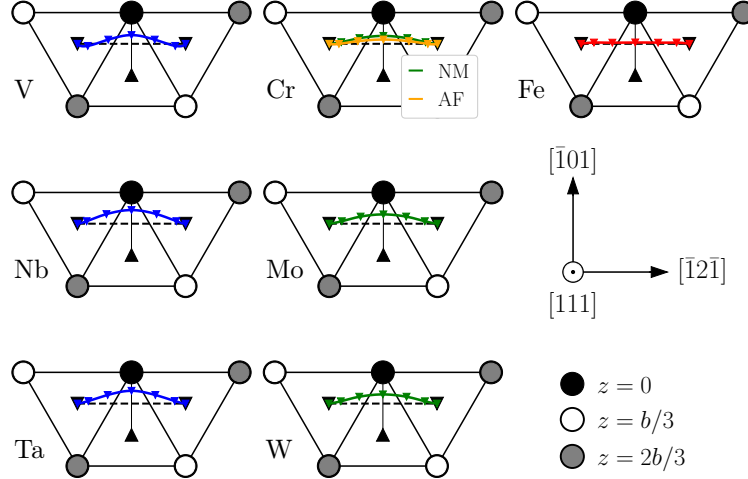


Figure 2: Trajectory of the $1/2[111]$ screw dislocation when gliding in the $(\bar{1}01)$ plane in all bcc transition metals extracted from the stress variations recorded along the NEB path using the dislocation setup *stress*. Symbols are *ab initio* data after post-processing, and solid lines are quadratic splines.

From the same NEB calculations, the stress variations recorded along the path allow to extract the variations of the relaxation volume tensor $\Delta\bar{\bar{\Omega}}$ of the screw dislocation core field (see section 3.1.3 in Methods). These variations have the following form for a $1/2\langle 111 \rangle$ screw dislocation gliding in a $\{110\}$ plane:

$$\Delta\bar{\bar{\Omega}}_{1/2\langle 111 \rangle} = \begin{bmatrix} \Delta\Omega_{11} & \Delta\Omega_{12} & 0 \\ \Delta\Omega_{12} & \Delta\Omega_{22} & 0 \\ 0 & 0 & \Delta\Omega_{33} \end{bmatrix}, \quad (2)$$

where the components $\Delta\Omega_{13}$ and $\Delta\Omega_{23}$, are zero, as previously reported for W [45, 79] and Cr [180]. The validity of this assumption was checked for all bcc metals following the method described by Kraych *et al.* [79], based on the symmetries between two NEB paths, from initial to final position, and from final to initial position. The non-zero components of the variation of the relaxation volume tensor are presented in Fig. 3 as a function of the dislocation position x for all bcc metals. Are also plotted the trace $\Delta\Omega_P$, which reflects coupling with pressure, and ellipticity $\Delta\Omega_e = \Delta\Omega_{22} - \Delta\Omega_{11}$ of the relaxation volume, linked to the T/C asymmetry [45, 79].

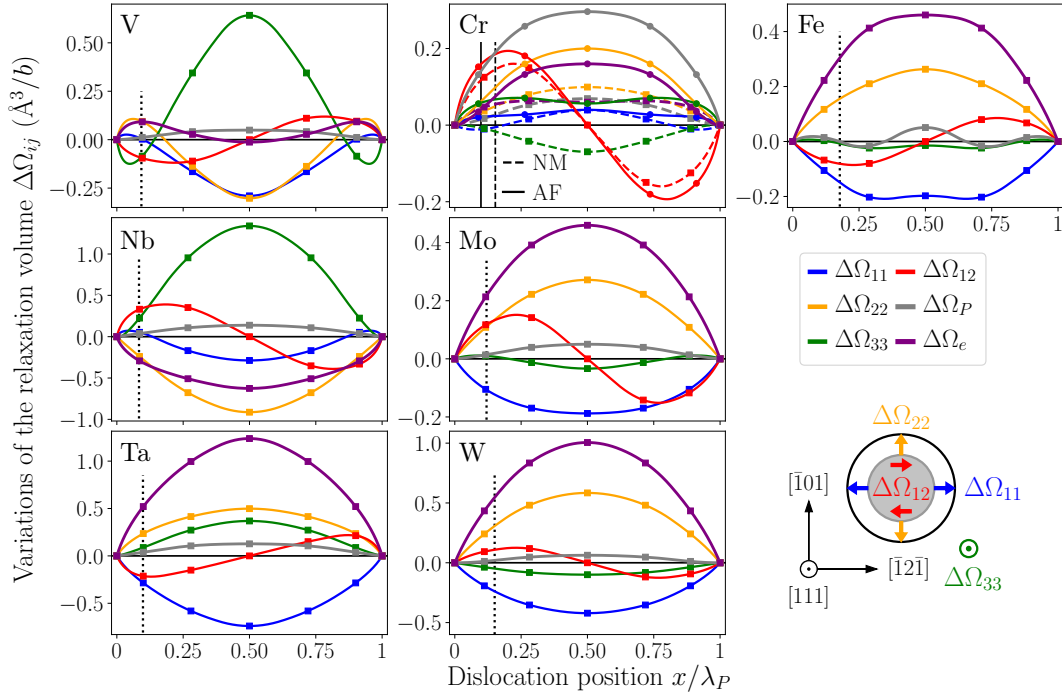


Figure 3: Variations of the relaxation volume $\Delta\Omega_{ij}$ of the $1/2\langle 111 \rangle$ screw dislocation (sketched in the lower right panel) as a function of its position x in the $\{110\}$ glide plane for all bcc transition metals. Squares are *ab initio* results and lines are quadratic splines. The trace and ellipticity of the tensor are also plotted. Different scales are used depending on the metal for clarity. Vertical dotted lines indicate the position of the inflexion point x^*/λ_P of the Peierls potential.

As reported in the case of Cr in Chapter 2, the dislocation trajectory and relaxation volume extracted using the stress variations along the NEB path are very sensitive to the values of the elastic constants. In particular, the symmetry of the trajectory and relaxation volume are not fully respected when using elastic constants of the perfect crystal. As presented in Appendix D, this can be fixed by slightly adjusting the elastic constants in order to enforce the expected symmetries. The validity of this approach was checked by calculating for W [45], Cr [180] and Mo the elastic constants of a simulation cell containing a $1/2\langle 111 \rangle$ screw dislocation dipole. The elastic constants slightly differ from the perfect crystal (up to 13% for the C_{15} and C_{44} components and less than 6% for all other constants in Cr, 18% and 15% for C_{15} and C_{44} respectively and less than 4% for all other components in Mo, and 6 and 7% for C_{15} and C_{44} respectively with less than 3% variation on all other elastic constants in W). Most importantly, the difference is of the same order as with the elastic constants obtained through the fitting procedure to enforce symmetry of the trajectory.

Variations of the relaxation volume (Fig. 3) show a large variety of different behaviors among bcc metals. No group tendency can be observed: in a same column of the periodic table, V, Nb, Ta on the one hand, Cr, Mo, W on the other hand, the same component of the relaxation volume can have different signs (see for instance $\Delta\Omega_{12}$). This makes the variations of the relaxation volume a strongly metal-dependent property.

Table 1: Parameters of the yield criterion for $\langle 111 \rangle \{110\}$ slip: Peierls stress τ_P (GPa), position x^* of the inflexion point of the Peierls potential (normalized by the distance λ_P between Peierls valleys), angle α^* ($^\circ$) made by the dislocation trajectory at this position, and derivatives $\Delta\Omega'_{ij}$ (\AA) of the relaxation volume with respect to the position x at the inflexion point x^* .

Element	τ_P	x^*/λ_P	α^*	$\Delta\Omega'_{11}$	$\Delta\Omega'_{22}$	$\Delta\Omega'_{33}$	$\Delta\Omega'_{12}$	$\Delta\Omega'_P$	$\Delta\Omega'_e$
V	1.03	0.093	-14.4	-0.101	-0.096	+0.222	-0.068	+0.026	+0.004
Nb	0.79	0.047	-17.4	-0.011	-0.354	+0.423	+0.343	+0.057	-0.343
Ta	0.87	0.083	-16.2	-0.288	+0.210	+0.131	-0.095	+0.053	+0.498
Cr (NM)	2.32	0.153	-13.5	+0.025	+0.050	-0.034	+0.067	+0.041	+0.025
Cr (AF)	1.98	0.099	-7.0	-0.013	+0.116	+0.041	+0.119	+0.171	+0.103
Mo	1.40	0.114	-13.9	-0.084	+0.113	-0.008	+0.078	+0.021	+0.198
W	2.36	0.129	-14.4	-0.168	+0.239	-0.042	+0.058	+0.029	+0.406
Fe	1.65	0.143	-0.5	-0.130	+0.117	-0.029	-0.042	-0.043	+0.247

No correlation can neither be found with elastic anisotropy characterized by the ratio $A = C_{44}/C'$ of shear moduli. We also note that the magnitude of the different $\Delta\Omega_{ij}$ components strongly depend on the metal, with weak variations in Cr, Mo and Fe, and high amplitudes in all others, the consequence of which on the predicted yield behavior will be discussed later. A striking feature of the variations of the relaxation volume is that both its trace $\Delta\Omega_P$ and component $\Delta\Omega_{33}$ along the dislocation line are non-negligible for some metals. The non-zero $\Delta\Omega_{33}$ components in V, Nb, Ta and Cr imply a non-negligible effect of an applied stress σ_{33} along the dislocation line. Also, the effect of pressure, carried by $\Delta\Omega_P$, should be important in Cr, and small but non-negligible in Nb, Ta and Mo. It is thus not possible to neglect the effect of hydrostatic pressure, nor of a tensile stress along the dislocation line when describing non-Schmid effects, contrary to yield criteria usually used for bcc metals [187]. This motivates the use of generalized yield criteria involving all stress components to properly account for these core properties of the screw dislocation [186, 207, 208].

1.3. Peierls enthalpy barrier under applied stress

With all core properties extracted from *ab initio* calculations, one can now write the Peierls enthalpy $\Delta H_P(x)$ of the screw dislocation gliding under an applied stress $\bar{\Sigma}$ as [79] (Eq. 7 in Chapter 2):

$$\Delta H_P(x) = V_P(x) - \Sigma_{yz} b x + \Sigma_{xz} b y(x) - \sum_{ij} \Sigma_{ij} \Delta\Omega_{ij}(x), \quad (3)$$

where $y(x)$ and $\Delta\bar{\Omega}(x)$ are parameterizations of the dislocation trajectory and relaxation volume along the minimum energy path for $\{110\}$ glide. An important consequence of the relaxation volume $\Delta\bar{\Omega}$ on the yield properties of bcc metals is carried by its ellipticity $\Delta\Omega_e = \Delta\Omega_{22} - \Delta\Omega_{11}$, linked to the change in the Peierls enthalpy barrier ΔH_P experienced by the screw dislocation when its glide plane is subjected to a normal stress [79] (Eq. 7). With a positive ellipticity, a glide plane subjected to a tensile stress results in a lowering of ΔH_P and thus of the yield stress. This is the case for W, as presented in Fig. 4a, an effect which was validated in W using direct *ab initio* calculations by Kraych *et al.* [79]. This behavior matches the T/C asymmetry generally observed in bcc metals, with easier plastic yield in tension than in compression. Surprisingly, Nb and V seem to deviate from this general behavior as $\Delta\Omega_e$ is negative in Nb and almost zero in V. In particular in Nb, one expects an increase of the Peierls enthalpy ΔH_P for a glide plane in tension. We checked this prediction by performing *ab initio* calculations in Nb of the dislocation Peierls enthalpy for a non-null stress component normal to the dislocation glide plane. The results are presented in Fig. 4b, where a stress σ_{22} is applied to the system, resulting, as predicted, in a lower barrier when the glide plane is in compression. Results of the model (dashed lines) are in good agreement with direct *ab initio* NEB calculations, in particular regarding the slope of the enthalpy barriers, defining the yield stress. Consequences of this peculiarity of Nb on its yield properties will be discussed in more details when comparing to experimental data in following sections.

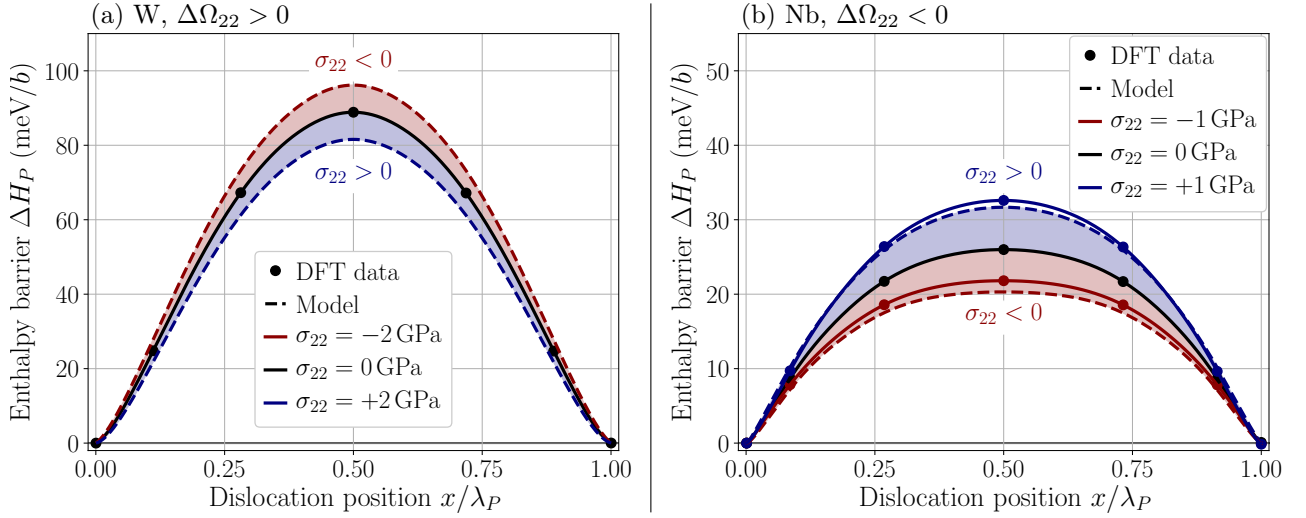


Figure 4: Peierls enthalpy barrier $\Delta H_P(x)$ of a $1/2\langle 111 \rangle$ screw dislocation gliding in a $\{110\}$ plane which is subjected to a tensile and compression non-glide stress Σ_{22} of magnitude σ_{22} in (a) W, and (b) Nb. Results of direct *ab initio* calculations in Nb are reported by solid lines and color circles, with the predictions of the model shown with dashed lines.

2. Uniaxial mechanical loading

The yield stress for any mechanical loading is defined as the stress state for which $\Delta H_P(x)$ (Eq. 7) ceases to have a saddle point. We illustrate in this section the approach by considering a uniaxial mechanical loading, *i.e.* a tension or compression test, and develop an analytical yield criterion based on the *ab initio* data obtained in the previous section. Full derivation of the model is given in more details in previous works [45, 79, 180] and in Chapter 2, with all assumptions given in Methods. The choice to focus on uniaxial loading is motivated by the availability of experimental data at low temperature for all bcc transition metals, and hence the possibility to compare the results of the presented yield criterion with experiments. However, we stress that the approach described here can be applied to any other mechanical loading.

2.1. Generalized yield criterion

We now extend the yield criterion presented in Chapter 2 for Cr to all other bcc transition metals using the core properties of the $1/2\langle 111 \rangle$ screw dislocation presented in the previous sections and listed in Tab. 1. Methods and details about the parameterization of the generalized yield criterion for uniaxial loading are given in Chapter 2, section 2.1. We recall the expression obtained for the yield stress in tension [180], which corresponds to Eq. 12 in Chapter 2:

$$\sigma_Y^T(\zeta, \chi) = \frac{2\tau_P}{\sin(2\zeta) \frac{\cos(\chi - \alpha^*)}{\cos(\alpha^*)} + \beta(\zeta, \chi)}, \quad (4)$$

with the corresponding criterion for compression obtained by substituting $\chi \rightarrow -\chi$, $\alpha \rightarrow -\alpha$ and $\beta \rightarrow -\beta$ in Eq. 4, resulting in the following expression:

$$\sigma_Y^C(\zeta, \chi) = \frac{2\tau_P}{\sin(2\zeta) \frac{\cos(\chi + \alpha^*)}{\cos(\alpha^*)} - \beta(\zeta, \chi)}, \quad (5)$$

and where β is a function of angles ζ and χ and components $\Delta\Omega_{ij}$ (Eq. 13 in Chapter 2):

$$\beta(\zeta, \chi) = \sin^2 \zeta \left[\frac{\Delta\Omega_e^*}{b} \cos(2\chi) + \frac{2\Delta\Omega_{12}^*}{b} \sin(2\chi) + \frac{\Delta\Omega_P^*}{b} \right] - (1 - 3\cos^2 \zeta) \frac{\Delta\Omega_{33}^*}{b}. \quad (6)$$

Parameters for the 0 K yield criterion are given in Tab. 1 for all bcc transition metals, which we now discuss the predictions in the following sections.

2.2. Variations among bcc transition metals

To better visualize the difference between tension and compression, the predicted slip activity, *i.e.* the distribution of primary slip system as a function of the orientation of the loading axis, is presented in Fig. 5 under both tensile and compressive mechanical loadings for all bcc transition metals. These stereographic projections show the slip system with the lowest yield stress according to Eq. 4 in tension (Eq. 5 in compression) among the twelve $\langle 111 \rangle \{110\}$ possible systems, similar to previously reported using different yield criteria [184, 185, 188]. The corresponding stereographic maps for bcc Cr were presented in Figs. 12 and 13 in Chapter 2 for the two NM and AF phases.

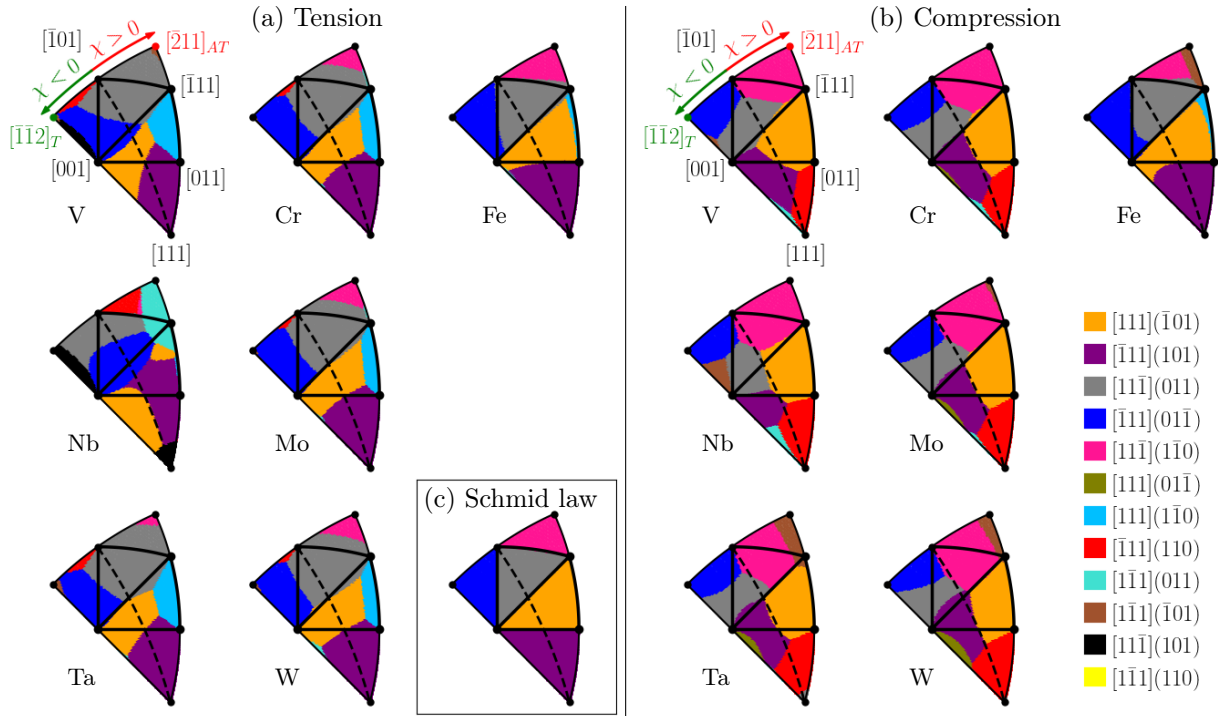


Figure 5: Predicted distribution of primary $\langle 111 \rangle \{110\}$ slip systems for all bcc transition metals at 0 K according to the yield criteria of Eqs. 4 and 5 under uniaxial (a) tension and (b) compression respectively. Results for Cr are presented for the non-magnetic (NM) phase. The distribution of primary slip systems predicted by the Schmid law, in either tension or compression, is shown in (c), which is common to all bcc transition metals.

As shown in Fig. 5a and b, the predicted slip activity deviates from the predictions of the Schmid law, shown in c, according to which the same single $\langle 111 \rangle \{110\}$ slip system should have the lowest yield stress in both tension and compression in any stereographic triangle delimited by axis $\langle 100 \rangle$ - $\langle 110 \rangle$ - $\langle 111 \rangle$, and should show the same distribution in all bcc transition metals. When non-Schmid effects are included, this simple distribution changes, with various coexisting primary slip systems in a same triangle, and a change of the minimum symmetry-equivalent region of the stereographic space from a single triangle, as obtained with the Schmid law, to two adjacent triangles.

Looking at the predicted slip activity, all bcc metals show a similar distribution, except Fe and Nb. Indeed, Fe is the only metal for which a marginal deviation from the Schmid law is predicted, due to its small deviation angle and also limited variation of its relaxation volume. On the contrary, tensile and compressive slip activities in Nb show major deviations with respect to the Schmid law and also to all other metals.

Most particularly, regions of the standard triangle are predicted to favor an anomalous slip system in tension ($[\bar{1}11](01\bar{1})$ in blue) and compression ($[11\bar{1}](011)$ in grey). This is a consequence of both a high deviation angle α^* and a large magnitude of $\Delta\Omega_{ij}$, with a negative ellipticity. Although Ta has also a high deviation angle, it does not appear as different from other metals as Nb. This difference between Nb and Ta lies in the high magnitude of the $\Delta\Omega_{33}$ component of the relaxation volume in Nb. Due to this component, yield stress in Nb is sensitive to a normal stress acting along the dislocation line. This coupling in Nb is responsible for the region in the central triangle of the stereographic projection where the $[\bar{1}11](101)$ (in purple) and $[11\bar{1}](011)$ (in grey) are predicted as primary slip systems in tension and compression respectively. The four other metals, namely V, Ta, Mo and W, display similar slip activity in both tension and compression. The main features are the activity of both the expected $[111](\bar{1}01)$ (orange) slip system with $[111](\bar{1}10)$ (sky blue) in tension and $[\bar{1}11](101)$ (purple) in compression over the standard stereographic triangle.

When we compare the predicted slip activity for Cr to all other bcc transition metals, we report a similar yield behavior to Ta, Mo and W both under uniaxial tension and compression. As can be seen in Tab. 1, the parameters of the yield criterion for both magnetic phases of bcc Cr are similar to these three other metals, except for the weaker magnitude of the variation of the relaxation volume tensor of the screw dislocation. Given the presented results, one can expect the plastic behavior of Cr to be similar to that of all other bcc metals, with similar qualitative features such as the T/AT and T/C asymmetries under uniaxial loading.

3. Comparison to experiments at low temperature

As presented in the previous sections, the yield criterion proposed in this work, based on *ab initio* calculations of the screw dislocation properties, gives a good qualitative reproduction of known features of the yield behavior of bcc transition metals under uniaxial loading, namely the T/AT and tension/compression asymmetries. We now compare the predictions of the model at 0 K with low temperature experimental data in terms of the variation of the yield stress and slip activity with the orientation of the loading axis.

3.1. Yield stress and slip activity

The *ab initio* yield stresses are presented in Fig. 6 for all bcc transition metals, with experimental data measured at 77 K for different loading orientations taken from various references (see Appendix A). To effectively compare the predictions of the yield criterion to experiments, it is necessary to account for the variations of the yield stress with the crystal orientation as non-Schmid effects make it impossible to

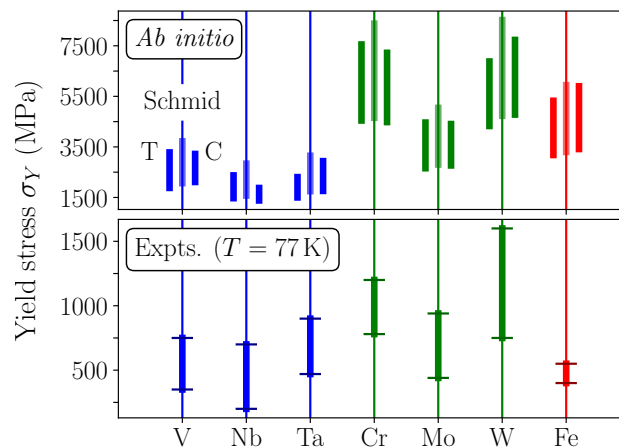


Figure 6: Comparison between the yield stress σ_Y predicted by the *ab initio* yield criterion and experimental data taken from various references at 77 K (see Appendix A for values and references). Experimental yield stresses range from their minimum to maximum over the whole stereographic space in both tension and compression. *Ab initio* data are plotted both according to the Schmid law (Schmid, center bar), in tension (T, left bar), and compression (C, right bar).

define a single experimental value. We therefore report for each element the range of yield stresses measured for different orientations of the loading axis and compare with the range predicted by the model over the whole stereographic space, accounting for all possible slip systems, from which the minimum and maximum predicted yield stresses are shown. The *ab initio* data are reported both according to the Schmid law and including non-Schmid effects in tension and compression to highlight the different ranges covered by the different predicted yield stresses. We observe that deviations from the Schmid law tend to narrow the width of the yield stress distributions, with lower stresses in tension than in compression except in Nb due to the negative ellipticity discussed above.

As already largely discussed in the literature [44, 65, 209], depending on the metal, atomistic calculations using either interatomic potentials or *ab initio* calculations overestimate the yield stress by a factor 2 to 4 with respect to experiments. This effect is not corrected by accounting for non-Schmid effects in the evaluation of the yield stress, as seen on Fig. 6, which was proposed as a possible explanation for such a discrepancy with experiments in previous works [210, 211]. Despite this scaling effect, we note that the model reproduces the hierarchy of yield stresses between metals, except for Fe which is found experimentally

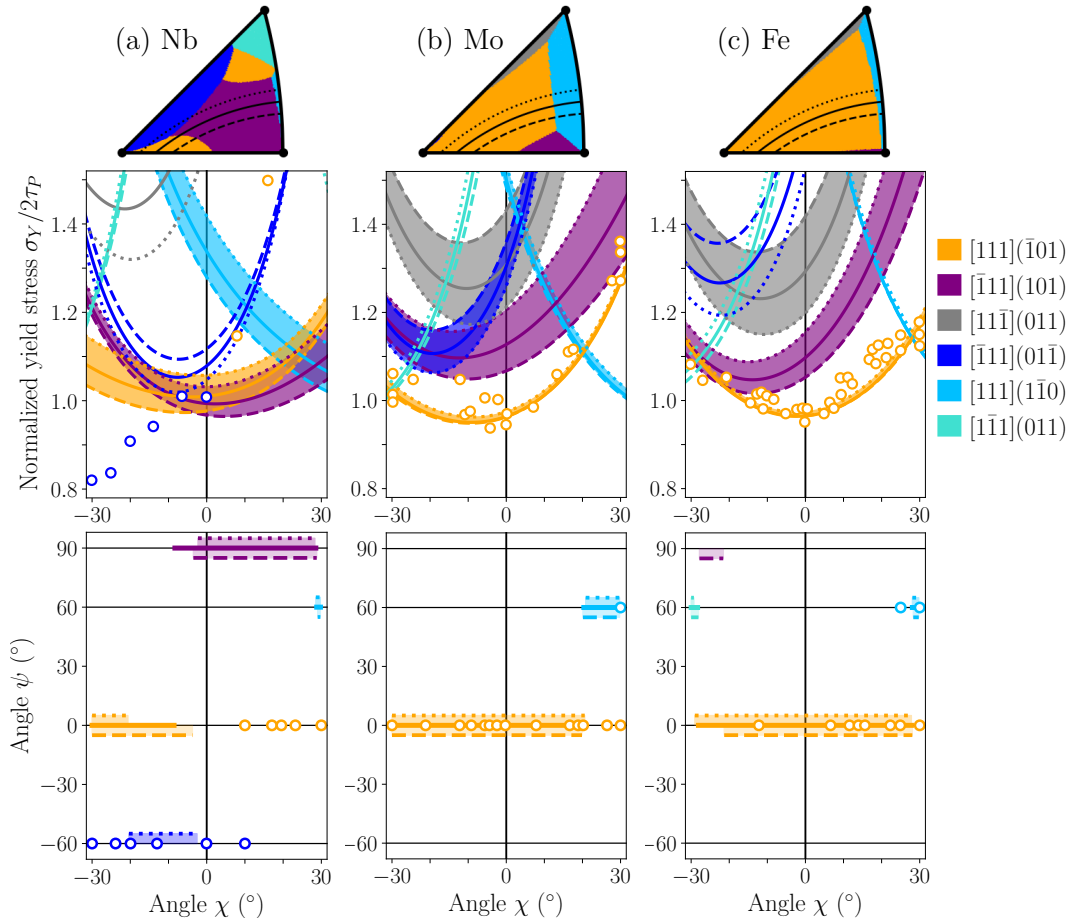


Figure 7: (Middle row) Normalized yield stress σ_Y / σ_Y^0 under uniaxial tension for each $\{111\}\{110\}$ slip system as a function of the angle χ for (a) Nb, (b) Mo, and (c) Fe along the $\zeta \in \{45^\circ; 48^\circ; 51^\circ\}$ lines shown in black in the stereographic triangles of the upper row. (Lower row) Corresponding angle ψ between the observed and the expected $(\bar{1}01)$ slip plane. Profiles for the three ζ -lines are shifted up and down for clarity. Experimental data in tension (open circles) were measured for $\zeta \simeq 47^\circ$ at 4.2 K for Nb [36], Mo [30] and Fe [35]. Experimental σ_Y are normalized by 570 MPa, 1100 MPa and 740 MPa for Nb, Mo and Fe respectively, and predicted σ_Y by $2\tau_P$ (see Tab. 1), which is the lowest value predicted by the Schmid law.

to have a narrower range of variations and, on average, a lower yield stress than all other metals, a specificity which is not captured by our model. In the following, yield stresses are rescaled to focus on their relative variations with respect to the loading axis rather than their absolute values.

We first compare the results of our model with experimental data in terms of the dependence of the yield stress and slip activity on the angle χ between the $\{110\}$ glide plane and the MRSSP. Only data measured at low enough temperature are relevant for the comparison since non-Schmid effects fade out when the temperature is increased up to the athermal temperature of the Peierls mechanism T_{ath} , where lattice friction becomes negligible [25, 45, 212]. Slip activity, *i.e.* active glide planes, is determined experimentally through the identification of slip traces left by dislocations on the surfaces of the deformed samples. The planes where the dislocations have slipped can then be defined by the angle ψ between the observed slip plane and the expected $(\bar{1}01)$ plane. Comparison between the yield criterion in tension (Eq. 4) and experiments is presented in Fig. 7 for a constant ζ angle, *i.e.* a constant angle between the tensile axis \vec{t} and the slip direction \vec{b} , as a function of the angle χ . Experimental data were measured at 4.2 K with $\zeta \simeq 47^\circ$ for Nb [36], Mo [30] and Fe [35]. Results for V and Ta under uniaxial tension with $\zeta \simeq 50^\circ$ are presented in Fig. 8 and compared with experimental data measured at 77 K taken from Bressers *et al.* [213] for V, and Nawaz and Mordike [33] for Ta. To emphasize on the sensitivity of the results on ζ , three different angles are plotted for the theoretical yield stresses: 45, 48, and 51° in Fig. 7 for Nb, Mo and Fe, and 48, 51, and 54° in Fig. 8 for V and Ta. The $\psi = f(\chi)$ plots in the lower row of Figs. 7 and 8 show the primary slip systems.

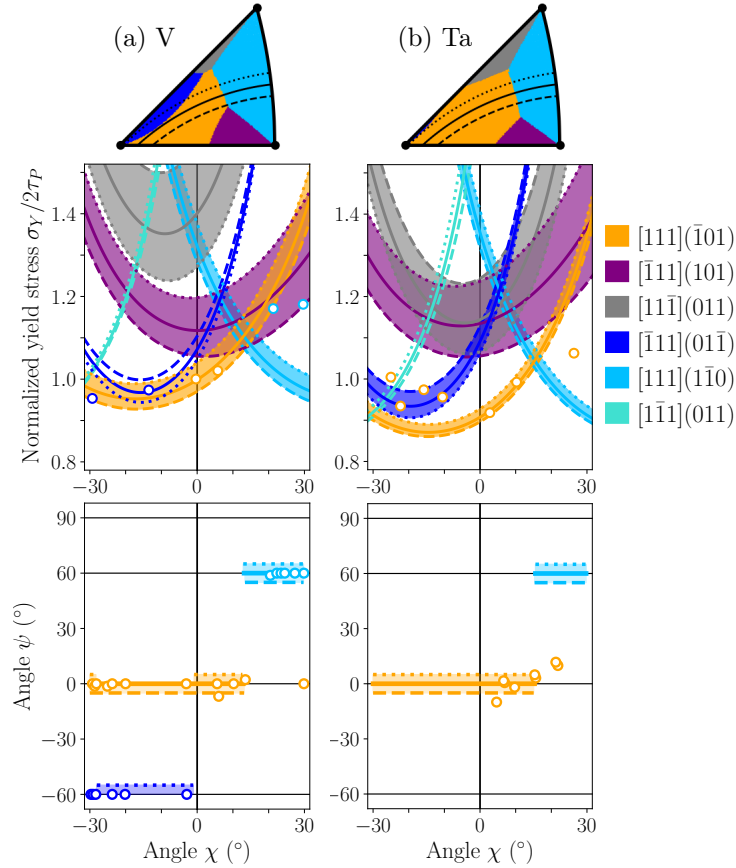


Figure 8: Normalized yield stress and angle ψ for V and Ta under uniaxial tension, with the same notations as in Fig. 7. Experimental data were measured at 77 K for $\zeta \simeq 50^\circ$ for both V [213] and Ta [33]. Experimental yield stresses are normalized by 500 and 510 MPa for V and Ta respectively.

The presented yield stress profiles highlight the departure from the Schmid law, characterized by the

T/AT asymmetry and a strong competition between slip systems. According to the Schmid law, only the $[111](\bar{1}01)$ system (orange) is expected over the range of orientations contained in the standard stereographic triangle delimited by axis $[001]$ - $[011]$ - $[\bar{1}11]$, resulting in $\psi(\chi) = 0$ for all χ angles. This is the case for Fe only (Fig. 7c), for which non-Schmid effects have a marginal impact. In the range of ζ angles considered here, we report a very good agreement with experimental data for Mo and Fe (Fig. 7b and c) in terms of both relative variation of the yield stress and active slip systems. The agreement for Nb is less satisfactory, especially regarding the yield stress for $\chi < 0$, where anomalous slip was reported experimentally [36], associated with a steep decrease of the yield stress not reproduced by the model. As will be detailed in the following Chapter 5, using TEM observations and atomistic simulations we proposed a new mechanism explaining such anomalous slip, which involves highly mobile multi-junctions between screw dislocations [214]. This effect can therefore not be understood from the glide properties of single dislocations, as considered in the present model. Regarding the predicted slip activity in Nb, the experimental $[\bar{1}11](0\bar{1}\bar{1})$ (blue, with $\psi = -60^\circ$) system is also predicted by the model for $\chi < 0$. In the $\chi > 0$ range, the authors report activity of the expected $[111](\bar{1}01)$ slip system (orange, with $\psi = 0$), while the model predicts the $[\bar{1}11](101)$ (purple, with $\psi = 90^\circ$) to require a lower yield stress. In terms of the yield stress, very few experimental values were reported by the authors for $\chi > 0$, not allowing for a proper comparison with the model.

Experimental slip activity measured for single crystals of V [213] and Ta [33, 215, 216] under uniaxial tension and compression at 77 K revealed wavy slip lines in a wide range of orientations tested by the authors, for which a precise identification of the active slip system was not possible at temperatures as low as 77 K (or $T_{\text{ath}}/5$ for both V and Ta). For this reason, only experimental data for which a precise slip system was determined are presented on Fig. 8. This temperature effect at 77 K on the measured slip activity does not however impact measurement of the yield stress, for which a precise definition holds up to the athermal temperature. A good agreement between predictions of the model and experiments is found for V, both in terms of yield stress and slip activity, except for $\chi > 20^\circ$ where the observed $[111](\bar{1}10)$ slip system (sky blue, with $\psi = +30^\circ$) is predicted to require a lower yield stress than observed experimentally. The same applies for Ta, for which the predicted slip activity in tension is similar to V, showing a satisfactory agreement in terms of the predicted relative variations of the yield stress. Very few experimental points are available in terms of slip activity in the same reference, caused by the temperature effect discussed above. Still, the predicted $[111](\bar{1}01)$ slip system (orange, with $\psi = 0$) for $\chi > 0$ is also observed experimentally, and is predicted over the entire range of χ angles, except for $\chi > +15^\circ$ where the $[111](\bar{1}10)$ (in sky blue, with $\psi = +30^\circ$) is predicted by the model, similar to V and Mo.

We now compare in Fig. 9 the predicted yield stress at 0 K with experimental data measured at 77 K for single crystals oriented along the edges of the standard stereographic triangle delimited by $[001]$ - $[011]$ - $[\bar{1}11]$ for W [217] under uniaxial tension in a, and Ta [218] in b and c under uniaxial tension and compression respectively. All yield stresses are normalized by the minimum yield stress $2\tau_P$ predicted by the Schmid law, as for results presented above, to focus only on its variations with orientation. A direct comparison with predictions at 0 K is legitimate since the 77 K temperature at which the reported experiments were conducted is sufficiently low compared to the athermal temperature of the Peierls mechanism for both W and Ta, of approximately 800 [29] and 400 K [216] respectively. As will be discussed in the following, dependence of the yield stress on the orientation of the loading axis is almost unchanged in this temperature range. Considering the case of W, the predicted yield stress is effectively lower for $[001]$ than $[\bar{1}11]$ orientation, which is also predicted by the Schmid law and is common to all bcc metals (see inset in Fig. 9a), but the yield criterion fails to reproduce the strong increase of the yield stress near $[011]$. Along the $[001]$ - $[011]$ edge of the triangle, the criterion predicts almost a flat variation of the minimum yield stress (thick black dashed line) because of the competition between the two $[111](\bar{1}01)$ (orange) and $[\bar{1}11](101)$ (purple), instead of the steep increase near $[011]$ observed experimentally. This discrepancy with experiments highlight the missing ingredients of the model for this particular region of the stereographic triangle close to $[011]$ in W, where glide of $1/2(111)$ screw dislocations in $\{112\}$ planes instead of $\{110\}$ has been reported experimentally [20, 26]. No precise atomistic mechanism has been proposed accounting for activity of $\langle 111 \rangle \{112\}$ slip systems up to date.

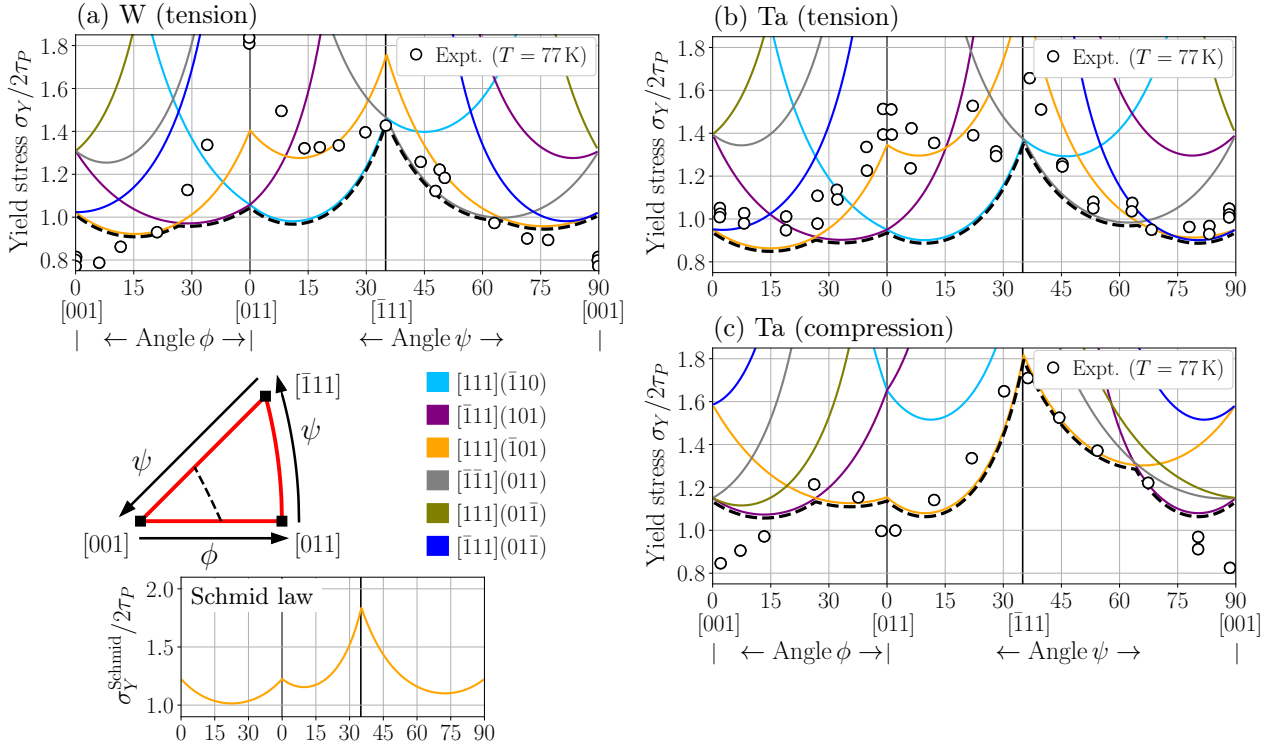


Figure 9: Variation of the predicted yield stress σ_Y at 0 K, normalized by $\sigma_Y^0 = 2\tau_P$, for $\{111\}\{110\}$ slip systems along the path defined by the $[001]$ - $[011]$ - $[\bar{1}11]$ edges of the standard stereographic triangle shown in the lower left for (a) W in tension, and Ta in (b) tension and (c) compression. Experimental data measured at 77 K are indicated by empty circles, and were taken from Bearmore and Hull [217] for W under uniaxial tension, normalized by 850 MPa, and from Byron and Hull [218] for Ta under uniaxial tension and compression, normalized by 550 MPa.

Now considering Ta, the predicted variations of the yield stress are in better agreement with experiments, in particular under compression (Fig. 9c), where the $[111](101)$ slip system expected from the Schmid law (orange) dominates across almost the whole range of orientations. The steep increase of the yield stress observed between $[011]$ and $[\bar{1}11]$ axis is well reproduced by the criterion in compression, and shows notable differences along the two other edges of the standard stereographic triangle with the experimental data in

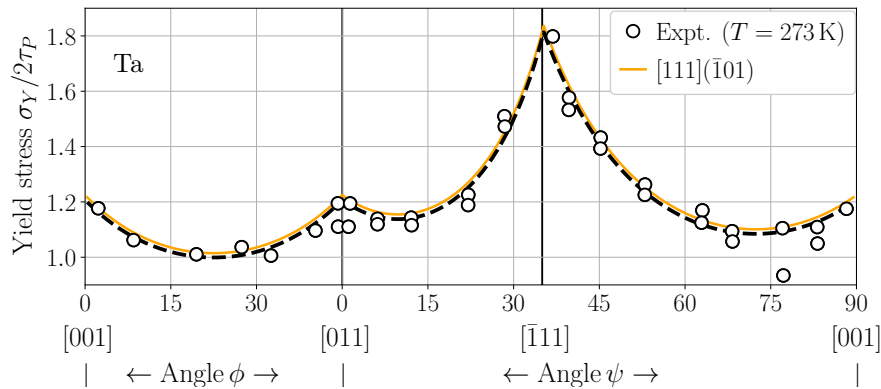


Figure 10: Comparison between the predictions of the Schmid law and experimental data of the yield stress of Ta single crystals under uniaxial tension along the edges of the standard $[001]$ - $[011]$ - $[\bar{1}11]$ stereographic triangle measured at a temperature of 273 K [218]. Experimental yield stresses are normalized by 160 MPa.

tension. The agreement with tensile data is less satisfactory, especially along the $[011]$ - $[\bar{1}11]$ edge where the $[111](\bar{1}10)$ system (sky blue) is predicted to require a lower yield stress. The predicted lower bound of the profile has a similar shape to W, while the yield stress for the $[111](\bar{1}01)$ system is predicted with a much steeper increase near $[\bar{1}11]$. Byron and Hull [218] also studied the profile of the tensile yield stress along the edges of the standard stereographic triangle at a temperature of 273 K, closer to the athermal temperature $T_{\text{ath}} \simeq 400$ K of the Peierls mechanism. The reported profiles in both tension and compression show a very good agreement with the predictions of the Schmid law, as presented in Fig. 10. This shows non-Schmid effects become less pronounced as the temperature is increased, up to T_{ath} where they ultimately vanish. A more detailed study of the temperature evolution of these effects is the focus of a following section.

3.2. Tension/compression asymmetry

We now focus on the asymmetry between tension and compression, comparing again predictions of the model with experimental data. A tension/compression (T/C) asymmetry has been observed experimentally in all bcc metals under uniaxial loading, over a wide range of crystal orientations [25, 42, 43]. In particular, the yield stress of bcc metals is generally lower in tension than in compression considering the same loading axis. This T/C asymmetry is analyzed as a function of the loading axis using the strength differential (SD) introduced by Gröger *et al.* [183, 184], expressed as:

$$\text{SD} = \frac{\sigma_T - \sigma_C}{(\sigma_T + \sigma_C)/2}, \quad (7)$$

where σ_T and σ_C are the absolute values of the yield stress in tension and compression respectively. Level plots of SD are presented in Fig. 11 for Nb, Ta, Mo, and W. Only these four metals are considered here for comparison to experiments, since data at low enough temperature is not available for other metals. The yield stress for Nb, Mo and Ta were mostly measured at 77 K, which is below the athermal temperature T_{ath} of the Peierls mechanism (between 300 and 400 K), and at 293 K for W, also below T_{ath} (around 800 K). Experimental values for T_{ath} are summarized in Appendix A. Other experimental data comparing tensile and compressive behaviors are available for Fe, Nb, Mo, Ta, and V but were however measured at least at

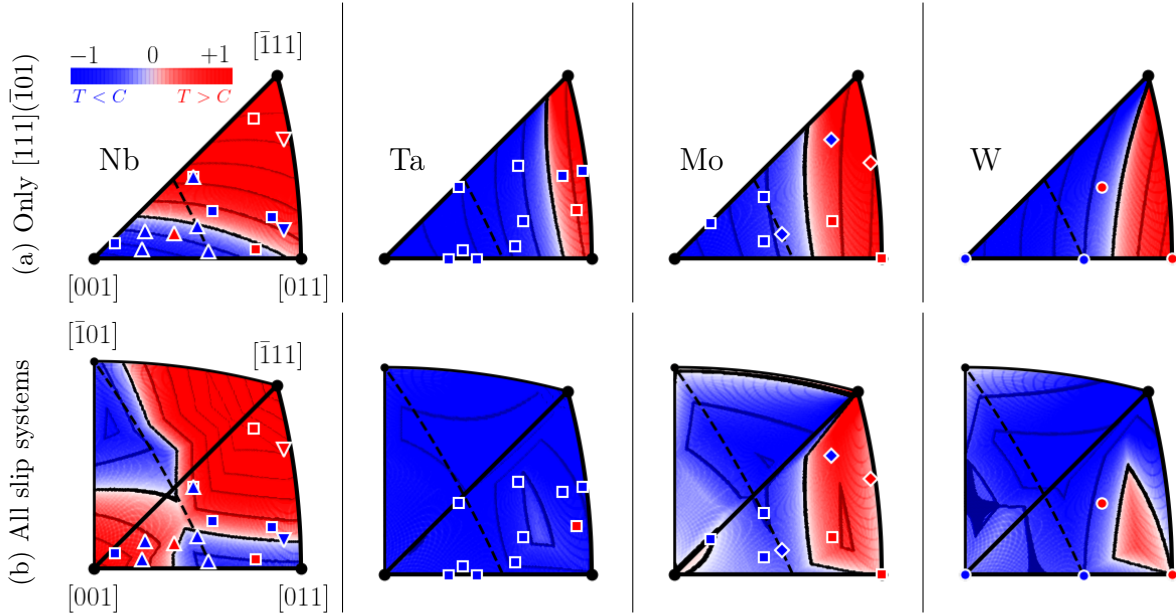


Figure 11: Strength differential (Eq. 7) of Nb, Ta, Mo, and W single crystals under uniaxial loading of (a) only the $[111](\bar{1}01)$ slip system, and (b) all $\langle 111 \rangle \{110\}$ slip systems. Experimental data at 77 K are indicated by colored squares (for Nb [13, 219], Ta [33, 220] and Mo [41, 221]), at 123 K by diamonds (for Mo [222]), at 158 K by upwards triangle (for Nb [223]), at 228 K by downwards triangles (for Nb [219]), and at 293 K by circles (for W [224]). Levels are indicated by dark lines every 0.1 step.

room temperature, which is too close to T_{ath} for these metals. Results for V and Fe, for which experimental data are missing, are presented in Fig. 12. All presented results are plotted considering only the primary expected slip system $[111](\bar{1}01)$ in the left column, and all $\langle 111 \rangle \{110\}$ slip systems in the right column, in order to stress the importance of accounting for all possible systems when describing the T/C asymmetry. Results for bcc Cr were presented in Chapter 2, Fig. 15, considering its two NM and AF phases.

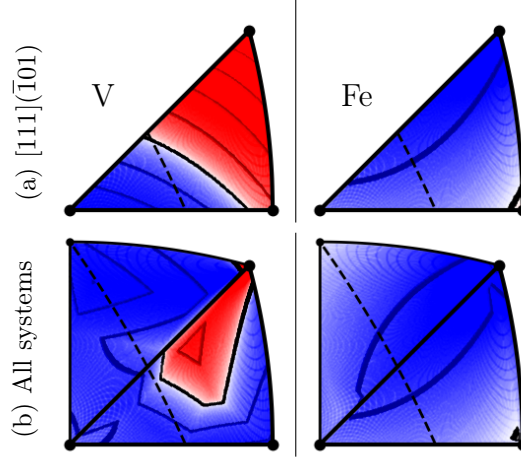


Figure 12: Strength differential of V and Fe single crystals under uniaxial loading considering (a) only the $[111](\bar{1}01)$ slip system predicted by the Schmid law, and (b) all $\langle 111 \rangle \{110\}$ slip systems. Notations and colors are identical as in Fig. 11.

When only the $[111](\bar{1}01)$ slip system is considered, all bcc metals presented in Figs. 11 and 12 show a non-negligible range of loading orientations for which compression activates slip more easily than tension (*i.e.* $SD > 0$, in red), except Fe for which the tensile yield stress is always lower. This is a direct consequence of the T/AT asymmetry of the $[111](\bar{1}01)$ slip system. Upon changing the sign of the applied stress (*i.e.* from $\sigma > 0$ in tension to $\sigma < 0$ in compression), the twinning region is reversed from $\chi < 0$ in tension, to $\chi > 0$ in compression. Hence, the yield stress is lower in compression than in tension near the $[011]-[\bar{1}11]$ edge of the standard stereographic triangle, and the opposite near the $[001]$ axis. In Mo and Ta, a small region where compression is easier than tension is predicted only in the part where $\chi > 0$. The location of this region is in qualitative agreement with experiments. However, this reasoning is too simplistic as active slip systems may differ inside the standard triangle when non-Schmid effects are accounted for. Hence, it is necessary to take all $\langle 111 \rangle \{110\}$ slip systems into account to have a correct representation of the T/C asymmetry and to compare with experiments. Two adjacent triangles are then plotted to describe the minimum symmetry-equivalent region of the stereographic projection.

When all slip systems are considered, the range of orientations where compression is easier than tension gets narrowed for Ta and W, while a similarly large or even wider range is observed for Nb and Mo. For Ta, the predicted yield stress is lower in tension than in compression for all orientations of the loading axis, in good agreement with experimental data [33, 216, 220], except near the $[011]-[\bar{1}11]$ edge. In this region, the authors report a lower compressive yield stress, not predicted by the model. Ta has the most pronounced T/C asymmetry in favor of tension among the four metals in Fig. 11, a consequence of the high positive magnitude of the ellipticity component $\Delta\Omega_e$ of its relaxation volume (see Tab. 1 and Fig. 3). The reverse effect is observed for Nb, and in V (see Fig. 12) to a lesser extent, for which the T/C asymmetry is predicted to be the most pronounced in favor of compression. A striking feature of this asymmetry in Nb is the lower compressive stress found for orientations near the center of the standard stereographic triangle, however comparing poorly with experimental data in this region. A large range of orientations close to the $[\bar{1}11]$ and $[001]$ corner orientations show a lower compressive yield stress, comparing well with experimental data close to $[\bar{1}11]$, but poorly near $[001]$. In this last region, *i.e.* $\chi < 0$, all authors reported anomalous slip for Nb samples deformed in either tension and compression, which cannot be captured by the presented model.

3.3. Tension/compression asymmetry at finite temperature

We now discuss the temperature evolution of the yield stress and tension/compression asymmetry through comparison with experimental data. As detailed in Chapter 2 section 3.2 in the case of Cr, the 0 K yield criterion can be extended to include finite temperature effects through a line tension model, whose parameters can be directly extracted from *ab initio* calculations [85, 191]. The expression of this finite temperature mobility law is given in Eq. 28 of Chapter 2. As discussed for Cr, this criterion qualitatively reproduces the progressive fade out of the yield stress and non-Schmid effects when the temperature approaches the athermal temperature T_{ath} of the Peierls mechanism, like presented in Figs. 19 and 20 for the T/AT asymmetry in the two NM and AF phases of bcc Cr. Similar behaviors can be obtained for all other bcc transition metals, as reported for W in Ref. [45], which are thus not presented here. The comparison between predictions of the model and experimental data in terms of the temperature evolution of the yield stress for W and Mo is instead presented in Appendix E.

The following results presented for Mo were obtained using the *ab initio* line tension $\Gamma_{\text{Mo}} = 2.86 \text{ eV}/\text{\AA}$ reported in the work of Dezerald *et al.* [191], where the line tension was calculated *ab initio* for all bcc transition metals except Cr. Evaluation of the line tension was performed again for W only in the present work, using the *ab initio* parameters and dislocation setup presented in the Methods, to ensure the consistency between the different properties extracted from our modeling. Using the method of Provile [85], we obtain a line tension $\Gamma_{\text{W}} = 3.41 \text{ eV}/\text{\AA}$, very close to the $3.89 \text{ eV}/\text{\AA}$ reported by Dezerald *et al.* for W [191], also comforting us in using previously published values for Mo. Comparison with experiments in terms of temperature evolution of the yield stress are presented in Fig. 13 for Mo single crystals of various orientations, tested under both uniaxial tension and compression [41]. Entropic contributions to kink-pair nucleation (see Chapter 2, section 3.2) are taken into account using $T_{\text{m}} = T_{\text{melt}} = 2895 \text{ K}$ in the predictions of the model, which are presented for the primary slip system only throughout the whole temperature range in both tension (solid lines) and compression (dashed lines).

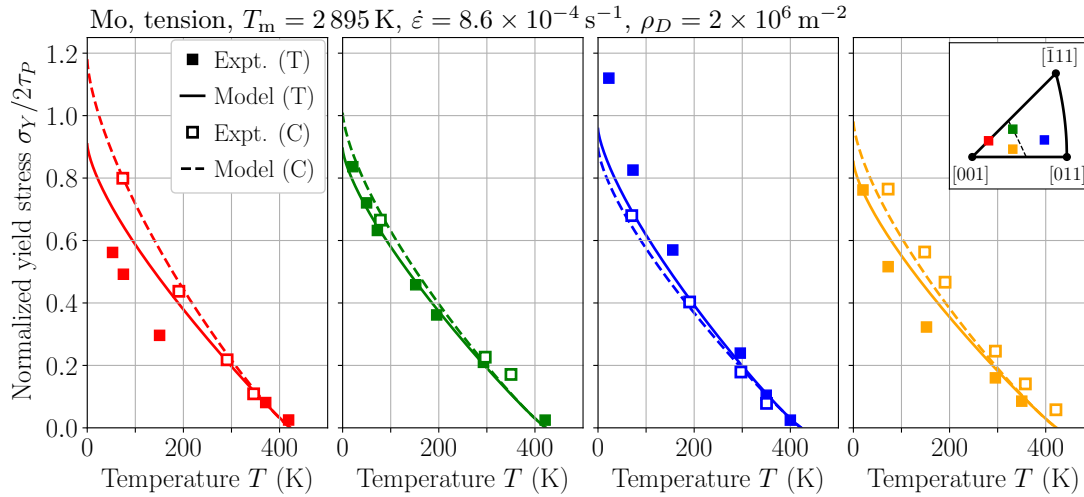


Figure 13: Comparison between experimental [41] and predicted normalized yield stresses in tension (solid lines) and compression (dashed lines). Predicted and experimental yield stresses are normalized by 2.8 and 1.8 GPa respectively.

We note that the sign of the T/C asymmetry predicted by the model, in the sense of the strength differential of Eq. 7, is in very good agreement for all four orientations, as also presented for Mo in Fig. 11 at 0 K. Variations of the yield stress with temperature has a similar shape for all four orientations, in either tension or compression. Apart from a scaling factor of approximately 1.6 between experiments and predictions, variations of both tensile and compressive predicted yield stresses are in good agreement with experiments, showing a pronounced T/AT asymmetry near 0 K. A strong T/C asymmetry is also reported

by the authors, especially for the red orientation, and almost identical tensile and compressive yield stresses for the green orientation, which are both reproduced by the model. The agreement is less satisfactory for the blue orientation, where the strong T/C asymmetry observed experimentally is not predicted. The two T/AT and T/C asymmetries both hold across the whole range of temperature, but become less pronounced near T_{ath} , where the yield stress falls to zero regardless of the orientation and sign of the applied stress, in agreement with the presented experimental data from Liu *et al.* [41], and the work of Seeger and Hollang [222], where Mo single crystals of three different orientations were subjected to cyclic tension/compression deformation in the temperature range from 123 to 460 K.

Conclusions of Chapter 4:

- Predictions of the model reproduce the known features of non-Schmid effects in the yield behavior of bcc transition metals under uniaxial loading. The T/AT asymmetry is predicted in all seven metals, whose amplitude only is metal dependent, linked to the deviation angle of the $\frac{1}{2}\langle 111 \rangle$ screw dislocation trajectory in $\{110\}$ planes. The variations of its relaxation volume tensor, responsible for the T/C asymmetry, show on the other hand much diverse behaviors among bcc metals, also indicating a non-negligible coupling with applied pressure or stresses resolved along the dislocation line for some metals. Consideration of all stress components is thus required when developing a yield criterion.
 - The criterion accurately predicts active $\langle 111 \rangle \{110\}$ slip system and the distribution of the T/C asymmetry observed experimentally in low temperature tension and compression tests.
 - Variations of the yield stress with the orientation of the loading axis are in qualitative agreement with experiments at low temperature, despite the overestimation of the Peierls stress, inherent to atomistic simulations and which is not resolved by accounting for non-Schmid effects, as proposed previously. There are still some discrepancies between experiments and the model, which includes glide properties of single dislocations only, notably on the edges of the standard stereographic triangle, and in the $\chi < 0$ region for Nb where anomalous slip is reported. Accounting for these effects require new mechanisms to be included in the yield criterion, which are the focus of the following two chapters.
 - As presented for Cr in Chapter 2, and extended to W in Ref. [45] and Mo here, the inclusion of the thermally activated glide of $\frac{1}{2}\langle 111 \rangle$ screw dislocations using a line tension model allows for prediction of the temperature dependence of the yield stress. The predicted decreasing yield stress and progressive fade out of non-Schmid effects with increasing temperature are in agreement with experiments.
-

Chapter 5 - Anomalous slip in bcc transition metals

Results of the yield criterion presented for $\langle 111 \rangle \{110\}$ slip across all bcc transition metals in the previous Chapter 4 show discrepancies with experimental data particularly for Nb, where anomalous slip is reported. Such anomalous slip is observed in all bcc metals, except Fe, with slip activity in non expected $\{110\}$ planes, where the required yield stress to activate such $\langle 111 \rangle \{110\}$ slip system is high, and cannot be accounted for when only considering motion of isolated dislocations. We present in this chapter a new mechanism to explain the occurrence of anomalous slip in all bcc transition metals at low temperature based on *in situ* TEM observations, realized by Daniel Caillard at CEMES (CNRS, Toulouse), coupled with atomistic simulations in Nb, which are also presented in details in Ref. [214].

1. Experimental literature review

We begin this chapter by a short review of experimental references reporting occurrence of anomalous slip in bcc transition metals. Experimental observation of anomalous slip has first been reported in Nb [225], and was since then extensively studied in different bcc transition metals. It is characterized by the occurrence of long and straight slip bands in non-expected $\{110\}$ planes with low resolved shear stresses, *i.e.* in planes where $1/2\langle 111 \rangle$ dislocations are subjected to quite low driving forces, *e.g.* about twice lower than for the primary activated slip system. This is clearly at variance with the usual behavior of bcc metals, where wavy and non-crystallographic slip bands correspond to the most activated slip systems (Literature review, section 1.2), which is also observed in bcc transition metals besides of anomalous slip.

Experimentally, anomalous slip exhibits several characteristic features giving precious indications about its possible origin. First, slip bands are very planar, and without so-called “dead bands”: when observed around samples with rounded section, the slip band contrast only decreases along a direction, which is intermediate between the two $1/2\langle 111 \rangle$ shear directions contained in the anomalous $\{110\}$ slip plane, and does not vanish, as expected when the shear direction is locally parallel to the surface. Anomalous slip thus corresponds to the cooperative motion of dislocations with two different $1/2\langle 111 \rangle$ Burgers vectors, which both belong to the anomalous $\{110\}$ slip plane. Second, anomalous slip is observed under uniaxial mechanical loading in both tension and compression, which rules out interpretations based on the role of non-glide stresses, *e.g.* stresses normal to the slip plane, on dislocation mobility [42, 226]. In particular, even if the slip activity differs at low temperature from the predictions of the Schmid law in almost all bcc metals (see Chapter 4, section 2.2), activity of single slip systems is insufficient to account for the absence of dead-bands in the experimental observations. It is also prominent for directions of tensile or compressive axis between the center of the standard stereographic triangle delimited by axis $[001]$ - $[011]$ - $[\bar{1}11]$ and its $[001]$ corner. Third, anomalous slip takes place only at low temperature, *i.e.* below the athermal temperature T_{ath} of the Peierls mechanism. In this temperature range, dislocations align along the direction parallel to their Burgers vector because of the high lattice friction experienced by this screw orientation. Occurrence of anomalous slip therefore appears as a consequence of the reduced mobility of $1/2\langle 111 \rangle$ screw dislocations at low temperature. TEM observations in Nb and Mo also show that straight screws are most often arranged in networks parallel to the anomalous slip bands [37–39, 227, 228]. These planar networks contain the two screw families activated in the bands, which react to form junctions with $\langle 100 \rangle$ Burgers vectors according to the reaction $1/2[111] + 1/2[\bar{1}1\bar{1}] \rightarrow [010]$. Finally, it is observed in high purity materials only, with suppression of anomalous slip with additional substitutional elements (*e.g.* rhenium in Ta [33]) or interstitial impurities (*e.g.* oxygen in V [229], or nitrogen in Nb [230] and Ta [231]). Anomalous slip is not observed in Fe across the wide range of orientations, conditions and temperatures tested in numerous experimental references, contrary to all other bcc metals. Experimental evidences of anomalous slip in all bcc metals, except Fe, are listed in Tab. 1.

Proposed models of anomalous slip are either based on surface effects easing glide of dislocations in the anomalous planes [38, 40, 227], or on the presence of the above-mentioned planar networks. As pointed by Taylor [42], surface effects fail to account for all characteristics of anomalous slip, in particular the

Table 1: Experimental observations of anomalous slip in pure bcc transition metals: deformation mode in tension, compression, or both with experimental reference; temperature range where anomalous slip is reported by the authors, the most relevant range is indicated in red and the range of temperature investigated in brackets; evidence of the occurrence of anomalous slip in the reported dislocation activity of two different dislocation families by TEM ("two b 's"), of through slip line analysis showing absence of dead bands ("no db "); orientation of the loading axis in the standard stereographic triangle with corner axis $[001]$ - $[011]$ - $[\bar{1}11]$; athermal temperature of the Peierls mechanism T_{ath} .

Metal	Deformation mode (T/C)	Temperature range of anomalous slip	Dislocation activity	Orientation of the loading axis	T_{ath}
V	Compression [31]	77-173 K (77-295 K)	No db	Center - near $[001]$	300 - 450 K [233, 234]
	Tension [213]	77 K (77-298 K)	/	/	
	Tension [232]	77 K (77 K)	No db	Between center and $[001]$	
Nb	Tension - [235] Compression	77 K (77 K)	/	/	275 - 375 K [237]
	Tension [36]	4.2-77 K (4.2-77 K)	/	Between center and $[001]$	
	Tension [37]	50 K	Two b 's	Near $[001]$	
	Tension [236]	77 K (77 K)	No db	Center - near $[001]$	
	Tension - [39] Compression	Below 200 K (77-473 K)	No db - two b 's	Between center and $[001]$	
Ta	Tension - [39] Compression	77 K (77-500 K)	No db	Center - between center and $[001]$	400 - 450 K [238]
	Tension - [216] Compression	4.2-77 K (4.2-450 K)	/	Near $[001]$	
	Tension - [33] Compression	77 K (77-293 K)	/	Center - near $[001]$ in tension	
Cr	Compression [34]	77 K (77 K)	/	Center	400 K [126]
Mo	Tension [239]	300 K (300 K)	Two b 's	Center	400 - 450 K [240]
	Compression [228]	300 K (300 K)	Two b 's	Center	
	Tension [38]	77 K (77 K)	Two b 's	/	
W	Tension [239]	300 K (300 K)	/	Center	600 - 800 K [29, 241]
	Compression [40]	300 K (300 K)	/	Center, $[\bar{1}510]$	

activation of two dislocation families. In models based on planar networks, the two dislocation families composing the network are assumed to move cooperatively in the anomalous plane, at a lower applied stress than isolated dislocations thanks to the easier nucleation of kinks on screw dislocations at the network nodes [34, 74, 242, 243]. *In situ* straining experiments in a TEM have shown that such a cooperative motion of dislocations inside the network do exist [37, 227]. However, the networks observed in TEM are so imperfect that it is difficult to imagine how they could glide as a whole over long distances. One thus still does not fully understand the exact origin of anomalous slip in bcc metals.

2. *In situ* straining experiments

In 2021, we have been contacted by Daniel Caillard, who realized *in situ* TEM straining experiments in single crystals of bcc Nb at low temperature, and proposed a new mechanism for explaining anomalous slip in bcc metals. In this respect, we performed atomistic simulations to help investigate this mechanism, which we now present the experimental part. All results are presented in extended data of Ref. [214].

2.1. Experimental methods

Experiments have been carried out in a high-purity (5N) Nb single crystal bought at Goodfellow containing less than 1 ppm of O, C, N, and Si, and less than 0.1 ppm of other elements. Nb microsamples have been cut in a (501) plane with a tensile loading direction $\vec{t} = [\bar{1}05]$, which is thus always vertical in the images. The horizontal direction is accordingly along the [010] axis. Referring to the stereographic projection in Fig. 4 (see upper right panel), the four dislocations of Burgers vectors $\vec{b}_1 = 1/2[\bar{1}\bar{1}\bar{1}]$, $\vec{b}_2 = 1/2[111]$, $\vec{b}_3 = 1/2[\bar{1}\bar{1}1]$ and $\vec{b}_4 = 1/2[\bar{1}1\bar{1}]$ are activated in planes $P_{12} = (10\bar{1})$, $P_{34} = (101)$ and $P_{23} = (0\bar{1}1)$. Nb microsamples are strained in the Gatan low-temperature straining holder working at 95 K. Samples are observed in a JEOL 2010-HC TEM operating at 200 kV.

2.2. Glide of isolated $1/2\langle 111 \rangle$ screw dislocations and networks in niobium

Observation of isolated $1/2\langle 111 \rangle$ screw dislocations gliding in Nb under strain, recorded *in situ* in TEM at different times, are presented in Fig. 1. Frames a) and b) follow the motion of the same dislocations at two different times, while frame c) is obtained by taking the difference between these two images, showing the dislocation motion in the time interval with initial and final positions appearing in black and white contrast respectively. The motion of this dislocation of Burgers vector $\vec{b}_4 = 1/2[\bar{1}\bar{1}\bar{1}]$ is sketched in d), with initial and final positions represented by solid and dashed lines respectively. The slip traces left on the thin foil surface by the gliding dislocations, noted 'tr', correspond to non-crystallographic slip planes. The four dislocation families appearing in Fig. 1, with different Burgers vectors \vec{b}_1 , \vec{b}_2 , \vec{b}_3 , and \vec{b}_4 , are identified and can be distinguished in the images thanks to their different directions and lengths in projection. The dislocations straighten along their screw orientation when gliding, with a slow and steady motion at an average velocity of the order of 5 nm/s, consistent with a conventional motion of screw dislocations at low temperature, controlled by the nucleation of kink-pairs.

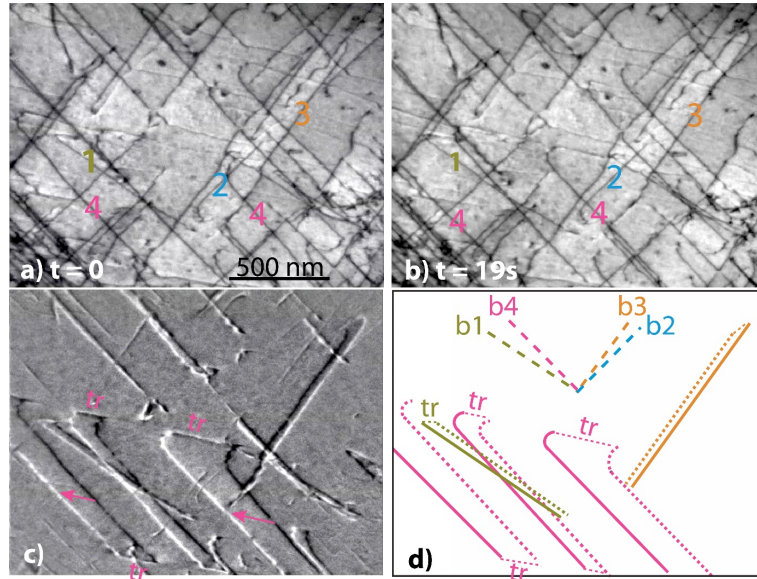


Figure 1: *In situ* TEM images recorded at different times, showing glide of isolated $1/2\langle 111 \rangle$ screw dislocations in Nb at 95 K.

Dislocation networks are also identified, with a motion imaged on Fig. 2. These networks are made of two interacting $1/2\langle 111 \rangle$ screw dislocation families with Burgers vectors $\vec{b}_1 = 1/2[\bar{1}\bar{1}\bar{1}]$ and $\vec{b}_2 = 1/2[111]$, and which form junctions with Burgers vector $\vec{b}_{JR} = [010]$. These networks glide in the $P_{12} = (10\bar{1})$ plane, containing the three dislocation families, at a velocity of about 15 nm/s for the fastest nodes, therefore only slightly higher than neighboring isolated screw dislocations. Networks are thus not much more mobile than individual dislocations. The often-proposed mechanism, with easy kink nucleation at the nodes leading to

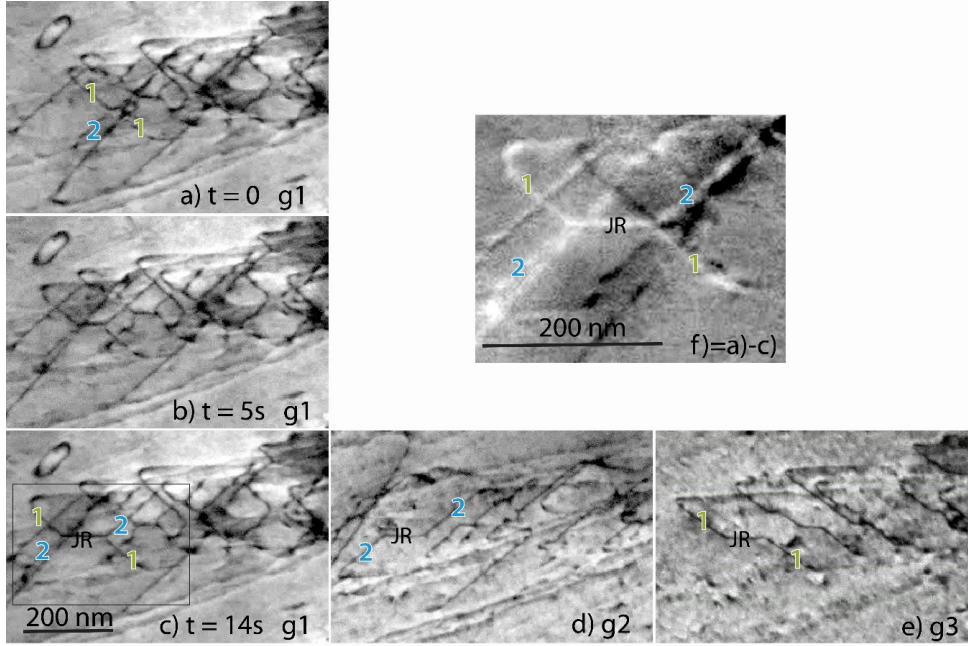


Figure 2: Glide of a network in Nb made of two interacting screw dislocation families with Burgers vectors $\vec{b}_1 = 1/2[\bar{1}1\bar{1}]$ and $\vec{b}_2 = 1/2[111]$, forming horizontal junctions with Burgers vector $[010]$ through the reaction $1/2[\bar{1}1\bar{1}] + 1/2[111] = [010]$. Diffraction vectors are $\vec{g}_1 = (010)$ (for which all dislocations are in contrast), $\vec{g}_2 = (011)$, and $\vec{g}_3 = (011)$.

fast glide of the network in the anomalous $\{110\}$ slip plane [74], is thus inoperative in real situations where dislocation networks are not perfectly planar. Similar observation of the motion of dislocation networks have been reported by Holzer *et al.* [34] in Cr at 77 K under compression, which was attributed by the authors to the occurrence of anomalous slip. However, as demonstrated here for Nb, such mechanism fails to account for all characteristic features of anomalous slip listed in section 1.

2.3. Rapid motion of multi-junctions in niobium

During the same *in situ* TEM straining experiments, it was observed in the same experiments a completely different and new behavior: a very fast motion of a group of four straight screw dislocations connected at a single node (Fig. 3). These dislocations glide cooperatively over large distances at a velocity higher than $50 \mu\text{m/s}$, thus several orders of magnitude higher than individual dislocations ($\simeq 5 \text{ nm/s}$ on Fig. 1) or dislocation networks ($\simeq 15 \text{ nm/s}$ on Fig. 2). This fast motion is generally issued from a dense region containing tangles of two or more dislocation families and leaves two sets of horizontal traces at the two foil surfaces corresponding to the two orthogonal glide planes $P_{12} = (\bar{1}01)$ and $P_{34} = (101)$. Twenty similar events have been recorded in different Nb samples, three of which are presented in Fig. 3, showing that such a motion is not unusual. The four screw dislocations connected at the node have necessarily different Burgers vectors that sum up to zero, explaining why no dislocation is left behind after the node has glided.

We see in the TEM images the cooperative glide of the four screw dislocations over a large distance in less than 40 ms, and have created two sets of slip traces on the two foil surfaces corresponding to planes $P_{12} = (10\bar{1})$ and $P_{34} = (101)$, clearly visible as horizontal lines with a white contrast in the image differences (iii). The node can only glide along the $[010]$ direction defined by the intersection of the two $\{110\}$ planes, thus constraining \vec{b}_1 and \vec{b}_2 on the one hand, and \vec{b}_3 and \vec{b}_4 dislocations on the other hand, to glide respectively in P_{12} and P_{34} planes. As this $[010]$ direction lies in the foil plane, this makes it possible to observe the fast motion of the four-dislocation node along this direction. Otherwise, the node would have rapidly disappeared at a surface. Since the four dislocations glide cooperatively at an abnormal high velocity in planes P_{12} and

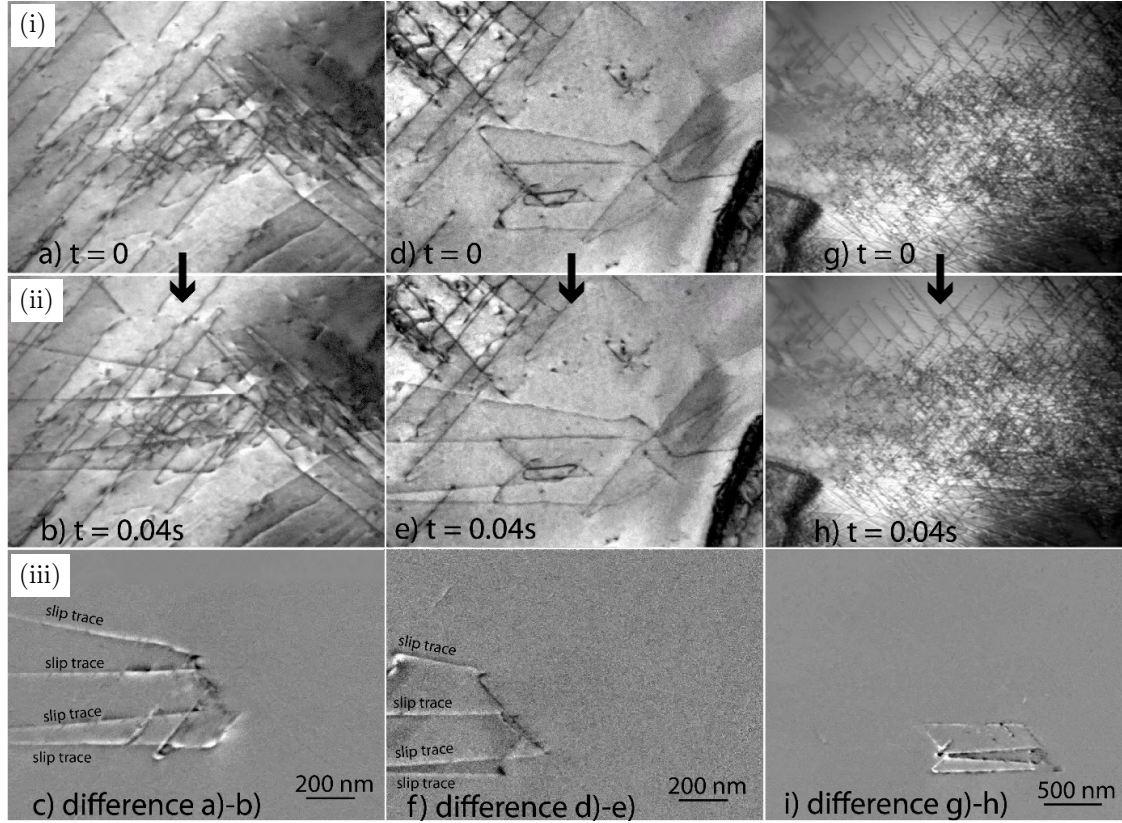


Figure 3: Three different events showing four $\frac{1}{2}\langle 111 \rangle$ screw dislocations connected to a node which glide cooperatively in two different planes over a large distance in less than 40 ms. The sets of slip traces left of the two foil surfaces correspond to planes $P_{12} = (10\bar{1})$ and $P_{34} = (101)$. The node is forced to glide along $[010]$, defined by the intersection of these two planes.

P_{34} where the driving resolved shear stress is not the highest (see Tab. 2), we believe that such a highly surprising behavior is the true origin of anomalous slip. The maximum Schmid factors are obtained for dislocations \vec{b}_3 and \vec{b}_4 gliding respectively in P_{23} and P_{14} , thus defining the primary slip systems (in red). *In situ* TEM tensile experiments (Fig. 3) show that the same \vec{b}_3 and \vec{b}_4 dislocations glide in P_{34} , despite the lower Schmid factor (indicated by a *) and that \vec{b}_1 and \vec{b}_2 dislocations glide in P_{12} (also indicated by a *).

Table 2: Schmid factors (SF) of the 12 different $\langle 111 \rangle \{110\}$ slip systems considering a $[\bar{1}05]$ tensile axis

Slip direction	Glide plane	SF	Slip direction	Glide plane	SF
$\vec{b}_1 = \frac{1}{2}[\bar{1}\bar{1}\bar{1}]$	$P_{13} = (110)$	0.063	$\vec{b}_1 = \frac{1}{2}[\bar{1}\bar{1}\bar{1}]$	$P_{12} = (10\bar{1})$	0.377*
$\vec{b}_3 = \frac{1}{2}[\bar{1}\bar{1}\bar{1}]$	$P_{13} = (110)$	0.094	$\vec{b}_2 = \frac{1}{2}[\bar{1}11]$	$P_{12} = (10\bar{1})$	0.377*
$\vec{b}_2 = \frac{1}{2}[\bar{1}11]$	$P_{24} = (\bar{1}10)$	0.063	$\vec{b}_1 = \frac{1}{2}[\bar{1}\bar{1}\bar{1}]$	$P_{14} = (011)$	0.314
$\vec{b}_4 = \frac{1}{2}[\bar{1}\bar{1}\bar{1}]$	$P_{24} = (\bar{1}10)$	0.094	$\vec{b}_4 = \frac{1}{2}[\bar{1}\bar{1}\bar{1}]$	$P_{14} = (011)$	0.471
$\vec{b}_3 = \frac{1}{2}[\bar{1}\bar{1}\bar{1}]$	$P_{34} = (101)$	0.377*	$\vec{b}_2 = \frac{1}{2}[\bar{1}11]$	$P_{23} = (01\bar{1})$	0.314
$\vec{b}_4 = \frac{1}{2}[\bar{1}\bar{1}\bar{1}]$	$P_{34} = (101)$	0.377*	$\vec{b}_3 = \frac{1}{2}[\bar{1}\bar{1}\bar{1}]$	$P_{23} = (01\bar{1})$	0.471

The detailed mechanism observed in the presented TEM observations is sketched in Fig. 4, with the corresponding TEM images. The observed time sequence a)-d) and its schematic description f)-k) show the

formation of a node connecting four $\frac{1}{2}\langle 111 \rangle$ screw dislocations and its rapid glide out of the observation zone. The starting configuration in **a)** is made of two $\frac{1}{2}\langle 111 \rangle$ screw dislocations $\vec{b}_1 = \frac{1}{2}[\bar{1}\bar{1}\bar{1}]$ and $\vec{b}_2 = \frac{1}{2}[111]$ reacting to form a junction JR of Burgers vector $\vec{b}_{JR} = [010]$. The three dislocations are contained in their common slip plane $P_{12} = (10\bar{1})$. Another screw dislocation $\vec{b}_3 = \frac{1}{2}[\bar{1}\bar{1}\bar{1}]$ glides to the bottom left in its slip plane $P_{23} = (0\bar{1}1)$ and intersects in **b)** the junction reaction JR. In the next frame **c)**, separated from the previous one by only 40 ms, the investigated process has already occurred, with the creation of four slip traces corresponding to glide planes $P_{12} = (10\bar{1})$ and $P_{34} = (101)$ and the disappearance of several dislocation segments. The image difference **e)** allows connecting these slip traces to the glide of the three previous screw dislocations and an additional dislocation $\vec{b}_4 = \frac{1}{2}[\bar{1}\bar{1}\bar{1}]$, which results from the reaction between \vec{b}_3 and the junction reaction JR, as sketched in **h)**. This fourth dislocation extends and forms in the plane P_{34} a screw dipole in **i)** which emerges at the bottom surface in **j)**. The whole configuration is then divided in two parts, a group of four screw dislocations connected to a node which rapidly glides to the left out of the observation zone and a remaining tangle on the right (see **k)**), where the screw segment 4 has shortened its length by cross-slip. The last image **d)** shows the subsequent evolution of the short segment 4 forming another screw dipole which is used to check that dislocation 4 has the expected Burgers vector \vec{b}_4 .

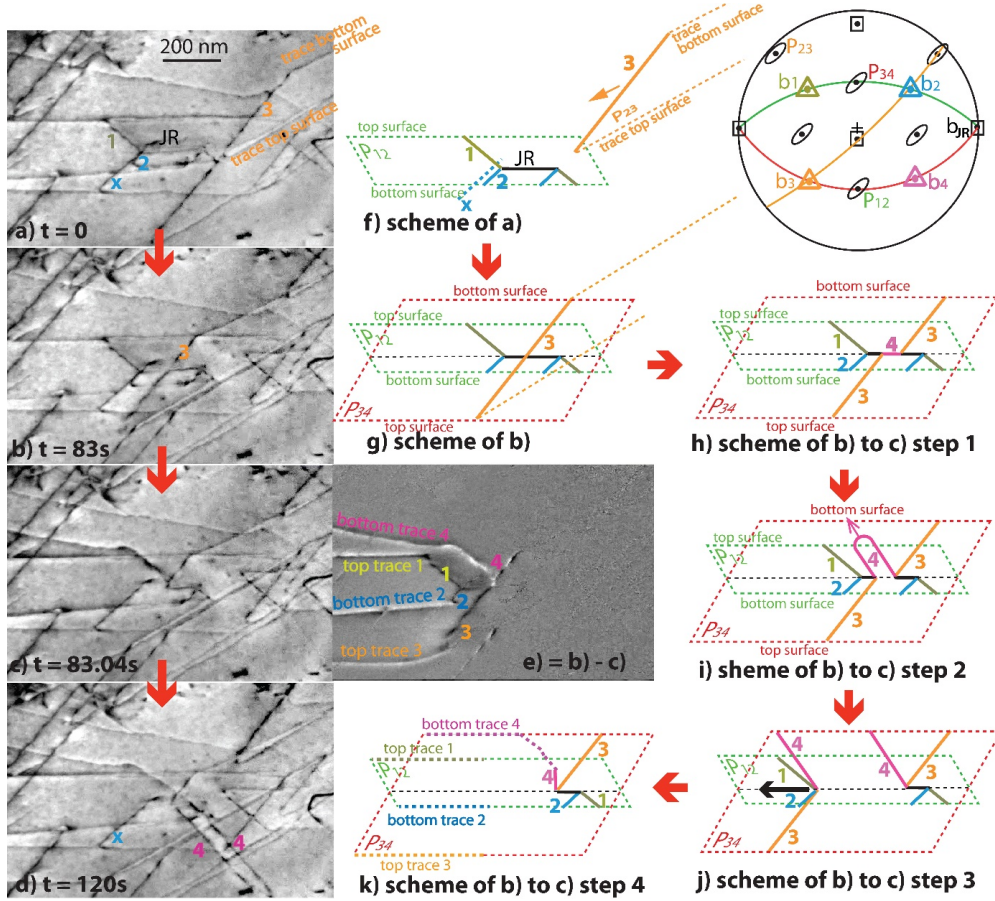


Figure 4: TEM images and sketch of the mechanism for the formation and glide of four-dislocation nodes observed in Nb.

3. Atomistic simulations and elastic model

We present in this section atomistic simulations performed in order to gain a better understanding of the

different steps of the mechanism proposed for anomalous slip presented in Fig. 4 in the previous section. All atomistic simulations presented here were performed using the LAMMPS code [157] with the interatomic potentials presented in section 1.4 in Methods. These atomistic simulations are coupled with simple elastic models, whose ingredients helped get insights on the energetic mechanisms at stake.

3.1. Relaxation of a four-dislocation node

We begin this section with molecular static relaxation of the node in Nb at 0 K, presented in the sketch of the mechanism in Fig. 4, to investigate the origin of the driving force explaining the fast motion of the four-dislocation node observed experimentally (less than 40 ms). The simulation cell used for the relaxation of the four-dislocation node, imaged experimentally in Fig. 3, is defined by the three vectors $X = 120 \times [010]$, $Y = 80 \times [001]$ and $Z = 80 \times [100]$, with free surfaces in all three Cartesian directions. Four screw dislocation segments with Burgers vectors $\vec{b}_1 = 1/2[\bar{1}\bar{1}\bar{1}]$, $\vec{b}_2 = 1/2[111]$, $\vec{b}_3 = 1/2[1\bar{1}\bar{1}]$ and $\vec{b}_4 = 1/2[\bar{1}\bar{1}1]$ are introduced so as to intersect on a node located in the simulation cell at the two thirds of the cell height, in the $X \parallel [010]$ direction. The four screw dislocation segments come out of the simulation cell on each external $[010]$ edge. The structure is then relaxed using molecular statics at zero temperature with the EAM potential of Fellingner *et al.* [158]. The initial configuration of the system is shown in dashed lines in Fig. 5, with the relaxed positions of atoms belonging to the dislocation cores after relaxation of the system represented by spheres.

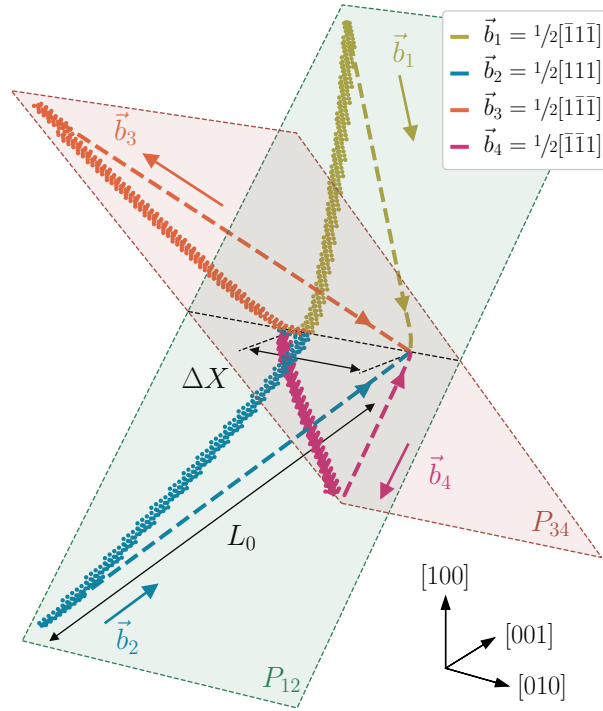


Figure 5: Molecular statics relaxation of the node connecting four screw dislocations with different Burgers vectors in Nb, each of an initial length L_0 . Colored spheres correspond to atoms belonging to the relaxed dislocation cores.

We note that relaxing such a node connecting four screw dislocations with Burgers vectors $\vec{b}_1 = 1/2[\bar{1}\bar{1}\bar{1}]$, $\vec{b}_2 = 1/2[111]$, $\vec{b}_3 = 1/2[1\bar{1}\bar{1}]$ and $\vec{b}_4 = -\vec{b}_1 - \vec{b}_2 - \vec{b}_3 = 1/2[\bar{1}\bar{1}1]$, one sees that the node prevents the dislocations from conserving their screw orientation, which glides along the $[010]$ direction over a distance ΔX . Dislocations instead relax to a mixed orientation in their P_{12} and P_{34} glide planes, with the node producing the kinks necessary to the dislocation motion. Further analysis with anisotropic elasticity theory, presented below, shows that the line tension exerted by the dislocations on the node is responsible for this relaxation

of the dislocations from a screw to a mixed orientation and that this behavior is generic to bcc metals. Once the dislocations have lost their screw character, they can glide without experiencing any noticeable lattice friction under a small applied stress, leading to the fast and long-distance motion observed in TEM. The four dislocations will then recover their screw character when they stop at an extrinsic obstacle (*e.g.* impurity, surface, grain boundary or another dislocation).

We now detail the formalism for the development of line energy model to study the elastic driving force for the displacement of the node. The elastic energy per unit length of a straight infinite dislocation line of Burgers vector \vec{b} and character θ is given by the following according to elasticity theory:

$$E(\theta) = \frac{b_i [K_{ij}(\theta)] b_j}{4\pi} \ln \left(\frac{R_\infty}{r_C} \right) = e(\theta) \ln \left(\frac{R_\infty}{r_C} \right), \quad (1)$$

where b is the norm of the Burgers vector, R_∞ is the outer cutoff radius for elastic interactions, r_C is the core cutoff radius where the long-range elastic interactions fade out, and \bar{K} is the Stroh tensor, function of the elastic constants of the material and the orientation of the dislocation line θ with respect to its Burgers vector. An analytical evaluation of the Stroh tensor in the frame of anisotropic elasticity theory is not possible for all character θ of the line, hence it is evaluated numerically using the BABEL package [165] with experimental elastic constants measured at 4.2 K (see Tab. 2 in the Literature review). The anisotropic elastic energies of $1/2\langle 111 \rangle$ dislocations are presented in Fig. 2 in the Literature review as a function of their character θ . Then, the elastic energy of a dislocation microstructure composed of several interconnected dislocation segments is described in the frame of the line-tension approximation, neglecting interactions between dislocation segments, with a total energy:

$$E^{elas}(\{X_i\}) = \left[\sum_i e(\theta_{i,i+1}) \times L_{i,i+1} \right] \ln \left(\frac{R_\infty}{r_C} \right), \quad (2)$$

where $\theta_{i,i+1}$ and $L_{i,i+1}$ are respectively the character and length of the segment joining nodes i and $i+1$ located at positions X_i and X_{i+1} . We stress that in such elastic model, all contributions due to interaction between dislocations and their cores are neglected.

We now use this line energy model to study the relaxation of the quadri-junction (QJ) formed by four intersecting $1/2\langle 111 \rangle$ screw dislocation segments connected at a node N, where the condition on the Burgers vectors $\vec{b}_1 + \vec{b}_2 + \vec{b}_3 + \vec{b}_4 = \vec{0}$ is satisfied. The system is composed of the four dislocation segments, which all intersect at the node N, and are linked to fixed points at their other ends (see the sketch of the system in Fig. 6). The dislocations, in their screw orientation, have an initial length L_0 . In the frame of the line energy model, the total elastic energy of the quadri-junction is:

$$E_{QJ}^{elas}(\theta) = 4e(\theta) \frac{L_0 \cos(\psi_0)}{\cos(\psi_0 - \theta)} \ln \left(\frac{R_\infty}{r_C} \right), \quad (3)$$

where θ is the character of the four $1/2\langle 111 \rangle$ dislocations connected at the node N. As observed in atomistic simulations, relaxation of the quadri-junction leads to glide of the node along the direction $[010]$ defined by the intersection of the slip planes of the four dislocations. After such a glide motion, each dislocation segment acquires the same character θ and has a length $L_0 \cos(\psi_0) / \cos(\psi_0 - \theta)$, where ψ_0 is the angle between the initial screw orientation of the segments and the (010) plane normal to the glide direction of the node. By minimizing the above Eq. 3 with respect to the character θ and replacing the cosines of the angle with its numerical values, we obtain the following equilibrium condition on the character minimizing the elastic energy of the quadri-junction:

$$\frac{e'(\theta_N)}{e(\theta_N)} = \tan(\psi_0 - \theta_N) = \frac{1 - \sqrt{2} \tan(\theta_N)}{\sqrt{2} + \tan(\theta_N)}, \quad (4)$$

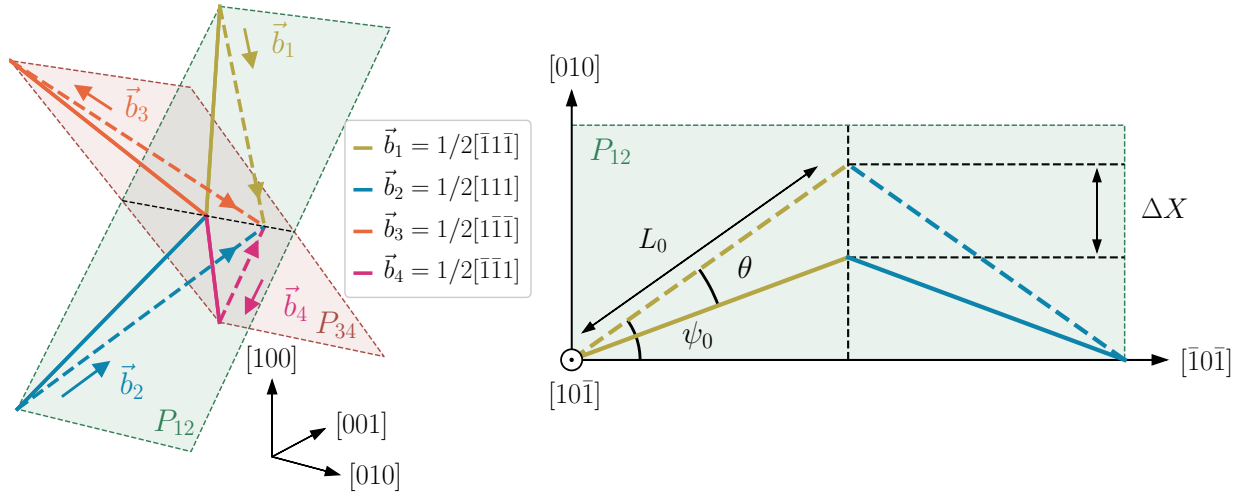


Figure 6: Definition of the notations introduced for the formulation of the line energy model of the four-dislocation node, with projection onto the $P_{12} = (10\bar{1})$ plane, showing the displacement of the node ΔX along the $[010]$ direction and character θ of the four $1/2\langle 111 \rangle$ dislocation segments of initial length L_0 .

which has to be solved numerically. The displacement of the node ΔX is then determined geometrically from the value of the equilibrium character θ_N , solution of Eq. 4, given by:

$$\frac{\Delta X}{L_0} = \sin(\psi_0) - \cos(\psi_0) \tan(\psi_0 - \theta_N) = \frac{\sqrt{3}}{3} \left[1 - \sqrt{2} \frac{e'(\theta_N)}{e(\theta_N)} \right], \quad (5)$$

showing the displacement ΔX of the node is proportional to the initial length L_0 of the dislocation segments. The results obtained using the line energy model are presented in Tab. 3 for all bcc transition metals, considering anisotropic elasticity theory with experimental elastic constants. In all bcc transition metals, relaxation of the quadri-junction forces the four dislocation segments to leave their screw orientation, with a mixed equilibrium character θ_N varying between 10 and 30°, depending on the elastic anisotropy ratio A of the bcc metal. The line tension exerted by the four dislocations on the node thus prevents the dislocations from keeping their screw orientation, as observed in our atomistic simulations in Nb presented in Fig. 5, thus allowing for easy glide of these four dislocations connected to the node.

Table 3: Elastic anisotropy ratio A , equilibrium character θ_N of the four dislocation segments, and displacement ΔX of the node normalized by the initial length L_0 of the dislocation segments obtained after relaxation of the four-dislocation node.

Metal	A	θ_N	$\Delta X/L_0$
Nb	0.50	25.7°	0.44
Cr	0.68	29.3°	0.49
Mo	0.77	24.8°	0.45
V	0.78	21.1°	0.37
W	1.00	21.2°	0.37
Ta	1.56	13.0°	0.24
Fe	2.38	10.0°	0.19

To validate the results of the line energy model, we compare its predictions with results of molecular statics relaxation of a four-dislocation node in both Nb and W, using the EAM potential of Fellingner *et al.*

[158] and the MEAM potential of Park *et al.* [89] for the two metals respectively. A qualitative agreement is found for both metals, as presented in Fig. 7. Like predicted by the model, the displacement ΔX of the node is proportional to the initial length L_0 of the dislocation segments, as $\Delta X(L_0) = a L_0$. The line energy model predicts a lower slope in W than in Nb, in agreement with the results of atomistic simulations. In both metals, the slope a observed in atomistic simulations is lower than the one predicted by the model. This difference may be the consequences of atomic effects in the dislocation core or of the elastic interactions between the different dislocation segments which are both neglected in the model.

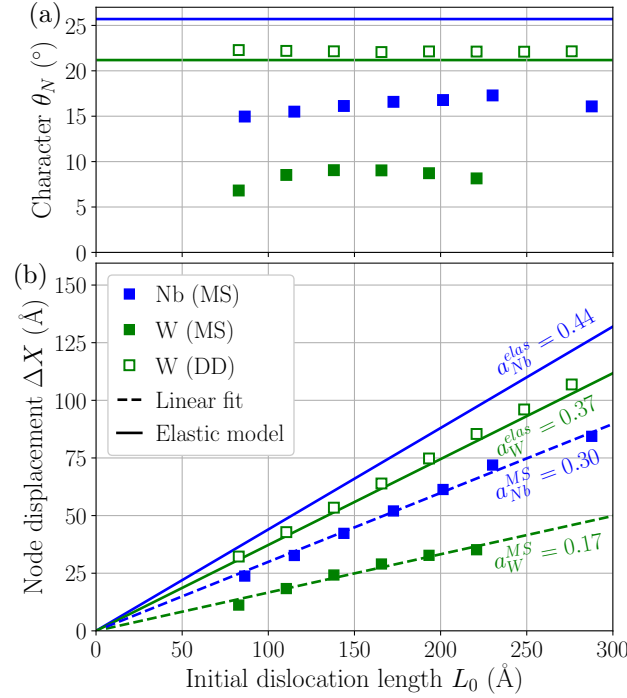


Figure 7: (a) Equilibrium character θ_N of the four segments, and (b) displacement of the node ΔX along the [010] axis as a function of the initial length L_0 of the screw segments. Predictions of the line energy model (solid lines) are compared to results of molecular statics relaxations in Nb and W (filled squares and dashed lines) and of DD simulations in W (open squares).

To better understand this difference between predictions of the line energy model and results of atomistic simulations, we perform additional simulations in W. As the elastic response of tungsten is close to isotropy, one can use isotropic dislocation dynamics (DD) simulations [244] to relax the four-dislocation node. These simulations only consider elasticity and neglect any core contributions, but, contrary to our simple line energy model, they take full account of elastic interactions between the different dislocation segments. These simulations are performed with the DDLab code developed by Wei Cai [245], using a Poisson's ratio $\nu = 0.27$ for W. Relaxation of a four-dislocation node with the isotropic DD code leads to $\Delta X/L_0 = 0.38$ (see Fig. 7b), in very good agreement with the value $\Delta X/L_0 = 0.37$ given by our line energy model. One can thus conclude that elastic interactions between segments have a negligible impact on the relaxation of the four-dislocation node, with dislocation line energies being the main driving force of this relaxation. The neglect of these elastic interactions in our line energy model is not the reason for the highest slope $\Delta X/L_0$ predicted by the model compared to atomistic simulations. The only contribution left to explain this difference is then the dislocation core energy. In bcc metals, the screw orientation of the $\frac{1}{2}\langle 111 \rangle$ dislocation gliding in a $\{110\}$ plane is a minimum of the core energy and corresponds to a marked cusp [246]. Hence, as the four intersecting segments change their characters to trigger the displacement of the node, the core energy, per unit of length, of the four dislocation segments increases. The force resulting from this core contribution tends to maintain the $\frac{1}{2}\langle 111 \rangle$ dislocation in their screw orientations, partly counterbalancing elastic effects. The neglect of this core contribution in our line energy model could thus be the reason why the model

overestimates the slope $\Delta X/L_0$ when compared to atomistic simulations.

Despite this difference on the slope $\Delta X/L_0$ with results of atomistic simulations, the line energy model allows rationalizing the driving forces for the relaxation of the four-dislocation node, showing that the minimization of the dislocation line energy is the main contribution preventing the dislocations to keep their screw orientations when they intersect at such a node. This displacement of the node proportional to the initial length of the four screw dislocation segments corresponds to the situation where no stress is applied to the dislocations. With an applied stress leading to a driving force on the dislocations, as the dislocations are not aligned anymore along their screw orientations, they will easily glide, thus leading to the long distance glide of the four dislocation node observed experimentally.

3.2. Formation of a four-dislocation node

Now that the mechanism leading to the fast motion of the node has been investigated, showing the spontaneous nucleation of kinks at the node driven by the line tension exerted by the four $1/2\langle 111 \rangle$ dislocations, we investigate the mechanism leading to its formation using atomistic simulations. The formation of the four-dislocation node in Nb is modeled in a simulation cell defined by the three vectors $X = 120 \times [010]$, $Y = 120 \times [101]$ and $Z = 40 \times [101]$, with free surfaces in all Cartesian directions, presented in Fig. 8.

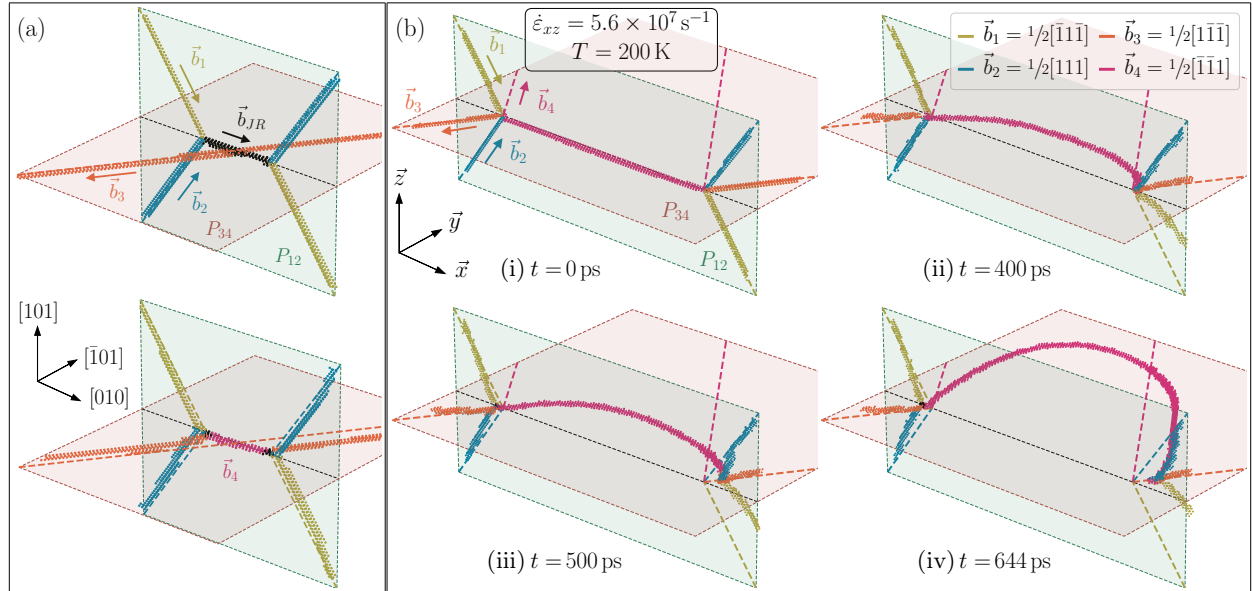


Figure 8: (a) A $\vec{b}_3 = 1/2[\bar{1}\bar{1}\bar{1}]$ screw dislocation reacts with a $\vec{b}_{JR} = [010]$ junction formed by the intersection between two screw dislocations $\vec{b}_1 = 1/2[\bar{1}\bar{1}\bar{1}]$ and $\vec{b}_2 = 1/2[111]$. Upon relaxation by molecular statics, a mixed $\vec{b}_4 = 1/2[\bar{1}\bar{1}\bar{1}]$ dislocation is formed, leading to two nodes connecting four different $1/2\langle 111 \rangle$ dislocations. (b) Upon straining in molecular dynamic simulations, the mixed \vec{b}_4 dislocation bows out and tends to its screw orientation (dashed lines) close to the node, which starts to glide.

The starting configuration is made of two screw dislocations $\vec{b}_1 = 1/2[\bar{1}\bar{1}\bar{1}]$ and $\vec{b}_2 = 1/2[111]$ which have reacted to form a screw junction with Burgers vector $\vec{b}_{JR} = 1/2[\bar{1}\bar{1}\bar{1}] + 1/2[111] = [010]$, introduced piecewise in the center of the simulation cell (see upper panel in Fig. 8a). The $[010]$ junction has a length of $20a_0$, with a_0 the lattice parameter. Atomistic simulations and anisotropic elasticity, both presented in the next section 3.3, show that such a reaction is energetically favorable in Nb. All dislocations, the two \vec{b}_1 and \vec{b}_2 screw dislocations and the \vec{b}_{JR} junction reaction, are contained in their common $P_{12} = (10\bar{1})$ slip plane. After relaxation of the junction, a third screw dislocation with Burgers vector $\vec{b}_3 = 1/2[\bar{1}\bar{1}\bar{1}]$ is introduced, and intersects the $[010]$ junction in its middle. Upon relaxation, the $[010]$ junction unzips, leading to the creation of a mixed dislocation with the fourth Burger vector $\vec{b}_4 = -\vec{b}_{JR} - \vec{b}_3 = 1/2[\bar{1}\bar{1}\bar{1}]$ and a length of

$20a_0$ located where the junction laid before its intersection (lower panel in Fig. 8a). Molecular dynamics simulations of the bowing of this \vec{b}_4 dislocation are presented in Fig. 8b, performed in the same dynamics cell as the static relaxations just described in Fig. 8a, but for an initial length of $80a_0$ of this \vec{b}_4 dislocation. The temperature is set to $T = 200$ K and the strain rate $\dot{\varepsilon}_{xz} = 5.6 \times 10^7 \text{ s}^{-1}$ (see Methods, section 2.2).

As the \vec{b}_4 segment bows out under the applied stress, a screw dipole starts to expand in the P_{34} plane. As soon as it reaches its screw orientation (indicated by dashed lines in Fig. 8b), a four-dislocation node is created. The whole configuration is then divided in two parts, also observed in TEM: a group of four screw dislocations connected to a node, which rapidly glide to the left, and a remaining dislocation tangle on the right (see TEM images presented in Fig. 3). The detailed mechanism proposed based on TEM observations presented in section 1 is thus confirmed by atomistic simulations, which allowed for determining both the driving force for the fast motion of the four-dislocation node, and its formation under dynamic conditions, where experiments did not allow for imaging the whole process. This new mechanism to explain anomalous slip thus occurs in four steps: **(1)** a $\langle 100 \rangle$ junction forms from two intersecting $1/2\langle 111 \rangle$ screw dislocations; **(2)** a third \vec{b}_3 screw dislocation intersects the junction to create a mixed \vec{b}_4 segment; **(3)** as the \vec{b}_4 dislocation bows out to create a screw dipole, a four-dislocation node connecting the four segments is created; **(4)** "free" nucleation of kinks at the node allows for the fast motion over long distances of the four dislocations in the two orthogonal P_{12} and P_{34} planes, as observed in TEM.

3.3. Formation of $\langle 100 \rangle$ junctions

These $\langle 100 \rangle$ junctions, resulting from the intersection between two $1/2\langle 111 \rangle$ screw dislocations, appear as an essential ingredient for the occurrence of anomalous slip at low temperature since they are necessary for the creation of glissile multi-junctions. We stress that since anomalous slip occurs only at low temperature, $1/2\langle 111 \rangle$ dislocations are aligned along their screw orientations due to the high lattice friction they experience. Therefore, we only consider formation of $\langle 100 \rangle$ junctions from two intersecting $1/2\langle 111 \rangle$ screw dislocations. At higher temperature, above the athermal temperature T_{ath} of the Peierls mechanism where lattice friction opposing dislocation glide vanishes (see experimental values in Tab. 1 for all bcc transition metals), $1/2\langle 111 \rangle$ dislocations can take any orientation of mixed character, facilitating formation of $\langle 100 \rangle$ junctions as detailed in Appendix F. We study in this section their spontaneous formation resulting from the intersection between two $1/2\langle 111 \rangle$ screw dislocations, using both molecular statics relaxations and a line energy model developed in the same formalism as presented in the previous section 3.1 for the relaxation of the four-dislocation node.

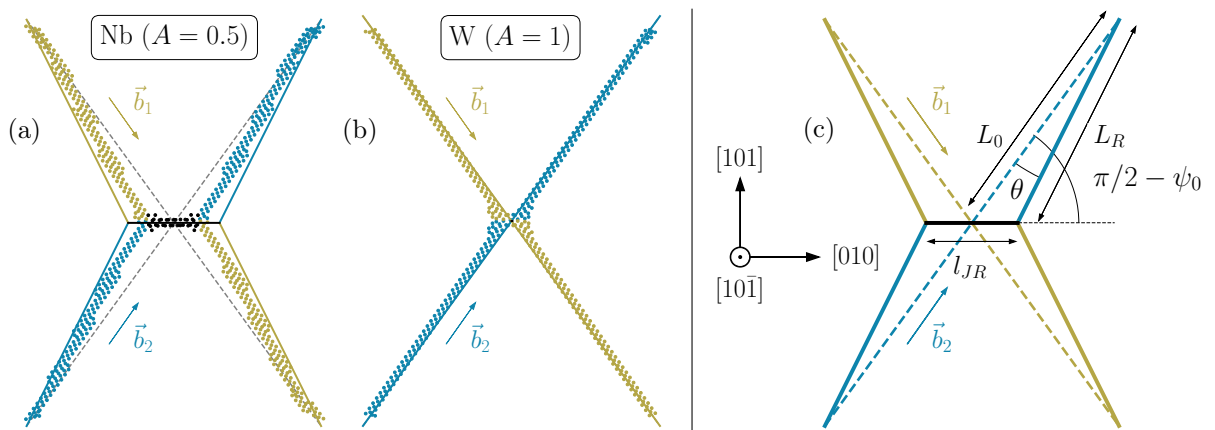


Figure 9: Superposition of the relaxed configuration obtained after molecular statics relaxation (colored spheres) and the predictions of the line energy model (solid lines) for two initially screw $1/2\langle 111 \rangle$ dislocations intersecting to form a $\langle 100 \rangle$ screw junction in (a) Nb and (b) W. (c) Sketch of the formation of a $[010]$ screw junction reaction of length l_{JR} resulting from the intersection of two initially screw dislocations of Burgers vectors $\vec{b}_1 = 1/2[111]$ and $\vec{b}_2 = 1/2[111]$.

For molecular statics relaxations, the geometry of the simulation cell is defined by the three vectors $X = 80 \times [010]$, $Y = 40 \times [101]$ and $Z = 20 \times [10\bar{1}]$, with periodic boundary conditions along X , and free surfaces in the Y and Z directions. Two $1/2\langle 111 \rangle$ screw dislocations having Burgers vectors \vec{b}_1 and \vec{b}_2 , satisfying $\vec{b}_1 + \vec{b}_2 = \vec{b}_{\text{JR}} = [010]$, are introduced in the cell, and cross each other at its center. The relaxed structures are presented in Fig. 9a and b in Nb and W respectively, where only atoms belonging to the dislocation cores are shown, and the starting configuration is represented by dashed grey lines.

Upon relaxation, we see the spontaneous formation of a $\langle 100 \rangle$ junction in Nb, but not in W. We also note that the two $1/2\langle 111 \rangle$ dislocations leave their initial screw character upon formation of the junction, taking a mixed orientation of character θ . To rationalize the driving force leading to the formation of these $\langle 100 \rangle$ junctions in bcc transition metals, in particular why it spontaneously forms in Nb and not W, we now consider the same system using a line energy model, based on the formalism introduced in section 3.1, sketched in Fig. 9c. For the formation of the $\langle 100 \rangle$ junction to be energetically favorable, the elastic energy needs to decrease upon its formation. The energy variation associated with the junction formation is:

$$\Delta E^{\text{elas}}(l_{\text{JR}}) = 4L_R E^{\langle 111 \rangle}(\theta) + l_{\text{JR}} E_{\text{screw}}^{\langle 100 \rangle} - 4L_0 E_{\text{screw}}^{\langle 111 \rangle}, \quad (6)$$

with L_0 and L_R the initial and relaxed lengths of the $1/2\langle 111 \rangle$ dislocation segments intersecting at the node, and l_{JR} the junction length (see sketch in Fig. 9c for notations). The $1/2\langle 111 \rangle$ dislocations are initially in screw orientation and have a character θ after formation of the junction, with the corresponding linear energy $E_{\text{screw}}^{\langle 111 \rangle}$ and $E^{\langle 111 \rangle}(\theta)$. $E_{\text{screw}}^{\langle 100 \rangle}$ is the linear energy of the junction reaction, which is of screw character here, but can also have other orientation as detailed in Appendix F and section 1.2 of the next chapter. The length of the junction reaction is found by minimizing Eq. 6. To do so, we need first to express the length L_R of the relaxed $1/2\langle 111 \rangle$ dislocation segments and their character θ as functions of l_{JR} . Simple geometry leads to the expression:

$$L_R = L_0 \sqrt{1 - 2 \sin(\psi_0) \frac{l_{\text{JR}}}{2L_0} + \left(\frac{l_{\text{JR}}}{2L_0}\right)^2} = L_0 \sqrt{1 - \frac{\sqrt{3}}{3} \frac{l_{\text{JR}}}{L_0} + \frac{1}{4} \left(\frac{l_{\text{JR}}}{L_0}\right)^2} \quad (7)$$

A good approximate of the above expression 7 is found considering a Taylor series expansion to the second order in l_{JR}/L_0 , resulting in the following:

$$\frac{L_R}{L_0} = 1 - \frac{\sqrt{3}}{6} \frac{l_{\text{JR}}}{L_0} + \frac{1}{12} \left(\frac{l_{\text{JR}}^2}{L_0^2}\right) + \mathcal{O}\left(\frac{l_{\text{JR}}^3}{L_0^3}\right) \quad (8)$$

For the line energy $E^{\langle 111 \rangle}(\theta)$, we take advantage of the fact that, in the absence of junction reaction (*i.e.* $l_{\text{JR}} = 0$), the two $1/2\langle 111 \rangle$ dislocations are in screw orientation (*i.e.* $\theta = 0$) and the energy is minimal for the screw dislocation. Thus, we have:

$$E^{\langle 111 \rangle}(\theta) = E_{\text{screw}}^{\langle 111 \rangle} + \frac{1}{2} \left. \frac{\partial^2 E^{\langle 111 \rangle}}{\partial \theta^2} \right|_{\theta=0} \theta^2 + \mathcal{O}(\theta^3) \quad (9)$$

Then, the character θ of the two intersecting $1/2\langle 111 \rangle$ is linked to the length l_{JR} of the junction reaction through the following relation:

$$\sin(\psi_0 - \theta) = \sin(\psi_0) - \frac{l_{\text{JR}}}{2L_0} \quad (10)$$

A Taylor series expansion of this relation for small characters θ leads to:

$$\theta^2 = \frac{1}{\cos^2(\psi_0)} \left(\frac{l_{\text{JR}}}{2L_0}\right)^2 + \mathcal{O}\left(\frac{l_{\text{JR}}^3}{L_0^3}\right) = \frac{6}{16} \frac{l_{\text{JR}}^2}{L_0^2} + \mathcal{O}\left(\frac{l_{\text{JR}}^3}{L_0^3}\right), \quad (11)$$

and then to:

$$E^{\langle 111 \rangle}(\theta) = E_{\text{screw}}^{\langle 111 \rangle} + \frac{3}{16} \left. \frac{\partial^2 E^{\langle 111 \rangle}}{\partial \theta^2} \right|_{\theta=0} \frac{l_{\text{JR}}^2}{L_0^2} + \mathcal{O}\left(\frac{l_{\text{JR}}^3}{L_0^3}\right) \quad (12)$$

Injecting the two Taylor series expansions of Eqs. 8 and 12 in the expression 6 for the variation of the elastic energy, we finally obtain:

$$\Delta E^{\text{elas}}(l_{\text{JR}}) = l_{\text{JR}} \left(E_{\text{screw}}^{\langle 100 \rangle} - 2 \frac{\sqrt{3}}{3} E_{\text{screw}}^{\langle 111 \rangle} + \left[\frac{1}{3} E_{\text{screw}}^{\langle 111 \rangle} + \frac{3}{2} \frac{\partial^2 E^{\langle 111 \rangle}}{\partial \theta^2} \Big|_{\theta=0} \right] \frac{l_{\text{JR}}}{L_0} + \mathcal{O} \left(\frac{l_{\text{JR}}^2}{L_0^2} \right) \right) \quad (13)$$

This function has a minimum for positive length l_{JR} of the junction only if the linear term is negative, thus resulting in the following condition:

$$E_{\text{screw}}^{\langle 100 \rangle} - 2 \frac{\sqrt{3}}{3} E_{\text{screw}}^{\langle 111 \rangle} \leq 0 \quad \rightarrow \quad \alpha_{\text{JR}}^{\text{elas}} = \frac{\sqrt{3}}{2} \frac{E_{\text{screw}}^{\langle 100 \rangle}}{E_{\text{screw}}^{\langle 111 \rangle}} \leq 1 \quad (14)$$

In the frame of isotropic elasticity theory, the ratio between the elastic energies of the two $1/2\langle 111 \rangle$ and $\langle 100 \rangle$ screw dislocations is equal to the ratio between the square of the norm of their Burgers vectors, resulting in $\alpha_{\text{JR}}^{\text{elas}} = 2/\sqrt{3} \simeq 1.15$. Hence, according to isotropic elasticity, no $\langle 100 \rangle$ screw junction should form spontaneously when two $1/2\langle 111 \rangle$ screw dislocations intersect. As shown in Fig. 9b, this result is confirmed by atomistic simulations performed in W, which is elastically isotropic (*i.e.* $A = 1$).

Now considering anisotropic elasticity, an analytical expression for the elastic energy of a screw dislocation is available for $1/2\langle 111 \rangle$ and $\langle 100 \rangle$ Burgers vectors [177, 178], for which the logarithmic prefactors are:

$$e_{\text{screw}}^{\langle 111 \rangle} = \frac{3a_0^2 C_{44}}{8\pi} \sqrt{\frac{9 + (1 + m_B)(2 + A)}{(1 + 2A)[1 + A(3 + m_B)]}} \quad \text{and} \quad e_{\text{screw}}^{\langle 100 \rangle} = \frac{a_0^2 C_{44}}{2\pi}, \quad (15)$$

where $A = 2C_{44}/(C_{11} - C_{12})$ is the elastic anisotropy ratio, and $m_B = (C_{11} + 2C_{12})/C_{44}$ is a modified bulk to shear moduli ratio. Their values are given in Tab. 1 for all bcc transition metals, derived from experimental elastic constants measured at 4.2 K. The ratio $\alpha_{\text{JR}}^{\text{elas}}$ then has an analytical expression:

$$\alpha_{\text{JR}}^{\text{elas}} = \frac{2}{\sqrt{3}} \sqrt{\frac{(1 + 2A)[1 + A(3 + m_B)]}{9 + (1 + m_B)(2 + A)}} \quad (16)$$

Taking $A = 1$ in the above expression of $\alpha_{\text{JR}}^{\text{elas}}$ gives the previous result of isotropic elasticity theory, $\alpha_{\text{JR}}^{\text{elas}} = 2/\sqrt{3} \simeq 1.15$. Considering elastic anisotropy, one obtains the values presented in Tab. 4 for all bcc transition metals. The condition for the $\langle 100 \rangle$ screw junction reaction to form is met by all metals satisfying $A \leq 0.8$ (*i.e.* V, Nb, Cr and Mo), almost independently of the value of m_B . Indeed, the elastic energy ratio $\alpha_{\text{JR}}^{\text{elas}}$ can be approximated as a unique function of the elastic anisotropy A given that $m_B \gg A$ (see Tab. 1):

$$\alpha_{\text{JR}}^{\text{elas}} \simeq \frac{2}{\sqrt{3}} \sqrt{\frac{A(1 + 2A)}{2 + A}} \quad (17)$$

The condition for the stability of the junction $\alpha_{\text{JR}}^{\text{elas}} \leq 1$ is then $8A^2 + A - 6 \leq 0$, which is satisfied for $A \leq (-1 + \sqrt{193})/16$, *i.e.* for an elastic anisotropy ratio A smaller than 0.8. For metals in which this condition is met, and thus the $\langle 100 \rangle$ screw junction reaction stable, the equilibrium length of the junction is the minimum of the function $\Delta E^{\text{elas}}(l_{\text{JR}})$ given by Eq. 13, leading to:

$$\frac{l_{\text{JR}}}{L_0} = \frac{2\sqrt{3}E_{\text{screw}}^{\langle 111 \rangle} - 3E_{\text{screw}}^{\langle 100 \rangle}}{2E_{\text{screw}}^{\langle 111 \rangle} + \frac{9}{2} \frac{\partial^2 E^{\langle 111 \rangle}}{\partial \theta^2} \Big|_{\theta=0}} = \frac{\sqrt{3}}{1 + \frac{9}{4E_{\text{screw}}^{\langle 111 \rangle}} \frac{\partial^2 E^{\langle 111 \rangle}}{\partial \theta^2} \Big|_{\theta=0}} (1 - \alpha_{\text{JR}}^{\text{elas}}) \quad (18)$$

We note that the length of the junction is proportional to the elastic coefficient $(1 - \alpha_{\text{JR}}^{\text{elas}})$. Nb, followed by Cr, have the smallest elastic ratios $\alpha_{\text{JR}}^{\text{elas}}$, indicating that two intersecting $1/2\langle 111 \rangle$ screw dislocations can easily and spontaneously form long $\langle 100 \rangle$ screw junctions in these two metals (see Tab. 4). Since the length

of these $\langle 100 \rangle$ junctions is maximum in these two metals, its probability to be intercepted by a third screw dislocation of Burgers vector \vec{b}_3 is thus maximized. This leads to easier formation of four-dislocation nodes following the process of Fig. 8, further responsible for the development of anomalous slip. This is consistent with experiments, mostly in Nb where anomalous slip is reported most often in experimental works, but also in Cr where Holzer *et al.* [34] recently reported such event on samples compressed at 77 K. In V and Mo, this $\alpha_{\text{JR}}^{\text{elas}}$ coefficient is close to 1, but still smaller, thus resulting in stable $\langle 100 \rangle$ screw junctions, but of a small length. Finally, in W, Ta and Fe, this coefficient is larger than 1, and these junctions are thus unstable. According to the presented model, the stability of the $\langle 100 \rangle$ screw junction reaction directly follows the variations of the elastic anisotropy ratio A , with an increasing stability for small value of A .

Table 4: Elastic anisotropy $A = 2C_{44}/(C_{11} - C_{12})$, logarithmic prefactors $e_{\text{screw}}^{\langle 111 \rangle}$ and $e_{\text{screw}}^{\langle 100 \rangle}$ of the elastic energy of $1/2\langle 111 \rangle$ and $\langle 100 \rangle$ screw dislocations (eV/Å), second derivative of the elastic energy of $1/2\langle 111 \rangle$ dislocation at the screw orientation (eV/Å), elastic ratio $\alpha_{\text{JR}}^{\text{elas}}$ defining the stability of the junction, normalized length l_{JR}/L_0 of the screw $\langle 100 \rangle$ junction, and corresponding character $\theta_{1/2\langle 111 \rangle}$ ($^\circ$) of the two $1/2\langle 111 \rangle$ dislocations after the formation of the junction.

Metal	A	$e_{\text{screw}}^{\langle 111 \rangle}$	$e_{\text{screw}}^{\langle 100 \rangle}$	$\left. \frac{\partial^2 E^{\langle 111 \rangle}}{\partial \theta^2} \right _{\theta=0}$	$\alpha_{\text{JR}}^{\text{elas}}$	l_{JR}/L_0	$\theta_{1/2\langle 111 \rangle}$
Nb	0.50	0.36	0.31	0.05	0.74	0.35	9.0°
Cr	0.68	0.82	0.85	0.06	0.90	0.15	3.6°
Mo	0.77	0.97	1.09	0.38	0.97	0.01	0.3°
V	0.78	0.35	0.39	0.23	0.98	0.01	0.3°
W	1.00	1.17	1.56	0.83	1.15	0	0°
Ta	1.56	0.50	0.89	1.01	1.56	0	0°
Fe	2.38	0.39	0.95	1.16	2.08	0	0°

These $\langle 100 \rangle$ junctions are observed in all bcc transition metals at low temperature [34, 37, 38, 247–249], having different lengths depending on the metal, as predicted by the presented atomistic simulations and line energy model. This agrees with the observation that activity of anomalous slip in bcc metals correlates with the elastic anisotropy ratio A , and is more prominent for small values, like in Nb ($A = 0.50$) [37, 250–252]. This is also the case for Cr ($A = 0.68$), where these $\langle 100 \rangle$ junctions are often reported experimentally [13, 34, 122, 123], and anomalous slip reported for orientations of the loading axis near the center of the standard stereographic triangle [34], where activity on anomalous slip planes is the most striking.

According to the line energy model, $\langle 100 \rangle$ screw junctions should form spontaneously from the interaction of two $1/2\langle 111 \rangle$ screw dislocations in bcc metals having $A < 0.8$. Looking at the relaxed configurations of the junction at 0 K presented in in Fig. 9 for two metals having different elastic anisotropy ratios, namely Nb and W with $A = 0.5 < 0.8$ and $A = 1 > 0.8$ respectively, we find a good agreement between the two models for both metals, with predictions of the line energy model shown with solid colored lines. We now further test the predictions of the line energy model in terms of the correlation between A and the stability of the $\langle 100 \rangle$ screw junction, and most particularly regarding the proportional relation predicted between the length l_{JR} of the junction and the initial length L_0 of the two intersecting $1/2\langle 111 \rangle$ screw dislocations. For this purpose, a similar setup is adopted, where two $1/2\langle 111 \rangle$ screw dislocations intersect in their middle, and are then relaxed at 0 K with molecular statics. We then vary their initial length L_0 and record the length of the junction l_{JR} . Results are presented in Fig. 10 in Nb and W, using the same interatomic potentials as previously cited.

Atomistic simulations confirm the creation of a $\langle 100 \rangle$ junction of screw character in Nb, with a length l_{JR} of the junction reaction varying linearly with the length L_0 of the two intersecting $1/2\langle 111 \rangle$ screw dislocations:

$$l_{\text{JR}}(L_0) = a L_0 + l_{\text{JR}}^0, \quad (19)$$

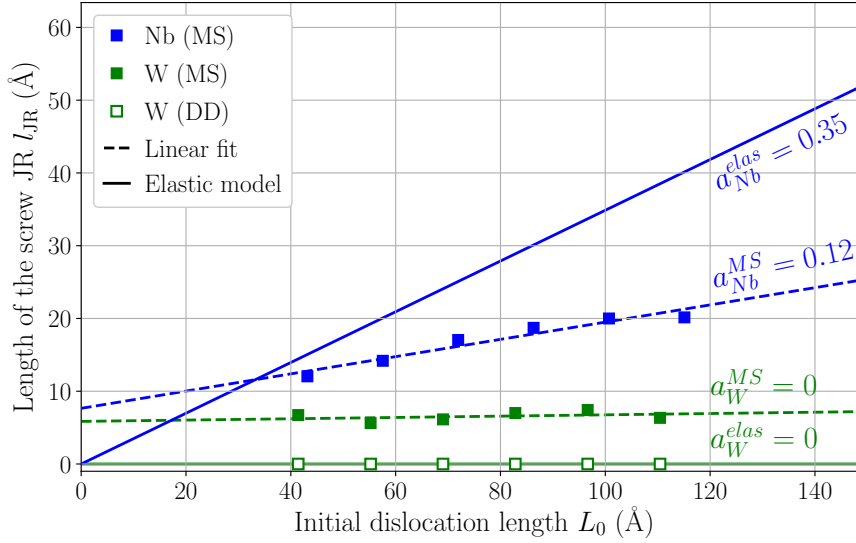


Figure 10: Length l_{JR} of the junction reaction produced by the intersection of two $1/2\langle 111 \rangle$ screw dislocations of length L_0 . Predictions of the line energy model (solid lines) are compared to results of molecular statics simulations (filled symbols and dashed lines) for Nb (blue) and W (green), and to results of DD simulations for W (open symbols).

where l_{JR}^0 is a small offset appearing in atomistic simulations, arising from the uncertainty associated with the measure of the junction length for small junctions. Like for the relaxation of the four-dislocation node, the slope a deduced from atomistic simulations is lower than the one predicted by the line energy model. Here also, one can suppose that this difference is caused by the neglect of the core contributions in the line energy model. $\langle 100 \rangle$ dislocations have indeed a higher core energy than $1/2\langle 111 \rangle$ dislocations. For the screw orientation, empirical interatomic potentials used in the present work lead to a core energy equal to 0.48 and 0.25 eV/Å respectively for $\langle 100 \rangle$ and $1/2\langle 111 \rangle$ screw dislocations in Nb (0.93 and 0.52 eV/Å in W) for the same core radius $r_C = b_{1/2\langle 111 \rangle} = a_0\sqrt{3}/2$. The higher core energy of the $\langle 100 \rangle$ screw dislocation adds a penalty for the spontaneous formation of $\langle 100 \rangle$ screw junctions, which is not considered in the line energy model developed here. It thus appears normal that this model overestimates the length of the junction compared to atomistic simulations accounting for every contributions. This model, which thus appears semi-quantitative, allows nevertheless to rationalize the impact of the elastic anisotropy on the creation of $\langle 100 \rangle$ junctions, showing that such junctions are spontaneously created when two $1/2\langle 111 \rangle$ screw dislocations intersect in bcc transition metals with an elastic anisotropy ratio A smaller than $\simeq 0.8$, and is further stabilized by a decreasing anisotropy ratio. Elasticity also predicts that formation of $\langle 100 \rangle$ screw junctions becomes unfavorable in metals where this ratio A is larger than $\simeq 0.8$. In particular, in the isotropic case of W ($A = 1$), atomistic simulations confirm that the interaction of two $1/2\langle 111 \rangle$ screw dislocations do not spontaneously lead to the creation of a $\langle 100 \rangle$ screw junction (see Fig. 9b).

3.3.1. Formation of $\langle 100 \rangle$ screw junctions under dynamic conditions

According to the results presented in the previous section, $\langle 100 \rangle$ screw junctions formed by two intersecting $1/2\langle 111 \rangle$ screw dislocations are not energetically favorable for metals with elastic anisotropy $A > 0.8$, which are an essential ingredient for the occurrence of anomalous slip in bcc metals. This appears in contradiction with the experimental observation of anomalous slip in W and Ta (see Tab. 1), for which $A \geq 1$. This apparent paradox finds a solution in the possibility for such $\langle 100 \rangle$ junctions to form under dynamic conditions from two intersecting $1/2\langle 111 \rangle$ screw dislocations, observed in W at 373 K during *in situ* straining experiments in TEM by Daniel Caillard, presented in Fig. 11a.

Despite the energy cost of these screw junctions in W, TEM observations reveal that the two interacting $1/2\langle 111 \rangle$ screw dislocations, of Burgers vectors $\vec{b}_1 = 1/2[\bar{1}11]$ and $\vec{b}_2 = 1/2[111]$ thus satisfying $\vec{b}_1 + \vec{b}_2 = [010]$,

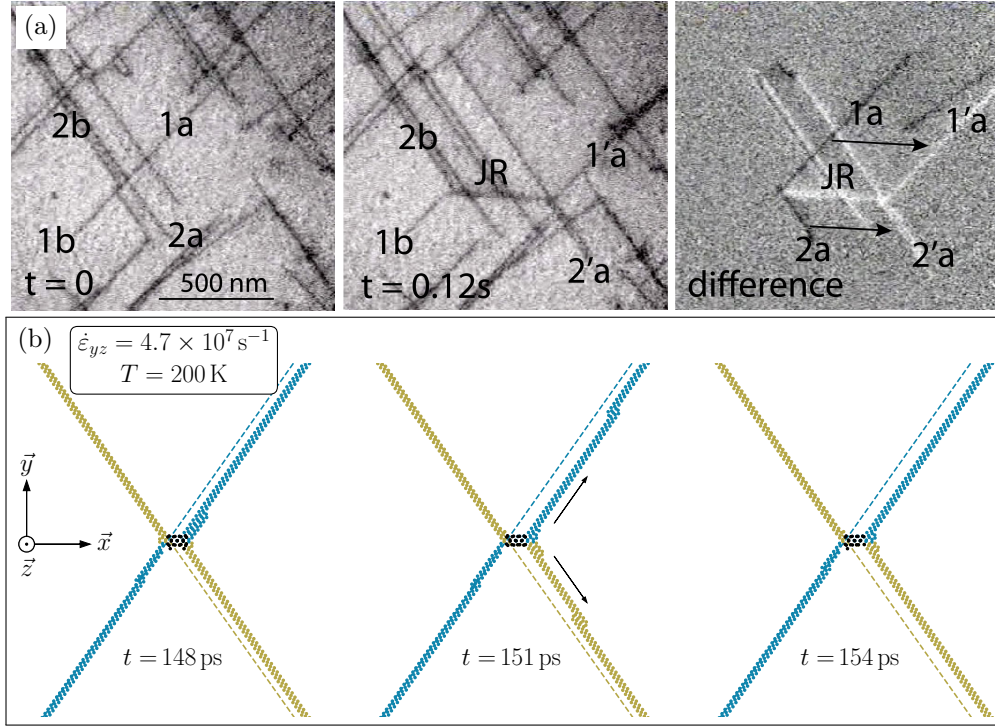


Figure 11: (a) Formation of a $[010]$ junction observed in tungsten by TEM with *in situ* straining experiments at 373 K. Two intersecting screw dislocations with different $1/2\langle 111 \rangle$ Burgers vector are observed at two different times. The difference image between the two frames shows that the right parts of the screw dislocations noted 1a and 2a have glided to the right while their left parts 1b and 2b remain fixed, leading to the creation of the JR. (b) Molecular dynamics simulations show the dynamical creation of a $[010]$ junction in tungsten operating through the nucleation of kinks at the node on the right dislocation segments.

glide under an applied stress only on one side of their contact point (1a and 2a dislocation segments in Fig. 11a), and remain immobile on the other side (1b and 2b dislocation segments in Fig. 11a). Therefore, a $\langle 100 \rangle$ junction is formed at their intersection, and can then extend under the effect of the applied stress. Now that the junction is sufficiently long, it can then be intersected by a third screw dislocation of Burgers vector \vec{b}_3 to form the multi-junction leading to anomalous slip according to the mechanism sketched in Fig. 4.

The extension of the $\langle 100 \rangle$ screw junction under applied stress is now studied using molecular dynamics straining simulations in W. The simulation cell used for this calculation is defined by vectors $X = 140 \times [010]$, $Y = 100 \times [011]$ and $Z = 30 \times [10\bar{1}]$, with periodic boundary conditions along the X direction only, and free surfaces along Y and Z directions. Two screw dislocations of Burgers vectors $\vec{b}_1 = 1/2[\bar{1}1\bar{1}]$ and $\vec{b}_2 = 1/2[111]$ are introduced in the simulation cell, and intersect at its center. The system is then relaxed with a molecular statics step at 0 K, resulting in the same relaxed structure as presented in Fig. 9b, with no $\langle 100 \rangle$ junction formed and a longer initial length L_0 of the two $1/2\langle 111 \rangle$ screw dislocations. A constant strain rate $\dot{\epsilon}_{xz} = 4.7 \times 10^7 \text{ s}^{-1}$ is then applied to the dislocations using flexible boundary conditions [167] (see Methods, section 3.2), resulting in an equal net force on the two $1/2\langle 111 \rangle$ screw dislocations contained in the simulation cell. The results of this calculation in W are presented in Fig. 11b, performed at 200 K.

The simulation starts from the relaxed configuration shown in Fig. 9b, thus without an initial $\langle 100 \rangle$ segment, since intersection between two $1/2\langle 111 \rangle$ screw dislocations do not spontaneously produce a junction in W. Three further snapshots of the simulation are shown, starting from a moment where the $\langle 100 \rangle$ junction has already formed, shown on the first presented step. After a short time and increment of strain, two kinks form on the right side of the junction, which then rapidly migrate along the two dislocation lines. This

leads to the extension of the $\langle 100 \rangle$ junction by an elementary step of $\lambda_P = a_0\sqrt{6}/3$, corresponding to the displacement of the two kinks on the right. Atomistic calculations allow for reconstruction of the proposed mechanism based on *in situ* straining experiments, responsible for the creation and elongation of $\langle 100 \rangle$ junctions under applied stress. In particular, atomistic simulations evidenced an easier nucleation of kinks along the $1/2\langle 111 \rangle$ dislocation lines on the side of the junction oriented in the direction of the applied stress. According to the proposed mechanism, it then allows for anomalous slip to occur in bcc transition metals having $A > 0.8$, in agreement with experiments, with however a lower probability since formation of junctions is still less favorable, and the $\langle 100 \rangle$ junctions produced are smaller. This also explains why no anomalous slip is observed in Fe, which has the highest elastic anisotropy ratio A among all bcc transition metals, and the reverse effect for Nb and Cr, which have the lowest A .

3.4. Discussion

These highly mobile multi-junctions offer a nice explanation to the occurrence of anomalous slip in bcc metals, starting from a large network of dislocations \vec{b}_1 and \vec{b}_2 , as sketched in Fig. 12. Such networks are created after activation of dislocations glide in their most favorable planes and result from mutual blocking of dislocations \vec{b}_1 and \vec{b}_2 which form arrays in the plane containing them. The formation of large planar arrays is helped by the associated decrease of the elastic energy, because of a substantial twist component. Incoming dislocations \vec{b}_3 , which glide in the primary P_{23} plane, will form many glissile multi-junctions when intersecting such networks. This will result in further glide of \vec{b}_1 and \vec{b}_2 dislocations in the P_{12} plane and in deviation of \vec{b}_3 dislocations from their primary to the P_{34} slip plane where they will glide with \vec{b}_4 dislocations. It is important to note that none of the four dislocations can cross slip during their cooperative glide motion, which results in a very planar slip in P_{12} and P_{34} planes. In this description, \vec{b}_3 and \vec{b}_4 dislocations glide in many parallel slip planes, thus producing fine slip traces, hardly visible, at the surface of the sample. On the other hand, all \vec{b}_1 and \vec{b}_2 dislocations glide in a single P_{12} plane, namely the plane of the starting network, which results in a very coarse and straight slip band characteristic of anomalous slip. This mechanism also agrees with the average shear direction intermediate between two Burgers vectors directions and with the absence of dead band usually observed in anomalous slip conditions.

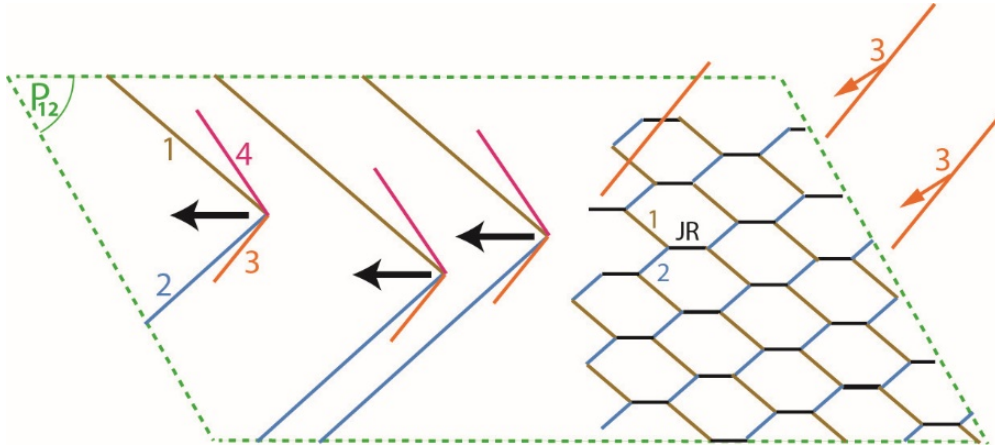


Figure 12: A network formed by \vec{b}_1 and \vec{b}_2 screw dislocations in P_{12} plane is intersected by dislocations \vec{b}_3 , which glide in the principal slip system. The interaction results in the creation of highly mobile junctions, leading to long-distance glide of \vec{b}_1 and \vec{b}_2 dislocations in a single P_{12} plane, and of \vec{b}_3 and \vec{b}_4 dislocation in many parallel P_{34} slip planes.

The existence of four-dislocation node in bcc metals has already been discussed by Bulatov *et al.* [86], but with dislocations belonging to three different $\{110\}$ planes intersecting along a $\langle 111 \rangle$ direction, thus with a mixed $\langle 100 \rangle$ junction reaction of character $\theta_{JR} = 54.7^\circ$ (see Appendix F). These multi-junctions were reported as strong anchoring points, leading to substantial strain hardening and acting as dislocation sources. The multi-junctions observed here are different, corresponding to four dislocations belonging to

two different $\{110\}$ planes intersecting along a $\langle 100 \rangle$ direction. As a result of their high mobility, they lead to the reverse effect and are a source of considerable softening, where anomalous slip takes place.

Conclusions of Chapter 5:

- Anomalous slip observed at low temperature in bcc metals arises from the unusual high mobility of multi-junctions formed by intersection between a $\langle 100 \rangle$ junction and moving $1/2\langle 111 \rangle$ screw dislocations. The proposed mechanism, based on *in situ* straining experiments in TEM, was investigated using atomistic simulations coupled with elastic considerations. The fast and cooperative motion of dislocations over long distances operates through easy nucleation of kinks at the node connecting the four $1/2\langle 111 \rangle$ dislocations, driven by the line tension exerted by the dislocations on the node.
 - Understanding and modeling the formation of these multi-junctions necessitates going beyond usual simplifications in dislocation theory, with elastic anisotropy being a key ingredient, and the possible creation in dynamic conditions of junctions otherwise found unstable based solely on energy.
 - Both displacement of the four-dislocation node and creation of the $\langle 100 \rangle$ screw junction is favored by a decreasing elastic anisotropy ratio A , like in Nb or Cr, and less favorable in metals with a large A like Fe. In particular, longer $\langle 100 \rangle$ junctions are produced in metals with a small A , thus maximizing the probability for such junction to be further intercepted by another $1/2\langle 111 \rangle$ screw dislocation, leading to anomalous slip. Such a qualitative criterion based on elasticity thus helps rationalizing occurrences of anomalous slip across bcc metals, with abundant evidences in Nb, and no observation at all in Fe.
-

Chapter 6 - $\langle 100 \rangle$ dislocations in bcc transition metals

As discussed in the previous chapter, $\langle 100 \rangle$ dislocations are observed in all bcc transition metals as junctions, created by two intersecting $1/2\langle 111 \rangle$ dislocations. However, these $\langle 100 \rangle$ dislocations are often not considered as a possible slip system when rationalizing the plastic deformation of these metals due to their longer Burgers vector. We discuss in the present chapter possibility for these $\langle 100 \rangle$ dislocations to participate to the plasticity of bcc transition metals.

1. Elasticity and $\langle 100 \rangle$ dislocations

1.1. Elasticity and relative stability of dislocations having different Burgers vectors

A common argument to discard $\langle 100 \rangle$ dislocations is based on their presumably higher elastic energy, due to the longer norm of their Burgers vector than $1/2\langle 111 \rangle$ dislocations. Indeed, in the frame of isotropic elasticity theory, the elastic energy of a dislocation is proportional to the square norm of its Burgers vector, with a minimum for the screw orientation (see Eq. 2 in the Literature review). Hence, dislocations having a Burgers vector equal to the smallest periodicity vector of the lattice are the most energetically favorable, which is $1/2\langle 111 \rangle$ for the bcc lattice. The second smallest periodicity vector of the bcc lattice is $\langle 100 \rangle$, slightly longer in norm than $1/2\langle 111 \rangle$, namely $b_{1/2\langle 111 \rangle} = a_0\sqrt{3}/2$ and $b_{\langle 100 \rangle} = a_0$ respectively, with a_0 the lattice parameter. According to isotropic elasticity, these $\langle 100 \rangle$ dislocations thus have a higher elastic energy than $1/2\langle 111 \rangle$, by approximately a factor 1.33. However, among all bcc transition metals, only W is elastically isotropic, *i.e.* with an elastic anisotropy $A = C_{44}/(C_{11} - C_{12}) = 1$. Now considering elastically anisotropic metals, *i.e.* $A \neq 1$, the situation is different. The elastic energy of these two dislocations are presented in

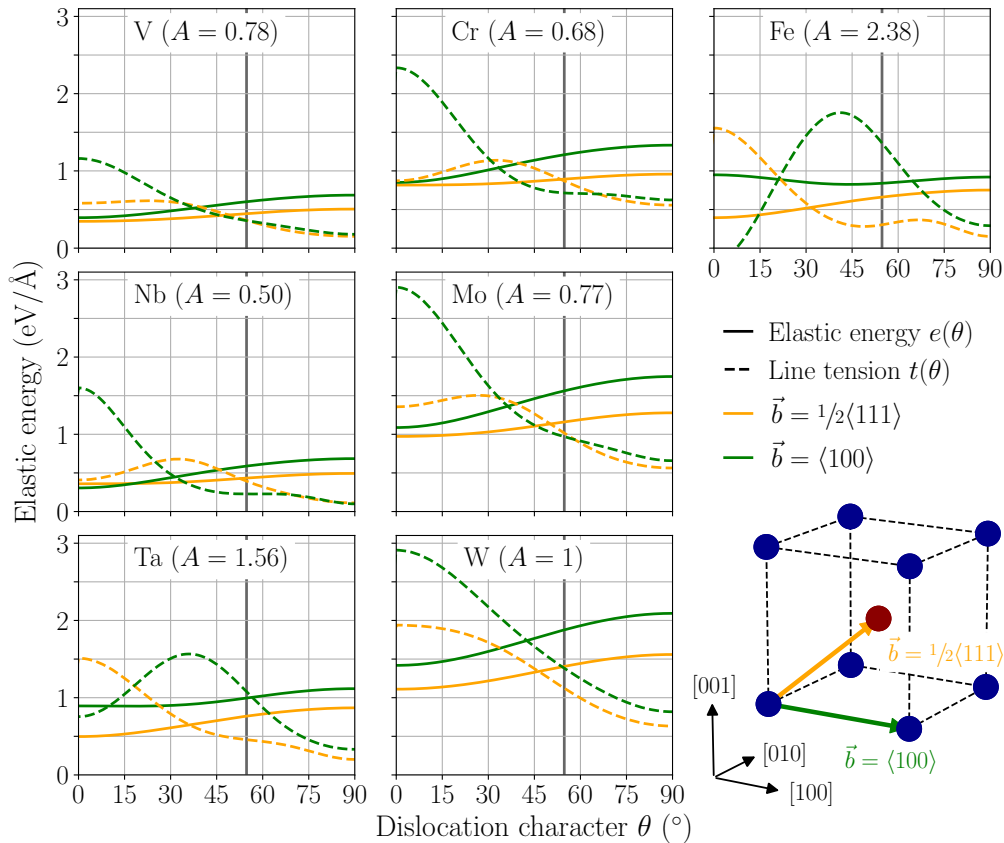


Figure 1: Pre-logarithmic factors to the elastic energy e (solid lines) and line tension t (dashed lines) of dislocations with Burgers vectors $1/2\langle 111 \rangle$ (orange) and $\langle 100 \rangle$ (green) as a function of their character θ for all bcc transition metals using experimental elastic constants at 4.2 K (see Tab. 1). Vertical lines indicate the mixed $\theta = 54.7^\circ$ orientation of the $\langle 100 \rangle$ dislocations.

Fig. 1 for all bcc transition metals as a function of their character θ , obtained using anisotropic elasticity [165], with the 4.2 K experimental elastic constants (see Tab. 1 in the Literature review).

Except for the isotropic case of W, which shows the expected hierarchy between the two types of dislocations, *i.e.* with an elastic energy proportional to the square of the norm of its Burgers vector, all other bcc metals show different behaviors, a direct consequence of the elastic anisotropy ratio A . Looking at the screw orientation, which minimizes the elastic energy for the two dislocations, although these $\langle 100 \rangle$ dislocations have a larger Burgers vector than $1/2\langle 111 \rangle$ dislocations, both have close core and elastic energy [129, 253]. This is true for all bcc metals having $A < 1$ (Nb, Cr, Mo and V), with the reverse effect for metals with $A \geq 1$ (W, Ta and Fe). Using the analytical expression for the elastic energy of both screw dislocations [177, 178] (Chapter 5, section 3.3), the ratio between the two screw dislocations is given by:

$$\frac{e_{\text{screw}}^{\langle 100 \rangle}}{e_{\text{screw}}^{1/2\langle 111 \rangle}} = \frac{4}{3} \sqrt{\frac{(1+2A)[1+A(3+m_B)]}{9+(1+m_B)(2+A)}} \simeq \frac{4}{3} \sqrt{\frac{A(1+2A)}{2+A}} \quad (1)$$

In particular, for metals having a strong elastic anisotropy defined by $A < 0.65$, the $\langle 100 \rangle$ screw dislocation actually has a lower elastic energy than the $1/2\langle 111 \rangle$ screw dislocation, which is the case for Nb ($A = 0.5$) and Cr ($A = 0.68$), as also pointed out by Reid [129]. Therefore, the conventional argument to discard $\langle 100 \rangle$ dislocations in the study of plasticity in bcc metals, based on isotropic elasticity theory, is not sufficient and one *a priori* needs to account for these dislocations. Besides, $\langle 100 \rangle$ dislocations do not disrupt the AF order of bcc Cr and thus do not create magnetic fault at low temperature, giving an additional reason to consider them in Cr.

The elastic line tension is also plotted on Fig. 1 as a function of the dislocation character for both Burgers vectors, which characterizes the ease to bend a straight dislocation line as a function of its orientation. We note that for all metals having $A \leq 1$, the minimum of the elastic energy of the $\langle 100 \rangle$ dislocation is found for the screw orientation, which also shows the maximum for the line tension. As a consequence, the screw orientation will be the most difficult to bend, further linked to the activation of Frank-Read sources. The reverse effect is found for metals having $A > 1$ (Ta and Fe), where a mixed character minimizes the elastic energy of $\langle 100 \rangle$ dislocations, while also maximizing their line tension.

1.2. Formation of $\langle 100 \rangle$ junctions in bcc metals

In the previous chapter, we discussed the stability of $\langle 100 \rangle$ junctions as part of the mechanism leading to anomalous slip, which requires formation of junctions from two intersecting $1/2\langle 111 \rangle$ dislocations of screw character. We now discuss all possible reactions leading to the formation of glissile $\langle 100 \rangle$ junctions, which can then act as sources for multiplication of $\langle 100 \rangle$ dislocations, for any character and glide plane of the two reacting $1/2\langle 111 \rangle$ dislocations. The $\langle 100 \rangle$ junction can only glide in a plane where both its Burgers \vec{b}_{JR} and line \vec{l}_{JR} vectors belong. In the present case, \vec{b}_{JR} is the sum of the Burgers vectors of the two intersecting $1/2\langle 111 \rangle$ dislocations. As for the line orientation \vec{l}_{JR} , it is defined as the intersection between their two glide planes. Therefore, the resulting junction can either be sessile (*i.e.* with no possible $\{110\}$ glide plane containing both its Burgers \vec{b}_{JR} and line \vec{l}_{JR} vectors), or glissile (*i.e.* at least one possible $\{110\}$ glide plane that contains both \vec{b}_{JR} and \vec{l}_{JR}). All nine possible combinations of two intersecting dislocations $\vec{b}_1 = 1/2[1\bar{1}1]$ and $\vec{b}_2 = 1/2[\bar{1}11]$ leading to the formation of a junction $\vec{b}_{\text{JR}} = \vec{b}_1 + \vec{b}_2 = [001]$ are presented in Fig. 2.

As pointed out by Spitzig and Mitchell [254], there are four types of reactions to consider among these nine combinations. The first possibility corresponds to the case where the two original habit planes are orthogonal to each other, which products a completely sessile junction, corresponding to Fig. 2e and i. The second case occurs when the two reacting $1/2\langle 111 \rangle$ dislocations are both on the same plane, which results in a completely glissile junction, as shown in Fig. 2a (corresponding to the one involved in the mechanism for occurrence of anomalous slip). A third possibility results in a $\langle 100 \rangle$ junction glissile in one of the two original habit planes of the two $1/2\langle 111 \rangle$ dislocations, for which several possible combinations are possible, shown in

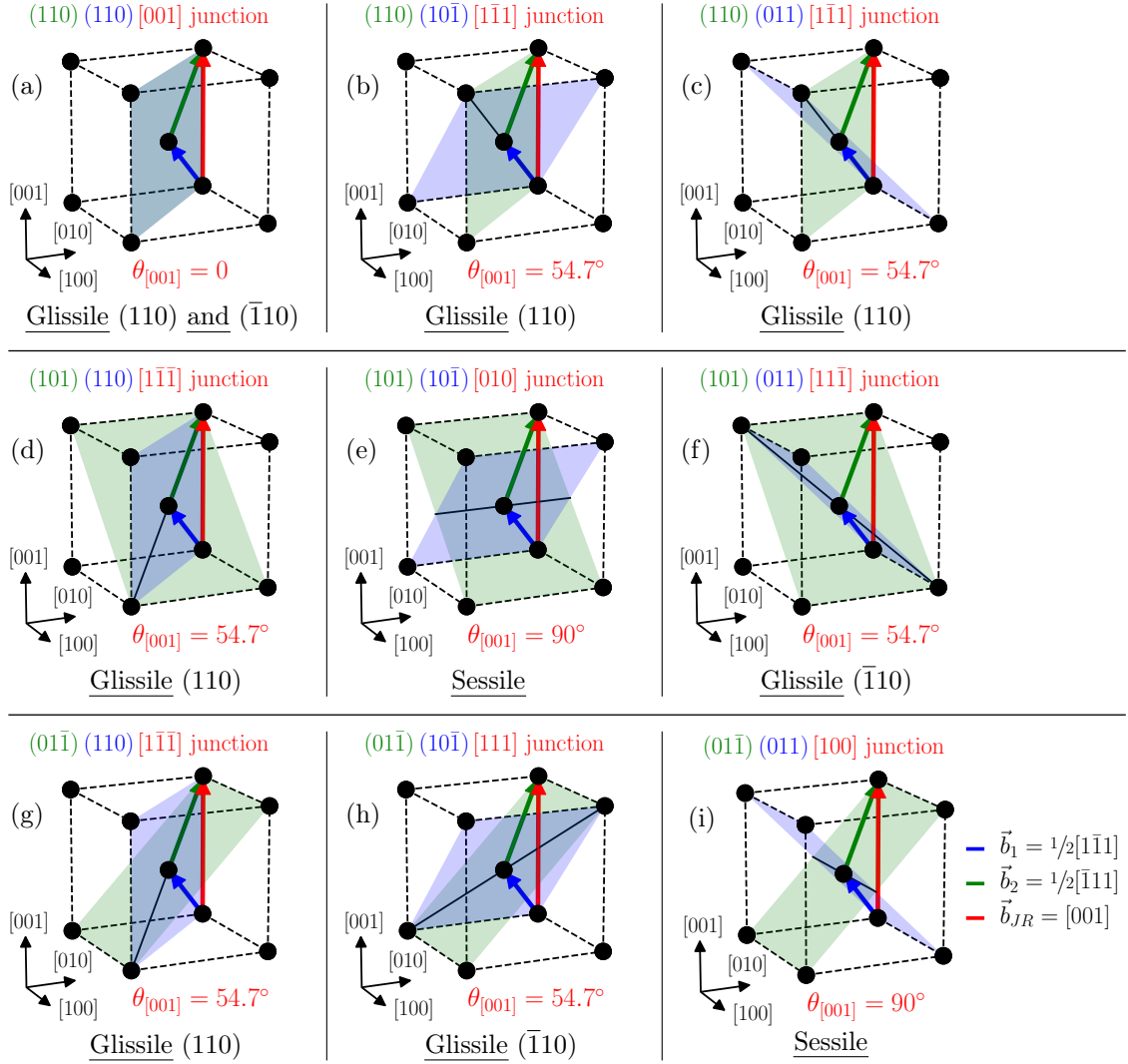


Figure 2: All possible combinations of the two $\vec{b}_1 = 1/2[1\bar{1}1]$ and $\vec{b}_2 = 1/2[\bar{1}11]$ screw dislocations leading to the formation of a JR of Burgers vector $\vec{b}_{JR} = \vec{b}_1 + \vec{b}_2 = [001]$, depending on their 3 possible $\{110\}$ glide planes. Combinations between different $1/2\langle 111 \rangle$ dislocations and leading to other Burgers vectors for the JR are equivalent to the ones presented here.

Fig. 2b, c, d and g. Finally, the junction can also be glissile in a different plane than the original habit planes of the two intersecting dislocations, corresponding to Fig. 2f and h. There are only three different possible characters for $\langle 100 \rangle$ junctions which are screw, a mixed orientation with $\theta = 54.7^\circ$ (see vertical line on Fig. 1) corresponding to a line along a $\langle 111 \rangle$ direction, and an edge character.

Other possibilities than presented in Fig. 2 would have been the formation of $\langle 110 \rangle$ junctions, following the reaction $\vec{b}_1 - \vec{b}_2 \rightarrow [1\bar{1}0]$. $\langle 110 \rangle$ dislocations are however not observed experimentally in any bcc metals, and are unstable according to elasticity theory. Indeed, the formation of $\langle 110 \rangle$ dislocations is not energetically favorable following this reaction, or the other possibility, which is $[100] + [010] \rightarrow [1\bar{1}0]$. Further analysis reveals that they can spontaneously dissociate into two $1/2\langle 111 \rangle$ or $\langle 100 \rangle$ dislocations, depending on the character of the junction formed. We also studied their stability using atomistic simulations, where molecular statics relaxation at 0 K in Nb, W, Mo and Ta confirmed this spontaneous dissociation.

As presented in the previous chapter while discussing occurrence of anomalous $\{110\}$ slip in bcc transition metals, the spontaneous formation of $\langle 100 \rangle$ junctions with a screw character (Fig. 2a) is governed by the elastic anisotropy of the metal, with an increase stability associated with low elastic anisotropy ratio A (Chapter 5, section 3.3). At low temperature where $1/2\langle 111 \rangle$ dislocations align along their screw orientation due to the strong lattice friction they experience, $\langle 100 \rangle$ junctions can only form as the product of the intersection between two $1/2\langle 111 \rangle$ screw dislocations. As presented in Appendix F, spontaneous formation of the screw junction from this reaction is energetically favorable only in metals with an elastic anisotropy $A \leq 0.8$, with a length proportional to the length of the two intersecting $1/2\langle 111 \rangle$ dislocations. Formation of a $\langle 100 \rangle$ junctions having the two other possible characters present in Fig. 2, *i.e.* mixed $\theta = 54.7^\circ$ and edge, is however not energetically favorable from intersection between two $1/2\langle 111 \rangle$ screw dislocations. Instead, there is a critical character θ^{JR} of the two reacting dislocations above which the reaction leading to the formation of the mixed and edge $\langle 100 \rangle$ junctions becomes possible. At higher temperature, above the athermal temperature of the Peierls mechanism, $1/2\langle 111 \rangle$ dislocations can take any character, since the high lattice friction experienced by the screw orientation has vanished. In these conditions, according to our line energy model and atomistic simulations presented in Appendix F, $\langle 100 \rangle$ junctions can form more easily, also in metals with $A > 0.8$, and for all three possible screw, mixed and edge characters.

Assuming $\langle 100 \rangle$ dislocations to primarily originate from such junctions, they are therefore expected at low temperature only in metals with a small elastic anisotropy ratio $A < 0.8$, which is the case for Nb and Cr. Indeed, one possibility is that such junctions act as sources for $\langle 100 \rangle$ dislocations, which can then multiply from these active sources. For metals having $A > 0.8$, two $1/2\langle 111 \rangle$ dislocations of a mixed character needs to cross to form a $\langle 100 \rangle$ junction of sufficient length to then act as dislocation sources, which is thus possible only at higher temperature where they do not align preferentially along their screw orientation. Among the nine combinations presented in Fig. 2, only the glissile reactions can act as sources, and since the two possibilities leading to a edge $\langle 100 \rangle$ junction are sessile, only junctions having a screw or a mixed $\theta = 54.7^\circ$ character can then act as sources.

1.3. Experimental observations of $\langle 100 \rangle$ dislocations

Given their close energetics compared to the conventional $1/2\langle 111 \rangle$ dislocations, there appears to be no valid argument based on elasticity theory to discard these $\langle 100 \rangle$ dislocations in rationalizing plasticity of bcc transition metals. To participate actively to the plastic deformation, a given slip system needs to be able to multiply to non-negligible proportion of mobile dislocations. For $\langle 100 \rangle$ dislocations, a possibility for such multiplication process would be for junctions discussed in the previous section 1.2 to act as active sources. As will be discussed, motion of these $\langle 100 \rangle$ dislocations have been observed at room temperature in Cr and Nb, and at higher temperature in other metals. We present in this section a review of experimental evidences of the presence and mobility of $\langle 100 \rangle$ dislocations across all bcc transition metals.

In Fe, Dingley and Hale [255] reported a large proportion of $\langle 100 \rangle$ dislocations observed in TEM in samples deformed at temperatures ranging from 156 to 673 K, with an approximate ratio of 1 $\langle 100 \rangle$ dislocation for 3 $1/2\langle 111 \rangle$. The authors also report constant proportions of the two Burgers vectors with temperature, showing no significant change of multiplication mechanism in this temperature range. However, the analysis performed by the authors used a single extinction criterion (*i.e.* $\vec{g} \cdot \vec{b}$ contrast) for determination of the Burgers vectors of dislocations, which was then corrected by Hale and Anderson Brown [123], who demonstrated the necessity to use at least two different extinction conditions for a precise evaluation of the Burgers vectors in presence. The authors considered both Fe and Cr for their study, first confirming the previous results in Fe using a single extinction vector, and a ratio of 3 $\langle 100 \rangle$ for 4 $1/2\langle 111 \rangle$ dislocations in Cr. However, using two extinction conditions, the authors reported less $\langle 100 \rangle$ dislocations in Fe, approximately 5%, which is still a non-negligible proportion, and was further confirmed by France and Loretto [256, 257].

$\langle 100 \rangle$ dislocations in bcc metals are most often the junction product resulting from the interaction of two $1/2\langle 111 \rangle$ dislocations, a reaction driven by elasticity [258]. At low temperature, where $1/2\langle 111 \rangle$ dislocations

are aligned along their screw orientation, according to atomistic simulations and the line energy model presented in the previous chapter (see section 3.3), the formation of these junctions is energetically favorable in all bcc metals with an elastic anisotropy ratio $A < 0.8$. This is the case for Nb ($A = 0.5$) [250, 259], Cr ($A = 0.67$) [34], Mo ($A = 0.77$) [38] and V ($A = 0.78$) [247], with a junction of length proportional to the length of the two intersecting $1/2\langle 111 \rangle$ dislocations, decreasing with increasing anisotropy ratio A . At higher temperature, above the athermal temperature of the Peierls mechanism, $1/2\langle 111 \rangle$ dislocations can take any character, and $\langle 100 \rangle$ junctions can form more easily, also in metals with $A > 0.8$. This agrees with experimental observations of longer $\langle 100 \rangle$ junction segments in Ta ($A = 1.56$) [248] at 463 K. Apart from these static observations in all bcc transition metals, evidence of long mobile segments of $\langle 100 \rangle$ dislocations are very scarce in the experimental literature, which is an essential condition for these dislocations to participate actively to the plastic deformation of these bcc metals.

However, in addition to the conventional $\langle 111 \rangle \{110\}$ slip system, experiments [13, 123] in samples of Cr have also reported glide of $\langle 100 \rangle$ dislocations in $\{110\}$ planes. Reid and Gilbert [13] observed with TEM in pure Cr deformed at 300 K slip traces corresponding to cross-slip events. As intersections between the primary and the cross-slipped $\{110\}$ planes were along $\langle 100 \rangle$ and not $\langle 111 \rangle$ directions, this event clearly indicates slip activity of $\langle 100 \rangle$ dislocations in bcc Cr, and with an ability to cross-slip at ambient temperature. Junctions with a $\langle 100 \rangle$ Burgers vector, formed by intersection between two $1/2\langle 111 \rangle$ dislocations, have been observed by TEM in polycrystalline samples by McLaren [122], Garrod and Wain [125], and Reid and Gilbert [13]. Such a junction has been observed recently by transmission electron microscopy in Cr by Holzer *et al.* [34] on compressed single crystals at a temperature of 77 K. However, these authors did not report any activity of the $\langle 100 \rangle \{110\}$ slip system for the different orientations of the compression axis they investigated. Similar observations in Nb of the activity of $\langle 100 \rangle$ dislocations gliding in $\{110\}$ planes were reported by both Reid *et al.* [251] and Foxall *et al.* [250], the latter also reporting evidence of long $\langle 100 \rangle$ dislocation segments.

Given the results of anisotropic elasticity theory (see section 1.1), one would expect similar proportions and activity of the two Burgers vectors. But even in Nb and Cr, in which $\langle 100 \rangle$ dislocations have close elastic energy compared to $1/2\langle 111 \rangle$, experimental observations systematically report much fewer $\langle 100 \rangle$ dislocations, and evidences of their activity are very scarce at low temperature (below ambient). Also, it is not clear if these dislocations are able to glide in other bcc transition metals at low temperature, since no experimental evidence of their motion is reported. As presented in the previous section 1.2, $\langle 100 \rangle$ junctions can only be formed at low temperature by two intersecting $1/2\langle 111 \rangle$ dislocations having a screw character. However, at higher temperature, where the lattice friction opposing $1/2\langle 111 \rangle$ screw dislocations vanishes, $\langle 100 \rangle$ junctions can form more easily from dislocations with a mixed character, and thus in all bcc transition metals as detailed in Appendix F. Therefore, one needs an explanation for the rather scarce experimental observations of the motion of $\langle 100 \rangle$ dislocations at low temperature.

2. Core properties and mobility of $\langle 100 \rangle$ screw dislocations

We study in this section the core properties and mobility of the $\langle 100 \rangle$ screw dislocation, first in the two NM and AF phases of bcc Cr, and then in all other bcc transition metals, using *ab initio* calculations. We focus on its screw orientation, assuming it represents the hindering character, like for $1/2\langle 111 \rangle$, and since it minimizes its elastic energy (see Fig. 1 in section 1.1).

2.1. $\langle 100 \rangle$ screw dislocations in chromium

The *ab initio* simulation cell used for the $\langle 100 \rangle$ screw dislocation contains 200 atoms per unit b length in the direction of the line, with the three periodicity vectors $\vec{p}_1 = 10 \times [100]$, $\vec{p}_2 = 10 \times [010]$, and $\vec{p}_3 = [001]$, and is constructed in a similar way as for $1/2\langle 111 \rangle$ screw dislocations. The crystal is oriented by the glide direction $X \parallel [110]$, the normal to the glide plane $Y \parallel [\bar{1}10]$, and the dislocation line $Z \parallel [001]$. The dislocations are arranged in dipoles in a quadrupolar array. The relaxed core structure of the $\langle 100 \rangle$ screw dislocation in the NM phase of bcc Cr is presented in Fig. 3.

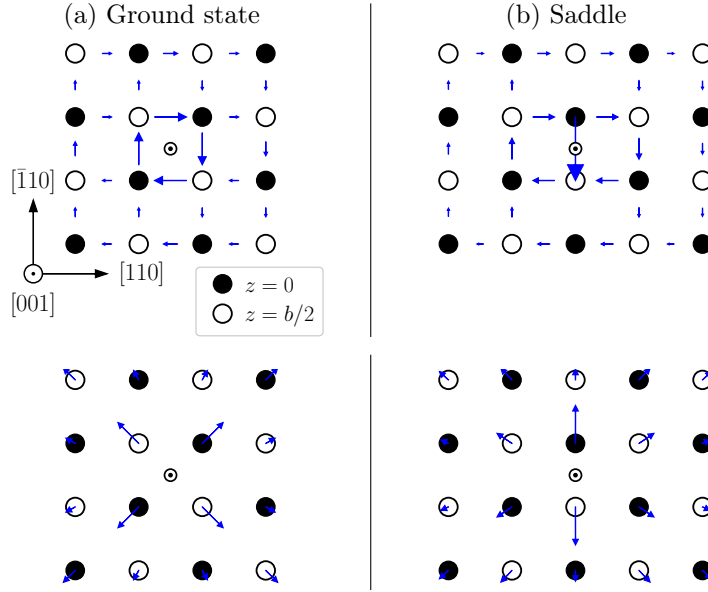


Figure 3: (Upper row) Differential displacement map showing the core structure of the $\vec{b} = [001]$ screw dislocation in the NM phase of bcc Cr in its (a) ground state and (b) saddle configurations. An arrow joining two atoms corresponds to a differential displacement of $b/2$ along $[001]$. (Lower row) Absolute displacement in the (001) plane magnified by a factor 10. Atoms are represented in different colors according to their height along $[001]$.

We consider two positions for the dislocation in the $\{100\}$ plane orthogonal to its line: one leads to the ground state, shown in Fig. 3a, where the dislocation is located at the center of four $\langle 100 \rangle$ atomic columns along the Z axis; and the other one leads to a configuration of higher energy, shown in Fig. 3b, where the dislocation is located between two atomic columns along a $\{110\}$ plane. We will show in the following that the latter actually coincides with the saddle point configuration when the $\langle 100 \rangle$ screw dislocation is gliding in a $\{110\}$ plane. We find a compact core structure for this $\langle 100 \rangle$ screw dislocation, with no spreading. Prior to the *ab initio* calculations presented in this section, the stability of dislocations having a $\langle 100 \rangle$ Burgers vector was checked using anisotropic elasticity theory, to search for possible dissociation into two $1/2\langle 111 \rangle$ partial dislocations. We find such dissociation to be energetically unfavorable, considering $\langle 100 \rangle$ dislocations of all character ranging from screw to edge. The core structures in the two considered configurations are identical in both NM and AF phases, with no magnetic fault introduced in the system as $\langle 100 \rangle$ is a periodicity vector of the AF order of bcc Cr. The edge component of the dislocation in its two configurations are presented in the lower row of Fig. 3, showing a slight dilatation of the atoms near the core of the $\langle 100 \rangle$ dislocation in the plane orthogonal to its line. The core energy of this $\langle 100 \rangle$ screw dislocation in its ground state configuration (Fig. 3a) is 0.718 and 0.737 eV/Å in the NM and AF phases respectively, using the same core radius $r_C = a_0\sqrt{3}/2$ as for $1/2\langle 111 \rangle$ screw dislocations. The energy of the metastable configuration shown in Fig. 3b, defined with respect to the ground state, is 25 and 20 meV/Å respectively in the NM and AF phases.

We then determine the Peierls energy barrier opposing glide of $\langle 100 \rangle$ screw dislocations in $\{110\}$ planes using the two *both* and *stress* NEB setups (see Methods, section 3). The resulting energy barriers ΔE_P and Peierls potentials V_P as a function of the dislocation position x , obtained after subtraction of the variation in the elastic energy of the dipole, are presented in Fig. 4a and b in the NM and AF phases respectively. We did not consider glide of these dislocations in the other possible planes, which are $\{100\}$, since no experimental observation report glide of any dislocation in these planes. Moreover, $\langle 100 \rangle$ dislocations would have to cross a $\langle 100 \rangle$ atomic column (see Fig. 3). The obtained Peierls potentials in $\{110\}$ planes have a similar shape in both magnetic phases of bcc Cr, with a lower energy maximum in the AF phase. The heights of these energy barriers are equal in both cases to the energy difference between the metastable configuration of Fig.

3b and the ground state. The height of the Peierls barrier obtained using setup *both* for the NEB calculation between two adjacent ground state configurations are indicated by grey crosses located at $\xi = 0.5$, showing an excellent agreement between the two methods, proving again the validity of the elastic correction.

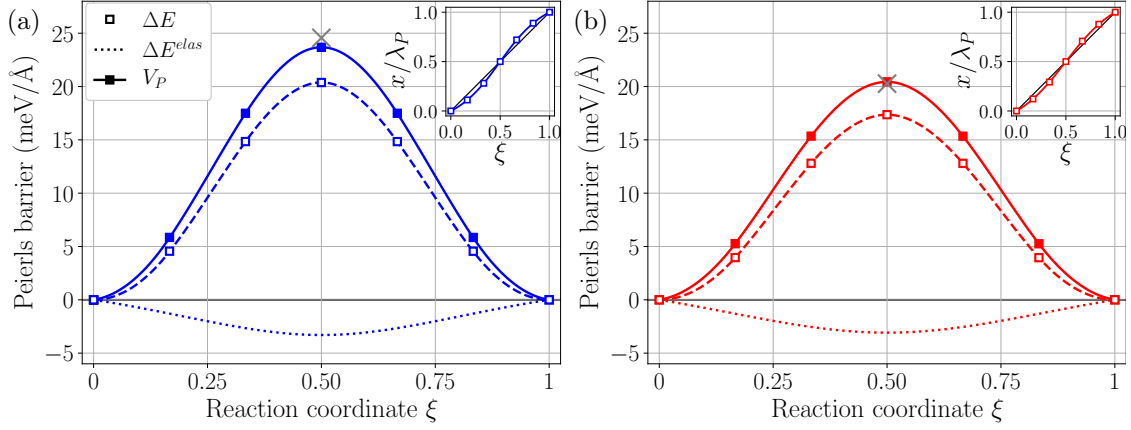


Figure 4: (a) Peierls potential V_P (solid lines) of a $\langle 100 \rangle$ screw dislocation gliding in a $\{110\}$ plane in (a) the NM, and (b) AF phases of bcc Cr as a function of the reaction coordinate ξ along the NEB path. The position x of the dislocation, normalized by the distance $\lambda_P = a_0\sqrt{2}/2$ between adjacent Peierls valleys, is shown in insets.

In the same way as for $1/2\langle 111 \rangle$ screw dislocations, the trajectory and variations of the relaxation volume of the dilatation field induced by the core of the $\langle 100 \rangle$ screw dislocation can be extracted from the variations of the stress recorded along the NEB path using setup *stress*. In the frame of the simulation cell, the relaxation volume tensor of the $\langle 100 \rangle$ screw dislocation has the following form along the path:

$$\bar{\bar{\Omega}}_{\langle 100 \rangle} = \begin{bmatrix} \Omega_{11} & 0 & 0 \\ 0 & \Omega_{22} & 0 \\ 0 & 0 & \Omega_{33} \end{bmatrix} \quad (2)$$

As reported for $1/2\langle 111 \rangle$ screw dislocations, post-processing of the stress variations recorded along the two $I \rightarrow F$ and $F \rightarrow I$ paths [79] show that components Ω_{13} and Ω_{32} are zero for the $\langle 100 \rangle$ screw dislocation gliding in a $\{110\}$ plane. As for Ω_{12} , the mirror symmetry of the $\{110\}$ glide plane imposes its nullity. This is the case for both NM and AF phases. Also, since no magnetic fault is generated by $\langle 100 \rangle$ dislocations in the AF phase, contrary to $1/2\langle 111 \rangle$, the dislocation trajectory and the variation of its relaxation volume can be directly extracted from the stress variations recorded along the NEB path using setup *stress*. The trajectory followed by the $\langle 100 \rangle$ screw dislocation along its minimum energy path when gliding in a $\{110\}$ plane is presented in Fig. 5a in the NM and AF phases, which have been shifted up and down for clarity. We note that the $\langle 100 \rangle$ screw dislocation, contrary to $1/2\langle 111 \rangle$, follows a straight trajectory between two adjacent Peierls valleys in a $\{110\}$ plane, and is almost identical in both magnetic phases. This is also a consequence of the mirror symmetry of the $\{110\}$ glide plane. Given that the trajectory of the $\langle 100 \rangle$ screw dislocation coincides with its macroscopic $\{110\}$ glide plane, $\langle 100 \rangle\{110\}$ slip systems will not exhibit any T/AT asymmetry, unlike $\langle 111 \rangle\{110\}$ slip systems. Variations of the relaxation volume as a function of the dislocation position x are presented in Fig. 5b and c in the NM and AF phases respectively. Although the relaxation volume remains diagonal upon crossing of the Peierls barrier, the high symmetry of the core dilatation field is broken along the path, with the development of an elliptic contribution $\Delta\Omega_e$, and a non-negligible trace $\Delta\Omega_P$. As a consequence, the yield stress of $\langle 100 \rangle$ screw dislocations should experience tension/compression asymmetry, and also be sensitive to an applied pressure. The variation of the relaxation volume tensor is similar in the NM and AF phases, except the $\Delta\Omega_{33}$ component, which is almost negligible in the AF phase.

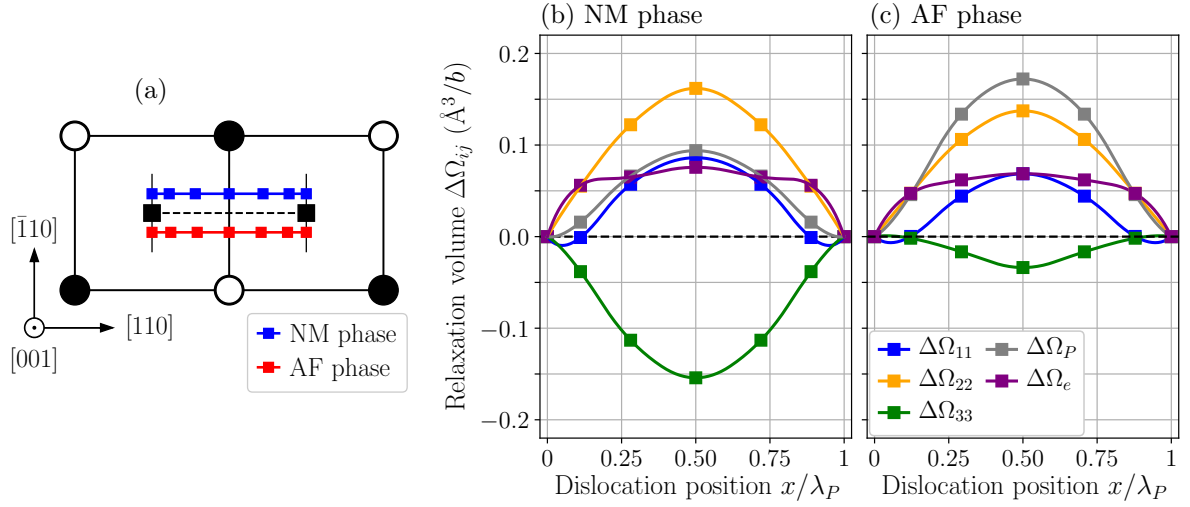


Figure 5: (a) Trajectory of a $[001]$ screw dislocation gliding in the $[110]$ plane in the NM (blue) and AF (red) phases of bcc Cr. Variations of the non-zero components of the relaxation volume tensor of the $[001]$ screw dislocation are presented in the (b) NM and (c) AF phases.

2.2. Competition between $1/2\langle 111 \rangle\{110\}$ and $\langle 100 \rangle\{110\}$ slip in chromium

The Peierls potentials V_P for both $1/2\langle 111 \rangle$ and $\langle 100 \rangle$ screw dislocations gliding in a $\{110\}$ plane are presented in Fig. 6 as a function of the dislocation position x in both NM and AF phases. The Peierls stress τ_P necessary to overcome the energy barrier is evaluated as the maximum slope of the Peierls potential V_P . Upon crossing the barrier, $1/2\langle 111 \rangle$ screw dislocations have to travel a longer distance than $\langle 100 \rangle$, namely $a_0\sqrt{6}/3$ and $a_0\sqrt{2}/2$. We find a Peierls stress of 2.2 and 1.7 GPa for the $\langle 100 \rangle$ screw dislocation gliding in a $\{110\}$ plane in the NM and AF phases respectively. For comparison, the Peierls stress for the $1/2\langle 111 \rangle$ screw dislocation was 2.3 and 2.0 GPa in the NM and AF phases. Thus, one sees that the Peierls stresses of the $1/2\langle 111 \rangle$ and $\langle 100 \rangle$ screw dislocations are comparable in both magnetic phases, and that the two $\langle 111 \rangle\{110\}$ and $\langle 100 \rangle\{110\}$ slip systems should be competitive on the basis of their mobilities. However, as we now know precisely the trajectory followed by the dislocation along its minimum energy path when gliding in a $\{110\}$ plane, and also the variations of its relaxation volume along this path, it is possible to study in more details the competition between these two slip systems, taking full account of non-Schmid effects. In particular, the

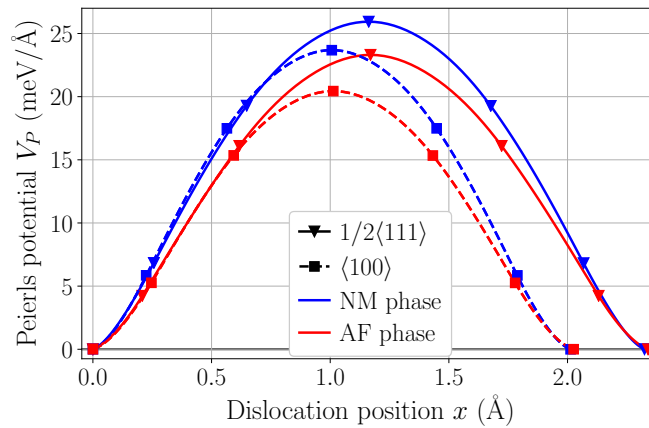


Figure 6: Peierls potential V_P of the $1/2\langle 111 \rangle$ (solid lines) and $\langle 100 \rangle$ (dashed lines) screw dislocations gliding in a $\{110\}$ plane in the NM (blue) and AF (red) phases of bcc Cr as a function of the dislocation position x .

dependence of the yield stress for both $\langle 111 \rangle \{110\}$ and $\langle 100 \rangle \{110\}$ slip systems can be studied as a function of the orientation of the loading axis taking non-Schmid effects into account, which allows for characterizing the competition between these different slip systems for all possible orientations of the tensile/compressive axis at 0 K in the NM and AF phases of bcc Cr. With three different $\langle 100 \rangle$ Burgers vectors, and two possible glide planes for each, there is a total of 6 different $\langle 100 \rangle \{110\}$ slip systems to consider for $\langle 100 \rangle$ dislocations.

Using the yield criteria of Eqs. 12 and 14 presented in section 2.1 of Chapter 2, the yield stress σ_Y of all slip systems of the $\langle 111 \rangle \{110\}$ and $\langle 100 \rangle \{110\}$ types is evaluated as a function of the orientation of the tensile axis in the region of the stereographic projection used in previous chapters (see for example Fig. 5 in Chapter 4). This region encapsulates the whole range of orientations to characterize the plastic anisotropy of both slip systems. The parameters of the yield criterion for $\langle 100 \rangle \{110\}$ slip system under uniaxial loading, extracted from the core properties and mobility of $\langle 100 \rangle$ screw dislocations in the previous section 2.1, are presented in Tab. 1 for the NM and AF phases of bcc Cr. One sees that, contrary to $\langle 111 \rangle \{110\}$ slip, the deviation angle α^* is zero for $\langle 100 \rangle$ screw dislocations gliding in $\{110\}$ planes, due to their straight trajectory along the minimum energy path between two adjacent Peierls valleys. Therefore, these systems do not exhibit T/AT asymmetry in the angle χ between the MRSSP and the glide plane. Also, the magnitude of the variations of the relaxation volume for this $\langle 100 \rangle$ screw dislocation is small compared to $1/2\langle 111 \rangle$, which should yield negligible non-Schmid effects also in terms of tension/compression asymmetry. Among these different components, the trace $\Delta\Omega_P$ has the highest magnitude in both magnetic phases, which will be responsible for non-negligible coupling with applied pressure.

Table 1: Parameters of the yield criterion for $\langle 100 \rangle \{110\}$ slip in bcc Cr considering both NM and AF phases: Peierls stress τ_P (GPa), position x^* of the inflexion point of the Peierls potential (normalized by the distance λ_P between Peierls valleys), and derivatives $\Delta\Omega'_{ij}$ (Å) of the relaxation volume with respect to the position x at the inflexion point x^* .

	τ_P	x^*/λ_P	α^*	$\Delta\Omega'_{11}$	$\Delta\Omega'_{22}$	$\Delta\Omega'_{33}$	$\Delta\Omega'_P$	$\Delta\Omega'_e$
NM phase	2.17	0.169	0	+0.069	+0.075	-0.086	+0.058	+0.007
AF phase	1.74	0.183	0	+0.049	+0.064	-0.014	+0.099	+0.015

The distributions of primary slip systems, *i.e.* whether $\langle 111 \rangle \{110\}$ or $\langle 100 \rangle \{110\}$, and the corresponding yield stress σ_Y in the NM phase are presented in Fig. 7 as a function of the loading axis according to the Schmid law, and including non-Schmid effects in tension and compression. The distribution of primary slip systems as predicted by the Schmid law is a direct image of the ratio between the Peierls stresses of $1/2\langle 111 \rangle$ and $\langle 100 \rangle$ screw dislocations gliding in $\{110\}$ planes, weighted by their respective Schmid factors. The regions colored in green represent the range of loading orientations where a $\langle 100 \rangle \{110\}$ system requires a lower stress to operate than any $\langle 111 \rangle \{110\}$ system. These regions are close to a $\langle 111 \rangle$ axis, where the maximum Schmid factor of a $\langle 111 \rangle \{110\}$ system is below 0.3 whereas it concentrates the orientations for which the Schmid factor of a $\langle 100 \rangle \{110\}$ is maximum, *i.e.* close to 0.5. According to these results, $\langle 100 \rangle$ slip should be observed for a large range of loading orientations in both tension and compression. The results in the AF phase, presented in Fig. 8, show the same qualitative features as in the NM phase. However, as the ratio between the Peierls stresses of the two $\langle 100 \rangle$ and $1/2\langle 111 \rangle$ screw dislocations gliding in a $\{110\}$ plane is slightly lower than in the NM phase (0.89 and 0.94 respectively, see Tab. 1), a larger range of loading orientations favors $\langle 100 \rangle \{110\}$ slip over $\langle 111 \rangle \{110\}$. When non-Schmid effects are taken into account, the region where $\langle 100 \rangle \{110\}$ slip systems are easier to activate is reduced in both tension and compression in the two NM and AF phases, due to the T/AT asymmetry of $\langle 111 \rangle \{110\}$ systems.

Looking at the distribution of the yield stress, its minimum value is found close to $\langle 111 \rangle$ axis, where a $\langle 100 \rangle \{110\}$ slip system is easier to activate. If these systems were not considered, we would have retrieve the results presented in Figs. 12 and 13 of Chapter 2 in the NM and AF phases respectively. As the Peierls stress of both screw dislocations is slightly lower in the AF than in the NM phase, the overall yield stress

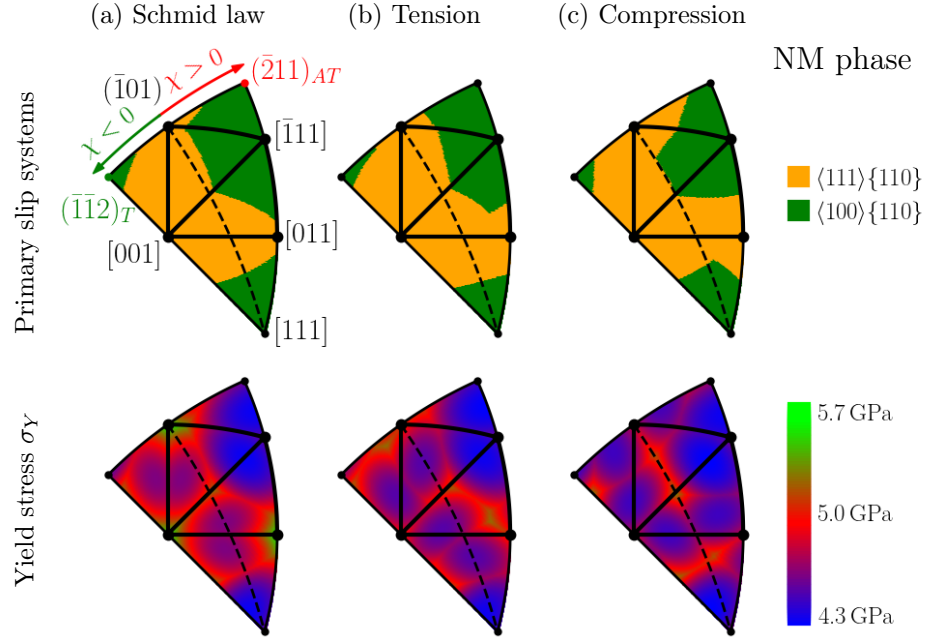


Figure 7: Type of primary slip systems, *i.e.* $\langle 111 \rangle \{110\}$ or $\langle 100 \rangle \{110\}$ (first row), with the corresponding yield stress σ_Y levels (second row) at 0 K as a function of the orientation of the loading axis in the NM phase of bcc Cr (a) according to the Schmid law, and including non-Schmid effects in (b) tension, and (c) compression.

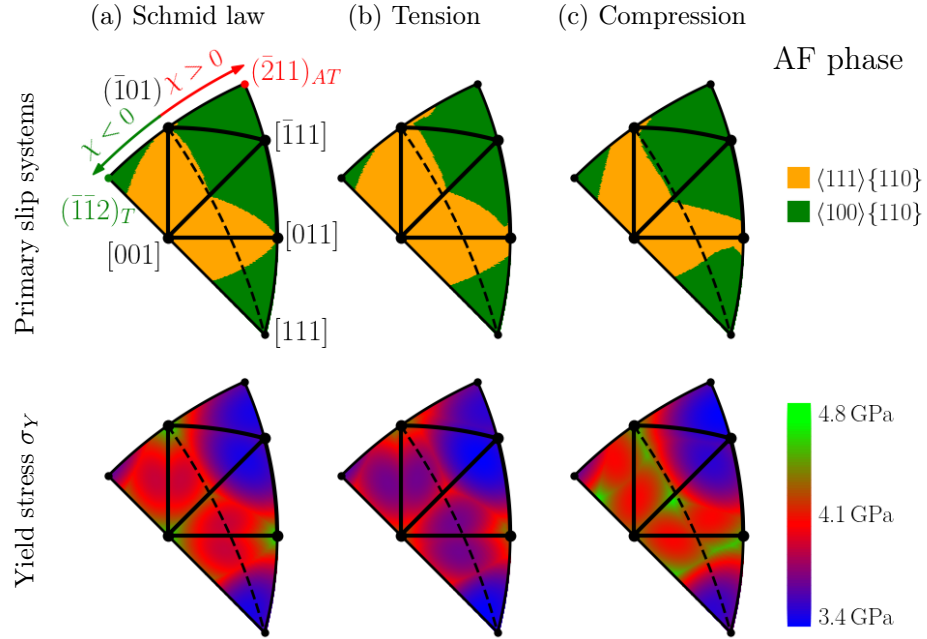


Figure 8: Competition between $\langle 111 \rangle \{110\}$ and $\langle 100 \rangle \{110\}$ slip systems in the AF phase of bcc Cr at 0 K.

required to activate slip is lower. However, the predicted primary slip systems are the same in the two magnetic phases, covering a more or less equivalent space in the stereographic projection.

Our *ab initio* modeling thus predicts $\langle 100 \rangle \{110\}$ slip to occur in a large portion of the standard stere-

ographic triangle at 0 K, mainly near $\langle 111 \rangle$ orientations (see Fig. 7) where slip systems having all three $\langle 100 \rangle$ Burgers vectors have the same Schmid factor. We stress that this conclusion assumes motion of $\langle 100 \rangle$ dislocations to be controlled by its screw orientation like for $1/2\langle 111 \rangle$. However, we will show in the following another line orientation impedes the motion of $\langle 100 \rangle$ dislocations at low temperature. Taking for instance a $[\bar{5}911]$ single crystal tested in compression by Holzer *et al.* [34] at 77 K, strong $\langle 100 \rangle\{110\}$ slip activity is expected. The predicted yield stress for the slip systems having the 6 highest Schmid factors are presented in Tab. 2, among which the two most stressed are of the $\langle 100 \rangle\{110\}$ type. For this orientation, the authors report slip activity on both $(\bar{1}01)$ and $(\bar{1}10)$ planes through the rotation of the sample towards the corresponding poles of the stereographic projection. They attributed this observation to the activity of a $\langle 111 \rangle\{110\}$ slip system for both observed slip planes. However, according to our yield criterion, the lowest yield stress for a $\langle 111 \rangle\{110\}$ slip system in compression for $(\bar{1}10)$ slip is 6.95 GPa in the AF phase, whereas it is only 3.68 GPa for a $\langle 100 \rangle\{110\}$ system, suggesting slip might have occurred through the operation of the $[001](\bar{1}10)$ slip system. As for slip on $(\bar{1}01)$ plane, it is probably due to the operation of the highly stressed $[111](\bar{1}01)$ system, but can also be interpreted as the operation of the $[010](\bar{1}01)$ slip system, which has a lower predicted yield stress in compression.

Table 2: Predicted yield stress for Cr single crystal under uniaxial compression along the $[\bar{5}911]$ axis investigated by Holzer *et al.* [34] at 77 K. Predicted yield stresses are presented considering the AF phase.

Slip system	SF	Schmid law	Compression
$[111](\bar{1}01)$	0.432	4.59 GPa	4.45 GPa
$[111](\bar{1}10)$	0.378	5.25 GPa	6.95 GPa
$[\bar{1}11](101)$	0.270	7.35 GPa	8.18 GPa
$[001](\bar{1}10)$	0.480	3.62 GPa	3.68 GPa
$[010](\bar{1}01)$	0.449	3.87 GPa	3.98 GPa
$[100](011)$	0.312	5.58 GPa	5.25 GPa

2.3. Thermal activation of $\langle 100 \rangle$ screw dislocations in chromium

We study in the present section if the stiff competition between the two $\langle 111 \rangle\{110\}$ and $\langle 100 \rangle\{110\}$ slip systems predicted at 0 K holds with temperature, accounting for the thermally activated glide of $\langle 100 \rangle$ screw dislocations through nucleation of kink-pairs. We use the same method as in Chapter 2 to evaluate the line tension Γ of the $\langle 100 \rangle$ screw dislocation using similar *ab initio* calculations [85, 191]. The resulting energies and fit to the model (see Chapter 2, section 3.1) are presented in Fig. 9 for both NM and AF phases, for which we find a line tension Γ of 2.84 and 2.60 eV/Å respectively.

Table 3: Parameters of the mobility law for the two $1/2\langle 111 \rangle\{110\}$ and $\langle 100 \rangle\{110\}$ slip systems in the NM and AF phases of bcc Cr: Peierls stress τ_P (GPa), line tension Γ (eV/Å), kink-pair formation energy ΔE_{kp} (eV), and parameters p and q of the Kocks' law in Eq. 23. The model is presented in details in Chapter 2, section 3.2.

	Slip system	τ_P	Γ	ΔE_{kp}	p	q
NM phase	$1/2\langle 111 \rangle\{110\}$	2.32	1.26	0.80	0.88	1.39
	$\langle 100 \rangle\{110\}$	2.17	2.84	1.04	0.87	1.35
AF phase	$1/2\langle 111 \rangle\{110\}$	1.98	3.01	1.27	0.89	1.33
	$\langle 100 \rangle\{110\}$	1.74	2.60	0.89	0.85	1.31

Contrary to $1/2\langle 111 \rangle$ screw dislocations, the line tension is very close for $\langle 100 \rangle$ in the two magnetic phases of bcc Cr, since there is no added resistance from the magnetic fault in the AF phase like for $1/2\langle 111 \rangle$. This results in the parameters of the yield criterion presented in Tab. 3 for the thermally activated term of the

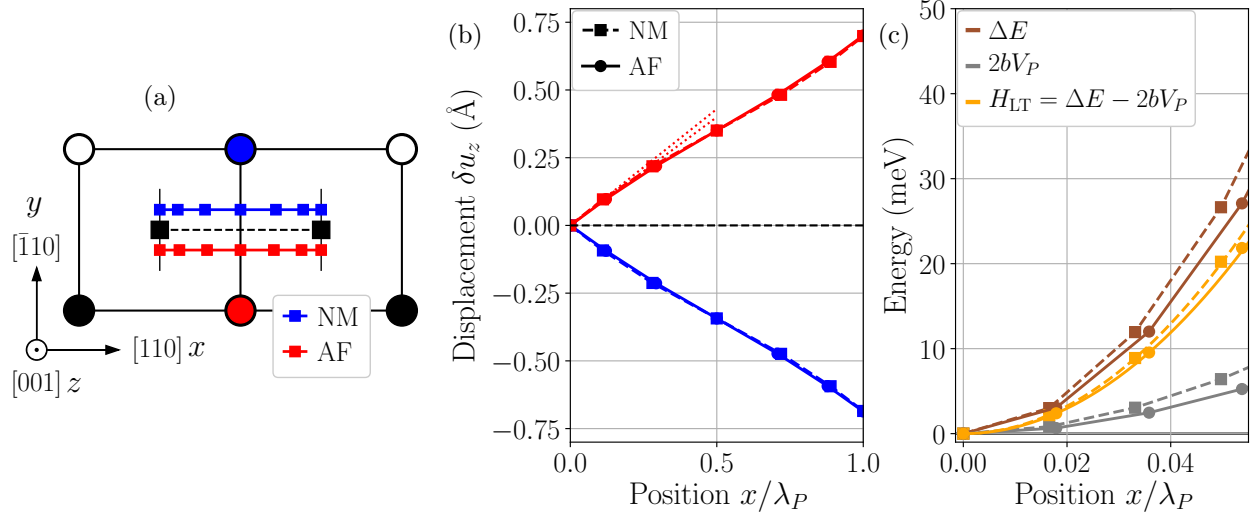


Figure 9: (a) Trajectory of the $[001]$ screw dislocation in the NM and AF phases showing in colors the two most displaced atomic columns in the $[001]$ direction. (b) Displacement δu_z of the two $[001]$ atomic columns shown in (a) along $[001]$ as a function of the dislocation position x projected along the $[110]$ direction. (c) Total energy difference ΔE (brown), change in Peierls energy $2bV_P$ (grey), and resulting line tension energy H_{LT} (orange) of a kinked $[001]$ screw dislocation in the NM (dashed squares) and AF (solid circles) phases as a function of its position x .

criterion of Eq. 28, detailed in Chapter 2, section 3.2, which is extended here to $\langle 100 \rangle \{110\}$ slip systems. The resulting flow stress evolution with temperature $\tau_P(T)$ for both types of slip systems in the two NM and AF phases of bcc Cr are presented in Fig. 10, considering an entropic contribution accounted for by the Meyer-Neldel compensation rule with $T_m = T_{\text{melt}} = 2180$ K. Different values are set for the dislocation density ρ_D to show the dependence of the athermal temperature T_{ath} on this parameter of the model, with a density set to the same value for both slip systems, *i.e.* $\rho_D^{1/2\langle 111 \rangle} = \rho_D^{\langle 100 \rangle}$.

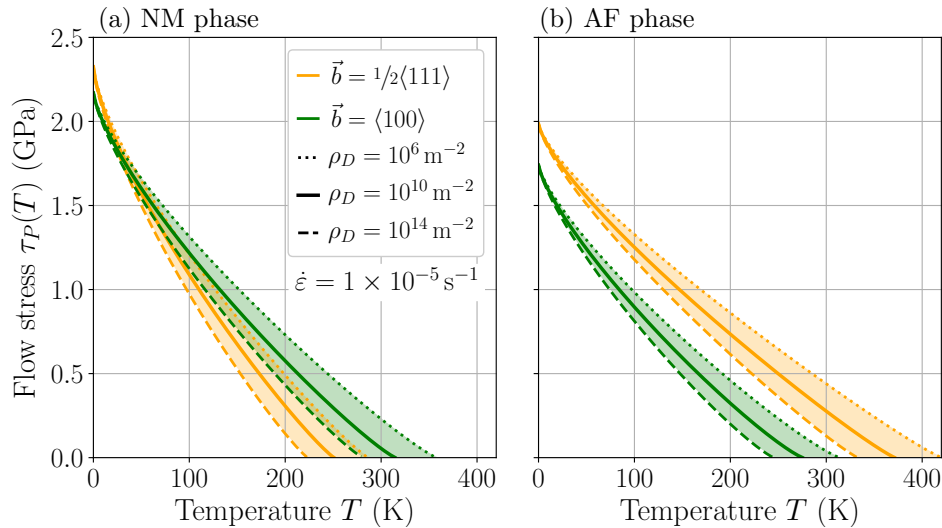


Figure 10: Flow stress $\tau_P(T)$ as a function of the temperature T for both $1/2\langle 111 \rangle$ (orange) and $\langle 100 \rangle$ (green) screw dislocations in the (a) NM and (b) AF phases of bcc Cr, considering different values for the dislocation density ρ_D ranging from 10^6 to 10^{14} m^{-2} at a fixed rate of plastic strain $\dot{\epsilon} = 1 \times 10^{-5} \text{ s}^{-1}$.

At 0 K, we retrieve the comparable Peierls stresses of the two slip systems in both magnetic phases of bcc Cr, as discussed in the previous section. Also, a similar athermal temperature is predicted for both slip systems, maintaining the competition throughout the whole temperature range up to T_{ath} . Indeed, the main dislocation dependent quantity entering the expression of the athermal temperature (see Eq. 30) is the kink-pair formation energy ΔE_{kp} , which is comparable for both $\langle 100 \rangle \{110\}$ and $\langle 111 \rangle \{110\}$ slip systems (see Tab. 3). Therefore, one expects the distribution of primary slip systems presented at 0 K in the previous section (see Figs. 7 and 8 for the NM and AF phases respectively) to hold with temperature, up to T_{ath} . Thus, it appears necessary to account for $\langle 100 \rangle$ screw dislocations to rationalize the plasticity of bcc Cr, with a competition between with glide of $1/2\langle 111 \rangle$ screw dislocations holding with increasing temperature. Given the strong competition predicted in Cr, one needs to check if it is the case in other bcc metals.

2.4. $\langle 100 \rangle$ screw dislocations in all bcc transition metals

We present in this section *ab initio* evaluation of the core properties and mobility of $\langle 100 \rangle$ screw dislocations at 0 K in all bcc transition metals, in order to compare to the results presented for Cr in the previous section. The core of the $\langle 100 \rangle$ screw dislocation obtained after relaxation with *ab initio* calculations has the same structure in all bcc transition metals as presented in Fig. 3a for Cr, showing a compact structure with a slight dilatation of the atoms in the vicinity of the core, whose magnitude depends on the metal. The configuration presented in Fig. 3b is always found metastable, with a higher energy than the ground state configuration, and corresponding to the configuration at the saddle point of the Peierls energy barrier in $\{110\}$ planes. The core energy of the $\langle 100 \rangle$ screw dislocation in its ground state is presented in Tab. 4 for all bcc transition metals, and compared to the results obtained for the $1/2\langle 111 \rangle$ screw dislocation.

Table 4: Core energy E_c (eV/Å) of the two $1/2\langle 111 \rangle$ and $\langle 100 \rangle$ screw dislocations in all bcc transition metals obtained using *ab initio* calculations and considering a core radius $r_c = b_{1/2\langle 111 \rangle} = a_0\sqrt{3}/2$ for both dislocations.

	V	Nb	Ta	Cr (NM)	Cr (AF)	Mo	W	Fe
$\vec{b} = 1/2\langle 111 \rangle$	0.16	0.14	0.19	0.43	0.44	0.42	0.58	0.29
$\vec{b} = \langle 100 \rangle$	0.40	0.44	0.59	0.72	0.74	0.79	1.13	0.71

Comparing the results for the two types of screw dislocations, we see that the core energy of the $\langle 100 \rangle$ screw dislocation is higher than for $1/2\langle 111 \rangle$ in all bcc metals, with a ratio of 2 to 3 between the two Burgers vectors depending on the metal. This higher core energy for $\langle 100 \rangle$ dislocations has also been reported by Bertin *et al.* [246] in various bcc transition metals using interatomic potentials. In their work, the authors also showed that the minimum of the core energy for $\langle 100 \rangle$ dislocations does not correspond to the screw orientation, but is found instead for a mixed character $\theta = 54.7^\circ$, which corresponds to a line oriented along a $\langle 111 \rangle$ direction, whose importance will be shown in the next section.

We now evaluate the Peierls potential of this $\langle 100 \rangle$ screw dislocation gliding in a $\{110\}$ plane using the same NEB calculations as performed for Cr in the previous section 2.1, with setups *both* and *stress*. The resulting Peierls potentials V_P obtained after correction of the variation of the elastic energy are presented in Fig. 11 in green as a function of the dislocation position x for all bcc transition metals. Similarly to $1/2\langle 111 \rangle$ dislocations, an adjustment of the elastic constants was needed to enforce the symmetry of trajectory for the $\langle 100 \rangle$ screw dislocation, which is presented in Appendix D. The Peierls potentials for a $1/2\langle 111 \rangle$ screw dislocation gliding in a $\{110\}$ obtained previously (see Chapter 4, Fig. 1) are also plotted in orange for comparison. We see that, like reported for Cr, the height of the barrier opposing glide of $\langle 100 \rangle$ screw dislocations in $\{110\}$ planes is similar to the one of $1/2\langle 111 \rangle$ screw dislocations for almost all bcc transition metals except V and Nb. In particular, the barrier is lower in Cr, and have very close values for both screw dislocations in Ta, Mo, W and Fe (within accuracy of *ab initio* calculations). The resulting Peierls stresses are presented in Tab. 5, with the values obtained previously for the $1/2\langle 111 \rangle$ screw dislocation also reported.

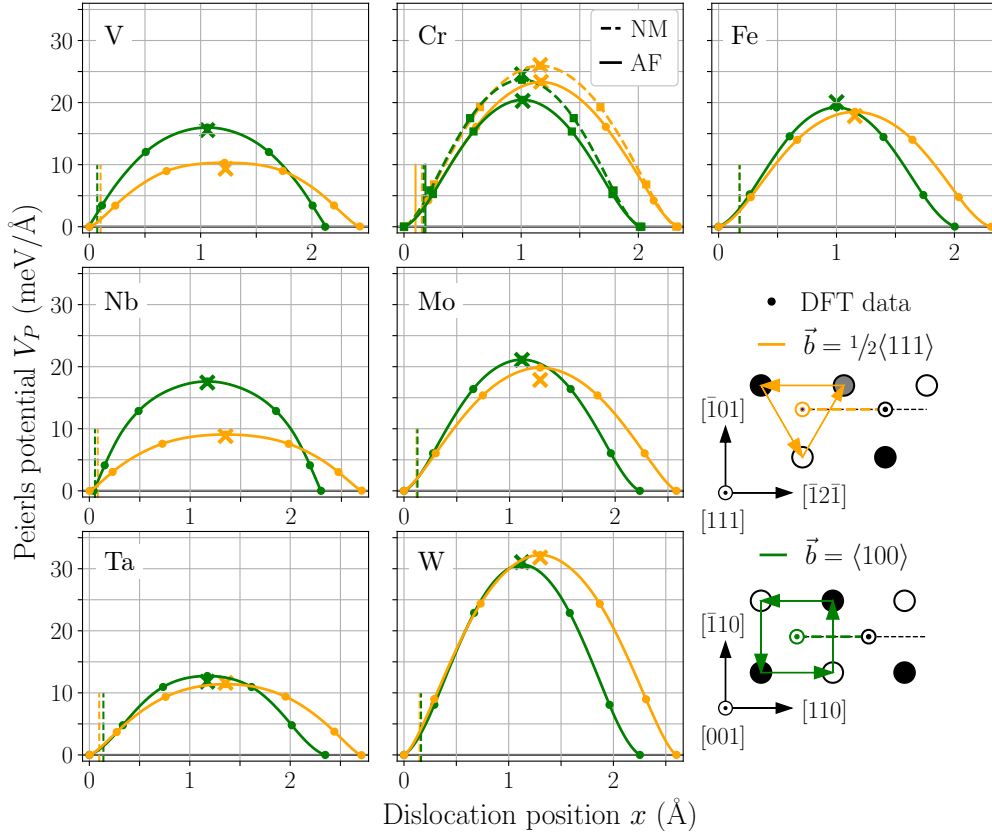


Figure 11: Peierls potential V_P (meV/Å) of both $1/2\langle 111 \rangle$ (orange) and $\langle 100 \rangle$ (green) screw dislocations gliding in a $\{110\}$ plane as a function of their position x for all bcc transition metals. All presented potentials are obtained using the *stress* setup, and after performing correction of the variation in elastic energy. Crosses located halfway along the paths indicate the height of the barrier obtained using the *both* setup.

Again, the Peierls stresses of the two systems are comparable in the majority of the seven bcc transition metals, which should result in the same competition as predicted in bcc Cr in the previous section.

Table 5: Parameters of the yield criterion for $\{100\}\{110\}$ slip: Peierls stress τ_P (GPa), with the value for the $1/2\langle 111 \rangle$ screw dislocation in the left column, position x^* of the inflexion point of the Peierls potential (normalized by the distance λ_P between Peierls valleys), and derivatives $\Delta\Omega'_{ij}^*$ (Å) of the relaxation volume with respect to the position x at the inflexion point x^* . The deviation angle α^* is zero in all metals for $\langle 100 \rangle\{110\}$ slip.

Element	$1/2\langle 111 \rangle\{110\}$	$\langle 100 \rangle\{110\}$						
	τ_P	τ_P	x^*/λ_P	$\Delta\Omega'_{11}^*$	$\Delta\Omega'_{22}^*$	$\Delta\Omega'_{33}^*$	$\Delta\Omega'_P$	$\Delta\Omega'_e$
V	1.03	1.61	0.071	+1.080	-1.067	+0.042	+0.055	-2.147
Nb	0.79	1.72	0.056	+1.567	-1.594	+0.084	+0.057	-3.161
Ta	0.87	0.94	0.140	+0.214	-0.171	-0.014	+0.030	-0.385
Cr (NM)	2.32	2.17	0.169	+0.069	+0.075	-0.086	+0.058	+0.007
Cr (AF)	1.98	1.74	0.183	+0.049	+0.064	-0.014	+0.099	+0.015
Mo	1.40	1.57	0.128	-0.034	+0.174	-0.092	+0.047	+0.208
W	2.36	2.09	0.163	+0.057	+0.089	-0.084	+0.062	+0.033
Fe	1.65	1.67	0.178	+0.094	-0.140	-0.033	-0.081	-0.237

To fully parametrize the yield criterion including $\langle 100 \rangle \{110\}$ slip systems, the trajectory and variations of the relaxation volume of the $\langle 100 \rangle$ screw dislocation upon crossing the Peierls barrier of Fig. 11 can be extracted using the setup *stress* as already done for $1/2\langle 111 \rangle$ in all bcc transition metals in Chapter 4, and also $\langle 100 \rangle$ screw dislocations in Cr in section 2.1. The variation of the relaxation volume of this $\langle 100 \rangle$ screw dislocation gliding in a $\{110\}$ plane is presented in Fig. 12 for all bcc transition metals, with the parameters of the yield criterion presented in Tab. 5. As reported for $1/2\langle 111 \rangle$, the variation of the relaxation volumes show a large variety of different behaviors among all bcc transition metals. However, some group tendencies can be observed for metals belonging to a same column of the periodic table. For V, Nb and Ta (group V), we find a negligible trace and component $\Delta\Omega_{33}$, with a negative ellipticity $\Delta\Omega_e$ of a high magnitude compared to other metals and results obtained for the $1/2\langle 111 \rangle$ screw dislocation. For Cr, Mo and W (group VI), a non-negligible trace and component $\Delta\Omega_{33}$ is found, with the same sign in the three metals, and also a positive ellipticity $\Delta\Omega_e$. Fe show a hybrid behavior between the two previous groups, with a weak magnitude for the variation of all components, but a non-negligible trace and $\Delta\Omega_{33}$, and negative ellipticity $\Delta\Omega_e$.

Using the yield criterion including core properties of this $\langle 100 \rangle$ screw dislocation, we can now study the competition between $\langle 111 \rangle \{110\}$ and $\langle 100 \rangle \{110\}$ slip in all bcc transition metals. Ranges of the predicted yield stress at 0 K for both slip systems, *i.e.* minimum to maximum values over the whole range of orientations and considering all possible slip systems of both types, are presented in Fig. 13 for all bcc transition metals. Results are shown according to the Schmid law, and including non-Schmid effects in both tension and compression. For all metals, the predicted distribution of the yield stress resembles the one presented in the NM phase of Cr in Fig. 7, unless the ratio between the Peierls stresses of the two systems drastically favors $\langle 111 \rangle \{110\}$ slip, which is the case for Nb, and in a lesser extent for V. In all other metals, the yield stress show the competition between the two systems, which is most pronounced in Ta, Cr, W and Fe. We also note that, since the Schmid factor for all $\langle 100 \rangle \{110\}$ slip systems tends to zero for loading axis close to

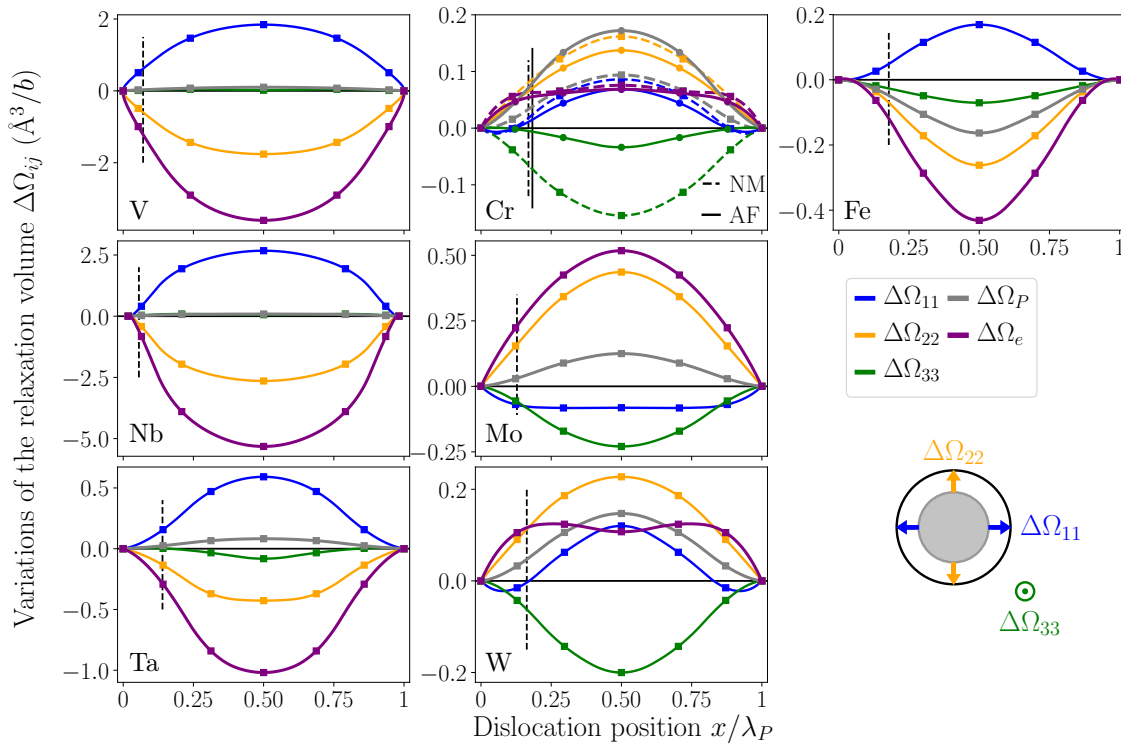


Figure 12: Variations of the relaxation volume $\Delta\Omega_{ij}$ ($\text{\AA}^3/b$) of the $\langle 100 \rangle$ screw dislocation as a function of its position x in the $\{110\}$ plane for all bcc transition metals. Vertical lines indicate the position of the inflexion point x^* of the Peierls potential.

a $\langle 100 \rangle$ orientation, the maximum value predicted by the model tends to infinity. As discussed in the case of Cr, the competition between the two slip systems is expected to be the most pronounced for loading axis near a $\langle 111 \rangle$ orientation, in both tension and compression.

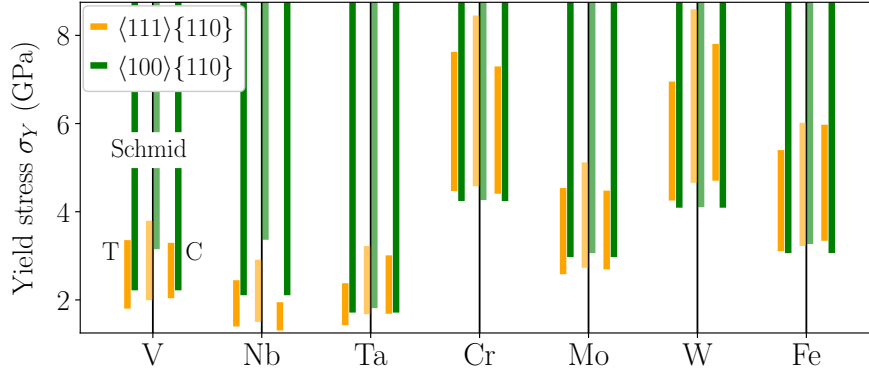


Figure 13: Range of yield stresses σ_Y predicted by the yield criterion at 0 K for both $\langle 111 \rangle \{110\}$ (orange) and $\langle 100 \rangle \{110\}$ (green) slip systems according to the Schmid law (middle bars), and including non-Schmid effects in tension (T, left bars) and compression (C, right bars), for all bcc transition metals. Results for Cr are presented in the NM phase.

Our *ab initio* results thus indicate that resolved shear stress necessary to activate glide of the $\langle 100 \rangle$ screw dislocations compares to $1/2\langle 111 \rangle$. However, the relative contribution of the different slip systems to the development of the plastic strain depends not only on the dislocation ease to glide, but also on the corresponding density of dislocations and their multiplication propensity. As discussed in section 1.3, a non-negligible proportion of $\langle 100 \rangle$ dislocations is reported experimentally compared to $1/2\langle 111 \rangle$ [123, 256, 257]. $\langle 100 \rangle$ dislocations are actually observed as junctions between intersecting $1/2\langle 111 \rangle$ dislocations in all bcc transition metals. These junctions could therefore act as sources of $\langle 100 \rangle$ dislocations for well oriented mechanical loadings. This will allow for the increase of $\langle 100 \rangle$ dislocation density, unless another character has a higher Peierls stress than the screw orientation and impedes the activation of $\langle 100 \rangle$ sources, thus explaining why motion of these $\langle 100 \rangle$ dislocations is not observed at low temperature in most bcc metals.

3. Larger scale simulations using molecular dynamics and interatomic potentials

We study in this section dislocation loops with both $1/2\langle 111 \rangle$ and $\langle 100 \rangle$ Burgers vectors, to compare their expansion under an applied stress. We also investigate $\langle 100 \rangle$ dislocation sources made of a junction between two intersecting $1/2\langle 111 \rangle$ dislocations, to search for a mechanism explaining the scarce experimental observations of the motion of $\langle 100 \rangle$ dislocations at low temperature, whereas our *ab initio* modeling predicts glide of the two screw dislocations in $\{110\}$ planes to be competitive at 0 K in almost all bcc transition metals.

3.1. Dislocation loops with $1/2\langle 111 \rangle$ and $\langle 100 \rangle$ Burgers vectors under strain

For a given slip system to actively participate to the plastic deformation, these dislocations must be able to effectively multiply to a representative density. Dislocation loops expand when subjected to an applied stress, with a shape dictated by elasticity at high temperature [260]. At low temperature, where the Peierls mechanism still holds, the high lattice friction of $1/2\langle 111 \rangle$ screw dislocations in bcc metals leads to a faceted growth of $1/2\langle 111 \rangle$ loops, with a channeled expansion along the screw direction of the dislocation line [261], since this screw orientation has the highest Peierls barrier among all characters. In the previous sections using *ab initio* calculations, competition between the two $\langle 111 \rangle \{110\}$ and $\langle 100 \rangle \{110\}$ slip systems was studied assuming motion of both dislocations is governed by the high lattice friction experienced by its screw orientation. However, we are not sure that this is also the case for $\langle 100 \rangle$ dislocations, thus motivating the study of these loops under applied stress, to determine the orientation of the line hindering the motion of these dislocations. We study loops having both $1/2\langle 111 \rangle$ and $\langle 100 \rangle$ Burgers vectors, in W, modeled using

the MEAM potential of Park *et al.* [89].

The simulation cell used for the growth of $1/2\langle 111 \rangle$ dislocation loop has a geometry defined by the three vectors $X = 87 \times [111]$, $Y = 35 \times [\bar{1}2\bar{1}]$, and $Z = 40 \times [\bar{1}01]$, with periodic boundary conditions in the three Cartesian directions. A circular dislocation loop having a $1/2[111]$ Burgers vector is introduced in the center of the simulation cell, and a shear strain ε_{xz} is then applied to the system by constraining the periodicity vectors of the simulation cell, resulting in a stress τ_{xz} resolved on the screw orientation. The loop starts to expand as to equilibrate the applied strain, with a decreasing stress until the loop has reached equilibrium. The configuration of a $1/2[111]$ loop after molecular statics relaxation at 0 K is presented in Fig. 14 under two different shear strains ε_{xz} , and a corresponding stress $\tau_{xz} = 2.5$ GPa measured after relaxation in both presented configurations of the loop.

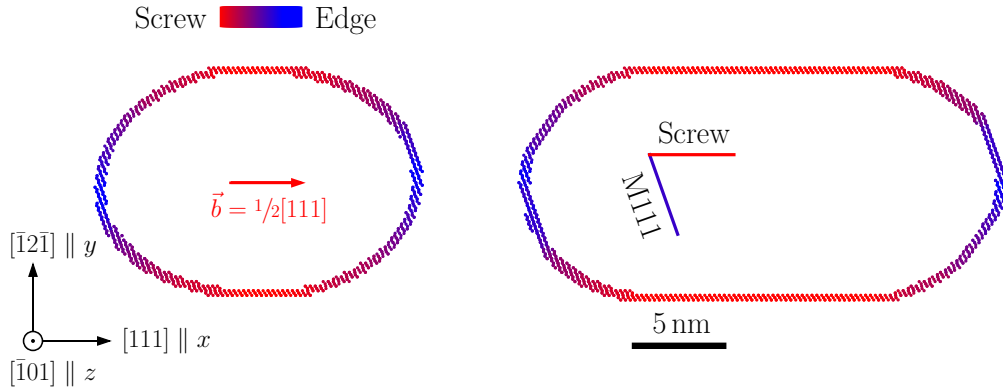


Figure 14: Molecular statics relaxation at 0 K of dislocation loops with $1/2[111]$ Burgers vector in W under a shear strain ε_{xz} . Atoms belonging to the dislocation core are represented as spheres, whose color depends on the local orientation of the line.

As the strain is increased, the expansion of the $1/2[111]$ dislocation loop is channeled along the direction of the screw orientation, due to the high lattice friction it experiences compared to all other line orientations. This results in a faceted growth of the loop as long as the Peierls stress of the screw orientation is not reached, with the creation of a $1/2[111]$ screw dislocation dipole. We also note the presence of small faceted segments along a mixed orientation, denoted M111 on Fig. 14, and corresponding to a line orientation along the $[1\bar{1}1]$ direction, with a mixed character $\theta = 70.5^\circ$. This orientation was previously studied by Kang *et al.* [261] in Ta using an interatomic potential. The authors reported this M111 orientation to have the second highest Peierls stress among all line orientations they tested, with similar consequences on the expansion of $1/2\langle 111 \rangle$ dislocation loops as presented here. To quantify the lattice friction experience by these different line orientations, we now evaluate the height of the Peierls barrier of a $1/2[111]$ dislocation gliding in the $(\bar{1}01)$ plane in W, using the MEAM potential of Park *et al.* [89]. For this purpose, the simulation cell contains a single dislocation with a line oriented along the periodic Y axis of the cell, and free surfaces in the two other directions, as sketched in Fig. 8 in Methods. The results are presented in Tab. 6, considering a line oriented along the four high-symmetry axis of the bcc lattice (*i.e.* $\langle 111 \rangle$, $\langle 112 \rangle$, $\langle 110 \rangle$ and $\langle 100 \rangle$).

Table 6: Height of the Peierls barrier E_P (meV/Å) opposing glide of a $1/2[111]$ dislocation in the $(\bar{1}01)$ plane for different line orientations \vec{l} corresponding to a character θ ($^\circ$). Results are presented in W modeled with the MEAM potential of Park *et al.* [89]. The line orientation with the highest barrier is indicated by a *, which is the screw for $1/2\langle 111 \rangle$ dislocations.

Line orientation \vec{l}		$[111]$	$[121]$	$[101]$	$[010]$	$[\bar{1}\bar{1}\bar{1}]$	$[\bar{1}\bar{2}\bar{1}]$
$\vec{b} = 1/2[111] \in (\bar{1}01)$	θ	0	19.5°	35.3°	54.7°	70.5°	90°
	E_P	43.8*	1.3	4.7	13.5	20.6	1.3

Apart from the screw orientation, which experiences the highest Peierls energy barrier E_P , we retrieve this mixed orientation with $\theta = 70.5^\circ$, corresponding to a line oriented along a different $\langle 111 \rangle$ direction than its Burgers vector, with a non-negligible energy barrier as previously reported in other bcc transition metals, both using interatomic potentials [261] or *ab initio* calculations [262]. This shows on the shape of the $1/2\langle 111 \rangle$ loop expanding under an applied strain presented in Fig. 14, where a small faceted segment with this mixed orientation appears on the left and right of the loop. However the energy barrier for the screw orientation of $1/2\langle 111 \rangle$ dislocations is at least twice higher using the MEAM potential for W, and also reported in the work of Romaner *et al.* [262] using *ab initio* calculations in various bcc transition metals. By applying a controlled shear stress to this non-periodic simulation cell until the dislocation glides over at least 1 nm, we evaluate the Peierls stress of the $1/2\langle 111 \rangle$ screw dislocation in a $\{110\}$ plane at 4.0 GPa in W. As measured after relaxation of the loop in both configurations presented in Fig. 14, the applied shear stress $\tau_{xz} = 2.5$ GPa falls below the Peierls stress τ_P of this screw dislocation. Thus, the loop can start to expand before the Peierls stress of the screw orientation is reached, indicating this orientation has indeed the highest barrier to overcome, and thus controls motion of $1/2\langle 111 \rangle$ dislocations. The study of the expansion of a dislocation loop therefore gives unbiased information on the orientation hindering the motion of these dislocations at low temperature.

We now perform identical simulations on a $\langle 100 \rangle$ dislocation loop, in a cell with periodicity vectors $X = 150 \times [010]$, $Y = 60 \times [101]$, and $Z = 40 \times [10\bar{1}]$, and periodicity along the three directions. Relaxed configurations of a $[010]$ loop at two different shear strains ε_{xz} are presented in Fig. 15, also in W.

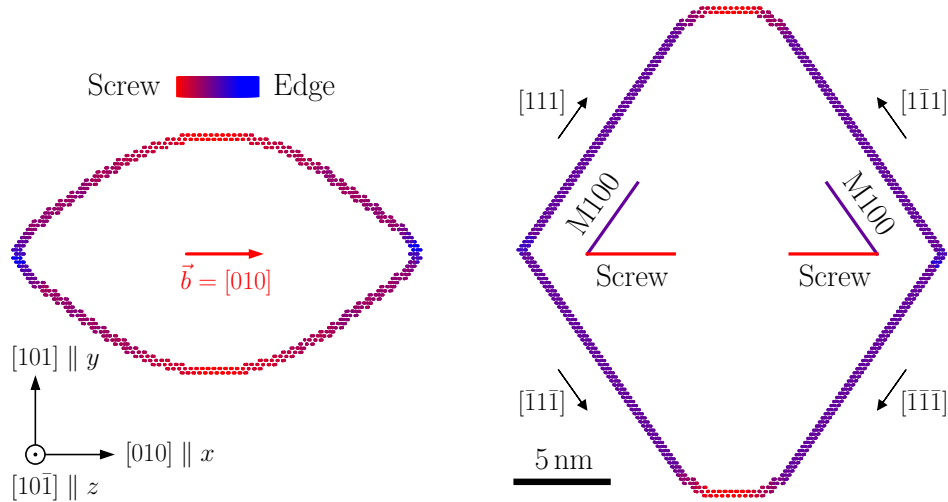


Figure 15: Molecular statics relaxation at 0 K of dislocation loops with $[010]$ Burgers vector in W under a shear strain ε_{xz} .

The configuration shown on the left is relaxed under a shear strain corresponding to a stress $\tau_{xz} = 3$ GPa, which is below the Peierls stress of 3.2 GPa found for the $\langle 100 \rangle$ screw dislocation. Thus, the loop does not expand below the Peierls stress of the $\langle 100 \rangle$ screw dislocation, contrary to $1/2\langle 111 \rangle$, where the loop had already started to expand before the Peierls stress of the screw orientation was reached through motion of mixed orientations. This indicates that for $\langle 100 \rangle$ dislocations, another line orientation must require a higher stress than the screw. This is further confirmed when the applied strain is increased up to a corresponding stress of 6 GPa, with the relaxed configuration presented on the right of Fig. 15. The shear stress is now above the Peierls stress of the screw orientation, which therefore starts moving in the Y direction. However, contrary to $1/2\langle 111 \rangle$, for which the hindering orientation is of screw character, the screw segments of the $\langle 100 \rangle$ dislocation start moving before another particular line orientation, matching the two $\langle 111 \rangle$ directions contained in the habit $\{110\}$ plane of the loop. Given the symmetry of the bcc lattice, these two $[111]$ and

$[1\bar{1}1]$ hindering orientations (for the $[010]$ loop of Fig. 15) lay at an angle of 70.5° between one another, therefore blocking both the expansion of the loop and the further creation of a dipole when the dislocation line aligns in one of these two orientations, even if the stress is increased. Indeed, the length of the screw segment of the loop shortens until this mixed orientation is matched, which we will refer in the following as the M100 dislocation. We now quantify the lattice friction experienced by different line orientations of this $[010]$ dislocation in W, using a similar dislocation setup as for the $1/2[111]$ dislocation in Tab. 6. The results are presented in Tab. 7 using the MEAM potential for W.

Table 7: Height of the Peierls barrier E_P (meV/Å) opposing glide of a $[010]$ dislocation in the $(\bar{1}01)$ plane for different line orientations \vec{l} corresponding to a character θ ($^\circ$). Results are presented in W modeled with the MEAM potential of Park *et al.* [89]. The line orientation with the highest barrier is indicated by a *.

Line orientation \vec{l}	θ	$[010]$	$[121]$	$[111]$	$[101]$
$\vec{b} = [010] \in (\bar{1}01)$	E_P	0	35.3°	54.7°	90°
		33.2	19.2	195.9*	51.2

As expected from the loop expansion, contrary to $1/2\langle 111 \rangle$ dislocation, the screw orientation of the $\langle 100 \rangle$ dislocation does not show the maximum energy barrier. Instead, the height of the Peierls barrier for the screw is of the same order as the edge orientation, and are both much lower than for the mixed orientation with $\theta = 54.7^\circ$, corresponding a line oriented along a $\langle 111 \rangle$ direction, *i.e.* the M100 dislocation. To confirm these results, the height of the Peierls barrier of the M100 dislocation in $\{110\}$ planes will be evaluated using *ab initio* calculations in the next section.

Identical molecular statics relaxations were also performed at 0 K in Nb, Mo and Ta (see references for the interatomic potentials in Methods, Tab. 4) to check for any metal-dependence of the locking mechanism presented here in W. We found no qualitative difference between these four metals, with a channeled growth of the $1/2\langle 111 \rangle$ loop, whereas the M100 dislocation impedes the expansion of the $\langle 100 \rangle$ loop. The choice to present these results in W is also motivated by its isotropic elasticity, for which the equilibrium shape and expansion of dislocation loops under an applied stress can thus be obtained within isotropic elasticity theory. In particular, the shape of these loops do not depend on its Burgers vector in the frame of isotropic elasticity theory, resulting theoretically in identical shapes for both $1/2\langle 111 \rangle$ and $\langle 100 \rangle$ loops in the absence of lattice friction. At higher temperature, above the athermal temperature T_{ath} , where the lattice friction experienced by dislocation vanishes, the equilibrium shape of the loop, driven by elasticity only, is an ellipse for the two Burgers vectors in isotropic W. At low temperature, orientations with the highest lattice friction dictate the shape of the loops. As evidenced here at 0 K, contrary to $1/2\langle 111 \rangle$, the hindering orientation of the $\langle 100 \rangle$ dislocation is this mixed M100 orientation aligned along $\langle 111 \rangle$ directions.

3.2. $\langle 100 \rangle$ dislocation sources

A common mechanism for dislocation multiplication relies on the activation of Frank-Read sources, emitting several dislocations from a dislocation segment pinned at its two ends by obstacles (*e.g.* impurities, interstitial atoms, other dislocations), which bends under an applied stress. Given that $\langle 100 \rangle$ dislocations are most often observed experimentally as the junction product of two intersecting $1/2\langle 111 \rangle$ dislocations, we investigate the possibility for these junctions to operate as active dislocation sources, essential for a slip system to yield a non-negligible participation to the plastic deformation. As discussed in section 1.2, these $\langle 100 \rangle$ junctions are completely glissile when formed by two dislocations having the same habit plane (see Fig. 2a). Such $\langle 100 \rangle$ junctions have a screw character, and as a result can glide in two different planes, which are orthogonal to each other given the symmetry of the bcc lattice. Taking the reaction between $\vec{b}_1 = 1/2[\bar{1}11]$ and $\vec{b}_2 = 1/2[111]$, which result in the formation of a junction $\vec{b}_{\text{JR}} = \vec{b}_1 + \vec{b}_2 = [010]$, such junction can glide in the two $P = (\bar{1}01)$ and $P' = (101)$ planes. When an applied stress is resolved in the

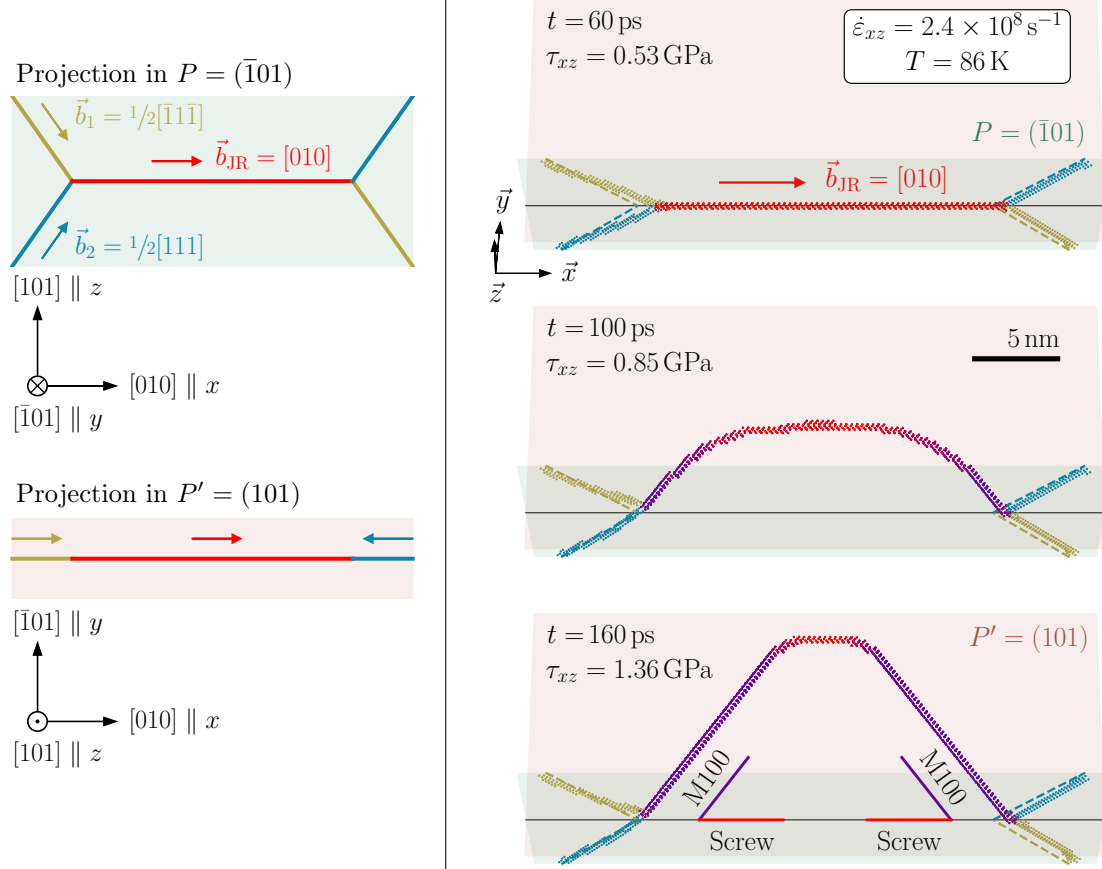


Figure 16: Molecular dynamics simulation of the bowing of a $[010]$ screw junction in the $P' = (10\bar{1})$ plane, formed by the interaction between two $1/2\langle 111 \rangle$ screw dislocations in the $P = (101)$ plane in W under stress. The character of the bowing $[010]$ segment is represented by the color of the atoms. The axis are $\vec{x} \parallel [010]$, $\vec{y} \parallel [101]$ and $\vec{z} \parallel [10\bar{1}]$.

habit plane P of the three dislocations, the network can glide in this plane (see sketch on the left side of Fig. 16). On the contrary, when the applied stress is resolved orthogonal to the habit plane, in the P' plane in this example, the $[010]$ junction can start to bend, and initiate a multiplication process similar to a Frank-Read source, where the two nodes of the junction act as pinning points for the $[010]$ segment. We now investigate such a process in W, starting from a $\langle 100 \rangle$ screw junction which has already formed. The simulation cell is defined by vectors $x \parallel [010]$, $y \parallel [101]$ and $z \parallel [10\bar{1}]$, with a junction oriented along its screw orientation with a length of 21 nm. We perform a molecular dynamics straining simulation of such a junction in W, at $T = 86$ K and a strain rate $\dot{\epsilon}_{xz} = 2.4 \times 10^8 \text{ s}^{-1}$, thus resolved in the P' plane. In these conditions, the two $1/2\langle 111 \rangle$ dislocations are not subjected to the applied strain, whereas the $\langle 100 \rangle$ junction is strained to move in the P' plane. Three snapshots of the simulations are presented in Fig. 16.

Up to a certain shear stress τ_{xz} (approximately 530 MPa in the present simulation, corresponding to the first presented snapshot), the $\langle 100 \rangle$ junction stays aligned along its screw orientation. When the applied stress gradually increases, the junction starts to bend to expand in the P' plane, whereas the two $1/2\langle 111 \rangle$ dislocations, both along their screw orientation, remain immobile. The $\langle 100 \rangle$ junctions then keeps expanding in the P' plane with increasing stress, while shortening along its screw orientation, before ultimately matching a $\langle 111 \rangle$ direction at both of its two ends, where the strong lattice friction of the M100 dislocation blocks further activation of the source. Therefore, this mixed orientation of $\langle 100 \rangle$ dislocations does not allow for such multiplication mechanism to actively operate, due to their high lattice friction and the symmetry

of the bcc lattice, as also observed in the previous section 3.1 considering expansion of the $\langle 100 \rangle$ dislocation loop. Indeed, since two hindering $\langle 111 \rangle$ orientations lay in a same $\{110\}$ plane at an angle 70.5° , further expansion of $\langle 100 \rangle$ dislocations along any orientation is prevented as soon as the line matches these two $\langle 111 \rangle$ orientations. This geometrical effect does not allow for the creation of a dipole, as would have been possible for a screw character since the two screw orientations make an angle 180° with each other. Further motion of $\langle 100 \rangle$ dislocations is therefore only possible at stresses above the Peierls stress of the M100 dislocation, or at higher temperature where lattice friction vanishes.

Given the similar results obtained in the four metals considered in the case of dislocation loops, the high lattice friction experienced by the M100 dislocation therefore appears as the limiting factor for activity of $\langle 100 \rangle \{110\}$ slip systems at low temperature. Another consequence of this hindering mixed M100 orientation is the locking of possible sources for $\langle 100 \rangle$ dislocations at low temperature, starting from junctions between two $\frac{1}{2}\langle 111 \rangle$ dislocations as presented in Fig. 16. The presented results thus explain a possibility for the lack of experimental observations of the motion of $\langle 100 \rangle$ dislocations in bcc transition metals at low temperature.

3.3. *Ab initio* calculation of the Peierls barrier of mixed $\langle 100 \rangle$ dislocations

We now evaluate the stability and Peierls energy barrier of the M100 mixed $\langle 100 \rangle$ dislocation, with a line oriented along $\langle 111 \rangle$, using *ab initio* calculations. Since dislocations having a non-negligible edge component (which is the case here with $\theta = 54.7^\circ$) induce a much larger displacement field in the plane orthogonal to their line than screw dislocations, a larger simulation cell is required for the calculation. The simulation cell containing 273 atoms per unit b length in the line direction is used, with a geometry defined by periodicity vectors $\vec{p}_1 = 7/2 \times [\bar{1}2\bar{1}] - 13/2 \times [\bar{1}01]$, $\vec{p}_2 = 7/2 \times [\bar{1}2\bar{1}] + 13/2 \times [\bar{1}01]$, and $\vec{p}_3 = 1/2[111]$ (see Tab. 5 in Methods). Similarly to the two $\frac{1}{2}\langle 111 \rangle$ and $\langle 100 \rangle$ screw dislocations, a dipole of M100 dislocations is introduced in the cell according to anisotropic elasticity theory. However, since the dislocation has an edge component, atoms need to be added along the cut surface of the dipole when introduced in the simulation cell. For the present quadrupolar arrangement and geometry of the cell, it corresponds to a total of 286 atoms after the dipole has been inserted. The relaxed configuration of the core of the mixed M100 dislocation in W is presented in Fig. 17.

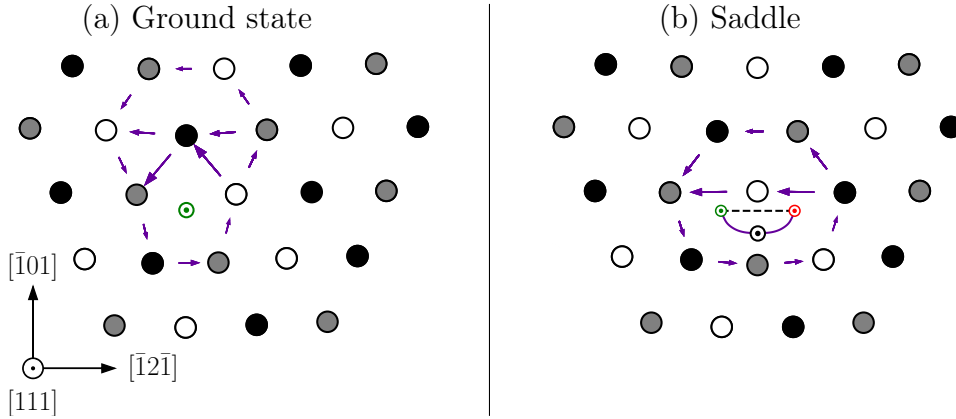


Figure 17: Screw component of the differential displacement map showing the core structure of a mixed $[100]$ dislocation (M100) with line direction $[111]$ in W in (a) its ground state configuration, and (b) at the saddle point upon crossing the Peierls barrier from the initial (green) to final (red) configurations. An arrow joining two atoms corresponds to a differential displacement of $b/2 = a_0/2$ along $[111]$. The trajectory of the dislocation is shown in solid line in (b).

The ground state configuration of the core is found after relaxation starting from the M100 dislocation positioned at the center of a triangle formed by three $[111]$ atomic columns, with a different shape than in the perfect crystal, since atoms have been added to the simulation cell. The second configuration presented corresponds to the saddle point of the Peierls barrier when this M100 dislocation glides in a $\{110\}$ plane from the green to the red positions indicated in Fig. 17b. We note that for both configurations, the relaxed

core of the M100 dislocation is compact, with no spreading in the (111) plane orthogonal to the line direction. Identical *ab initio* calculations of this mixed M100 dislocation were also performed in Nb and Cr, for which experimental evidence of the motion of $\langle 100 \rangle$ dislocations have been reported, and to test possible metal-dependent effect based on their different electronic structure. In Cr, the calculations were performed in the NM phase to reduce the computational time needed to account for magnetism, and also motivated by the previous results indicating the marginal influence of magnetism on the plasticity of Cr. The two relaxed configurations of the core are found identical to the results presented for W in Fig. 17 in both Cr and Nb, with a compact structure and no spreading of the core in the (111) plane. We now evaluate the Peierls energy barrier of the mixed M100 dislocation gliding in a $\{110\}$ plane using setup *stress* for the NEB calculation with 11 intermediate images. The resulting Peierls potentials are presented for Nb, Cr (NM phase) and W in Fig. 18 after correction of the variation in the elastic energy of the dipole upon crossing the barrier. Results obtained for the $\langle 100 \rangle$ screw dislocation (see Fig. 11) are reported in red for comparison.

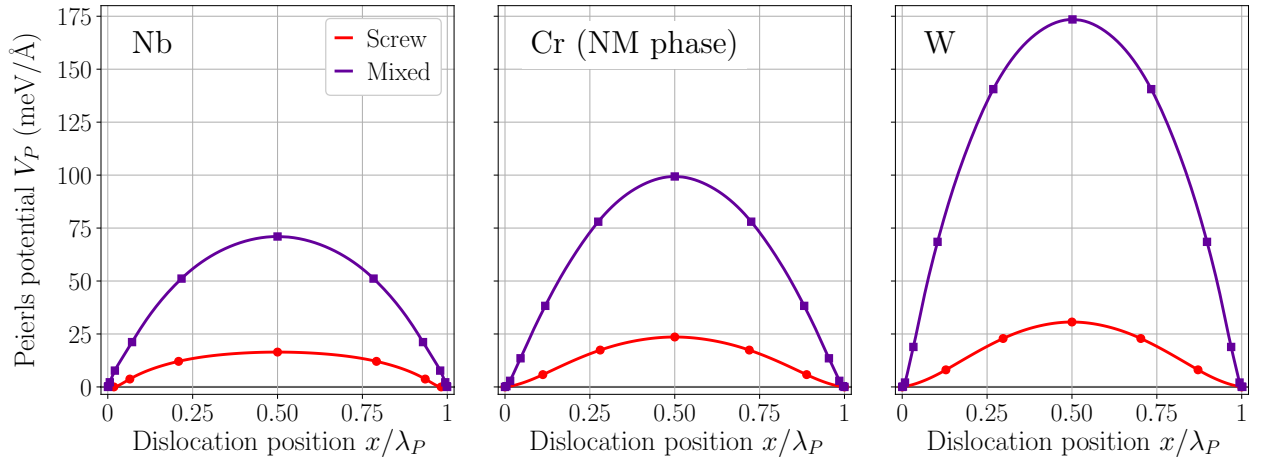


Figure 18: Peierls potential V_P as a function of the dislocation position x for a screw (red) and a mixed M100 (purple) $\langle 100 \rangle$ dislocation gliding in a $\{110\}$ plane obtained using *ab initio* calculations in Nb, Cr (NM phase), and W.

The Peierls potential for the mixed M100 orientation shows a much higher energy barrier in $\{110\}$ planes than for the screw orientation of the $\langle 100 \rangle$ dislocation in the three metals considered here, with a ratio of 4.3, 4.2 and 5.7 in Nb, Cr and W respectively. We also note that the shape of the potential is much steeper near the bottom of Peierls valleys, resulting in a very high Peierls stress of 9.5, 8.9 and 15.0 GPa respectively, to be compared to the much lower values found for the screw orientation presented in Tab. 5. Even if these simulations appear rough due to the small simulation cells accessible to *ab initio* calculations, the presented results constitute a good estimate of the true Peierls potential of this M100 dislocation. Indeed, given that its core is compact and does not spread in the (111) plane, such a size effect is therefore limited. The strong deformation induced by its core in the (111) plane could also yield size dependent effects. However, using the MEAM potential for W [89] in much larger simulation cells, we found a similar ratio of 5.9 between the height of the barrier of the screw and mixed $\langle 100 \rangle$ dislocation (compared to 5.7 in the *ab initio* calculations for W presented in Fig. 18), with fast convergence of the height of the barrier for the M100 dislocation with respect to the size of the simulation cell. Therefore, it appears that the high lattice friction experienced by this M100 mixed orientation is the true limiting factor for the multiplication of $\langle 100 \rangle$ dislocations at low temperature, and which is generic to all bcc transition metals (at least the ones presented here). Indeed, as presented in the previous sections 3.1 and 3.2, given the geometry of the bcc lattice, with two $\langle 111 \rangle$ orientations making an angle of 70.5° with each other, both expansion of $\langle 100 \rangle$ loops and activation of their Frank-Read sources is hindered by the reduced mobility of the M100 orientation.

3.4. Discussion

Long segments of mixed $\langle 100 \rangle$ dislocations lying along a $\langle 111 \rangle$ direction have been observed experimentally in Ta deformed at 77 K by Welsch *et al.* [263, 264], indicating the locking mechanism evidenced here at low temperature by our atomistic simulations. Such $\langle 100 \rangle$ dislocations are also observed in samples of W and Mo under high-temperature creep conditions ($0.5 - 0.7 T_{\text{melt}}$, with T_{melt} the melting point of 2895 and 3695 K in Mo and W respectively) [265, 266]. The authors report block boundaries where dislocations with a $\langle 100 \rangle$ Burgers vector are already present in the sample by the time the networks are formed during these high-temperature mechanical testing. Large proportion of $\langle 100 \rangle$ dislocations are also observed after rolling at high temperature ($0.5 - 0.7 T_{\text{melt}}$) in Mo and W single crystals [267, 268]. Motion of $\langle 100 \rangle$ dislocations at high temperature was also suspected by Dingley and Hale [255], and Carrington *et al.* [269] in Fe, and also observed at room temperature in Cr [13, 122] and Nb [250, 251], as discussed in section 1.3.

In this temperature range, where $1/2\langle 111 \rangle$ dislocations do not align preferentially along their screw orientation anymore, formation of $\langle 100 \rangle$ junctions are energetically favorable in all bcc transition metals, resulting from two intersecting mixed $1/2\langle 111 \rangle$ dislocations (see Appendix F). Assuming these reactions are the principal source for creation of $\langle 100 \rangle$ dislocations, junctions can then act as sources to account for their multiplication. However, the temperature must be sufficiently high for the M100 dislocation to glide without experiencing the extreme lattice friction evidenced here. These high-temperature experimental observations of the motion of $\langle 100 \rangle$ therefore indicate the locking mechanism along $\langle 111 \rangle$ directions vanishes at high temperatures. At these elevated temperatures, $\langle 100 \rangle$ dislocations are then allowed to actively glide and multiply, with a presumed non-negligible contribution to the plastic deformation of bcc transition metals. Therefore, one needs to account for $\langle 100 \rangle$ dislocations when rationalizing plasticity of these metals not only through formation of junctions responsible for strain hardening, but also through their motion, thus allowing them to carry plastic deformation at high temperature.

Conclusions of Chapter 6:

- Considering anisotropic elasticity theory, the two $1/2\langle 111 \rangle$ and $\langle 100 \rangle$ dislocations show comparable energies, especially for metals with an anisotropy ratio $A < 1$ (V, Nb, Cr and Mo), thus invalidating the common argument used to discard $\langle 100 \rangle$ dislocations in the study of their plasticity.
- These $\langle 100 \rangle$ dislocations are observed in all bcc transition metals, mostly as junctions formed at the intersection between two $1/2\langle 111 \rangle$ dislocations. However, experimental evidence of their motion at low temperature is scarce, only reported in Cr and Nb at room temperature.
- *Ab initio* modeling of $\langle 100 \rangle$ screw dislocations in bcc Cr showed their activity in $\{110\}$ planes is competitive with respect to the conventional $1/2\langle 111 \rangle$, particularly for a loading axis close to a $\langle 111 \rangle$ direction. Including the effect of temperature in the frame of the line tension model also showed this competition to hold up to the athermal temperature of the Peierls mechanism in Cr.
- A systematic study of the mobility of this $\langle 100 \rangle$ screw dislocation across all bcc transition metals using *ab initio* calculations showed that the results obtained in Cr apply to other metals, with a competitive activity of the two $1/2\langle 111 \rangle$ and $\langle 100 \rangle$ screw dislocations in $\{110\}$ planes.
- Further investigation on the expansion of dislocation loops under an applied stress showed that, contrary to $1/2\langle 111 \rangle$, for which the loop expands to create a screw dipole, the loop with a $\langle 100 \rangle$ Burgers vector locks in a diamond-like shape as soon as it aligns along one of the two $\langle 111 \rangle$ directions contained in the habit plane of the loop. This mixed M100 dislocation also hinders activation of possible $\langle 100 \rangle$ dislocation sources, from junctions formed between two $1/2\langle 111 \rangle$ dislocations. *Ab initio* evaluation of the Peierls energy barrier opposing their glide confirmed these M100 dislocations are the true limiting factor to the multiplication of $\langle 100 \rangle$ dislocations at low temperature.
- At high temperature, where the high lattice friction experienced by these M100 dislocations vanishes, activity of $\langle 100 \rangle$ dislocations in $\{110\}$ planes is expected, *a priori* yielding a non-negligible contribution to the plastic deformation of bcc transition metals, as reported experimentally in W and Mo [265–268].

Conclusions and outlook

Through the atomistic simulations of the core properties and mobility of dislocations presented in this work across all bcc transition metals, both using *ab initio* calculations and interatomic potentials, the following conclusions were drawn:

- At low temperature, magnetism has a marginal impact on the properties of $\frac{1}{2}\langle 111 \rangle$ screw dislocations in bcc Cr, except for the generation of magnetic faults caused by the disruption of the low-temperature AF order by their Burgers vector, constraining them to coexist and move pairwise. These collinear faults however disappear below the Néel temperature T_N of 311 K, letting $\frac{1}{2}\langle 111 \rangle$ dislocations free to move without dragging magnetic faults.
- Parametrization of a generalized yield criterion based on the core properties and mobility of $\frac{1}{2}\langle 111 \rangle$ screw dislocations gliding in $\{110\}$ planes allows for prediction of slip activity and variations of the yield stress with the orientation of the loading axis, across all pure bcc transition metals. By comparing predictions of the model between the different metals, we showed that Cr has a similar yield behavior to other bcc transition metals. Comparison to experimental data at low temperature in different bcc metals demonstrated the ability of the criterion to reproduce the T/AT and T/C asymmetries observed experimentally, with strong metal-dependent behaviors, also allowing to validate predictions made in Cr for which experimental data is missing.
- This systematic study across all bcc transition metals showed the importance to account for all components of the stress tensor to develop a yield criterion, in particular regarding effects of applied pressure and stresses along the dislocation line. We report unexpected behaviors in terms of T/C asymmetry in Nb and Mo, for which a wide range of loading orientations show a lower yield stress in compression, whereas the contrary is expected and observed in other bcc transition metals.
- Accounting for the thermally activated glide of $\frac{1}{2}\langle 111 \rangle$ screw dislocations through nucleation of kink-pairs, the effect of temperature was included in the yield criterion. With increasing temperature, up to the athermal limit of the Peierls mechanism, we show a progressive fade out of non-Schmid effects, both in terms of yield stress variations and predicted slip activity.
- *In situ* straining experiments of Daniel Caillard (CEMES, CNRS, Toulouse) in TEM, coupled with atomistic simulations highlighted a new mechanism explaining occurrence of anomalous slip in bcc transition metals, based on the high mobility of multi-junctions formed by four $\frac{1}{2}\langle 111 \rangle$ screw dislocations. Atomistic simulations show the spontaneous nucleation of kinks at the four-dislocation node, thus allowing these screw dislocations to glide cooperatively over long distances without experiencing lattice friction. The observed multi-junctions rely on the prior formation of $\langle 100 \rangle$ junctions from two intersecting $\frac{1}{2}\langle 111 \rangle$ screw dislocations, thus required for occurrence of anomalous slip. The stability of these junctions at low temperature, where $\frac{1}{2}\langle 111 \rangle$ dislocations align along their screw orientation, is linked to the elastic anisotropy of the metal, with a increased stability in metals with an anisotropy ratio smaller than one. This is the case for Nb and Cr, and correlates well with the profuse occurrence of anomalous slip observed experimentally in Nb.
- Apart from junctions responsible for hardening, activity of $\langle 100 \rangle$ dislocations was reported in Nb and Cr at room temperature, raising questions about the conditions under which they can carry deformation in bcc transition metals. Based on anisotropic elasticity theory, these $\langle 100 \rangle$ dislocations have close energetics compared to the conventional $\frac{1}{2}\langle 111 \rangle$, despite the higher norm of their Burgers vector. Further investigation with *ab initio* calculations showed their stability in all bcc transition metals, with a competitive glide of the two $\frac{1}{2}\langle 111 \rangle$ and $\langle 100 \rangle$ screw dislocations in $\{110\}$ planes. However, we showed that contrary to $\frac{1}{2}\langle 111 \rangle$, a line orientation other than screw impedes the motion of $\langle 100 \rangle$ dislocations at low temperature, namely a mixed orientation along $\langle 111 \rangle$ directions, showing a Peierls barrier five times higher than the screw. Due to the symmetry of the bcc lattice, where two $\langle 111 \rangle$ directions lay at an angle 70.5° , the high lattice friction experienced by this mixed orientation does not allow for their multiplication at low temperature. With junctions that can act as sources, activity of $\langle 100 \rangle$ dislocations nevertheless needs to be considered as a possibility. However, their motion may only

be possible at a high enough temperature for the lattice friction experienced by the M100 dislocation vanishes. Experimental validation is still required for both the low temperature locking mechanism, and this possible motion of these $\langle 100 \rangle$ dislocations at high temperature, dictated by elasticity.

In addition to these conclusions, several points still need to be addressed. In particular, now that we have a good understanding of the plasticity of pure bcc Cr, one needs to qualify the influence of impurities and substitutional elements on the mobility of dislocations. Most particularly, the ductile to brittle transition temperature of Cr, linked in the first order to the activity of dislocations, strongly depends on the purity of the sample, which can vary by up to 500°C depending on alloying elements [5]. Recent studies coupling *ab initio* calculations with *in situ* straining experiments in TEM performed by Daniel Caillard [20, 270], both Lüthi *et al.* [271–273] in Fe, and Hachet *et al.* [193, 274] in W, showed the resurgence of the Peierls mechanism above its athermal temperature T_{ath} due to carbon atoms impeding the motion of dislocations, this mechanism holding up to even higher temperatures. Such modeling of the mobility of dislocations in presence of impurities could help explain the dependence of the brittle to ductile transition temperature of Cr, with application for the coatings subjected to working conditions in nuclear plants where various impurities are found (oxygen, hydrogen, nitrogen, sulfur), and also interstitial elements.

Comparison between predictions of the yield criterion for $1/2\langle 111 \rangle\{110\}$ slip and experimental data helped highlighting some discrepancies. Among those remains the overestimation of the yield stress at 0 K, despite the good agreement found with experiments in terms of its variations with orientation of the loading axis. This discrepancy, common to all atomistic simulations, is not resolved by accounting for non-Schmid effects, as discussed in this work. Proville *et al.* [65] showed a non-negligible contribution of the zero-point energy to the Peierls energy barrier experienced by $1/2\langle 111 \rangle$ screw dislocations gliding in $\{110\}$ planes at 0 K, with a substantial lowering of the barrier when entropic contributions are included. Calculations were performed using an EAM interatomic potential to reduce the computational time required for evaluation of this entropic contribution, which was out of the reach of an *ab initio* evaluation. With the recent improvement of computational resources, an *ab initio* evaluation of the zero-point energy of simulation cells containing a dislocation dipole becomes accessible, which will help understanding the origin of this overestimation of the Peierls stress. Such *ab initio* calculations are nevertheless restricted to the study of straight infinite dislocations, in 1b-high simulation cells. To study kinked dislocation lines, requiring larger system sizes, one can rely on recent developments in machine-learning interatomic potentials suited for the study of plasticity of bcc transition metals [87, 88]. These potentials are adjusted on *ab initio* data, and allows for a good reproduction of the fine core properties of screw dislocations when included in the training procedure (*e.g.* trajectory in $\{110\}$ planes, variations of its relaxation volume tensor, Peierls potential), which then allows for a direct evaluation of the zero-point energy contribution to the Peierls energy barrier of a large simulation cell containing a kinked dislocation.

In this work, comparison between experiments and predictions of the proposed "*ab initio*" yield criterion assumes the macroscopic yield behavior can be derived solely from mobility of isolated dislocations. Such an assumption *a priori* holds at low temperature, where plasticity of bcc transition metals is governed by the slow glide of screw dislocations, impeded by a strong friction with the lattice. There are however conditions under which this assumption does not hold, for instance at higher temperature where lattice friction has vanished. We also showed the importance of accounting for multi-dislocation processes in the investigated mechanism explaining anomalous slip. Such elemental processes involved in the plasticity of bcc transition metals can be accessed with atomistic simulations, as exemplified in the present work for both possible motion of $\langle 100 \rangle$ dislocations and the motion of highly mobile multi-junctions. The macroscopic yield behavior of these metals can then be derived including all relevant mechanisms quantified at the atomic scale, relying on a multiscale modeling scheme, where each scale informs the next and uses different simulation tools. Such a multi-scale modeling approach can be achieved using for instance dislocation dynamics as a first step towards plasticity of the polycrystal, which rely on mobility laws for dislocations that can be derived from the lower scale. In this respect, the developed yield criterion can be used to test its ability to compare to the macroscopic yield behavior of bcc transition metals observed experimentally. In particular, our *ab initio*

modeling evidenced the importance to account for all components of the applied stress tensor, including ones that are neglected in most criteria used in large scale simulations. Additionally, now that all physical ingredients derived from the core properties of the $\frac{1}{2}\langle 111 \rangle$ screw dislocations have been integrated, new possibilities need to be investigated to explain the remaining discrepancies with experiments. For example, the yield stress along the edges of the standard stereographic triangle shows variations which are not reproduced by the proposed yield criterion. For these orientations, activity of multiple slip systems is both predicted and observed. Possible routes for resolving these discrepancies could thus be the integration of multi-dislocation processes as both a source of hardening, but also of softening (*e.g.* anomalous slip), or through motion of $\langle 100 \rangle$ dislocations. Activity of multiple $\frac{1}{2}\langle 111 \rangle \{110\}$ slip systems is both predicted and observed in these regions should favor formation of $\langle 100 \rangle$ junctions, since intersection between two $\frac{1}{2}\langle 111 \rangle$ dislocations is more probable. These $\langle 100 \rangle$ junctions can act as a source of hardening at low temperature, since their motion is impeded by the lattice friction experienced by their mixed $\langle 111 \rangle$ orientation.

Also, mobility of $\frac{1}{2}\langle 111 \rangle$ dislocations in $\{112\}$ planes is observed experimentally in pure bcc transition metals [20, 21], for which an explanation still lacks. Several atomistic mechanisms have been proposed but not confirmed experimentally, including a transition in the core structure of the $\frac{1}{2}\langle 111 \rangle$ screw dislocation at low temperature [275], or their alternate motion on two $\{110\}$ planes [28], with an average $\{112\}$ macroscopic glide plane. Arguments based on the symmetry of the compact core structure of the $\frac{1}{2}\langle 111 \rangle$ screw dislocation allow for rationalizing their glide in $\{110\}$ planes, in which they do not have to cross an atomic column during their motion. Possible routes for explaining coexistence of these two different glide planes would be a difference in the kink-pair nucleation energy of the screw dislocation in these two planes. A transition in the hierarchy between the two profiles as a function of the applied stress would indeed account for both glide planes to be active under certain loading conditions.

As presented in the last chapter, mobility of $\langle 100 \rangle$ dislocations is predicted at high enough temperatures, at which the strong lattice friction experienced by the hindering mixed M100 dislocation vanishes, therefore allowing for these dislocations to effectively multiply and carry plastic deformation. In particular, a strong activity of $\langle 100 \rangle \{110\}$ slip systems is predicted for uniaxial tension/compression along a loading axis close to a $\langle 111 \rangle$ direction, where the Schmid factors of these systems are maximum. To test this assumption in experimental conditions, a single crystal of ultra-pure Cr with a $\langle 111 \rangle$ axis was ordered, to perform tensile and compressive *in situ* experiments in TEM from room temperature to at least 350° C. Apart from these *in situ* straining tests, a sample of the $\langle 111 \rangle$ single crystal was compressed at 350° C to carry *post mortem* observations in TEM. These two tests are performed in parallel, in a attempt to correlate the dynamic motion of dislocations observed under *in situ* straining conditions to the dislocation microstructures generated upon application of the strain, also allowing to test possible artefacts associated with *in situ* tests (*e.g.* local heat concentration due to the irradiation of the sample by the electron beam). These tests are done in collaboration with Estelle Meslin (CEA, SRMP) and Daniel Caillard (CEMES, CNRS, Toulouse). Depending on the results obtained for Cr, similar experiments in Nb would then be interesting, in search for the activity of $\langle 100 \rangle$ dislocations as a function of temperature, since activity of $\langle 100 \rangle$ dislocations was already reported experimentally in these two metals through *post mortem* observations in TEM [13, 250].

Synthèse en français

Le contexte de cette thèse, intitulée "étude à l'échelle atomique de la plasticité du chrome et des autres métaux de transition cubiques centrés", s'inscrit dans la recherche de solutions pour prévenir à la rupture de la gaine combustible des réacteurs à eau pressurisée en conditions accidentelles. Dans ces conditions, la température peut rapidement atteindre des niveaux extrêmes, accélérant l'oxydation de la gaine, et pouvant entraîner sa rupture. Une solution développée par le CEA pour limiter cette oxydation est l'emploi d'un revêtement en chrome (Cr), connu pour sa résistance à la corrosion. Ainsi, la couche de Cr doit être en mesure d'accommoder la déformation qui lui est imposée par la gaine et le combustible en se déformant plastiquement, tout en garantissant l'absence de fissures qui pourraient lui faire perdre ses propriétés protectrices.

Le chrome (Cr) est l'un des sept métaux de transition cubiques centrés (CC) purs, dont la plasticité opère à basse température par le mouvement de dislocations. Celles-ci sont caractérisées par leur vecteurs de Burgers \vec{b} , le plus communément égal au plus court vecteur de périodicité du réseau, soit $1/2\langle 111 \rangle$ pour les métaux CC, et glissant principalement dans les plans $\{110\}$ à basse température. Dans cette gamme de température, ces dislocations s'alignent préférentiellement selon leur orientation vis, du fait de la grande friction de réseau ressentie par cette orientation. Elles doivent ainsi surmonter cette friction pour se déplacer, représentée par un potentiel dit de Peierls et ayant la périodicité du réseau. Lorsque la température augmente, la contrainte nécessaire au déplacement des dislocations diminue progressivement, jusqu'à ce que la friction de réseau disparaisse, dans le régime athermique de la plasticité où celle-ci est contrôlée par l'élasticité. Cependant, très peu d'études portant sur la plasticité du Cr sont disponibles, à la fois expérimentalement et théoriquement, contrairement aux autres métaux CC, ne permettant pas de conclure sur son comportement plastique par rapport à ces autres métaux.

Parmi les sept purs métaux CC, le Cr est le seul avec un ordre magnétique proche de l'antiferromagnétisme (AF) en-dessous de la température ambiante. Plus précisément, il s'agit d'une onde de densité de spins (ou *spin density wave* en anglais, SDW), correspondant à une modulation quasi sinusoïdale de l'amplitude des moments magnétiques selon une direction $\langle 100 \rangle$ du cristal. Cependant, la DFT prédit la phase AF comme la structure magnétique la plus stable, la SDW ayant toujours une énergie plus haute peu importe sa périodicité, la phase non-magnétique (NM) étant la moins stable. En regardant maintenant les constantes élastiques de ces différentes phases magnétiques, nous nous apercevons que les structures AF et SDW ont des propriétés élastiques très proches. Ainsi, puisque nous sommes intéressés dans cette étude aux dislocations, lesquelles dépendent entre autres des constantes élastiques du métal, la phase SDW sera par la suite approchée par la phase AF. Ce choix est aussi motivé par l'ordre AF local le long de la propagation de la SDW. Par la suite, nous avons étudié les fautes d'empilement généralisées, donnant l'énergie nécessaire pour cisailier le cristal d'un vecteur faute (assimilé au vecteur de Burgers des dislocations) dans un plan de faute (assimilé au plan de glissement des dislocations). En cisailant le cristal de Cr dans sa phase AF d'un vecteur $1/2\langle 111 \rangle$ contenu dans plusieurs plans, nous avons observé la création de fautes magnétiques, causées par la rupture de l'ordre AF par ces vecteurs. L'amplitude des moments magnétiques diminue à proximité du plan de faute, créant

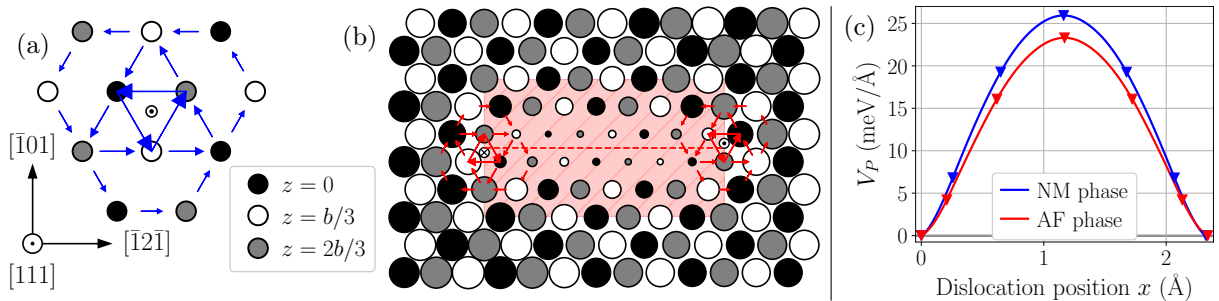


Figure 1: Composante vis du cœur de la dislocation vis $1/2\langle 111 \rangle$ dans les phases (a) NM et (b) AF du Cr. Dans la phase AF, les atomes sont représentés avec un diamètre proportionnel à leur moment magnétique. (c) Potentiel de Peierls V_P de la dislocation vis $1/2\langle 111 \rangle$ glissant dans un plan $\{110\}$ du Cr.

une structure similaire à une paroi magnétique, et d'énergie $16 \text{ meV}/\text{\AA}^2$.

En étudiant maintenant la structure de cœur des dislocations vis $1/2\langle 111 \rangle$ en calculs *ab initio*, une faute magnétique de structure similaire à la faute précédente est aussi générée par le cisaillement induit par les dislocations (Fig. 1b). Cependant, la structure de cette dislocation vis est identique dans les deux phases NM et AF. Nous avons ensuite évalué la friction de réseau s'opposant au glissement de ces dislocations vis dans les plans $\{110\}$ par calcul *ab initio* de la barrière de Peierls, de hauteur comparable dans les deux phases NM et AF du Cr (Fig. 1c). Le seul effet notable du magnétisme est donc la création de fautes magnétiques, responsable d'une contrainte de rappel d'environ 1 GPa à température nulle. Cette contrainte est donc trop importante pour autoriser les dislocations $1/2\langle 111 \rangle$ à exister seules, la faute devant être fermée par une autre dislocation. Nous avançons ainsi la possibilité que celles-ci soient contraintes à coexister et à se déplacer par paires, créant une superdislocation de vecteur de Burgers total $\langle 111 \rangle$ dissociée en deux dislocations $1/2\langle 111 \rangle$ séparées par une faute magnétique, cette hypothèse nécessitant une validation expérimentale.

Ainsi, les résultats précédents obtenus dans le Cr indiquent que la principale conséquence du magnétisme sur sa plasticité est la génération de fautes magnétiques. Cependant, cette observation n'est faite jusqu'ici qu'à température nulle, interrogeant donc sur le comportement de ces fautes à température finie. Pour se faire, un modèle d'interaction de type Heisenberg-Landau a été développé, permettant de reproduire à la fois les propriétés énergétiques à 0 K et la température de Néel T_N du Cr, *i.e.* la température de transition vers la phase paramagnétique (PM) caractérisée par un désordre magnétique à longue portée. Les paramètres du modèle ont ensuite été ajustés sur les énergies magnétiques *ab initio* de diverses phases du Cr. Les configurations d'équilibre atteintes à température finie sont ensuite explorées par le biais d'un échantillonnage de Metropolis Monte Carlo, uniquement sur les moments magnétiques et gardant les atomes fixes. L'étude de la transition ordre-désordre, allant de la phase AF à PM, montre la disparition progressive de l'ordre magnétique à longue distance à mesure que la température augmente, jusqu'à disparaître au-delà de T_N . Dans cette phase PM, le moment magnétique moyen reste cependant non-nul, montrant que le désordre de cette phase est causé par la désorientation entre les spins, en accord avec l'expérience. Considérant maintenant la faute magnétique bornée par deux dislocations vis $1/2\langle 111 \rangle$ générée par le cisaillement de leur vecteur de Burgers, nous avons observé que celle-ci disparaît à une température inférieure à T_N , laissant place à une structure non-colinéaire s'étalant dans l'intégralité du volume de la boîte de simulation. Ainsi, compte tenu des propriétés similaires des dislocations vis $1/2\langle 111 \rangle$ dans les deux phases NM et AF, puisque la faute magnétique disparaît à température finie, le magnétisme n'a *a priori* d'impact sur la plasticité du Cr qu'à très basse température, et la phase NM constitue au-delà une bonne approximation pour l'étude de sa plasticité. Cette simplification est utilisée par la suite afin de comparer la plasticité du Cr aux autres métaux CC, afin notamment d'évaluer s'il présente un comportement similaire.

La plasticité des métaux de transition CC présente des caractéristiques contredisant la loi de Schmid, obéissant par les métaux cubiques à faces centrées notamment. Ces écarts à la loi de Schmid sont observés dans l'ensemble des métaux CC, principalement à basse température où leur plasticité est contrôlée par le mouvement des dislocations vis $1/2\langle 111 \rangle$ et dont les propriétés à l'échelle atomique peuvent être reliées au comportement macroscopique de ces métaux. Expérimentalement, il est observé d'une part une asymétrie dite de maillage/antimaillage, avec un sens de cisaillement plus "facile" lors d'essais de chargement uniaxial, et d'autre part un comportement différent selon le signe de la contrainte, en particulier une limite élastique plus faible en traction qu'en compression. À l'aide de calculs *ab initio*, il a été démontré précédemment que ces effets sont dus à deux caractéristiques des dislocations vis $1/2\langle 111 \rangle$: leur trajectoire déviée dans les plans $\{110\}$, responsable de l'asymétrie maillage/antimaillage; et un champ de dilatation induit par leur cœur, conduisant à l'asymétrie traction/compression.

En s'appuyant sur les propriétés *ab initio* de la dislocation vis, il est ainsi possible de développer un critère d'écoulement plastique dans l'ensemble des sept métaux de transition CC : vanadium (V), niobium (Nb), tantale (Ta), chrome (Cr), molybdène (Mo), tungstène (W), et fer (Fe). Les résultats de cette étude systématique sont présentés dans le cas d'un chargement uniaxial (représenté schématiquement Fig. 2a), pour lequel une grande variété de données expérimentales est disponible, permettant une comparaison aux prédictions du

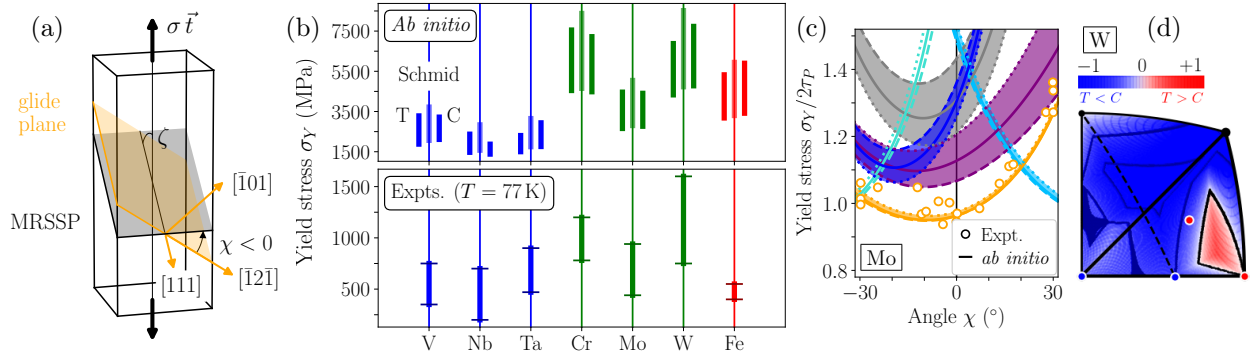


Figure 2: (a) Schéma d'un essai de chargement uniaxial montrant le plan de glissement de la dislocation en orange et le plan de scission résolue maximale en noir. (b) Comparaison entre la limite élastique σ_Y prédite par le critère d'écoulement à 0 K ("Ab initio") et des données expérimentales à 77 K ("Expts.") pour l'ensemble des métaux de transition CC. (c) Comparaison à l'expérience en terme de la variation de la limite élastique σ_Y avec l'angle χ dans le Mo. (d) Distribution de l'asymétrie traction/compression en fonction de l'orientation de l'axe de chargement dans le W.

modèle. Il en ressort que la contrainte nécessaire à l'activation et l'activité des différents systèmes de glissement, dépendent fortement du métal. Les prédictions sont en bon accord avec l'expérience, reproduisant les asymétries maillage/antimaillage (Fig. 2c) et traction/compression (Fig. 2d), mais conduisant néanmoins à des contraintes trop élevées (Fig. 2b), un désaccord communément observé entre simulations atomiques et expérience. Il est prédit pour certains métaux une contrainte d'activation inférieure en compression qu'en traction, en accord avec l'expérience. La variation de la contrainte d'écoulement plastique avec l'orientation du chargement et la température, dont l'effet est intégré par un modèle de tension de ligne, montre que les écarts à la loi de Schmid disparaissent progressivement à mesure que la température augmente. Ce critère, dont les paramètres sont issus directement de calculs *ab initio*, permet une comparaison satisfaisante avec l'expérience, et constitue un outil pour comparer les différents métaux CC entre eux, ayant notamment permis de conclure que le Cr présente un comportement plastique similaire.

Plusieurs désaccords sont néanmoins observés entre les résultats du critère ici développé et l'expérience, et ce en particulier dans le cas du Nb où le glissement anormal est observé. Ce phénomène est caractérisé par l'observation de l'activité de dislocations $1/2\langle 111 \rangle$ dans des plans $\{110\}$ où la contrainte résolue est faible, observé dans l'ensemble des métaux de transition CC purs (excepté le Fe) à basse température. Les résultats présentés par la suite s'appuient sur des essais de traction *in situ* sur des échantillons de Nb dans un microscope électronique à transmission (MET) réalisés par Daniel Caillard (CEMES, CNRS, Toulouse). Dans ces expériences est observé le mouvement rapide et simultané de quatre dislocations $1/2\langle 111 \rangle$ connectées à un nœud (Fig. 3a). Ces dislocations laissent des traces de glissement dans deux plans $\{110\}$ orthogonaux, l'un d'entre eux correspondant au plan anormal où la force résolue sur les dislocations est faible. Le nœud est alors contraint de se déplacer selon la direction définie par l'intersection de ces deux plans.

Afin de mieux appréhender le mécanisme à l'origine de ce déplacement rapide, nous avons étudié le nœud où se joignent les quatre dislocations $1/2\langle 111 \rangle$ à l'aide de simulations atomiques, ici présenté dans le Nb. En relaxant le système, le nœud empêche les dislocations de rester alignées selon leur orientation vis (pointillés sur la Fig. 3b), et relaxent vers une orientation mixte. Une fois celle-ci atteinte, les dislocations peuvent alors glisser dans les deux plans $\{110\}$ sans ressentir de friction avec le réseau, expliquant le mouvement rapide observé expérimentalement sur de longues distances. Nous avons aussi montré que la tension de ligne élastique est la principale force motrice de ce mécanisme, ce qui en fait un mécanisme générique aux métaux de transition CC. La formation de ces jonctions multiples a ensuite été étudié à l'aide de simulations atomiques, à partir du mécanisme observé expérimentalement, et se déroule en quatre étapes : (1) une jonction vis $\langle 100 \rangle$ est formée par l'intersection entre deux dislocations vis $1/2\langle 111 \rangle$; (2) cette jonction est intersectée par une troisième dislocations vis $1/2\langle 111 \rangle$ ce qui crée une dislocation $1/2\langle 111 \rangle$ avec le quatrième vecteur de Burgers là où la jonction se trouvait avant intersection; (3) ce segment se courbe ensuite sous l'application

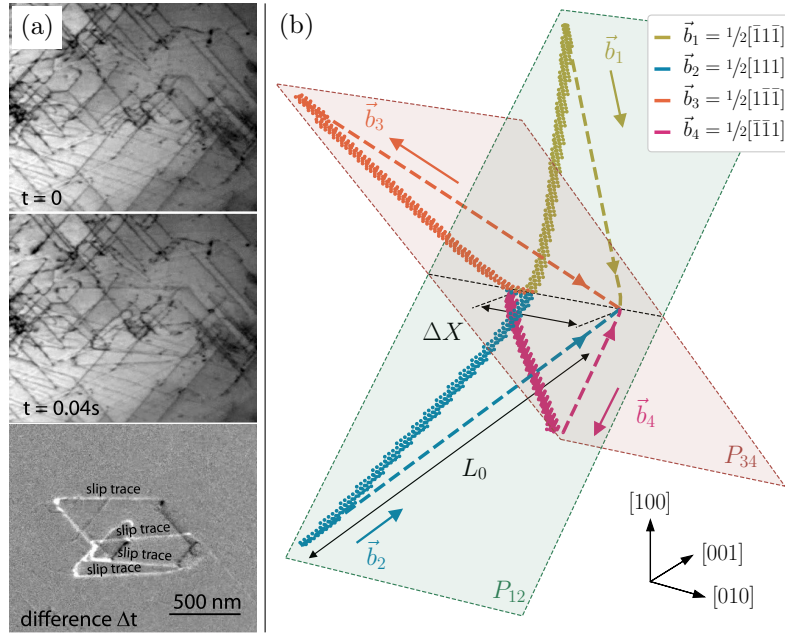


Figure 3: (a) Clichés MET d'une même zone de l'échantillon acquis à $\Delta t = 40$ ms d'intervalle. L'image différentielle (panneau du bas) permet de mieux visualiser le glissement rapide du nœud, laissant des traces de glissement correspondant aux quatre dislocations $1/2\langle 111 \rangle$ dans les deux plans orthogonaux $P_{12} = (10\bar{1})$ et $P_{34} = (101)$. (b) Relaxation en simulation atomique de ce même nœud, montrant les quatre dislocations $1/2\langle 111 \rangle$ initialement vis relaxant vers une orientation mixte, entraînant ainsi le mouvement du nœud selon la direction $[010]$.

d'une contrainte et tend ainsi vers son orientation vis; (4) lorsque celle-ci est atteinte, le nœud est formé, entraînant le glissement rapide selon le mécanisme présenté en Fig. 3b. Ainsi, la formation de jonctions $\langle 100 \rangle$ apparaît comme une condition nécessaire pour que ce mécanisme puisse opérer. Aussi, nous avons montré que la longueur de celles-ci est liée à l'anisotropie élastique du métal, favorisant ainsi l'activité du glissement anormal dans les métaux où ces jonctions sont les plus stables, comme le Nb et le Cr par exemple.

Enfin, nous nous sommes intéressés aux propriétés des dislocations de vecteur de Burgers $\langle 100 \rangle$, observées expérimentalement dans tous les métaux de transition CC sous forme de jonctions entre dislocations $1/2\langle 111 \rangle$, et nécessaires à l'activité du glissement anormal. Peu d'observations expérimentales mentionnent l'activité de ces dislocations $\langle 100 \rangle$ à basse température, cependant observées sous forme de longs segments dans une quantité non négligeable à plus haute température. Néanmoins, ces dislocations $\langle 100 \rangle$ ne sont communément pas considérées comme un système de glissement possible, pouvant donc générer de la déformation plastique. Cette simplification est basée sur un résultat de la théorie élastique isotrope, selon laquelle l'énergie élastique d'une dislocation est proportionnelle à la norme au carré de son vecteur de Burgers, les dislocations $\langle 100 \rangle$ étant donc d'énergie plus élevée que $1/2\langle 111 \rangle$. Prenant en compte l'anisotropie élastique, ces deux dislocations alignées selon leurs orientations vis ont une énergie élastique comparable dans plusieurs métaux (V, Nb, Cr et Mo), invalidant ainsi l'argument élastique isotrope utilisé pour ne pas considérer les dislocations $\langle 100 \rangle$.

Afin de savoir si l'activité de ces dislocations est comparable aux conventionnelles $1/2\langle 111 \rangle$, nous avons évalué par calculs *ab initio* la barrière de Peierls s'opposant au glissement des dislocations vis $\langle 100 \rangle$ dans les plans $\{110\}$, et ce dans l'ensemble des métaux de transition CC. Dans la plupart de ces métaux, la hauteur de la barrière comme la contrainte de Peierls est comparable pour les deux systèmes de glissement $\langle 111 \rangle\{110\}$ et $\langle 100 \rangle\{110\}$, suggérant donc une activité compétitive. Nous avons ensuite étendu le critère d'écoulement plastique présenté précédemment aux systèmes $\langle 100 \rangle\{110\}$ de manière à étudier la compétition entre eux en fonction de l'orientation du chargement mécanique, considérant que leur mobilité à basse température est pilotée par leurs orientations vis respectives. Ce critère prédit une vaste gamme d'orientations favorisant

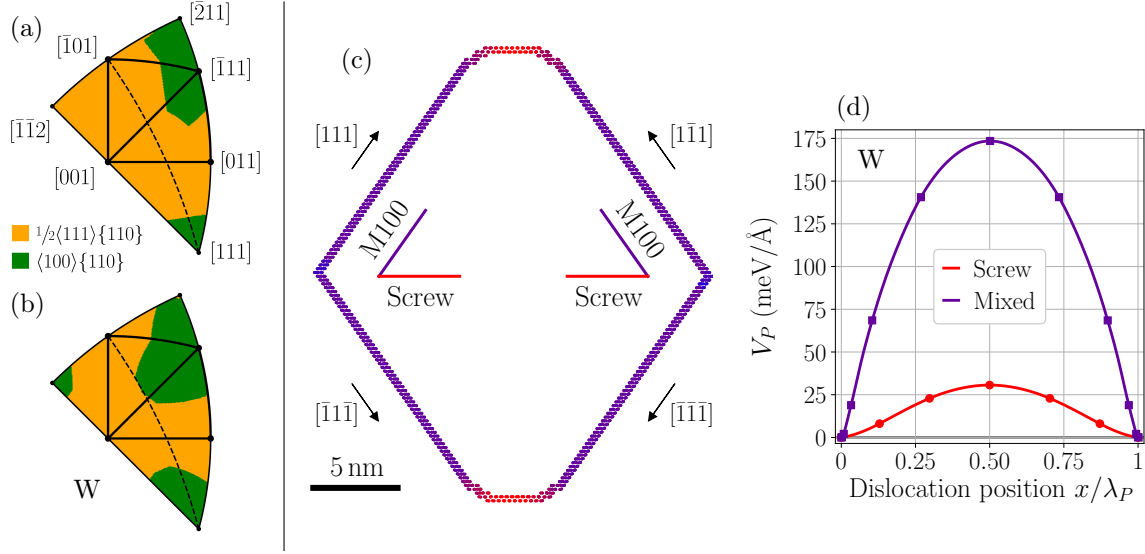


Figure 4: Système de glissement primaire parmi les vis $1/2\langle 111 \rangle$ (orange) et $\langle 100 \rangle$ (vert) glissant dans les plans $\{110\}$ en fonction de l'orientation de l'axe de chargement dans le W en (a) traction et (b) compression. (c) Configuration d'équilibre à 0 K d'une boucle de dislocation $\langle 100 \rangle$ soumise à une déformation, la couleur des atomes représentant l'orientation locale de la ligne. (d) Potentiel de Peierls *ab initio* V_P d'une dislocation $\langle 100 \rangle$ vis (rouge) et mixte (violet) glissant dans un plan $\{110\}$ dans le W.

l'activité de systèmes $\langle 100 \rangle \{110\}$, en particulier proche d'un axe $\langle 111 \rangle$ (voir Fig. 4a et b). Ainsi, ce critère prédit une plus forte activité de dislocations $\langle 100 \rangle$ à basse température qu'observé expérimentalement, même pour des axes de chargement proches de $\langle 111 \rangle$. Une contradiction apparaît donc, à moins qu'un autre mécanisme ne s'oppose à leur mouvement à basse température.

Notamment, ce critère est basé sur l'hypothèse que ces dislocations $\langle 100 \rangle$ ressentent la plus forte friction de réseau lorsqu'elles sont alignées selon leur orientation vis, de manière identique aux dislocations $1/2\langle 111 \rangle$. Pour tester cette hypothèse, nous avons étudié l'expansion d'une boucle de dislocation $\langle 100 \rangle$ sous contrainte, de manière à sonder les orientations bloquantes de la ligne à basse température. Après relaxation de la déformation imposée, la forme de la boucle montre que son expansion est bloquée dès que la ligne s'oriente selon une direction $\langle 111 \rangle$ (Fig. 4c). La très forte friction ressentie par cette orientation mixte a ensuite été confirmée par calculs *ab initio* dans plusieurs métaux, montrant une barrière cinq fois plus élevée que pour l'orientation vis (voir Fig. 4d pour le cas du W). Il apparaît donc que le mouvement des dislocations $\langle 100 \rangle$ est limité à basse température par cette orientation mixte, un phénomène *a priori* générique à l'ensemble des métaux de transition CC. Ainsi, il se pourrait que leur activité ne soit possible qu'à plus haute température, lorsque la friction de réseau disparaît, en accord qualitatif avec les observations expérimentales. Dans cette gamme de température, les dislocations $\langle 100 \rangle$ seraient alors en mesure de contribuer de manière non négligeable à la plasticité des métaux de transition CC.

Bibliography

References

- [1] J.-C. Brachet, I. Idarraga-Trujillo, M. Le Flem, M. Le Saux, V. Vandenberghe, S. Urvoy, E. Rouesne, T. Guilbert, C. Toffolon-Masclat, M. Tupin, C. Phalippou, F. Lomello, F. Schuster, A. Billard, G. Velisa, C. Ducros, F. Sanchette, Early studies on Cr-Coated Zircaloy-4 as enhanced accident tolerant nuclear fuel claddings for light water reactors, *J. Nucl. Mater.* 517 (2019) 268–285. doi:10.1016/j.jnucmat.2019.02.018.
- [2] J. Yang, M. Steinbrück, C. Tang, M. Große, J. Liu, J. Zhang, D. Yun, S. Wang, Review on chromium coated zirconium alloy accident tolerant fuel cladding, *J. Alloys and Compounds* 895 (2022) 162450. doi:10.1016/j.jallcom.2021.162450.
- [3] E. Kashkarov, B. Afornu, D. Sidelev, M. Krinitcyn, V. Gouws, A. Lider, Recent advances in protective coatings for Accident Tolerant Zr-based fuel claddings, *Coatings* 11 (2021) 557. doi:10.3390/coatings11050557.
- [4] H. Chen, X. Wang, R. Zhang, Application and development progress of Cr-based surface coating in nuclear fuel elements: II. Current status and shortcomings of performance studies, *Coatings* 10 (2020) 835. doi:10.3390/coatings10090835.
- [5] R. Wadsack, R. Pippan, B. Schedler, Chromium a material for fusion technology, *Fusion Eng. Des.* 58–59 (2001) 743–748. doi:10.1016/S0920-3796(01)00554-3.
- [6] E. Fawcett, Spin-density-wave antiferromagnetism in chromium, *Rev. Mod. Phys.* 60 (1988) 209–283. doi:10.1103/RevModPhys.60.209.
- [7] Y. F. Gu, H. Harada, Y. Ro, Chromium and chromium-based alloys: Problems and possibilities for high-temperature service, *JOM* 56 (2004) 28–33. doi:10.1007/s11837-004-0197-0.
- [8] I.-C. Choi, C. Brandl, R. Schwaiger, Thermally activated dislocation plasticity in body-centered cubic chromium studied by high-temperature nanoindentation, *Acta Mater.* 140 (2017) 107–115. doi:10.1016/j.actamat.2017.08.026.
- [9] P. Anderson, J. Hirth, J. Lothe, *Theory of dislocations*, Cambridge University Press, 2017.
- [10] A. N. Stroh, Dislocations and cracks in anisotropic elasticity, *Philos. Mag.* 3 (1958) 625–646. doi:10.1080/14786435808565804.
- [11] A. N. Stroh, Steady state problems in anisotropic elasticity, *J. Math. Phys.* 41 (1962) 77–103. doi:10.1002/sapm196241177.
- [12] A. Argon, *Strengthening Mechanisms in Crystal Plasticity*, Oxford University Press, 2007. doi:10.1093/acprof:oso/9780198516002.001.0001.
- [13] C. N. Reid, A. Gilbert, Dislocation structure in chromium, chromium-rhenium, and chromium-iron alloys, *J. Less Common Met.* 10 (1966) 77–90. doi:10.1016/0022-5088(66)90116-0.
- [14] D. I. Bolef, Elastic Constants of Single Crystals of the bcc Transition Elements V, Nb, and Ta, *J. Appl. Phys.* 32 (1961) 100–105. doi:10.1063/1.1735933.
- [15] K. J. Carroll, Elastic Constants of Niobium from 4.2 to 300 K, *J. Appl. Phys.* 36 (1965) 3689–3690. doi:10.1063/1.1703072.
- [16] D. I. Bolef, J. de Klerk, Anomalies in the elastic constants and thermal expansion of chromium single crystals, *Phys. Rev.* 129 (1963) 1063–1067. doi:10.1103/PhysRev.129.1063.
- [17] D. I. Bolef, J. De Klerk, Elastic Constants of Single-Crystal Mo and W between 77 and 500 K, *J. Appl. Phys.* 33 (1962) 2311–2314. doi:10.1063/1.1728952.
- [18] D. Dever, Temperature dependence of the elastic constants in α -iron single crystals: relationship to spin order and diffusion anomalies, *J. Appl. Phys.* 43 (1972) 3293–3301. doi:10.1063/1.1661710.
- [19] E. Clouet, *Ab initio* models of dislocations, in: *Handbook of Materials Modeling : Methods: Theory and Modeling*, 2018, pp. 1–22. doi:10.1007/978-3-319-42913-7_22-1.
- [20] D. Caillard, Geometry and kinetics of glide of screw dislocations in tungsten between 95K and 573K, *Acta Mater.* 161 (2018) 21–34. doi:10.1016/j.actamat.2018.09.009.
- [21] D. Caillard, Kinetics of dislocations in pure Fe. Part I. In situ straining experiments at room temperature, *Acta Mater.* 58 (2010) 3493–3503. doi:10.1016/j.actamat.2010.02.023.
- [22] F. Louchet, L. P. Kubin, D. Vesely, In situ deformation of b.c.c. crystals at low temperatures in a high-voltage electron microscope Dislocation mechanisms and strain-rate equation, *Philos. Mag.* 39 (1979) 433–454. doi:10.1080/01418617908239283.
- [23] D. Caillard, TEM in situ straining experiments in Fe at low temperature, *Philos. Mag. Lett.* 89 (2009) 517–526. doi:10.1080/09500830903127518.
- [24] C. R. Weinberger, B. L. Boyce, C. C. Battaile, Slip planes in bcc transition metals, *Int. Mater. Rev.* 58 (2013) 296–314. doi:10.1179/1743280412Y.0000000015.
- [25] J. W. Christian, Some surprising features of the plastic deformation of body-centered cubic metals and alloys, *Metall. Trans. A* 14 (1983) 1237–1256. doi:10.1007/BF02664806.
- [26] A. S. Argon, S. R. Maloof, Plastic deformation of tungsten single crystals at low temperatures, *Acta Metall.* 14 (1966) 1449–1462. doi:10.1016/0001-6160(66)90165-9.
- [27] W. A. Spitzig, A. S. Keh, The effect of orientation and temperature on the plastic flow properties of iron single crystals, *Acta Metall.* 18 (1970) 611–622. doi:10.1016/0001-6160(70)90090-8.
- [28] C. Marichal, H. Van Swygenhoven, S. Van Petegem, C. Borca, {110} Slip with {112} slip traces in bcc Tungsten, *Sci Rep* 3 (2013) 2547. doi:10.1038/srep02547.
- [29] D. Brunner, Temperature dependence of the plastic flow of high-purity tungsten single crystals, *IJMR* 101 (2010) 1003–1013, publisher: Hanser Verlag. doi:10.3139/146.110362.
- [30] K. Kitajima, Y. Aono, E. Kuramoto, Slip systems and orientation dependence of yield stress in high purity molybdenum single crystals at 4.2K and 77K, *Scripta Metall.* 15 (1981) 919–924. doi:10.1016/0036-9748(81)90278-7.

- [31] R. Creten, J. Bressers, P. de Meester, Anomalous slip in high-purity vanadium crystals deformed in compression, *Mat. Sci. Eng.* 29 (1977) 51–53. doi:10.1016/0025-5416(77)90145-8.
- [32] A. J. Garratt-Reed, G. Taylor, Stress-strain curves for niobium crystals deformed at temperatures below ambient, *Philos. Mag.* 33 (1976) 577–590. doi:10.1080/14786437608221120.
- [33] M. H. A. Nawaz, B. L. Mordike, Slip geometry of tantalum and tantalum alloys, *Phys. Stat. Sol. (a)* 32 (1975) 449–458. doi:https://doi.org/10.1002/pssa.2210320213.
- [34] J. Holzer, Z. Chlup, T. Kruml, R. Gröger, Plastic deformation of magnetically isotropic Cr single crystals compressed at 77 K, *Int. J. Plast.* 138 (2021) 102938. doi:10.1016/j.ijplas.2021.102938.
- [35] Y. Aono, E. Kuramoto, K. Kitajima, Plastic deformation of high-purity iron single crystals, *Rep. Res. Inst. Appl. Mech.* 29 (1981) 127–193.
- [36] Y. Aono, E. Kuramoto, K. Kitajima, Orientation dependence of slip in niobium single crystals at 4.2 and 77 K, *Scripta Mater.* 18 (1984) 201–205. doi:10.1016/0036-9748(84)90508-8.
- [37] F. Louchet, L. P. Kubin, Dislocation substructures in the anomalous slip plane of single crystal niobium strained at 50 K, *Acta Metall.* 23 (1975) 17–21. doi:10.1016/0001-6160(75)90064-4.
- [38] H. Matsui, H. Kimura, Anomalous {110} slip in high-purity molybdenum single crystals and its comparison with that in V(a) metals, *Mater. Sci. Eng.* 24 (1976) 247–256. doi:10.1016/0025-5416(76)90118-X.
- [39] W. Wasserbäch, Anomalous Slip in High-Purity Niobium and Tantalum Single Crystals, *Phys. Stat. Sol.* 147 (1995) 417–446. doi:10.1002/pssa.2211470213.
- [40] C. Marichal, K. Srivastava, D. Weygand, S. Van Petegem, D. Grolimund, P. Gumbsch, H. Van Swygenhoven, Origin of Anomalous Slip in Tungsten, *Phys. Rev. Lett.* 113 (2014) 025501. doi:10.1103/PhysRevLett.113.025501.
- [41] G. C. Liu, S. S. Lau, J. E. Dorn, The plastic deformation behavior of Mo single crystals under compression, *Phys. Stat. Sol. (a)* 11 (1972) 645–651. doi:https://doi.org/10.1002/pssa.2210110228.
- [42] G. Taylor, Thermally-activated deformation of BCC metals and alloys, *Progress in Materials Science* 36 (1992) 29–61. doi:10.1016/0079-6425(92)90004-Q.
- [43] S. Takeuchi, T. Hashimoto, K. Maeda, Plastic Deformation of bcc Metal Single Crystals at Very Low Temperatures, *Transactions of the Japan Institute of Metals* 23 (1982) 60–69. doi:10.2320/matertrans1960.23.60.
- [44] L. Dezerald, L. Ventelon, E. Clouet, C. Denoual, D. Rodney, F. Willaime, Ab initio modeling of the two-dimensional energy landscape of screw dislocations in bcc transition metals, *Phys. Rev. B* 89 (2014) 024104. doi:10.1103/PhysRevB.89.024104.
- [45] E. Clouet, B. Bienvenu, L. Dezerald, D. Rodney, Screw dislocations in bcc transition metals: from *ab initio* modeling to yield criterion, *Comptes Rendus Physique* 22 (2021) 1–34. doi:10.5802/crphys.75.
- [46] V. Vitek, R. C. Perrin, D. K. Bowen, The core structure of $1/2\langle 111 \rangle$ screw dislocations in bcc crystals, *Philos. Mag.* 21 (1970) 1049–1073. doi:10.1080/14786437008238490.
- [47] S. Takeuchi, Core structure of a screw dislocation in the bcc lattice and its relation to slip behaviour of α -iron, *Philos. Mag.* 39 (1979) 661–671. doi:10.1080/01418617908239296.
- [48] S. L. Dudarev, P. M. Derlet, A ‘magnetic’ interatomic potential for molecular dynamics simulations, *J. Phys.: Condens. Matter* 17 (2005) 7097–7118. doi:10.1088/0953-8984/17/44/003.
- [49] L. Ventelon, F. Willaime, Generalized stacking-faults and screw-dislocation core-structure in bcc iron: A comparison between ab initio calculations and empirical potentials, *Philos. Mag.* 90 (2010) 1063–1074. doi:10.1080/14786431003668793.
- [50] V. Vitek, J. W. Christian, Computer simulation of the screw dislocation motion in bcc metals under the effect of the external shear and uniaxial stresses, *Proc. Royal Soc. London* 352 (1976) 109–124. doi:10.1098/rspa.1976.0166.
- [51] A. Seeger, C. Wüthrich, Dislocation relaxation processes in body-centred cubic metals, *Nuovo Cimento B* 33 (1976) 38–75. doi:10.1007/BF02722472.
- [52] W. Xu, J. A. Moriarty, Atomistic simulation of ideal shear strength, point defects, and screw dislocations in bcc transition metals: Mo as a prototype, *Phys. Rev. B* 54 (1996) 6941–6951. doi:10.1103/PhysRevB.54.6941.
- [53] M. S. Duesbery, V. Vitek, Plastic anisotropy in bcc transition metals, *Acta Mater.* 46 (1998) 1481–1492. doi:10.1016/S1359-6454(97)00367-4.
- [54] K. Ito, V. Vitek, Atomistic study of non-Schmid effects in the plastic yielding of bcc metals, *Philos. Mag.* 81 (2001) 1387–1407. doi:10.1080/01418610108214447.
- [55] M. Wen, A. H. W. Ngan, Atomistic simulation of kink-pairs of screw dislocations in body-centred cubic iron, *Acta Mater.* 48 (2000) 4255–4265. doi:10.1016/S1359-6454(00)00288-3.
- [56] G. Wang, A. Strachan, T. Çağın, W. A. Goddard, Kinks in the $a/2\langle 111 \rangle$ screw dislocation in Ta, *Journal of Computer-Aided Materials Design* 8 (2001) 117–125. doi:10.1023/A:1020038515726.
- [57] A. H. W. Ngan, M. Wen, Dislocation kink-pair energetics and pencil glide in body-centered cubic crystals, *Phys. Rev. Lett.* 87 (2001) 075505. doi:10.1103/PhysRevLett.87.075505.
- [58] S. I. Rao, C. Woodward, Atomistic simulations of $a/2\langle 111 \rangle$ screw dislocations in bcc Mo using a modified generalized pseudopotential theory potential, *Philos. Mag.* 81 (2001) 1317–1327. doi:10.1080/01418610108214443.
- [59] G. Wang, A. Strachan, T. Çağın, W. A. Goddard, Role of core polarization curvature of screw dislocations in determining the peierls stress in bcc Ta: A criterion for designing high-performance materials, *Phys. Rev. B* 67 (2003) 140101. doi:10.1103/PhysRevB.67.140101.
- [60] L. H. Yang, P. Söderlind, J. A. Moriarty, Accurate atomistic simulation of $a/2\langle 111 \rangle$ screw dislocations and other defects in bcc tantalum, *Philos. Mag.* 81 (2001) 1355–1385. doi:10.1080/01418610108214446.
- [61] M. Mrovec, D. Nguyen-Manh, D. G. Pettifor, V. Vitek, Bond-order potential for molybdenum: Application to dislocation behavior, *Phys. Rev. B* 69 (2004) 094115. doi:10.1103/PhysRevB.69.094115.
- [62] P. A. Gordon, T. Neeraj, Y. Li, J. Li, Screw dislocation mobility in bcc metals: the role of the compact core on double-kink

- nucleation, *Modelling Simul. Mater. Sci. Eng.* 18 (2010) 085008. doi:10.1088/0965-0393/18/8/085008.
- [63] M. I. Mendelev, S. Han, D. J. Srolovitz, G. J. Ackland, D. Y. Sun, M. Asta, Development of new interatomic potentials appropriate for crystalline and liquid iron, *Philos. Mag.* 83 (2003) 3977–3994. doi:10.1080/14786430310001613264.
- [64] D. Rodney, L. Ventelon, E. Clouet, L. Pizzagalli, F. Willaime, Ab initio modeling of dislocation core properties in metals and semiconductors, *Acta Mater.* 124 (2017) 633–659. doi:10.1016/j.actamat.2016.09.049.
- [65] L. Proville, D. Rodney, M.-C. Marinica, Quantum effect on thermally activated glide of dislocations, *Nature Mater.* 11 (2012) 845–849. doi:10.1038/nmat3401.
- [66] M.-C. Marinica, L. Ventelon, M. R. Gilbert, L. Proville, S. L. Dudarev, J. Marian, G. Bencteux, F. Willaime, Interatomic potentials for modelling radiation defects and dislocations in tungsten, *J. Phys.: Condens. Matter* 25 (2013) 395502. doi:10.1088/0953-8984/25/39/395502.
- [67] K. Edagawa, T. Suzuki, S. Takeuchi, Motion of a screw dislocation in a two-dimensional Peierls potential, *Phys. Rev. B* 55 (1997) 6180–6187. doi:10.1103/PhysRevB.55.6180.
- [68] K. Edagawa, T. Suzuki, S. Takeuchi, Plastic anisotropy in bcc transition metals, *Mater. Sci. Eng.* 234–236 (1997) 1103–1105. doi:10.1016/S0921-5093(97)00386-9.
- [69] L. Dezerald, D. Rodney, E. Clouet, L. Ventelon, F. Willaime, Plastic anisotropy and dislocation trajectory in BCC metals, *Nature Commun.* 7 (2016) 11695. doi:10.1038/ncomms11695.
- [70] C. Woodward, S. I. Rao, Ab initio simulation of isolated screw dislocations in bcc Mo and Ta, *Philos. Mag.* 81 (2001) 1305–1316. doi:10.1080/01418610108214442.
- [71] L. Ventelon, F. Willaime, E. Clouet, D. Rodney, Ab initio investigation of the Peierls potential of screw dislocations in bcc Fe and W, *Acta Mater.* 61 (2013) 3973–3985. doi:10.1016/j.actamat.2013.03.012.
- [72] J. Chaussidon, M. Fivel, D. Rodney, The glide of screw dislocations in bcc Fe: Atomistic static and dynamic simulations, *Acta Mater.* 54 (2006) 3407–3416. doi:10.1016/j.actamat.2006.03.044.
- [73] R. Gröger, V. Vitek, Explanation of the discrepancy between the measured and atomistically calculated yield stresses in body-centred cubic metals, *Philos. Mag. Lett.* 87 (2007) 113–120. doi:10.1080/09500830601158781.
- [74] V. V. Bulatov, W. Cai, Nodal effects in dislocation mobility, *Phys. Rev. Lett.* 89 (2002) 115501. doi:10.1103/PhysRevLett.89.115501.
- [75] E. Clouet, L. Ventelon, F. Willaime, Dislocation core energies and core fields from first principles, *Phys. Rev. Lett.* 102 (2009) 055502. doi:10.1103/PhysRevLett.102.055502.
- [76] E. Clouet, Dislocation core field. I. Modeling in anisotropic linear elasticity theory, *Phys. Rev. B* 84 (2011) 224111. doi:10.1103/PhysRevB.84.224111.
- [77] E. Clouet, L. Ventelon, F. Willaime, Dislocation core field. II. Screw dislocation in iron, *Phys. Rev. B* 84 (2011) 224107. doi:10.1103/PhysRevB.84.224107.
- [78] C. Crussard, F. Aubertin, Nouvelle méthode de précision pour la mesure de la maille individuelle des grains. application à l'étude de l'écrouissage et de la recristallisation, *Rev. Met. Paris* 46 (1949) 354–359.
- [79] A. Kraych, E. Clouet, L. Dezerald, L. Ventelon, F. Willaime, D. Rodney, Non-glide effects and dislocation core fields in bcc metals, *npj Computational Materials* 5 (2019) 1–8. doi:10.1038/s41524-019-0247-3.
- [80] J. D. Eshelby, R. E. Peierls, The determination of the elastic field of an ellipsoidal inclusion, and related problems, *Proc. Royal Soc. London* 241 (1957) 376–396. doi:10.1098/rspa.1957.0133.
- [81] J. D. Eshelby, R. E. Peierls, The elastic field outside an ellipsoidal inclusion, *Proc. Royal Soc. London* 252 (1959) 561–569. doi:10.1098/rspa.1959.0173.
- [82] E. Clouet, C. Varvenne, T. Jourdan, Elastic modeling of point-defects and their interaction, *Comput. Mater. Sci.* 147 (2018) 49–63. doi:10.1016/j.commatsci.2018.01.053.
- [83] T. Suzuki, H. Koizumi, H. O. K. Kirchner, Plastic flow stress of b.c.c. transition metals and the Peierls potential, *Acta Metall.* 43 (1995) 2177–2187. doi:10.1016/0956-7151(94)00451-X.
- [84] L. A. Zepeda-Ruiz, A. Stukowski, T. Oppelstrup, V. V. Bulatov, Probing the limits of metal plasticity with molecular dynamics simulations, *Nature* 550 (2017) 492–495. doi:10.1038/nature23472.
- [85] L. Proville, L. Ventelon, D. Rodney, Prediction of the kink-pair formation enthalpy on screw dislocations in α -iron by a line tension model parametrized on empirical potentials and first-principles calculations, *Phys. Rev. B* 87 (2013) 144106. doi:10.1103/PhysRevB.87.144106.
- [86] V. V. Bulatov, L. L. Hsiung, M. Tang, A. Arsenlis, M. C. Bartelt, W. Cai, J. N. Florando, M. Hiratani, M. Rhee, G. Hommes, T. G. Pierce, T. D. de la Rubia, Dislocation multi-junctions and strain hardening, *Nature* 440 (2006) 1174–1178. doi:10.1038/nature04658.
- [87] A. M. Goryaeva, J.-B. Maillat, M.-C. Marinica, Towards better efficiency of interatomic linear machine learning potentials, *Comput. Mater. Sci.* 166 (2019) 200–209. doi:10.1016/j.commatsci.2019.04.043.
- [88] A. M. Goryaeva, J. Dérès, C. Lapointe, P. Grigorev, T. D. Swinburne, J. R. Kermode, L. Ventelon, J. Baima, M.-C. Marinica, Efficient and transferable machine learning potentials for the simulation of crystal defects in bcc Fe and W, *Phys. Rev. Materials* 5 (2021) 103803. doi:10.1103/PhysRevMaterials.5.103803.
- [89] H. Park, M. R. Fellingner, T. J. Lenosky, W. W. Tipton, D. R. Trinkle, S. P. Rudin, C. Woodward, J. W. Wilkins, R. G. Hennig, Ab initio based empirical potential used to study the mechanical properties of molybdenum, *Phys. Rev. B* 85 (2012) 214121. doi:10.1103/PhysRevB.85.214121.
- [90] L. M. Corliss, J. M. Hastings, R. J. Weiss, Antiphase antiferromagnetic structure of chromium, *Phys. Rev. Lett.* 3 (1959) 211–212. doi:10.1103/PhysRevLett.3.211.
- [91] H. Bjerrum Møller, K. Blinowski, A. R. Mackintosh, T. Brun, Magnetic scattering of neutrons in chromium, *Solid State Communications* 2 (1964) 109–114. doi:10.1016/0038-1098(64)90248-0.
- [92] C. R. Fincher, G. Shirane, S. A. Werner, Magnetic excitations in chromium, *Phys. Rev. B* 24 (1981) 1312–1322. doi:

- 10.1103/PhysRevB.24.1312.
- [93] V. S. Golovkin, V. N. Bykov, V. A. Levдик, Anomalies in the magnetic structure of chromium, Soviet Phys. JETP-USSR 22 (1966) 754.
- [94] D. Mannix, P. de Camargo, C. Giles, A. de Oliveira, F. Yokaichiya, C. Vettier, The chromium spin density wave: magnetic X-ray scattering studies with polarisation analysis, Eur. Phys. J. B 20 (2001) 19–25. doi:10.1007/s100510170281.
- [95] V. L. Jacques, D. Le Bolloc'h, S. Ravy, C. Giles, F. Livet, S. B. Wilkins, Spin density wave dislocation in chromium probed by coherent X-ray diffraction, Eur. Phys. J. B 70 (2009) 317–325. doi:10.1140/epjb/e2009-00231-3.
- [96] U. Köbler, S. M. Dubiel, On the magnetic anisotropy of chromium, Z. Physik B - Condensed Matter 61 (1985) 257–262. doi:10.1007/BF01317792.
- [97] E. Fawcett, Spin fluctuations in the paramagnetic phase of Cr and Cr(V) alloys, Physica B: Condensed Matter 180-181 (1992) 179–181. doi:10.1016/0921-4526(92)90699-S.
- [98] B. H. Grier, G. Shirane, S. A. Werner, Magnetic excitations in chromium. II, Phys. Rev. B 31 (1985) 2892–2901. doi:10.1103/PhysRevB.31.2892.
- [99] S. A. Werner, A. Arrott, H. Kendrick, Temperature and magnetic field dependence of the antiferromagnetism in pure chromium, Phys. Rev. 155 (1967) 528–539. doi:10.1103/PhysRev.155.528.
- [100] G. E. Bacon, N. Cowlam, Magnetic studies of annealed and alloyed chromium by neutron diffraction, J. Phys. C: Solid State Phys. 2 (1969) 238–251. doi:10.1088/0022-3719/2/2/306.
- [101] I. S. Williams, R. Street, Magnetic ordering in strained chromium, Philos. Mag. B 3 (1981) 893–906. doi:10.1080/01418638108222355.
- [102] I. S. Williams, E. S. R. Gopal, R. Street, The specific heat of strained and annealed chromium, J. Phys. F: Met. Phys. 9 (1979) 431–445. doi:10.1088/0305-4608/9/3/007.
- [103] I. S. Williams, R. Street, Investigation of thermal hysteresis near the Neel transition in chromium, J. Phys. F: Met. Phys. 10 (1980) 2551–2553. doi:10.1088/0305-4608/10/11/026.
- [104] K. R. A. Ziebeck, J. G. Boom, P. J. Brown, H. Capellmann, J. A. C. Bland, Observation of spatial magnetic correlations in the paramagnetic phase of chromium using polarised neutrons and polarisation analysis, Z. Physik B - Condensed Matter 48 (1982) 233–239. doi:10.1007/BF01420585.
- [105] D. G. Van Campen, M. L. Knierim, L. E. Klebanoff, Persistence of atomic magnetism in the paramagnetic phase of chromium, Phys. Rev. B 43 (1991) 11668–11675. doi:10.1103/PhysRevB.43.11668.
- [106] D. G. Laurent, J. Callaway, J. L. Fry, N. E. Brener, Band structure, Fermi surface, Compton profile, and optical conductivity of paramagnetic chromium, Phys. Rev. B 23 (1981) 4977–4987. doi:10.1103/PhysRevB.23.4977.
- [107] A. W. Overhauser, Spin-density waves in an electron gas, Phys. Rev. 128 (1962) 1437–1452. doi:10.1103/PhysRev.128.1437.
- [108] W. M. Lomer, Electronic structure of chromium group metals, Proc. Phys. Soc. 80 (1962) 489–496. doi:10.1088/0370-1328/80/2/316.
- [109] S. B. Palmer, E. W. Lee, The elastic constants of chromium, Philos. Mag. 24 (1971) 311–318. doi:10.1080/14786437108227390.
- [110] S. Shallcross, A. E. Kissavos, V. Meded, A. V. Ruban, An *ab initio* effective Hamiltonian for magnetism including longitudinal spin fluctuations, Phys. Rev. B 72 (2005) 104437. doi:10.1103/PhysRevB.72.104437.
- [111] K. Hirai, Total energy calculation for spin-density wave chromium, J. Phys. Soc. Jpn. 67 (1998) 1776–1783. doi:10.1143/JPSJ.67.1776.
- [112] S. Cottenier, B. D. Vries, J. Meersschant, M. Rots, What density-functional theory can tell us about the spin-density wave in Cr, J. Phys.: Condens. Matter 14 (2002) 3275–3283. doi:10.1088/0953-8984/14/12/314.
- [113] R. Soulaïrol, C.-C. Fu, C. Barreteau, Structure and magnetism of bulk Fe and Cr: from plane waves to LCAO methods, J. Phys.: Condens. Matter 22 (2010) 295502. doi:10.1088/0953-8984/22/29/295502.
- [114] V. Vanhoof, M. Rots, S. Cottenier, Spin-density wave in Cr: Nesting versus low-lying thermal excitations, Phys. Rev. B 80 (2009) 184420. doi:10.1103/PhysRevB.80.184420.
- [115] R. Hafner, D. Spišák, R. Lorenz, J. Hafner, Magnetic ground state of Cr in density-functional theory, Phys. Rev. B 65 (2002) 184432. doi:10.1103/PhysRevB.65.184432.
- [116] A. Farrell, P.-K. Wu, Y.-J. Kao, T. Pereg-Barnea, Incommensurate spin density wave as a signature of spin-orbit coupling and precursor of topological superconductivity, Phys. Rev. B 94 (2016) 214424. doi:10.1103/PhysRevB.94.214424.
- [117] K. W. Katahara, M. Nimalendran, M. H. Manghnani, E. S. Fisher, Elastic moduli of paramagnetic chromium and Ti-V-Cr alloys, J. Phys. F: Met. Phys. 9 (1979) 2167–2176. doi:10.1088/0305-4608/9/11/008.
- [118] E. E. Lahteenkorva, J. T. Lenkkeri, Effects of magnetic order on elastic moduli of chromium, J. Phys. F: Met. Phys. 11 (1981) 767–773. doi:10.1088/0305-4608/11/4/010.
- [119] Y. N. Smirnov, V. Finkel, Crystal structure of chromium at 113–373 K, Soviet Phys. JETP-USSR 20 (1965) 315.
- [120] R. Street, Elasticity and anelasticity of chromium, Phys. Rev. Lett. 10 (1963) 210–211. doi:10.1103/PhysRevLett.10.210.
- [121] A. V. Sameljuk, A. D. Vasilev, S. A. Firstov, Low temperature deformation and fracture behaviour of [100] and [110] chromium single crystals, Int. J. Refract. Met. Hard Mater. 14 (1996) 249–255. doi:10.1016/0263-4368(95)00046-1.
- [122] A. C. McLaren, Dislocation substructures in deformed and recovered chromium, Aust. J. Phys. 17 (1964) 447–451. doi:10.1071/ph640447.
- [123] K. F. Hale, M. H. Brown, Experimental determination of Burgers vectors of dislocations, Proc. R. Soc. Lond. A 310 (1969) 479–491. doi:10.1098/rspa.1969.0088.
- [124] C. N. Reid, A. Gilbert, G. T. Hahn, Dislocation and deformation modes in chromium single crystals, Trans. AIME 239 (1967) 467–473.
- [125] R. I. Garrod, H. L. Wain, Dislocation arrangements and brittleness in chromium, J. Less Common Met. 9 (1965) 81–94.

- doi:10.1016/0022-5088(65)90086-X.
- [126] M. J. Marcinkowski, H. A. Lipsitt, The plastic deformation of chromium at low temperatures, *Acta Met.* 10 (1962) 95–111. doi:10.1016/0001-6160(62)90055-X.
 - [127] R. Ravlić, M. Bode, A. Kubetzka, R. Wiesendanger, Correlation of dislocation and domain structure of Cr(001) investigated by spin-polarized scanning tunneling microscopy, *Phys. Rev. B* 67 (2003) 174411. doi:10.1103/PhysRevB.67.174411.
 - [128] M. Kleiber, M. Bode, R. Ravlić, R. Wiesendanger, Topology-induced spin frustrations at the Cr(001) surface studied by spin-polarized scanning tunneling spectroscopy, *Phys. Rev. Lett.* 85 (2000) 4606–4609. doi:10.1103/PhysRevLett.85.4606.
 - [129] C. Reid, Dislocation widths in anisotropic bcc crystals, *Acta Metall.* 14 (1966) 13–16. doi:10.1016/0001-6160(66)90266-5.
 - [130] Y.-S. Lin, M. Mrovec, V. Vitek, A new method for development of bond-order potentials for transition bcc metals, *Modelling Simul. Mater. Sci. Eng.* 22 (2014) 034002. doi:10.1088/0965-0393/22/3/034002.
 - [131] R. Gröger, V. Vitek, Single crystal yield criterion for chromium based on atomistic studies of isolated $1/2[111]$ screw dislocations, *Int. J. Plast.* 132 (2020) 102733. doi:10.1016/j.ijplas.2020.102733.
 - [132] P. Hohenberg, W. Kohn, Inhomogeneous electron gas, *Phys. Rev.* 136 (1964) B864–B871. doi:10.1103/PhysRev.136.B864.
 - [133] W. Kohn, L. J. Sham, Self-consistent equations including exchange and correlation effects, *Phys. Rev.* 140 (1965) A1133–A1138. doi:10.1103/PhysRev.140.A1133.
 - [134] J. P. Perdew, K. Burke, M. Ernzerhof, Generalized gradient approximation made simple, *Phys. Rev. Lett.* 77 (1996) 3865–3868. doi:10.1103/PhysRevLett.77.3865.
 - [135] G. Kresse, J. Furthmüller, Efficiency of *ab initio* total energy calculations for metals and semiconductors using a plane-wave basis set, *Comput. Mater. Sci.* 6 (1996) 15–50. doi:10.1016/0927-0256(96)00008-0.
 - [136] H. J. Monkhorst, J. D. Pack, Special points for brillouin-zone integrations, *Phys. Rev. B* 13 (1976) 5188–5192. doi:10.1103/PhysRevB.13.5188.
 - [137] P.-W. Ma, S. L. Dudarev, Constrained density functional for noncollinear magnetism, *Phys. Rev. B* 91 (2015) 054420. doi:10.1103/PhysRevB.91.054420.
 - [138] A. Schneider, Corrélations entre le magnétisme, la thermodynamique et la diffusion dans les alliages fe-mn cubiques centrés : des premiers principes aux températures finies, Ph.D. thesis (2019). URL <http://www.theses.fr/2019SACL367/document>
 - [139] D. Nguyen-Manh, S. L. Dudarev, Model many-body stoner hamiltonian for binary fccr alloys, *Phys. Rev. B* 80 (2009) 104440. doi:10.1103/PhysRevB.80.104440.
 - [140] E. C. Stoner, R. Whiddington, Collective electron specific heat and spin paramagnetism in metals, *Proc. Roy. Soc. A* 154 (1936) 656–678. doi:10.1098/rspa.1936.0075.
 - [141] C. Barreateau, D. Spanjaard, M.-C. Desjonquères, An efficient magnetic tight-binding method for transition metals and alloys, *Comptes Rendus Physique* 17 (2016) 406–429. doi:10.1016/j.crhy.2015.12.014.
 - [142] R. Soulaïrol, C.-C. Fu, C. Barreateau, Magnetic and energetic properties of low-index Cr surfaces and Fe/Cr interfaces: A first-principles study, *Phys. Rev. B* 84 (2011) 155402. doi:10.1103/PhysRevB.84.155402.
 - [143] J. Tranchida, S. J. Plimpton, P. Thibaudau, A. P. Thompson, Massively parallel symplectic algorithm for coupled magnetic spin dynamics and molecular dynamics, *J. Comput. Phys.* 372 (2018) 406–425. doi:10.1016/j.jcp.2018.06.042.
 - [144] M. Y. Lavrentiev, D. Nguyen-Manh, S. L. Dudarev, Cluster expansion models for fccr alloys, the prototype materials for a fusion power plant, *Comput. Mater. Sci.* 49 (2010) S199–S203. doi:10.1016/j.commatsci.2010.04.033.
 - [145] R. Cardias, C. Barreateau, P. Thibaudau, C. C. Fu, Spin dynamics from a constrained magnetic tight-binding model, *Phys. Rev. B* 103 (2021) 235436. doi:10.1103/PhysRevB.103.235436.
 - [146] L. Bergqvist, A. Taroni, A. Bergman, C. Etz, O. Eriksson, Atomistic spin dynamics of low-dimensional magnets, *Phys. Rev. B* 87 (2013) 144401. doi:10.1103/PhysRevB.87.144401.
 - [147] A. Bergman, A. Taroni, L. Bergqvist, J. Hellsvik, B. Hjörvarsson, O. Eriksson, Magnon softening in a ferromagnetic monolayer: A first-principles spin dynamics study, *Phys. Rev. B* 81 (2010) 144416. doi:10.1103/PhysRevB.81.144416.
 - [148] C. Etz, L. Bergqvist, A. Bergman, A. Taroni, O. Eriksson, Atomistic spin dynamics and surface magnons, *J. Phys.: Condens. Matter* 27 (2015) 243202. doi:10.1088/0953-8984/27/24/243202.
 - [149] M. Trochet, F. Soisson, C.-C. Fu, M. Y. Lavrentiev, Influence of magnetic excitation and vibrational entropy on the phase diagram of fccr alloys, *Comput. Mater. Sci.* 199 (2021) 110698. doi:10.1016/j.commatsci.2021.110698.
 - [150] D. Nguyen-Manh, M. Y. Lavrentiev, S. L. Dudarev, Magnetic properties of point defect interaction with impurity atoms in fccr alloys, *J. Nucl. Mater.* 386-388 (2009) 60–63. doi:10.1016/j.jnucmat.2008.12.059.
 - [151] M. Y. Lavrentiev, S. L. Dudarev, D. Nguyen-Manh, Magnetic cluster expansion model for high-temperature magnetic properties of iron and iron–chromium alloys, *J. App. Phys.* 109 (2011) 07E123. doi:10.1063/1.3556900.
 - [152] M. Y. Lavrentiev, S. L. Dudarev, D. Nguyen-Manh, Magnetic cluster expansion simulations of fccr alloys, *J. Nucl. Mater.* 386-388 (2009) 22–25. doi:10.1016/j.jnucmat.2008.12.052.
 - [153] A. Schneider, C.-C. Fu, F. Soisson, C. Barreateau, Atomic diffusion in α -iron across the curie point: An efficient and transferable *ab initio* based modeling approach, *Phys. Rev. Lett.* 124 (2020) 215901. doi:10.1103/PhysRevLett.124.215901.
 - [154] A. Schneider, C.-C. Fu, O. Waseda, C. Barreateau, T. Hickel, Ab initio based models for temperature-dependent magnetochemical interplay in bcc femn alloys, *Phys. Rev. B* 103 (2021) 024421. doi:10.1103/PhysRevB.103.024421.
 - [155] V.-T. Tran, C.-C. Fu, A. Schneider, Effective interaction model for coupled magnetism and phase stability in bcc feco

- systems, Comput. Mater. Sci. 183 (2020) 109906. doi:10.1016/j.commatsci.2020.109906.
- [156] E. Bitzek, P. Koskinen, F. Gähler, M. Moseler, P. Gumbsch, Structural relaxation made simple, Phys. Rev. Lett. 97 (2006) 170201. doi:10.1103/PhysRevLett.97.170201.
- [157] S. Plimpton, Fast parallel algorithms for short-range molecular dynamics, J. Comput. Phys. 117 (1995) 1–19. doi:10.1006/jcph.1995.1039.
- [158] M. R. Fellinger, H. Park, J. W. Wilkins, Force-matched embedded-atom method potential for niobium, Phys. Rev. B 81 (2010) 144119. doi:10.1103/PhysRevB.81.144119.
- [159] C. Yang, L. Qi, Modified embedded-atom method potential of niobium for studies on mechanical properties, Computational Materials Science 161 (2019) 351–363. doi:10.1016/j.commatsci.2019.01.047.
- [160] G. J. Ackland, R. Thetford, An improved n-body semi-empirical model for body-centred cubic transition metals, Philos. Mag. 56 (1987) 15–30. doi:10.1080/01418618708204464.
- [161] L. Bergqvist, A. Bergman, Realistic finite temperature simulations of magnetic systems using quantum statistics, Phys. Rev. Mater. 2 (2018) 013802. doi:10.1103/PhysRevMaterials.2.013802.
- [162] W. Setyawan, S. Curtarolo, High-throughput electronic band structure calculations: Challenges and tools, Comput. Mater. Sci. 49 (2010) 299–312. doi:10.1016/j.commatsci.2010.05.010.
- [163] C. H. Woo, H. Wen, A. A. Semenov, S. L. Dudarev, P.-W. Ma, Quantum heat bath for spin-lattice dynamics, Phys. Rev. B 91 (2015) 104306. doi:10.1103/PhysRevB.91.104306.
- [164] L. P. Kadanoff, W. Göetze, D. Hamblen, R. Hecht, E. A. S. Lewis, V. V. Palciauskas, M. Rayl, J. Swift, D. Aspnes, J. Kane, Static phenomena near critical points: Theory and experiment, Rev. Mod. Phys. 39 (1967) 395–431. doi:10.1103/RevModPhys.39.395.
- [165] E. Clouet, BABEL software.
URL <http://emmanuel.clouet.free.fr/Programs/Babel/index.html>
- [166] G. Henkelman, H. Jónsson, Improved tangent estimate in the nudged elastic band method for finding minimum energy paths and saddle points, J. Chem. Phys. 113 (2000) 9978–9985. doi:10.1063/1.1323224.
- [167] D. Rodney, Activation enthalpy for kink-pair nucleation on dislocations: Comparison between static and dynamic atomic-scale simulations, Phys. Rev. B 76 (2007) 144108. doi:10.1103/PhysRevB.76.144108.
- [168] R. Pynn, W. Press, S. M. Shapiro, S. A. Werner, Second and third harmonics of the spin density wave in chromium metal, Phys. Rev. B 13 (1976) 295–298. doi:10.1103/PhysRevB.13.295.
- [169] Y. Tsunoda, Y. Nakai, N. Kunitomi, Phase relation between sdw and strain wave in chromium, Solid State Commun. 16 (1975) 443–445. doi:10.1016/0038-1098(75)90107-6.
- [170] Y. Tsunoda, M. Mori, N. Kunitomi, Y. Teraoka, J. Kanamori, Strain wave in pure chromium, Solid State Commun. 14 (1974) 287–289. doi:10.1016/0038-1098(74)90855-2.
- [171] S. Iida, Y. Tsunoda, Y. Nakai, N. Kunitomi, Third harmonics of spin density wave in cr and its alloys, J. Phys. Soc. Jpn. 50 (1981) 2587–2594. doi:10.1143/JPSJ.50.2587.
- [172] C. F. Eagen, S. A. Werner, A neutron diffraction investigation of the sinusoidal atomic displacement wave in pure chromium, Solid State Commun. 16 (1975) 1113–1116. doi:10.1016/0038-1098(75)90017-4.
- [173] P. M. Marcus, S.-L. Qiu, V. L. Moruzzi, The mechanism of antiferromagnetism in chromium, J. Phys.: Condens. Matter 10 (1998) 6541–6552. doi:10.1088/0953-8984/10/29/014.
- [174] C. Kittel, Introduction to solid state physics, Wiley, New York, 1966.
- [175] V. Vitek, Intrinsic stacking faults in body-centred cubic crystals, Philos. Mag. 18 (1968) 773–786. doi:10.1080/14786436808227500.
- [176] C. R. Weinberger, B. L. Boyce, C. C. Battaile, Slip planes in bcc transition metals, Int. Mater. Rev. 58 (2013) 296–314. doi:10.1179/1743280412Y.0000000015.
- [177] A. K. Head, The energy of a screw dislocation in a cubic crystal, Phys. Stat. Sol. (b) 5 (1964) 51–54. doi:10.1002/pssb.19640050105.
- [178] A. J. E. Foreman, Dislocation energies in anisotropic crystals, Acta Metall. 3 (1955) 322–330. doi:10.1016/0001-6160(55)90036-5.
- [179] M. S. Duesbery, Z. S. Basinski, On non-glide stresses and their influence on the screw dislocation core in body-centred cubic metals I. The Peierls stress, Proc. R. Soc. Lond. A 392 (1984) 145–173. doi:10.1098/rspa.1984.0027.
- [180] B. Bienvenu, E. Clouet, *Ab initio* modeling of slip activity in body-centered cubic chromium, Acta Mater. 224 (2022) 117485. doi:10.1016/j.actamat.2021.117485.
- [181] B. Bienvenu, E. Clouet, L. Dezerald, D. Rodney, *Ab initio* informed yield criterion accross body-centered cubic transition metals, Acta Mater. 236 (2022) 118098. doi:10.1016/j.actamat.2022.118098.
- [182] V. Vitek, M. Mrovec, J. L. Bassani, Influence of non-glide stresses on plastic flow: from atomistic to continuum modeling, Mat. Sci. Eng. A 365 (2004) 31–37. doi:10.1016/j.msea.2003.09.004.
- [183] R. Gröger, A. G. Bailey, V. Vitek, Multiscale modeling of plastic deformation of molybdenum and tungsten: I. Atomistic studies of the core structure and glide of $1/2 < 111 >$ screw dislocations at 0K, Acta Mater. 56 (2008) 5401–5411. doi:10.1016/j.actamat.2008.07.018.
- [184] R. Gröger, V. Racherla, J. L. Bassani, V. Vitek, Multiscale modeling of plastic deformation of molybdenum and tungsten: II. Yield criterion for single crystals based on atomistic studies of glide of $1/2 < 111 >$ screw dislocations, Acta Mater. 56 (2008) 5412–5425. doi:10.1016/j.actamat.2008.07.037.
- [185] Z. M. Chen, M. Mrovec, P. Gumbsch, Atomistic aspects of $1/2 < 111 >$ screw dislocation behavior in α -iron and the derivation of microscopic yield criterion, Modelling Simul. Mater. Sci. Eng. 21 (2013) 055023. doi:10.1088/0965-0393/21/5/055023.
- [186] H. Lim, C. R. Weinberger, C. C. Battaile, T. E. Buchheit, Application of generalized non-Schmid yield law to low-

- temperature plasticity in bcc transition metals, *Modelling Simul. Mater. Sci. Eng.* 21 (2013) 045015. doi:10.1088/0965-0393/21/4/045015.
- [187] R. Gröger, Which stresses affect the glide of screw dislocations in bcc metals?, *Philos. Mag.* 94 (2014) 2021–2030. doi:10.1080/14786435.2014.904058.
- [188] R. Gröger, Symmetry-adapted single crystal yield criterion for non-Schmid materials, *Int. J. Plast.* 146 (2021) 103101. doi:10.1016/j.ijplas.2021.103101.
- [189] K. Srivastava, D. Weygand, D. Caillard, P. Gumbsch, Repulsion leads to coupled dislocation motion and extended work hardening in bcc metals, *Nature Commun.* 11 (2020) 5098. doi:10.1038/s41467-020-18774-1.
- [190] K. Srivastava, R. Gröger, D. Weygand, P. Gumbsch, Dislocation motion in tungsten: Atomistic input to discrete dislocation simulations, *Int. J. Plast.* 47 (2013) 126–142. doi:10.1016/j.ijplas.2013.01.014.
- [191] L. Dezerald, L. Proville, L. Ventelon, F. Willaime, D. Rodney, First-principles prediction of kink-pair activation enthalpy on screw dislocations in bcc transition metals: V, Nb, Ta, Mo, W, and Fe, *Phys. Rev. B* 91 (2015) 094105. doi:10.1103/PhysRevB.91.094105.
- [192] U. F. Kocks, A. S. Argon, M. F. Ashby, Progress in materials science, in *Thermodynamics and Kinetics of Slip*, Vol. 19, Pergamon Press, Oxford, UK, 1975.
- [193] G. Hachet, D. Caillard, L. Ventelon, E. Clouet, Mobility of screw dislocation in bcc tungsten at high temperature in presence of carbon, *Acta Mater.* 222 (2022) 117440. doi:10.1016/j.actamat.2021.117440.
- [194] T. D. Swinburne, M.-C. Marinica, Unsupervised calculation of free energy barriers in large crystalline systems, *Phys. Rev. Lett.* 120 (2018) 135503. doi:10.1103/PhysRevLett.120.135503.
- [195] W. Meyer, H. Neldel, Relation between the energy constant and the quantity constant in the conductivity-temperature formula of oxide semiconductors, *Z. Tech. Phys.* 18 (1937) 588–593.
- [196] R. Soulaïrol, C. Barreteau, C.-C. Fu, Interplay between magnetism and energetics in fccr alloys from a predictive non-collinear magnetic tight-binding model, *Phys. Rev. B* 94 (2016) 024427. doi:10.1103/PhysRevB.94.024427.
- [197] F. Ducastelle, Order and Phase Stability in Alloys, in: *Interatomic Potential and Structural Stability*, Springer Series in Solid-State Sciences, Berlin, Heidelberg, 1993, pp. 133–142. doi:10.1007/978-3-642-84968-8_14.
- [198] M. A. Ruderman, C. Kittel, Indirect exchange coupling of nuclear magnetic moments by conduction electrons, *Phys. Rev.* 96 (1954) 99–102. doi:10.1103/PhysRev.96.99.
- [199] X. Wu, Z. Liu, T. Luo, Magnon and phonon dispersion, lifetime, and thermal conductivity of iron from spin-lattice dynamics simulations, *J. App. Phys.* 123 (2018) 085109. doi:10.1063/1.5020611.
- [200] R. Przeniosło, P. Fabrykiewicz, I. Sosnowska, D. Wardecki, W. A. Stawinski, H. Y. Playford, R. Hempelmann, M. Bukowski, Crystallite size effect on the monoclinic deformation of the bcc crystal structure of chromium, *Physica B: Condensed Matter* 530 (2018) 183–190. doi:10.1016/j.physb.2017.10.086.
- [201] J. Lagoute, S. L. Kawahara, C. Chacon, V. Repain, Y. Girard, S. Rousset, Spin-polarized scanning tunneling microscopy and spectroscopy study of chromium on a Cr(001) surface, *J. Phys.: Condens. Matter* 23 (2011) 045007. doi:10.1088/0953-8984/23/4/045007.
- [202] M. Kleiber, M. Bode, R. Ravlić, N. Tezuka, R. Wiesendanger, Magnetic properties of the cr(001) surface studied by spin-polarized scanning tunneling spectroscopy, *J. Mag. Mag. Mater.* 240 (2002) 64–69. doi:10.1016/S0304-8853(01)00739-9.
- [203] P. G. Evans, E. D. Isaacs, G. Aeppli, Z. Cai, B. Lai, X-ray microdiffraction images of antiferromagnetic domain evolution in chromium, *Science* 295 (2002) 1042–1045. doi:10.1126/science.1066870.
- [204] G. Hausch, Magnetic exchange energy contribution to the elastic constants and its relation to the anomalous elastic behaviour of invar alloys, *Phys. Stat. Sol. (a)* 15 (1973) 501–510. doi:10.1002/pssa.2210150215.
- [205] D. Hinzke, N. Kazantseva, U. Nowak, O. N. Mryasov, P. Asselin, R. W. Chantrell, Domain wall properties of fept: From bloch to linear walls, *Phys. Rev. B* 77 (2008) 094407. doi:10.1103/PhysRevB.77.094407.
- [206] C. R. Weinberger, G. J. Tucker, S. M. Foiles, Peierls potential of screw dislocations in bcc transition metals: Predictions from density functional theory, *Phys. Rev. B* 87 (2013) 054114. doi:10.1103/PhysRevB.87.054114.
- [207] A. Koester, A. Ma, A. Hartmaier, Atomistically informed crystal plasticity model for body-centered cubic iron, *Acta Mater.* 60 (2012) 3894–3901. doi:10.1016/j.actamat.2012.03.053.
- [208] G. Po, Y. Cui, D. Rivera, D. Cereceda, T. D. Swinburne, J. Marian, N. Ghoniem, A phenomenological dislocation mobility law for bcc metals, *Acta Mater.* 119 (2016) 123–135. doi:10.1016/j.actamat.2016.08.016.
- [209] C. Woodward, S. I. Rao, Flexible *ab initio* boundary conditions: Simulating isolated dislocations in bcc mo and ta, *Phys. Rev. Lett.* 88 (2002) 216402. doi:10.1103/PhysRevLett.88.216402.
- [210] D. Cereceda, M. Diehl, F. Roters, P. Shanthraj, D. Raabe, J. M. Perlado, J. Marian, Linking atomistic, kinetic monte carlo and crystal plasticity simulations of single-crystal tungsten strength, *GAMM-Mitteilungen* 38 (2015) 213–227. doi:10.1002/gamm.201510012.
- [211] D. Cereceda, M. Diehl, F. Roters, D. Raabe, J. M. Perlado, J. Marian, Unraveling the temperature dependence of the yield strength in single-crystal tungsten using atomistically-informed crystal plasticity calculations, *Int. J. Plast.* 78 (2016) 242–265. doi:10.1016/j.ijplas.2015.09.002.
- [212] K. Edagawa, T. Suzuki, S. Takeuchi, Motion of a screw dislocation in a two-dimensional Peierls potential, *Phys. Rev. B* 55 (1997) 6180–6187. doi:10.1103/PhysRevB.55.6180.
- [213] J. Bressers, P. De Meester, Slip plane choice in vanadium at deformation temperatures $T \leq 0.15 T_m$, *J. Less Common Met.* 84 (1982) 11–23. doi:10.1016/0022-5088(82)90123-0.
- [214] D. Caillard, B. Bienvenu, E. Clouet, Anomalous slip in body-centred cubic metals, *Nature*, in press (2022).
- [215] K. D. Rogausch, B. L. Mordike, Proc. 2nd Intern. Conf. Strength of Metals and Alloys (1970) 168.
- [216] S. Takeuchi, E. Kuramoto, T. Suzuki, Orientation dependence of slip in tantalum single crystals, *Acta Metall.* 20 (1972) 909–915. doi:10.1016/0001-6160(72)90084-3.

- [217] P. Beardmore, D. Hull, Deformation and fracture of tungsten single crystals, *J. Less Common Met.* 9 (1965) 168–180. doi:10.1016/0022-5088(65)90094-9.
- [218] J. F. Byron, D. Hull, Plastic deformation of tantalum single crystals: I. The surface morphology of yield, *J. Less Common Met.* 13 (1967) 71–84. doi:10.1016/0022-5088(67)90048-3.
- [219] L. N. Chang, G. Taylor, J. W. Christian, Stress asymmetries in the deformation behaviour of niobium single crystals, *Acta Metall.* 31 (1983) 37–42. doi:10.1016/0001-6160(83)90061-5.
- [220] G. Webb, R. Gibala, T. Mitchell, Interstitial solution hardening and slip asymmetry in tantalum, *Inst of Metals, United Kingdom*, 1973, iNIS Reference Number: 5124585.
- [221] H.-J. Kaufmann, A. Luft, D. Schulze, Deformation mechanism and dislocation structure of high-purity molybdenum single crystals at low temperatures, *Crystal Research and Technology* 19 (1984) 357–372. doi:10.1002/crat.2170190312.
- [222] A. Seeger, L. Hollang, The Flow-Stress Asymmetry of Ultra-Pure Molybdenum Single Crystals, *Materials Transactions, JIM* 41 (2000) 141–151. doi:10.2320/matertrans1989.41.141.
- [223] D. K. Bowen, J. W. Christian, G. Taylor, Deformation properties of niobium single crystals, *Can. J. Phys.* 45 (1967) 903–938. doi:10.1139/p67-069.
- [224] K. J. Bowman, R. Gibala, Stress asymmetry in cyclic deformation of b.c.c. metals, *Acta Metall.* 40 (1992) 193–200. doi:10.1016/0956-7151(92)90213-X.
- [225] M. S. Duesbery, R. A. Foxall, A detailed study of the deformation of high purity niobium single crystals, *Philos. Mag.* 20 (1969) 719–751. doi:10.1080/14786436908228040.
- [226] S. Takeuchi, E. Kuramoto, Anomalous slip in a bcc crystal observed in computer simulation of screw dislocation motion, *Scripta Metall.* 8 (1974) 785–789. doi:10.1016/0036-9748(74)90294-4.
- [227] H. Saka, K. Noda, T. Imura, H. Matsui, H. Kimura, HVEM in-situ observation of anomalous (101) slip in molybdenum, *Philos. Mag.* 34 (1976) 33–48. doi:10.1080/14786437608228172.
- [228] L. L. Hsiung, On the mechanism of anomalous slip in bcc metals, *Mater. Sci. Eng.* 528 (2010) 329–337. doi:10.1016/j.msea.2010.09.017.
- [229] J. Bressers, R. Creten, Suppression of anomalous slip by oxygen interstitials in vanadium, *Scripta Metall.* 11 (1977) 33–36. doi:10.1016/0036-9748(77)90008-4.
- [230] D. K. Bowen, G. Taylor, The deformation behaviour of dilute niobium-nitrogen alloys, *Acta Metall.* 25 (1977) 417–436. doi:10.1016/0001-6160(77)90233-4.
- [231] R. Lachenmann, H. Schultz, The influence of interstitial nitrogen on the asymmetry of the yield stress of tantalum, *Scripta Metall.* 6 (1972) 731–736. doi:10.1016/0036-9748(72)90133-0.
- [232] G. Taylor, R. Bajaj, O. N. Carlson, Anomalous slip in high-purity vanadium crystals, *Philos. Mag.* 28 (1973) 1035–1042. doi:10.1080/14786437308220966.
- [233] C. T. Wang, D. W. Bainbridge, The deformation mechanism for high-purity vanadium at low temperatures, *Metall. Mater. Trans. B* 3 (1972) 3161–3165. doi:10.1007/BF02661327.
- [234] D. L. Harrod, R. E. Gold, Mechanical properties of vanadium and vanadium-base alloys, *Int. Met. Rev.* 25 (1980) 163–222. doi:10.1179/imtr.1980.25.1.163.
- [235] C. J. Bolton, G. Taylor, Anomalous slip in high-purity niobium single crystals deformed at 77 K in tension, *Philos. Mag.* 26 (1972) 1359–1376. doi:10.1080/14786437208220348.
- [236] W. Wasserbäch, V. Novák, Optical investigation of anomalous slip-line patterns in high purity niobium and tantalum single crystals after tensile deformation at 77 K, *Mat. Sci. Eng.* 73 (1985) 197–202. doi:10.1016/0025-5416(85)90308-8.
- [237] F. Ackermann, H. Mughrabi, A. Seeger, Temperature- and strain-rate dependence of the flow stress of ultrapure niobium single crystals in cyclic deformation, *Acta Metall.* 31 (1983) 1353–1366. doi:10.1016/0001-6160(83)90006-8.
- [238] M. Werner, Temperature and strain-rate dependence of the flow stress of ultrapure tantalum single crystals, *Phys. Stat. Sol. (a)* 104 (1987) 63–78. doi:https://doi.org/10.1002/pssa.2211040105.
- [239] L. Kaun, A. Luft, J. Richter, D. Schulze, Slip Line Pattern and Active Slip Systems of Tungsten and Molybdenum Single Crystals Weakly Deformed in Tension at Room Temperature, *Phys. Stat. Sol. (b)* 26 (1968) 485–499. doi:10.1002/pssb.19680260212.
- [240] F. Guiu, P. L. Pratt, The Effect of Orientation on the Yielding and Flow of Molybdenum Single Crystals, *Phys. Stat. Sol. (b)* 15 (1966) 539–552. doi:10.1002/pssb.19660150214.
- [241] R. H. Schnitzel, Deformation of tungsten single crystals from 77°C to 800°C, *J. Less Common Met.* 8 (1965) 81–89. doi:10.1016/0022-5088(65)90099-8.
- [242] H. Matsui, H. Kimura, Anomalous {110} slip and the role of co-planar double slip in bcc metals, *Scripta Metall.* 9 (1975) 971–978. doi:10.1016/0036-9748(75)90554-2.
- [243] J. Yang, Z. Zhang, Z. Zhang, Quantitative understanding of anomalous slip in mo, *Philos. Mag.* 95 (2015) 2026–2045. doi:10.1080/14786435.2015.1045567.
- [244] V. V. Bulatov, W. Cai, *Computer simulations of dislocations*, Oxford Univ. Press, Oxford, 1966.
- [245] DDLAB.
URL <http://micro.stanford.edu/~caiwei/Forum/2005-12-05-DDLab/>
- [246] N. Bertin, W. Cai, S. Aubry, V. V. Bulatov, Core energies of dislocations in bcc metals, *Phys. Rev. Mat.* 5 (2021) 025002. doi:10.1103/PhysRevMaterials.5.025002.
- [247] Y. Huang, R. J. Arsenault, The effect of oxygen on the dislocation structures in vanadium, *Mater. Sci. Eng.* 12 (1973) 111–118. doi:10.1016/0025-5416(73)90134-1.
- [248] R. J. Arsenault, A. Lawley, Work hardening and dislocation structure in ta and ta-base alloys, *Philos. Mag.* 15 (1967) 549–565. doi:10.1080/14786436708220902.
- [249] C. Y. Chiem, W. S. Lee, The influence of dynamic shear loading on plastic deformation and microstructure of tungsten

- single crystals, *Mater. Sci. Eng.* 187 (1994) 43–50. doi:10.1016/0921-5093(94)90329-8.
- [250] R. A. Foxall, M. S. Duesbery, P. B. Hirsch, The deformation of niobium single crystals, *Can. J. Phys.* 45 (1967) 607–629. doi:10.1139/p67-052.
- [251] C. N. Reid, A. Gilbert, G. T. Hahn, Twinning, slip and catastrophic flow in niobium, *Acta Metall.* 14 (1966) 975–983. doi:10.1016/0001-6160(66)90218-5.
- [252] R. J. Wasilewski, R. Hutchings, M. H. Loretto, Slip on {110} in <001> nb single crystals deformed in compression at 77 k, *Philos. Mag.* 29 (1974) 521–535. doi:10.1080/14786437408213236.
- [253] B. Bienvenu, C. C. Fu, E. Clouet, Impact of magnetism on screw dislocations in body-centered cubic chromium, *Acta Mater.* 200 (2020) 570–580. doi:10.1016/j.actamat.2020.09.041.
- [254] W. A. Spitzig, T. E. Mitchell, Dislocation arrangements in tantalum single crystals deformed in tension at 373°K, *Acta Metall.* 14 (1966) 1311–1323. doi:10.1016/0001-6160(66)90248-3.
- [255] D. J. Dingley, K. F. Hale, N. P. Allen, Burgers vectors of dislocations in deformed iron and iron alloys, *Proc. Royal Soc. London* 295 (1966) 55–71. doi:10.1098/rspa.1966.0225.
- [256] L. K. France, M. H. Loretto, G. V. Raynor, The influence of the size of diffracting vectors on the visibility of dislocations in α -iron, *Proc. Royal Soc. London* 307 (1968) 83–96. doi:10.1098/rspa.1968.0176.
- [257] L. K. France, M. H. Loretto, Field-ion microscope evidence for the existence of an a <110> dislocation in iron, *Philos. Mag.* 19 (1969) 873–876. doi:10.1080/14786436908216341.
- [258] Y. T. Chou, Dislocation reactions and networks in anisotropic bcc crystals, *Mater. Sci. Eng.* 10 (1972) 81–86. doi:10.1016/0025-5416(72)90071-7.
- [259] A. J. Garratt-Reed, G. Taylor, Optical and electron microscopy of niobium crystals deformed below room temperature, *Philos. Mag. A* 39 (1979) 597–646. doi:10.1080/01418617908239294.
- [260] S. Aubry, S. P. Fitzgerald, S. L. Dudarev, W. Cai, Equilibrium shape of dislocation shear loops in anisotropic α -fe, *Modell. Simul. Mater. Sci. Eng.* 19 (2011) 065006. doi:10.1088/0965-0393/19/6/065006.
- [261] K. Kang, V. V. Bulatov, W. Cai, Singular orientations and faceted motion of dislocations in body-centered cubic crystals, *PNAS* (2012). doi:10.1073/pnas.1206079109.
- [262] L. Romaner, T. Pradhan, A. Kholobina, R. Drautz, M. Mrovec, Theoretical investigation of the 70.5° mixed dislocations in body-centered cubic transition metals, *Acta Mater.* 217 (2021) 117154. doi:10.1016/j.actamat.2021.117154.
- [263] G. Welsch, R. Gibala, T. E. Mitchell, Structure of dislocations in tantalum and tantalum-nitrogen alloys, *Acta Metall.* 23 (1975) 1461–1468. doi:10.1016/0001-6160(75)90155-8.
- [264] G. Welsch, R. Gibala, T. E. Mitchell, Dislocation substructures in tantalum and tantalum–nitrogen alloys deformed at 77 k, *Phys. Stat. Sol. (a)* 30 (1975) 117–132. doi:10.1002/pssa.2210300112.
- [265] M. Myshlyayev, I. Khodos, O. Senkov, Y. Romanov, Dislocation structure of block boundaries in monocrystalline molybdenum and tungsten., *Physics of Metals and Metallography* 47 (1979) 163–174.
- [266] M. Myshlyayev, Y. Romanov, O. Sen'kov, I. Khodos, V. Glebovskij, High temperature creep and dislocation structure of tungsten monocrystals, *Problemy Prochnosti* 5 (1979) 26–34.
- [267] L. N. Pronina, S. Takeuchi, K. Suzuki, M. Ichihara, Dislocation structures in rolled and annealed (001)[110] single-crystal molybdenum, *Philos. Mag.* 45 (1982) 859–865. doi:10.1080/01418618208239908.
- [268] L. Pronina, I. Aristova, A. Mazilkin, Orientational dependence of the dislocation structure in rolled single crystals of tungsten, *Physics of The Solid State* 38 (1996) 442–447.
- [269] W. Carrington, K. F. Hale, D. McLean, N. P. Allen, Arrangement of dislocations in iron, *Proc. Royal Soc. London* 259 (1960) 203–227. doi:10.1098/rspa.1960.0219.
- [270] D. Caillard, An in situ study of hardening and softening of iron by carbon interstitials, *Acta Mater.* 59 (2011) 4974–4989. doi:10.1016/j.actamat.2011.04.048.
- [271] L. Ventelon, B. Lüthi, E. Clouet, L. Proville, B. Legrand, D. Rodney, F. Willaime, Dislocation core reconstruction induced by carbon segregation in bcc iron, *Phys. Rev. B* 91 (2015) 220102. doi:10.1103/PhysRevB.91.220102.
- [272] B. Lüthi, L. Ventelon, D. Rodney, F. Willaime, Attractive interaction between interstitial solutes and screw dislocations in bcc iron from first principles, *Comput. Mater. Sci.* 148 (2018) 21–26. doi:10.1016/j.commatsci.2018.02.016.
- [273] B. Lüthi, F. Berthier, L. Ventelon, B. Legrand, D. Rodney, F. Willaime, *Ab initio* thermodynamics of carbon segregation on dislocation cores in bcc iron, *Mod. Simul. Mater. Sci. Eng.* 27 (2019) 074002. doi:10.1088/1361-651X/ab28d4.
- [274] G. Hachet, L. Ventelon, F. Willaime, E. Clouet, Screw dislocation-carbon interaction in BCC tungsten: an ab initio study, *Acta Mater.* 200 (2020) 481–489. doi:10.1016/j.actamat.2020.09.014.
- [275] A. Seeger, U. Holzwarth†, Slip planes and kink properties of screw dislocations in high-purity niobium, *Philos. Mag.* 86 (2006) 3861–3892. doi:10.1080/14786430500531769.
- [276] T. E. Mitchell, R. J. Fields, R. L. Smialek, Three-stage hardening in vanadium single crystals, *J. Less Common Met.* 20 (1970) 167–170. doi:10.1016/0022-5088(70)90104-9.
- [277] J. Bressers, M. Heerschap, P. De Meester, Deformation properties of vanadium single crystals, *J. Less Common Met.* 22 (1970) 321–326. doi:10.1016/0022-5088(70)90082-2.
- [278] H. Yoshinaga, K. Toma, K. Abe, S. Morozumi, The Portevin-Le chatelier effect in vanadium, *Philos. Mag.* 23 (1971) 1387–1403. doi:10.1080/14786437108217009.
- [279] U. Holzwarth, A. Seeger, *Proc. 9th Intern. Conf. Strength of Metals and Alloys* (1991) 577.
- [280] J. Nagakawa, M. Meshii, The deformation of niobium single crystals at temperatures between 77 and 4.2 K, *Philos. Mag. A* 44 (1981) 1165–1191. doi:10.1080/01418618108235801.
- [281] S. Takeuchi, K. Maeda, Slip in high purity tantalum between 0.7 and 40 K, *Acta Metall.* 25 (1977) 1485–1490. doi:10.1016/0001-6160(77)90078-5.
- [282] R. J. Arsenault, An investigation of the mechanism of thermally activated deformation in tantalum and tantalum-base

- alloys, *Acta Metall.* 14 (1966) 831–838. doi:10.1016/0001-6160(66)90003-4.
- [283] L. Hollang, D. Brunner, A. Seeger, Work hardening and flow stress of ultrapure molybdenum single crystals, *Mater. Sci. Eng. A* 319–321 (2001) 233–236. doi:10.1016/S0921-5093(01)01002-4.
- [284] E. Kuramoto, Y. Aono, K. Kitajima, K. Maeda, S. Takeuchi, Thermally activated slip deformation between 0.7 and 77 K in high-purity iron single crystals, *Philos. Mag. A* 39 (1979) 717–724. doi:10.1080/01418617908239302.
- [285] T. Takeuchi, R. Honda, K. Iwayama, T. Taoka, Tensile Deformation of Iron Single Crystals Having the [100] and [110] Axes between -70°C and 250°C, *Jpn. J. Appl. Phys.* 6 (1967) 1282. doi:10.1143/JJAP.6.1282.
- [286] D. Brunner, J. Diehl, Temperature and Strain-Rate Dependence of the Tensile Flow Stress of High-Purity α -Iron below 250 K. I. Stress/Temperature Regime III, *Phys. Stat. Sol. (a)* 124 (1991) 455–464. doi:https://doi.org/10.1002/pssa.2211240210.
- [287] T. L. Altshuler, J. W. Christian, W. Hume-Rothery, The mechanical properties of pure iron tested in compression over the temperature range 2 to 293°K, *Philos. Trans. R. Soc. Lond. A* 261 (1967) 253–287. doi:10.1098/rsta.1967.0004.
- [288] A. Sato, M. Meshii, Asymmetry in yield stress and irradiation softening of high purity iron single crystals, *Scripta Met.* 8 (1974) 851–859. doi:10.1016/0036-9748(74)90306-8.
- [289] D. Brunner, V. Glebovsky, The plastic properties of high-purity w single crystals, *Mater. Lett.* 42 (2000) 290–296. doi:10.1016/S0167-577X(99)00200-1.
-

Appendices

Appendix A. Experimental yield stresses and athermal temperatures

We present in this appendix a summary of the experimental yield stresses σ_Y measured at low temperature across all bcc transition metals under uniaxial mechanical loading in tension and/or compression, presented in Tab. A.1, with the athermal temperature of the Peierls mechanism T_{ath} and the melting point T_m . Are indicated under brackets for each presented data the test temperature, experimental strain rate $\dot{\epsilon}$, and the orientation of the loading axis defined by angles ζ and χ .

Table A.1: Experimental yield stress σ_Y (MPa) for all bcc transition metals measured at low temperature, and athermal temperature of the Peierls mechanism T_{ath} (K). Values are taken from various references indicated in each row with details about the experimental conditions. The melting point T_m (K) is indicated as a reference temperature for each metal.

	Yield stress σ_Y (MPa)	T_{ath} (K)	T_m (K) [174]
V	400 [233] (77 K, $6.7 \times 10^{-5} \text{ s}^{-1}$, center orientation)	300 [233] 450 [234] 400 [276, 278]	2 200
	350 [276] (77 K, $6.7 \times 10^{-4} \text{ s}^{-1}$, center orientation)		
	500 [277] (77 K, $1.0 \times 10^{-4} \text{ s}^{-1}$, center orientation)		
	750 [278] (77 K, $3.3 \times 10^{-5} \text{ s}^{-1}$, center orientation)		
Nb	900 [43] (4.2 K, $8.0 \times 10^{-5} \text{ s}^{-1}$, [011]- $\bar{1}$ 11] edge)	300 [43, 279] 275 – 375 [237]	2 750
	500 – 900 [36] (4.2 K, $1.7 \times 10^{-4} \text{ s}^{-1}$, $\zeta \simeq 47^\circ$)		
	600 – 1 200 [280] (4.2 K, $4.6 \times 10^{-4} \text{ s}^{-1}$, center orientation)		
	270 – 600 [36] (77 K, $1.7 \times 10^{-4} \text{ s}^{-1}$, $\zeta \simeq 47^\circ$)		
Ta	200 – 700 [32, 280] (77 K, $6 \times 10^{-4} \text{ s}^{-1}$, [001]-[011]- $\bar{1}$ 11] triangle)	400 [216, 282] 400 – 450 [238]	3 290
	700 [281] (4.2 K, $1.0 \times 10^{-4} \text{ s}^{-1}$, center orientation)		
	500 – 900 [218] (77 K, $4.0 \times 10^{-4} \text{ s}^{-1}$, edges of triangle)		
Cr	470 – 560 [33] (77 K, $6.0 \times 10^{-5} \text{ cm/min}$, $\zeta \simeq 50^\circ$)	420 [126]	2 180
	970 [126] (77 K, $8.3 \times 10^{-5} \text{ s}^{-1}$, polycrystal)		
Mo	780 – 1 200 [34] (77 K, $1.0 \times 10^{-5} \text{ s}^{-1}$, [001]-[011]- $\bar{1}$ 11] triangle)	450 [41, 83] 400 – 450 [240]	2 895
	1 140 – 1 600 [30, 36] (4.2 K, $1.7 \times 10^{-4} \text{ s}^{-1}$, $\zeta \simeq 47^\circ$)		
	1 620 [283] (4.2 K, $8.6 \times 10^{-4} \text{ s}^{-1}$, center orientation)		
	440 – 740 [41] (77 K, $3.3 \times 10^{-5} \text{ s}^{-1}$, [001]-[011]- $\bar{1}$ 11] triangle)		
W	500 – 940 [30] (77 K, $1.7 \times 10^{-4} \text{ s}^{-1}$, $\zeta \simeq 47^\circ$)	800 [29] 600 [241]	3 695
	1 600 [29] (60 K, $8.7 \times 10^{-4} \text{ s}^{-1}$, center orientation)		
Fe	750 – 1 500 [26, 217] (77 K, $4.0 \times 10^{-4} \text{ s}^{-1}$, edges of triangle)	300 [284] 400 [285, 286]	1 810
	720 – 850 [35, 36] (4.2 K, $1.7 \times 10^{-4} \text{ s}^{-1}$, $\zeta \simeq 47^\circ$)		
	750 – 950 [284] (4.2 K, $8.0 \times 10^{-5} \text{ s}^{-1}$, center and [001]-[011] edge)		
	700 [287] (20.4 K, $5.0 \times 10^{-4} \text{ s}^{-1}$, center orientation)		
	450 – 550 [288] (60 K, $5.0 \times 10^{-4} \text{ s}^{-1}$, $\zeta \simeq 45^\circ$)		
	400 – 500 [35] (77 K, $1.7 \times 10^{-4} \text{ s}^{-1}$, $\zeta \simeq 47^\circ$)		

Appendix B. Orientation and surface dependence of the energy of the magnetic fault bounded by two $\frac{1}{2}\langle 111 \rangle$ screw dislocations with the tight binding model

We study in this appendix the impact of the orientation and surface of the fault plane on the energy γ of the magnetic fault bounded by two $\frac{1}{2}\langle 111 \rangle$ screw dislocations using the TB model presented in Methods, section 1.2, and which gives a very satisfactory agreement with *ab initio* calculations in terms of bulk properties and core energy of the dislocation. The calculation is performed in the 273 atom supercell, with periodicity vectors $\vec{p}_1 = 7/2 [\bar{1}2\bar{1}] - 13/2 [\bar{1}01]$, $\vec{p}_2 = 7/2 [\bar{1}2\bar{1}] + 13/2 [\bar{1}01]$, and $\vec{p}_3 = 2 \times \frac{1}{2} [111]$, where the total energy contained in the simulation cell is:

$$E^{\text{tot}} = E^{\text{bulk}} + E^{\text{elas}} + 2E^{\text{core}} + E^{\text{fault}} \quad (\text{B.1})$$

The orientation of the fault plane Θ with respect to the $(\bar{1}01)$ plane is imposed by moving the two dislocations of the dipole as sketched on Fig. B.1a. As the distance between the two dislocations, and with their periodic images, varies from one position to another, the elastic contribution to the energy E^{elas} changes, which is evaluated for each position using the BABEL package [165]. In each calculation, atomic positions are not relaxed, but are fixed to the predictions of anisotropic elasticity theory. The core energy E^{core} of the two $\frac{1}{2}\langle 111 \rangle$ screw dislocations is assumed to be independent on their environment, which was checked in Chapter 2 with respect to the size of the simulation cell (see section 1.2). This core energy is then fixed to the TB

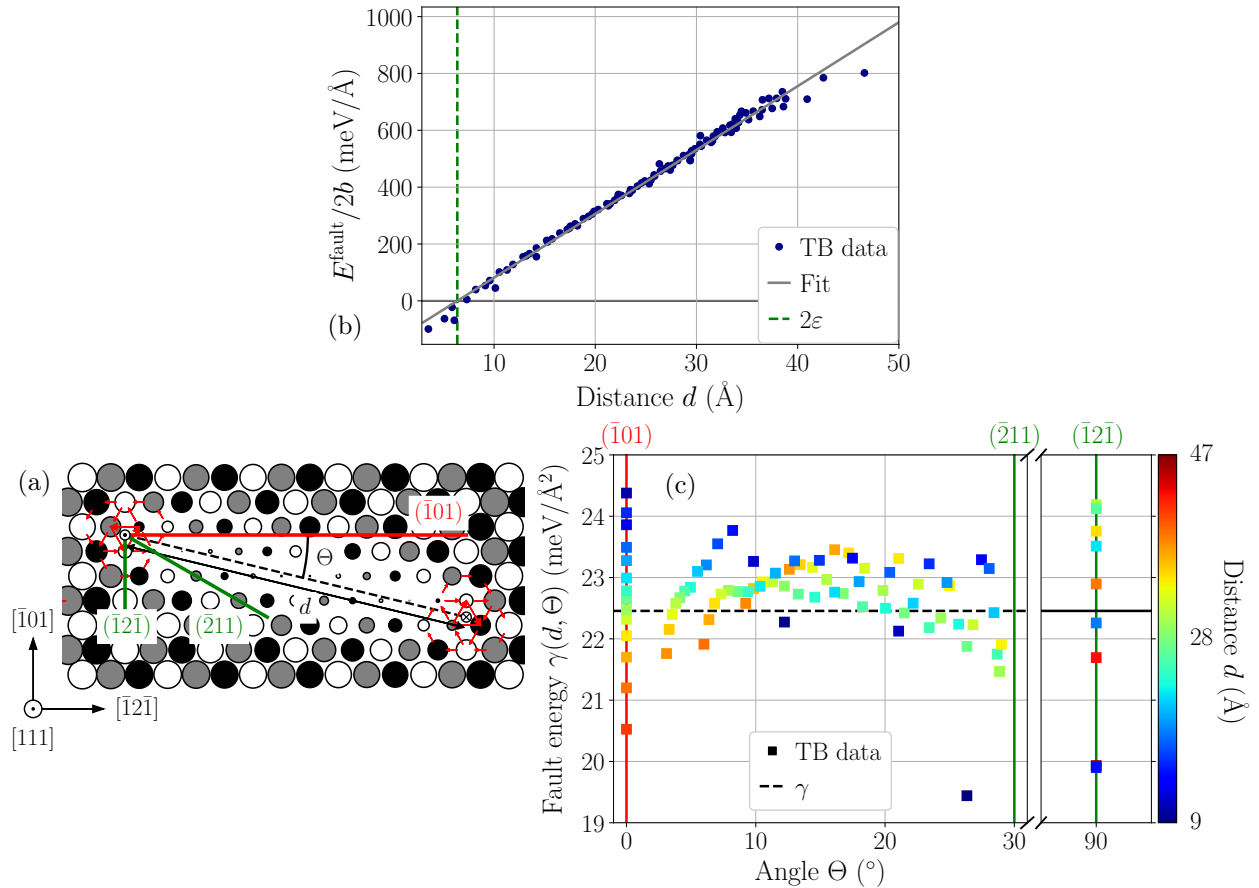


Figure B.1: Dependence of the magnetic fault surface energy γ (meV/Å²) on the orientation of its habit plane Θ with respect to the $(\bar{1}01)$ plane, and surface $S^{\text{fault}} = h \times (d - 2\varepsilon)$ obtained using the TB model in the 273 atom supercell.

result obtained using the relaxed *ab initio* structure as input, $E^{\text{core}} = 524 \text{ meV}/\text{\AA}$. Accounting for a region of radius ε near the core the two dislocations and where the energy of the magnetic fault cannot be properly defined due to local effects, *i.e.* neither described by elasticity nor included in the range of the magnetic fault, the magnetic fault then covers a surface $S^{\text{fault}} = h(d - 2\varepsilon)$, with $h = 2b$ the height of the simulation cell in the direction of the line. Assuming the fault energy E^{fault} to be proportional to its surface, *i.e.* $E^{\text{fault}} = \gamma \times 2b(d - 2\varepsilon)$, leads to the following expression per unit length:

$$\frac{E^{\text{fault}}}{2b} = \gamma \times (d - 2\varepsilon) = \frac{E^{\text{tot}} - E^{\text{bulk}} - E^{\text{elas}} - 2E^{\text{core}}}{2b}, \quad (\text{B.2})$$

which can be fitted to a linear function of the distance d to obtain γ and ε simultaneously. The results for all scanned positions of the two dislocations are presented in Fig. B.1b. The agreement with the linear fit is very good, resulting in a fault energy $\gamma = 22.5 \text{ meV}/\text{\AA}^2$ and a radius $\varepsilon = 3.2 \text{ \AA}$ below which the fault energy does not vary linearly with the distance d between the two dislocations. The magnetic fault energy is also presented as a function of the orientation of its habit plane Θ with respect to the $(\bar{1}01)$ plane (red in Fig. B.1a) in Fig. B.1c, with all TB data plotted in different colors according to the distance d covered by the magnetic fault. This shows that γ does not depend on the relative orientation of the two $1/2\langle 111 \rangle$ bounding dislocations, nor on the distance between them. If the magnetic fault had shown a preferred orientation, this would have constrained $1/2\langle 111 \rangle$ dislocations to glide in these planes, in order to reduce the energy of the fault they drag behind them, which is not the case at 0 K according to these results.

Appendix C. Free energy of model magnetic fault variations with temperature

The object of this appendix is to give analytical expressions of the magnetic free energy of a fault having different model temperature evolution. Two different magnetic energy profiles are considered here, similar to the two variations found through the heating and cooling cycles of the infinite magnetic faults presented in section 2.1 of Chapter 3: a constant energy up to a given temperature T_0 ; and a linearly decreasing energy up to T_0 . The magnetic free energy ΔF^{mag} of a fault with energy ΔE^{mag} is known at zero temperature, where we have $\Delta F^{\text{mag}}(T = 0 \text{ K}) = \Delta E^{\text{mag}}(T = 0 \text{ K})$ since the entropic contribution is zero at $T = 0 \text{ K}$. An alternative way to evaluate analytically its free energy as a function of temperature is thus:

$$\Delta F^{\text{mag}}(\beta) = \frac{1}{\beta} \int_{\beta'=\beta_{\text{ref}}}^{\beta} \Delta E^{\text{mag}}(\beta') d\beta' \quad \leftrightarrow \quad \Delta F^{\text{mag}}(T) = T \int_{t=T}^{T_{\text{ref}}} \frac{\Delta E^{\text{mag}}(t)}{t^2} dt \quad (\text{C.1})$$

In the case of the magnetic faults presented in Chapter 3, a reference temperature $T_{\text{ref}} = 5T_N/4$ is chosen, above which the magnetic energy of all defects studied here vanish, namely the infinite magnetic fault and the magnetic contribution to the core energy of $1/2\langle 111 \rangle$ screw dislocations as discussed in section 2.3.

Appendix C.1. Constant magnetic fault energy

Considering a magnetic fault of constant energy γ up to a given temperature T_0 :

$$\Delta E^{\text{mag}}(T) = \begin{cases} \gamma, & \text{for } T < T_0 \\ 0, & \text{for } T \geq T_0 \end{cases} \quad (\text{C.2})$$

Integration over the temperature range between 0 K and T_{ref} gives:

$$\Delta F^{\text{mag}}(T) = T \int_{t=T}^{T_0} \frac{\gamma}{t^2} dt = \boxed{\gamma \left(1 - \frac{T}{T_0} \right) \text{ for } T < T_0} \quad (\text{C.3})$$

This model evolution corresponds to the energy of the non-collinear structure found upon cooling a crystal rigidly sheared by a $1/2\langle 111 \rangle$ vector (see Fig. 10 in section 2.1).

Appendix C.2. Linearly decreasing magnetic fault energy

We now consider a magnetic fault whose energy decreases linearly to zero at T_0 , similar to the evolution of the collinear fault energy below $T_N/2$ found upon heating a crystal containing an infinite magnetic fault (Fig. 10 in section 2.1), or bounded by two $1/2\langle 111 \rangle$ screw dislocations (Fig. 18 in section 2.3). The energy of such magnetic fault is given by:

$$\Delta E^{\text{mag}}(T) = \begin{cases} \gamma \left(1 - \frac{T}{T_0} \right), & \text{for } T < T_0 \\ 0, & \text{for } T \geq T_0 \end{cases} \quad (\text{C.4})$$

An integration over the temperature range using Eq. 28 results in the following:

$$\Delta F^{\text{mag}}(T) = T \int_{t=T}^{T_0} \frac{\gamma}{t^2} \left(1 - \frac{t}{T_0} \right) dt = \boxed{\gamma \left(1 - \frac{T}{T_0} \right) - \frac{\gamma T}{T_0} \ln \left(\frac{T_0}{T} \right) \text{ for } T < T_0} \quad (\text{C.5})$$

Appendix D. Adjustment of the elastic constants to ensure the symmetry of the $\frac{1}{2}\langle 111 \rangle$ and $\langle 100 \rangle$ screw dislocations trajectory in $\{110\}$ planes

As detailed in section 3.1.3 of the Methods, an adjustment of the elastic constants from the values of the perfect crystal is required to enforce the symmetry of the dislocation trajectory along the NEB path, notably to ensure $x(\xi = 0) = 0$ and $x(\xi = 1) = \lambda_P$, which is detailed here for both $\frac{1}{2}\langle 111 \rangle$ and $\langle 100 \rangle$ screw dislocations, with the correction performed in all bcc transition metals.

Appendix D.1. $\frac{1}{2}\langle 111 \rangle$ screw dislocation

Only the elastic constants C_{44} and C_{15} are modified to enforce this relation, using the stress differences between the initial and final configurations given by *ab initio* calculations. The values for the rotated bcc unit-cell and the fitted values necessary to ensure both conditions are satisfied are presented in Tab. D.1. The elastic constants of a simulation cell containing a $\frac{1}{2}\langle 111 \rangle$ screw dislocation dipole are also evaluated for W, Mo, and the NM phase of Cr, and are presented in the 'Dislocated crystal' row. We note that the elastic constants of the dislocated crystal vary by a similar amount from the bulk values as the fitted values chosen to ensure the conditions on the dislocation trajectory. These elastic constants, with respect to the perfect crystal, show a variation up to 13% for the C_{15} and C_{44} components and less than 6% for all other constants in Cr, 18% and 15% for C_{15} and C_{44} respectively and less than 4% for all other components in Mo, and 6 and 7% for C_{15} and C_{44} respectively with less than 3% variation on other components in W.

Table D.1: Lattice parameter a_0 (Å), and elastic constants C_{ij} (in GPa) rotated in the frame of the $\frac{1}{2}\langle 111 \rangle$ screw dislocation ('Perfect crystal'), corrected values used to extract the screw dislocation trajectory and relaxation volume ('Fit'), and values of a cell containing a $\frac{1}{2}\langle 111 \rangle$ screw dislocation dipole ('Dislocated crystal'). Adjusted values (C_{15} and C_{44}) are in italic.

	a_0		C_{11}	C_{12}	C_{13}	C_{15}	C_{33}	C_{44}	C_{66}
V	2.998	Perfect crystal	233	163	175	20	221	47	35
		Fit	233	163	175	18	221	48	35
Nb	3.308	Perfect crystal	217	151	164	17	204	42	33
		Fit	217	151	164	15	204	42	33
Ta	3.322	Perfect crystal	288	154	145	-12	296	59	67
		Fit	288	154	145	-9.1	296	55	67
Cr (NM phase)	2.847	Perfect crystal	420	164	191	38	394	155	128
		Dislocated crystal	416	174	195	33	382	135	118
		Fit	420	164	191	32	394	138	128
Cr (AF phase)	2.865	Perfect crystal	338	86	117	45	306	157	126
		Fit	338	86	117	35	306	140	126
Mo	3.159	Perfect crystal	416	175	195	27	396	140	120
		Dislocated crystal	413	182	197	22	381	119	115
		Fit	416	175	195	21	396	122	120
W	3.186	Perfect crystal	495	207	211	5.1	492	148	144
		Dislocated crystal	499	213	210	5.4	487	137	143
		Fit	495	207	211	4.5	492	141	144
Fe	2.829	Perfect crystal	320	142	129	-18	333	76	89
		Fit	320	142	129	-17	333	71	89

Appendix D.2. $\langle 100 \rangle$ screw dislocation

In the frame of the $\langle 100 \rangle$ screw dislocation, the elastic tensor is:

$$\bar{\bar{C}}_{\langle 100 \rangle} = \begin{bmatrix} C_{11} & C_{12} & C_{13} & 0 & 0 & 0 \\ C_{12} & C_{11} & C_{13} & 0 & 0 & 0 \\ C_{13} & C_{13} & C_{33} & 0 & 0 & 0 \\ 0 & 0 & 0 & C_{44} & 0 & 0 \\ 0 & 0 & 0 & 0 & C_{44} & 0 \\ 0 & 0 & 0 & 0 & 0 & C_{66} \end{bmatrix}, \quad (\text{D.1})$$

so that only one component of the elastic tensor needs to be adjusted to ensure $x(\xi = 1) = \lambda_P$:

$$4C_{44}b^2\lambda_P = hS\Delta\sigma_{32}(\xi = 1) \quad (\text{D.2})$$

Given that, for the $\langle 100 \rangle$ screw dislocation gliding in a $\{110\}$ plane, we have $h = b = a_0$ and $\lambda_P = a_0\sqrt{2}/2$, the above condition results in the following expression for the C_{44} elastic constant:

$$C_{44} = \frac{hS\Delta\sigma_{32}(\xi = 1)}{4b^2\lambda_P} = \frac{S\Delta\sigma_{32}(\xi = 1)}{2a_0^2\sqrt{2}} \quad (\text{D.3})$$

The elastic constants of the rotated unit-cell ('Perfect crystal') and the fitted values to enforce the above condition ('Fit') are reported in Tab. D.2 for all bcc transition metals. We note that this adjustment is very small, even compared to the one performed in the previous section for the $1/2\langle 111 \rangle$ screw dislocation, except in Nb for which this correction corresponds to a variation of -30% with respect to bulk values.

Table D.2: Elastic constants C_{ij} (in GPa) rotated in the frame of the $\langle 100 \rangle$ screw dislocation ('Perfect crystal'), and corrected values used to extract the screw dislocation trajectory ('Fit'). Adjusted values for C_{44} are indicated in *italic*.

		C_{11}	C_{12}	C_{13}	C_{33}	C_{44}	C_{66}
V	Perfect crystal	233	187	151	269	<i>24</i>	59
	Fit	233	187	151	269	<i>24</i>	59
Nb	Perfect crystal	216	177	138	255	<i>20</i>	59
	Fit	216	177	138	255	<i>14</i>	59
Ta	Perfect crystal	296	143	169	270	<i>76</i>	50
	Fit	296	143	169	270	<i>69</i>	50
Cr (NM phase)	Perfect crystal	415	219	151	483	<i>98</i>	166
	Fit	415	219	151	483	<i>102</i>	166
Cr (AF phase)	Perfect crystal	343	152	63	432	<i>96</i>	185
	Fit	343	152	63	432	<i>97</i>	185
Mo	Perfect crystal	428	227	170	485	<i>100</i>	157
	Fit	428	227	170	485	<i>99</i>	157
W	Perfect crystal	507	226	217	517	<i>141</i>	150
	Fit	507	226	217	517	<i>141</i>	150
Fe	Perfect crystal	320	116	155	281	<i>102</i>	63
	Fit	320	116	155	281	<i>109</i>	63

Appendix E. Influence of the entropic contribution on the predicted flow stress

Appendix E.1. Comparison with experiments

We compare in this appendix the predicted temperature evolution of the tensile yield stress for single crystals of W and Mo with center orientation $[\bar{1}49]$, *i.e.* $\zeta = 50^\circ$ and $\chi = 0$, with experimental data from Brunner and Glebovsky [289] and Hollang and Seeger [283] respectively. For a tensile loading axis having this orientation, the 0 K yield criterion in tension (Eq. 12 in Chapter 2) predicts the lowest yield stress for $[111](\bar{1}01)$ (orange) and $[\bar{1}11](101)$ (purple) slip systems for both W and Mo, which have similar slip activity at 0 K as presented in Chapter 4, Fig. 5. The variation of the yield stress for both slip systems is plotted as a function of temperature in Fig. E.1 for different dislocation densities ρ_D ranging from 10^6 to 10^{12} m^{-2} , both neglecting entropic contributions (*i.e.* $T_m \rightarrow \infty$) and using the Meyer-Neldel compensation rule with the melting point for both materials, 3695 and 2895 K for W and Mo respectively [174].

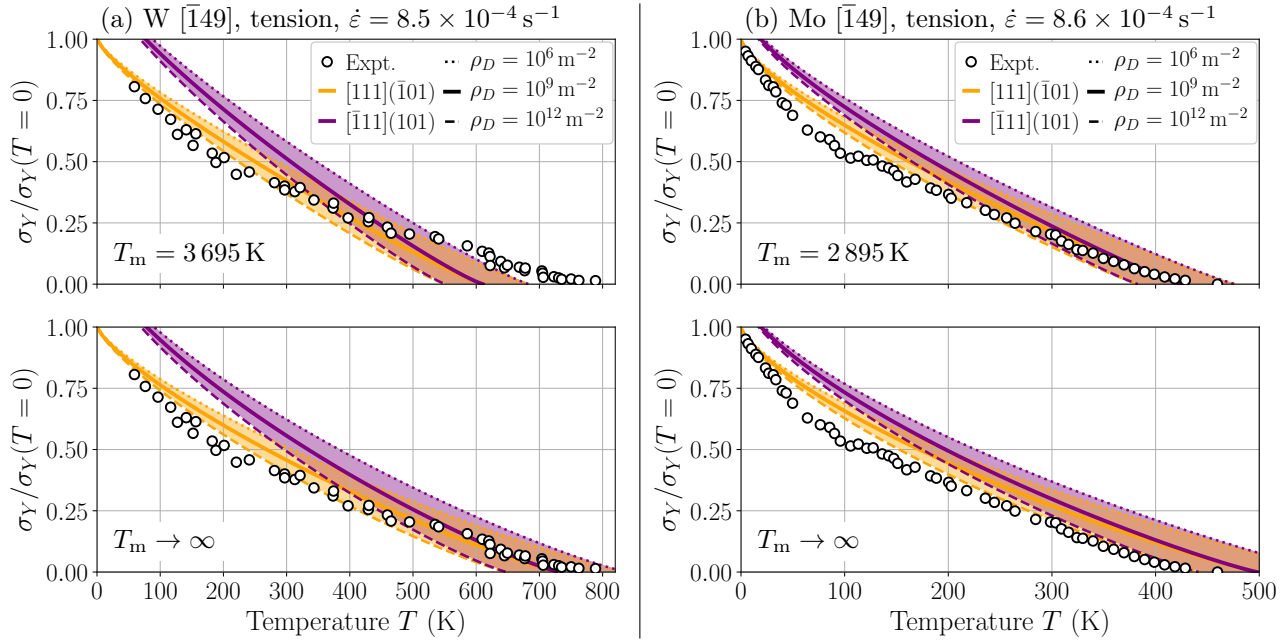


Figure E.1: Predicted and experimental yield stresses σ_Y as a function of temperature for (a) W, and (b) Mo single crystals of orientation $[\bar{1}49]$ tested under uniaxial tension. Predicted yield stresses are normalized by their value at 0 K, 4.1 and 2.4 GPa for W and Mo respectively. Experimental data for W are taken from Brunner and Glebovsky [289] and are normalized by 2.0 GPa, and from Hollang and Seeger [283] for Mo, normalized by 1.5 GPa.

The strain rate $\dot{\epsilon}$ is set to the experimental value, indicated above each of the two plots in Fig. E.1. In these two experimental works, the dislocation density is unknown, thus justifying for the choice of a range of different possible values in the model. However, in a later experimental study of the temperature dependence of the yield stress of W single crystal having a similar orientation ($\zeta = 45.6^\circ$ and $\chi = 0$), the authors report an estimated dislocation density $\rho_D = 5.5 \times 10^9 \text{ m}^{-2}$ [29]. For similar samples of Mo, no estimation of ρ_D is reported in the literature. This value for W is used as a reference to highlight the effect of the dislocation density on the temperature evolution of the tensile yield stress. All other parameters of the model are kept fixed, according to experimental conditions for $\dot{\epsilon}$, and *ab initio* calculations for all other parameters of Eq. 28. As expected, and also reported for Cr in Chapter 2, both experimental and predicted flow stresses decrease with temperature. They show a steep decrease near 0 K, before reaching a more linear variation with temperature, with a similarly convex evolution in both metals and regardless of entropic effects. Competition between the two primary slip systems is stiff at 0 K, but the yield stress

difference between the two becomes lower with increasing temperature, before ultimately vanishing before the athermal temperature. The agreement found with experiments is rather satisfactory, keeping in mind that predicted and experimental stresses do not share the same scale, with a scaling factor of 2.0 and 1.6 for W and Mo respectively. The same scale is however used in temperature, showing the dependence of the athermal temperature T_{ath} on the dislocation density ρ_D . A good agreement in terms of T_{ath} with the experimental values of 800 and 450 K in W and Mo is obtained setting ρ_D to 10^{10} and 10^{12} m^{-2} respectively when entropic contributions are neglected (*i.e.* $T_m \rightarrow \infty$, lower row of Fig. E.1), and 10^4 and 10^9 respectively using the Meyer-Neldel compensation rule with $T_m = T_{\text{melt}}$ (upper row of Fig. E.1). This is particularly satisfactory since predictions of the model do not use any fitting parameter. Further study on the sensibility of the flow stress to entropic contributions in the frame of the Meyer-Neldel compensation rule is presented in the next section for both W and Mo.

Appendix E.2. Influence of the approximation for the entropic contribution

As discussed in the previous section, the entropic contribution to the kink-pair nucleation free energy ΔG_{kp} has an impact on the predicted temperature dependence of the yield stress $\sigma_Y = f(T)$. The Meyer-Neldel compensation rule, *i.e.* assuming this entropic contribution is proportional to the kink-pair nucleation enthalpy ΔH_{kp} , is a first step towards a better inclusion of these effects in the kink-pair nucleation process at finite temperatures. We study in this section the influence of the Meyer-Neldel parameter on the predicted flow stress in the frame of the Schmid law, since a similar effect holds *a priori* when non-Schmid effects are included. The two cases where T_m is taken equal to the melting point of the material T_{melt} and infinity, *i.e.* where entropic contributions are neglected, are already discussed in section 3.2. The temperature evolution of the yield stress for W and Mo single crystals under uniaxial tension along a $[\bar{1}49]$ axis are presented in Fig. E.2 using different values of the Meyer-Neldel temperature, and compared to experiments.

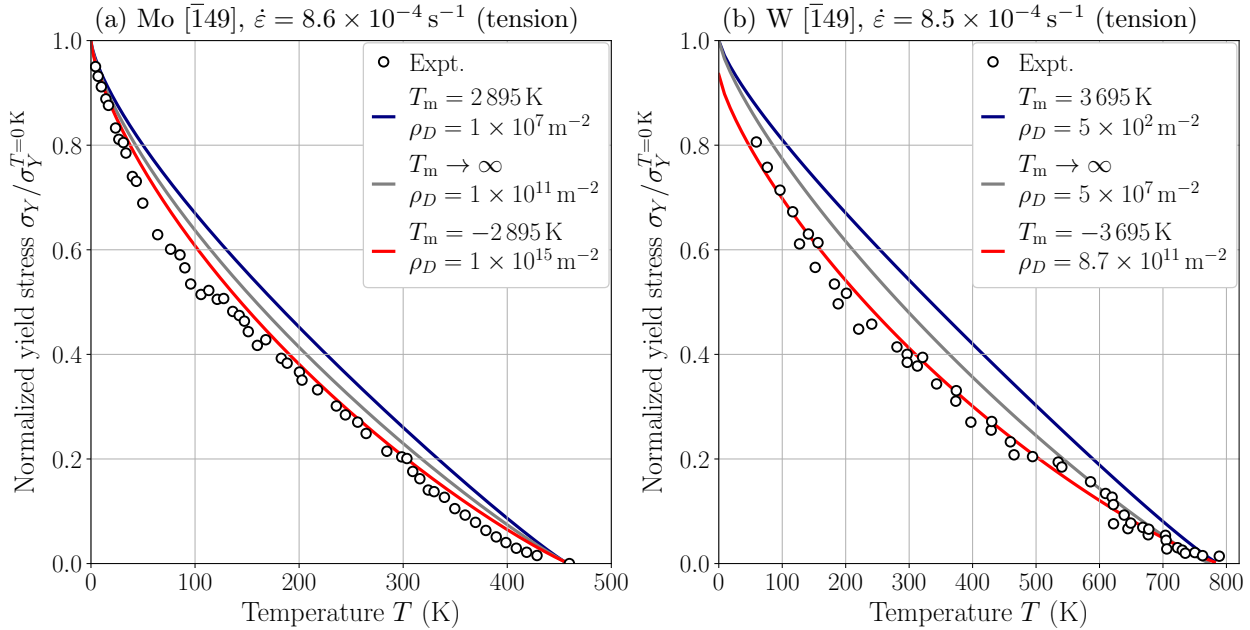


Figure E.2: Normalized yield stress as a function of temperature for (a) Mo and (b) W single crystals with center orientation $[\bar{1}49]$ considering $T_m = T_{\text{melt}}$ in blue, $T_m \rightarrow \infty$ in grey, and $T_m = -T_{\text{melt}}$ in red. Experimental data are taken from Hollang and Seeger [283] for Mo, and Brunner and Glebovsky [289] for W.

In order to reproduce the experimental athermal temperature T_{ath} , a lower dislocation density ρ_D is required when entropic contributions are accounted for using $T_m = T_{\text{melt}}$ (dark blue) than for $T_m \rightarrow \infty$ (grey) in both W and Mo, whose value in the first case is unrealistic for W ($\rho_D = 1 \times 10^2 \text{ m}^{-2}$, with an experimental estimated density $\rho_D \simeq 5 \times 10^9 \text{ m}^{-2}$). Neglecting entropic contributions also gives a more pronounced cusp in

the temperature evolution of the yield stress, which is even more accentuated using a negative Meyer-Neldel temperature $T_m = -T_{\text{melt}}$ (red curves in Fig. E.2). This cusp in the intermediate temperature range is also responsible for a steeper increase of the yield stress near 0 K, which is in better agreement with experiments for both W and Mo. Using this negative temperature in the entropic contribution, a higher dislocation density is required to reproduce the experimental T_{ath} , still remaining in a realistic range.

Appendix F. Formation of $\langle 100 \rangle$ junctions of different characters from interaction between mixed $1/2\langle 111 \rangle$ dislocations

We further investigate here formation of $\langle 100 \rangle$ junctions from two intersecting $1/2\langle 111 \rangle$ dislocations. In Chapter 5, we only focused on the formation of such junctions from two intersecting screw dislocations. This case is representative of the situation at low temperature, where $1/2\langle 111 \rangle$ align along their screw orientation due to the strong lattice friction they experience. However, at higher temperature, most particularly above the athermal temperature T_{ath} of the Peierls mechanism where lattice friction vanishes, $1/2\langle 111 \rangle$ dislocations do not align preferentially along their screw orientation but can take any character. Since all line orientations move at the same velocity, this allows for dislocations of mixed character to form $\langle 100 \rangle$ junctions.

Based on the same formulation of the elastic energy as the line model presented in section 3.3 of Chapter 5, we study here the length of the junction reaction l_{JR} as a function of the initial character θ of the two intersecting $1/2\langle 111 \rangle$ dislocations to stress that the preferred alignment of these dislocations along their screw orientation at low temperature is a limiting factor in the formation of such $\langle 100 \rangle$ junctions. Three orientations of the $\langle 100 \rangle$ junction are considered, which are the only possible characters formed upon interaction of the two $1/2\langle 111 \rangle$ dislocations, depending on their $\{110\}$ glide planes, following the three reactions:

$$1/2[1\bar{1}1] \in (110) + 1/2[\bar{1}11] \in (110) \rightarrow [001] \parallel [001] \quad (\text{F.1})$$

$$1/2[1\bar{1}1] \in (\bar{1}01) + 1/2[\bar{1}11] \in (110) \rightarrow [001] \parallel [1\bar{1}1] \quad (\text{F.2})$$

$$1/2[1\bar{1}1] \in (\bar{1}01) + 1/2[\bar{1}11] \in (101) \rightarrow [001] \parallel [010] \quad (\text{F.3})$$

These three possible character are the screw ($\theta_{\text{screw}} = 0$) following F.1, a mixed orientation with $\theta_{\text{mixed}} = 54.7^\circ$ corresponding to a line along a $\langle 111 \rangle$ direction following F.2 (which corresponds to the M100 dislocation studied in Chapter 6, sections 3.2 and 3.3, and having the highest Peierls energy barrier among all possible line orientations for the $\langle 100 \rangle$ dislocation), and edge ($\theta_{\text{edge}} = 90^\circ$) following F.3. As presented in Fig. 2 of Chapter 6, among the nine combinations between the two $1/2\langle 111 \rangle$ dislocation leading to the possible formation of a junction, only one has a screw character, two are of edge character but however completely sessile, and the seven others have a mixed M100 orientation, partially glissile. The logarithmic prefactor e to the elastic energies for these three orientations are listed in Tab. F.1 for all bcc transition metals using the experimental elastic constants at 4.2 K of Tab. 1 in the Literature review.

Table F.1: Elastic anisotropy $A = 2C_{44}/(C_{11} - C_{12})$, logarithmic prefactors $e_{\text{screw}}^{(100)}$, $e_{\text{mixed}}^{(100)}$ and $e_{\text{edge}}^{(100)}$ of the elastic energy of screw, mixed and edge $\langle 100 \rangle$ screw dislocations, and critical character θ^{JR} of the two $1/2\langle 111 \rangle$ dislocations from which a $\langle 100 \rangle$ junction of non-zero length is spontaneously formed from the interaction between the two $1/2\langle 111 \rangle$ dislocations.

Metal	A	$e_{\text{screw}}^{(100)}$	$e_{\text{mixed}}^{(100)}$	$e_{\text{edge}}^{(100)}$	$\theta_{\text{screw}}^{\text{JR}}$	$\theta_{\text{mixed}}^{\text{JR}}$	$\theta_{\text{edge}}^{\text{JR}}$
Nb	0.50	0.31	0.59	0.69	0°	15.3°	24.0°
Cr	0.68	0.85	1.21	1.33	0°	11.3°	17.0°
Mo	0.77	1.09	1.56	1.75	0°	12.1°	18.0°
V	0.78	0.39	0.60	0.69	0°	13.0°	19.7°
W	1.00	1.42	1.88	2.09	2.5°	11.9°	16.9°
Ta	1.56	0.89	1.00	1.12	8.0°	11.0°	15.0°
Fe	2.38	0.95	0.84	0.92	13.0°	9.9°	12.0°

We note that, contrary to the $1/2\langle 111 \rangle$ dislocation, the screw orientation does not systematically minimize the elastic energy of $\langle 100 \rangle$ dislocations. This elastic effect is more pronounced for metals having $A > 1$, *i.e.* Ta and Fe, as also presented in Fig. 1 of Chapter 6. Thus, depending on the character of the $\langle 100 \rangle$ junction

formed by the interaction between two $\frac{1}{2}\langle 111 \rangle$ dislocations, different behaviors are expected depending on the elastic anisotropy. The length of a junction of three different characters resulting from the intersection between two $\frac{1}{2}\langle 111 \rangle$ dislocations of character θ are presented in Fig. F.1 for all bcc transition metals. In the presented model, we assume the system to have the same geometry as for the formation of the screw $\langle 100 \rangle$ junction, sketched in Chapter 5 Fig. 9c, regardless of the character of the junction formed, *i.e.* screw, mixed or edge. Instead, only the elastic energy $E^{(100)}$ appearing in Eq. 6 is changed to match the character of the junction of interest.

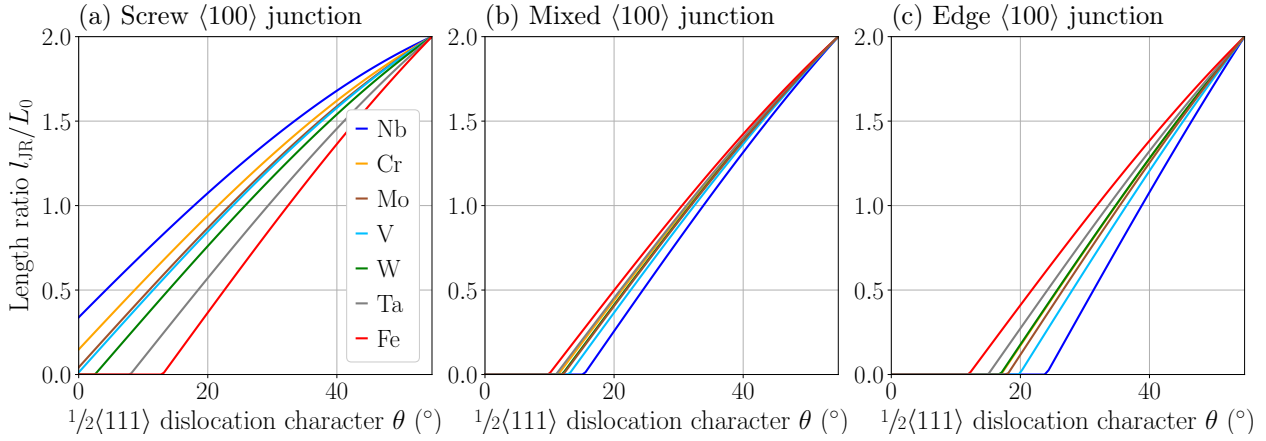


Figure F.1: Length l_{JR} predicted by the line energy model for a (a) screw, (b) mixed ($\theta = 54.7^\circ$), and (c) edge $\langle 100 \rangle$ junction formed by intersection of two $\frac{1}{2}\langle 111 \rangle$ dislocations of initial character θ , normalized by their initial length L_0 .

As detailed in section 3.3 of Chapter 5, formation of the $\langle 100 \rangle$ screw junction is favored by a decreasing elastic anisotropy ratio A . Its spontaneous formation from two intersecting $\frac{1}{2}\langle 111 \rangle$ dislocations of screw character is predicted for $A < 0.8$, corresponding to Nb, Cr, Mo and V. From Fig. F.1a, we also note that longer $\langle 100 \rangle$ screw junctions are also predicted to form in these four metals when the two $\frac{1}{2}\langle 111 \rangle$ dislocations are not aligned along their screw orientation, but for any mixed character θ . This effect of the anisotropy ratio A reflects in the critical character θ^{JR} above which a $\langle 100 \rangle$ junction of non-zero length is

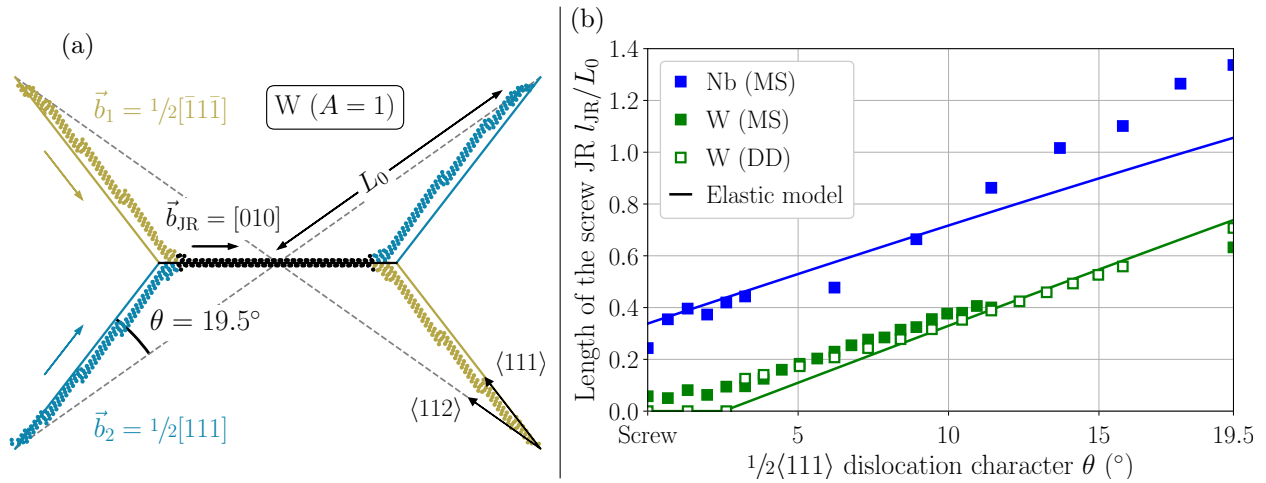


Figure F.2: (a) Screw $[010]$ junction created upon intersection of two mixed $\frac{1}{2}\langle 111 \rangle$ dislocations \vec{b}_1 and \vec{b}_2 of character $\theta = 19.5^\circ$ obtained after molecular statics relaxation (colored spheres), and with the line energy model (solid lines) in W. (b) Length l_{JR}/L_0 of the screw JR formed upon intersection of two mixed $\frac{1}{2}\langle 111 \rangle$ dislocations in Nb and W obtained with molecular statics relaxations (filled squares), the line energy model (solid lines), and isotropic DD simulations (open squares, for W only).

spontaneously produced after intersection between the two $\frac{1}{2}\langle 111 \rangle$ dislocations. For metals with $A < 0.8$, this critical character θ^{JR} is zero for the screw junction, whereas an increasing θ^{JR} is required as A increases, for instance in W, Ta and Fe by order of increasing A . The existence of this critical character shows that, at higher temperature, when $\frac{1}{2}\langle 111 \rangle$ dislocations are not preferentially aligned along their screw orientation, $\langle 100 \rangle$ screw junctions can form in any bcc metal. The produced junctions are nevertheless shorter in metals having a high anisotropy ratio A . This prediction is in agreement with experimental observations of long $\langle 100 \rangle$ junctions in all bcc transition metals above the athermal temperature of the Peierls mechanism.

Focusing only on the screw $\langle 100 \rangle$ junction, we now compare the above predictions of the line energy model with molecular statics relaxations at 0 K in Nb and W, presented in Fig. F.2. A satisfactory agreement is found between the two models for both Nb and W, most particularly regarding the existence and the value of the critical character $\theta_{\text{screw}}^{\text{JR}}$ of the two $\frac{1}{2}\langle 111 \rangle$ dislocations above which a $\langle 100 \rangle$ screw junction forms spontaneously in W, evaluated at 2.5° and 2.8° according to the line energy model and atomistic simulations respectively. The later is confirmed by isotropic DD simulations in W, again in very good agreement with both models and an identical predicted critical character $\theta_{\text{screw}}^{\text{JR}} = 2.8^\circ$. Predictions of the line energy model for Nb are also in good agreement with results of atomistic simulations, with spontaneous formation of a $\langle 100 \rangle$ screw junction for all characters θ of the two intersecting dislocations. As also predicted by the model, and confirmed here by molecular statics relaxations, the length of the junction produced increases with an increasing character θ of the two $\frac{1}{2}\langle 111 \rangle$ dislocations, for which a good agreement is found in both Nb and W. As an example, we show in Fig. F.2a the relaxed configuration resulting from the intersection between two $\frac{1}{2}\langle 111 \rangle$ dislocations of mixed character $\theta = 19.5^\circ$ in W, corresponding to a line oriented along a $\langle 112 \rangle$ direction, with the results of the line energy model indicated by solid colored lines.

Now considering the results of the line energy model for the mixed M100 and edge $\langle 100 \rangle$ junctions in Fig. F.1b and c respectively, we note that the intersection between two $\frac{1}{2}\langle 111 \rangle$ screw dislocations does not lead to spontaneous formation of the junction in any bcc metal. A mixed critical character θ^{JR} is instead required for the formation of these two junctions to be energetically favorable. Contrary to the screw $\langle 100 \rangle$ junction, whose formation is favored by a decreasing elastic anisotropy A , the mixed junction forms preferentially in metals with higher anisotropy ratio $A > 1$. This is also the case for the edge $\langle 100 \rangle$ junction, whose formation is even more favorable than the screw junction in Fe, which has the highest ratio A . This is a direct consequence of the lower elastic energy found for the edge than the screw $\langle 100 \rangle$ dislocation in Fe, as listed in Tab. F.1 for all bcc transition metals. For the two mixed and edge orientations of the junction, a higher critical character of the two intersecting $\frac{1}{2}\langle 111 \rangle$ dislocations is nevertheless required for the formation of the junction to be energetically favorable in all metals except for Fe, where this character is minimum for the edge $\langle 100 \rangle$ junction. For all three of its possible orientations, we note that the length l_{JR} of the junction always increases with the character θ of the two intersecting $\frac{1}{2}\langle 111 \rangle$ dislocations.

Titre: Modélisation atomique de la plasticité du chrome et des autres métaux de transition cubiques centrés

Mots clés: Modélisation, Chrome, Dislocations, Plasticité, Magnétisme, *Ab initio*

Résumé: L'objet de cette thèse est d'étudier la plasticité du chrome, envisagé comme revêtement des gaines combustibles en zirconium, et qui dans ces conditions doit être capable de supporter la déformation qui lui est imposée sans se fracturer. Le chrome est l'un des sept métaux de transition purs à structure cubique centrée, étant cependant l'unique d'entre eux ayant une structure magnétique proche de l'antiferromagnétisme à température inférieure à l'ambiante. A l'échelle atomique, la déformation plastique de ces métaux à basse température s'opère principalement par le mouvement des dislocations vis de vecteur de Burgers $\frac{1}{2}\langle 111 \rangle$, subissant une friction importante avec le réseau cristallin. Or, la plasticité du chrome soulève encore de nombreuses questions (types de dislocations, effet du magnétisme), et a été l'objet de peu d'étude visant à caractériser son comportement mécanique. En comparant le chrome aux autres métaux cubiques centrés, cette étude a permis de conclure sur les similitudes et différences que celui-ci présente.

A l'aide de calculs *ab initio*, les propriétés des dislocations vis $\frac{1}{2}\langle 111 \rangle$ ont été étudiées dans les deux phases non-magnétique et antiferromagnétique du chrome, de manière à caractériser l'influence du magnétisme sur sa plasticité à basse température. Cette étude a révélé que la seule conséquence du magnétisme est la génération de fautes magnétiques lorsque les dislocations cisailent le cristal, puisque leur vecteur de Burgers ne respecte pas l'ordre magnétique du chrome à basse température. Ainsi, les dislocations $\frac{1}{2}\langle 111 \rangle$ sont contraintes à se déplacer en traînant derrière elles une faute. Celle-ci a ensuite été étudiée à température finie par simulations Monte Carlo couplées à un modèle de Heisenberg développé pour cette étude, mettant en évidence

leur disparition à une température inférieure à la transition vers le désordre magnétique, proche de l'ambiante, laissant les dislocations libres de se déplacer sans traîner de faute. Le magnétisme n'a donc un impact sur la plasticité du chrome qu'à très basse température, où ces fautes existent.

Tenant compte des propriétés atomiques des dislocations, ainsi que de leur mouvement thermiquement activé par germination de doubles décrochements à l'aide d'un modèle de tension de ligne, nous avons ensuite développé une loi d'écoulement plastique donnant la limite d'élasticité en fonction du chargement mécanique et de la température, jusqu'à la température athermale. Par le biais d'une étude systématique sur l'ensemble des métaux cubiques centrés, pour lesquels une grande variété de données expérimentales est disponible, les prédictions du modèle ont pu à la fois être comparées à l'expérience ainsi qu'entre métaux, de manière à confirmer que le comportement plastique du chrome est semblable à l'ensemble de ces métaux. Cette approche systématique permettant à la fois de mieux comprendre la plasticité du chrome et des autres métaux cubiques centrés s'est ensuite étendue à l'étude d'un nouveau mécanisme expliquant le glissement anormal à basse température observé expérimentalement, s'opérant par un mouvement coopératif de plusieurs dislocations entraînant leur déplacement rapide, reproduit par nos simulations atomiques. Nous nous sommes enfin intéressés aux propriétés de dislocations ayant un vecteur de Burgers $\langle 100 \rangle$, d'énergie proche des dislocations $\frac{1}{2}\langle 111 \rangle$ et observées dans l'ensemble de ces métaux, afin d'expliquer dans quelles conditions celles-ci pourraient participer à la déformation plastique, nos simulations montrant un blocage des mécanismes de multiplication de ces dislocations.

Title: Atomic scale modeling of plasticity in chromium and other body-centered cubic transition metals

Keywords: Modeling, Chromium, Dislocations, Plasticity, Magnetism, *Ab initio*

Abstract: The object of this thesis is to study plasticity of chromium, considered as a coating layer of zirconium fuel claddings, and in these conditions needs to be able to accommodate the deformation which is imposed to it without cracking. Chromium is one of the seven pure body-centered cubic transition metals, however the only one with a magnetic structure close to antiferromagnetism at temperatures below ambient. At the atomic scale, plastic deformation of these metals at low temperature is mainly governed by the motion of screw dislocations with a $\frac{1}{2}\langle 111 \rangle$ Burgers vector, which experience a strong friction with the crystal lattice. However, plasticity of chromium still raises numerous questions (types of dislocations, influence of magnetism), and has been the focus of a few studies aiming at characterizing its mechanical behavior. Comparing chromium to the other body-centered cubic metals, this work helped conclude on the similarities and differences it presents.

Using *ab initio* calculations, properties of $\frac{1}{2}\langle 111 \rangle$ screw dislocations were studied in the two non-magnetic and antiferromagnetic phases of chromium, in order to qualify the impact of magnetism on its plasticity at low temperature. This study revealed the only consequence of magnetism is the generation of magnetic faults when these dislocations shear the crystal, since their Burgers vector disrupts the magnetic order of chromium at low temperature. Thus, $\frac{1}{2}\langle 111 \rangle$ dislocations are constrained to move while dragging a magnetic fault behind them. This fault was then studied at finite temperature using Monte Carlo simulations coupled with a Heisenberg model developed for this work, evidencing their disappearance at a temperature be-

low the transition to magnetic disorder, close to ambient, letting dislocations free to move without dragging magnetic faults. Magnetism therefore has an impact on the plasticity of chromium at very low temperature only, where these faults exist.

Accounting for the atomic properties of dislocations, as well as their thermally activated glide through nucleation of kink pairs using a line tension model, we then developed a plastic flow law predicting the yield stress as a function of the mechanical loading and the temperature, until the athermal temperature. Through a systematic study across all body-centered cubic metals, for which numerous experimental data are available, predictions of the model were both compared to experiments and between metals, in order to confirm the plastic behavior of chromium is comparable to the other metals. This systematic approach allowing at the same time for a better understanding of the plasticity of chromium and the other body-centered cubic metals was then extended to the study of a new mechanism explaining anomalous slip at low temperature observed experimentally, operating through a cooperative motion of multiple dislocations leading to their fast motion, reproduced by our atomistic simulations. We then looked at the properties of dislocations having a $\langle 100 \rangle$ Burgers vector, with close energy compared to $\frac{1}{2}\langle 111 \rangle$ and observed in all these metals, to explain under which conditions they can participate to the plastic deformation, our atomistic simulations showing a locking of the multiplication mechanisms of these dislocations.